PADERBORN UNIVERSITY

Contributions to differential phase contrast imaging

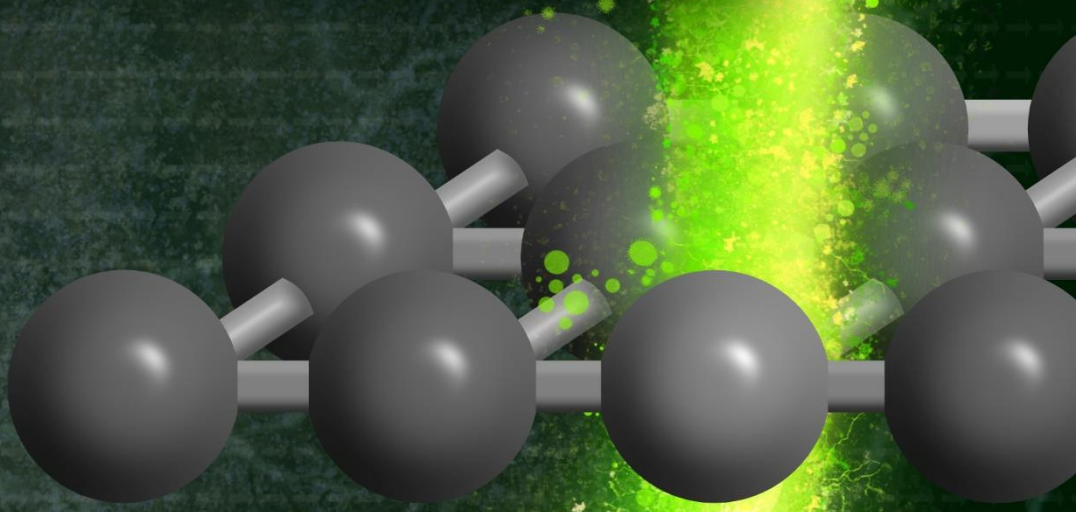

Dissertation

zur Erlangung des Doktorgrades
der Naturwissenschaften

von der
Fakultät für Naturwissenschaften
der Universität Paderborn

Vorgelegt von Julius Bürger

1. Gutachter: Prof. Dr. Jörg K. N. Lindner
2. Gutachter: Prof. Dr. Knut Müller-Caspary
3. Gutachter: Prof. Dr. Donat J. As

Vorgelegt am 22.12.2023.

Kurzzusammenfassung:

Die differentielle Phasenkontrastmikroskopie (DPC) ist eine Technik in der Rastertransmissionselektronenmikroskopie (STEM), die die Abbildung und Quantifizierung von elektrischen Feldern in Festkörpern ermöglicht. In Verbindung mit der modernen Korrektur von Linsenfehlern können elektrische Felder mit subatomarer Auflösung untersucht werden. Dies macht STEM-DPC zu einer vielversprechenden Methode, um die Verteilung des elektrischen Feldes und der Ladungsdichte einzelner Atome genau zu bestimmen. Die Anforderungen an eine quantitative DPC-Mikroskopie sind jedoch hoch, da die messbare Feldverteilung durch zahlreiche Faktoren beeinflusst ist. In dieser Arbeit werden verschiedene Einflüsse auf die DPC-Abbildung, wie z.B. Linsenfehler, dynamische Beugungseffekte, Bildrauschen, Probenverkippung sowie der verwendete Detektor, experimentell und mit Hilfe von Multislice-Simulationen untersucht. Mit Fokus auf die DPC-Abbildung mit einem segmentierten Detektor wird gezeigt, wie sich einzelne Einflüsse auf die DPC-Messung auswirken und wie sie leicht erkannt werden können. Es werden neue Methoden zur Minimierung der Einflüsse vorgestellt, z.B. ein Verfahren zur Ermittlung des optimalen Fokus sowie ein Verfahren zur Reduzierung des Einflusses der Verwendung von segmentierten Detektoren. Abschließend werden Anwendungsbeispiele der DPC-Mikroskopie an elektrischen Feldern in Silizium, Indiumarsenid sowie defektfreiem und defektbehaftetem zweidimensionalen Wolframdiselenid gezeigt.

Abstract:

Differential phase contrast (DPC) imaging is a scanning transmission electron microscopy (STEM) technique, which allows the visualisation and quantification of electric field distributions of solids. Paired with state-of-the-art lens aberration correction, electric fields can be investigated with exceptional spatial resolution, which is far below the typical distance of atoms in solids. This renders STEM-DPC a promising method to accurately reveal the electric field and charge density distributions around individual atoms. However, the requirements for quantitative DPC are high, as the measured field distributions are influenced by numerous factors. In this thesis, various influences on the DPC image including residual lens aberrations, dynamic diffraction effects, image noises, specimen tilt as well as the detector are investigated both experimentally and with the help of multislice image simulations. With focus on DPC imaging with a segmented detector, it is demonstrated how individual influences affect the DPC measurement and how they can be readily detected. New methods for minimisation of influences are presented, e.g. a method to find the optimum focus as well as a novel procedure to reduce the influence of the segmented detector. Finally, application examples of DPC imaging of atomic electric fields in silicon, indium arsenide as well as multilayers of pristine and defective two-dimensional tungsten diselenide are shown.

Table of contents

List of abbreviations

AFM	Atomic force microscope
(A)BF	(Annular) bright-field
CBED	Convergent beam electron diffraction
CCD	Charge-coupled device
CFEG	Cold-field emission gun
CMOS	Complementary metal-oxide semiconductor
CoM	Centre of mass
CVD	Chemical vapor deposition
dDPC	Differentiated differential phase contrast
DPC	Differential phase contrast
DPCTF	Differential phase contrast transfer function
EDS	Energy-dispersive X-ray spectroscopy
EELS	Electron energy loss spectroscopy
EFTEM	Energy-filtered TEM
FIB	Focused ion beam
FL	Frozen lattice
(HA)ADF	(High-angle) annular dark-field
IAMSR	Increased azimuthal momentum space resolution
iDPC	Integrated differential phase contrast
LSO	Lutetium oxyorthosilicate
MBE	Molecular beam epitaxy
PACBED	Position-averaged convergent beam electron diffraction
PDMS	Polydimethylsiloxane
PL	Photoluminescence
PMMA	Polymethylmethacrylate
PSD	Position sensitive diode
QD	Quantum dot
SAAF	Segmented annular all-field
SAED	Selected-area electron diffraction pattern
(S)TEM	(Scanning) transmission electron microscopy or (scanning) transmission electron microscope
TDS	Thermal diffuse scattering
TMD	Transition metal dichalcogenides
VLM	Visual light microscope
(W)POA	(Weak) phase object approximation
WZ	Wurtzite
YAG	Yttrium aluminium garnet
ZB	Zinc blende

1. Introduction

Differential phase contrast (DPC) imaging is one of the most promising methods in scanning transmission electron microscopy (STEM) as it is among the only few techniques which allow for the visualisation and quantification of electric and magnetic field distributions in solid specimens [1]. Even though DPC imaging was already proposed in the early 1970s by Rose, Dekkers and de Lang [2–4], it has recently become one of the most popular and exciting methods in the research field of electron microscopy. This is due to state-of-the-art lens aberration correction, the consequential increase in spatial resolution of modern transmission electron microscopes [5–7], and the resulting capability to investigate electric fields at sub-atomic resolution [8, 9]. Until now, DPC has been applied to investigate long-range field distributions, such as magnetic domain walls [10, 11], skyrmions [12] and magnetic stray fields [13] as well as electric fields at hetero interfaces [14–16], p-n-junctions [17–21], and nano-emitters [22]. Due to the high-resolution possible with aberration-corrected microscopes, DPC was recently applied to quantify sub-atomically resolved electrostatic fields and charge density distributions in 3D [8, 9, 15, 23–30] and 2D [31–35] materials.

In DPC imaging, the interaction of an incident electron beam with the electromagnetic fields inside the specimen is utilised. This interaction is based on the Lorentz force and results in a redistribution of beam intensity due to a transfer of momentum perpendicular to the propagation direction of the incident electron beam. For homogeneous electric fields, the interaction can be compared to the one for electrons in a plate capacitor, leading to a rigid displacement of the electron beam intensity in the detection plane. Electric field distributions which are inhomogeneous across the beam diameter do not lead to a rigid displacement of the beam. Instead, the intensity is redistributed within the beam [9, 27, 36]. This is typical for DPC imaging at atomic resolution due to the strongly decaying potentials of individual atoms. It was described by Müller et al. [9] that accurate quantitative electric field investigations at atomic resolution are only possible if the specimen is sufficiently thin. Atomic electric field measurements are achieved by measuring the quantum mechanical expectation value of the transferred momentum which is detectable as the centre of mass (CoM) of the intensity distribution on the detector. Therefore, a position sensitive detector such as a segmented [37–39] or pixelated detector [9, 40] is necessary which enables the detection of the CoM of the post-specimen intensity distribution for each pixel of the scan.

Quantifying atomic electric fields accurately remains challenging because the DPC signal is affected by various influences. These influences include lens aberrations impacting the incident electron beam, dynamic diffraction effects which are unavoidable especially for thick specimens, the specimen tilt, and the type and shape of the detector used. For example, when using a segmented detector, the measured CoM is only an approximation of the true CoM, as a segmented detector only consists of a few segments which do not enable to evaluate the detailed intensity distribution

across each segment [41]. It is necessary to understand how and to what extent these influences impact the DPC images, as these might hamper correct image interpretation.

In this thesis, the influences on the DPC signal of electric fields at atomic resolution are investigated by utilising measured and simulated DPC images. Among the investigated influences are the detector extension and rotation of segmented detectors, the energy of incident electrons, lens aberrations, dynamic diffraction effects, which occur with increasing specimen thickness, specimen tilt, and image noise. In addition, methods to minimise these influences are given, e.g. a method to find the optimum defocus during DPC experiments. The methods are based on the so-called scattergram, which is a two-dimensional histogram of the transferred momentum distribution. Moreover, a novel method, the so-called scattergram filtering, is introduced which allows to reveal the spatial distribution of characteristic scattergram features in DPC images.
To investigate the influence of the detector type, DPC images of Si in [110] zone-axis orientation acquired with a segmented and a pixelated detector are compared. So far this has only been achieved using image simulations or a single 4D-STEM image [36, 42, 43]. For the latter the true CoM or the one obtained from virtual segments projected onto the pixelated detector in post-processing are utilised. Based on this, crucial parameters for the similarity of DPC images with segmented detectors and pixelated detectors are identified and discussed. This is followed by investigations on the optimum detector rotation and extension to generate a DPC image with a segmented detector which is as close as possible to the one measurable with a pixelated detector. In addition, a method to minimise the impact of the low momentum space resolution of segmented detectors on the DPC images is described and experimentally validated. This method utilises a series of DPC images acquired at different detector rotations.
The scope of this work includes exemplary analyses of sub-atomically resolved electric field and charge density distributions of selected materials, e.g. Si in [110] zone-axis orientation. In addition, the atomic electric field and charge density distributions of an InAs nano-island are investigated. As the InAs island contains several twin boundaries which might change the local electric field distribution, DPC imaging is also conducted to analyse the electric field distribution in the vicinity of one of the twin boundaries. As accurate quantitative DPC imaging is only possible for specimen thicknesses in the single digit nanometre regime [9], two-dimensional materials including graphene and 2D transition metal dichalcogenides are particularly suitable for the application and optimisation of quantitative DPC imaging [31–34]. Due to the reduced dimensionality of 2D materials, vacancy-type defects can be assumed to have a drastic influence on the electric field distribution, ultimately affecting the optoelectronic properties. In this thesis, bi- and trilayers of 2D WSe_2 are investigated. This includes the measurement of the electric field and charge density distributions of a pristine as well as a defective lattice.

This thesis is structured as follows. In Chapter 2, the fundamentals of STEM and DPC imaging are given. The latter includes descriptions of the DPC contrast mechanisms

with focus on the measurement of electric fields at atomic resolution, suitable detectors, the signal acquisition, as well as the calculation of charge densities. Chapter 2 additionally presents a description of the fundamentals of multislice STEM image simulations implemented in Dr. Probe [44], which is the simulation software used in this thesis. In Chapter 3, the microscopes used in this thesis and their components are described. As DPC images are acquired with a segmented as well as a pixelated detector, the characterisation of the detectors and calibrations for quantitative electric field measurements is described. In Chapter 4, the post-processing steps to obtain calibrated electric field maps and charge density distributions are discussed. This chapter covers descriptions of algorithms to reduce image noise, to precisely determine the position of atomic columns, and to increase the momentum space resolution of segmented detectors. The above-mentioned influences on the DPC signal are investigated in Chapter 5 using multislice image simulations and experimental DPC images. In Chapter 6, DPC measurements of Si are presented which include the comparisons of segmented and pixelated DPC images, the optimisation of the segmented detector response function and momentum space resolution of segmented detector. Chapter 6 additionally covers the investigation of atomic electric fields in InAs as well as at a twin-boundary in InAs. Finally, the electric field and charge density distributions in bi- and trilayer WSe_2 and the characterisation of different vacancy-type defects are presented. The main conclusions are summarized in Chapter 7. This thesis is completed by supplementary simulations on the influence of lens aberrations, dynamic effects, and the description of methods for the correction of machine-related image artefacts which are presented in the Appendix.

2. Fundamentals

Differential phase contrast (DPC) imaging is a method in the scanning mode of a transmission electron microscope. To explain the fundamentals of DPC imaging, first an introduction into (scanning) transmission electron microscopy ((S)TEM) is given in Chapter 2.1. The description of (S)TEM covers a fundamental description of the required electron optical system, a mathematical description of the electron wave incident on the specimen, a general overview on the interactions between the incident electrons and the specimen as well as the explanation of the concept of (weak) phase object approximation. Additionally, the contrast mechanisms in the conventional (high-angle) annular dark-field ((HA)ADF) imaging mode and two commonly applied analytical methods, namely electron energy-loss spectroscopy (EELS) and energy-filtered transmission electron microscopy (EFTEM), are explained. Chapter 2.2 then discusses the theory of differential phase contrast imaging, including a classical picture of the origin of the DPC signal, the influence of inhomogeneous potentials on the DPC signal as well as a quantum mechanical treatment of DPC imaging. Furthermore, different detectors for DPC imaging and their impact on DPC images are discussed. In Chapter 2.3 the basics of multislice image simulations using Dr. Probe are elucidated. Multislice image simulations are performed for HAADF and DPC images in this thesis.

2.1. (Scanning) transmission electron microscopy

One of the most versatile instruments for detailed characterisation of materials is the (scanning) transmission electron microscope ((S)TEM) [45–48]. (S)TEMs are e.g. widely applied for the in-depth analysis of structural, physical and chemical properties of semiconductors, metals, ceramics and beyond. Among the specimen properties are the crystal structure, strain on a nanometre scale, type and density of crystallographic defects, plasmonic properties as well as chemical composition and electric or magnetic fields [1, 46, 48, 49]. Since comprehensive descriptions of (S)TEM imaging fill complete textbooks, only the basics necessary for the understanding of this thesis will be given in the following. For detailed description, the reader is referred to refs. [45, 47, 50–52].

In general, the resolution of any microscope with a probe that has wave characteristics is mainly limited by diffraction. The resolution limit δ, which is defined as the minimum distance of two point-shaped objects, which can be observed as separated objects, can be approximated by the Rayleigh criterion. δ is determined by the wavelength λ, refractive index μ of the viewing medium as well as the collection semi-angle of the magnifying lens β [50]:

$$\delta = \frac{0.61 \cdot \lambda}{\mu \cdot \sin(\beta)}. \tag{1}$$

A (S)TEM uses electrons, which according to de Broglie have a wavelength $\lambda = h/p$. Here h is the Planck's constant and p the particle momentum. In a (S)TEM, the electrons are accelerated with an acceleration voltage U typically ranging from 30 kV to 300 kV. Such high acceleration voltages lead to electron velocities corresponding to a substantial fraction of the speed of light c and to a relativistic wavelength given by [50]

$$\lambda = \frac{h}{\sqrt{2m_0 eU\left(1 + \frac{eU}{2m_0 c^2}\right)}}, \tag{2}$$

with e the charge and m_0 the rest mass of the electron. Electrons that are accelerated with a voltage of 200 kV have a relativistic wavelength of $\lambda_{200\mathrm{kV}} = 2.51 \cdot 10^{-12}$ m. Therefore, the spatial resolution possible with a TEM in principle is in the single digit picometer range. However, actual resolving powers are significantly smaller due to the presence of lens aberrations including the spherical aberration and other machine-related instabilities. By correcting these residual lens aberrations with state-of-the-art lens aberration correctors, resolutions below 50 pm are possible today [53–55].

2.1.1. TEM and STEM imaging

The working principle of a (S)TEM can be coarsely divided into two major operational modes, namely TEM and STEM, which are determined by the way of illuminating the specimen.

In the TEM mode a broad parallel electron beam is incident on a rather large area of the specimen. After the incident wave has interacted with the specimen potentials, the so-called exit wave is projected onto a camera. Due to the broad and parallel illumination, the image and all pixels of the image are obtained in a parallel way. No further details on the conventional TEM mode are given at this point because the differential phase contrast is a method using the scanning mode of the (S)TEM.

In STEM, the electron beam is focused to a spot as small as possible and scanned across the specimen. A schematic of the layout of the illumination system including the electron beam's path in STEM is depicted in Fig. 1. The layout matches the ones of microscopes used in this thesis. However, also different layouts are possible, e.g. without a corrector for lens aberrations. The electrons of the electron beam are emitted by an electron gun. The instruments used here have a cold-field emission gun (CFEG) providing a narrow energy distribution and a high spatial coherence.

The electrons accelerated to energies of 30 keV to 300 keV pass three condenser lenses and a condenser aperture which are used to obtain a focused convergent beam. In addition, a pair of scan coils move the beam across the specimen by a double deflection. A double deflection (indicated by two red lines) is mandatory to obtain equally shaped electron waves and maintain the electron wave's phase front at each beam position. Optionally, a so-called C_s-corrector for the probe-side correction of lens aberrations is installed in the microscope between the second condenser lens aperture

and the scan coils. C_s denotes a particularly important optical lens aberration called spherical aberration, which has a considerable influence on the spatial resolution of the microscope (see Chapter 2.1.2).

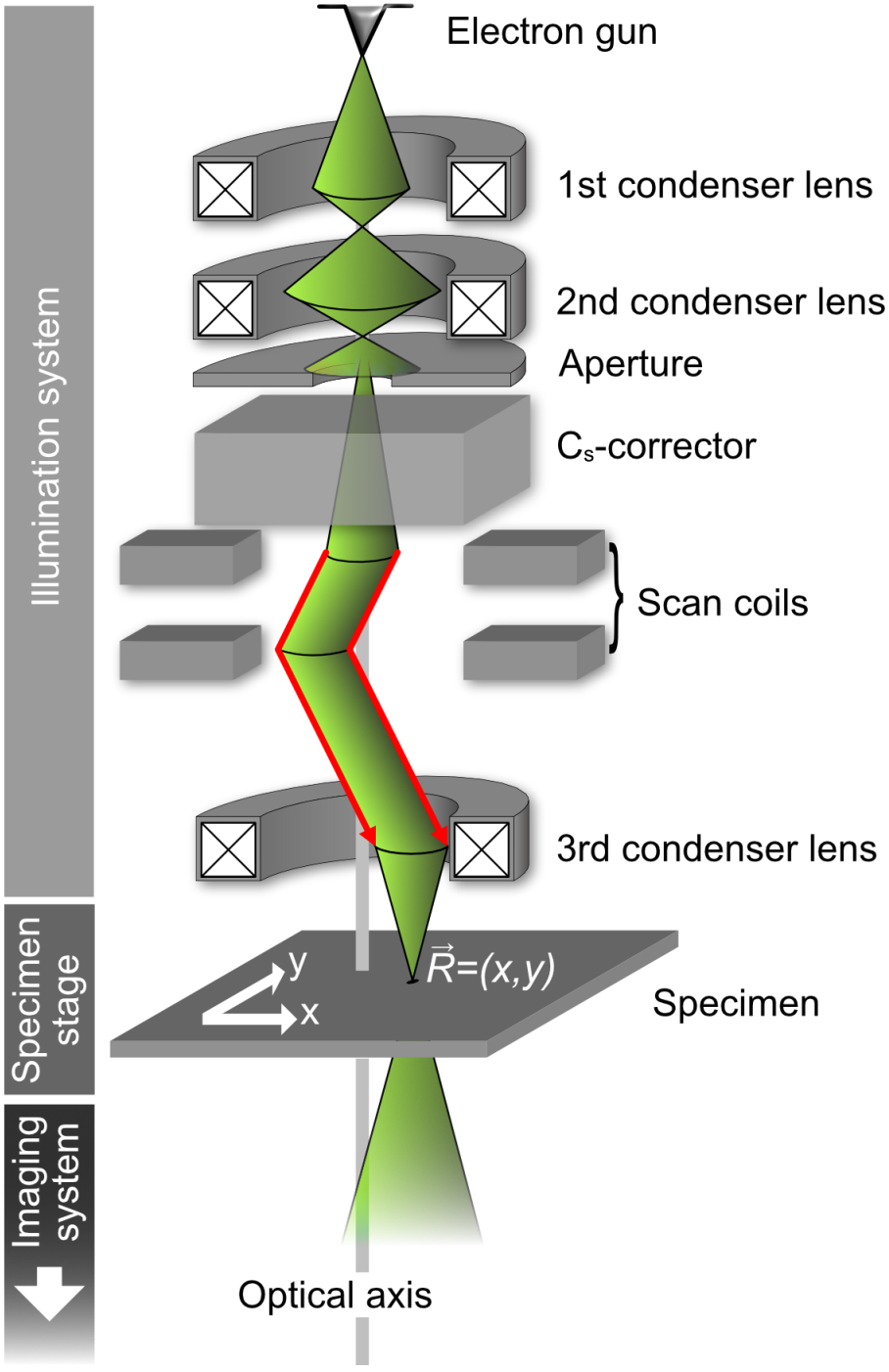

Figure 1: Schematic of the electron beam path and layout of the illumination system of a STEM.

As a result, a convergent electron beam is finely focused onto the specimen at scan position $\vec{R}$ corresponding to real space coordinates (x, y) in the specimen plane. The intensity distribution of the incident electron beam is one of the most important properties, as it determines the spatial resolution of a STEM (Chapter 2.1.2).

The convergent electron beam interacts with the specimen at each beam position of the scan as detailed in Chapter 2.1.3. At each beam position, the electron wave is

projected by the imaging system onto a certain detector, which measures the intensity in a certain angular interval of the electron beam intensity distribution. Furthermore, it is also possible to measure other signals such as X-rays or the energy distribution of the electron beam at each pixel. The latter is achieved with the help of electron energy loss spectroscopy (EELS) which is described in Chapter 2.1.6 along with energy-filtered TEM (EFTEM).

Several things need to be emphasised. First, STEM images are acquired in a serial way, i.e. pixel by pixel. Second, a second pair of deflector coils, so-called descanning coils [56], typically bring the beam back to the optical axis. However, as these are not installed on the microscopes used, they are neglected in the schematic in Fig. 1. At atomic resolution, the scanned area is typically in the range of only a few nanometres. Thus, the missing descanning coils can fairly be neglected for conventional STEM imaging. Third, the lenses of the imaging system below the specimen are not shown in Fig. 1 for simplicity. These lenses have a small influence on the spatial resolution in STEM. Fourth, the imaging system lenses do not project an image of the electron beam but a magnified convergent-beam electron diffraction (CBED) pattern onto the detector. The detector collection angles can thus be described by reciprocal space coordinates $\vec{k}_\perp = (k_x, k_y)$ with respect to the optical axis at $\vec{k}_\perp = (0,0)$. Here, $\vec{k}_\perp$ denotes the components of wavevector perpendicular to the optical axis. The reciprocal coordinates can also be given by the transferred momentum perpendicular to the optical axis $\vec{p}_\perp = \hbar\vec{k}_\perp$, with $\hbar$ the reduced Planck constant. The wavenumber of the incident electron wave parallel to the optical axis $|\vec{k}_0| = 1/\lambda$ can be calculated using the wavelength.

2.1.2. Description of electron waves in STEM

To understand the contrasts of STEM images and to do STEM image simulations, a mathematical description of the propagation of the electron wave $\psi(\vec{k}_\perp)$ from the electron gun to the detection plane including the interaction with the specimen is necessary [47, 57]. Fig. 2(a) illustrates the propagation of the electron wave and shows the involved components: the electron gun, the probe forming lens system focusing the electron beam onto the sample and the imaging system projecting the electron wave onto the detector after it has interacted with the specimen. A formalism for the electron wave propagation and its resulting intensity distribution in the detection plane has been achieved by Cowley [58–60]. Detailed descriptions can be found in the original literature as well as many textbooks, for example in references [47, 50, 57]. The following chapter briefly summarises the formalism for the electron wave $\psi(\vec{k}_\perp)$. Note that similarly to optics, the intensity $I(\vec{k}_\perp) = |\psi(\vec{k}_\perp)|^2 = \psi(\vec{k}_\perp) \cdot \psi^*(\vec{k}_\perp)$ is given by the product of the wave function with its complex conjugate $\psi^*(\vec{k}_\perp)$.

An ideal coherent electron source can be assumed to be point-like, which can be mathematically described by a Dirac delta function $\delta(\vec{r})$ at the real space coordinate $\vec{r}$ of the electron gun tip [57]. The shape of a real electron gun tips is, however, not point-like and therefore leads to a reduced spatial coherence of the electron waves [50].

However, assuming a coherent electron source is still a reasonable approximation, as the coherence width of CFEGs is larger than the width of the condenser aperture [58].
After the emission and acceleration of the electron beam, the focusing of the beam is achieved via the probe forming lens system (Fig. 2(a)) which includes several condenser lenses and an aperture. The impact of the aperture and the aberrations of the lenses can be summarised in an optical transfer function $O(\vec{k}_\perp)$ altering the phase and the amplitude of the electron wave. The electron wave $\psi_i(\vec{r})$ incident on the specimen with real space coordinates $\vec{r} = (x, y)$ in the specimen plane from a point-like electron source is thus given by

$$\psi_i(\vec{r}) = \mathcal{F}\left[\underbrace{A(\vec{k}_\perp)\exp\left(\mathrm{i}\chi(\vec{k}_\perp)\right)}_{=O(\vec{k}_\perp)} \cdot \psi_g\right]. \tag{3}$$

Here, $\mathcal{F}$ denotes the Fourier transform, $A(\vec{k}_\perp)$ the aperture function, $\chi(\vec{k}_\perp)$ the aberration phase function, which is also called the aberration phase plate, and ψ_g the electron wave emitted from the electron gun, which is $\psi_g = 1$ for a point-like electron source. The aperture function $A(\vec{k}_\perp)$ in reciprocal space coordinates k_x and k_y as well as a corresponding line profile in k_x direction are exemplarily depicted in Fig. 2(b). The position and extension of the line profile can be deduced from the red marked line. As can be seen from Fig. 2(b), the aperture function is 1 for $|\vec{k}_\perp| \leq k_{\max}$ and 0 outside the aperture hole. As a result, the aperture function with an extension of $k_{\max}$ determines the convergence semi-angle $\alpha \approx k_{\max} \cdot \lambda$. The convergence semi-angle α is depicted in Fig. 2(a).
If no lens aberrations are present, the electron beam intensity $I_i(x, y)$ incident on the specimen has the form of an Airy disc which is exemplarily depicted in Fig. 2(c). Fig. 2(c) additionally shows a line profile of the electron beam intensity that is incident on the specimen. It can be seen that the intensity distribution is neither point-like nor spatially limited, as the intensity of rings (in two-dimensional representation in Fig. 2(c)) and the side maxima (in the line profile in Fig. 2(c)) never reach zero due to a proportionality to the squared Bessel function of the first kind of order one [50]. Since the side maxima have a reduced intensity, the resolution of the STEM is significantly determined by the extension of the central maximum. The extension of the central maximum, which can also be described by the distance δ_s between the first minima (Fig. 2(c)), can be approximated by $\delta_s = 1.22\,\lambda/\alpha$. It is important to note that the convergence semi-angle α has an influence on the obtainable resolution. Increasing the convergence semi-angle increases the resolution, as the extension δ_s of the central maximum of the Airy disc decreases.
Besides the convergence semi-angle, residual lens aberrations influence the obtainable resolution as they result in a reciprocal space coordinate dependent z-height of the focal plane. This is schematically depicted in Fig. 2(d) using geometrical optics. The grey lines represent trajectories of the electron beams. It is visible that

beams farther away from the optical axis experience a stronger focusing than beams close to the axis. As a result, the minimum extension of the beam is increased, and the possible resolution reduced. In Fig. 2(d), this behaviour is rotational symmetric around the optical axis, i.e. similar for all azimuthal angles θ around the optical axis. The aberration corresponding to the scenario in Fig. 2(d) is the spherical aberration which in addition to defocus and two-fold astigmatism, which both can be easily corrected, is one of the most crucial lens aberrations in electron microscopy. Ideally, all electrons are focused into a single small spot with infinitesimal extension if no lens aberrations are present.

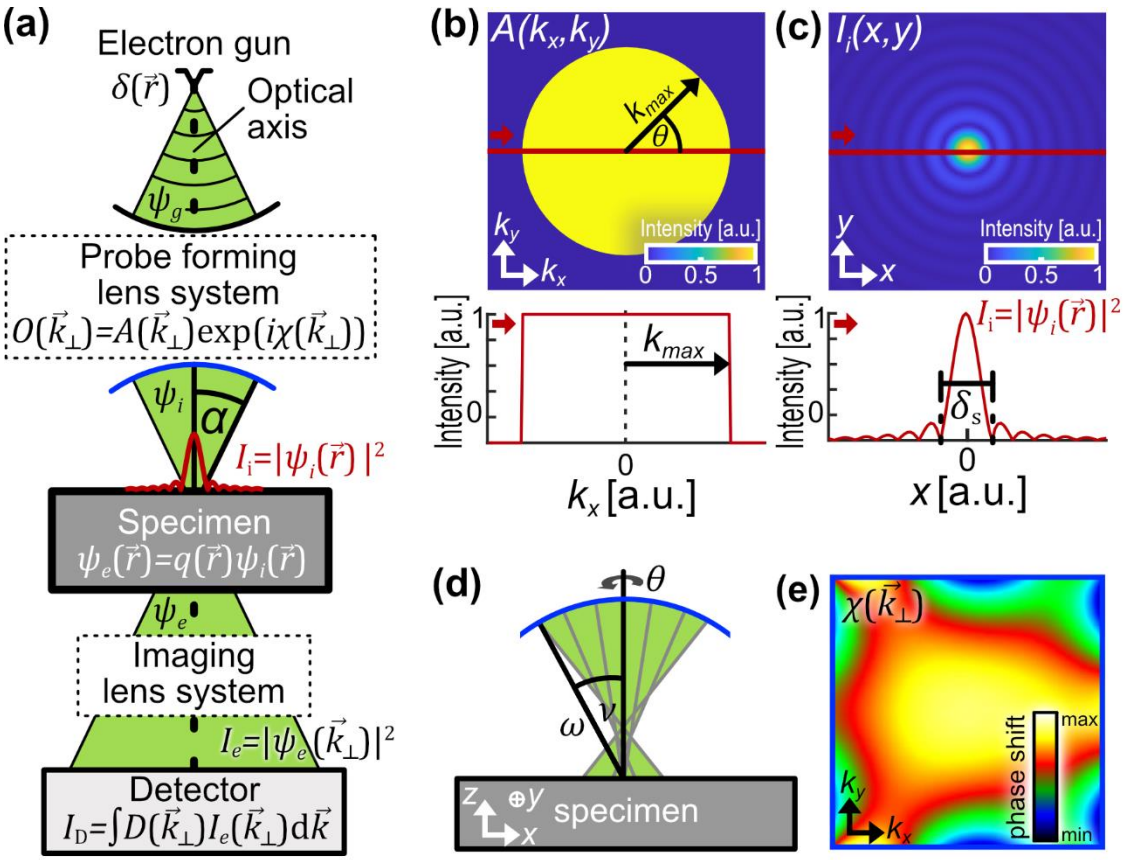

Figure 2: (a) Illustration of the electron wave propagation and interaction in a STEM. (b) Aperture function $A(\vec{k}_\perp)$ with line profile. (c) Intensity distribution of the incident electron beam $I_i(x,y) = |\psi_i|^2$ with corresponding line profile. (d) Illustration of a convergent electron probe incident on the entrance surface of the specimen including lens aberrations. The lens aberration phase plate is described by the angle ω and adds phase shifts to the electron beam as a function of ω. Such a phase plate is shown in (e), which is mainly dominated by six-fold astigmatism (A_5) and axial coma (B_2). (a) and (d) adapted from [57].

There are several ways to mathematically describe the lens aberrations, which can be either based on wave or geometrical optics [57]. To include lens aberrations in the optical transfer function $O(\vec{k}_\perp)$, the aberration function $\chi(\vec{k}_\perp)$ is used to alter the phase of the electron wave (see Eq. 3) in dependency of the reciprocal space coordinate. In the following the wave optical description by Sawada et al. is considered [57], in which the aberration phase function is represented by

$$\chi(\omega) = \frac{2\pi}{2 \cdot \lambda}\left(\sum_{m,n} \frac{1}{m+n} C_{mn}\, (\omega^*)^{\mathrm{m}} \omega^n \; + \mathrm{c.c.}\right). \tag{4}$$

Here, C_{mn} represents the aberration coefficient of a certain lens aberration and $c.c.$ the complex-conjugate of the first summand in the parentheses. The parameter m and n in Eq. 4 determine the order and symmetry of the lens aberration. Instead of using the reciprocal space coordinates $\vec{k}_\perp = (k_x, k_y)$, Sawada et al. [57] introduce the angle $\omega = \upsilon \cdot \exp[i\theta] = \lambda(k_x + ik_y)$ which describes the angle to the optical axis using an azimuthal angle θ and a polar angle ν. The angle to the optical axis ω, the azimuthal angle θ and polar angle ν are depicted in Fig. 2(d).

Various notations of the aberration coefficients can be found in the literature. In this thesis, mainly the notation according to Haider et al. is used [5]. The lens aberration, the coefficients C_{mn} in Eq. 4 and the corresponding Haider notation are compiled in Table 1. It is to note that in this thesis C_s is also used for the spherical aberration coefficient C_3 and f for defocus C_1.

Table 1: Low-order lens aberrations including the order and symmetry of the aberration function, aberration coefficients C_{mn} and the corresponding Haider notation [5].

Aberration {wave aberration order, symmetry}	$\boldsymbol{C_{mn}}$	**Haider-Notation**
Defocus f {2,0}	C_{11}	C_1
Two-fold astigmatism {2,2}	C_{20}	A_1
Axial coma {3,1}	C_{21}	B_2
Three-fold astigmatism {3,3}	C_{30}	A_2
Spherical aberration C_s {4,0}	C_{22}	C_3
Star aberration {4,2}	C_{31}	S_3
Four-fold astigmatism {4,4}	C_{40}	A_3
Axial coma fourth order {5,1}	C_{32}	B_4
Third order lobe aberration {5,3}	C_{41}	D_4
Five-fold astigmatism {5,5}	C_{50}	A_4
Fifth order spherical aberration {6,0}	C_{33}	C_5
Six-fold astigmatism {6,6}	C_{60}	A_5

Rotationally symmetric magnetic lenses which are commonly used in electron microscopes impose a non-negative and non-zero spherical aberration on the beam. In contrast to optical lenses, it is not possible to correct spherical aberration with rotationally symmetric magnetic lenses [61]. This problem is overcome with the so-called C_s-corrector, consisting of (typically) two magnetic multipoles and several transfer lenses [5–7]. Magnetic multipoles reduce spherical aberration at the expense of higher-order lens aberrations. For example, if a C_s-corrector with two magnetic hexapoles is used, lens aberrations up to the 5th geometrical order can be corrected. With such a C_s-corrector, the residual lens aberrations are dominated by six-fold

astigmatism leading to an electron beam with six-fold symmetry of the phase plate. An example is shown in Fig. 2(e).

Mathematically, all lens aberrations induced by the probe forming lens system are incorporated in the wave function $\psi_i(\vec{r})$ of the electron beam which is incident on the specimen according to Eq. 3. The interaction of the incident electron wave $\psi_i(\vec{r})$ with a sufficiently thin specimen can be described following the formulation by Cowley [58]:

$$\psi_e(\vec{k}_\perp) = \mathcal{F}^{-1}[q(\vec{r}) \cdot \psi_i(\vec{r})] = Q(\vec{k}_\perp) \otimes O(\vec{k}_\perp), \tag{5}$$

with $\psi_e(\vec{k}_\perp)$ the exit wave, as well as $Q(\vec{k}_\perp)$ and $q(\vec{r})$ the reciprocal and real space representations of the specimen transmission function. $\mathcal{F}^{-1}$ denotes the inverse Fourier transform and $\otimes$ a convolution. Especially the specimen transmission function, which can include phase shifts as well as absorption, has a strong influence on the complexity of mathematical descriptions, as described in Chapter 2.1.4. The intensity distribution in the detection plane is given by

$$I(\vec{k}_\perp) = \left|Q(\vec{k}_\perp) \otimes O(\vec{k}_\perp)\right|^2. \tag{6}$$

Measuring the intensity $I_D(\vec{R})$ on a detector D (Fig. 2(a)), which has a certain extension and shape in the reciprocal space at each pixel $\vec{R} = (x, y)$ of the scan, can be described mathematically by an integration of the intensity distribution with the detector response function $D(\vec{k}_\perp)$:

$$I_D(\vec{R}) = \int D(\vec{k}_\perp) I(\vec{k}_\perp) d\vec{k}_\perp. \tag{7}$$

For a simple bright-field detector this detector response function D is equal to 1 as long as $\vec{k}_\perp$ is within the detector area.

2.1.3. Electron – solid interactions

When a high-energy electron beam impinges on a specimen, the electrons of the electron beam interact with the specimen in numerous ways. Those which are typically considered in analytical and conventional (S)TEM imaging of solid specimen are depicted in Fig. 3.

Since TEM specimens have a typical thickness of $t < 100$ nm, a fraction of incident electrons passes through the specimen without any interaction. These electrons, which transmit the specimen without changing their direction or energy, can be summarised as the direct beam. Electrons, which change their direction and sustain their kinetic energy, are referred to as elastically scattered electrons. Electrons which loose or gain kinetic energy by interaction with the specimen, are inelastically scattered electrons. One example in which the incident electron loses energy is an inner shell ionisation event, where a knock-off of a core-near electron results in an unoccupied state. This hole is recovered by a recombination process of a less bound core electron and the excess energy is released by characteristic X-ray radiation (Fig. 3), which can be used

to locally determine the atomic composition of the material. The corresponding method is called energy-dispersive X-ray spectroscopy, abbreviated as EDS. Further inelastic processes include the excitation of surface or bulk plasmons as well as the interaction with phonons.

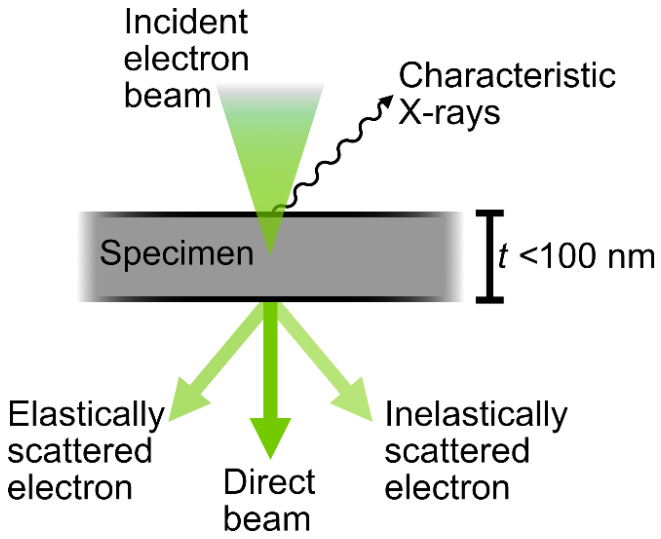

Figure 3: High-energy electron beam incident on a solid specimen resulting in emitted characteristic X-rays and transmitted electrons including the direct beam, as well as elastically and inelastically scattered electrons. Adapted from [50].

Elastically scattered electrons comprise Bragg diffracted electrons, which experience a change in direction due to the crystal structure of the specimen and ultimately generate a diffraction pattern in the detection plane. In crystalline material, the change in direction of diffracted beams is correlated to an angle which is given via the Bragg equation [50]:

$$2d_{hkl} \sin \theta_{\mathrm{Bragg}} = n\lambda, \tag{8}$$

in which θ_{Bragg} is the Bragg angle of diffraction, d_{hkl} the lattice plane spacing, n the order of diffraction and λ the electron wavelength. The diffraction pattern in the detection plane thus includes information on the lattice plane spacings perpendicular to the optical axis and can therefore be used to study the crystal structure, orientation, and defects of the specimen. When using a convergent instead of a parallel electron beam, diffraction leads to a pattern of discs instead of spots on the detector. Diffraction with convergent electron beams is referred to as convergent-beam electron diffraction (CBED). The Bragg equation still suffices to describe the angular relation between the discs. The disc radius is determined by the convergence semi-angle.

In addition to the previous classifications, it is also possible to subdivide the signals of the scattered electrons into coherently and incoherently scattered electrons. In coherent imaging the phase relationship is preserved. This is mainly the case for beams that have been scattered to small polar angles. Incoherently scattered electrons do not retain their phase relationship. This type of signal increases at high polar angles to the optical axis and, e.g. arises due to Rutherford forward scattering of electrons at

the nucleus of the atoms inside the specimen which have fluctuating positions due to thermally induced lattice vibrations [56]. This interaction is also referred to as inelastic thermal diffuse scattering (TDS) if it includes the interaction of the electron beam with phonons [62]. These (thermal diffuse) scattered electrons are typically considered for Z-contrast (atomic number Z) imaging using a high-angle annular dark-field HAADF detector. Details on HAADF imaging are given in Chapter 2.1.5.

2.1.4. Phase object approximations

A (scanning) transmission electron microscope image using electrons for signal generation is always a (beam position related) measurement of intensity in specific scattering angle intervals of the exit wave intensity distribution. This measurement is used to quantitatively deduce one of the material properties, e.g. atomic potentials. However, as only the result of the beam specimen interaction is measurable by the exit wave intensity and not the electron propagation within the specimen structure, inferring exact specimen properties is challenging. Moreover, as the specimen is analysed at a certain orientation to the electron beam direction, only information projected in that direction can be deduced.

To allow for contrast interpretation and ultimately obtain quantitative information without knowing the exact beam path, approximations are needed [50]. One of these approximations is the phase object approximation (POA), which assumes that the specimen only changes the phase ϕ of the electron beam and not its amplitude. Within the POA, the absorption μ of the electron beam intensity is therefore neglected (Eq. 9). Moreover, if the specimen is very thin, the specimen can be treated within the weak phase object approximation (WPOA) assuming that phase changes are small and linear. The influence of the specimen potential can then be approximated using a series expansion of the transmission $q(\vec{r})$ function, in which high order terms are additionally neglected [50]:

$$q(\vec{r}) = \exp(-i\phi - \mu) \underbrace{\approx}_{\text{POA}} \exp(-i\phi) = \exp\left(-i\sigma V_p(\vec{r})\right) \underbrace{\approx}_{\text{WPOA}} 1 - i\sigma V_p(\vec{r}). \tag{9}$$

The phase shift ϕ of the electron wave corresponds to the product of the projected specimen potential $V_p(\vec{r})$ at coordinate $\vec{r}$ and the interaction constant $\sigma = (m_{\text{rel}}\lambda)/(2\pi\hbar^2)$ with m_{rel} the relativistic electron mass, $\hbar$ the reduced Planck constant, and λ the wavelength. It is thus assumed that the phase shift is proportional to the specimen potential which is projected in beam direction (negative z-direction in Fig. 2(d)). The projected specimen potential is given via integrating the specimen potential along the complete specimen thickness t:

$$V_p(x,y) = \frac{1}{t}\int_0^t V(x,y,z)\mathrm{d}z. \tag{10}$$

The integration of the specimen potential along the z-axis thus reduces the specimen potential from a three-dimensional potential to a two-dimensional one.

One of the drawbacks of the (W)POA is the neglection of the curvature of the Ewald sphere and the ignoration of Fresnel propagation, i.e. evolution of the electron wave inside the specimen [63]. At some thicknesses both approximations thus break down. The limit depends on the scattering power of atoms in the material [64]: Heavy atoms exhibit a lower validity range of the (weak) phase object approximation than lighter atoms. According to ref. [63], the limit for the weak phase object approximation is given by $\lambda t k_{\max}^2 \leq 0.25$, with $k_{\max}$ the highest wavenumber measurable with the detector. The thickness of true weak phase objects is therefore in the range of a few Å for typical acceleration voltages and polar detection angles considered in a (S)TEM. The thickness limits for the validity of the (W)POA also depend on the atomic number of the specimen. Since such specimen thicknesses are practically impossible for many material systems, the measurable specimen potentials are always an approximation of the real specimen potentials.

2.1.5. STEM (high-angle) annular dark-field and bright-field imaging

In conventional STEM imaging several detector geometries are commonly exploited to select a certain contrast mechanism, e.g. coherent or incoherent scattering [56]. Among these detectors are the bright-field (BF) and the annular dark-field (ADF) detector, which are depicted in Fig. 4(a). The latter is also referred to as a high-angle annular dark-field (HAADF) detector if it detects electrons that are scattered to very high angles to the optical axis, typically > 5° [56]. Fig. 4(a) also includes a simplified representation of the detected electrons that are exploited with both detectors, namely the direct beam and scattered electrons.

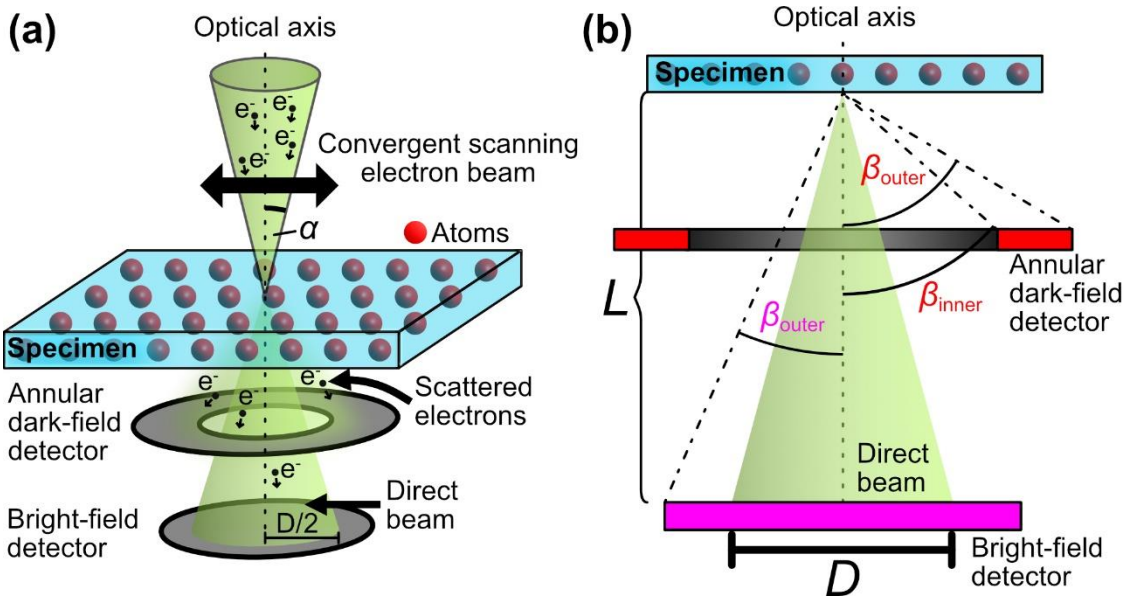

Figure 4: (a) Schematics of the contrast mechanism in STEM and the intensity on dark-field and bright-field detectors. (b) Detectors below the specimen and the influence of the camera length L on the collection angles and the diameter D of the direct beam on the detector.

The BF detector shown in Fig. 4(a) is primarily used to measure the intensity variation in the direct beam from scan position to scan position and typically also collects diffracted beams. The bright-field detector is centred on the optical axis similar to a DPC detector. Therefore, both types of detectors cannot simultaneously acquire a signal if the DPC detector does not have a hole in the centre. It is worth to note that DPC detectors can also be used to acquire a BF signal by integrating the intensity on the complete detector, i.e. a summation of the intensity on all segments. The ADF detector collects all electrons of the intensity distribution which have been incoherently scattered into large polar angles. All electrons scattered into polar angles within the hole of the annular detector do not contribute to the image. However, depending on the collection angles of the ADF detector an ADF image might contain some diffraction contrast.

The adjustment of the inner and outer collection angles β_{inner} and β_{outer} (Fig. 4(b)) of both the BF and the ADF detector can be achieved by changing the camera length L of the microscope. The camera length principally is the distance between detector and specimen, which is constant in an electron microscope. The camera length adjustment is realised by changing the magnifying optics of the projection lens system (below the specimen). With the camera length L adjusted, the diameter D_{beam} in CBED follows from the convergence semi-angle (Fig. 4):

$$D_{\mathrm{beam}} \approx 2\alpha \cdot L. \tag{11}$$

As the convergence semi-angle α of the incident electron beam remains constant despite changing the camera length L, the detector collection angles depend on the camera length.

The geometry and extension of the considered detector play an important role because individual types of interactions of the electron beam with the specimen are correlated with characteristic scattering angles to the optical axis. For example, Bragg diffracted electrons can be measured at polar angles close to the optical axis [56]. Furthermore, Rutherford forward scattering leads to a deflection of the incident electrons into high polar angles. The resulting scattered intensity distribution of an atom depends on its atomic number Z^n with exponent n, which is a function of the scattering angle. This dependency of n arises from the atomic form factor, which describes the scattering power of an isolated atom as a function of the scattering angle. The atomic form factor depends on the atomic species and decreases with increasing scattering angle. At low polar angles to the optical axis, the scattered intensity is proportional to $Z^{2/3}$. Incoherent scattering of electrons to high polar scattering angles follows a Z^2-dependency [56, 65, 66].

Since collection angles of HAADF detectors reach very high polar angles and therefore fulfil a Z^2 condition, the intensity distribution in STEM HAADF images readily allows to determine the spatial position of atoms or atomic columns. Fig. 5 exemplarily shows an atomically resolved STEM HAADF image of Si in [110] zone-axis orientation. Bright spots in this image arise due to the scattering of the electron beam at individual atoms

of spatially separated atomic columns. The atomic columns in Fig. 5 comprise approximately 40 atoms stacked on top of each other. It is to note that the measurable peak intensity of an atomic column does not linearly depend on the number of atoms, although each atom acts as an individual scattering centre. This is due to a combination of channeling [67] and thermal diffuse scattering effects [62, 68]. To account for these effects the peak intensity in HAADF is therefore typically described as a $Z^{(2-x)}$ -contrast, with a parameter x between 0.3 and 0.7 depending on the material [68, 69]. This power law dependency of Z^n breaks down at low acceleration voltages and at heavy atoms, since the validity of the first Born approximation vanishes at low kinetic energies for strong scatterers [69].

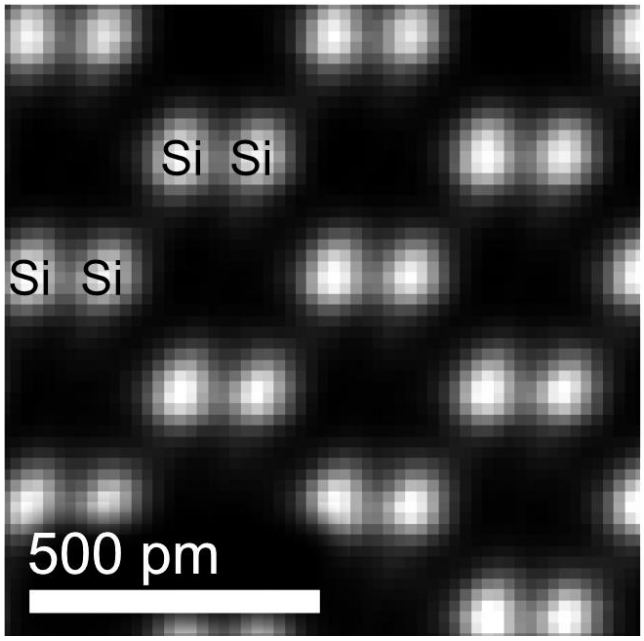

Figure 5: STEM HAADF image of Si in [110] zone-axis orientation. This image was acquired on a *JEOL* JEM-ARM200F at an acceleration voltage of 200 kV and at a camera length of 12 cm. The HAADF collection angles are given in Chapter 3.3. A description of the applied denoising technique can be found in Chapter 4.4.2. The specimen thickness amounts to $\approx 30\,\mathrm{nm}$. Hence, atomic columns comprise approximately 40 Si atoms stacked in projection. Imaging parameters are listed in Table 33 in the Appendix.

As still a monotonic increase of peak intensity of atomic columns is observed with increasing thickness, HAADF imaging is thus typically used to study the composition of materials [66] without applying further analytical techniques such as EELS or EDS. Recently, the intensity distribution in HAADF images and in particular the intensity distribution at individual atomic columns have been exploited to count the number of atoms in an atomic column or estimate the chemical composition [70–72]. Such investigations based on the HAADF image necessitate extensive simulations and precise knowledge on the number of detected atoms.

2.1.6. Electron energy loss spectroscopy and energy-filtered TEM

The electrons in the detection plane of the (S)TEM can be largely subdivided into elastically or inelastically scattered electrons. These inelastic interactions include the inner shell ionisation of atoms, the excitation of surface and bulk plasmons as well as an interaction with phonons [73]. All inelastic interactions result in a kinetic energy loss E of the incident electron, which can be found in interaction-dependent intervals of kinetic energy. It is furthermore to note that the incident electron is scattered through a characteristic angle. This characteristic angle $\varepsilon_{\mathrm{Scat}}$ can roughly be estimated by $\varepsilon_{\mathrm{Scat}} = (E/E_0) \cdot ((E_0 + E_{\mathrm{rest}})/(E_0 + 2E_{\mathrm{rest}}))$, with the energy loss E, the incident

electron beam energy E_0 and the electron rest energy E_{rest} = 511 keV [27, 73]. At an acceleration voltage of 200 kV, characteristic scattering angles arising from inner shell ionisations (E in the range from 30 eV to 200 eV) are below 5 mrad. For comparison, incident electrons with the same kinetic energy that excited a bulk plasmon (energy loss of about 25 eV) can most likely be found at an angle of 0.07 mrad.

As the energy loss is characteristic for the interaction as well as the involved materials, the energy distribution of the electrons can also be used for the analysis of materials, e.g. to atomically resolve the chemical composition [74], to map plasmonic resonances of metallic nanostructures [75–77], to distinguish between sp^2 and sp^3 hybridised carbon and to differentiate polymers showing similar contrasts in conventional (S)TEM (e.g. polymethylmethacrylate and polystyrene) [78–82], and to quantify bandgap energies of semiconductors [83].

Such analyses are achieved with electron energy-loss spectroscopy (EELS) in STEM and energy-filtered TEM (EFTEM) by separating the electrons according to their kinetic energy through a magnetic prism, which is installed either within or at the end of the imaging system. As both methods, EFTEM and EELS, fill complete textbooks [50–52, 73], only a brief description is given. Moreover, as EELS and EFTEM are utilised in this thesis exclusively to determine the thickness of the specimen, only this application is explained in the following.

In EELS, a spectrum of the energy loss distribution of the post-specimen electron beam is projected onto a camera. The spectrum in STEM EELS is acquired at each beam position of a scan or at specific points. Analysis of the energy loss related interaction processes are done subsequently.

In EFTEM, the optics behind the magnetic prism is used to project an image onto the camera, to which only electrons with a certain kinetic energy are contributing. The filtering is achieved by a slit-like aperture behind the magnetic prism. The width of the slit determines the interval of kinetic energies contributing to the filtered image. This interval is typically referred to as an energy window. As changing the magnetic field strength of the magnetic prism is impracticable due to hysteresis and subsequent instabilities, the acceleration voltage is slightly changed (in the range of few hundred eV) to adjust the energy interval of the energy window.

The fraction of inelastically scattered electrons increases with increasing thickness following a Poisson distribution. Thus, the intensity ratio of elastically and inelastically scattered electrons allows to determine the relative thickness in terms of the mean free path λ_{mfp} of electron scattering events. This is exploited in the log-ratio method (also referred to as t/λ-method) [73, 84, 85] which estimates the relative specimen thickness by

$$\frac{t}{\lambda_{\mathrm{mfp}}} = \ln\left(\frac{I_t}{I_0}\right), \tag{12}$$

with I_0 the intensity of elastically scattered electrons and I_t the summed intensity of elastically and inelastically scattered electrons. In EELS, I_0 and I_t are obtained as the

area under the zero-loss peak (ZLP) and the complete spectrum, respectively. The ZLP contains all electrons which have not experienced any change in energy. In EFTEM, an elastic image, i.e. an image with the energy window centred around the ZLP, and an unfiltered image (without filter) are acquired. By aligning both images, the relative specimen thickness can be calculated at each pixel in multiples of λ_{mfp}.
It is possible to convert the relative thickness into an absolute thickness if λ_{mfp} of the investigated material is known. To calculate the mean free path, the atomic number-dependent model by Malis et al. [52] and the density-dependent model by Iakoubovskii et al. [85] are commonly applied. Only the latter model takes the convergence semi-angle α and spectrometer's collection semi-angle β into account. The model of Iakoubovskii is therefore an improvement in accuracy of thickness determination for most materials. The t/λ-method allows for absolute thickness accuracies below 10% for $t = 4 \cdot \lambda_{\mathrm{mfp}}$ [73]. When applied to very thin specimen $(t < 0.1 \cdot \lambda_{\mathrm{mfp}})$, the t/λ-method typically overestimates the specimen thickness due to increased energy loss from surface effects [73].

2.2. Theory of differential phase contrast in STEM

This chapter describes the theory of differential phase contrast (DPC) imaging. DPC is a technique in the STEM mode of a transmission electron microscope and allows for the measurement and visualisation of electric and magnetic field distributions in a solid specimen. The high-resolution capability of modern STEMs even enables to investigate electric fields and charge density distributions at subatomic resolution. Due to this, DPC imaging is a possible method for the investigation of the influence of chemical bonding on charge and electric field distributions [86].
The signal of DPC measurements is derived from the redistribution of intensity resulting from the interaction of the incident electron beam with the specimen potentials. As this thesis focusses on the investigation of electric fields and influences on the DPC signal at atomic resolution, this chapter only includes the description for electric fields. Descriptions of the differential phase contrast signal arising from magnetic fields can be found in references [38, 87].
Fig. 6 shows a sketch of the DPC technique, including all necessary components namely a scanning convergent electron beam impinging on a specimen with electric fields and a position sensitive detector. At each beam position $\vec{R} = (x, y)$ the incident electron beam interacts via the Coulomb force with the present atomic electric fields. This leads to changes of the convergent-beam electron diffraction pattern (intensity distribution $I(k_x, k_y)$), which is projected onto the detector. To measure such changes induced by the electric fields, a position sensitive detector is mandatory. Depending on the homogeneity of the specimen potentials across the beam diameter, the intensity redistribution in the detection plane can be a rigid deflection of the electron beam or can result in an intensity gradient across the direct beam.
This chapter is subdivided as follows. In Chapter 2.2.1, the interaction of the electron beam with homogeneous electric fields is described both classically in the particle and

in the wave picture, assuming a plate-capacitor-like appearance of the specimen's potential at each pixel of the scan. In Chapter 2.2.2, limitations of the plate capacitor approximation are explained, originating from electric field distributions which exhibit variations in magnitude and direction across the probe diameter. Such inhomogeneous electric fields are typically present at atomic resolution. Chapter 2.2.2 expands the description of differential phase contrast by including the influence of inhomogeneous electric fields. Chapter 2.2.2 covers a quantum mechanical description of the measurable DPC signal of inhomogeneous electric fields. Chapter 2.2.3 explains the working principles of different types of detectors suitable for DPC imaging and, furthermore, exemplifies the signal acquisition and display of a DPC image acquired with a segmented detector. Finally, Chapter 2.2.4 describes how charge density distributions are deduced from a DPC measurement.

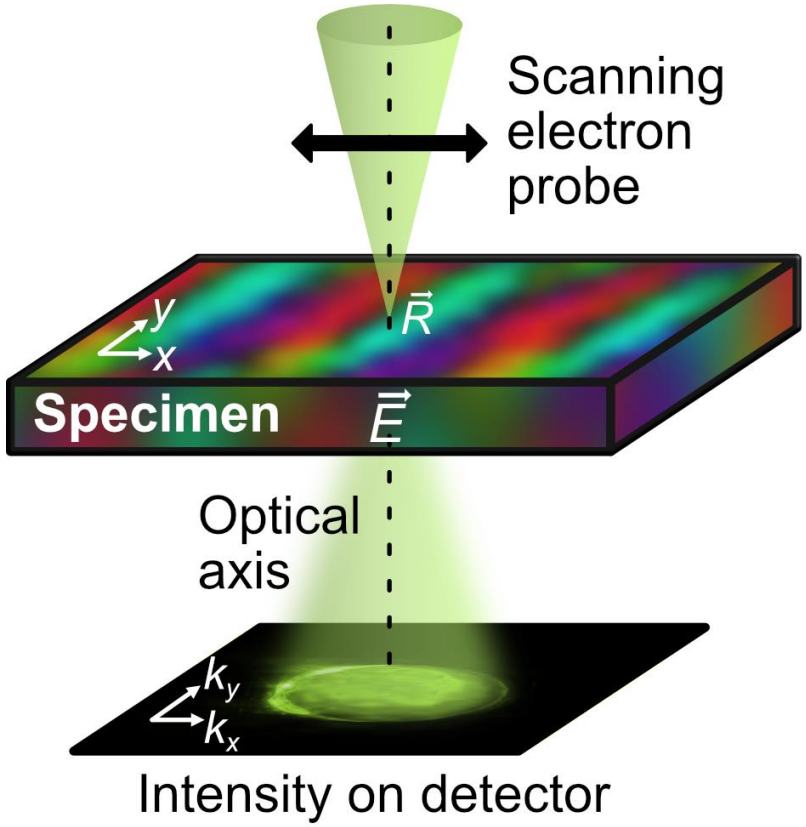

Figure 6: Schematic of differential phase contrast imaging. In STEM, a convergent electron beam is incident on the specimen and interacts with the electric fields inside the specimen. After interaction, the exit wave is projected onto a detector. The depicted intensity in the detection plane is obtained from multislice image simulations using Dr. Probe (Chapter 2.3).

2.2.1. Plate capacitor approximation

To understand the contrast mechanism of DPC one can assume a single fast-moving electron in a homogeneous electric field [1, 38], comparable to the movement of an electron in the homogeneous field of a plate capacitor. Hence, the following description in the particle picture is often referred to as the plate capacitor approximation.

Fig. 7(a) illustrates the trajectory of the electron which is incident in z-direction with a momentum p_0 on the homogeneous electric field. The electric field is described by its extension t in z-direction and its electric field vectors pointing in negative x-direction. After interaction with the electric field, the electron is projected onto a detector.

The interaction of the incident electron with the electric field can be described by the Coulomb component of the Lorentz force. In Fig. 7(a), this Coulomb interaction results in a deflection in opposite direction of the electric field components, i.e. in positive x-direction. The deflection angle $\varepsilon_{\mathrm{el}}$ can be derived from the transferred momentum $p_\perp$ and the incident momentum p_0 using the paraxial approximation [38, 51], which is possible since typical deflection angles of DPC are <5 mrad. Both, p_0 and $p_\perp$, are exemplarily depicted in Fig. 7(a).

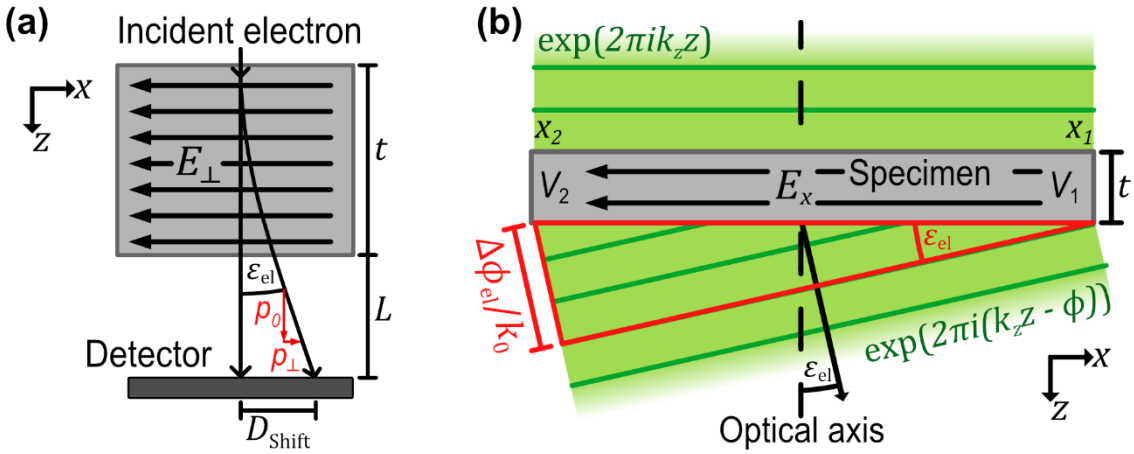

Figure 7: Illustrations of (a) the electron trajectory in a plate capacitor and (b) the deflection of electron waves due to electrostatic potentials inside a specimen. (a) adapted from [51] and (b) adapted from [38].

By inserting expressions for $p_0 = m_{\mathrm{rel}} v_{\mathrm{rel}}$ and $\vec{p}_\perp = e\vec{E}_\perp t / v_{\mathrm{rel}}$, which include the elementary charge e as well as the relativistic electron mass and velocity m_{rel} and v_{rel}, the deflection angle

$$\varepsilon_{\mathrm{el}} \approx \frac{\vec{p}_\perp}{p_0} = -\frac{e}{m_{\mathrm{rel}} \cdot v_{\mathrm{rel}}^2} \cdot \vec{E}_\perp \cdot t \propto \vec{E}_\perp \cdot t \tag{13}$$

can be calculated. It exhibits a proportionality to the electric field $\vec{E}_\perp$ and the extension t of the electric field in z-direction [38, 51]. Importantly, the deflection angle $\varepsilon_{\mathrm{el}}$ is a vectorial quantity because it possesses components in x- and y-direction. Moreover, the extension of electric field in z-direction corresponds to the specimen thickness.

Until now the wave character of the incident electron beam and its convergent shape (given by the convergence angle α) are neglected. In the following a wave optical description of the interaction of an incident electron beam with the electric fields in a specimen is given. For simplicity, however, a plane wave is assumed without loss of generality. The description follows the work by Zweck et al. [38]. Fig. 7(b) schematically depicts a planar electron wave which is deflected by the electric field inside a specimen. The incident electron wave is described by its wavelength λ (Eq. 2) or in reciprocal

space by a wavenumber $k_0 = 2\pi/\lambda$. It is to note that Zweck et al. [38] use the angular wavenumber.

A deflection of the electron beam, as it may be caused by a phase object, can be described as a result of phase shifts ϕ_{el} imposed on the beam by an electrostatic potential $V_{\mathrm{el}}(x, y, z)$. The phase shift may be written as [38]

$$\phi_{\mathrm{el}} = \underbrace{\frac{e}{\hbar v_{\mathrm{rel}}}}_{=\xi} \int_0^t V_{\mathrm{el}}(x, y, z)\, \mathrm{d}z, \tag{14}$$

which includes a pre-factor ξ, comprising the reduced Planck constant $\hbar$, the elementary charge e and relativistic electron velocity v_{rel}. It is to note that utilizing the phase object approximation, projected potentials are considered which are represented by $V_{\perp,\mathrm{el}} = 1/t \cdot \int_t V_{\mathrm{el}} \mathrm{d}z$.

From electrostatic theory it is known that electric fields $\vec{E}$ are the negative gradient of the electrostatic potentials, $\vec{E} = -\nabla V_{\perp,\mathrm{el}}$. Thus, specimens exhibit electric fields if a gradient in electrostatic potential is present, e.g. at a pn-junction [17]. This scenario is depicted in Fig. 7(b), where an electric field is present due to different electrostatic potentials, V_1 and V_2, at positions x_1 and x_2, respectively. A mean inner potential V_0 is neglected in the schematic in Fig. 7(b) because a specimen with constant mean inner potential and with constant thickness would just lead to a constant phase shift. However, the influence of the mean inner potential must be considered for a specimen with thickness modulations, e.g. for a wedge shaped specimen, because the electron wave experiences stronger phase shifts at the thicker side [14].

By rewriting Eq. 14 in a differential form, only considering the x-direction and exchanging the derivative of the electrostatic potential with the electric field, one obtains the following equation for the phase differential $\mathrm{d}\phi_{el}/\mathrm{d}x$ (adapted from [38]):

$$\frac{\mathrm{d}\phi_{el}}{\mathrm{d}x} = \xi \underbrace{\left(\frac{\mathrm{d}V_{\perp,\mathrm{el}}}{\mathrm{d}x}\right)}_{=-E_x} \cdot t = -\xi \cdot E_x \cdot t\,. \tag{15}$$

Here again a proportionality of the phase gradient to the electric field and the specimen thickness can be observed (compare Eq. 13).

Similar to the description in the particle picture a deflection angle can be determined. This is achieved from geometrical considerations. Fig. 7(b) includes a (red) triangle denoting the distance $\Delta\phi_{el}/k_0$ the electron beam with phase shift $\Delta\phi_{el}$ has travelled. The deflection angle is then given in paraxial approximation by

$$\varepsilon_{el} \approx \sin(\varepsilon_{el}) = \frac{\Delta\phi_{el}}{k_0} \cdot \frac{1}{(x_2 - x_1)} = \frac{1}{k_0} \cdot \left(\frac{\mathrm{d}\phi_{el}}{\mathrm{d}x}\right) = -\frac{\xi}{k_0} E_x t. \tag{16}$$

In both the particle as well as the wave optical description, the electrons leave the specimen in an angle $\varepsilon_{\mathrm{el}}$ to the incident propagation direction. In the microscope, the electron beam intensity distribution $I(\vec{k}_\perp) = \psi(\vec{k}_\perp) \cdot \psi^*(\vec{k}_\perp)$ is measured with a detector

at a distance L (camera length) to the specimen. In the detection plane the deflection leads to a displacement D_{Shift}(Fig. 7(a)) of the electron beam intensity which is given by [38]:

$$D_{\mathrm{Shift}} = \varepsilon_{\mathrm{el}} \cdot L. \tag{17}$$

From Chapter 2.1.2 it is known that the intensity distribution on the detector is measured in reciprocal space coordinates. This is indicated in Fig. 6 by the (k_x, k_y) coordinate system. The displacement D_{Shift} to the optical axis is thus a measure of lateral wavevector or the lateral momentum transfer resulting from the Coulomb interaction of the electron beam.

$$p_\perp = \hbar k_\perp = \varepsilon_{\mathrm{el}} p_0, \tag{18}$$

with $k_\perp = (k_x, k_y) = \varepsilon_{\mathrm{el}} k_0$.

2.2.2. Homogeneous and inhomogeneous specimen potentials

In the previous chapter, the origin of the differential phase contrast signal was described in a wave optical as well as a particle picture by assuming a homogeneous electric field. These descriptions, however, only consider a single electron or a planar electron wave which is incident on a homogeneous electric field. In a STEM, however, a convergent electron beam with a certain intensity distribution is used (Chapter 2.1.2). In addition, the electron beam is incident on a specimen, which does not necessarily consist entirely of homogeneous electric fields. This is particular the case when doing DPC at atomic resolution. The following chapter therefore describes, how homogeneous and inhomogeneous electrostatic potentials influence the intensity distribution in the detection plane.

Fig. 8(a) shows the intensity distribution in the detection plane, when no electric field $\vec{E}_\perp = 0$ is present. The left side depicts a schematic of the electron beam, while the intensity distribution in the detection plane is shown on the right side. As can be seen from the intensity distribution in Fig. 8(a), a shadow image of the aperture function is measurable in the detection plane. Note that the aperture function defines the convergence angle by k_{max} in reciprocal space (Chapter 2.1.2). As no electric field is present and the aperture is centred on the optical axis, the intensity distribution in the detection plane is also centred. Therefore, no transferred momentum $\vec{p}_\perp = 0$ perpendicular to the optical axis can be measured.

If a homogeneous electric field is present $\vec{E}_\perp \neq 0$ (Fig. 8(b)), the disc is rigidly shifted by a reciprocal vector $k_\perp$, which corresponds to a transferred momentum $\vec{p}_\perp = \hbar\vec{k}_\perp \neq 0$. In other words, homogeneous electric fields lead to a displacement of the direct beam in the detection plane without changing its shape or inner intensity distribution. Fig. 8(a) and Fig. 8(b) contain dashed circles which depict the edge of the direct beam in the absence (blue) and presence (red) of electric fields. Fig. 8(c) shows line profiles of the

intensity distribution in Figs. 8(a, b). The rigid shift is also visible in the line profiles depicting a rigid displacement of the intensity distribution. The rigid shift model has been applied to investigate rather homogeneous electric field distributions at p-n junctions and semiconductor heterojunctions [14, 17, 88], which have a lateral extension significantly larger than the probe diameter.

At atomic resolution, this simple rigid shift model breaks down, as the atomic potentials strongly vary across the probe diameter. This was described in [9] and is due to the rapid decay of screened atomic potentials near atomic column positions and the width of the intensity distribution of the incident beam (Chapter 2.1.2). However, it was experimentally demonstrated in [8] and [9] on the example of $SrTiO_3$ that DPC imaging at atomic resolution can be accomplished.

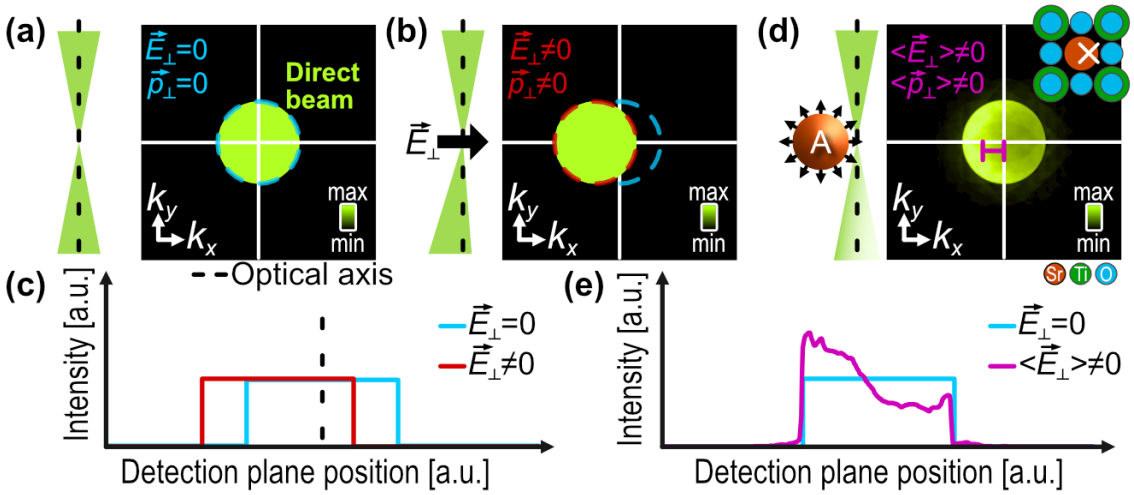

Figure 8: (a) Intensity distribution in the detection plane in the absence of any electric field. The direct beam is perfectly centred on the optical axis. (b) Influence of homogeneous electric fields on the intensity distribution in the detection plane. (c) Line profiles of the intensity distribution in the detection plane in (a) and (b). The respective line profiles range in k_x-direction across the complete intensity distribution and have an infinitesimal width in k_y-direction. The dashed circles in (a) and (b) illustrate the edge of the direct beam in absence (blue) and presence (red) of electric fields. (d) Intensity distribution in the detection plane after interaction with a 2.73 nm thick $SrTiO_3$ specimen structure. A list of parameters for the CBED simulation in (d) is compiled in Table 8 in the Appendix. (a, b, d) are split into a left- and a right-hand side. On the left-hand side the electron beam path is depicted. The right-hand side shows the intensity distribution on the detection plane. Similar to (c), (e) depicts line profiles of the intensity distribution in the detection plane, again across the complete intensity distribution in k_x-direction. (e) additionally contains the line profile obtained from (a) for comparison.

To exemplify the influence of inhomogeneous electric fields on the intensity distribution in the detection plane, Fig. 8(d) shows a multislice simulation of the CBED intensity distribution (Chapter 2.3) in the detection plane, after the incident electron wave has interacted with a 2.73 nm thick $SrTiO_3$[001] specimen structure. This CBED pattern is obtained at a beam position which is close to a Sr atomic column. The respective position is indicated by a white cross in the specimen structure of the $SrTiO_3$ model in Fig. 8(d). Electrons which are incident at this position, are attracted by the not fully screened atomic nuclei. However, instead of a rigid deflection of the electron beam towards the atomic column, an intensity redistribution in the direct beam is observed. This can be seen in Fig. 8(d), in which the intensity inside the direct beam at the side

towards the atomic column is increasing. Such a behaviour has also been described in literature [8, 9, 19, 27, 36, 89].
This intensity redistribution is also visible in corresponding line profiles in Fig. 8(e). As the beam is incident at a position on the right-hand side of a Sr atomic column, the intensity redistribution leads to an intensity increase on the left-hand side of the direct beam. Due to thickness dependent coherent interference effects and (multiple) scattering, the mean intensity in the direct beam is reduced. The overall intensity of the purple line profile obtained from beam position is therefore rescaled by a factor of 1.4.
Since a rigid displacement of the direct beam cannot be observed when investigating inhomogeneous specimen potentials, the plate capacitor approximation in a classical description (Chapter 2.2.1) is not sufficient. Müller et al. [9] therefore formulate a quantum mechanical description based on expectation values for the transferred momentum $\langle \vec{p}_\perp \rangle$ and the projected electric field $\langle \vec{E}_\perp \rangle$. By applying the Ehrenfest theorem and assuming a non-propagating electron probe, they find [9]:

$$\langle \vec{E}_\perp \rangle(\vec{R}) = -\frac{v_{\mathrm{rel}}}{e \cdot t} \cdot \langle \vec{p}_\perp \rangle(\vec{R}). \tag{19}$$

Here, v_{rel} denotes the relativistic electron velocity, e the elementary charge and t the specimen thickness. Assuming a non-propagating probe means neglecting any broadening and intensity change of the electron beam in the specimen. The beam therefore must only interact with the specimen potentials projected in z-direction at beam position $\vec{R}$. Simply put, the electron beams intensity must stay within the current voxel (pixel extended in z-direction to the full specimen thickness). In addition, the specimen must fulfil the phase object approximation [90]. Hence, Eq. 19 is only valid for small specimen thicknesses in the range of 2 nm [9]. While this limits the thickness range in which DPC can be quantitatively applied, reasonable qualitative DPC mapping can be achieved even at larger thicknesses of approximately 20 nm [43, 91].
Furthermore, it is to note that $\langle \vec{E}_\perp \rangle(\vec{R})$ is not the expectation value of the true electric field within the specimen at beam position $\vec{R}$. Instead $\langle \vec{E}_\perp \rangle(\vec{R})$ is a convolution of the true projected electric field $\langle \vec{E}_\perp^T \rangle(\vec{R})$ with the inversion of the incident probe intensity $I_i(-\vec{R})$ [9, 27]:

$$\langle \vec{E}_\perp \rangle(\vec{R}) = \langle \vec{E}_\perp^T \rangle(\vec{R}) \otimes I_i(-\vec{R}). \tag{20}$$

As the intensity $I_i = |\psi_i(\vec{r})|^2$ of the incident electron wave $\psi_i(\vec{k}_\perp)$ is governed by the aperture function and more importantly the lens aberration phase plate, careful adjustments of focus [36, 43, 91] and other residual lens aberrations [91] are required for DPC imaging.

2.2.3. Detectors and signal acquisition

To investigate the electric field distribution in a specimen via DPC, a suitable detector is necessary which allows to condense the inhomogeneous but detailed CBED

intensity distribution into the expectation value of transferred momentum. The expectation value for the momentum itself is defined in quantum mechanics as [9]:

$$\langle \vec{p}_\perp \rangle = \int \vec{p}_\perp I_e(\vec{p}_\perp) \mathrm{d}p_x \mathrm{d}p_y, \tag{21}$$

where $I_e(\vec{p}_\perp) = \psi_e \cdot \psi_e^*$ is the post-specimen intensity distribution in the detection plane. The increments dp_x and dp_y denote the directional components of the two-dimensional vector of transferred momentum $\vec{p}_\perp$.

In DPC imaging, the application of this equation is achieved by calculating the centre of mass (CoM) of the intensity distribution in momentum space. As the mapping of the intensity of an electron wave can only be achieved with a finite resolution in reciprocal space, which is e.g. determined by the number of pixels of a camera, the CoM is calculated by

$$\langle \vec{p}_{\mathrm{CoM},\perp} \rangle = \frac{\Sigma_{\mathrm{px}} \, \vec{p}_{\perp,\mathrm{px}} I_e(\vec{p}_{\perp,\mathrm{px}})}{\Sigma_{\mathrm{px}} \, I_e(\vec{p}_{\perp,\mathrm{px}})}, \tag{22}$$

including a summation of the intensity of all pixels weighted by the momentum space coordinate of the corresponding pixel. This CoM $\langle \vec{p}_{\mathrm{CoM},\perp} \rangle$ is also referred to as the (transferred) first moment. As a DPC detector should be capable to determine the CoM signal with sufficient precision, the momentum space resolution plays a crucial role [9] but a sampling of a few mrad per pixel typically suffices [27].

Currently employed detectors are depicted in Fig. 9. These include a segmented (Fig. 9(a)) [37, 39, 92], a pixelated (Fig. 9(b)) [9, 10, 40, 93] and a non-pixelated detector (Fig. 9(c)) [94], the latter being based on position sensitive diodes.

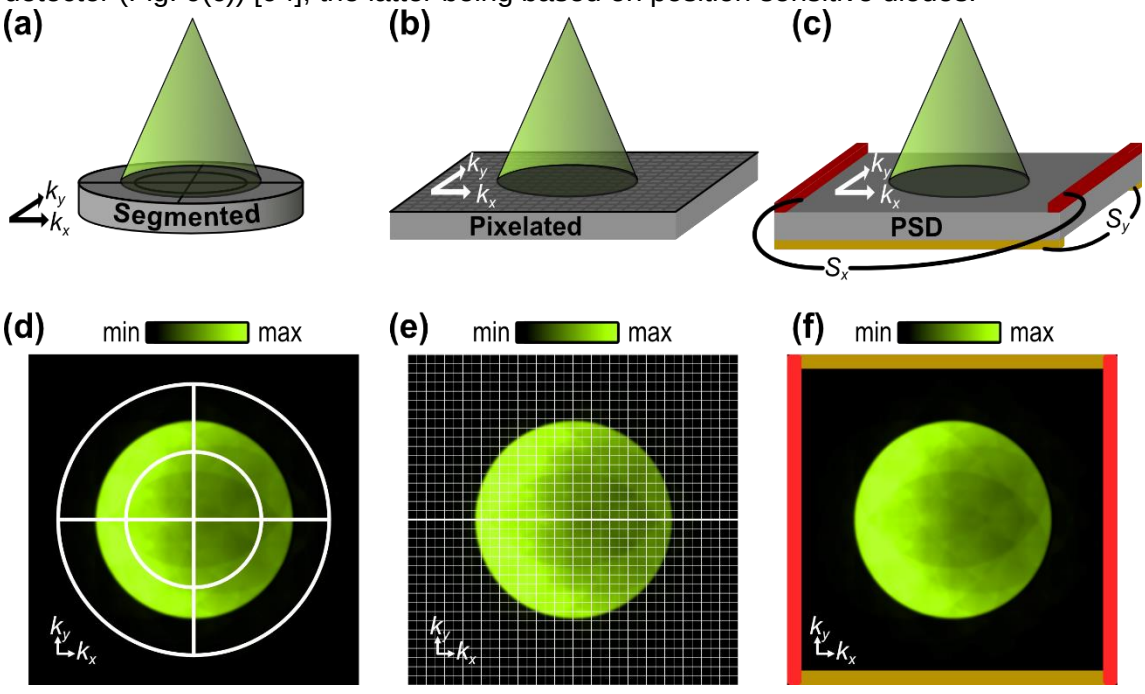

Figure 9: Three-dimensional sketches of (a) a segmented, (b) a pixelated and (c) a position sensitive diode detector, with (d-f) corresponding illustrations of the evaluation of the CBED intensity distribution in the detection plane. The intensity distribution is the one from Fig. 8.

It was already proposed in the 1970s by Rose [3] as well as Dekkers and Lang [4] to use a segmented detector for phase contrast imaging in STEM. The first segmented detector was realised by Chapman et al. [11] which was a split-detector consisting of two segments. Today's segmented detectors are usually divided into four quadrants [92], which can additionally contain further, but equally sized ring-shaped detector segments or a central hole [37–39]. Among these are the 16-fold segmented detector of Shibata et al. [39] and the eight-fold segmented detector [92] depicted in Fig. 9(a). The latter includes two polar detection intervals, which are both divided into four quadrants. The segments of a segmented detector typically consist of a scintillator material, e.g. lutetium oxyorthosilicate (LSO) or yttrium aluminium garnet (YAG), which are individually coupled into photomultipliers via fibre optics. Due to the fast decay time of scintillator materials and the individual read-out of only a few detector segments, intensities on the detector segments can be measured in a few microseconds and the DPC signal can be calculated in real-time. Segmented detectors are therefore particularly suited for in-situ investigations [26] or imaging of beam sensitive materials, which require a fast scanning of the electron beam. Segmented detectors obtain a DPC signal by comparing the intensities on diametrically opposed detector segments.

Pixelated detectors acquire an image of the intensity distribution at each beam position of the scan. STEM images obtained with a pixelated detector are therefore also referred to as 4D-STEM images, because each pixel (two real space coordinates) of the two-dimensional STEM image contains a two-dimensional image of the intensity distribution (two reciprocal space coordinates) [40, 95]. Since the camera resolves the intensity distribution in momentum space, images with a pixelated detector are also termed momentum-resolved STEM images [21, 25]. Typical pixelated detectors are based on charge-coupled device (CCD) [43, 49, 96] or complementary metal-oxide-semiconductor (CMOS) [97] technology. Simply put, the working principle of a pixelated detector (Fig. 9(b)) is like that of a fast camera [40]. Since the intensity distribution is captured with a typical resolution of several hundred by several hundred pixels (e.g. 512x512 pixels), using a pixelated detector facilitates a more accurate quantification of the CoM (Eq. 22) [9]. When analysing long-range electric fields leading to rigid deflections of the incident electron beam, it is also possible to obtain the DPC signal by detecting the edge position of the direct beam on the camera or finding the beam position via the optimum cross-correlation with the edges of an ideal beam [10, 49]. Besides typical pixel acquisition times in the millisecond range, 4D-STEM images generate up to tens or even hundreds of gigabytes of data volume per image, which is usually condensed into a DPC image only through time-consuming post-processing.

Non-pixelated detectors are intended to combine the accuracy of the CoM determination of pixelated detectors with the fast read-out speed of segmented detectors. Such a non-pixelated detector based on a position sensitive diode (PSD) has been developed and successfully employed by Schwarzhuber et al. [94]. An illustration of such a PSD based on a p-i-n-junction which is read-out by four opposing

electrodes is displayed in Fig. 9(c). The CoM of the intensity distribution is measured by evaluating the signals arriving at the four electrodes around the p-i-n junction.
It should be noted that non-pixelated and segmented detectors do not allow for direct DPC image and contrast interpretations as it is possible with pixelated detectors. This is due to the fact that non-pixelated and segmented detectors do not record the electron intensity distribution in the detection plane with a sufficient resolution in momentum space. In case of the segmented detectors, each detector segment intersects only a certain part of the diffraction pattern meaning that intensity modulations within individual segments cannot be considered. This is clear from Fig. 9(d), in which the intensity distribution in the detection plane is depicted and overlayed by the silhouette of an eight-fold segmented detector. Analogously, the same intensity distribution is shown in Figs. 9(e, f) on a pixelated as well as non-pixelated detector, respectively.
Since only the overall intensity and not the detailed intensity distribution is measured on each detector segment, features in the DPC image may also arise from the geometry and collection angles of the segmented detector, as will be shown in this thesis. To include the influence of the detector, Close et al. [36] developed an expression for the measurable electric field distribution based on a detector response function $D(\vec{k}_\perp)$ for segmented detectors. The detector response function accounts for the way the detector collects the intensity distribution. Using segmented detectors, the detector response function to measure the transferred momentum is defined as [36, 41]

$$D(\vec{k}_\perp) = \begin{cases} k_i & \text{if } I(\vec{\mathrm{k}}_\perp) \text{ is in the } i\text{th segment,} \\ 0 & \text{else.} \end{cases} \tag{23}$$

which links the intensity on a certain detector segment i to the geometrical centre of mass k_i of the detector segment i in momentum space.
This detector response function is included in a differential phase contrast transfer function (DPCTF) $h^{\mathrm{DPCTF}}(\vec{K})$, which also accounts for the properties of the incident beam via the aperture function $A(\vec{k}_\perp)$ and the lens aberration function $\chi(\vec{k}_\perp)$. The DPCTF is defined as [41]:

$$\begin{aligned} h^{\mathrm{DPCTF}}(\vec{K}) = \frac{1}{\vec{K}} \int A(\vec{k}_\perp) D(\vec{k}_\perp) \Big[& A(\vec{k}_\perp - \vec{K}) \exp\left(-i\chi(\vec{k}_\perp - \vec{K}) + i\chi(\vec{k}_\perp)\right) \\ & - A(\vec{k}_\perp + \vec{K}) \exp\left(-i\chi(\vec{k}_\perp + \vec{K}) - i\chi(\vec{k}_\perp)\right) \Big] d\vec{k}_\perp \end{aligned} \tag{24}$$

Here, $\vec{K}$ denotes the Fourier space coordinate of $\vec{R}$. According to Seki et al. [41] the measurable electric field distribution $\langle \vec{E}_\perp \rangle(\vec{R})$ can be described by a convolution of the true electric field in the specimen $\langle \vec{E}_\perp^T \rangle(\vec{R})$ with the inverse Fourier transform of the DPCTF $h^{\mathrm{DPCTF}}(\vec{K})$:

$$\langle \vec{E}_\perp \rangle(\vec{R}) = \langle \vec{E}_\perp^T \rangle(\vec{R}) \otimes \mathcal{F}^{-1}\left[h^{\mathrm{DPCTF}}(\vec{K})\right]. \tag{25}$$

Eq. 25 can thus be understood as an expansion of Eq. 20, as it includes the detector response function.

All in all, the segmentation of the detector influences the measured momentum transfer depending on how the segments intersect the intensity distribution of the beam after the beam has interacted with the specimen [41, 42, 98]. As a result the measurement with segmented detectors provides only an approximated first moment due to the reduced resolution in momentum space, leading to a reduction in measurable field magnitude [42] and artefacts in the DPC image. The artefacts in the DPC image are introduced when using segmented detectors possessing a quadrant geometry since the diffraction pattern projected on the detector exhibits a certain but typically different symmetry [99] depending on the crystalline specimen structure. This for example leads to difficulties in image interpretation close to a heterointerface of two materials [10, 16] with different crystal structures due to the different diffraction patterns and other effects such as dynamical diffraction. To reduce such influences, Seki et al. [100] recently developed a precession diffraction method using a series of tilts of the incident electron beam to reduce the influence of diffraction on the DPC images.
To reduce the influence of detector response function, Seki et al. have also shown that the true electric field magnitude can be approximated via a scaling factor [41]. However, this scaling does not reduce the directionality of image artefacts. Müller-Caspary et al. [42] propose a method to reduce the anisotropy of segmented detector response functions by using a Fourier-transform-based method, which they state might be problematic if the DPC image shows significant scan distortions.

In the following, an example for HAADF and DPC images at atomic resolution are shown in Fig. 10. These images are obtained from a 11.32 nm thick $SrTiO_3$ specimen structure in [001] zone-axis orientation and simulated by assuming an eight-fold segmented detector for DPC imaging. The simulations are based on the multislice algorithm Dr. Probe (Chapter 2.3) and use simulation parameters that match realistic (S)TEM operation conditions, e.g. the direct beam extending to half the outer annular ring of an eight-fold segmented detector as in Fig. 9(d). All other simulation parameters are given in Table 9 in the Appendix.
Fig. 10(a) shows the HAADF image, which can be simultaneously acquired to the DPC image. The HAADF image reveals the typical Z^{2-x} contrast described in Chapter 2.1.5, as Sr, Ti-O and O columns show a decreasing intensity. For identification of atomic columns, the projected $SrTiO_3$ crystal structure is illustrated in the lower right corner of each image in Fig. 10. Fig. 10(b) depicts the intensities incident on the four segments of the outer annulus. These segments are referred to as segments 5, 6, 7, 8 and their intensities are denoted by S_5, S_6, S_7 and S_8. It can be clearly seen in Fig. 10(b) that the intensity distribution strongly depends on the segment used. The difference in intensity dominantly arises from beam position dependent asymmetric intensity redistribution within the direct beam. Fig. 10(c) shows the S_x and S_y signals, which are the components of the DPC signal in x- and y-direction. These difference signals are obtained by using following equation for the x- and y-components:

$$S_{x;y} = \frac{(S_5 \pm S_6 - S_7 \mp S_8)}{(S_5 + S_6 + S_7 + S_8)} \tag{26}$$

Here, the upper cases of the $\pm$ and $\mp$ operators correspond to the S_x signal and the lower to the S_y signal, respectively. This way of determining the difference signal has been successfully applied in many publications [14, 37, 38] for homogeneous electric fields. It is again to note that the difference signals shown above give only an approximated CoM of the intensity distribution in the detection plane when investigating atomic electric fields [42]. Nevertheless, despite possible inaccuracies due to the approximation, the difference signals are related to the intensity redistribution in x- and y-directions and thus have been employed in early DPC studies at atomic resolution [8].

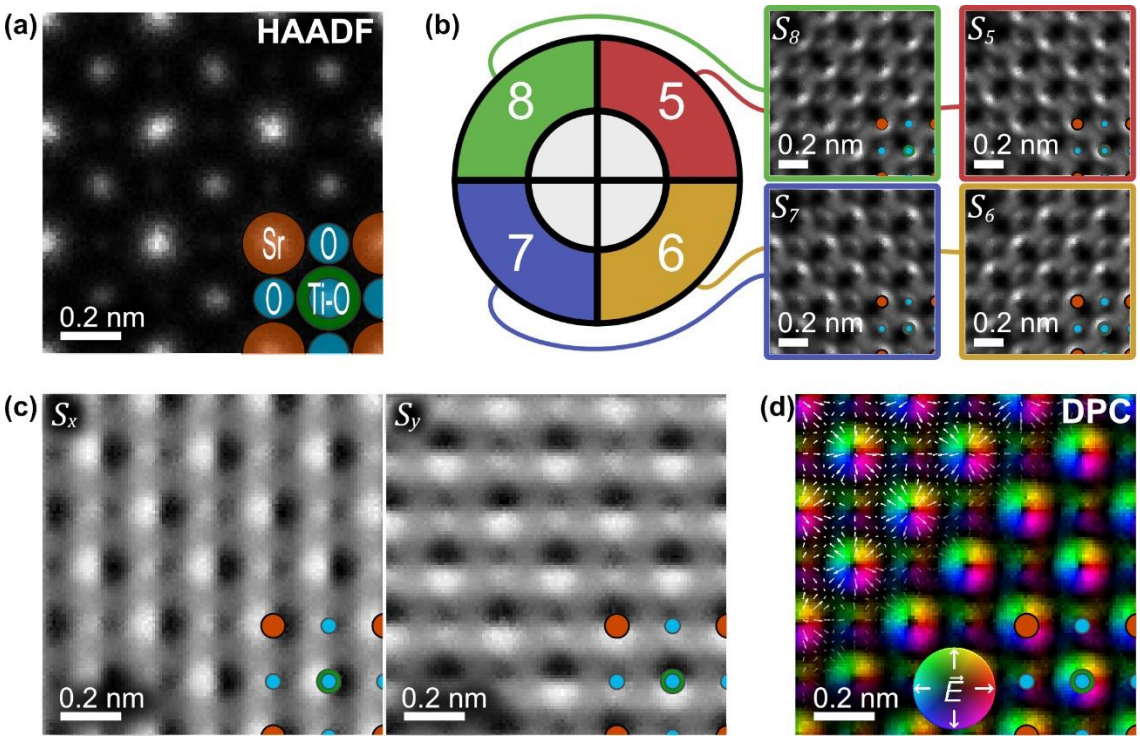

Figure 10: (a) HAADF image of $SrTiO_3$ in [001] zone-axis orientation. (b) STEM images obtained from segments 5, 6, 7 and 8 of the outer ring of an eight-fold segmented detector. (c) x- and y-components of the differential phase contrast signal. (d) Colour-coded representation of the differential phase contrast signals, indicating the electric field distribution. In all subfigures, a sketch of the considered $SrTiO_3$ crystal structure is given in projection. Images were obtained from multislice image simulations for a $SrTiO_3$ specimen thickness of 11.32 nm. A list of simulation parameters is compiled in Table 9 in the Appendix.

The components of the difference signal are typically combined in a vector map showing the deflection, transferred momentum or electric field distribution. Throughout this thesis, this vector map is referred to as the DPC image and is displayed either as an arrow-map or as a colour-coded image. Fig. 10(d) shows the colour-coded DPC image of the difference signals in Fig. 10(c). In the colour-coded DPC image, the colour indicates the direction and the colour intensity the magnitude of the displayed quantity, e.g. the electric field distribution indicated by the circular colour scale (also named colour wheel) in Fig. 10(d). Superimposed white arrows in parts of the DPC image indicate the electric field distribution as a vector map. As can be seen in Fig. 10(d)

rotational electric fields around atomic columns are evident. As these electric fields of individual atoms appear to be rotational symmetric and therefore contain all colours of the colour scale, they are referred to as colour wheels. Such rotational electric fields around individual atomic columns in $SrTiO_3$[001] have also been experimentally observed by Shibata et al. [24] using a segmented detector. Fig. 10 additional reveals the high capability of DPC imaging of light elements. This is particularly evident for the O atomic columns, which are clearly revealed by a rotational electric field distribution in the DPC image, while they are almost invisible in the HAADF image. DPC is therefore also a promising technique to investigate low-Z materials [86].

2.2.4. Specimen potentials and charge densities

Besides investigation of electric fields, phase contrast images obtained by using differential phase imaging can furthermore be used to calculate the specimen potentials and the charge density. Analysis of specimen potentials is possible with integrated DPC (iDPC), in which an integration based on a Fourier theorem is applied [89]. As the DPC imaging is particularly suited to investigate low-Z materials due to its contrast mechanism, iDPC is typically applied to reveal light elements such as oxygen or lithium in materials which consist of heavy and light elements [28, 86]. iDPC is also applied to investigate electron beam sensitive materials [101] such as zeolites [102] and metal-organic frameworks [103, 104].

From Maxwell's theory it is known that the divergence of the electric field distribution is related to the charge density [27]. Imaging of charge densities is therefore also referred to as differentiated DPC (dDPC). The charge density ρ is obtained by differentiating the measured projected electric field distribution $\vec{E}_\perp$ [9, 27]:

$$\rho = \varepsilon_0 \cdot \nabla \cdot \vec{E}_\perp \tag{27}$$

Here, ∇ denotes the two-dimensional Nabla operator used for differentiation of the projected electric field in x and y-direction and ε_0 the vacuum permitivity. The charge density consists of negative electrons ρ^e as well as positive protons ρ^p and the overall charge density $\rho = \rho^e + \rho^p$ is the sum of both. Since the measured electric field distribution is convolved by the incident electron beam intensity distribution I_i (Eq. 20), the true charge density ρ is also probe-convolved, i.e. $\rho = \left[\left(\rho^{\mathrm{T}} \otimes I_i\right)\right]$ with ρ^{T} the true charge density. The DPC measurement can therefore determine charge densities only with the spatial resolution of the microscope.

2.3. Multislice image simulations using Dr. Probe

To extract quantitative information from DPC measurements, the influence of parameters such as the specimen thickness, specimen tilt, lens aberration, detector response function and acceleration voltage on the obtainable DPC signal must be gaugeable. Since some of these parameters are difficult to adjust precisely or to measure, it is advantageous to investigate their influence numerically with the help of

computer simulations. Therefore, STEM image simulations based on the multislice algorithm implemented in Dr. Probe [44] are performed in this thesis. Dr. Probe is particularly suited for simulations of atomically resolved (S)TEM images and diffraction patterns because it considers a quasi-elastic interaction of the incident electron wave with the specimen structure, i.e. scattering with insignificant energy loss. In the following, the multislice algorithm is described with a special note on simulation parameters which considerably affect the obtainable DPC image. Further information on Dr. Probe and application examples in context of (integrated) differential phase contrast imaging can be found in references [44, 91, 105, 106].

The multislice algorithm is based on a wave-optical approach, in which an incident electron wave interacts with the potential of a specimen structure which is subdivided into small potential slices. The slices ideally contain only one atomic plane, and thus the propagation of an electron wave from atom to atom inside the specimen can be included. Multislice image simulations therefore overcome the limits of a description with the phase object approximation (Chapter 2.1.4), which assume a non-propagating electron probe and a projection of potentials.

Similar to the description of electron waves in a STEM in Chapter 2.1.2, the incident electron wave $\psi_i(\vec{k})$ can be described in reciprocal space coordinates $\vec{k} = (k_x, k_y)$ by a plane wave, which is altered by an aperture function and a coherent lens aberration phase function (see Chapter 2.1.2) [44]. As the incident wave interacts with the specimen potentials distributed in real space, the incident wave $\psi_{i=0}(\vec{r}) = \mathcal{F}^{-1}[\psi_{i=0}(\vec{k})]$ is transformed into real space coordinates by an inverse Fourier transform denoted by $\mathcal{F}^{-1}$.

The incident wave $\psi_{i=0}(\vec{r})$ interacts with the specimen potentials of slice i. This interaction is described by a multiplication with the specimen transmission function $q_i(\vec{r})$ of slice i. Afterwards the electron wave is Fresnel propagated onto the next slice $i+1$ by a multiplication with operator $P_i(\vec{k})$. The propagation of the electron wave is conducted in reciprocal space, such that the electron wave incident on slice $i+1$ is given by

$$\psi_{i+1}(\vec{r}) = \mathcal{F}^{-1}\left[P_i(\vec{k})\,\mathcal{F}[q_i(\vec{r})\,\psi_i(\vec{r})\right]. \tag{28}$$

The interaction and subsequent propagation of the electron wave is iterated until the target slice e or specimen thickness t is reached. Details on the propagation operator can be found in [44].

The specimen transmission function, which is also called phase grating, assumes that the electron wave function is only subjected to phase changes. Thus, the relation $q(\vec{r}) = \exp(i\sigma V_p)$, which is also considered in the phase object approximation (Eq. 9), is adapted and the overall projected potential V_p is replaced by the projected potential $V_{i,p}$ of the individual slice i. The specimen transmission function of slice i is given by $q_i(\vec{r}) = \exp\left(i\sigma V_{i,p}(\vec{r})\right)$ with the interaction constant $\sigma = m_{\mathrm{rel}}\lambda/(2\pi\hbar^2)$. The interaction constant includes the wavelength λ, the relativistic electron mass m as well as the

reduced Planck constant $\hbar$. Numerically the projected potential $V_{i,p}$ can be calculated by integrating the potential along the complete slice thickness from $t(i)$ to $t(i+1)$:

$$V_{i,p}(\vec{r}) = \int_{t(i)}^{t(i+1)} V(\vec{r},z)\mathrm{d}z \approx \int_{-\infty}^{+\infty} V_i(\vec{r},z)\mathrm{d}z = \mathcal{F}^{-1}[V_i(\vec{k},0)]. \quad (29)$$

As a slice ideally contains only one atomic plane, it is possible to further approximate the potential $V(\vec{r},z)$ by assuming a full potential $V_i(\vec{r},z)$ of atoms which possess a position in slice i (integration from $-\infty$ to $+\infty$ instead of $t(i)$ to $t(i+1)$). This allows to describe the projected potential of slice i in real space by an inverse Fourier transform of the projected potential in reciprocal space $V_i(\vec{k},0)$.

This is beneficial since the projected potential in reciprocal space $V_i(\vec{k},0)$ can be expressed by a sum of atomic form factors $f_\kappa^e(|\vec{k}|)$ of atomic species κ. Dr. Probe uses the atomic form factors published by Weickenmeier and Kohl [107] and their implementation follows

$$V_i(\vec{k},0) = V_{i,p}(\vec{k}) = \frac{2\pi\hbar^2}{m_0 \cdot a \cdot b}\sum_{\kappa=1}^{N_\kappa} f_\kappa^e(|\vec{k}|)\sum_{l=1}^{N_{\kappa,i}} \eta_{\kappa,l} e^{-2\pi i\vec{k}\vec{R}_{\kappa,l}}, \quad (30)$$

in which $\eta_{\kappa,l}$ denotes a factor for the partial site occupancy, $e^{-2\pi i\vec{k}\vec{R}}$ a phase factors to modify the atomic form factor according to atom position $\vec{R}_{\kappa,l}$, m_0 the electron rest mass, and $a \cdot b$ the lateral extension of the specimen structure, also referred to as supercell. $N_{\kappa,i}$ expresses the number of atoms of species κ in slice i and N_κ the number of atomic species κ. The pre-factor is necessary for a normalisation due to periodic boundary conditions.

It is important to note that the specimen potentials are generated from atomic form factors and do not include effects of bonding. Furthermore, the specimen potential slices are calculated with a reciprocal space resolution of $N_a \times N_b$. This resolution influences the accuracy of the calculation. Moreover, as N_a and N_b denote the number of discrete points of the reciprocal space, they also determine the maximum considered wavenumber which amounts to $k_{\max} \leq 1/3\min(N_a/a, N_b/b)$. As a result, it is possible to calculate the largest scattering angle $\theta_{\max}$, which amounts to $2\sin(\theta_{\max}/2) = \lambda k_{\max}$. The largest detection angle $\beta_{\max} < \theta_{\max}$ should not be larger than the largest scattering angle $\theta_{\max}$.

To include the interaction with phonons (thermal diffuse scattering) Dr. Probe uses the frozen-lattice (FL) approach [62, 108]. The FL approach applies random displacements to the atoms around their equilibrium position. This would correspond to a snapshot of atom positions during lattice vibration and is reasonable, as the atoms may be considered stationary during interaction with the electron beam [108]. The displacements follow a normal probability distribution, and the magnitude of the displacement is given a Debye-Waller factor $B = 8\pi^2\langle u_s^2\rangle$, which includes the isotropic equivalent mean square displacement amplitude $\langle u_s^2\rangle$.

For each slice of the input structure several FL configurations are calculated, the number of which can be chosen in Dr. Probe. Note that the number of slices of the

input structure is not necessarily the total number of slices of the simulation, as, for example, a unit cell can be used as an input file and then repeated to increase the specimen thickness. FL configurations are, however, only calculated for the input structure. To calculate the transmission functions at each pixel, Dr. Probe randomly selects one of the pre-calculated FL configurations for the slice potentials.

In experiments, a residual specimen tilt is sometimes present despite precise adjustments. It is therefore essential to enable the incorporation of specimen tilt in multislice simulations. In general there are different options available to include specimen tilt in multislice image simulations [109], namely tilt of the whole specimen, tilt of the beam or use of a tilted propagator which propagates the electron wave diagonally to the optical axis. Dr. Probe offers to tilt the specimen or the beam. Since only the latter does not cause increased computational effort for the calculation of the phase gratings, specimen tilt is modelled by tilting the beam.

Based on the previous descriptions, the Dr. Probe software primarily conducts the following two steps at each pixel to calculate a STEM image: First, the multislice algorithm is iteratively applied to the specimen structure to simulate the interaction of the incident electron beam with the specimen. Second, the STEM image acquisition is done by read-out of the resulting, post-specimen electron wave's intensity distribution with detector(s). The number and shape of detectors can be freely adjusted, e.g. to construct a segmented detector. Besides STEM images it is possible to calculate the CBED pattern intensity $I(\vec{k})$ as well as the real space probe intensity $I(\vec{r})$. This can be achieved after each iteration of the multislice algorithm and gives insights on the propagation of beam intensities within the specimen.

Chapter summary

- Modern aberration corrected scanning transmission electron microscopes (STEM), allow for atomic resolution imaging of solid materials, exploiting elastic and inelastic as well as coherent and incoherent scattering.
- Electrons, which are scattered to high polar angles in a Rutherford forward scattering process are considered in conventional high-angle annular dark-field (HAADF) imaging. The HAADF image contrast is roughly proportional to the atomic number Z^2. HAADF imaging has become a standard technique to detect the position of atomic columns or single atoms with accuracies < 10 pm.
- A thin specimen can be described by the (weak) phase object approximation, which allows to deduce quantitative information on the specimen potential without knowing the exact propagation of electron beam within the specimen. A true phase object only changes the phase of the incident electron beam and not its amplitude.
- Differential phase contrast (STEM-DPC) is a STEM method aiming to measure electric fields at atomic resolution. It relies on the measurement of transferred momentum imposed on the beam by Lorentz forces in electric as well as magnetic fields.

- The transferred momentum can only be measured with suitable detectors, which include segmented, pixelated, and non-pixelated detectors.
- For quantitative conversion of DPC images into electric field or charge density maps, the specimen must be a phase object and the beam must not propagate between pixels. The specimen thickness must therefore be in single digit nanometre range. Qualitative imaging can be conducted with thicker specimens and is useful for the detection of low-Z elements.
- Measured electric fields are influenced by the intensity distribution of the incident electron beam and in case of segmented detectors also by the detector response function. The detector response function is governed by the shape, the extension, and the orientation of the detector.

- STEM image simulations with a multislice algorithm are based on a wave-optical approach in which an incident electron wave interacts with the potential of a sample structure subdivided into small potential slices. This allows to study the propagation of the electron beam within the specimen and predict the detailed intensity distribution in the detection plane and in a DPC image.

3. Characterisation of the microscopes

This chapter describes the layout of the used microscopes, the signal acquisition and the calibration of DPC images. The two used microscopes, a JEM-ARM200F ACCELARM and a JEM-ARM200F NeoARM (in the following referred to as the NeoARM), are both manufactured by *JEOL* Ltd. (Tokyo, Japan). The description focusses on the layout of the JEM-ARM200F, as it is the microscope that is primarily used for the acquisition of DPC images in this thesis. Differences to the NeoARM are given at the end of this section. The description includes all the components required for the acquisition of DPC images as well as for further analytical analyses. Concurrently, the position of certain components in the column of the microscope are highlighted. The knowledge of the positions of components is mandatory for calibration of the microscope.

The JEM-ARM200F can be operated at acceleration voltages of 30 kV, 60 kV, 80 kV and 200 kV. The latter acceleration voltage offers the highest spatial resolution of approximately 70 pm (guaranteed by the manufacturer). This high resolution is made possible by a probe-side installed aberration corrector (C_s-corrector) which is an ASCOR corrector from CEOS GmbH (Heidelberg, Germany). Its working principle relies on two magnetic hexapole lenses in combination with transfer lens doublets, which allow for correction of lens aberrations up to the fifth geometrical order. With appropriate tuning of the C_s-corrector, even a spatial resolution in the range of 50 pm is possible at 200 kV.

A sketch of the layout of the microscope can be seen in Fig. 11. Electrons emitted by the cold-field electron gun (CFEG) are first accelerated by the accelerating tube and afterwards focused onto the specimen. The lens system above the specimen contains three condenser lenses, one of which is the condenser mini-lens directly above the specimen, two aperture drives (CL1 and CL2) sitting below the second condenser lens and each consisting of four individual apertures, and the C_s-corrector. In addition, deflector coils for the alignment of the microscope and scanning of the beam are installed. The deflector coils contain pairs of coils for gun alignment, spot alignment as well as condenser lens alignment. The illumination system also contains condenser lens stigmator coils, which are able to correct two-fold astigmatism in STEM and ellipticity of the incident beam in TEM mode.

The specimen is inserted into the microscope using a specimen holder which is mounted on a goniometer with a lock-load system to maintain the vacuum conditions. This goniometer allows to move the specimen in x-, y- and z-direction. In addition, the goniometer itself offers the tilting of the specimen by a rotation of the complete goniometer having its rotation axis in the x-direction. The EM01360RSTHB double-tilt holder manufactured by *JEOL* Ltd. has an additional step motor-driven tilting-axis for the specimen socket and is typically used as the specimen holder in this thesis. This additional tilting-axis is mandatory for the analysis of crystalline specimen, as the specimen must be carefully oriented in zone-axis orientation, not only to allow for high

resolution images, but also to allow for correct quantification of projected electric fields by DPC.

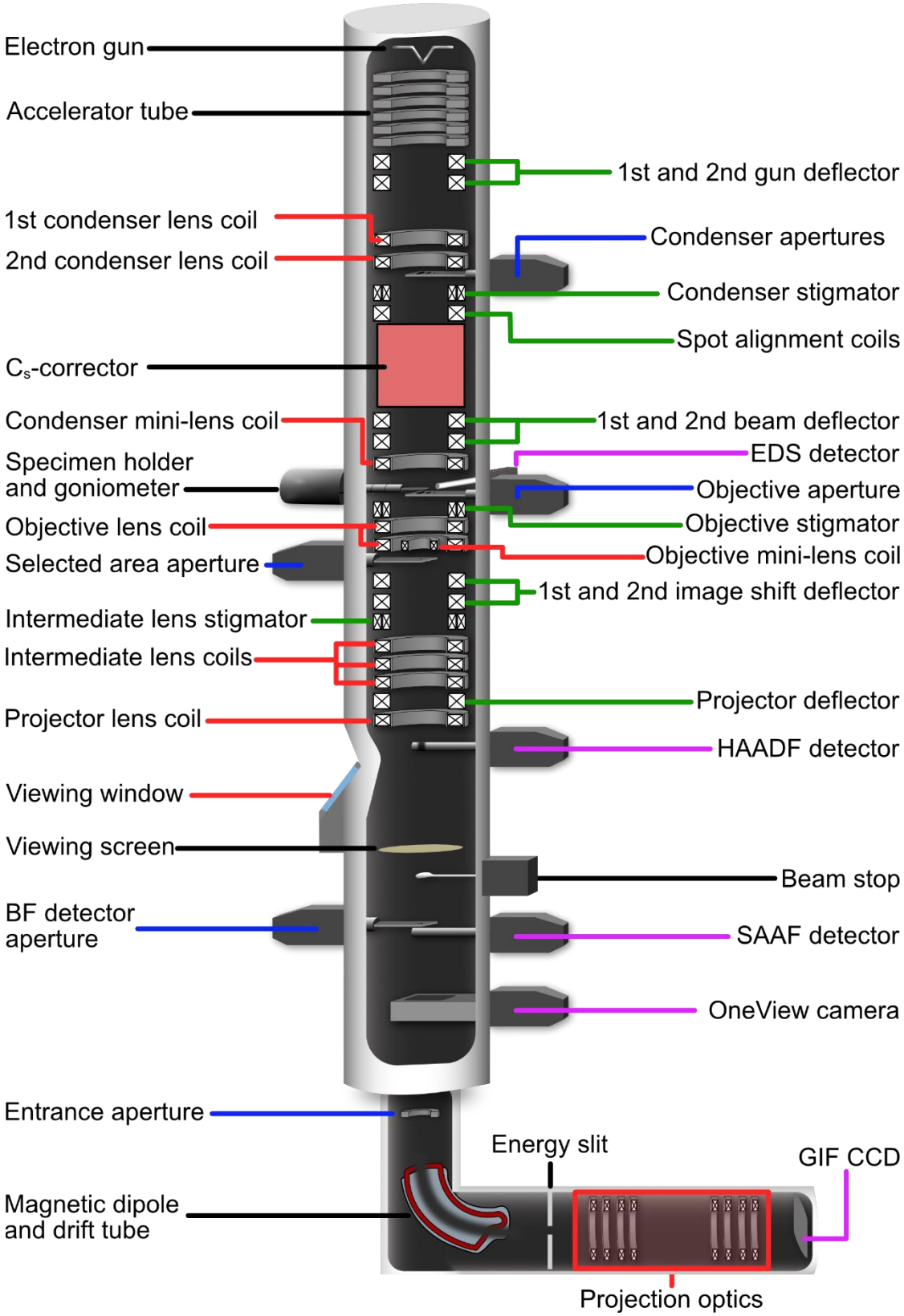

Figure 11: Sketch of the microscope layout of the *JEOL* JEM-ARM200F. For explanation of the components, the reader is referred to the main body of the text. Red-marked lines denote lenses, black-marked lines utility such as viewing screen, drift tube and electron gun, blue-marked lines apertures, green-marked lines stigmators and deflection coils and pink-marked lines detectors and cameras.

Below the specimen, an objective lens aperture can be placed to increase the contrast and select certain diffracted beams to contribute to a TEM image. This objective lens aperture is followed by an objective lens consisting of two objective lens coils as well as a mini-lens coil and subsequent selected-area aperture. Three intermediate lens coils and a final projector lens project the beam onto any detector, camera or viewing screen in the viewing chamber.

For imaging in STEM mode, an annular detector is positioned directly after the projection lens. This annular detector is typically used for high-angle annular dark-field (HAADF) imaging and is therefore referred to as the HAADF detector. A brief characterisation of the detector and its collection angles is given in Chapter 3.3. Furthermore, an eight-fold segmented detector is installed. This segmented annular all-field (SAAF) detector is the detector used for the acquisition of DPC images and therefore a detailed characterisation of it is given in Chapter 3.1. This detector can also work as a bright-field detector. An additional bright-field aperture is placed directly above the SAAF detector to select certain polar collection angle intervals in conventional STEM bright-field imaging. The SAAF detector is installed above a camera, which is a *GATAN* (Pleasanton CA, USA) OneView CMOS camera allowing for a resolution of 4096x4096 pixels.

For analytical investigations, the microscope is equipped with a *JEOL* SDD detector for energy-dispersive X-ray spectroscopy (EDS) analysis and a *GATAN* GIF-Quantum ER energy filter with a GIF CCD camera for energy-filtered TEM (EFTEM) and electron energy loss spectroscopy (EELS). The latter includes an entrance aperture, a drift tube, an energy slit (for energy-filtered TEM) and a projection optic consisting of several lenses and magnetic multipoles for aberration corrections. The energy filter can be used either in imaging or spectral mode and offers a dual mode, enabling an almost simultaneous measurement of two energy regions, e.g. the zero-loss region as well as a region containing an ionisation edge of an element.

The NeoARM at the University of Augsburg differs only by a few components. Regarding DPC, the main difference is the STEMx system by *GATAN* for hardware synchronized fast read-out of the OneView camera, allowing for acquisition of 4D-STEM images at 300 frames per second. In addition, a *GATAN* PEELS instead of the GIF-Quantum ER is installed on the NeoARM, which only allows to conduct STEM EELS analysis of specimen but not EFTEM. Furthermore, the electron-optical column in the NeoARM has a high-resolution pole piece, while the JEM-ARM200F has an ultra-high-resolution pole piece built in. This slightly increases the resolution of the JEM-ARM200F. However, as the resolution depends on the actual state of correction of residual lens aberrations, it is not useful to give a value for the difference in resolving power. Otherwise, the microscopes are comparable. This is particularly due to the fact that both microscopes are equipped with an ASCOR C_s-corrector. Thus, the obtainable image quality with both microscopes is quite the same.

3.1. Segmented detector sensitivities and calibrations

For DPC imaging with the JEM-ARM200F at Paderborn University the eight-fold segmented annular all-field (SAAF) detector is used. This detector consists of eight scintillator segments, which consist of lutetium oxyorthosilicate and are fibre-optically coupled to individual photomultipliers. The measurable signals after the photomultipliers are then read-out using eight individual 32-bit analog-to-digital converters allowing for the measurement of smallest intensity differences. Further details on a comparable segmented detector which has 16 instead of 8 segments can be found in reference [39].

A sketch of the detector illuminated by a simulated but typical convergent electron beam diffraction pattern is shown in Fig. 12(a). The SAAF detector is split into polar collection intervals each consisting of four segments. These collection intervals are denoted as Layer1 and Layer2 throughout this thesis. The inner ring (Layer1) comprises detector segments 1, 2, 3 and 4. The outer Layer2 consists of detector segments 5, 6, 7 and 8. Layer2 features a ring shape, and its polar collection interval is characterised by the inner collection angle β_{inner} as well as by the outer polar collection angle β_{outer}. The inner collection angle β_{inner} determines also the outer polar collection angle of Layer1. A speciality of the SAAF detector is its rotatability by an azimuthal angle of 90°. The precision by which the detector can be rotated was not investigated. However, angles with a precision of ±0.01° can be set in the software for controlling the detector rotation φ. Rotating the detector by 90° takes a few seconds depending on the range to be driven. Thus, changing the detector rotation is only practicable in between DPC measurements.

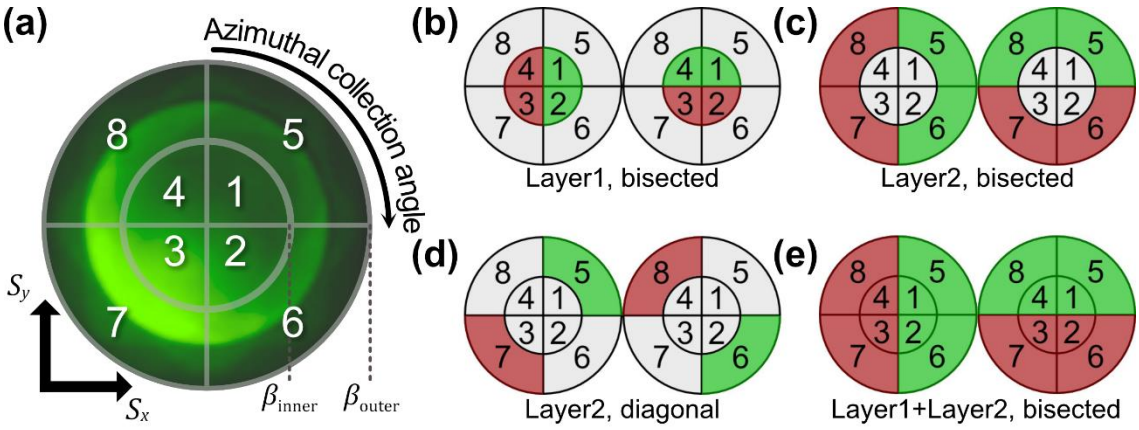

Figure 12: (a) Schematics of the segmented annular all-field detector with its eight segments. Different detector settings for the acquisition of DPC images with the bisected settings using the (b) inner and (c) outer segments as well as a (d) diagonal segmentation of Layer2 and (e) a bisected approach of the entire detector. Each individual figure shows two detectors with a green and a red marked area. The purpose of the red and green marked area is given in the main body of the text. The left detector schematics in (b-e) exemplify the calculation of the S_x difference signal, while the right ones show the determination of S_y difference signal.

Gain and offset of the photomultipliers are automatically levelled by using an auto-gain function of the software delivered by the manufacturer. This ensures that the

measurable signals on different detector segments are similar for homogeneous illumination conditions. Homogeneous illumination conditions imply a uniform intensity of the beam which is perfectly centred on the detector and thus illuminates an evenly large area of all detector segments. For the auto-gain function, a convergent electron beam in vacuum at the same camera length and probe size as during the subsequent DPC measurement but with a larger extension than the detector is used. The larger extension is achieved by using a larger condenser lens aperture than in the DPC measurement. Thus, the current density of the beam during the auto-gain calibration is like the one during the measurement.

Images are acquired using the software delivered by the manufacturer, i.e. *SAAF Center* in case of the ARM200F. For each detector segment, an image is stored as a 32-bit .tiff-file in an unsigned greyscale data type. In addition, also the S_x and S_y difference signals, i.e. the difference of the intensities in the green minus the intensity of the red coloured detector segments in Figs. 12(b-e), as well as the colour-coded DPC image are stored. Further details on the detector settings and signal calculation are described in Chapter 3.1.1.

There are two different methods for acquiring a DPC image with such a segmented detector. Both methods with corresponding calibration between the difference signals $S_{x,y}$ and the deflection angle $\varepsilon_{x,y}$ are described in the following. In the first method, the calibration of difference signals is conducted in post-processing using a calibration factor (Chapter 3.1.1). The second method uses calibrated centres of mass of individual detector segments to calculate the overall centre of mass of the intensity distribution on the segmented detector (Chapter 3.1.2). The latter therefore requires measurements of the inner collection angle β_{inner} as well as the outer collection angle β_{outer}. It is to note that both methods give qualitatively the same measurable electric or magnetic field distribution as they both use the same measured intensities. However, as the calibrations are done separately, they might differ in the obtainable field magnitudes. Investigations on the differences are given in Chapter 6.1.3.

3.1.1. Signal-based calibration factor

In the first method of acquiring DPC images, the detector approximates the centre of mass of the post-specimen intensity distribution by comparing the intensities of combinations of opposing segments. In contrast to the second method, this one does not require the explicit knowledge of the polar and azimuthal collection angles of the detector. It can therefore be readily applied and is implemented in the software for live observation by the manufacturer.

Figs. 12(b-e) show different detector segment combinations for the acquisition of the DPC image. In all these figures, the intensities collected with a combination of segments inside the red marked area are subtracted from the ones in the green marked area. These combinations are referred to as different detector settings. Using only the segments of Layer1 in a bisected way (Fig. 12(b)) is referred to as the “Layer1, bisected” setting. Fig. 12(c) shows the “Layer2, bisected” setting, in which the

segments of Layer2 are combined in a bisected way. A diagonal setting using only the segments of Layer2 is displayed in Fig. 12(d) and using all segments of the detector in a bisected way ("Layer1+Layer2, bisected") is shown in Fig. 12(e). The mathematical equations for the calculation of the difference signals, S_x and S_y, are given in Table 2. The intensities detected by individual segments i are given by S_i.

In this thesis, the first method to acquire DPC images is used for most experimental and simulated DPC images if not stated otherwise. More importantly, DPC images are acquired using the "Layer2, bisected" setting, i.e. intensities of Layer2 are solely used and segments are combined in a bisected manner. According to literature, using only Layer2 gives a good approximation of the real centre of mass of the intensity distribution of the electron beam [36] and a larger ratio between the difference signal and the base signal, which is the overall intensity on the detector [38].

Table 2: Equations for the difference signals S_x and S_y acquired with an eight-fold segmented detector and with the detector segment combinations illustrated in Fig. 12.

Detector setting	$\boldsymbol{S_x}$	$\boldsymbol{S_y}$
Layer1, bisected	$\frac{(S_1+S_2-S_3-S_4)}{(S_1+S_2+S_3+S_4)}$	$\frac{(S_1-S_2-S_3+S_4)}{(S_1+S_2+S_3+S_4)}$
Layer2, bisected	$\frac{(S_5+S_6-S_7-S_8)}{(S_5+S_6+S_7+S_8)}$	$\frac{(S_5-S_6-S_7+S_8)}{(S_5+S_6+S_7+S_8)}$
Layer2, diagonal	$\frac{(S_5-S_7)}{(S_5+S_6+S_7+S_8)}$	$\frac{(S_6-S_8)}{(S_5+S_6+S_7+S_8)}$
Layer1+Layer2, bisected	$\frac{(S_1+S_2-S_3-S_4+S_5+S_6-S_7-S_8)}{(S_1+S_2+S_3+S_4+S_5+S_6+S_7+S_8)}$	$\frac{(S_1-S_2-S_3+S_4+S_5-S_6-S_7+S_8)}{(S_1+S_2+S_3+S_4+S_5+S_6+S_7+S_8)}$

To convert the resulting difference signals pixel by pixel into calibrated quantities such as the deflection angle $\varepsilon_{x,y}$ or the transferred momentum $p_{\perp;x,y}$ perpendicular to the optical axis, a calibration factor $c_{\mathrm{cal},\varepsilon}$ is necessary. Here, the indices denote that the following equations of this chapter are applicable to components in x- and in y-direction. The deflection angle can be obtained from the difference signals S_x and S_y using

$$\varepsilon_{x,y} = \frac{S_{x,y}}{c_{\mathrm{cal},\varepsilon}}. \tag{31}$$

The x- and y-components of the transferred momentum $p_{\perp;x,y}$ can then be calculated using the calibrated deflection angle $\varepsilon_{x,y}$:

$$p_{\perp;x,y} \approx \varepsilon_{x,y} \cdot k_0 \cdot \hbar = \frac{S_{x,y}}{c_{\mathrm{cal},\varepsilon}} \cdot k_0 \cdot \hbar. \tag{32}$$

Here, k_0 denotes the wavenumber of the incident electron beam and $\hbar$ the reduced Planck constant. The transferred momentum, wavenumber and deflection angle can in general be used in an intermixed way for a qualitative description of DPC images, as they are only differing by a multiplication with a constant.

The calibration factor $c_{\mathrm{cal},\varepsilon}$ can be determined before or even after the actual DPC measurements and the calibrated quantities are calculated in post-processing steps. The procedure for the acquisition of an appropriate calibration factor is based on a known convergent-beam electron diffraction pattern of any monocrystalline material and intentional deflections of the beam on the detector as well as the camera. This method is already briefly described in reference [91]. In the following, it is explained in detail.

As a first step, the angle increment corresponding to the size of a pixel of the OneView camera is determined, i.e. the pixel length is converted into a deflection angle. It is to note that the angle per pixel particularly depends on the camera length as well as the acceleration voltage. Therefore, the following procedure needs to be conducted when changing any of the above-mentioned parameters. The determination of camera pixel's angle increments is achieved by using a characteristic feature of a convergent-beam electron diffraction pattern. For example, as shown in the schematics in Figs. 13(a, b), a pair of Kikuchi lines or two separated diffraction discs, which both have an angular spacing corresponding to two times the Bragg angle (Eq. 8), can be used. The latter is typically only applicable in the LowMag-mode of the TEM, because of the necessary small convergence semi-angles and high camera lengths. The Kikuchi lines can be used to calibrate the camera for DPC images acquired with small camera lengths and high convergence semi-angles, which are typical for high-resolution STEM.

Fig. 13(c) exemplifies the procedure by showing a CBED pattern of a monocrystalline Si specimen in [110] orientation. This image was captured on the OneView camera using a camera length of 12 cm and a 150 µm condenser lens aperture with a convergence semi-angle of approximately 120 mrad. Several pairs of excess and defect Kikuchi lines are observable, e.g. the ±(004) with twice the Bragg angle of $2\theta_B = 18.48$ mrad. By measuring the pixel distance of the ±(004) at the considered camera length of 12 cm, which is also used for all DPC measurements with the *JEOL* JEM-ARM200F, the angle increment of a camera pixel amounts to (8.9 ± 0.9) µrad. This value is determined by using the mean value and standard deviation derived from ten different line profiles with a line profile width of 50 pixels for integration.

For the next steps (Figs. 13(d, e)), the microscope must be in a mode with a stationary beam, i.e. a non-scanning beam. The direct beam must not interact with any electric or magnetic field inside a specimen, because a homogeneous intensity distribution in the direct beam is necessary. Therefore, the beam is optimally placed in a vacuum region of a non-magnetic specimen. The beam is then deflected by using the projector lens deflector coils (Fig. 13(d)) and its position is measured by determining the centre of mass of the complete intensity distribution on the camera. The measured displacement of the beam is assigned to a deflection angle by using the above-described camera pixel angle increment.

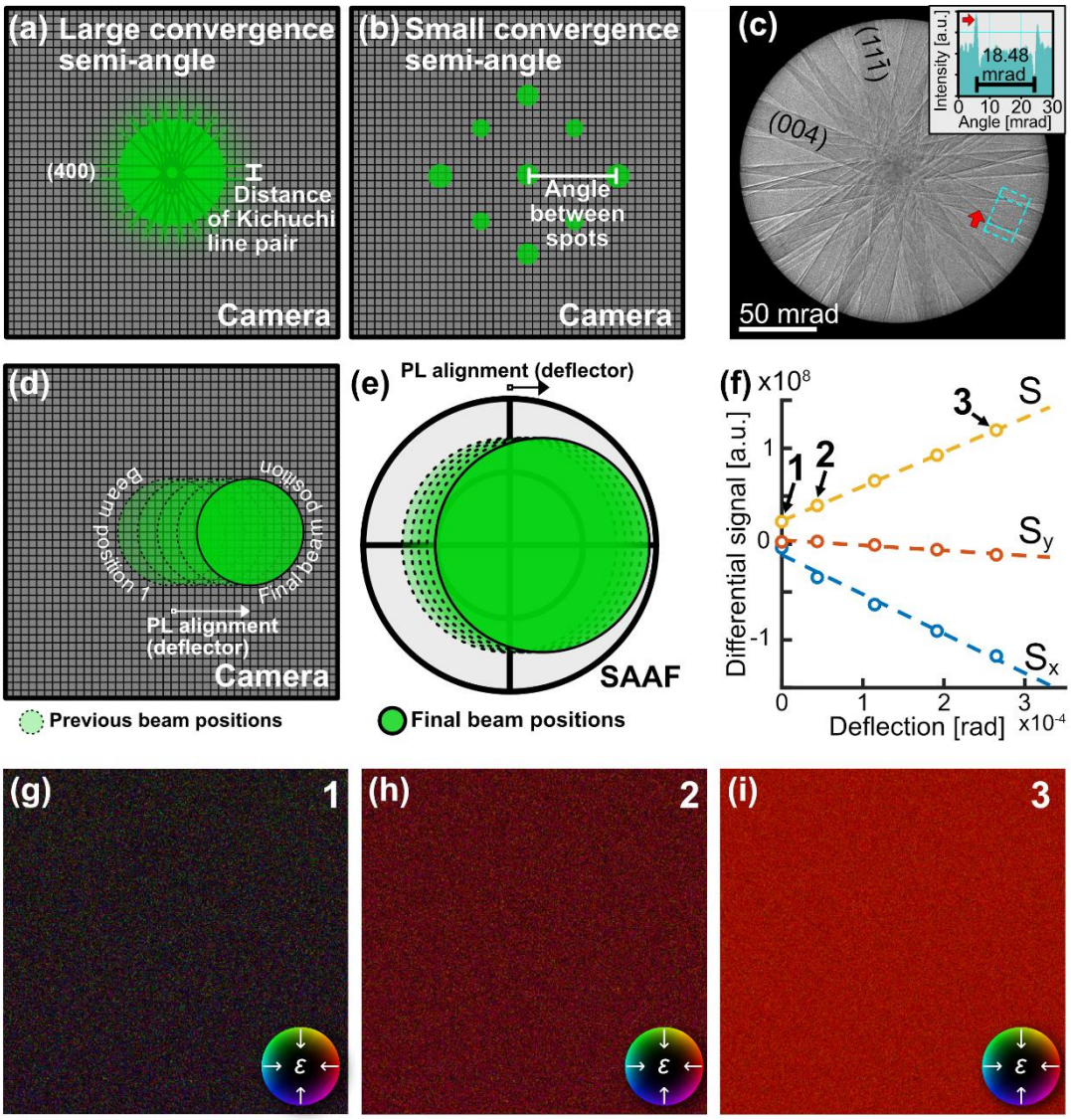

Figure 13: (a) Sketch of the diffraction pattern used for the camera calibration, The diffraction pattern containing Kikuchi lines present in the CBED pattern. (b) For high camera lengths in combination with small convergence semi-angles, the resulting diffraction discs can be used as an alternative to (a). (c) CBED pattern of Si in [110] zone-axis orientation with integrated line profile of the marked area. The red arrow denotes the direction of the line profile. The angular distance between defect and excess Kikuchi lines was used to calibrate the line profile as well as the CBED pattern. This CBED pattern has been acquired with the NeoARM at a camera length of 20 cm and with a 150 µm CL2 aperture. (d-e) Sketches of the procedure for determining the calibration factor. (d) The beam is intentionally deflected on the camera in defined steps using the projector lens deflector. (e) It is subsequently deflected on the SAAF detector with the same steps. (f) Mean difference signals of a 512 x 512 pixel DPC image plotted against the deflection angle. Linear fits of the difference signals S_x and S_y and the overall difference signal S are marked by dashed lines. (g-i) Exemplary DPC images for the measurement points marked as 1 (g), 2 (h) and 3 (i) in (f). All images in (g-i) were normalised to their maximum DPC signal. Thus, only the dominance of the red colour and not the intensity of the colour-coded DPC image can be used as an indicator for deflection magnitude. Lists of imaging parameters for (c) and (g-i) are given in Table 34 and Table 35 in the Appendix.

The deflection is performed in defined steps (Fig. 13(d)), leading to an almost equiangular distribution of data points when finally evaluated (Fig. 13(f)). It is to note that the measured beam position might be influenced by machine instabilities resulting from temperature or hysteresis induced drift of the lenses. This is accounted for by doing the measurement at least 2 h after switching the microscope in the

corresponding mode and by doing the deflection angle measurement as fast as possible, typically within a minute. Although the measurement must be conducted fast, sufficient intensities are necessary to reduce the influence of noise on the determination of beam positions.

Afterwards the beam is deflected with the same step size on the SAAF detector as depicted in Fig. 13(e). Analogously, the difference signals are measured at each step. Here, also a stationary beam is used, which needs to be perfectly centred on the detector before doing the procedure on the SAAF. At each step, a DPC image with 512x512 pixel is captured and the mean difference signal of all pixels is determined. The high number of pixels allows to account for noises arising from the detection process and the maximum dwell time of 1000 µs for a pixel.

Finally, the measured mean difference signals are plotted against the corresponding deflection angles. The resulting plots for the S_x, S_y and the overall $S = (S_x^2 + S_y^2)^{0.5}$ signal are depicted in Fig. 13(f). In Fig. 13(f), unexpected large magnitudes of the mean difference signals for a perfectly centred beam are observed, whereas a magnitude of zero is expected. The deviations of the mean difference signals from zero are due to image noise. Furthermore, the comparably large mean magnitude of the overall difference signal S can be explained by the fact that the S_x and S_y signals have positive and negative values, while the overall difference signal magnitude S only has positive values.

The calibration factor $c_{\mathrm{cal},\varepsilon}$ being the slope of a linear fit is deduced from the overall signal S (Fig. 13(f)). It is to note that an overall difference signal of approximately 10^8 is an order of magnitude below the maximum arising from the 32-bit resolution (signed data type ≈$2.1 \cdot 10^9$). The 32-bit resolution is not only setting the minimum detectable difference in deflection angle but also limits its maximum due to possible saturation of the AD converters, since the measured difference signals depend on the gain and offset settings of the individual photomultipliers. For optimum calibration, the range of deflection angles considered for calibration should, therefore, depend on the expected angles during the measurement. For high-resolution DPC imaging, it typically suffices to acquire a calibration factor for deflections below 1 mrad.

Since the calibration factor depends on the extension of the beam, which is predetermined by the camera length and lens settings of each individual microscope, the calibration factor is not transferrable to other microscopes, although they might have the same configuration. In addition, a new calibration factor has to be calculated if the gain of the individual photomultipliers is changed. One of the used calibration factors for the Paderborn JEM-ARM200F at an acceleration voltage of 200 kV and a camera length of 12 cm amounts to $c_{\mathrm{cal},\varepsilon} = (2.4 \pm 1.1) \cdot 10^{11}$ rad^{-1}. This calibration factor was determined from five beam deflection steps. The calibration factor also reveals the limit of the detector, which is in the mrad regime for the used combination of detector gain settings, camera length and size of condenser lens aperture as the bit depth is otherwise exceeded.

Figs. 13(g-i) exemplarily show colour-coded DPC images acquired with a stationary beam in vacuum and with different beam deflections corresponding to the data points denoted by 1, 2 and 3 in Fig. 13(f). Although all DPC images are normalised to their highest difference signal, a clear trend is visible. With increasing deflection of the stationary beam by the PL alignment, pixels exhibiting a red colour are becoming increasingly dominant. Following the chosen colour code, this is also in good agreement to the measured difference signals in x- and y-direction shown in Fig. 13(f) as both the S_x and the S_y become more negative with increasing deflection. Negative S_x lead to colours on the right half of the colour wheel and negative S_y values are found on the top half of the colour wheel. Thus, if both the S_x and S_y signal are negative, an orange colour can be expected.

3.1.2. Centre of mass and collection angles of segments

In addition to the post-acquisition calibration of the DPC images, it is also possible to use the collection angles and in particular the geometrical centre of mass of the detector segments in momentum space for the calculation of transferred momenta in x- and y-direction. The determination of transferred momenta then follows Eq. 22, in which p_i denotes the individual centre of mass of the detector segment i (p_i is denoted as $p_{\perp,\mathrm{px}}$ in Eq. 22, representing the geometrical centre of mass of a pixel).
Fig. 14(a) schematically illustrates a single detector segment in polar coordinates with polar angle β and azimuthal angle ϑ. The calculation of the geometrical centre of mass is based on the collection angle intervals of the detector segment, spanning an azimuthal range of $2\vartheta_1 = \pi/2$ (quadrant detector) and polar range of $\Delta\beta = \beta_{\mathrm{outer}} - \beta_{\mathrm{inner}}$ ($\beta_{\mathrm{inner}} = 0$ for Layer1). Instead of representing the geometrical centre of mass of each detector by an angle, the polar component of the $k_{i,\mathrm{Polar}}$ wavenumber perpendicular to the optical axis is used. To calculate $k_{i,\mathrm{Polar}}$ for segment i in polar coordinates, following equation can be used [36]:

$$k_{i,\mathrm{Polar}}(\beta,\vartheta) = k_0 \cdot \frac{\int_{-\vartheta_1}^{\vartheta_1}\int_{\beta_{\mathrm{inner}}}^{\beta_{\mathrm{outer}}} \beta\cos(\vartheta)\,\beta\,d\beta d\vartheta}{\int_{-\vartheta_1}^{\vartheta_1}\int_{\beta_{\mathrm{inner}}}^{\beta_{\mathrm{outer}}} \beta\,d\beta d\vartheta} = k_0 \cdot \frac{2\sin\vartheta_1(\beta_{\mathrm{outer}}^3 - \beta_{\mathrm{inner}}^3)}{3\,\vartheta_1(\beta_{\mathrm{outer}}^2 - \beta_{\mathrm{inner}}^2)} \quad (33)$$

When using this equation for the calculation of DPC signal, it is assumed that the sensitivity of the detector is homogeneous across the complete detector segment.
In Cartesian coordinates, the x- and y-components of the geometrical centre of mass of wavenumber perpendicular to the optical axis of each individual segment i can then be calculated using

$$k_{i,x} = k_{i,\mathrm{Polar}} \cdot \cos(\theta_i - \varphi) \quad (34)$$

and

$$k_{i,y} = k_{i,\mathrm{Polar}} \cdot \sin(\theta_i - \varphi), \quad (35)$$

in which θ_i denotes the azimuthal centre of mass of the detector segment and φ the clockwise detector rotation. For example, for a detector rotation of 0°, θ_5 of segment 5 shown in Fig. 12(a) amounts to 45° and θ_6 to 315°.

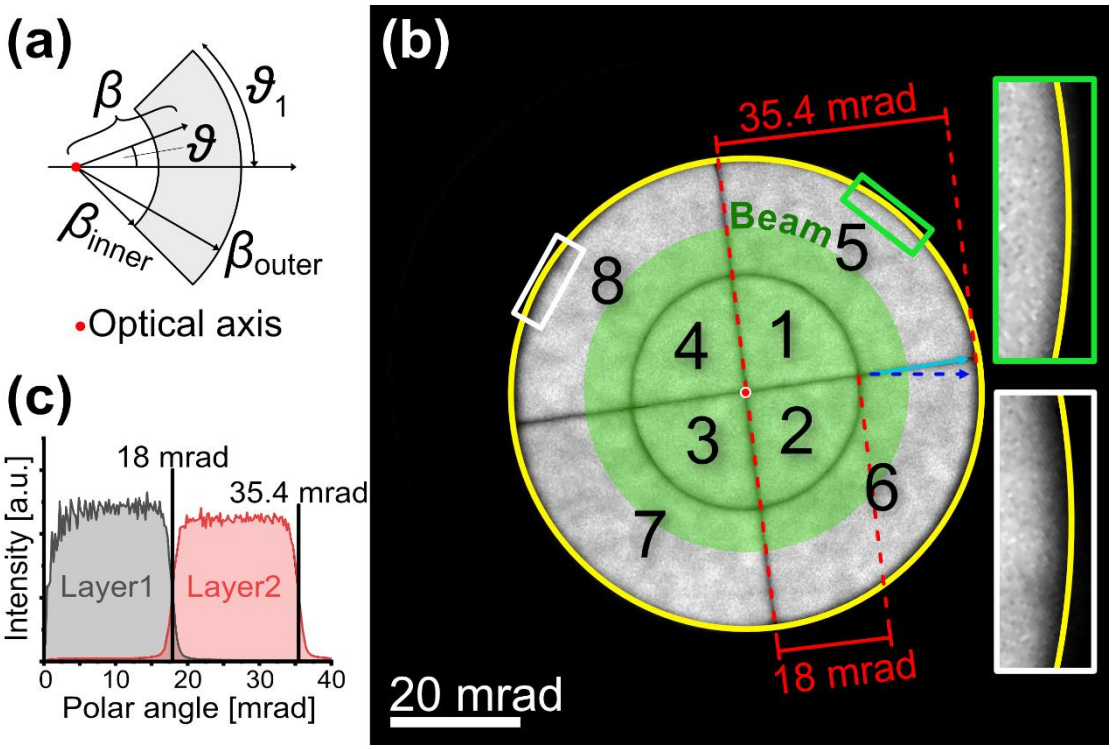

Figure 14: (a) Schematics for the definition of azimuthal ϑ and polar angles β of a detector segment with a polar collection interval ranging from β_{inner} to β_{outer} (adapted from [36]). Due to the segmentation into four quadrants, the azimuthal collection interval spans from $-\vartheta_1$ to $+\vartheta_1$ with $\vartheta_1 = \pi/4$. (b) Detector response function obtained by scanning a finely focused beam across the detector. The red dashed lines denote the inner and outer polar collection angles of $\beta_{\text{inner}} = 18$ mrad and $\beta_{\text{outer}} = 35.4$ mrad. The yellow circle is centred on the detector centre (optical axis) and used to show the geometrical shape of the detector. The white and green framed insets show the direction dependent extension of the detector. The semi-transparent green disc exemplifies the illuminated area of a convergent electron beam with a convergence semi-angle of 25 mrad at a camera length of 12 cm. For the calibration of the image, the reader is referred to the main body of the text. (c) Radial intensity profiles of the detector response function (b) for the segments of Layer1 and Layer2. These profiles are obtained by calculating the mean intensity on a complete circumference of a circle with a radius given by the polar angle. Imaging parameters of (b) are given in Table 36 in the Appendix.

Ultimately the transferred momentum $\vec{p}(\vec{R}) = (p_{\perp;x}, p_{\perp;y}) = \hbar \cdot \vec{k} = \hbar \cdot (k_x, k_y)$ at probe position $\vec{R}$ can be determined using the following equations which are based on Eq. 22 for the individual component in x- and y-direction

$$p_{\perp;x} = \hbar \cdot \frac{\sum_i k_{i,x} \cdot I_i}{\sum_i I_i} \tag{36}$$

and

$$p_{\perp;y} = \hbar \cdot \frac{\sum_i k_{i,y} \cdot I_i}{\sum_i I_i}. \tag{37}$$

In the above equations, I_i denotes the intensity measured with the ith segment. As this way of calculating the signals requires the polar and azimuthal collection angles, these

need to be determined before calculating the DPC image. However, this can also be done in post-processing if images of the intensities on the individual detector segments are stored.

In the following, the polar and azimuthal collection angles of the detector segments are measured. This is achieved by scanning a finely focused probe across the detector and in particular by using the STEM alignment mode, in which the projector lenses form an image of the probe in the detection plane. The resulting image is shown in Fig. 14(b). This image can be seen as the detector response function or the local sensitivity of the detector as the dwell time is the same for each pixel of the scan and the focused beam can be assumed to have a constant intensity. The angular calibration of this image is obtained by an analogous scan of the beam on the camera with the same extension of the scanned area, i.e. at the same magnification. Since the angle increment of a camera pixel at a given camera length is known from a CBED-based calibration (Chapter 3.1.1), the angular calibration of Fig. 14(b) is achieved by overlaying the scanned image of the detector response function with the scanned area on the camera. For visualisation purposes, the approximate extension of the beam on the detector is indicated by a semi-transparent green disc considering a convergence semi-angle of 25 mrad which is typically employed for DPC measurements at 200 kV and with $L =$ 12 cm as well as a CL2 aperture of 40 µrad.

The polar collection angles β_{inner} and β_{outer} can then be determined using radial intensity profiles of each individual layer by calculating the mean value of the detector response function along a complete circumference of a circle with radius β to the detector centre. The radial intensity profiles of the detector response function of Layer1 and Layer2 for a camera length of 12 cm are depicted in Fig. 14(c). By measuring the position of the crossing of the profiles of Layer1 and Layer2, β_{inner} of Layer2 amounts to 18 mrad. The same value is also usable for the outer polar collection angle of Layer1. The outer polar collection angle of Layer2 is estimated by the position of half the intensity at the outer edge of Layer2 and amounts to 35.4 mrad. The azimuthal distribution of detector segments leads to an equiangularly splitting into azimuthal collection intervals of 90°. The azimuthal detector rotation φ can be deducted from the angle between the x-direction (bright blue arrow) of the detector and the fast scan axis (dashed blue arrow). Here, the detector rotation φ amounts to 9°. These angles are not only important for the determination of the transferred momenta in the experiment, but also for DPC images simulations. For all DPC image simulations, if not otherwise stated, these estimated detector collection angles are used.

From Figs. 14(b, c), several other characteristics of the detector are noticeable. The signal generated by the detector is not homogeneous across a detector segment. This can be deduced from brighter and darker areas on the detector in Fig. 14(b) and noise-like fluctuations of the line profiles in Fig. 14(c). Possible explanations for this are contamination on the detector surface and deviations in local quantum efficiency of the detector segments. As the final DPC image is calculated using the intensity on complete detector segments, these local deviations in sensitivity cannot be accounted

for. Furthermore, the mean intensity in Layer1 is higher than in Layer2. This arises from a non-perfect auto-gain calibration but can be neglected if only one layer is used for the acquisition of DPC images. Another issue with scintillator-based devices that have several pixels or segments is that the process of photon generation within the scintillator and the transfer of photons to the photomultipliers is complex, as it depends on the path of the electrons in the scintillator as well as on possible photon scattering and reflection of the photons at the scintillator interface [110]. Especially the later might lead to the detection of intensity even if the beam is not incident on the corresponding segment. This hopping of photons between Layer1 to Layer2 is visible in the line profiles in Fig. 14(c) at β_{inner}, as the line profile of Layer2 and Layer1 extend into the area of their counterparts. Furthermore, it is visible that the detector has an ellipsoidal shape. This is particularly evident from the perfect yellow circle, which is centred on the detector, and the insets in Fig. 14(b) showing a magnified area of the detector edge. It is visible that the detector perfectly hits the yellow circle in the green marked inset while it barely touches it in the white marked area. This ellipsoidal shape also remains during rotation of the detector. A possible explanation for this deviation from a perfectly round detector is a tilted installation of the detector. The difference in extension of the detector segments direction also changes the sensitivity in the respective directions as the fraction of the detector's illuminated area is different. This imposes an anisotropy in momentum space sensitivity. Further investigations and a method to reduce the momentum space anisotropy are given in Chapter A.1.4 in the Appendix. The ellipsoidal shape might also introduce a certain gradient to the radial intensity profiles shown in Fig. 14(c), especially at the edges of the detector segments.

3.2. Pixelated detector signal generations and calibrations

The NeoARM's OneView camera is calibrated in the same way as the OneView in the JEM-ARM200F by exploiting a convergent-beam electron diffraction pattern with characteristic features. The description of the calibration process can be found in Chapter 3.1.1. As the camera is used with a binned resolution of 512x512 pixels instead of 4096x4096 pixels, the calibration process of the camera is done with the same binning. The binning is necessary as it allows for a hardware-synchronised read-out with a frame rate of 300 frames per second, which drastically reduces the influence of specimen drift and amount of data generated along DPC image acquisition. As a result of the calibration, the angle increment of a camera pixel at a camera length of 40 cm, which is used in this thesis for all 4D-STEM DPC images, is (0.206 ± 0.001) mrad. The angle increment of a camera pixel is analogously determined using the mean value and standard deviation of the distance of characteristic features, which are derived from 10 different line profiles with a line profile width of 20 pixels for integration (not shown here).

Figs. 15(a, b) illustrate the calculation of the DPC signal from a convergent-beam electron diffraction pattern which is captured at one of the scan positions of a complete 4D-STEM DPC image. The CBED pattern was captured from a (23.0 ± 0.7) nm thick Si

specimen oriented in [110] zone-axis orientation and with the lowest possible dwell time of 3.3 ms and a convergence semi-angle of $\alpha = (27.3 \pm 0.4)$ mrad (indicated by a red arrow in Fig. 15(a)). The DPC signal is calculated in two different ways, the centre of mass of the intensity on the complete camera, which is commonly applied in literature [9, 10, 15, 25, 31] and the virtual segmentation of the camera. The calculation of the centre of mass (CoM) fulfils Eq. 22 and the determination of transferred momentum is split into the component in x-direction

$$p_{\perp;x} = \hbar \cdot \frac{\sum_{x,y} k_x(u,v) \cdot I(u,v)}{\sum_{x,y} I\,(u,v)} \tag{38}$$

and the component in y-direction

$$p_{\perp;y} = \hbar \cdot \frac{\sum_{x,y} k_y(u,v) \cdot I(u,v)}{\sum_{x,y} I\,(u,v)}. \tag{39}$$

In these equations, the intensity $I(u,v)$ is given by the intensity measured in a camera pixel (indicated in the inset in Fig. 15(a)) with coordinates u and v. Note that u and v are in the same direction as x and y if the rotation of directionalities due to the Lorentz force acting on the beam in the projection lenses is properly corrected (Chapter A.1.1). The parameter $k_{x,y}(u,v)$ denotes the x- and y-components of the wavenumber of a certain camera pixel and is determined by the angle increment of a camera pixel multiplied with the pixel's distance to the optical axis. More precisely, the parameter $k_{x,y}(u,v)$ is given in paraxial approximation by $k_{x,y}(u,v) = \varepsilon_{x,y}(u,v) \cdot k_0$ with the components of the deflection angle $\varepsilon_{x,y}(u,v)$ and the wavenumber of incident electron beam k_0. Therefore, the components of the deflection angle $\varepsilon = (\varepsilon_x, \varepsilon_y)$ are depicted in Fig. 15(a), which can be transferred to the wavenumber using above equation. In this thesis, the reference pixel for the CoM determination, which defines the optical axis, is determined by the central pixel of the camera (marked by a red dot in Fig. 15(a)). As the central pixel of the camera is not necessarily corresponding optical axis of the microscope, this results in an offset imposed on the measured CoM at all pixels. This offset is corrected by subtracting the mean DPC signal magnitude from the DPC image after image calculation.

The determined CoM for the example in Fig. 15(a) is marked by a purple dot. For the CBED pattern shown in Fig. 15(a), the deflection angle derived from the CoM amounts to $|\varepsilon| = 6.95$ mrad. This would correspond to a wavenumber perpendicular to the optical axis of $|k| = \left(k_x^2 + k_y^2\right)^{0.5} = 17.46$ nm^{-1} and a transferred momentum of $|p| = \hbar \cdot |k| = 1.2 \cdot 10^{-23}$ N·s.

In comparison to the DPC image calculation using the CoM, the determination of a DPC image based on using virtual segments is more similar to the acquisition of DPC images with segmented detectors. However, as the virtual segments can be freely projected onto the camera, using a pixelated detector with virtual segments offers a manifold of possibilities for investigation and finetuning of the DPC image acquisition. For example, the number of annular detector segments, the azimuthal distribution of segments, e.g. eight instead of four segments, the inner and outer polar collection

angles of detector segments as well as the detector rotation can be freely chosen. In this thesis, only a segmentation corresponding to the described eight-fold segmented detector is used and the collection angles as well as the detector rotation are varied.

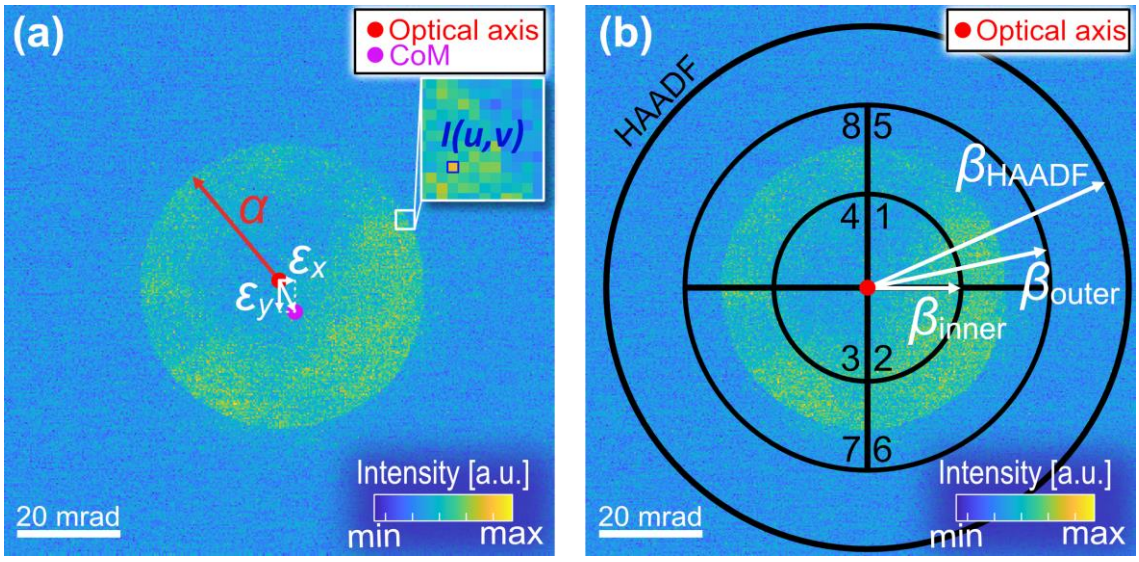

Figure 15: (a) Convergent-beam electron diffraction pattern of a (23.0 ± 0.7) nm thick Si specimen oriented in [110] zone-axis orientation with a convergence semi-angle $\alpha = (27.3 \pm 0.4)$ mrad. This CBED pattern is obtained during a 4D-STEM image acquisition with a dwell time of 3.3 ms. The determined centre of mass (CoM) and the optical axis, which corresponds to the geometrical centre of the direct beam, are marked by a purple and a red dot, respectively. The inset shows a magnified area at the edge of the direct beam and indicates the intensity $I(u,v)$ at a pixel (u,v). (b) The same CBED pattern, but with virtual detector segments. The polar collection angles $\beta_{\mathrm{inner}} =$ 18 mrad and $\beta_{\mathrm{outer}} = 35.4$ mrad are arbitrarily chosen for visualisation. The HAADF detector starts at a polar angle of 50 mrad. The ordering and orientation of segments shown in (b) corresponds to a detector rotation of 0°. Further details are listed in Table 37 in the Appendix.

Fig. 15(b) depicts the same CBED pattern already shown in Fig. 15(a) and includes superimposed detector segments which are marked by black lines. The detector segments are additionally marked with numbers that follow the same numbering as the ones of the SAAF detector and the segments of Layer2 range from polar collection angles of $\beta_{\mathrm{inner}} = 18$ mrad to $\beta_{\mathrm{outer}} = 35.4$ mrad. In addition, as a relatively large camera length of 40 cm is used, no physical HAADF detector can be used during the acquisition. At this camera length, the HAADF detector partially would block the beam, which would drastically alter the measurable DPC signal. Thus, the dark-field signal can only be obtained by a summation of the intensity of all camera pixels lying outside of the inner collection angle β_{HAADF} of the virtual HAADF detector (Fig. 15(b)).

The DPC signal is ultimately determined by the calculation of intensity in a virtual detector segment and by applying the method described in Chapter 3.1.2, which is based on the determination of transferred momentum using the geometrical centre of masses of the virtual detector segments. The intensity of a detector segment is obtained by a summation of the intensity on the camera pixels lying inside the corresponding virtual detector segment. By applying this method using the detector segments of Layer2, the determined deflection angle amounts to $|\varepsilon| = 1.69$ mrad. This corresponds to a wavenumber of $|k| = 4.26\ \mathrm{nm}^{-1}$ and a transferred momentum of

$|p| = 2.3 \cdot 10^{-24}$ N·s, both perpendicular to the optical axis. The large difference in deflection angle, wavenumber and transmitted pulse determined with the virtual detector segments and the CoM of the intensity distribution on the camera is due to the rather inhomogeneous intensity distribution and the fact that only Layer2 is used for image acquisition. Using a different detector setting, e.g. Layer1+Layer2, and detector extension, which can be adjusted via the camera length, as well as the detector orientation would result in different signals. This is further investigated in Chapter 6.1.4. However, it is to note that due to the detector response function and the rather large extension of the segments in momentum space as well as the usage of the geometrical centre of masses of the detector segments, virtual and physical segmented detector can only measure approximated centres of mass of the intensity distribution on the detector [36].

3.3. Annular dark-field detector

The scintillator-based annular dark-field detector, which is used for the acquisition of HAADF images, sits directly below the projection lenses as can be seen in Fig. 11. Depending on the camera length different polar collection angle intervals can be achieved for the detection of scattered electrons. As the contrast of HAADF images and the relative contrasts of atomic columns in HAADF images strongly depends on the polar collection angles of the detector, it is mandatory to investigate the HAADF detector and its collection angles. Thus, the HAADF detector is briefly investigated in the following.

An image of the detector response function of the annular dark-field detector can be seen in Fig. 16. It was similarly acquired as the detector response function of the SAAF detector by scanning a finely focused probe across the detector surface. Brighter areas within the detector convert the incoming electrons into an increased signal and can therefore be assigned to areas with higher sensitivity. It is to note that there is a circular area of the detector, which shows an overall brighter contrast than the rest of the detector. As this feature is not centred on the detector, it might impose a certain directionality of sensitivity to the scattered electrons. The effect of the detector non-uniformity is intensively studied in reference [111]. As a result, deviations from the theoretical contrast in the range of 10% can be expected [111]. For qualitative imaging, this does not pose a significant influence as the signal in HAADF imaging results from incoherent scattering. Furthermore, the mounting of the HAADF detector can be seen in the detector response function, leading to a blurred edge of the detector.

By using the calibration of the camera and scanning the beam on the camera as well as on the HAADF detector, the polar collection angles of the HAADF detector can be estimated. The detector annulus spans a polar angle interval of 158 mrad. The inner hole of the detector spans a polar angle interval of 106 mrad. This is indicated by the blue lines in Fig. 16. The optical axis, which is determined by the centre of the scanning area, is denoted by a yellow dot in Fig. 16. As the beam was centred on the SAAF detector before acquiring the image shown in Fig. 16, a discrepancy between

the geometrical centres of the HAADF detector and the SAAF detector can be observed. This discrepancy can be seen from the two blue lines with different lengths. Although this offset is present, a constant inner collection angle of 53 mrad can be assumed.

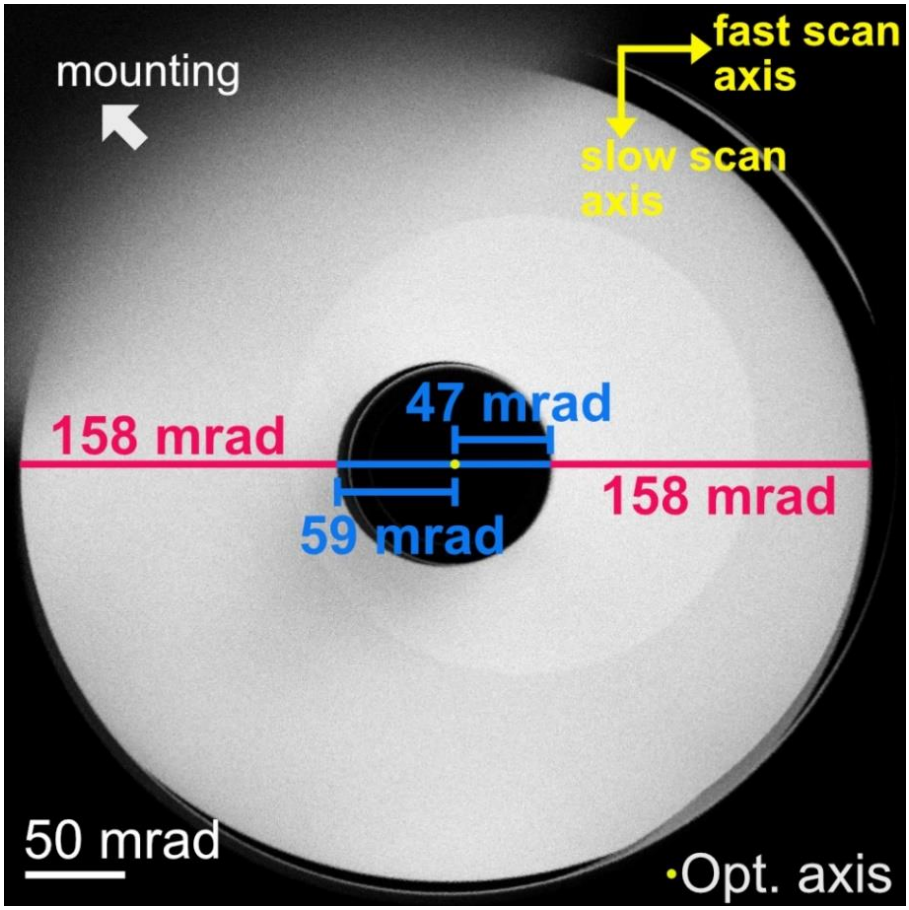

Figure 16: Detector response function of the annular dark-field detector. This image is acquired by scanning a finely focused probe across the detector. The acquisition process is similar to the process described for the SAAF detector in Chapter 3.1. Further imaging parameters are listed in Table 38 in the Appendix.

Chapter summary

- In this thesis, two microscopes, a *JEOL* JEM-ARM200F and a *JEOL* JEM-ARM200F NeoARM (referred to as the NeoARM), are used which are both equipped with a cold-field emission gun and a CEOS ASCOR C_s-corrector. The most important differences regarding this thesis are:
  - Segmented annular all-field detector (SAAF) in the ARM200F allowing dwell times in the µs range
  - Pixelated detector (*GATAN* OneView with fast read-out package) in the NeoARM allowing dwell times in the ms range
  - Ultra-high-resolution pole piece in the ARM200F and high-resolution pole piece in the NeoARM

- DPC signals can be obtained with the segmented detector by comparing intensities of opposing detector segments.

- Using pixelated detectors, the DPC signal can be determined from the centre of mass of the intensity distribution on the detector as well as by summing up the intensity in detector segments virtually projected onto the pixelated detector.

- For quantitative analysis a calibration is mandatory, which allows to convert the difference signal to a transferred momentum and a wavenumber perpendicular to the optical axis as well as a deflection angle.
- The transferred momentum, wavenumber and deflection angle can be in general used in an intermixed way for a qualitative description of DPC image, as they are only differing by a multiplication with a constant.

- Two calibrations are described for the segmented detector which rely on a known diffraction pattern captured with the camera and
  - scanning the beam across the detector to measure the geometrical centre of masses of the detector segments as well as
  - intentionally deflecting the beam with the projector lens deflectors on the camera and the SAAF detector measuring the signal difference as a function of the deflection.
- Azimuthal and polar collection angles of the SAAF and the annular dark-field detector are determined as they are necessary for comparable multislice image simulations.

4. Post-processing of DPC images

After acquisition, the captured intensities on the eight segments, the resulting difference signals in k_x- and k_y-direction, and the calculated colour-coded DPC image are stored in a 32-bit .tiff image format by the software delivered by the manufacturer. In order to obtain quantitative values from the images, the DPC images have to be processed. This is done with the self-written stand-alone *MATLAB* software "*DPCToolbox*", which is freely available from the author and the attached CD. In this software, all tools for the optimisation and quantitative analysis of DPC images used in this thesis are included. Furthermore, most of the visualisations and plots are achieved with this software. In addition, there are some machine-dependent influences on the images that must be eliminated prior to the quantitative analysis as they might lead to artefacts hampering correct image interpretation. Many of these artefacts can be corrected with this software. The correction of machine-dependent artefacts, which are partly unavoidable during the measurement, are described in the Appendix in Chapter A.1. One of the artefacts is the rotation of the deflection direction due to the Lorentz force, which acts on the electron beam in the magnetic fields of lenses between the specimen and the detector. The correction is described in Chapter A.1.1. After correction, the k_x- and k_y-directions are aligned with the x- and y-directions in real space, i.e. a deflection to the right side of the DPC image is correctly measured as a deflection to the right side. Thus, k_x and x as well as k_y and y can be interchangeably used in terms of directionality.

For each individual image pixel (x, y), the software recalculates the difference signals in x- and y-direction plus the colour-coded DPC image from the intensities of the individual segments (32-bit .tiff file). With the calibration procedure and the resulting calibration factor described in Chapters 3.1 and 3.2, the difference signal S_x and S_y can be converted into calibrated maps of a certain quantity, such as the deflection angle in [rad], the wavenumber perpendicular to the optical axis in [1/nm] and the transferred momentum in [$\hbar$/nm]. In this section, mainly the transferred momentum perpendicular to the optical axis will be used. Since there is no rigid deflection of the electron beam when investigating atomic electric fields, the use of the term deflection might therefore lead to a misunderstanding. However, all the procedures shown are also applicable to the expectation values of the other calibrated quantities as they are linked to the expectation value of transferred momentum by a scaling factor.

This chapter starts with the description of the calculation of the electric field and charge density distribution in Chapter 4.1 and includes the calculation of specimen thickness. The so-called scattergram, which is a two-dimensional histogram of the displayed quantity in the DPC image, and its calculation are then explained in Chapter 4.2. In addition, the novel scattergram filter, which is a filter to investigate characteristic features in momentum space, and its application are also shown in Chapter 4.2. The main difference between pixelated and segmented detectors is the possible resolution in momentum space. Since the SAAF detector is rotatable by 90°, a method to

increase the azimuthal momentum space resolution is given in Chapter 4.3. At atomic resolution, the beam is typically scanned with very low dwell-times to reduce the influence of specimen drift. This introduces considerable image noise. Chapter 4.4 therefore explains the algorithms used to reduce image noise in atomically resolved DPC images. Finally, routines for the determination of atomic column positions are given in Chapter 4.5.

4.1. Quantitative DPC imaging

This chapter describes how electric fields and charge densities are calculated from the calibrated transferred momentum distributions. According to Eq. 13 and Eq. 19, the exact specimen thickness is required in addition to the transferred momentum. Therefore, the following chapter describes the determination of a thickness map that accurately quantifies the specimen thickness at each pixel of the DPC image (Chapter 4.1.1). Subsequently, the formulas implemented in the *DPCToolbox* software for calculating the electric fields and charge densities are described (Chapter 4.1.2).

4.1.1. Determination of specimen thickness

According to the classical and quantum mechanical description of DPC contrast (Eq. 13 and Eq. 19), the specimen thickness at each pixel (x, y) enters inversely into the calculation of electric field magnitudes. The local thickness of the specimen thus has a strong influence on the field magnitude calculated from the calibrated difference signals. So far, the application of an accurate thickness map in DPC imaging has been barely discussed in literature. It furthermore remains challenging when specimens with inhomogeneous composition are investigated. In the following, three different approaches for the calculation of an accurate thickness map $t(\vec{R})$ depending on the probe position $\vec{R} = (x, y)$ are described. From a microscopist's point of view, the determination of specimen thickness should always be conducted prior to DPC analysis since contamination might build up during DPC image acquisition. Moreover, the methods for the calculation of the specimen thickness map are identical for electric and magnetic fields. Therefore, the presented methods are also relevant for magnetic field investigations.

In the first approach, the local thickness is determined using the HAADF signal and the EFTEM log-ratio method [73]. Since HAADF images are acquired simultaneously with DPC images, the HAADF image always shows the same image area as the DPC image. As described in Chapter 2.1.5, the intensity measurable at a pixel depends on the projected atomic number, which depends on the chemical elements and on the thickness present at a pixel. If the material consists of a single crystallographic phase, i.e. no variation of chemical composition is present in the investigated area, the HAADF intensity is primarily influenced by the morphology of the specimen. Using the EFTEM or STEM-EELS log-ratio method, minimum and maximum thickness in the area can be estimated and thus the HAADF intensity converted to a thickness value in the range of

minimum to maximum thickness. This approach is suitable for specimens with a homogeneous chemical composition.
In the second approach, a thickness map is loaded into the *DPCToolbox* software. This can be a section of the EFTEM thickness map, or a constructed thickness map for specimens with phases of different chemical compositions. For a constructed thickness map, which can be a greyscale .tiff file, the intensity must correspond to the local specimen thickness. These true thickness values can be determined via a EFTEM thickness map. Therefore, this approach can be used for the calculation of specimen structures with phases of different chemical composition.
The third approach is to create a thickness map with constant thickness. This thickness map can be used, e.g. for DPC images with atomic resolution for which a homogeneous thickness is expected. The specimen thickness can be obtained from EFTEM or EELS measurements using the log-ratio method at the location where DPC measurements are subsequently made. As only atomically resolved electric field maps are shown in this thesis, this is the only method used for the calculation of specimen thicknesses.

4.1.2. Electric fields and charge densities

For the calculation of electric field maps, the deflection angle $\varepsilon_{x,y}(\vec{R})$ or the transferred momentum $p_{\perp,x,y}(\vec{R})$ resulting from the calibration process and the specimen thickness $t(\vec{R})$ are necessary. The calibration process is described in Chapters 3.1 and 3.2 and converts the measured signal $S_{x,y}$ via a calibration factor $c_{\mathrm{cal},\varepsilon}$ into corresponding quantities. Based on [51] the components of the electric field are calculated as

$$E_{\perp;x,y}(\vec{R}) = -\frac{\varepsilon_{x,y}(\vec{R})\cdot m_{\mathrm{rel}}\cdot v_{\mathrm{rel}}^2}{e\cdot t(\vec{R})} = -\frac{p_{\perp,x,y}(\vec{R})\cdot m_{\mathrm{rel}}\cdot v_{\mathrm{rel}}^2}{p_0\cdot e\cdot t(\vec{R})} = -\frac{S_{x,y}(\vec{R})}{c_{\mathrm{cal},\varepsilon}}\cdot\frac{m_{\mathrm{rel}}\cdot v_{\mathrm{rel}}^2}{e\cdot t(\vec{R})}, \tag{40}$$

with m_{rel} the relativistic mass, v_{rel} the relativistic velocity of electrons, e the elementary charge and p_0 the incident momentum parallel to the optical axis. It is to note that the electric field is always antiparallel to the transferred momentum and all electric field magnitudes are normalised by the local specimen thickness. The electric field is thus given in units of [V/nm].
The charge density $\rho(\vec{R})$ is given as the result of the multiplication of the divergence of the electric field $\vec{E}_{\perp}(\vec{R})$ with the vacuum permittivity ε_0. Gauß' law states that:

$$\rho(\vec{R}) = \nabla\cdot\begin{pmatrix}E_{\perp;x}\\E_{\perp;y}\end{pmatrix}\cdot\varepsilon_0 = \left(\frac{\partial E_{\perp;x}(\vec{R})}{\partial x}+\frac{\partial E_{\perp;y}(\vec{R})}{\partial y}\right)\cdot\varepsilon_0. \tag{41}$$

The 2D divergence is calculated using the gradient of electric field components $E_{\perp;x}(\vec{R})$ and $E_{\perp;y}(\vec{R})$. These gradients are calculated with a built-in *MATLAB* function based on a Sobel gradient operator. In this thesis, the charge density is a volume density and is given in units of [C/m^3].

4.2. Scattergram and scattergram filtering

DPC images, like all other measurements, can be analysed in a myriad of ways, such as line profiles, mean values of regions of interests and many more. In this thesis several influences on DPC images are investigated in Chapter 5, which typically act on all pixels, but might be different from pixel to pixel. Thus, it is beneficial to not only analyse a certain area or an average signal but the entire signal distribution of the DPC image and determine the changes to the DPC signal as well as characteristic features arising from the influences.

One possible method to investigate any field quantity displayed in the DPC image (e.g. deflection angle, transferred momentum, electric field magnitude) is the so-called scattergram, which is a two-dimensional histogram of the displayed field quantity. In the following, the scattergram is presented using the transferred momentum distribution $\vec{p}_\perp(\vec{R})$.

$SrTiO_3$ has served as a test material in many TEM investigations due to its high beam stability and relatively simple unit cell containing atoms with high and low atomic number. It was impressively used in one of the first STEM DPC images at sub-atomic resolution by Shibata et al. [8, 24]. Thus, $SrTiO_3$ is also considered in the following. Fig. 17(a) depicts a simulated DPC image of $SrTiO_3$ in [001] zone-axis orientation. This DPC image simulation was obtained using the mutlislice algorithm Dr. Probe [44] and assuming a segmented detector. It is to note that the scattergram is not only applicable when using segmented detectors but is useful with any DPC detector (Chapter 2.2.3). The DPC image shows the transferred momentum using a colour code. The directionalities of the colour code are given by the arrows within the wheel-like colour scale in the lower right corner.

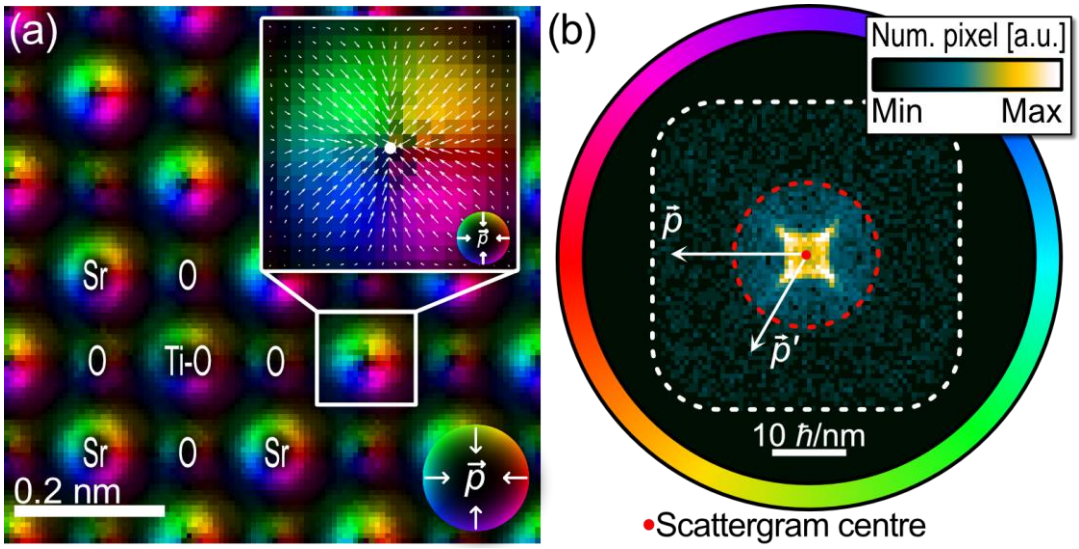

Figure 17: (a) Simulated DPC image $SrTiO_3$ in [001] zone-axis orientation with an inset showing a magnified DPC image of a Sr atomic column superimposed with electric field vectors (quiver plot). The white dot in the inset denotes a rough estimation of the the atomic column position. (b) correpsonding scattergram showing the number of pixels in a certain interval of transferred momentum direction and magnitude with two exemplarily marked transferred momenta $\vec{p}$ and $\vec{p}'$. A list of simulation parameters is compiled in Table 10 in the Appendix.

In Fig. 17(a), rotational-symmetric colour wheels are visible around each atomic column which are exemplarily indicated by their respective elemental composition in Fig. 17(a). To illustrate the calculation of the scattergram, the inset in Fig. 17(a) shows a quiver plot (white arrows, here without any calibration) of the transferred momentum distribution around an atomic column. The atomic column position is depicted by a white dot. As can be seen, around the atomic column a transferred momentum towards the atomic column is evident, which is also expected due to the Coulomb interaction with the screened potential of the positively charged nucleus. The magnitude of transferred momentum indicated by the length of the arrows increases and then decreases with increasing distance to the atomic column centre due to the projected potential landscape. Following the colour code, a red pixel corresponds to a transferred momentum to the left and a yellow pixel corresponds to an arrow pointing to the lower left.

Fig. 17(b) displays the scattergram calculated from the DPC image shown in Fig. 17(a). The scattergram is a two-dimensional histogram, it depicts the accumulated number of pixels $N_{\mathrm{acc.,px}}\left(\vec{p}_{\perp}(\vec{R})\right)$ with a transferred momentum in a certain interval of transferred momenta of the total DPC image or a selected region of interest of it. The scattergram thus is a representation of the momentum space.

The momentum space intervals are characterised by the direction and magnitude of transferred momentum which would analogously correspond to azimuthal and polar deflection intervals. The ordering of the pixels in the scattergram also follows the colour code. This means that the direction of transferred momentum is given by an azimuthal ordering around the scattergram centre and the magnitude is given by the distance to the centre of the scattergram. For reference, the coloured frame around the scattergram is provided. Pixels allocated far off the scattergram centre result from DPC image pixels exhibiting strong deflections. Following this distribution, e.g. a red pixel in the DPC image with high magnitude of transferred momentum corresponds to a scattergram pixel at the end of the arrow marked by $\vec{p}$ shown in Fig. 17(b). Analogously, a dim yellow pixel in the DPC image would correspond to a scattergram pixel at the end of the arrow marked by $\vec{p}'$. Here, both arrows represent the transferred momentum direction and magnitude. Furthermore , it is to note that the coloured frame around the scattergram and the scattergram distribution are typically rotated by 180° around the scattergram centre (e.g. shown in Fig. 18) as the electric field distribution is typically displayed with the coloured DPC image. A rotation of 180° compensates for the anti-parallel directionalities of electric field and transferred momentum distribution.

The resolution and displayed range of the transferred momentum space within the scattergram can be arbitrarily chosen by the maximum considered transferred momentum magnitude and by setting the image resolution of the scattergram, which determines the size of the $\vec{p}_{\perp}(\vec{R})$ intervals. This means that it is possible to calculate a scattergram with 2048x2048 pixels from a DPC image with 64x64 pixels. However, due to the cumulative process to calculate the scattergram intensity distribution it is not always useful to have a higher number of pixels in the scattergram than in the DPC

image. Furthermore, the calibration and thus the size of a scattergram pixel in momentum space is given by the maximum displayed transferred momentum divided by half the number of scattergram pixels in one direction (centre to periphery). In this thesis, all scattergrams of DPC measurements and simulations are calculated with the same number of pixels as the corresponding DPC image and are obtained using the *DPCToolbox*.

The scattergram in Fig. 17(b) exhibits several characteristic features. Listing them in an order with decreasing extension, the features include a broad rectangular background feature with rounded corners (marked by a dashed white line), a disc-like feature (dashed red circle), and a square like feature with four minor side lobes in the centre of the scattergram. It is beneficial to know the origin of the transferred momenta in the DPC image which are responsible for these characteristic features inside the scattergram. Therefore, to reveal the spatial distribution of characteristic scattergram features in DPC images, a novel method, the so-called scattergram filtering, is introduced in the following.

For the scattergram filtering, an aperture function $a(\vec{p}_\perp)$ with the same number of pixels and momentum space resolution as the scattergram is used which equals to 1 for a transferred momentum lying inside the aperture and 0 outside the aperture. The aperture shape is only limited by the number of scattergram pixels. Thus, shapes like a circular spot, a wedge, a square and combinations of the afore-mentioned aperture types can be applied. For scattergram filters with a low number of scattergram pixels, round aperture features are subjected to squaring. In scattergram filtering, the filtered DPC image is calculated by multiplying the value of the aperture function with the given $\vec{p}_\perp(\vec{R})$ at probe position $\vec{R} = (x, y)$. Thus, the filtered image $\vec{p}_{\perp;\mathrm{filtered}}(\vec{R}) = a(\vec{p}_\perp) \cdot \vec{p}_\perp(\vec{R})$ shows only those features of the initial DPC image exhibiting deflection magnitudes and directions which are selected by the scattergram filter aperture. The calculation of scattergram-filtered images is also done using the *DPCToolbox*.

The scattergram filtering is demonstrated in the following on the DPC image and corresponding scattergram already shown in Fig. 17. Fig. 18 displays the simulated DPC image and the corresponding scattergram achieved with a specimen thickness of 3.51 nm at a defocus of -2 nm and without further lens aberrations in an unfiltered (a-b) and filtered state (c-j). Further information on the simulation parameters is given in Table 10 in the Appendix.

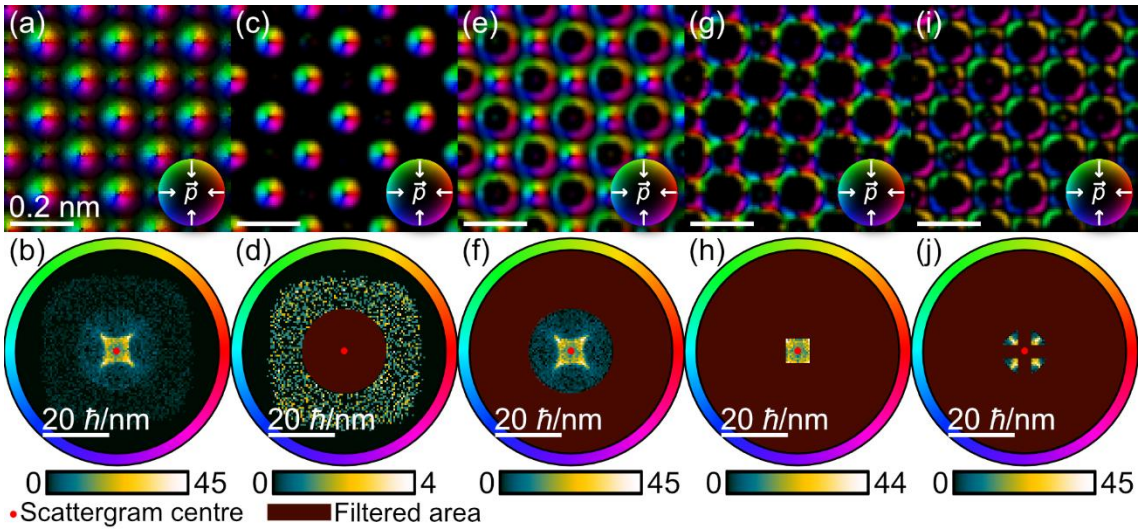

Figure 18: (a) DPC image simulation with corresponding scattergram (b) of a 3.51 nm thick $SrTiO_3$ structure in [001] zone-axis orientation simulated at a defocus of -2 nm and without other lens aberrations. (c-d) DPC image simulation and scattergram, where only those $\vec{p}$ with lead to the colour wheel distribution of Sr and TiO columns pass the filter. (e-f) DPC image simulations with corresponding scattergram after application of a filter exhibiting deflections mainly at oxygen sites. (g-h) DPC image simulations and scattergram, where the filter selected the inner part of the scattergram. The scattergram exhibits a square-like feature and with minor side lobes. The latter are analysed in more detail using a filter on these side lobes. The corresponding DPC image simulation and scattergram are displayed in (i-j). The filtered area is marked by a dim red colour in all scattergrams. Simulation parameters are compiled in Table 10 in the Appendix.

Several characteristic features in the unfiltered scattergram in Fig. 18(b) can be seen, whose origin in the DPC image can be revealed by scattergram filtering. The filtered area is always indicated by a dim red area. Since the magnitude of transferred momentum increases from the centre of the scattergram towards the periphery, the characteristic round shaped feature far off the scattergram centre is expected to arise from the strong atomic potentials at atomic columns. As it is observable from Figs. 18(c-d), where an aperture filter is used, only the transferred momenta near the atomic positions of Sr and Ti-O columns but not the pure O columns contribute to this part of the scattergram. Furthermore, Figs. 18(e-f) display the DPC image and scattergram of the inner part of the scattergram which was filtered in Fig. 18(d). The scattergram in Fig. 18(f) exhibits a central disc, which contains a pronounced square with minor side lobes. While the round shaped intensity in the scattergram can be linked to the oxygen sites, the square with side lobes results from the transferred momentum distribution at interatomic positions. The square-like feature with minor side lobes is studied in more detail in Figs. 18(g-h). These features arise from the diffraction effects and the extension of the beam, as will be discussed in Chapter 5. In addition, the small distances of Sr and Ti-O columns to the O columns in <100> direction lead to the square-like feature. As can be seen from the DPC image and scattergram in Figs. 18(i-j), the minor side lobes of the square-shaped central part of the scattergram emerge from transferred momenta at pixels halfway between the atomic columns. These features in the DPC image leading to minor side lobes in the scattergram extend especially in <110> directions.

4.3. Increasing azimuthal momentum space resolution

Image artefacts [91, 112] which are typically accompanied by reduced measurable DPC signal magnitudes [41] can occur due to the low momentum space resolution of segmented detectors (Chapter 2.2.3). For segmented detectors with a quadrant geometry, for example, the detector response function exhibits a four-fold symmetry [98, 112]. The signal obtained from a CBED pattern with a six-fold symmetry thus changes depending on the orientation of the detector response function. The influence of the detector response function of a segmented detector on DPC images is investigated and discussed in great detail in Chapter 5.1. Additionally, its impact on the obtainable iDPC images can also be found in references [98, 112]. The influence of the momentum space resolution on the measurable DPC signal has been theoretically described by Seki et al. [41] (Eq. 24 and following). According to this theoretical description, the measurable DPC signal at each probe position is given by a convolution of the true electric field, the incident beam's intensity distribution and the detector response function. Therefore, one of the goals is to reduce the influence of the detector response function on the measurable DPC signal by increasing the polar and azimuthal momentum space resolution of segmented detectors.

For this, Li et al. recently proposed a post-processing method that considers the in-plane rotation of either the segmented detector or the specimen [112] and, hence, allows to increase the azimuthal momentum space resolution. It is to note that the rotation of the specimen also changes the orientation (rotation) between the CBED pattern and the detector response function. According to Li et al. [112], the difference signals with increased azimuthal momentum space resolution are obtained by virtually spliting the detector into a multi-segment detector and using several DPC images that are acquired with different orientations of the CBED pattern and the detector. The number of detector segments of the multi-segment detector depends on the number of steps of detector or specimen rotation. The calculation of the difference signals is based on a linear combination of the intensities measured with certain opposing segments [112]. The actual number of necessary equations and combination of intensities on the opposing detector segments depends on the number of detector rotation steps. This virtually allows to calculate difference signals from detector segments that extend across smaller azimuthal collection intervals than the quadrants of the native detector. Li et al. [112] were able to prove that even dynamical diffraction contrasts which increase with increasing specimen thickness [91] can be drastically reduced. The improvements have also been experimentally shown by iDPC images of an InGaN/GaN quantum well structure [112].

The method proposed by Li et al. only allows to calculate the difference signals of opposing detector segments. It is, however, beneficial to know the intensity distribution in the detection plane with increased azimuthal momentum space resolution. Besides reducing artefacts in the DPC image, increasing the momentum space resolution is therefore also benefecial as it helps to examine the intensity distribution in the

detection plane to better understand contrast mechanisms in DPC images. In the following a different method is proposed, which allows to reveal the intensity distribution on the detector with increased azimuthal momentum space resolution (IAMSR) by creating a multi-segment detector through post-processing. It is therefore referred to as the IAMSR method. The DPC signal is afterwards calculated using the geometrical centre of masses of the virtually created detector segments in a similar way as described in Chapter 3.1.2. Similar to the method proposed by Li et al. [112], IAMSR-DPC images can be achieved by rotating the detector or the specimen. This chapter's purpose is to describe the basics behind the IAMSR method. An example of application, proof of principle and quantitative comparison to the DPC image obtained from the CoM of the intensity distribution on a pixelated detector are given in Chapter 6.1.5.

When rotating the detector, the segments collect electrons in different azimuthal angle intervals of the momentum space. This can be seen in Fig. 19(a), where a sketch of the eight-fold segmented SAAF detector is shown for a detector rotation of 0° (straight black line). Additionally, the azimuthal collection intervals for detector rotations of 10° and 20° are depicted by the dashed black and dashed red lines.

Fig. 19(b) shows a typical CBED pattern for a 30.72 nm thick Si specimen structure calculated with the multislice algorithm Dr. Probe [44]. The CBED pattern was simulated for Si[110] at a beam position 0.01 nm right of a Si atomic column (blue dot in Fig. 20(a)). The resulting CBED pattern shows an intensity redistribution in the direct beam with an increased intensity deflected in the direction of the atomic column position. Intensities of the CBED pattern in Fig. 19(b) are given as a fraction of the total beam intensity. A compilation of simulation parameter is given in Table 11 in the Appendix.

As the CBED's intensity distribution in the detection plane is unaffected by the detector rotation, the measured intensities of the detector segments only depend on the collection intervals. This can already be seen in Fig. 19(b) where the silhouette of the detector (grey lines) for a detector rotation of 0° is plotted on top of a CBED pattern. Additionally, azimuthal collection angles of a detector rotated by 60° are depicted by the red straight lines.

The intensities on the segments of a segmented detector are depicted in Fig. 19(c) and Fig. 19(d) for a detector rotation of 0° and 60°, respectively. These intensities experimentally correspond to the integrated intensity in the azimuthal and polar collection interval of a detector segment and are obtained from the CBED pattern and internally calculated by Dr. Probe. The color scale again depicts the beam intensity. It is clearly observed that the measurable intensities of the individual detector segments change when rotating the detector. The change in intensities on the detector segment, when the detector is rotated, predominantly depends on the homogeneity of the CBED intensity. The intensities of the detector segments shown in Figs. 19(c, d) are in good agreement to the CBED intensity distribution in Fig. 19(b). This is particularly evident for segment eight.

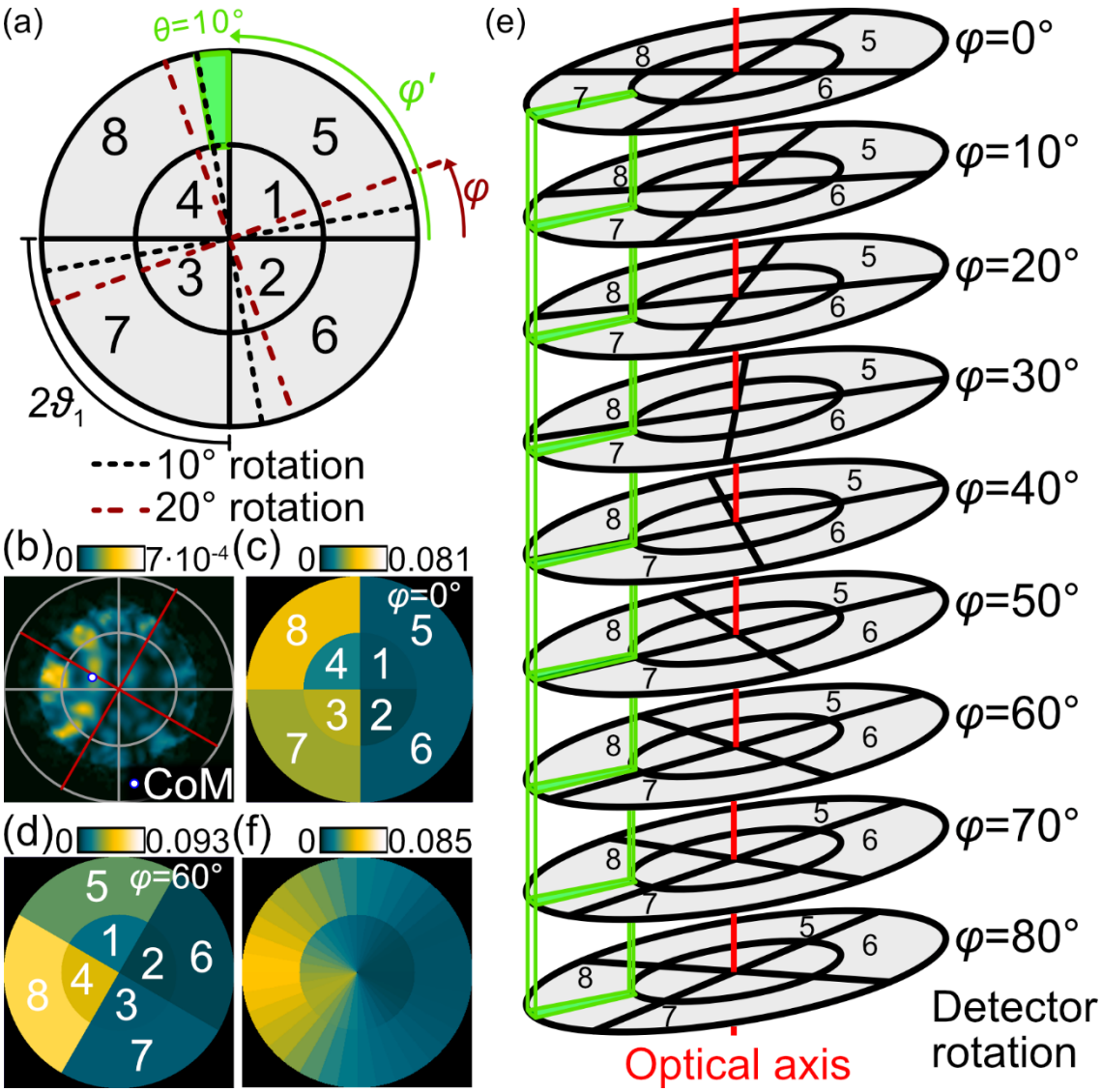

Figure 19: (a) Sketch of the detector under different detector rotations. The azimuthal intervals for the collection of electrons are depicted by the straight solid (detector rotation of 0°) and dashed (detector rotation of 10°) black line, as well as by a straight dashed red line (detector rotation of 20°). (b) CBED pattern of a 30.72 nm thick Si[110] crystal at a beam position marked by the bright blue dot in Fig. 20(b). The beam is shifted by 0.1 nm to the right side of a Si atomic column. Intensities are given as a fraction of the incident electron beam intensity. Intensities collected with the segmented DPC detector for a detector rotation of (c) 0° and (d) 60°. Integrated intensities are again normalised to correspond to a fraction of the incident beam intensity. (e) Sketch of an azimuthal angle interval to be calculated for a detector undergoing a rotation series with a step size of 10°. The green marked area hits different segments of the detector along the rotation. (f) Calculated intensity after applying the IAMSR method with the same step size. A list of simulation parameter is compiled in Table 11 and Table 12 in the Appendix.

To increase the azimuthal momentum space resolution, the IAMSR method uses the changes in intensity on the segments of a genuine quadrant detector under detector rotation. Assuming that the intensity distribution of the CBED pattern in all pixels of the DPC images remains constant during the acquisition of a detector rotation series, the IAMSR method divides the momentum space into smaller azimuthal momentum space intervals according to the number of rotation steps of the detector rotation series. These azimuthal momentum space intervals can be interpreted as virtual detector segments which, in accordance with Li et al. [112], together are referred to as a multi-

segment detector. The angular size of the virtual detector segments is given by step size of detector rotation. It should be noted that in the IAMSR method, the intensity on the virtual detector segments is obtained only from individual STEM images acquired with the individual detector segments and not by projecting the virtual segments onto a measured (4D-STEM) CBED intensity distribution.

Fig. 19(e) exemplarily shows such a virtual detector segment on Layer2 of the SAAF detector which is marked by the green area and spans an azimuthal range of 10°. This virtual detector segment and the genuine detector are illustrated for different rotations of the genuine detector ranging from 0° to 90° with step size of 10°. As the detector is rotated in steps of 10°, only the relative azimuthal position of the virtual detector segment on the detector changes, while its distance to the optical axis from β_{inner} to β_{outer} and the relative position to the CBED pattern remain constant. The relative position to the detector is described by the azimuthal step size θ and azimuthal angle φ' to the x-axis of the detector (Fig. 19(a)). It can be seen in Fig. 19(e) that the virtual detector segment is located in detector segments 7 and 8 depending on the detector rotation.

The IAMSR method approximates the intensity $S_{k,\mathrm{VS}}(\beta_{\mathrm{inner}}, \beta_{\mathrm{outer}}, \theta, \varphi')$ in a virtual segment k by averaging the intensities $S_{i,j}$ measured with a certain genuine detector segment i for the detector rotation step j of the detector rotation series. The selection rule of the genuine detector segment i contributing to average intensity is a function of the detector rotation $\varphi = j \cdot \theta$. In simple terms, only those segments of the genuine detector contribute to $S_{k,\mathrm{VS}}$ in which the virtual detector segment is located for a certain detector rotation φ. Mathematically, the intensity $S_{k,\mathrm{VS}}$ in the virtual detector segment is then calculated using

$$S_{k,\mathrm{VS}}(\beta_{\mathrm{inner}}, \beta_{\mathrm{outer}}, \varphi') = \frac{\sum_{j=0}^{n=\left(\frac{90°}{\theta}\right)-1} S_{i,j}\,(\beta_{\mathrm{inner}}, \beta_{\mathrm{outer}}, \varphi)}{n}. \tag{42}$$

Due to the quadrant symmetry, a DPC image with a detector rotation of 90° is not necessary. Therefore, the last term is to be neglected and the number n of images acquired with different detector rotations is given by $n = 90°/\theta - 1$. The number of detector rotations n must be an integer value, as it is necessary that the virtual detector segments do not spread over two segments of the genuine detector.

For the green virtual detector segment in Fig. 19(e), applying this method results in the intensity S_7 of segment 7 being used for detector rotations from 0° to 40° and the intensity S_8 of segment 8 being used for all other rotations.

An example for the intensity on the multi-segment detector after applying the IAMSR method is depicted in Fig. 19(f). The intensity on the multi-segment detector is obtained for the same position of the Si[110] specimen as used in Figs. 19(b, c, d). For this, the IAMSR method uses the images acquired with the individual detector segments of a DPC image series with a detector rotation step size of 10° resulting in virtual detector

segments that each span an azimuthal angle interval of 10°. The obtained intensity distribution is in good agreement to the intensities of the CBED pattern in Fig. 19(b).
In the following, the intensities of the virtual detector segments of a multi-segment detector after applying the IAMSR method are exemplarily investigated for a 5x5 matrix of beam positions around an atomic column in Si[110] and, in particular, by a qualitative comparison with the analogeously acquired CBED patterns (Fig. 20). The IAMSR method is applied using STEM image simulations acquired for the individual segments of the segmented detector (not shown here). These STEM image simulations are obtained with detector rotations ranging from 0° to 80° in steps of 10°.
The corresponding HAADF image (Fig. 20(a)), the CBED patterns (Fig. 20(b)) and the DPC image series used for the calculation of intensities on the multi-segment detector (Fig. 20(c)) were all obtained with Dr. Probe [44]. The beam positions are indicated by the red and bright blue dots in the simulated HAADF image in Fig. 20(a). The defocus was set to f = -6 nm to allow for a maximum obtainable DPC signal and all other lens aberrations were assumed to be zero (further information on the influence of the defocus and residual lens aberrations can be found in Chapter 5.2 and Chapter 5.5). The sample thickness was intentionally chosen to be 30.72 nm (40 unit cells stacked in beam direction) to show the results of the IAMSR method, when strongly inhomogeneous intensity distributions are present in the CBED pattern. Further details on the simulation parameters can be found in Table 11 and Table 12 in the Appendix.

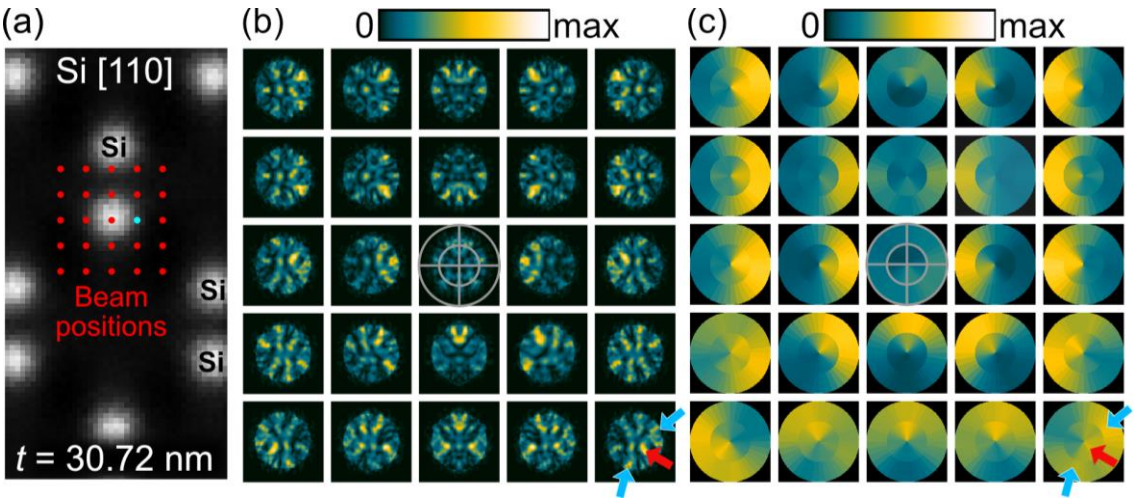

Figure 20: (a) Section of a Dr. Probe simulated STEM HAADF image of Si[110]. (b) 5x5 tableau of simulated CBED patterns for the beam positions marked by the red and blue dots in (a). The specimen thickness amounts to 30.72 nm and except for a defocus of f = -6 nm no other lens aberrations are assumed. The momentum space was calculated with a resolution of 500x500 pixels. (c) Calculated intensity on the detector after applying the IAMSR method with a step size of 10°. For each detector rotation, a simulation with the same parameters as in (a) was acquired and the intensities of the detector segments under detector rotation are obtained from individual image simulations and not from the CBED pattern.

From the theory of differential phase contrast imaging it is expected that intensity gradients across the CBED pattern are observable if the beam sits close to an atomic column. The gradient is in direction of the atomic column. Thus, the highest intensities can be expected in direction of the atomic column. However, as it is demonstrated in

the framework of this thesis (Chapter 5), any quantitative analysis is not reasonable for high thicknesses (also $t = 30.72$ nm) due to an inhomogeneous CBED intensity distribution which is a result of the beam extension, inhomogeneous potentials and dynamic diffraction effects [91]. Such inhomogeneous intensity distributions can be seen in the CBED patterns in Fig. 20(b). Nonetheless, at beam positions close to the atomic column, a significantly higher average intensity in the direction of the atomic column can be seen in the CBED pattern in Fig. 20(b). Fig. 20(c) displays the intensities on the multi-segment detector for the same beam positions after applying the IAMSR method.

Comparing the simulated CBED images and the intensity on the multi-segment detector, a strong similarity of the intensity distribution in azimuthal direction is observed for all beam position. However, the intensity distribution in polar direction can not be resolved in greater detail, as the polar collection angles of Layer1 and Layer2 in the detection plane are fixed by the camera length. It is observed that especially for beam positions close to the atomic columns, the intensity on the multi-segment detector in Fig. 20(c) is very similar to the CBED's intensity distribution in Fig. 20(b). As previously described, a large fraction of the beam intensity is deflected to the atomic column position. This is also observed in the intensity of the multi-segment detector Fig. 20(c). In addition, there is also a good agreement at other beam positions as e.g. in lower right corner. Here, it can be seen that the intensity inhomogeneities in the CBED pattern, which would lie on the segmented detector in Layer1, are well mapped. These features are indicated by red arrows in the CBED pattern but also in the intensity of the multi-segment detector. Moreover, changes in the intensity distribution on Layer2 are also observable with the mutli-segment detector. The areas of good agreement are exemplarily marked by blue arrows in Figs. 20(b, c).

To calculate the DPC signal from the intensity distribution on the multi-segment detector after applying the IAMSR method, the DPC signal evaluation method based on the geometrical centre of masses of individual virtual detector segments (described in Chapter 3.1.2) is applied. For the calculation of geometrical centre of masses of the virtual detector segments $k_{x;k,\mathrm{CoM}}$ and $k_{y;k,\mathrm{CoM}}$, the azimuthal angle interval is set to $\vartheta_1 = \theta/2$ (Eq. 33 and following). The CoM of the intensity distribution in momentum space coordinates is given by

$$p_{x;\mathrm{CoM}} = \hbar \cdot \frac{\sum_k k_{x;k,\mathrm{CoM}} \cdot S_{k,\mathrm{VS}}}{\sum_k S_{k,\mathrm{VS}}} \tag{43}$$

and

$$p_{y;\mathrm{CoM}} = \hbar \cdot \frac{\sum_k k_{y;i,CoM} \cdot S_{k,VS}}{\sum_k S_{k,\mathrm{VS}}}. \tag{44}$$

The index k is chosen for the respective layer configuration and only accounts for the virtual segments of e.g. Layer2. The DPC signal and colour-coded DPC signal are afterwards calculated in a similar way as described in Chapter 2.2.3 and Chapter 3.1.2. Examples for the application of the IAMSR method are given in Chapter 6.1.5. This includes a comparison with the CoM signal of the 4D-STEM image and results in a drastic improvement in similarity between images obtained with a pixelated and segmented detector, the latter is obtained with the IAMSR method. It is noteworthy that Chapter 6.1.5 should be understood as a proof of principle. To apply the IAMSR method on an image series which is experimentally and purely obtained on a segmented detector, the measured images must be carefully aligned to ensure the equality of the potential landscape for all pixels. This can be achieved by using rigid or non-rigid image registration techniques [113], which are described in Chapter 4.4.2.

4.4. Noise reduction

Due to the finite dose conditions in (scanning) transmission electron microscopy, noise is present in any image [114, 115]. It is thus a limiting factor regarding the accuracy of measuring a certain observable. For example, the determination of a position of an atomic column is strongly influenced by the noise, since the position is typically determined by the intensity profile of a certain atomic column [116] (further details can be found in Chapter 4.5). When using scintillator-based STEM detectors which are (fibre-optically) coupled into a photomultiplier [110], the signal noise of a single detector segment follows a Poisson distribution due to the detection process and the particle nature of an electron [110, 114, 117]. However, further detector noises are often disregarded, although they have a significant influence on the standard deviation of the measured signal. Detector noises include thermal noise of the analog-to-digital converters [118, 119], inhomogeneous quantum efficiency across the scintillator material [111] as well as in the photomultiplier [120], and dark currents in photomultipliers [121]. Segmented detectors also suffer from photons which move between different detector segments [110].

The signal-to-noise ratio in STEM can be influenced already during the measurement by increasing the electron dose at each pixel during the scan. This can be achieved by adjusting the probe current or the dwell time.

There are many denoising algorithms available for post-processing of (S)TEM images [122, 123]. Since the essential data of a DPC measurement can be reduced to the difference signals S_x and S_y, a noise-reduced DPC image can be obtained by reducing the noise in both difference signals. Many of the noise reduction algorithms apply a convolution with a smoothing kernel [123]. This typically leads to a blurring of the image and thus to a loss of spatial resolution. One of these algorithms which is also applied in this thesis is the Gaussian image filter described in Chapter 4.4.1. There are also algorithms that drastically reduce noise by averaging the intensities of image segments or a series of STEM images with a minimal loss of spatial resolution. These include rigid and non-rigid registration [124, 125], which are described in Chapter 4.4.2.

4.4.1. Gaussian filter

A Gaussian image filter uses a two-dimensional Gaussian function as a convolution kernel and works as a low-pass filter [123, 126, 127]. In a simpler picture [126] it can be understood as a convolution of the intensity at each pixel (x, y) with a Gaussian function $G(x, y)$ given by

$$G(x,y) = \frac{1}{2\pi\sigma}\exp\left(-\frac{x^2+y^2}{2\sigma^2}\right). \tag{45}$$

This Gaussian function determines the values of the kernel, and the extension of the kernel is given by the standard deviation σ of the Gaussian distribution. The convolution kernel and its extension thus determine the influence of neighbouring pixels. While at low standard deviations σ the emphasis of the filtering is on the central pixel, at higher σ the influence of neighbouring pixel is increasing. Gaussian image filtering is also included in the *DPCToolbox* application and based on a function built-in in *MATLAB*. The extension of the kernel in units of pixels is always a positive odd number. The pixel size of the kernel of the *MATLAB* function is always $2 \cdot \lceil 2 \cdot \sigma \rceil + 1$, in which $\lceil\ \rceil$ denotes the ceiling function. Although the 2D Gaussian never reaches zero, this kernel size suffices as pixels at a distance of 3σ have a negligible influence.
The Gaussian image filter is applied in this thesis for denoising of single DPC images. Therefore, it is used to individually denoise the S_x and S_y difference images. The colour-coded DPC image and other calibrated DPC images are recalculated after denoising. Furthermore, the Gaussian denoising also plays a central role in the non-rigid registration described in Chapter 4.4.2, as it is used to cohere a moving matrix via blurring. Moreover, the Gaussian blurring is also utilised to find starting parameters for the atomic column position fitting algorithm described in Chapter 4.5.

4.4.2. Rigid- and non-rigid registration

Optimally, noise reduction algorithms reduce image noise without compromising spatial resolution. However, the application of convolutional image filters such as the above-mentioned Gaussian image filter reduces the image resolution by blurring the images. This is not beneficial, as the resolution is one of the key aspects when analysing e.g. atomic electric field distributions. As the image noise depends on the number of detected electrons, the electron dose per pixel can be increased to reduce the image noise. However, this is typically not feasible for STEM images with subatomic resolution since low dwell times per pixel must be used to achieve negligible specimen drift. Low dwell times also enable the imaging of beam sensitive material, which show disintegration at certain dose levels [128].
One way to artificially increase the dwell time and hence reduce the noise in STEM images without compromising spatial resolution is the acquisition of an image series and a subsequent averaging of the image intensities [113, 125]. As there might be the possibility of macroscopic drift, local distortions of the crystal structure and dynamic processes such as jitter of atomic position between the subsequent images [125], the

images must be registered and aligned prior to superposition. Several registration routines are described in the literature [129, 130], which are for example already used in medicine for CT scans [131]. Many of the registration algorithms align distinctive features, e.g. points, surfaces or edges [132]. This is however a difficult task for STEM images if the images are noisy, i.e. the noise level is above the true signal, the latter resulting from the electron specimen interaction [125]. Among the registration techniques, which directly use the intensity of the image, are the rigid and non-rigid registration [125]. Especially the latter has already been tested in STEM on various material systems [113, 133], e.g. beam sensitive zeolite specimen [125]. Therefore, both are considered in this thesis and used in combination as described below.

The description of both rigid and non-rigid registration of images in general is only given briefly. Further details can be found in the original publications [113, 125, 132]. Afterwards, the procedure for obtaining registered DPC images is explained.

Although typically several images are registered to the same reference image during rigid and non-rigid registration, in the following, only two subsequent images $g(x,y)$ and $f(x,y)$ of an image series are to be registered. Registration in the following means to find a transformation matrix or displacement field which is applied to assimilate the images and the position of the features inside the image. The latter process is referred to as alignment. It is to note that the image $f = f_0$ is registered to the image g. Image $g(x,y)$ is therefore in the following referred to as the reference image. Furthermore, the coordinates (x,y) of an image are assumed to form a periodic grid. After the registration is achieved not only for two images but for a complete stack of images using the rigid or non-rigid registration, the average intensity at all pixels (x,y) of the aligned images are calculated resulting in a noise reduced image.

The goal of the rigid registration is to find a translational and rotational transformation matrix $\Upsilon(x,y)$ so that $\Upsilon \circ f \approx g$. This transformation matrix $\Upsilon(x,y)$ gives the relative position of a pixel in image f for a pixel in g, which is a displacement in case of a motion between subsequent images. This transformation conserves the grid of image pixels as can be seen in the schematics in Fig. 21(a). The alignment of images is exemplarily shown in Fig. 21(a) by the blue marked area as well as blue lines. This alignment is achieved by a warping [134], i.e. applying the calculated transformation matrix Υ which was found by the registration to the image g. This results in the warped image $f' = \Upsilon \circ f$. To measure the similarity of images after registration and alignment, typically the cross-correlation coefficient of f' and g is used [125]. Since the image intensities in subsequent images might not only vary due to image noise but also due to jitter of atomic positions and distortion of the crystal lattice, the superposition of registered images might lead to a blurring of features and a loss of resolution [113]. To overcome this limitation, local distortions between $g(x,y)$ and $f(x,y)$ must be considered.

This is achieved in the non-rigid registration by loosening the rigidness of the grid and allowing pixels to be freely moved by a deformation matrix (displacement field) as can be seen in the sketch in Fig. 21(b). As the complete mathematical description is

beyond the scope of this thesis, the basic principle of the algorithm is described only briefly. Similar to the rigid registration, the goal of the non-rigid registration is to find matrix Υ that can warp the moving image f so that ideally $\Upsilon \circ f = g$ is satisfied. As such a registration of images was typically conducted to overlay and align subsequently acquired images, the term "moving image" stems from a possible temporal movement of the specimen or its structure between the images. In case of the non-rigid registration, the displacement field allows for a non-parametric and non-rigid deformation of image f. The calculation of the displacement field is typically based on a gradient flow method and implemented in the *DPCToolbox* software using the “imregdemons()”-function built-in in *Matlab* [132].

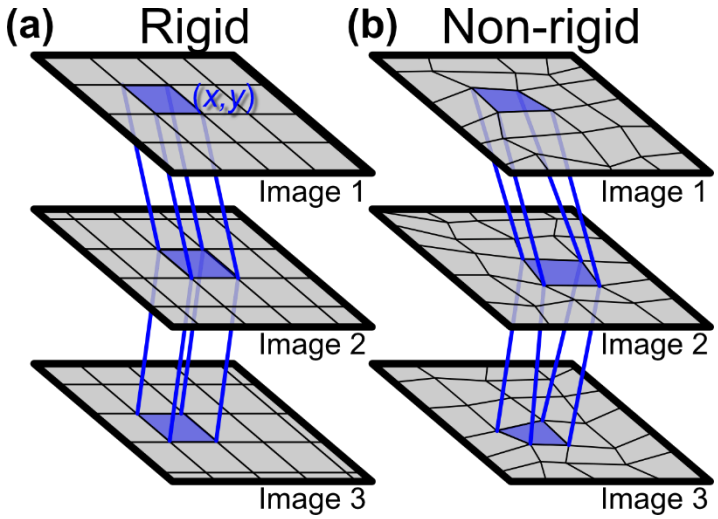

Figure 21: Schematics of the (a) rigid and (b) non-rigid registration. Images 1 to image 3 are aligned with (a) a rigid grid. (b) For the non-rigid registration, the rigid grid is loosened to align pixels. The blue line indicates the displacement. Adapted from [113].

The utilised gradient flow method [132] assumes that the intensity of a certain object is unchanged between subsequent frames although its position has changed by a certain displacement. The displacement field is then the displacement of all features or pixels when each pixel is considered as a feature between two consecutive images.

The calculation of the final displacement field is an iterative process. In the following, the index i denotes the step of the iteration starting at $i = 0$. The displacement field v_i (which is a two-dimensional vector field) also referred to as the velocity resulting from the flow and displacement of features between subsequent images at iteration step i is then given by [132]

$$v_i = \frac{\big(g(x,y) - f_i(x,y)\big) \cdot \vec{\nabla} g(x,y)}{\Big(\vec{\nabla} g(x,y)\Big)^2 + \big(g(x,y) - f_i(x,y)\big)^2}. \tag{46}$$

Here, $\vec{\nabla}$ denotes the gradient operator and $g(x,y)$ and $f_i(x,y)$ correspond to the intensity distributions of reference image and the registered image. The latter is updated with each iteration through warping $f_i = \Upsilon' \circ f_0$ using the displacement field Υ' which is also updated using $\Upsilon' = \Upsilon - v_i$ at each iteration. Due to noise in the images, strongly varying gradients might result in locally strong deformation of the displacement field. Therefore, a displacement field smoothing is applied using a Gaussian blurring

before warping. This smoothing is referred to as a field smoothing and is given by the standard deviation of the two-dimensional Gaussian function (σ in Eq. 45). After the final iteration, the image to be registered f_0 is warped with the displacement field Υ' and $f_i = \Upsilon' \circ f_0$ obtained by warping.

Usually, there is no convergence criterion used to finish the calculation of the displacement fields. In general, it is possible that the algorithm converges in a minimum of cross-correlation. However, it is also possible that this is a local but not global minimum. To prevent this, a multilevel scheme is utilised allowing for a coarse to fine registration by adjusting the grid resolution through binning [125]. For example, if the images to be aligned have a resolution of 512x512 pixels, the coarse registration is conducted with binned images. Using a binning factor two, an image with 512x512 pixels has a resolution of 256x256 as each pixel is derived from a 2x2-pixel array of the original image. After image registration on the coarse level, the resolution of the displacement field is adjusted via interpolation to fit to the image resolution of the subsequent level and the displacement field is again iteratively updated using the gradient flow method.

Fig. 22 exemplarily displays the non-rigid registration using a reference image, which is obtained from a rigid registration and shown in Fig. 22(a), and a moving image in Fig. 22(b). The moving image is the image which should be registered to the reference image. Further details on using a rigidly registered image as a reference are given at the end of this section. Figs. 22(a, b) show an HAADF image of Si in [110] zone-axis orientation for both the reference and the moving image. After registration, applying the calculated displacement field by warping the moving image, the aligned image is obtained, which is displayed in Fig. 22(c). For the calculations, a two-level scheme with 300 iterations on each level and a field smoothing of 2 pixels are used. Figs. 22(a-c) contain white and red markers for visualisation of the difference between the reference, moving and aligned image on the example of an atomic column which is surrounded by the markers. While a rather large proportion of the intensity arising at the atomic column in the reference image is found on the right side of the red marker in Fig. 22(a), the intensity of the respective atomic column in the moving image (Fig. 22(b)) is found between the white and red marker. After registration and alignment, the intensity is similarly found at the right side of the red marker in Fig. 22(c). The effects of a registration of a noisy moving image to a noise reduced image are evident. These effects include a more homogeneous intensity distribution of atomic columns, a more round shaped atomic column, and the reduction of flags, which are exemplarily marked by green ellipses and commonly observed in STEM imaging due to beam position instabilities [135]. Furthermore, the components of the calculated displacement field in x- and y-direction are depicted in Figs. 22(d, e). It is to note that these components of the displacement field show the displacement of pixels to reach from Fig. 22(b) to Fig. 22(c). The colour scale gives the displacement in units of pixels and red arrows in the colour scales depict the directions of displacement for positive and negative values. Fig. 22(f) shows the displacement field magnitude obtained from a superposition of x-

and y-directions. The colour scale again is in units of pixels. Fig. 22(f) shows the direction of the complete displacement field by means of a vector plot. From Figs. 22(d-f) a dominant displacement to the right is evident which is in good agreement to the estimated differences between Fig. 22(b) and Fig. 22(c).

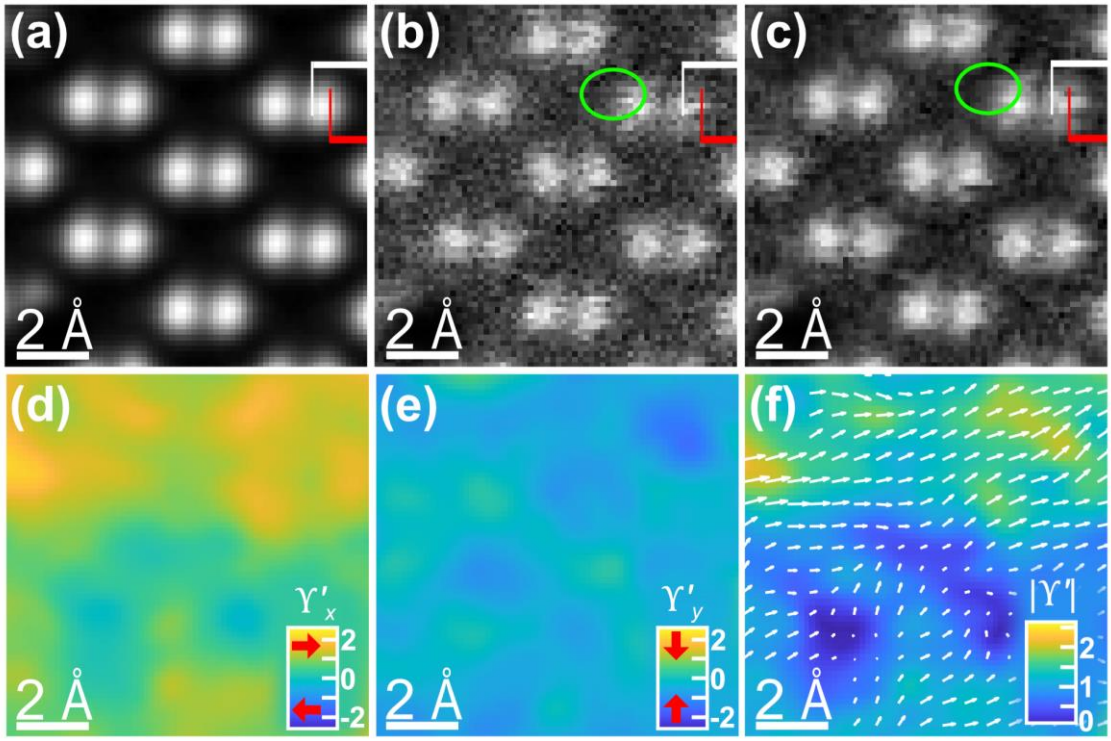

Figure 22: (a) Reference image. (b) Image before and (c) after registration and warping. Components of the calculated displacement field Υ' in (d) x- and (e) y-direction. (f) Magnitude of displacement field overlayed with the vector plot of displacement field. The displacement field depicts the displacement from (a) to (b) in units of pixels. For the calculations, a two-level scheme was used with 300 iterations on each level. A binning of two is applied at the coarse level and a field smoothing of 2 pixels is used. The reader is referred to the main body of the text for further explanations on the annotations and Table 39 in the Appendix for further experimental details.

The following describes in more detail how rigid and non-rigid registration are applied in this thesis in order to obtain denoised DPC images. Instead of using images of an image series, image sections of a single large-area atomically resolved image are registered and aligned. These image sections are in the following referred to as the image stack. For rigid and non-rigid registration, a DPC image and the simultaneously acquired HAADF image are measured with at least 512x512 pixels. It is important to note that the registration is always conducted using the HAADF image, since the HAADF signal is proportional to the projected atomic number and thus, depends on the exact positions of atomic nuclei in the image. The displacement field calculated with the HAADF image are then used for warping and aligning of the DPC related images the transformation matrix and.

A large-area HAADF image acquired during a DPC measurement is exemplarily displayed in Fig. 23(a). From this large-area image, a reference region is selected which is demarked by a mint-coloured frame. To find an appropriate stack of image sections, first the cross-correlation coefficients between the reference image section

(mint-coloured frame) and all other possible sections of the image with the same extension are calculated. Analogously, this can be described by scanning the reference image across the full-scale image and calculating the cross-correlation coefficient between the reference image and the image section at each scan position. This scanning is indicated by the dashed yellow boxes in Fig. 23(a) and leads to a cross-correlation coefficient map, which is depicted in Fig. 23(b). Image areas with a good similarity result in cross-correlation coefficients close to one. Such image areas are exemplarily indicated by the black and blue frames in Fig. 23(b). Second, all image section which exceed a manually selected cross-correlation threshold are added to the image stack. Simultaneously, the sections of the DPC related images are also added to this image stack. Such an image stack which consists of N_{I} images is exemplarily sketched in Fig. 23(c). The number N_{I} of image sections depends on the size of the reference image and the manually set threshold cross-correlation coefficient. A threshold coefficient leading to a reasonable number of image sections in the image stack can be deduced from the cross-correlation map in Fig. 23(b).

Figs. 23(d, e) show the HAADF image, the difference signals S_x and S_y as well as the colour-coded DPC image for image 1 and image 2 of the image stack. For all image types a good agreement is observed. Despite image noise, also rather strong variations in the HAADF image at interatomic pixels are observed (marked by yellow circles), which can be ascribed to atoms or molecules diffusing within or on the surface of the material [136].

As the images in the image stack already have a good cross-correlation coefficient, the rigid registration is conducted by simply calculating the mean value of intensity at all pixels and for all images of the image stack without further determining a transformation matrix. This is reasonable if the analysed specimen is monocrystalline without any defects, and the drift is negligible or almost constant during the acquisition of the images. For an image stack consisting of 200 images, which was determined from the large-area HAADF image in Fig. 23(a), the HAADF image, S_x and S_y as well as the colour-coded DPC image are displayed in Fig. 23(f). As can be seen in Fig. 23(f), the rigid registration improves the signal-to-noise reduction in all images. A detailed investigation on the effectiveness of the rigid registration and in particular the influence on the signal-to-noise ratio as well as image resolution is not intended in this thesis.

For the non-rigid registration, a reasonable reference image is necessary. It is possible to use one of the image sections as the reference image. However, this would possibly not reduce image artefacts, as the intensity distributions of the images to be aligned are also registered to features which are e.g. caused by noise. Using a theoretical or simulated image is possible, due to the effectiveness of the non-rigid registration. But such an approach would in a way be a self-fulfilling prophecy and is therefore not justifiable. In this thesis, the rigidly registered image (Fig. 23(f)) is used as the reference image during non-rigid registration. This allows a simple and efficient way to further improve the image quality by slightly improving the intensity distributions of all individual images in the image stack through a non-rigid registration.

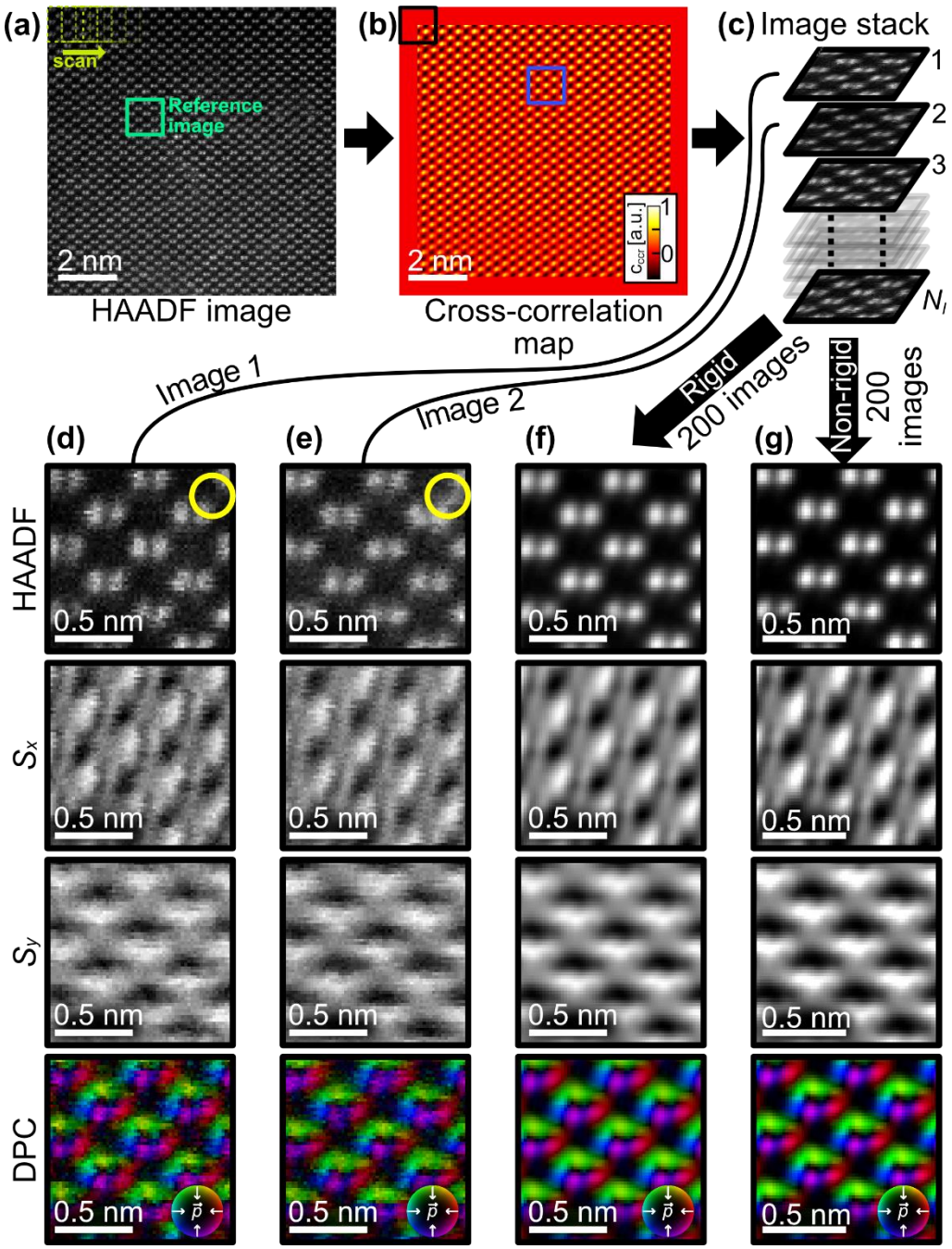

Figure 23: (a) 512x512 pixel large-area HAADF image of Si[110]. Yellow dashed frames indicate the scanning procedure to calculate the cross-correlation map with the mint-marked reference image. (b) Cross-correlation map obtained by calculating the cross-correlation coefficient c_{corr} between mint-coloured frame and any other image section of the same size in (a). The cross-correlation coefficient is always plotted at the central pixel of the image section. (c) Image stack consisting of N_{I} images sections exceeding a manually chosen cross-correlation coefficient threshold of 0.73. HAADF, S_x, S_y and colour-coded DPC image, of (d) image 1 of the image stack, (e) image 2 of the image stack, (f) 200 images aligned using rigid registration and (g) 200 non-rigidly aligned images. The images in (c-g) have a size of 64x64 pixel. Experimental details can be found in Table 40 in the Appendix.

Images after non-rigid registration are shown in Fig. 23(g). The non-rigid registration leads to further improvement and allows noise reduction without compromising spatial resolution too much, as the atomic columns in the non-rigidly registered HAADF image are less blurred than in rigid registration. However, quantitative investigation on the

influence of the registration techniques on the signal-to-noise as well as image resolution should be subject of future research.

4.5. Determination of atomic column positions

The exact positions of atomic columns or even single atoms at surfaces, defects and interfaces play a key role in a variety of properties of the materials [113]. Therefore, in many state-of-the-art investigations of advanced material systems, it is important to be able to determine these positions. This is in particular made possible by the advent of C_s-correction and the fact that the (annular) dark-field (ADF) signal gives robust signals regarding the positions of atoms [137]. For example, the bond contraction at interfaces of Pt catalyst particles has been studied with sub-picometre precision [113]. Furthermore, the diffusion of atoms can be studied by taking snapshots of the dynamic motion with fast scan speed ADF images and determination of atom positions within subsequent frames [136, 138]. Another example is the measurement of distortions of oxygen octahedra in perovskites of the form TO_6 [139] (with T being a transition metal atom) or ABO_3 [140] (with A and B representing a variety of possible cations) which have a significant effect on magnetic and electrical properties. Especially the precise determination of the position of light elements such as oxygen is made possible by the advances in annular bright-field (ABF) imaging and the combination of both ADF and ABF [139]. Besides the atomic column position, the determination of relative number of atoms and even an estimation of the chemical composition in atomic columns is possible with ADF [70–72, 137, 141]. Knowing the number of atoms is crucial when investigating nanometre sized particles because the number of atoms is directly related to the morphology of a nanoparticle [113, 142]. The morphology has been shown to play a key role in the catalytic activity of a nanometre sized catalyst particle [113, 141, 143]. Regarding the chemical composition, it has been shown by van Aert et al. [137] that the chemical composition even of an unknown atomic column can be assessed based on the dark-field signal.

The position and chemical composition of each atomic column is also a key parameter regarding the electric field distribution measured by DPC. For example, local distortions of the lattice will influence the local charge distribution and thus change the electric field distribution. Moreover, it is expected that atomic columns with different atomic species and number of atoms should generate different DPC signals. In addition, knowing the exact position of atomic columns is beneficial to fully understand the electric field distribution which may have rather complex distributions. These complex electric field distributions might arise due to the fact that, in contrast to the incoherent HAADF signal, DPC uses the bright-field signal, which is dominated by coherent contrast mechanisms, which behave non-monotonically with specimen thickness [109]. Thus, the measured electric field distribution is susceptible to various influences, as will be shown in Chapter 5. Colour wheels which are expected in the colour-coded DPC signal, are sometimes not present or resolvable although the dark-field signals indicate

that the resolution of the measurement is sufficient. In this context, the atomic column positions help to understand the field distribution at hand.

There are several routines described in literature that allow for the determination of atomic column positions as well as the number of atoms. Most of these routines consider a rather simple model for the intensity distribution of an atomic column, namely a two-dimensional Gaussian function. Despite its simplicity, the two dimensional Gaussian function typically suffices to describe the intensity distribution of an atomic column, although it does not fully account for all influences on the intensity distribution such as detector noise, thermal diffuse scattering and dynamical electron diffraction effects [70]. For the determination of the atomic column position, typically fitting of a superposition of two dimensional Gaussian functions [70–72, 113, 137–141] is used. In addition, the calculation of the centre of mass of intensity distribution in a region of interest covering the complete atomic column [139] can also be conducted to find the atomic column positions. Although the determination of the centre of mass of an atomic column can be considered as a robust tool, more precise positions can be obtained from the two-dimensional Gaussian fit [140]. By utilizing two-dimensional Gaussian functions, it was shown that the determination of atomic column position with a precision in sub-picometer range is possible [113]. Furthermore, also atomic column intensities (amplitude auf Gaussian function), an analogue to the scattering cross section (volume below the two-dimensional Gaussian function [144]), as well as the ellipticity of the atomic column can only be deduced using the two-dimensional Gaussian fit. The scattering cross-section as well as the peak intensity can be used to estimate the number of atoms as well as the chemical composition [144].

To precisely determine the atomic column position, initial atom positions must be estimated, which are refined with the calculation of centre of mass or fitting of a two dimensional Gaussian function [140]. In this thesis, a *MATLAB* script is implemented in the *DPCToolbox*. This script is based on finding local maxima in the dark-field image to estimate the atomic column positions. Similar procedures are used in references [109, 145]. Subsequently two-dimensional Gaussian functions are fitted to the intensity distribution in a region of interest around the estimated atomic column positions. The deduced centre positions and amplitudes of the fitted two-dimensional Gaussian functions are used for the position as well as the “type” of the respective atomic column. The term “type” assigns the atomic columns to different numbers of atoms or different chemical compositions.

An illustration of the determination algorithm of atomic column positions is shown in Fig. 24. The HAADF image for which the atomic columns are to be determined is shown in Fig. 24(a). This HAADF image shows WSe_2 close to [0001] zone-axis orientation. To estimate the atomic column positions, the image is first blurred using a Gaussian image filter (described in Chapter 4.4.1). In Fig. 24(b) a Gaussian image filter with a standard deviation of 2.5 pixels is applied to blur the image and reduce the impact of noise on the localization of maxima. Afterwards, the local maxima are determined which are indicated by the coloured dots in Fig. 24(c) and plotted on top of

the original HAADF image. Local maxima at the image edges are not considered since it is not clear if they are the overall maximum of an atomic column.

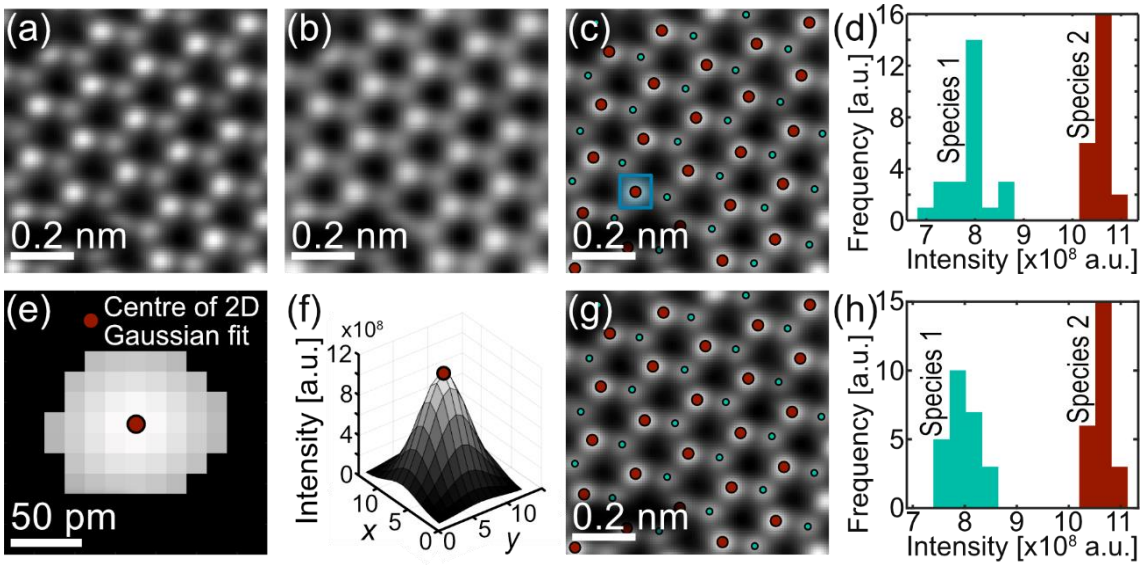

Figure 24: Illustration of the procedure for the determination of atomic column positions on the example of a HAADF image of WSe_2 imaged in [0001] direction after non-rigid registration. (a) Original HAADF image. (b) HAADF image after blurring by a Gaussian image filter ($\sigma = 2.5$ pixel). (c) Original HAADF image overlayed with atomic column positions determined from local intensity maxima. Atomic column positions are indicated by coloured circles. (d) Histogram of the intensities at the determined atomic column positions exhibiting two distinct features indicated by mint and red colour. These features, due to their difference in mean intensity, can be assigned to different atomic species. The same colour code is applied to (c). (e) Intensity distribution surpassing a set threshold value and obtained from a region of interest of the original image, marked by a blue box in (c). (f) Result of the fit of a two-dimensional Gaussian function to the intensity distribution in (e). (g) Original HAADF image overlayed by the atomic column positions determined through fitting two-dimensional Gaussian functions to the intensity distributions of the regions of interest of atomic column positions estimated by the local maxima. (h) Histogram of the peak height of the fitted Gaussian functions which is resembling the intensity of the respective atomic columns. Experimental details are compiled in Table 41 in the Appendix.

The dots in Fig. 24(c) exhibit different colours that assign a certain intensity interval to the atomic columns. The assignment of colour is made using the intensities at the estimated local maxima and by determining certain intensity intervals which belong to a characteristic feature in the histogram of peak intensities as shown in Fig. 24(d). In the histogram, two distinct features can be seen, a rather broadly distributed feature at lower intensities and a narrow, almost peak-like feature at higher intensities. Since the contrast in dark-field images depends on the projected atomic number, these intensities also represent the chemical composition. Thus, the atomic species can be assigned to the respective column. Without going further into detail on the influence of possible stacking orders of W and Se atoms and the number of layers on the HAADF signal, the red-marked atomic column in Fig. 24(c) corresponds to a pure W atomic column and the mint-marked atomic column to pure Se, respectively.

After rough estimation of atomic column positions by finding the local maxima in the blurred image, the distance to the next nearest neighbours of each atomic column is determined. This distance is used to cut out a certain region of interest of the intensity distribution around each estimated peak position. This cut-out region thus includes

mainly the intensity distribution arising from a single atomic column, which is later used for fitting a two-dimensional Gaussian function. The cut-out region of interest has typically a rectangular size with side lengths determined by the distance to the nearest atomic column.

When determining the atomic column position, the scattering cross-section of neighbouring atoms might partially overlap with the one of the atomic column under consideration. This is typically the case for dumbbells, whose distance is close to the resolution limit, e.g. in case of Si in [110] zone-axis orientation, and due to a blurring by the point spread function of the incident electron beam. Since the scattering cross-section of neighbouring atoms might have a drastic influence on the precision of atomic column position determination, a fraction (typically 50%) instead of the complete distance to the next neighbouring atomic column is used as a side length for the cut-out region of interest. In addition, a threshold intensity $I_{\mathrm{th}} = \eta(I_{\mathrm{max}} - I_{\mathrm{min}}) + I_{\mathrm{min}}$ derived with the minimum I_{min} and maximum intensity I_{max} of the region of interest and a threshold factor η ($0 < \eta < 1$). Applying this intensity threshold sets all pixels with intensities below I_{th} to 0.

An example for a cut-out area of interest showing the intensity distribution of a W atomic column is given in Fig. 24(e). Here, 50% of the distance to the next neighbouring atom is used as a side length of the cut-out area, and only intensities above $\eta = 0.6$ of the intensity are considered. This is reasonable, when precisely determining the atomic column positions. Applying an intensity threshold and reducing the size of the region of interest would probably not generate robust evidence for atom counting based on the scattering cross-section. Since knowing the exact number of atoms is not necessary in this thesis, thresholding of intensities is reasonable.

To determine the exact position (x_0, y_0) of the atomic column, a two-dimensional Gaussian function $G_{\mathrm{Fit}}(x, y)$ is fitted to the intensity distribution of the region of interest of the original HAADF image after applying the intensity threshold. This fit function has the form

$$G_{\mathrm{Fit}}(x, y) = I_{\mathrm{peak}} \cdot \exp\left(-\frac{(x - x_0)^2}{2\sigma_x^2} - \frac{(y - y_0)^2}{2\sigma_y^2}\right), \tag{47}$$

in which I_{peak} denotes the amplitude, σ_x and σ_y the standard deviations in x- and y-direction and x_0 and y_0 the central positions of the two-dimensional Gaussian function. The parameters x and y also denote the pixel coordinates of the cut-out region of interest in the original image. Fitting is conducted using the built in “fit()”-function of *MATLAB*, which considers non-linear least square fitting with a maximum number of iterations of 1000, as well as a tolerance of fitting coefficients of 10^{-6} and fitting model of 10^{-6} as a stopping criterion. These stopping criteria are typically reached within the considered maximum number of iterations. A contour plot of the two-dimensional Gaussian function is displayed in Fig. 24(f) and the calculated position of the Gaussian function is given by the red dot. This position is also indicated in Fig. 24(e) by the red-marked dot. It is to note that the sampling (pixel number) has no significant influence on the determination of atomic column position if the HAADF image is acquired with

atomic resolution and exhibits only negligible noise [141, 144]. By fitting two-dimensional Gaussian functions, atomic column positions can be the determined with subpixel precision. This approach is therefore also used for precise measurements of stress and strain in materials [143]. In the example in Fig. 24(g), the positions are again indicated by the dots overlayed on top of the original HAADF image. The assignment of column type is again conducted using a histogram (Fig. 24(h)) which displays the number of atomic columns in a certain range of peak intensity I_{peak}. The assignment is similarly conducted as described for Fig. 24(d).

Besides being used to determine the atomic column positions from HAADF images, this method is analogously applied to the positive part of the DPC-derived charge densities to automatically measure the charge density at atomic columns. The estimation of the peak charge density and its position are obtained by simply exchanging the HAADF image with the charge density map. Without approving the physical correctness of the assumed model, also a Gaussian function is fitted to the charge density. The separate treatment of HAADF and charge density is necessary due to the fact that the DPC signal uses the bright-field part of the intensity distribution in the detection plane and positions derivable from ABF as well as ADF signals are differently influenced by specimen tilt [109]. The deviations of atomic column positions in ABF and ADF depend, among other things, on the thickness as well as the atomic species in the atomic columns [109]. In addition, further influences such as the illumination conditions lead to deviations in the measured atomic column positions. Further influences on the DPC signal are discussed in the following Chapter 5.

Chapter summary

- This Chapter covers post-processing algorithms for quantitative analysis, denoising and reduction of the influence of the detector response function on DPC images acquired with a segmented detector. These algorithms as well as others (described in Chapter A.1) are implemented in the *DPCToolbox*, which is available from the author or the attached CD.

- Electric fields are calculated from calibrated quantities, such as the transferred momentum, the wavenumber perpendicular to the optical axis and the deflection angle.
- The specimen thickness is considered in the calculation of electric fields at each pixel of the DPC image.
- At atomic resolution, the specimen thickness is assumed to be constant across the image and measured by using either electron energy loss spectroscopy or energy filtered TEM within the log-ratio method (t/λ method).
- Charge densities are calculated from the electric field vectors using the Maxwells equation.

- To investigate the complete field distribution, the so-called scattergram, which is a two-dimensional histogram, can be used.

- The ordering of pixels in the scattergram follows the colour code. Pixels far of the scattergram centre correspond to pixels with high magnitudes. The azimuthal allocation of pixels is determined by the direction of field quantity.

- The novel scattergram filtering allows to determine and visualise the position of pixels leading to a characteristic feature in the scattergram.
- Exploiting the rotatability of the SAAF detector, the azimuthal momentum space resolution can be increased and an approximated intensity on a multi-segment detector consisting of virtual segments can be calculated.

- Image noise is present in any STEM image and can be reduced in post-processing by several techniques.
- In this thesis Gaussian image filtering and rigid as well as non-rigid registration are used.

- Atomic column positions are determined from HAADF images, which are simultaneously acquired to the DPC image, by fitting two-dimensional Gaussian functions to the intensity distribution of individual atomic columns.

5. Influences on DPC signal

This chapter investigates various influences on the DPC signal which result from machine-related parameters such as the segmentation of the detector and the lens aberrations as well as specimen-related parameters such as the specimen thickness and tilt. Some of the results have already been published [91]. Although the findings are explicitly given for segmented detectors, most of the results can also be applied to other detectors described in Chapter 2.2.3.

5.1. Detector response function of segmented detectors

When analysing crystalline materials with a finite thickness, diffraction is an unavoidable effect that occurs during (S)TEM investigations and influences the intensity distribution in the detection plane. The effect of diffraction is depicted in the sketch in Fig. 25(a) in which a convergent electron beam is incident on a crystalline specimen with lattice planes oriented parallel to the direction of electron beam propagation. Diffraction arises from those lattice planes, leading to the formation of diffracted beams forming a field of waves around the direct beam. Due to diffraction a broadening of the electron beam intensity distribution occurs within the specimen, which – for simplicity – is only sketched beyond the beam cross-over.

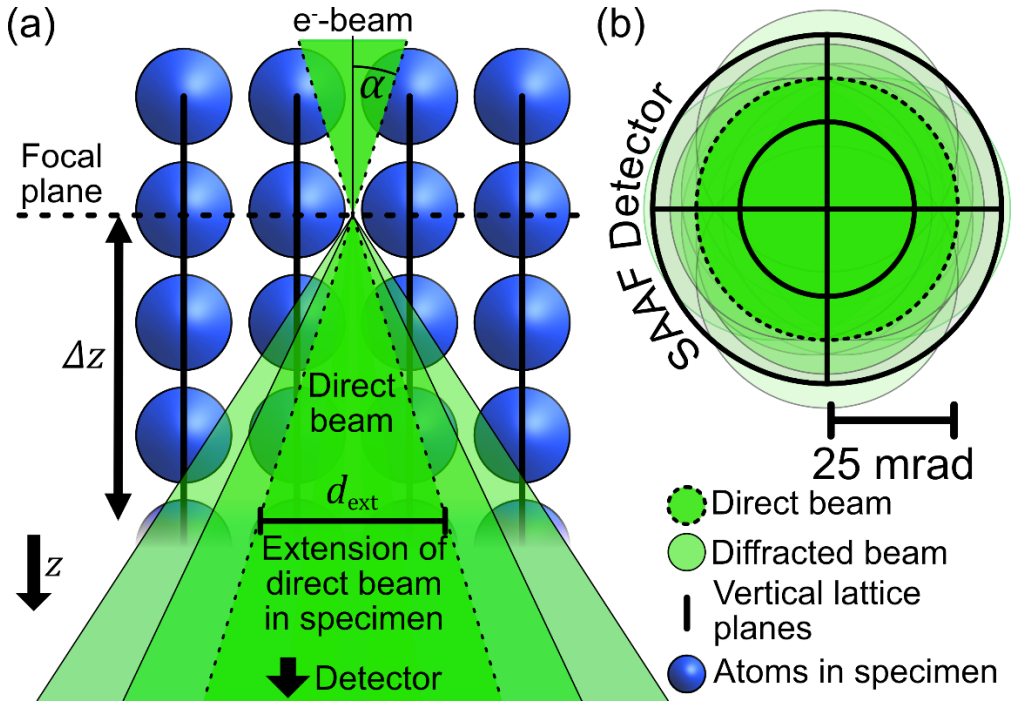

Figure 25: (a) Convergent beam incident on a crystalline specimen leading to the formation of diffracted beams (only sketched beyond the focal plane) and thus an enlarged divergence angle after the cross-over at the focal plane. The beam is afterwards projected onto the detector. (b) Illustration of diffraction discs and direct beam and their position for a typical CBED pattern of Si[110] on the segmented annular all-field. The convergence angle in (b) is 25 mrad corresponding to a typical value during DPC measurements.

The diffraction angles are calculated using Bragg's equation (Eq. 8) and are typically less than the convergence angle during high-resolution analysis (exemplary Bragg

angles in Si are given in Chapter 3.1). Hence, diffracted beams overlap with the direct beam during high-resolution analysis adding up to the complexity of the intensity distribution in the detection plane. The intensity of diffracted beams is a function of specimen thickness and can be assessed within the dynamic theory of electron diffraction [50]. A measure for the occurrence of diffraction is the extinction length ξ_g for a certain set of lattice planes $g = (hkl)$ which, in the Laue-case, describes the thickness at which intensity has been diffracted from the direct beam completely into a diffracted beam and back into the direct beam. The extinction length amounts to $\xi_g = \xi_{220}(\mathrm{Si}) = 112\,\mathrm{nm}$ for 200 keV electrons propagating along the [110] direction of a silicon crystal [91]. This means that for very small thicknesses, the formation of diffracted beams is smaller.

After the beam has interacted with the specimen, the electron beam is projected on the detector, with the direct beam and diffracted beams forming overlapping discs on the detector. The position and overlap of diffraction discs on the detector are illustrated in Fig. 25(b) for an electron beam with a convergence semi-angle of 25 mrad incident on a silicon single crystal in [110] zone-axis orientation. It is clearly visible that the diffraction discs overlap with the direct beam.

The extension of the beam within the specimen not only changes due to the formation of diffracted beams but also due to the cone-like shape of the incident beam. This can be seen in Fig. 25(a) where the beam diameter d_{ext} increases with distance Δz to the focal plane. The extension of the beam follows a simple tangent function, namely $d_{\mathrm{ext}}(\Delta z) = 2 \cdot \tan(\alpha) \cdot \Delta z$ if beam broadening due to elastic and inelastic scattering can be neglected. In this function, Δz describes the distance to the focal plane and α the convergence semi-angle. Considering a specimen thickness of 30 nm and having the focal plane on the entrance plane of the specimen, the extension of the beam on the exit plane amounts to 1.5 nm, which is much wider than the typical distance of atoms in crystalline materials. This ultimately leads to the finding that in a thick specimen the electron beam is not only influenced by the projected potential of a single atomic column but by several atomic columns. As a result, the electron beam experiences a strongly inhomogeneous potential landscape across the beam diameter, especially at large distances to the focal plane. The exclusive influence of inhomogeneous electric fields on the DPC signal was simulatively investigated by Müller-Caspary et al. [27] by assuming a plate capacitor with varying plate spacing, finding a reduction in measurable transferred momentum with decreasing plate spacing. The intensity redistribution due to inhomogeneous specimen potentials across the beam and diffraction effects is further investigated in Fig. 26. For this, Fig. 26 displays simulated CBED patterns for five different beam positions in $SrTiO_3$ in [001] zone-axis orientation which are projected on the SAAF detector (marked by a red circle). The beam positions are marked by the crosses in the upper row in Fig. 26 which depicts sketches of the projected unit cell of $SrTiO_3$. The exact beam positions are (0.27 nm, 0.31 nm), (0.28 nm, 0.30 nm), (0.29 nm, 0.29 nm), (0.30 nm, 0.28 nm), and (0.31 nm, 0.27 nm) of the $SrTiO_3$ cubic unit cell with a lattice parameter of 0.3905 nm and the centre of origin

(0 nm, 0 nm) at the lower left Sr atomic column. The CBED patterns are simulated for specimen thicknesses of 1.95 nm, 3.51 nm, 5.47 nm as well as 8.97 nm with a convergence semi-angle of 25 mrad. The focus is set to the entrance slice of the specimen structure and the displayed CBED pattern at each beam position are a result of 100 calculations with different frozen-lattice configurations accounting for thermal fluctuations of the atomic positions.

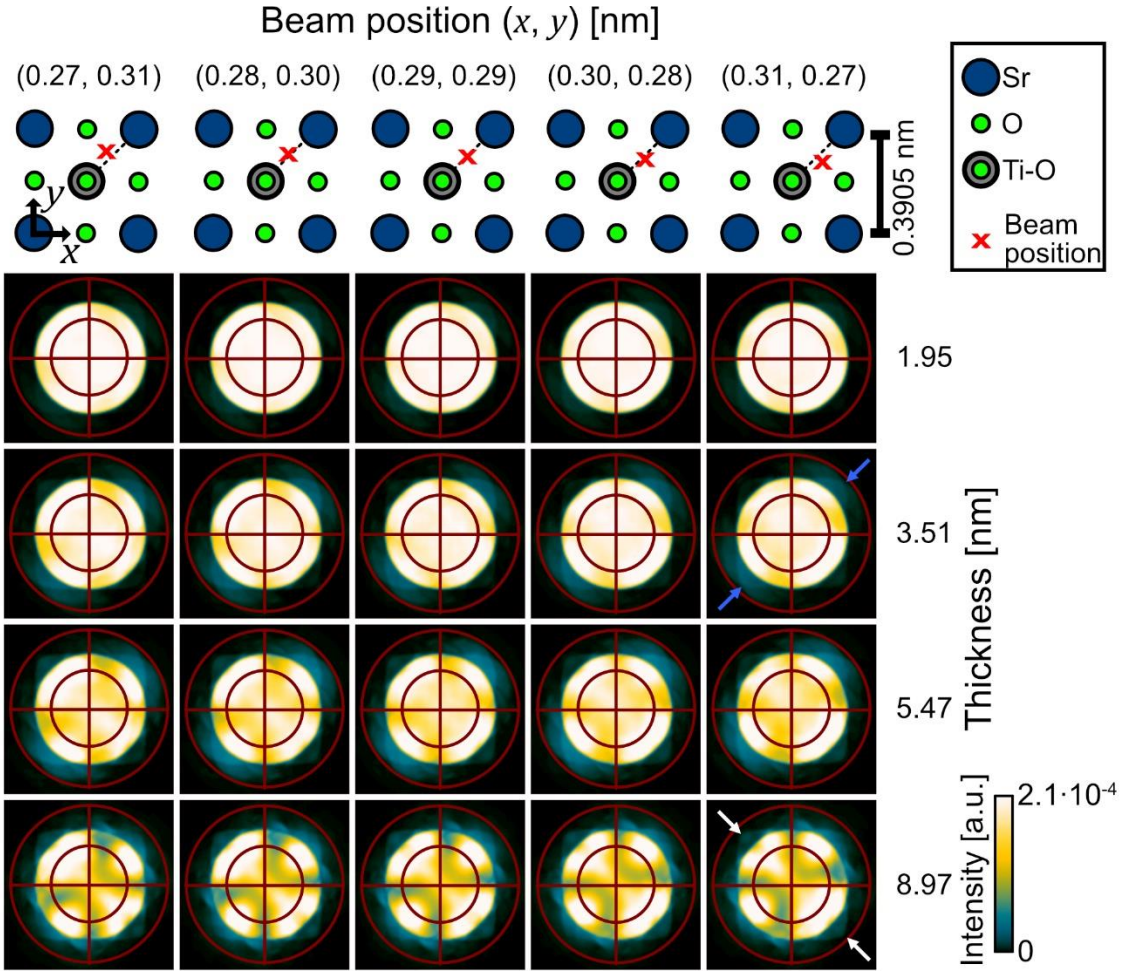

Figure 26: Upper row, sketch of the $SrTiO_3$ crystal structure viewed along the [001] zone-axis. In addition, the beam positions are marked by red crosses which more precisely sit at (0.27 nm, 0.31 nm), (0.28 nm, 0.30 nm), (0.29 nm, 0.29 nm), (0.30 nm, 0.28 nm), and (0.31 nm, 0.27 nm) of the $SrTiO_3$ cubic unit cell. Simulated CBED pattern from Dr. Probe are given for the beam positions and at specimen thicknesses of 1.95 nm, 3.51 nm, 5.47 nm and 8.97 nm. Adapted from [91]. A list of simulation parameter is given in Table 13 in the Appendix.

At a specimen thickness of 1.95 nm, the CBED pattern exhibits an almost homogeneous intensity distribution in the direct beam and almost no intensity outside. With increasing thickness, the proportion of intensity outside the direct beam increases. The intensity outside the direct beam especially arises from diffracted beams as can be seen by the round features outside the direct beam, which are already visible at a specimen thickness of 3.51 nm (indicated by blue arrows). More importantly, the intensity distribution inside the direct beam exhibits an inhomogeneous pattern. The inhomogeneous intensity distribution inside the direct beam reflects the arrangement of scattering atoms in the vicinity of the position at which the beam impinges on the

specimen. This can be seen in particular by the two-fold symmetry of the intensity distribution in the CBED pattern at the (0.29 nm, 0.29 nm) beam position exactly on the connecting axis between the Ti-O and Sr atomic columns. Beam positions which are diametrically shifted off the <110> connecting axis (marked by a dashed line in the upper row in Fig. 26) show a slightly but also diametrically shifted intensity distribution in the direct beam. This is also evident in the intensity of diffracted beams, which are exemplarily marked by two white arrows at a specimen thickness of 8.97 nm. The intensity of diffracted beams on the upper left quadrant exhibits a lower intensity than the ones on the lower right quadrant.

Since the intensity distribution in the detection plane shows a certain symmetry [99] and the detector intersects this intensity with a certain symmetry due to its equiangular azimuthal division into quadrants, artefacts in the DPC image can occur at points that do not lie at a high-symmetry point in the projected crystal lattice. The resulting artefacts can be found at atomic as well as intermediate resolution. Line-like features were observed in [91] at interatomic pixels of atomically resolved DPC image simulations of $SrTiO_3$. These artefacts, which are found to exhibit a stripe-like spatial distribution in the DPC image, are investigated in detail in Chapter 5.2 and include a change in direction and magnitude of the measurable transferred momentum. It is already evident from Fig. 26 that quantitative DPC imaging is strongly influenced by diffraction at a high specimen thickness. At intermediate resolution, difficulties in interpretation of electric fields in the vicinity of or across heterointerfaces are found [14, 29, 88, 146]. The difficulties arise from a change in mean inner potential of both materials [29]. In addition, difficulties presumably arise due to the fact that two material phases at the heterointerface possess different crystal structures and therefore lead to different diffraction patterns [29]. The resulting CBED patterns in the vicinity of the heterointerface might possess a strongly inhomogeneous intensity distribution which are then evaluated by a detector with a specific detector response function.

To describe the formation of these stripe-like artefacts in more detail, the detector response function must be considered. In this context, Seki et al. [41] have developed an expression for the measurable electric field distribution that includes the detector response function $D(\vec{k}_\perp)$. This expression can be found in Eq. 24 in which the detector response function is included in the differential-phase-contrast transfer function. There are several publications investigating the influence of the detector response function [41, 42, 98]. This is typically achieved by including a comparison of segmented DPC signals and CoM signals of pixelated detectors [36, 41, 42]. One of the drawbacks of DPC measurements with segmented detectors is that only an approximated and typically reduced [42] first moment magnitude can be measured due to the reduced resolution in momentum space. Shibata et al. and Seki et al. describe that the true electric field magnitude can be approximated via a scaling factor [24, 41]. Müller-Caspary et al. [42] propose a method to reduce the anisotropy of the segmented detector response function using a Fourier-transform-based method. They note that this may be problematic if the DPC image has significant scan distortions.

As the influence of detector response function on the measurement can only be reduced by optimising the collection angles of the detector, but not removed, it is important to investigate possible artefacts of DPC images, when using a segmented detector with a quadrant detector response function. Since the detector response function is determined by the polar and azimuthal detection angles, the following analysis of the influence of the detector response function is split accordingly.

5.1.1. Polar collection angles

One of the experimental parameters to adjust the detector response function and in particular the polar collection angles is the camera length which influences the extension of intensity distribution in the detection plane. As described in Chapter 2.1.5, an increase in camera length corresponds to a magnification of the electron beam's intensity distribution after interaction with the specimen increasing the extension of direct and diffracted beams on the detector. It is to note that the convergence angle remains constant. Thus, the choice of camera length corresponds to a change of the detector response function.

Close et al. [36] have investigated the influence of the beam extension on the detector for a 16-fold segmented detector by considering DPC simulations for different beam extensions. These beam extensions include direct beams that intersect the detection plane at polar angles corresponding to half or exactly one annular ring of the four layered (four annular rings) detector segment. By comparing Fourier coefficients of calculated potential with those obtained from a pixelated detector, it was found that the best agreement between pixelated and segmented detectors is achieved when the direct beam extends to half of the second layer. This would correspond to the scenario shown in Fig. 27(a). This is also in good agreement to the findings in [27] where it is stated that for inhomogeneous potentials the strongest intensity differences due to the redistribution of intensity are typically detectable at the edges of the direct beam.

The influence of the illuminated detector area on the extension and shape of measurable electric field distribution around individual atomic columns has not yet been analysed in great detail. In addition, it might also be possible to reduce the influence of diffraction phenomena on the DPC signal by selecting a proper camera length. In the following, the influence of the beam extension on the detector is studied based on simulations.

Fig. 27(a) shows a sketch of the beam extension on the eight-fold segmented SAAF detector with $\beta_{\mathrm{inner}} = 0.5 \cdot \beta_{\mathrm{outer}}$ the inner and the outer polar collection angles of Layer2. The polar extension of the direct beam is given by the convergence semi-angle α which is not changed by adjusting the camera length. Hence, the collection angles β_{inner} and β_{outer} can be described as a function of α and a parameter d which scales the size of the detector in the detection plane. In the following, $d = 1$ if β_{inner} is equal to α and $d = 2$ if $\beta_{\mathrm{outer}} = \alpha$. The polar collection angle β_{inner} can be calculated by $\beta_{\mathrm{inner}} = \alpha/d$. Analogously, β_{outer} is given by $\beta_{\mathrm{outer}} = 2 \cdot \alpha/d$.

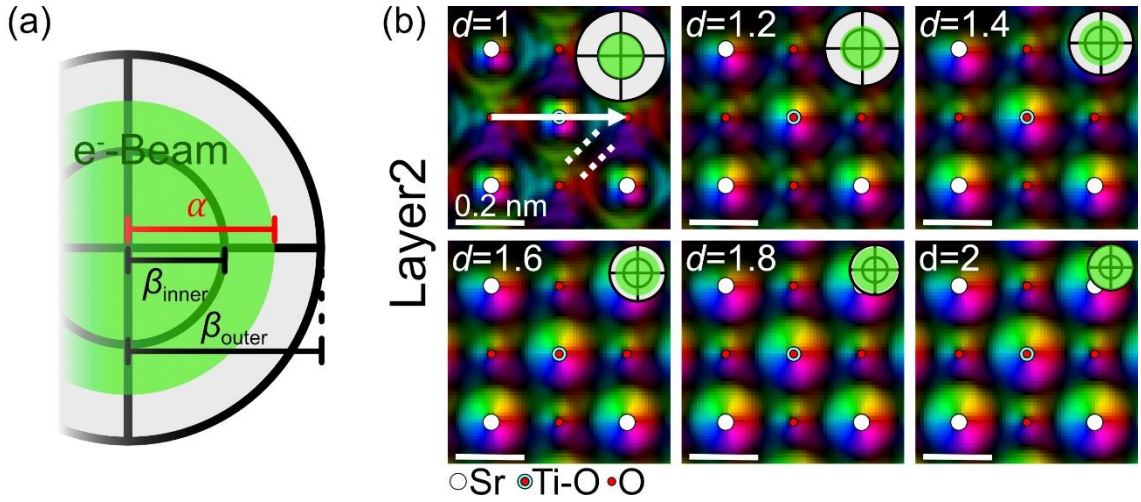

Figure 27: (a) Sketch of the direct beam on the segmented detector with detector collection angles β_{inner} and β_{outer}. The beam extension on the detector depends on the selected camera length and is examined here in dependence of the parameter d (see text). (b) Simulated DPC images of $SrTiO_3$ in [001] zone-axis orientation for beam extensions between $d = 1$ (direct beam extends to the inner collection angle β_{inner}) and $d = 2$ (the direct beam extends to the outer collection angle β_{outer}). All DPC images are calculated using detector segments of Layer2. A list of parameters for the multislice image simulations shown in (b) are compiled in Table 14.

To allow for comparability between the simulations and the experiment, Table 3 depicts the inner and outer collection angles as a function of d using a convergence semi-angle of $\alpha = 25$ mrad. These angles are used for the simulations. Table 3 additionally lists the corresponding experimental camera lengths for the JEM-ARM200F, which should be chosen, to obtain analogous collection angles. As there are typically only a few fixed camera length settings available at the microscope, the beam extension on the detector can also be manually changed by increasing the excitation of the projector lenses. The extension of the beam on the detector needs to be carefully determined as the electric field distribution is strongly influenced by the beam extension on the detector (shown below).

Table 3: Inner and outer collection angle, β_{inner} and β_{outer} of detector Layer2 depending on the parameter d. In addition, the experimental camera lengths L matching the beam extension on the detector for the given values of d are depicted.

d [a.u.]	1	1.2	1.4	1.6	1.8	2
β_{inner} [mrad]	25.00	20.83	17.86	15.63	13.89	12. 50
β_{outer} [mrad]	50.00	41.67	35.71	31.25	27.78	25.00
L [cm]	8.64	10.37	12.1	13.82	15.55	17.28

The influence of the beam extension on the obtained DPC signal is investigated in Fig. 27(b) for values of d between $d = 1$ and $d = 2$. All DPC images simulations are achieved using the segments of Layer2 in a bisected way. The simulation parameters for the images are compiled in Table 11 in the Appendix. These include a considered specimen thickness of 6.25 nm, and a defocus of $C_1 = -3$ nm below the entrance slice of the specimen structure. Sketches in the upper right corner of the DPC images

illustrate the detector and beam extensions. It is to note that all DPC images are individually normalised.

For a value of $d = 1$ the direct beam does not hit the detector segments of Layer2. The signal is therefore solely resulting from diffracted beams and scattered electrons. However, small rotationally symmetric electric field distributions can be observed close to the centre of Sr and Ti-O atomic columns (Fig. 27(b)). At the O-containing atomic columns, the typical colour distribution is also observed, however, a round shape is not evident. The field distribution resembles a cross. These features exhibit a continuous transition to other oxygen columns by line-like features, which are indicated by parallel dashed white lines.

With increasing beam extension on the detector, the colour wheels around all atomic columns become more pronounced and additionally exhibit a larger extension. Especially the enlarged extension of the distribution of DPC signal with high magnitude around atomic columns is interesting to recognize, as this would lead to completely different charge densities and might lead to a broadening of the positively charged nuclei. Moreover, the line-like features in the DPC image at interatomic pixels, which are exemplarily indicated by parallel dashed white lines for $d = 1$, are reduced with increasing direct beam extension on the detector. This can be possibly explained by the fact that the contribution of diffracted beams to the overall intensity distribution is decreasing. Increasing the beam extension would therefore reduce the magnitude of artefacts in the electric field distribution at interatomic pixels.

Since the signal on Layer2 does not originate from the direct beam at $d = 1$, it is interesting to investigate how the DPC signal behaves when all layers contribute to it. DPC images calculated from the intensities of all segments, i.e. a combination of Layer1 and Layer2 are displayed in Fig. 28. In contrast to the DPC images from the segments of Layer2, a beam extension dependent broadening of colour wheels around atomic columns is not observed when all detector segments are used, and the direct beam extension is increased. Additionally, it can be observed that the colour wheel-like DPC signal distributions are slightly squared.

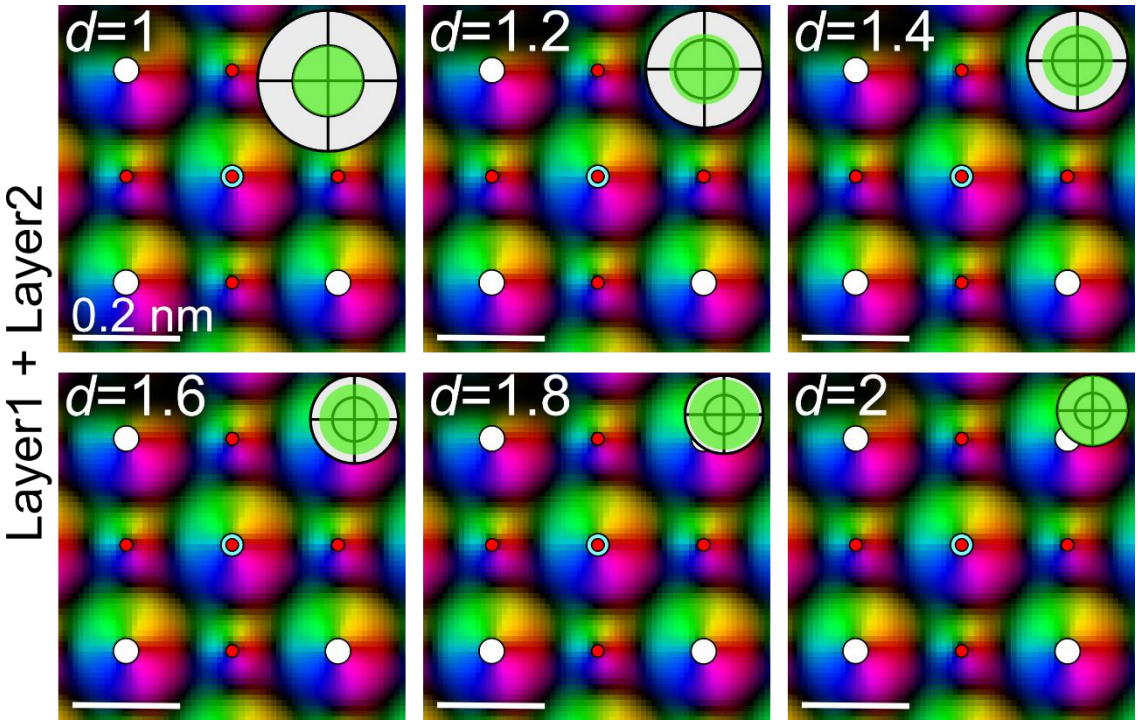

Figure 28: DPC image simulations for $SrTiO_3$ in [001] zone-axis orientation in dependency of the beam extension on the detector. The atomic column positions of the corresponding atomic species are marked with the coloured dots. The corresponding atomic species can be obtained from the legend in Fig. 27(b). Simulation parameters are given in Table 15 in the Appendix.

The broadening of the field structures around atomic column positions is further analysed with the line profiles of the deflection magnitude depicted in Fig. 29. The position of the line profile is shown by the arrow displayed in Fig. 27(b) and extends from a pure oxygen column to another pure oxygen column in [010] direction. As can be seen from the line profiles in Fig. 29(a), the deflection distribution shows a broadening of the feature with increasing beam extension if the segments of Layer2 are used. However, the maximum magnitude across the line profile is not altered with increasing the extension of the direct beam on the detector. It is to note that the deflection magnitude does not reach zero on the respective atomic column position due to the pixelation of simulated images. Furthermore, for a beam extension of $d = 1$ a local maximum is observed between the O and Ti-O atomic column. Fig. 29(b) shows analogously acquired line profiles of the deflection magnitude obtained using all segments. Although the extension of the direct beam on the detector changes, the deflection exhibits very similar magnitudes and features. This is particularly visible from the good agreement of line profiles at positions far of the Ti-O atomic column position. Moreover, the position of local minima remains constant for all beam extensions. Only the deflection distribution close to the Ti-O atomic column position is prone to changes. This would influence the electric field distribution and subsequently calculated charge densities but would have a smaller effect than the changes observed when only using the detector segments of Layer2 for the calculation of the DPC image.

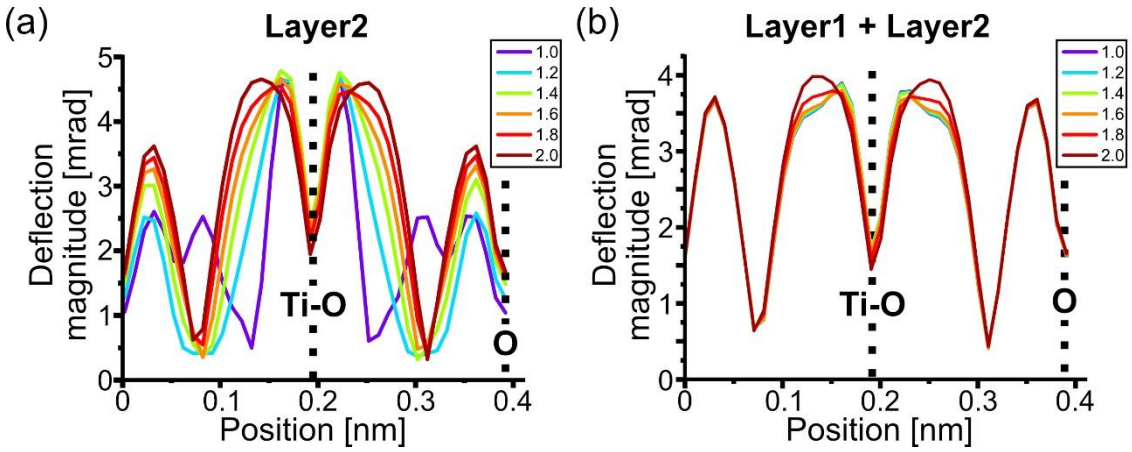

Figure 29: (a) Line profiles of the deflection magnitude calculated using the detector segments of Layer2 across a unit cell of $SrTiO_3$ for beam extensions d ranging from 1 to 2. The line profile position can be deduced from Fig. 27(b). Positions of the Ti-O and O columns are marked. (b) Line profiles of the deflection magnitude calculated from the intensities from the entire detector in a bisected manner. Simulation parameters for the corresponding multislice image simulations in Fig. 27(b) and Fig. 28 are compiled in Table 14 and Table 15 in the Appendix.

5.1.2. Detector rotation

Besides the polar collection angles of the detector, it is crucial to understand how and to what extend the azimuthal detector orientation with respect to the diffraction pattern influences the features in the DPC image. This has so far been only investigated for integrated DPC (iDPC) images [98] displaying the specimen potentials, which are calculated in post-processing based on a Fourier integration method. It is obvious that features in the measurable DPC image resulting from a certain detector orientation crucially impact also other quantities such as the iDPC signal or charge densities at atomic resolution which are calculated in post-processing. Therefore, detailed investigations on the influences of the detector orientation on the pure DPC signal are important. The question ultimately arises as to whether there is an optimal detector orientation with respect to the typically symmetrical diffraction pattern.

The detector orientation can be adjusted in different ways: Rotating the specimen or the detector. Rotating the specimen can be achieved with any microscope. Nevertheless, this might end up in being a tedious process if a dedicated rotation specimen holder is not available. In such a case, the orientation can only be adjusted by retracting, manually rotating the specimen, and inserting the specimen holder again into the microscope. Nowadays, some segmented detectors, such as the one in the JEM-ARM200F, allow azimuthal rotation so that the detector can be aligned with the symmetry of the diffraction pattern.

In the following, the influence of the detector rotation on the obtainable DPC signal is examined. It is to note that the detector rotation angles φ are defined as an anticlockwise rotation with respect to an orientation at which the S_x-direction of the detector is aligned with the x-direction of the image. A description of how to determine the detector rotation is given in Chapter 3.1.2.

Fig. 30(a) shows the simulated DPC images of a 24.58 nm thick Si specimen viewed along the [110] direction. Here a defocus of C_1 = -2 nm below the entrance slice of the

specimen structure is selected to obtain a good correlation to the electric field distribution of one unit cell. Details concerning the optimum defocus and the defocus dependent correlation of the measured electric field distribution to the real field distribution of one unit cell are given in Chapter 5.2. A convergence semi-angle of 25 mrad was chosen, which corresponds well to the typically used convergence semi-angle in the experiments shown in Chapter 6. All DPC images in Fig. 30(a) are calculated using Layer2 in a bisected way.

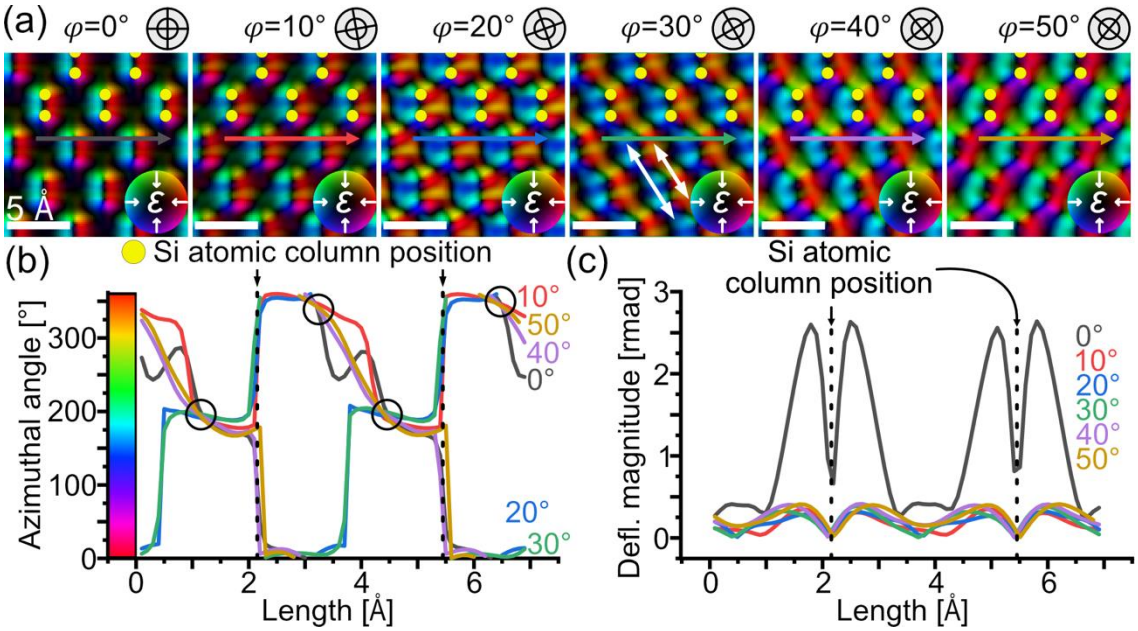

Figure 30: (a) Simulated DPC images for detector rotations of 0°, 10°, 20°, 30°, 40° and 50°. The detector is rotated in an anticlockwise manner. The thickness of the specimen structure amounts to 24.58 nm, which is far above the threshold value at which the measured DPC signals correspond to actual values of the electrostatic potential present in the specimen. However, as the thickness of the Si specimen can typically only be prepared in the range of 20 nm to 30 nm, even by FIB, this thickness helps to understand the effects influencing the DPC measurements at typical specimen thicknesses besides having an almost completely built-up diffraction pattern as this thickness is a substantial fraction of the extinction length. All images are calculated with a convergence semi-angle of 25 mrad and a defocus of -2 nm without other lens aberrations. (b) Line profiles of azimuthal angle of the deflection direction to the x-axis of the DPC image for all detector rotations in (a). Line profiles are marked by the arrows in (a). The colour code on the left side of the plot gives a reference to the colour code in the DPC image. (c) Line profiles of the deflection magnitude for all detector rotations in (a). A list of parameters considered for the multislice image simulations is given in Table 16 in the Appendix.

As can be seen from the DPC image for a detector rotation of $\varphi = 0°$ in Fig. 30(a), the electric field distribution around the silicon dumbbells indicated by yellow dots is very much pronounced and exhibits colour wheels around each individual atomic column. In the areas between the two atomic columns of the Si dumbbells, where the atomic potentials overlap, a superposition of the potentials resulting in a reduction of the measurable electric field magnitude is observed. This is also the case for other positions, where the deflections from individual atomic potentials point in opposing directions. With increasing detector rotation, the deflection distribution is drastically changed especially in areas between the atomic column positions, giving rise to stripe-like features which are especially visible for a detector rotation of $\varphi = 30°$. The stripe-

like features extend in diagonal directions from dumbbell to dumbbell and are exemplarily indicated by the white arrows. A possible explanation for the occurrence of changes especially between the dumbbell positions is that the DPC signal is not dominated by the electric field close to the focus plane at those areas, but drastically influenced by a combination of inhomogeneous intensity due to diffraction effects and the detector response function. In addition, the deflection in the vicinity of atomic columns (areas of strong deflection magnitudes around dumbbells) is also altered with the detector rotation. While the deflection distribution for a detector rotation of 0° is very much spatially compressed around a dumbbell, a very broad deflection distribution, which also extends to half the distance to the next dumbbell, is observed at a detector rotation of 20°.

For a quantitative comparison between the DPC images simulated for different detector rotations, line profiles of the azimuthal deflection angle as well as the deflection magnitude are depicted in Figs. 30(b, c). In both figures, the atomic column positions are marked by dashed lines. The azimuthal angle of deflection to the x-axis of the detector exhibits strong deviations between the line profiles acquired for different detector rotations. However, close to the atomic column positions, the deflection directions are quite similar for all detector rotations and are close to 180° azimuthal deflection angle on the left and close to 0° on the right of the atomic column position. This can be explained by the strong atomic potentials close to the atomic columns. It should be noted that due to the present rotational periodicity and the arrangement of the values in an interval of 360° interruptions in the line profiles occur at positions where the values go beyond the interval limits. In addition, regions in which all curves intersect are observed at the right and left of the atomic positions. These regions are highlighted by circles in Fig. 30(b). While the azimuthal angle changes the most drastically in the region far of the atomic column positions for a detector rotation of 0° or very abruptly for detector rotations of 20° and 30°, all other detector rotations show a more gradual change in deflection rotation and regions with almost constant deflection direction.

Concerning the deflection magnitude (Fig. 30(c)), the difference in magnitude between a detector rotation of 0° and all other detector rotations is evident. This might be due to the way the symmetry of the CBED pattern is aligned on the symmetric segmented detector. The overall maximum of deflection magnitude is always observed close to the atomic column position amounting to 2.6 mrad for a detector rotation of 0° and 0.4 mrad for a detector rotation of 50°. Hence, the deflection magnitude and the measurable electric fields in the experiment will be different by a factor of 6.5 depending on the detector rotation. In addition to the difference in deflection magnitude, the extension of areas with high deflection magnitude broadens with detector rotation, as already observed in Fig. 30(a).

In the following the influence of the detector rotation on measured DPC images of Si[110] is investigated experimentally and compared to DPC image simulations. This investigation also utilises the scattergram. The scattergram, which is employed in reference [91] to detect influences, such as lens aberrations and specimen tilt, has proven to be a versatile tool to investigate and characterise features with a high frequency of occurrence in the measured DPC image and the related calibrated electric field as well as the deflection distributions. The scattergram is thus a promising tool to investigate the combined influences of detector response function and diffraction effects on the DPC images as it allows for investigations on the complete deflection distribution and not only a line profile.

All measured images are acquired for a (30 ± 2) nm thick Si specimen and noise-reduced using the non-rigid image registration to ensure sufficient resolution in the momentum space (further details of the influence of noise on the momentum space resolution are given in Chapter 5.7). The detector was rotated in an anticlockwise manner to the dumbbell axis in steps of 10°. The simulated DPC images were obtained using a structure thickness of 30.72 nm and a defocus of -6 nm without other lens aberrations. Fig. 31 depicts the measured and simulated DPC images with the corresponding scattergrams for detector rotations φ of 0°, 30° and 40°. In addition, the simultaneously acquired HAADF images are displayed together with the measured DPC image. These detector rotations are chosen as examples. DPC measurements and image simulations including other detector rotations can be found in Fig. 85 and Fig. 86 in the Appendix.

The DPC image and HAADF image of Si[110] with a detector rotation of 0° to the dumbbell axis are displayed in Fig. 31(a). Here, a detector rotation of 0° corresponds to the case in which the p_x-direction of the detector is aligned with the x-direction of the scan. The latter is aligned with the dumbbell axis. This scenario is indicated by the coordinate system (upper half of Fig. 31(a)) as well as the detector sketch including a red arrow for p_x-direction in the lower right corner of the HAADF image. As expected, the DPC image shows an overlap of two rotational symmetric colour wheels at each dumbbell arising from the rotational symmetric potential around each individual atomic column. Since the atomic columns have a projected spacing of only 136 pm, reduced field magnitudes are measured along connecting axis, as the opposing field vectors cancel each other out in the region of overlap. Moreover, the DPC image shows weak deflections at interatomic positions. The corresponding scattergram depicted in Fig. 31(a) exhibits several characteristic features. The scattergram shows an off-centre maximum, a bowtie-like structure having its long axis in p_y-direction (marked by the two arrows) and a broad rounded distribution of deflections. A possible explanation for the formation of an off-centre maximum in the measured scattergram is a small specimen tilt (here, about 5 mrad), as already discussed in a previous publication [91] and investigated in Chapter 5.6. Furthermore, an increased number of transferred momenta leading to a line-like feature at the top end of the bowtie-like structure in the scattergram is observed and marked by a white circle.

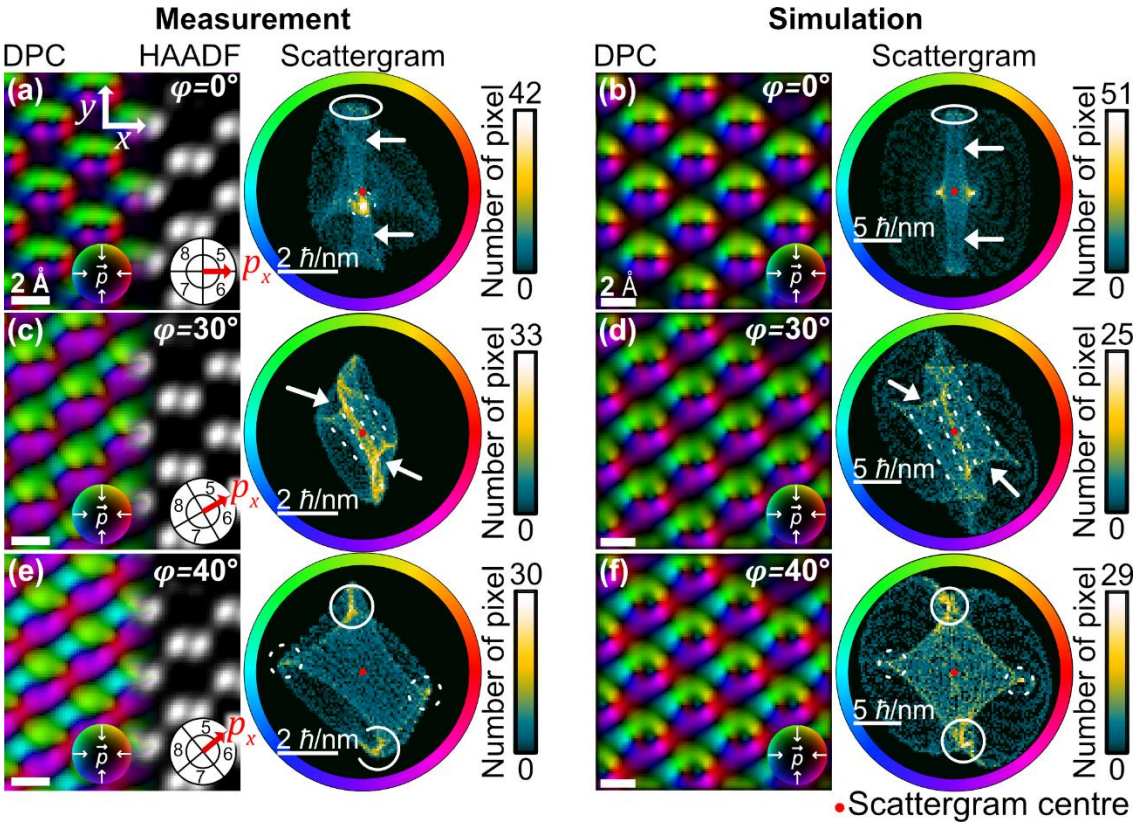

Figure 31: (a-f) Comparison of measured and simulated DPC images with corresponding scattergrams for detector rotations of 0°, 30° and 40°. (a, c, e) Measured DPC images and scattergrams for a (30 ± 2) nm thick Si specimen analysed in [110] zone-axis orientation. The sketches of the detector in the lower right corner of the measurements illustrate the detector orientation to the crystal structure. (b, d, f) DPC simulations and corresponding scattergrams of a 30.72 nm thick Si[110] structure using a defocus of -6 nm with the same detector rotations as used in (a, c, e). The reader is referred to the main body of the text for explanations on the arrows, the circles, and the lines in the scattergrams. Experimental parameters for (a, c, d) can be found in Table 42. Simulation parameters of the multislice image simulations shown in (b, d, f) are listed in Table 17.

The associated DPC image simulation and the scattergram in Fig. 31(b) are in good agreement to the measured DPC data. The simulated DPC image shows two slightly overlapping colour wheels for each dumbbell. The corresponding scattergram exhibits characteristic features, which are quite similar to the scattergram of the measured DPC image. However, in comparison to the measured scattergram in Fig. 31(a), the simulated scattergram in Fig. 31(b) exhibits not only one but two off-centre maxima which are displaced in p_x-direction. The two off-centre maxima arise from weak transferred momenta in the regions of overlap atomic potentials and at interatomic pixels as will be further investigated below. Moreover, the simulated scattergram exhibits an elongated rectangular feature expanding in p_y-direction which is slightly compressed at the ends and marked by white arrows in Fig. 31(b). This feature is very similar to the bowtie-like feature of the measured scattergram in Fig. 31(a) and shows a line-like feature at the ends, one of which is exemplarily marked by a white circle. Some minor differences of the measured and simulated scattergrams presumably arise from the presence of residual lens aberration (discussed in Chapter 5.5) in combination with a slight specimen tilt, which is not taken into account in the simulations. Another

explanation for the difference of measured and simulated scattergram features is the neglect of amorphous layers in the simulated structure.

Comparing the magnitudes of the transferred momenta in the measurements and in the simulations, it can be seen that the transferred momenta are much stronger in the simulations. This can also be explained by presence of lens aberrations (Chapter 5.5) as well as the presence of amorphous layers on top and bottom of the Si specimen in the measurements reducing the proportion of crystalline material in the 30 nm thick Si specimen. Moreover, the scattergram of the simulated DPC image exhibits wave-like features (indicated by a white line), which are not observed in case of the measurement. This wave-like features arise due to the neglect of image noise and lattice vibrations (frozen lattice configurations) as well as the grid of scan positions.

The DPC image measured with a detector rotation of $\varphi = 30°$ shown in Fig. 31(c) exhibits dominant green and purple stripe-like features. This is a result of the detector geometry and the symmetry of the diffraction pattern. The formation of stripe-like features is also observed in the corresponding DPC image simulation for a detector rotation of 30° in Fig. 31(d). Both scattergrams for the measured and simulated DPC image at a detector rotation of 30° show elongated distributions with crescent-like features at the ends (marked by white arrows) and a step like behaviour across the elongated scattergram features (white dashed lines). The similarity of the two scattergrams is obvious and on the one hand confirms the correlation between measurement and simulation and on the other hand highlights the fact that fine differences of the transferred momentum distribution can be detected by utilising the scattergram. Again, the fine differences are due to a small specimen tilt and possible residual lens aberrations absent in the simulation. Using such a DPC measurement to calculate charge densities or to interpret features of the electrostatic field distribution due to bonding would lead to a completely different result than in the case of a detector rotation of 0°.

Figs. 31(e, f) depict the measured and simulated DPC images and corresponding scattergrams for a detector rotation of 40°. While the stripe-like features which were apparent for a detector rotation of 30° (Figs. 31(c, d)) get less dominant, interatomic pixels show much increased transferred momenta. This is the reason for a much wider rectangular structure instead of the elongated rectangular feature in the scattergram, which is visible for a detector rotation of 0° (Fig. 31(b)). This feature is terminated in both the simulation and the measurement by intensity maxima at the corners, as it is indicated by the white dashed and solid circles. In addition, it is skirted by a broader extended round intensity distribution. This round intensity distribution shows a lower extension in the case of the measurement than in the case of the simulation, but this can be explained by slightly different defoci (Chapter 5.2). The intensity maxima in the corners of the scattergram feature, outlined with a white solid line, show significantly higher intensity than those marked with a dashed line in both the measurement and simulation.

The influence of detector rotation generally depends on the symmetry of the crystal structure. In the case of Si[110], the diffraction pattern possesses a two-fold axial symmetry. Therefore, due to the possibility to rotate the detector by 90°, all possible scenarios of azimuthal detector orientation can be imaged. For crystals with higher axial symmetry in beam direction, a smaller possible rotation range of the detector is necessary due to higher symmetry of the diffraction pattern.

To better understand the origin of characteristic scattergram features and their dependence on the detector rotation, a novel technique, the so-called scattergram filtering, has been developed in this work and is used to reveal the position of features in the DPC image which contribute to characteristic scattergram features. Details on the scattergram filtering are given in Chapter 4.2. In the following, all filtered scattergrams depict the transferred momentum distribution in units of $\hbar \cdot \mathrm{nm}^{-1}$ with the scattergram having the same number of pixels as the corresponding DPC image.
Fig. 32 displays a series of scattergram-filtered DPC images of the measurement and simulation for Si[110] using a detector rotation of 0°. Scattergram-filtered DPC images for detector rotations of 30° and 40° are depicted in Fig. 33. The unfiltered experimental and unfiltered simulated DPC images with corresponding scattergrams are displayed in Figs. 32(a-d) (also displayed in Fig. 31(a, b)), respectively.
The DPC image and scattergram after scattergram filtering using a circular aperture that is centred on the off-centre maximum are depicted in Figs. 32(e, f). By scattergram filtering, all pixels of the DPC image that have transferred momenta inside the circular aperture are removed, i.e. their difference signals are set to zero. Since the magnitude of transferred momentum increases from the centre of the scattergram towards the scattergram periphery and the aperture is placed close to the scattergram centre, the resulting scattergram and DPC image features correspond to transferred momenta with high magnitudes in the DPC image. This can be seen in the filtered DPC image in Fig. 32(e), in which mostly the dominant transferred momenta close to the Si dumbbells contribute and transferred momenta at interatomic positions are removed. That interatomic pixels are removed will become clearer below when investigating the DPC image (Figs. 32(q-t)) to which the inverse filter is applied. The filtered DPC measurement is in good agreement to the filtered simulation (Figs. 32(g, h)), for which a centred circular aperture with a diameter that exceeds the distance of both peaks close to the scattergram centre was used. After filtering, only regions of the DPC image take part in the image formation that are close to the atomic column positions.

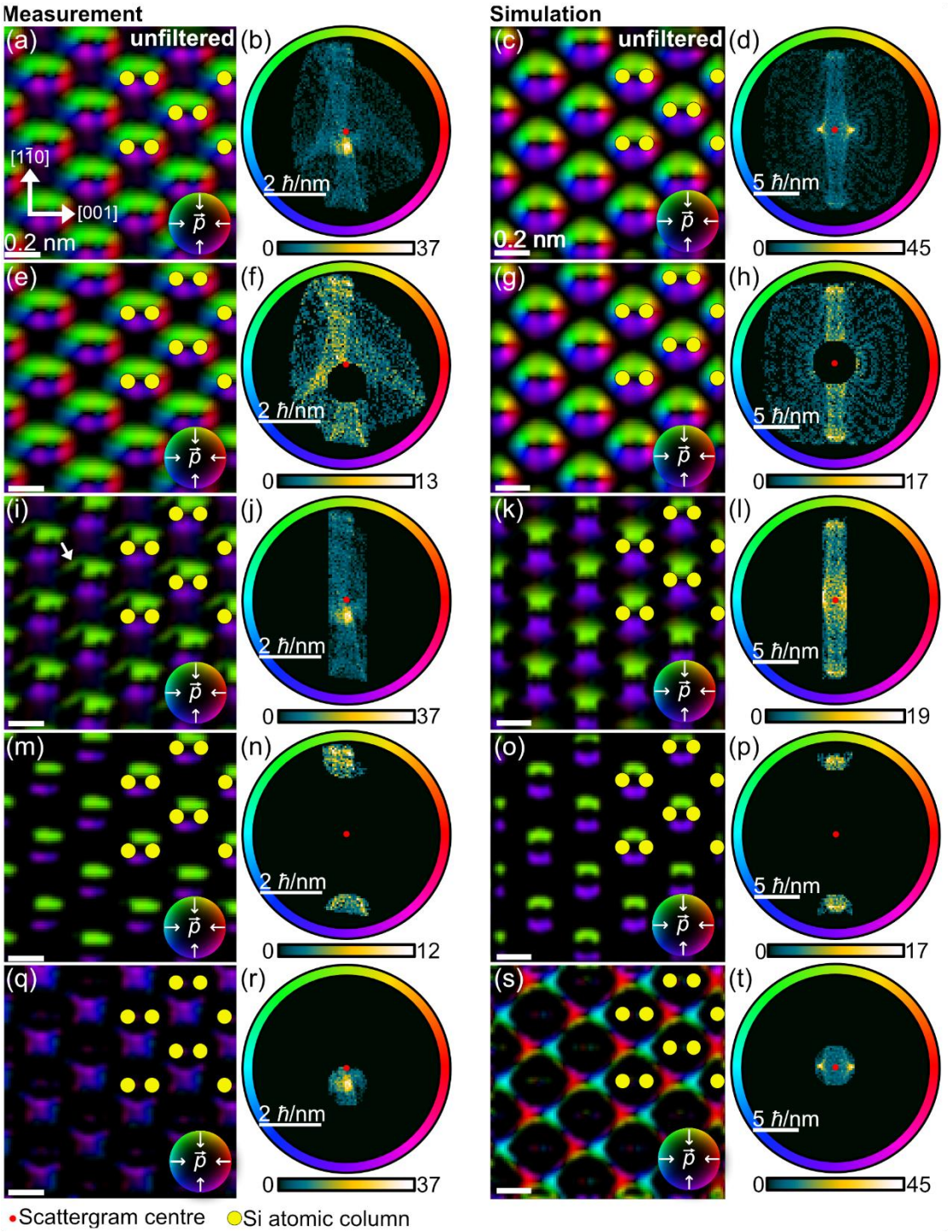

Figure 32: (a) Unfiltered DPC measurement with (b) corresponding scattergram for a (30 ± 2) nm thick Si specimen analysed in [110] zone-axis orientation. (c) Corresponding simulation and (d) scattergram achieved with a defocus of -6 nm and without other lens aberrations. (e) DPC measurement scattergram-filtered by an off-centre circular aperture with (f) corresponding scattergram. (g) DPC image simulation and (h) scattergram, where only deflections from pixels close to the silicon dumbbells pass the filter. (i) DPC image after applying a rectangular filter extending in p_y-direction on the (j) scattergram. (k) Filtered DPC image simulations and (l) corresponding scattergram after application of a similar rectangular filter. (m) Filtered DPC measurement and (n) scattergram after filtering line-like features at the end of the bowtie- or box-like scattergram features. (o) DPC image simulations and (p) scattergram after application of a similar filter to reveal the position of line-like features of the rectangular scattergram feature. (q) Filtered DPC measurement with (r) corresponding scattergram after using a circular aperture on the off-centre maximum in the scattergram distribution. (s) DPC image of the central part of the (t) scattergram distribution arising from transferred momenta at interatomic pixels. Simulation parameters of the multislice image simulation are listed in Table 17. Experimental parameters can be found in Table 42.

The regions of the measured and simulated DPC images leading to the characteristic bowtie-like or elongated box-like feature in the scattergram are analysed in Figs. 32(i-l). In this case, a rectangular filter, which removes all transferred momenta outside the filter aperture, was used. The measurement (Figs. 32(i, j)) and the simulation (Figs. 32(k, l)) are in good agreement, as the remaining transferred momenta are arranged as a bar-like structure above and below the silicon dumbbells. For both the measurement and the simulations, bar-like structures above the dumbbells have a strong green colour, while the ones below have a purple colour. The origin of the bars can be explained by the superimposed projected potentials of the atomic columns of the silicon dumbbells. In addition, the bar-like green features in the measurement show a tail-like extension, which is located at the upper left corner of each dumbbell. This tail-like feature arises at interatomic pixels and points in the $<1\bar{1}1>$ direction. The tail-like structure is exemplarily marked with an arrow in Fig. 32(e). In contrast to the measurement, this tail-like structure is not visible in the simulation in Fig. 32(g). These tail-like features are a result of the specimen tilt which is not considered in the simulations.

The scattergrams in Fig. 32(j) and especially in Fig. 32(l) exhibit an additional line-like feature at the ends of the bowtie-like or elongated box-like feature, which is investigated in more detail in Figs. 32(m-p). This line-like structure is filtered for both the measurement and the simulation by two apertures. The resulting scattergrams are shown in Figs. 32(n, p). As the line-like features are also present in the bowtie-like or elongated box-like feature, it is obvious that their corresponding pixels in the DPC image are part of the bar-like structures in the filtered DPC images in Figs. 32(i, k). This is approved by the filtered DPC images (Figs. 32(m, o)) in which again bar-like features but with smaller extension than in Figs. 32(i, k) are found parallel to the axis connecting the atomic columns of a dumbbell. It is interesting to note that the bar-like features in Figs. 32(m, o) cover a large proportion of the area of the bar-like structures in Figs. 32(I, k) although the aperture filters only act on a rather small area of the scattergram. The overlapping potentials above and below the dumbbells lead to dominant, almost unidirectional transferred momenta resulting in the line-like feature at the ends of the bowtie- or box-like scattergram features.

The positions of transferred momenta in the unfiltered DPC measurement contributing to the off-centre maximum in the corresponding scattergram are depicted in Fig. 32(q). For this purpose, an off-centre aperture filter is applied, and the resulting scattergram is displayed in Fig. 32(r). For comparison, the filtered simulated DPC image of the characteristic features close to the scattergram centre is displayed in Fig. 32(s). For this, a centred circular filter is used on the scattergram (Fig. 32(t)). As can be seen from the DPC image in Figs. 32(q, r), the transferred momenta passing through the filter arise at interatomic pixels where weak deflections are expected. Compared to the unfiltered DPC images, these features are more readily recognisable due to the normalisation of the DPC image after filtering. The shape and position in the filtered measurement and the filtered simulation are in good agreement as both exhibit a star-

like shape. In the measured DPC images, these pixels exhibit a purple colour, while in the simulated DPC images a distorted inverse colour wheel with dominating red and bright blue colours is observed. These star-like shaped features are connected by line-like features in direction of the spikes of the star-like shape. The purple colour corresponding to an almost unidirectional transfer of momentum at interatomic pixels in the measured DPC image can be explained by a specimen tilt. The domination bright blue and red colours possibly mean that electrons at interatomic pixels are more likely deflected in <001> than in <1$\bar{1}$0> directions.

Fig. 33 depicts the filtered DPC images and image simulations with corresponding scattergrams for azimuthal detector rotation angles φ of 30° (Figs. 33(a-h)) and 40° (Figs. 33(i-t)) around the optical axis. The original DPC images and unfiltered scattergrams for a detector rotation of 30° can be seen in Figs. 33(a, b) for the measurement and in Figs. 33(c, d) for the simulation. Figs. 31(e-h) analogously depict the DPC images and scattergrams of the corresponding simulations for a detector rotation of 40°.

Fig. 33(e) shows the measured DPC image obtained with a detector rotation of 30° in which only the transferred momenta leading to the crescent-like features in the unfiltered scattergram pass the filter. The corresponding scattergram is depicted in Fig. 33(f). To obtain the filtered DPC image, two circular apertures were positioned around each of the crescent-like features. The corresponding simulation in Figs. 33(g, h) shows structures after scattergram filtering that are very similar to those of the measurement. It is clearly visible that both the simulation and the measurement after filtering show distinctive green- and purple-coloured areas extending from dumbbell to dumbbell. They are in good agreement as purple-coloured areas in both the measurement and simulation widen in the middle (indicated by white arrow). In the simulation, however, both the green and purple features show a point symmetry about the centre of the dumbbells. This is not visible in the measurement due to the existing specimen tilt. The difference of green- and purple-coloured features would have a major impact on the conversion into electric fields and the calculation of charge densities.

Fig. 33(m) depicts the filtered DPC image at a detector rotation of 40°, in which only the maxima of the scattergram distribution at the corners of the rectangular feature pass the filter (Fig. 33(n)). The simulation, after applying a similar filter, is shown in Figs. 33(o, p). A good agreement between the simulation and the measurement is observed, as only structures above and below the dumbbells can be seen in both the measurement and simulation. However, the simulation shows finer details, such as the lobes that appear near the atom positions. One possible explanation for the missing of these finer details in the experimental image is the resolution of the microscope, which has a drastic effect on the resolution of details of the DPC signal distribution.

Figs. 33(q-t) show the filtered DPC images and corresponding scattergrams for the same detector rotation as in Figs. 33(i-l) with two circular apertures placed on the other two corners of the rectangular structure, where maxima with high intensity are visible.

The simulation and measurement reveal structures in the momentum distribution on the right and on the left side of the dumbbells.

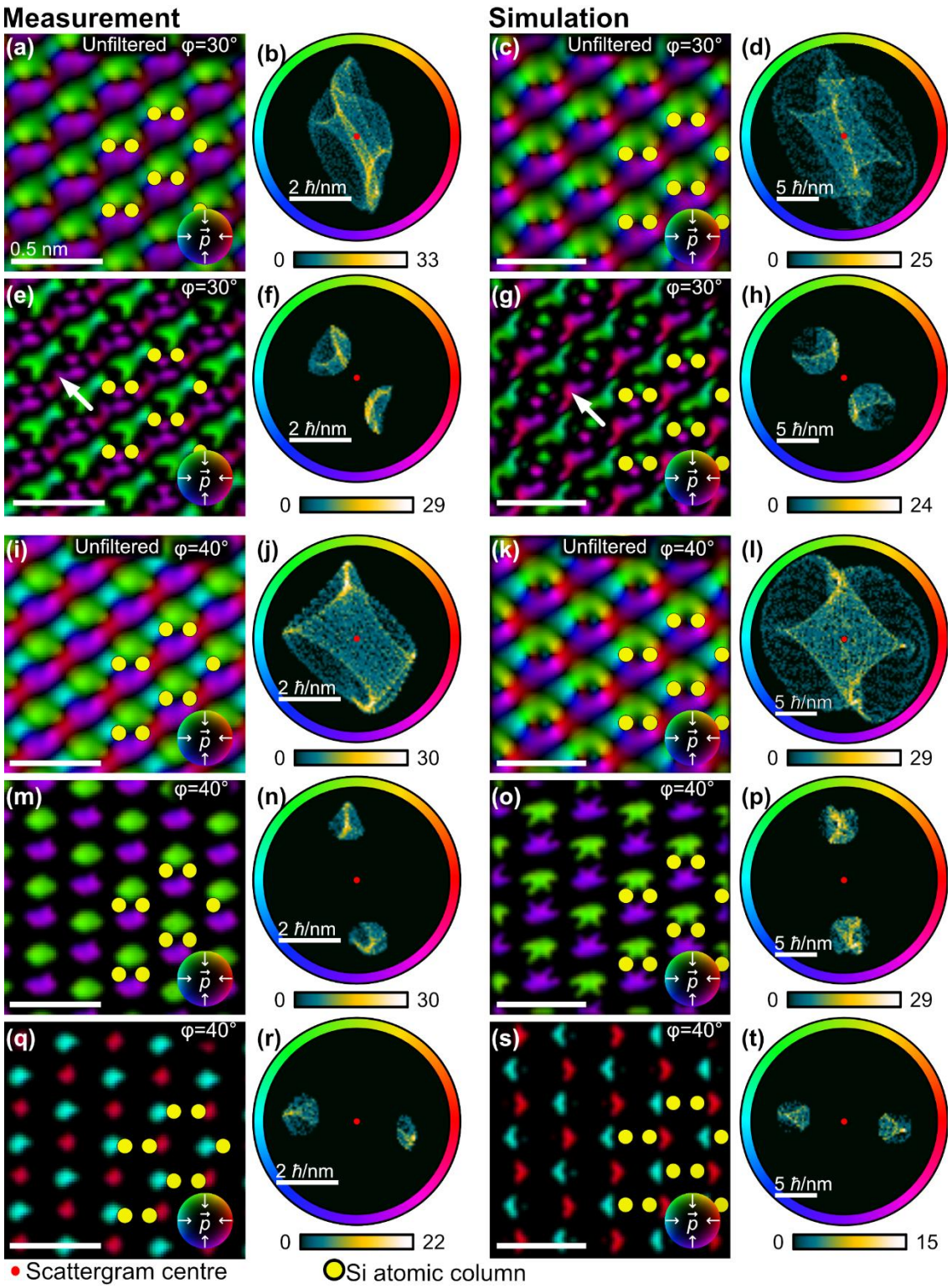

Figure 33: Measured and simulated unfiltered DPC images and corresponding scattergrams for a detector rotation of (a-d) 30° and (i-l) 40°. Scattergram-filtered DPC images and image simulations with corresponding scattergrams for azimuthal detector rotations of 30° (e-h) and 40° (m-t). Simulation parameters of the multislice image simulations shown in (c, g, k, o, s) are listed in Table 17. Experimental parameters can be found in Table 42.

Summarizing the results displayed in Fig. 32 and Fig. 33, it is obvious that transferred momenta with high magnitudes are typically generated in the vicinity of atomic columns. Transferred momenta with weaker magnitudes that can be found close to the centre of the scattergram mostly originate from regions between the atomic column positions. It is important to note that regardless of their magnitude, DPC image features are crucially influenced by the detector orientation. This is evident from the drastic impact of the detector rotation on the observable characteristic scattergram features. In this respect, the scattergram and its filtering are effective tools for the analysis of the detector rotation.

To investigate to what extend the detector rotation influences the direction and magnitude of the obtainable DPC signal, DPC image simulations were performed with detector rotations ranging from 0° to 80° in steps of 10°. The detector rotation of 0° corresponds to the case in which the p_x-direction of the detector is aligned with the x-direction of the image. Furthermore, the simulations were achieved using a specimen thickness of 30.72 nm, an underfocus of -6 nm and the segments of Layer2 in a bisected way. The original simulations including the HAADF and the DPC images as well as calculated maps of the electric field magnitude and the charge density are displayed in Fig. 87 and Fig. 88 in the Appendix. Further details of the simulation parameters are given in Table 18 in the Appendix. Next, the standard deviation of the azimuthal deflection direction (Fig. 34(a)) and polar deflection magnitude (Fig. 34(b)) were determined for each pixel from the simulated DPC images. The standard deviations indicate how much a pixel's measurable deflection direction and magnitude measured at each pixel are prone to changes arising from different detector rotations.
The standard deviation of the azimuthal deflection direction (Fig. 34(a)) reveals that the detector rotation most drastically changes the azimuthal deflection direction at interatomic pixels. As the maximum standard deviation amounts to 73.8°, it is obvious that rotating the detector can completely change the observable features in DPC images and related quantities such as the charge density distribution especially at interatomic pixels. Line-like features of strong standard deviation are observable which protrude in <1$\bar{1}$0> directions. One of the line-like features is exemplarily marked by white dotted lines in (Fig. 34(a)). The occurrence of the line-like features can possibly be explained by the fact that the beam interacts with a mostly symmetric potential at the corresponding pixels due to the crystal structure and its extension in the specimen. This ultimately leads to strongly symmetric intensity distributions on the detector especially in the region of the direct beam of the CBED pattern. As a result, measurable DPC signals at these pixels are particularly sensitive to the detector orientation.
The map of the standard deviation of the deflection magnitude (Fig. 34(b)) also shows strong differences in the measurable deflection magnitude for detector rotations between 0° and 80°, mostly at pixels located at a far distance from the atomic column positions. A reduced change in deflection magnitude along the detector rotation is

observed at high symmetry points, as exemplified by the red arrows in (Fig. 34(b)). A possible explanation for this is the high symmetry of the CBED pattern at such positions, which mostly influences the deflection direction and not its magnitude along the rotation of the detector.

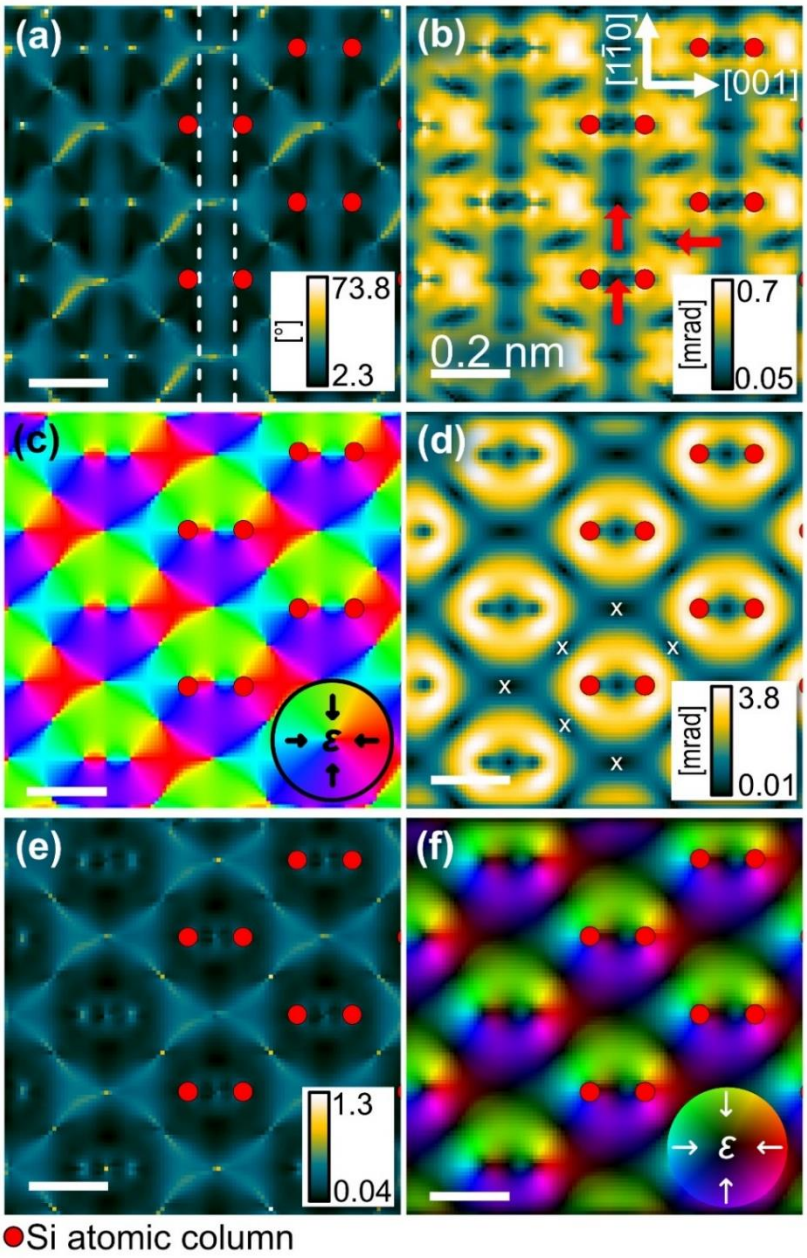

Figure 34: Pixelwise standard deviation of (a) the azimuthal deflection direction and (b) the deflection magnitude in Si in [110] zone-axis orientation obtained from a simulation series for different detector rotations. Images are acquired with Layer2 in a bisected way. Pixelwise mean value of (c) azimuthal deflection direction and (d) deflection magnitude. (e) Standard deviation of deflection magnitude normalised by the mean value. (f) Colour-coded DPC image obtained from the mean values of deflection direction and magnitude. A list of simulation parameters is given in Table 18 in the Appendix.

Figs. 34(c, d) depict maps of the mean value of the deflection direction and the deflection magnitude, respectively. Rotational symmetric deflection directions around the atomic columns are evident in Fig. 34(c) from the almost perfect colour wheel distributions which are centred on the atomic columns (marked with red dots). These

colour wheel distributions are only distorted in the region of potential overlap. The mean value of deflection magnitude (Fig. 34(d)) shows highest magnitudes of up to 3.8 mrad on the left and right side of the dumbbells and, as expected, strongly reduced magnitudes at high symmetry points of the projected crystal (exemplarily marked by white crosses). It should be emphasised that standard deviations of the deflection magnitude (Fig. 34(b)) of 0.7 mrad are a considerable fraction of the mean deflection magnitude. This once again highlights the influence of detector rotation on the measured field magnitude. Thus, any small differences in field magnitude due to bonding might be falsely identified by the use of a segmented detector.

Fig. 34(e) displays the map of the relative standard deviation of deflection magnitude. The relative standard deviation is the standard deviation of deflection magnitude normalised by its mean value. The maximum of the relative standard deviation amounts to 1.3 which indicates that measurable deflection magnitudes are enormously influenced by the detector rotation. It is also obvious that interatomic pixels are most likely influenced by the detector rotation. Fig. 34(f) shows the colour-coded mean DPC image. The mean DPC image is calculated from the mean deflection direction and magnitude. Here, rotational symmetric fields around individual atomic columns are evident.

It is interesting to determine which of the considered detector rotation generates the DPC image which is the most similar to the mean DPC image. This is investigated in Fig. 35 showing the cross-correlation coefficients of the mean DPC image and the DPC image simulations achieved with different detector rotations. Cross-correlations are calculated for the direction, magnitude as well as the combination of direction and magnitude. For the combination of direction and magnitude, the cross-correlation coefficients of the direction and magnitude were multiplied. From Fig. 35 it is obvious that detector rotations which are close to 0° or a multiple of 90° achieve the highest similarity to the mean DPC signal. This can be explained by the symmetry CBED pattern. Additionally, a good correlation is observed for a detector rotation of 40°.

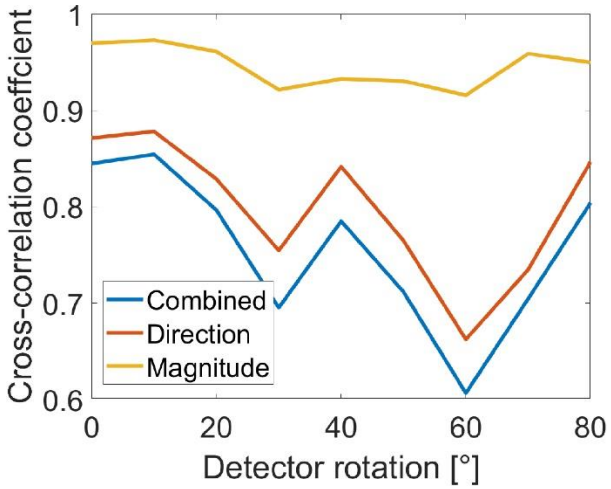

Figure 35: Cross-correlation coefficients of the mean DPC image and the individual DPC image simulations calculated for the direction, magnitude and a combination of direction and magnitude in dependence of the detector rotation.

As will be shown in Chapter 5.2, the results are also focus-dependent as the measurable DPC signal is strongly sensitive to defocus. However, the analysis presented above indicates how strongly the measurable field magnitudes are influenced by the detector rotation. It is also to be expected that the influence of the detector rotation is reduced with smaller specimen thicknesses due to reduced diffraction effects.

5.2. Specimen thickness and defocus

It has already been reported in literature that the specimen thickness has a drastic influence on the DPC signal magnitude [36, 43]. These investigations have been conducted using DPC image simulations mostly on $SrTiO_3$ in [001] zone-axis orientation for segmented [36] as well as pixelated detectors [43]. The main result of these investigations is that a maximum specimen thickness of about 5 nm is allowed for the quantification of atomic electric fields [27, 43]. This is due to the fact that the image contrast in DPC measurements is related to the gradient of the electron wave's phase [90], which is only measurable as long as the specimen fulfils the phase object approximation [27, 36]. However, it was also reported that more qualitative information about the field structure can be obtained even with specimen thicknesses as large as ~20 nm [43]. At such a thickness DPC images with rotational symmetric fields around atomic columns resembling the field structure of a unit cell can still be obtained.

For quantitative atomic electric field analysis, a specimen thickness of about

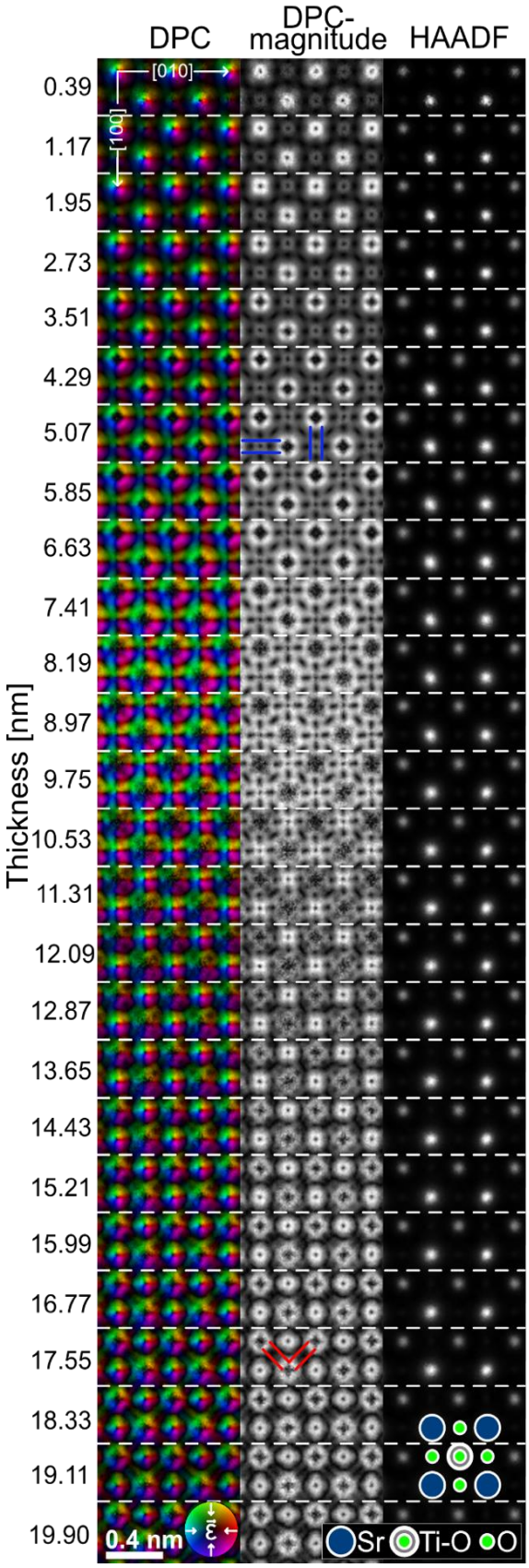

Figure 36: Influence of the specimen thickness on simulated DPC images of $SrTiO_3$ in [001] zone-axis orientation with corresponding DPC signal magnitude and HAADF image. The reader is referred to the main body of the text for explanation on the annotations. A list of simulation parameters can be found in Table 19.

5 nm is difficult to prepare as most materials tend to bend or have a large native oxide layer on the top and bottom surface. Therefore, the influence of the specimen thickness on the shape and features inside the DPC image as well as the magnitude must be known for correct image interpretation. Besides the specimen thickness, the defocus also influences the measured field maps [36, 43]. This has been investigated in literature finding that the optimum defocus is close to half the specimen thickness [43]. This is also the case in annular bright-field imaging [43, 147, 148] which mainly uses the direct beam similar to DPC. Furthermore, solid routines for finding an optimum defocus for HAADF imaging have been reported [149], but these cannot be so straightforwardly transferred to DPC analyses [91, 148].

Thus, in the following the influence of specimen thickness and defocus are investigated particularly focussing on electric field investigations at sub-atomic resolution. The influence of thickness and defocus are separately investigated and an “in-line” routine for optimizing the defocus is developed. All findings have been reported in a publication [91]. The results are briefly presented here.

Although it was already reported in literature that the optimum defocus for the acquisition of DPC images shown in Fig. 36 is close to half the specimen thickness [43], in the following, the focus is set to the entrance plane. This allows to investigate the influence of the specimen thickness decoupled from the influence of defocus. Fig. 36 displays DPC image simulations of $SrTiO_3$ in [001] zone-axis orientation as a function of the specimen thickness. Starting with a specimen thickness of a single unit cell, the specimen thickness is increased in steps of two unit cells. All simulations in Fig. 36 are normalised to their maximum intensity to allow for investigation of structures, which arise with increasing specimen thickness. It is to note that this would correspond to a realistic experimental situation, in which measurable image intensities are amplified to be close to saturation in the brightest pixel. Furthermore, the DPC signal magnitude and the simulated HAADF intensity are shown along with the DPC maps in Fig. 36. Atomic column positions are obtained from the HAADF image due to its Z contrast and exemplarily marked at the lower right corner of the tableau.

It is observed in Fig. 36 that the colour wheel-like DPC signal distributions around atomic columns, which are very similar to the experimental results reported by Shibata et al. [24], broaden with increasing specimen thickness. In addition, stripe-like features arise at interatomic pixels especially parallel to low index lattice planes, e.g. lines parallel to {100} at a thickness of 5.07 nm. This is due to diffraction induced redistribution of intensity in combination with the detector response function as described in Chapter 5.1. A further increase of the specimen thickness leads in DPC images to stronger intensities at oxygen atomic columns than on Sr or Ti-O columns, and stripe-like features in <110> type directions arise above a specimen thickness of about 16 nm. These stripe-like features are exemplarily marked by red parallel lines in the DPC magnitude image for a thickness of 17.55 nm in the middle column of Fig. 36. In contrast to the DPC signal, the HAADF images show less dependence on the specimen thickness. This is in good agreement with the literature [147]. Thus, HAADF

images allow for a robust image interpretation over a wide range of specimen thicknesses, as only the intensity of atomic columns increases with increasing specimen thickness. However, due to the Z^{2-x} contrast pure oxygen columns exhibit a lower intensity than the other atomic columns and are therefore less visible than in the DPC images.

The influence of defocus on the DPC image has been investigated by Addiego et al. [43] for $SrTiO_3$ and pixelated detectors by comparing the DPC images obtained with the focus at the entrance plane, half the specimen height and the exit plane of the specimen. In addition, Robert et al. have investigated the influence of defocus on momentum-resolved DPC images as well as HAADF images, finding a focus mismatch between both [148].

Since the focus can be almost freely chosen with sub-nanometre precision, microscopist need to know in detail how the DPC images change with defocus. This is even more important because the defocus can only be corrected “in-line” during DPC imaging and not afterwards. Therefore, Fig. 37 shows the combined influence of the specimen thickness and defocus for specimen thicknesses ranging from 0.39 nm to 19.92 nm and defoci from 5 nm (overfocus) to -10 nm (underfocus) in steps of 1 nm. A defocus value of 0 nm corresponds to the situation in which the beam is focused on the entrance plane of the specimen. It is to note that small deviations in specimen thickness arise between Fig. 36 and Fig. 37 due to different frozen-lattice configurations. The intensity scales are kept constant for all image simulations. This allows to also observe changes in the DPC signal magnitude. These intensity changes are also observable during experiments, as the contrast and brightness settings of the DPC detection process are typically kept constant during focusing. When analysing the desired area having a certain thickness, the observable image intensities would also change when altering the defocus. Tableaus of DPC images as a function of defocus and specimen thickness, in which all individual DPC image simulations are normalised to their maximum intensity, can be found in the Appendix (Fig. 89, Fig. 90 and Fig. 91).

As can be seen in Fig. 37, finding the optimum defocus is crucial for DPC imaging, as significant changes in the DPC image can be observed. When the beam is focused above the entrance plane of the specimen very small overall intensities are detected. The contrast is low in comparison to other defocus values and an inversion of the colour distribution around atomic columns can be observed (well visible in the individually normalised DPC image in Fig. 89). An inversion of colour distribution means that all deflections are rotated by 180°. This inversion is particularly evident for a thickness of about 5.86 nm (compare images for defocus values of 5 nm and -5 nm). With increasing specimen thickness, the DPC signal vanishes for overfocus conditions.

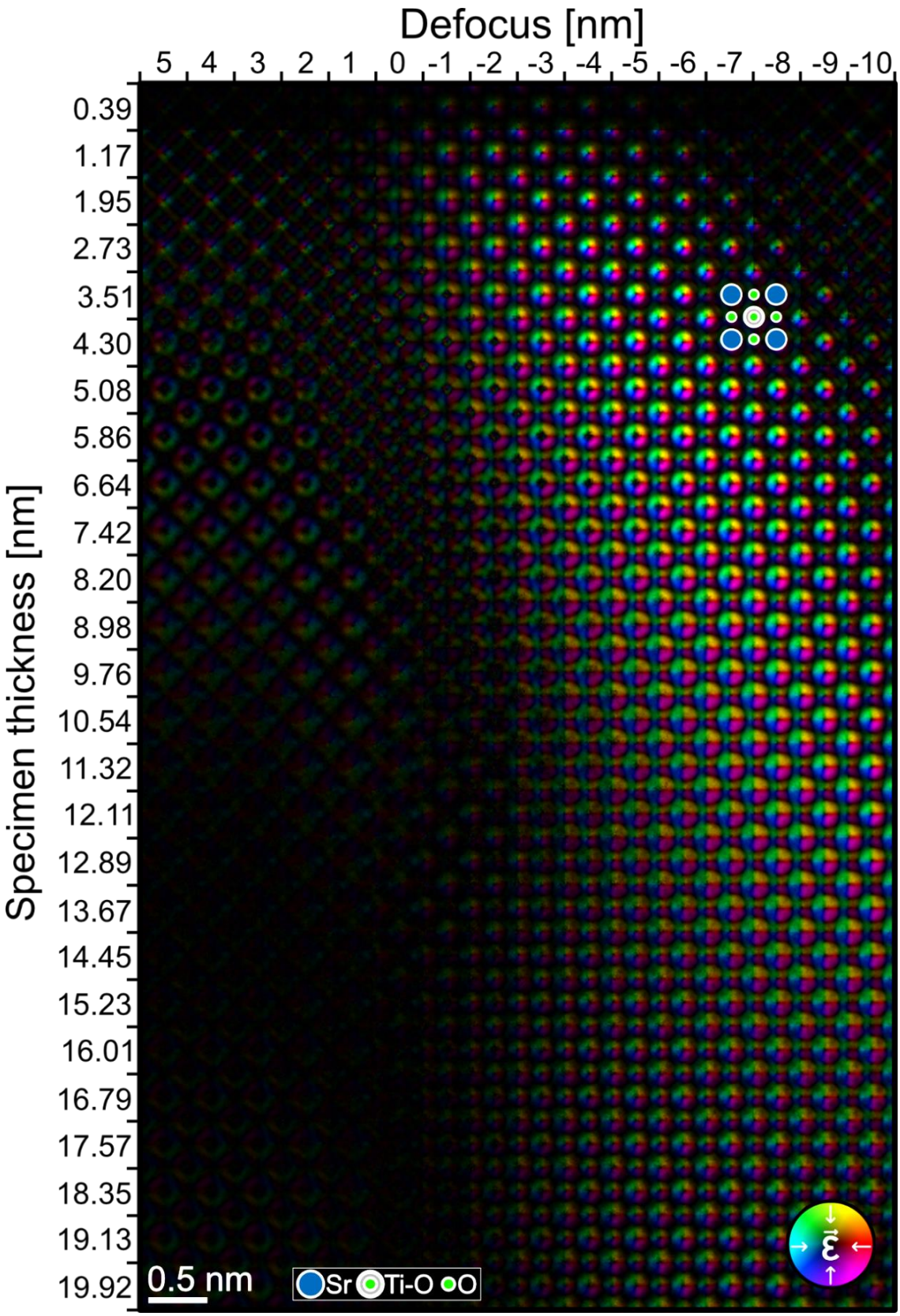

Figure 37: DPC image simulations of $SrTiO_3$ in [001] zone-axis orientation probing the influence of the specimen thickness and defocus on the obtainable DPC images. The intensity scale is identical for all considered simulations. Except of defocus no other lens aberrations are assumed in the calculation. Positions of Sr, Ti-O and O atomic columns are exemplarily marked. Tableaus of individually normalised DPC image simulations for the same defocus and thickness ranges are displayed in Fig. 89, Fig. 90 and Fig. 91. Simulation parameters are listed in Table 20.

When adjusting the focus to underfocus conditions, the colour wheel distribution first switches to the expected distribution, having the red colour on the right side of the atomic column. In addition, the extension of the colour wheel passes through a maximum. This is especially well visible for thicknesses below 8.20 nm. Moving the beam further to underfocus conditions leads to a spatial compression of the colour wheels around the atomic column positions and more importantly to a maximum DPC signal magnitude for certain underfoci. For a 5 nm thick specimen, focusing the beam on the entrance plane leads to blurred colour wheels, which show less contrast in the regions of overlap due to their high extension. The extension of these colour wheels decreases for defoci between -3 nm and -8 nm (below half the specimen thickness and below the specimen exit plane).

For larger specimen thicknesses above 13 nm almost uniform colour wheels are observed for all considered underfoci. This can also be seen in the colour wheels which have approximately the same extension regardless of the underfocus at the largest considered sample thickness. A compression of the extension and stronger contrasts between O and Sr as well as Ti-O columns are expected for higher underfoci but not shown here. The DPC images for the largest specimen thickness do not resemble the DPC images of a unit cell for all considered defoci, which is mainly evident from the differences between pure O and Sr columns. Therefore, it is necessary to analyse the ranges of specimen thickness and defocus which allow the measurement of quantitatively interpretable DPC images. This is investigated below by analysing the achievable mean DPC signal magnitude and the similarity of the DPC image to the DPC image of a unit cell, which is measured by the cross-correlation of both images.

To this end, Fig. 38(a) displays the mean DPC signal magnitude as a function of specimen thickness and defocus. The mean DPC signal is obtained by calculating the pixel-by-pixel average of the simulated DPC image for a certain combination of defocus and specimen thickness. It is observed that increased mean DPC signal magnitudes are measurable at specimen thicknesses for certain defoci. For $SrTiO_3$, the highest mean DPC signal magnitudes are achieved for defoci in between half the specimen thickness and the exit plane. The overall maximum of mean DPC signal magnitude can be obtained for specimen thicknesses between 6 nm and 7.5 nm using a underfocus of -4 nm to -5 nm. It is to note that these thickness and defocus combinations are only valid for $SrTiO_3$ and might change considerably when other Z-materials with different Coulomb potential are investigated. Investigations of the defocus-dependent mean DPC signal magnitude for Si[110] with a thickness of 30.72 nm are given in Chapter A.2.3 in the Appendix.

To further investigate the optimum defocus, a linear fit was applied to the maximum mean DPC signal magnitudes of all specimen thicknesses t, leading to the following relation for the optimum defocus C_1 [91]:

$$C_1\,[\text{nm}] = (-0.57 \pm 0.01) \cdot t\,[\text{nm}] + (-0.4 \pm 0.1)\,\text{nm}. \tag{48}$$

This linear fit is marked as a red dashed line in Fig. 38(a). Negative values of C_1 correspond to underfocus conditions.

Fig. 38(b) displays the cross-correlation coefficients of the images for the considered specimen thickness-defocus-combinations and the DPC image of a specimen with the thickness of one unit cell. This cross-correlation coefficient is used to quantitatively determine the similarities between any of the simulated DPC images and the image of one unit cell. The optimum defocus for a certain thickness is defined as the one at which the obtainable DPC image exhibits the highest similarity to the image of a unit cell, as diffraction contrasts and other effects might otherwise introduce artefacts to the DPC image, facilitating misinterpretations. It is found that the DPC image as closest as possible to the image of a unit cell is obtained for defoci below the specimen exit plane for specimen thicknesses below 10 nm. For higher specimen thicknesses, even an acceptable correlation is obtained when the beam is focused between half the specimen thickness and the exit plane. This is in good agreement to the findings of Addiego et al [43]. It is still worth to note that the ratios of DPC signal magnitudes of pure O, Sr and Ti-O atomic columns might not represent the theoretical ratios obtained for a single unit cell thick specimen as observed in Fig. 37.

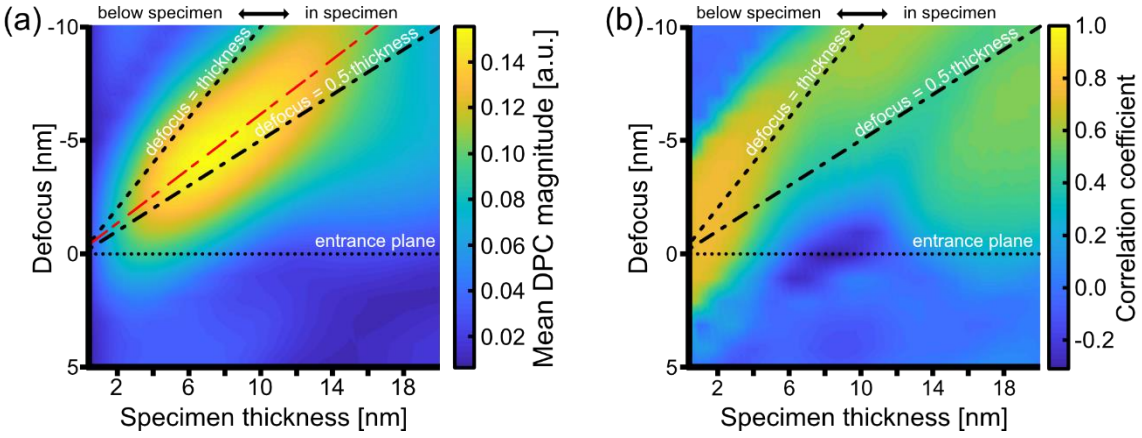

Figure 38: (a) Pixel-by-pixel average of the DPC signal magnitude (mean DPC magnitude) as a function of specimen thickness and defocus. A focus of C_1=0 nm corresponds to a situation in which the beam is focused on the entrance plane of the specimen (marked by a dotted black line). Half the specimen thickness is marked by a dashed-dotted black line, and the specimen exit plane by a dashed black line. The red dashed line displays a linear fit to the defocus and specimen thicknesses at which the maximum DPC signal is observed. (b) Cross-correlation coefficient between images simulated for the given specimen thicknesses plus defoci and the DPC image of a single unit cell. Simulation parameters of the related multislice image simulations are given in Table 20.

Overall, Fig. 38 highlights that the focus for the maximum mean DPC signal is different from the focus where the DPC image resembles best to the DPC image of a unit cell. However, Fig. 38 allows to derive a recipe for the “in-line” optimisation of the defocus, where the measured image is close to that of a unit cell. If the exact relation between the optimum defocus for the maximum mean DPC signal magnitude and the defocus for the optimum cross-correlation is known, one can readily reach the optimum defocus at which the DPC image resembles the image of one unit cell, by simply adjusting the defocus by the known value given by these simulations. This recipe has been

successfully applied for finding the right focus in iDPC measurements of a cuprate superconductor consisting of $La_2CuO_{4+\delta}$ and $La_2O_{2+\delta}$ spacer layers to reveal that excess oxygen atoms are located in the spacer layer [105].

In addition to the DPC image contrasts, the measurable image intensities are important and depend on specimen thickness. One might expect a linear increase with thickness. However, it can be seen in Fig. 38(a) that a global maximum of the measurable image intensity forms. The image intensity as a function of the specimen thickness will therefore be analysed in more detail in the following.
Fig. 39 shows the image-integrated, arithmetic mean DPC signal and the image-integrated DPC signal normalised to the thickness as a function of the specimen thickness, determined from simulated images in Fig. 37. The focus for each thickness is chosen in such that image intensities are maximised (dashed red line in Fig. 38(a) and Eq. 48). As can be seen from Fig. 39, the mean magnitude of the DPC signal first increases with increasing specimen thickness because the number of scatterers leading to an intensity redistribution on the detector increases. It reaches a maximum at approximately 9 nm. At a specimen thickness of about 9 nm the maximum obtainable DPC signal is achievable with a defocus of -5.6 nm, i.e. slightly below the specimen half-thickness. Beyond a specimen thickness of 9 nm diffraction effects, the extension of the electron beam inside the specimen seeing an inhomogeneous potential landscape, as well as the detector response function led to a reduction of detectable DPC signal magnitude.

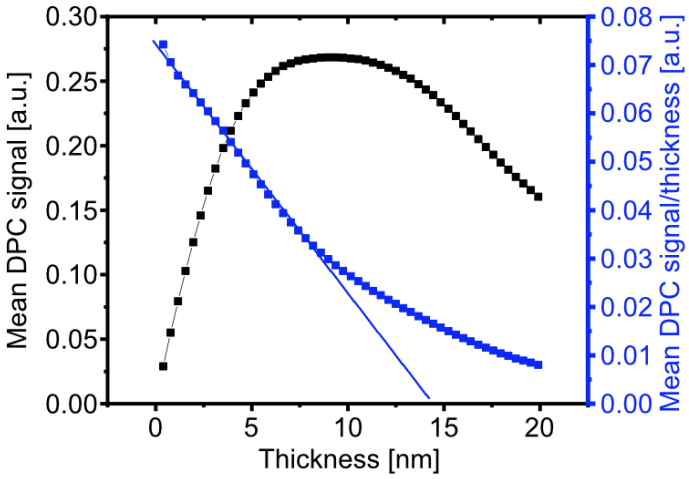

Figure 39: DPC signal magnitude averaged over a DPC image of $SrTiO_3$[001] and mean DPC signal magnitude normalised to the specimen thickness as a function of the specimen thickness. The focus is obtained from the fit in Fig. 38 which is marked by the red dashed curve. The resulting fit for the optimum defocus guaranteeing for maximum obtainable DPC signal is C_1=(-0.57 ± 0.01) · t + (-0.4 ± 0.1) nm, in which negative values correspnd to an underfocus.

The thickness normalised DPC magnitude in Fig. 39 shows a linear decrease up to a specimen thickness of 8 nm. This contrasts with an expected constant value for the thickness normalised DPC signal and shows that the measured projected signal is always lower than the signal measurable for a single unit cell. This indicates that

already very few atoms at the surface of a specimen strongly modify the beam impinging on the subsequently following atomic layers, i.e. DPC is extremely sensitive to dynamic effects. However, it is necessary to be able to calculate the electric field correctly in order to determine, e.g. charge densities correctly. Therefore, a method for correcting the signal reducing effects on the DPC signal is described below.

To account for the detector response function, Shibata et al. used a scaling factor to match the obtained DPC signal acquired with an segmented detector to the one of a first moment detector [24, 41]. However, to reveal the true electric field distribution, also the diffraction effects and the influence of beam extension needs to be considered. Since DPC primarily uses the direct beam, parallels can be drawn with bright-field imaging. The bright-field contrasts in general consist of a phase term S_ϕ, a diffraction term S_{diff} and a scattering term S_{scat} [150]. If diffraction and scattering have a negligible influence on the signal, which is particularly the case for small specimen thicknesses, the reduction in image contrast can be approximated by a compensation term $-k_{\mathrm{comp}} \cdot t$, in which k_{comp} is a compensation coefficient and t the specimen thickness. As can be seen from Fig. 39, this linear dependency is fulfilled for specimen thicknesses below 8 nm. Thus, the DPC signal magnitude $S_{\mathrm{DPC,comp}}$ corresponding to the multiple of the signal magnitude of a unit cell can be derived by applying this compensation coefficient to the measured DPC signal magnitude S as follows:

$$S_{\mathrm{DPC,comp}} = S - k_{\mathrm{comp}} \cdot t. \tag{49}$$

The compensation coefficient of the linear fit which is marked by a blue line in Fig. 39 amounts to $k_{\mathrm{comp}} = (-2.6 \pm 0.3) \cdot 10^{-3}\ \mathrm{nm}^{-1}$. By applying this correction before converting the signal magnitude into calibrated electric field values, the true electric field corresponding to the field magnitude of a unit cell can be obtained. Nevertheless, as the DPC signal is strongly focus dependent, this correction is only valid in case of DPC images with maximised mean signal magnitudes.

5.3. Acceleration voltage

The incident electron beam interacts via the Lorentz force with the electric and magnetic fields inside the specimen. As a result, a momentum $p_{\perp,x} = e \cdot \left(E_x \cdot t/v_{\mathrm{rel}} + B_y \cdot t\right)$ perpendicular to the optical axis is transferred onto the incident electrons (note that the indices of the electric and the magnetic field depict one of the vectorial components). The transferred momentum depends on the specimen thickness t, the elementary charge e, the reduced Planck's constant $\hbar$, and only for the electric and not the magnetic part of the Lorentz force on the relativistic electron velocity v_{rel} [38]. The relativistic electron velocity v_{rel} is a function of the acceleration voltage and results in increased transferred momenta and deflection angles for decreased acceleration voltages [38]. If both the electric field E_x and the magnetic field B_y contribute to the DPC image, the ratio of the influence of magnetic and electric fields can therefore be adjusted, since only the transferred momentum resulting from an electric field depends

on v_{rel} [38]. In addition to the transferred momentum as a function of the acceleration voltage, the diffraction phenomena that occur in the detection plane are also dependent on the acceleration voltage. This can be seen from the Bragg equation (Eq. 8) considering the wavelength of the electrons, which is dependent on the acceleration voltage. The Bragg angle depends on the distance d_{hkl} of lattice planes leading to diffraction. In high-resolution STEM, overlapping diffraction discs are present, as Bragg angles are typically much smaller than the typically selected convergence semi-angles of approximately 25 mrad. Due to the superposition of diffraction discs with the direct beam and interference phenomena, this results in intensity modulations [38, 91] in the detection plane that go beyond the simple intensity gradient due to the inhomogeneous potentials present at the location to be examined.

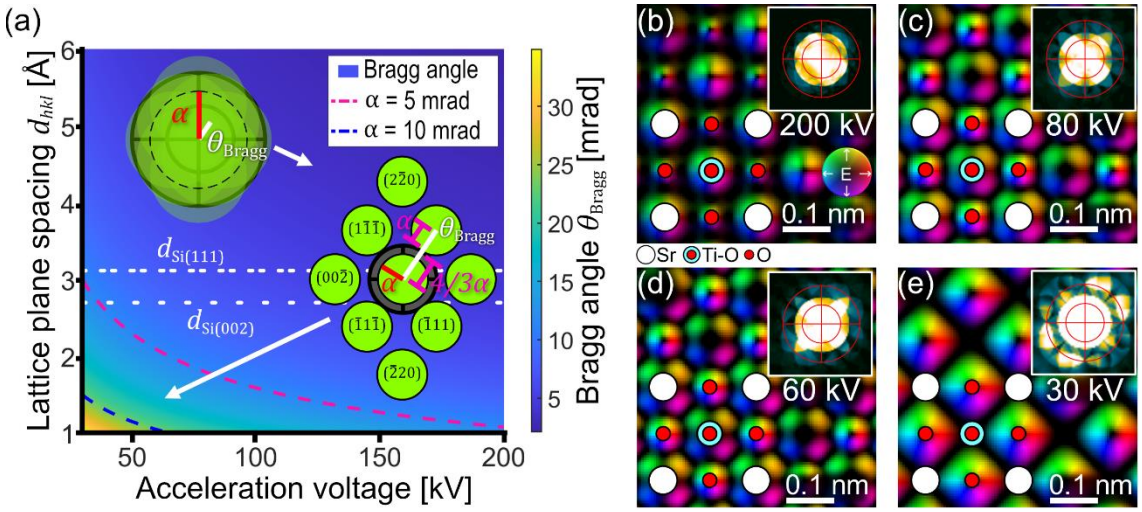

Figure 40: (a) Bragg angle θ_{Bragg} as a function of the lattice plane spacing d_{hkl} and the acceleration voltage. Insets show the two scenarios in which the Bragg angle θ_{Bragg} is smaller or greater than the convergence semi-angle α. The red and blue dashed lines indicate the threshold lattice plane spacing below which the condition $\theta_{\mathrm{Bragg}} > 7/3\,\alpha$ is fulfilled. For further explanations, the reader is referred to the main body of the text. Multislice DPC image simulations of a 6.25 nm thick $SrTiO_3$ structure in [001] zone-axis orientation which are achieved with acceleration voltages of (b) 200 kV, (c) 80 kV, (d) 60 kV and (e) 30 kV. In all image simulations a defocus of -3 nm below the entrance slice of the specimen structure is considered. Insets in (b-d) depict the CBED intensity distribution in the detection plane. The detector segments are indicated by red lines. Simulation parameters are listed in Table 21.

The inset in the top left of Fig. 40(a) illustrates this scenario, in which the Bragg angle θ_{Bragg} is smaller than the convergence semi-angle α of the direct beam. Zweck et al. state that the diffraction discs should be separated to minimise intensity modulations within the direct beam [38]. Fig. 40(a) therefore shows the Bragg angle θ_{Bragg} as a function of the acceleration voltage and the lattice planes spacings. To prevent diffracted spots from contributing to the measurement of the transferred momentum, they should not hit the detector. This is fulfilled if the Bragg angle θ_{Bragg} is $\theta_{\mathrm{Bragg}} > 7/3\,\alpha$ considering a direct beam that extends to half the outer detector segments. The factor 7/3 arises due to the fact that the detector extends to 4/3 α and another α is required to ensure that the diffraction discs do not overlap with the detector. This scenario is sketched in the lower right corner of Fig. 40(a) for a CBED

pattern from a face-centred cubic crystal structure including several diffraction discs and the detector.

Combinations of lattice plane spacings and acceleration voltages for which these conditions are fulfilled are indicated by the red and blue dotted lines for convergence semi-angles of 5 mrad and 10 mrad, respectively. These lines represent the upper limits of lattice plane spacings, which are “allowed” for the two considered convergence angles, as a function of the acceleration voltage. It should be noted that the distance between the diffraction discs below the curves monotonously increases allowing to only use the direct beam for DPC image acquisition. In addition, also off-axis DPC using one of the diffracted beams is possible to apply a filtering in momentum space during analysis quite similar to off-axis EELS [151]. This approach has so far not been investigated and is beyond the scope of this thesis. Moreover, Fig. 40(a) shows that even at a convergence semi-angle of 10 mrad and an acceleration voltage of 30 kV, a maximum lattice plane spacing of about 1.5 Å is allowed for diffraction spots to appear separated from each other in the detection plane. Since 1.5 Å is close to the resolving power of state-of-the-art microscopes at low keV, the diffraction phenomena would be reduced, however, imaging of sub-atomically resolved potentials is difficult to conduct.

For example, if silicon should be analysed in [110] zone-axis orientation, then the {002} diffraction discs fulfil the condition using a convergence semi-angle of 5 mrad at an acceleration voltage of 30 kV. However, the {111} diffraction discs would still not fulfil the condition and thus influence the measurement of transferred momentum due to an insufficiently small lattice plane spacing. Both lattice plane spacings are indicated in Fig. 40(a) by the white dashed lines. It can be seen in Fig. 40(a) that with the available acceleration voltages on the JEM-ARM200F and a convergence semi-angle of 25 mrad which is typical for high-resolution imaging, there is always an overlap of diffraction discs. Therefore, the question remains whether and to what extent artefacts arise due to the overlapping diffraction discs in the intensity distribution on the detector. This will be investigated in the following for the available acceleration voltages of the JEM-ARM200F.

Figs. 40(b-e) show multislice DPC image simulations of $SrTiO_3$ in [001] zone-axis orientation acquired with acceleration voltages of 200 kV, 80 kV, 60 kV and 30 kV. The simulation parameter for the images shown are similar except of the acceleration voltage. The specimen thickness amounts to 6.25 nm, and the defocus is set at -3 nm below the entrance slice of the specimen structure. The inner and outer polar collection angles of the detector segments resemble the ones used in the experiment at which half of Layer2 is illuminated with the direct beam using a convergence semi-angle of 25 mrad. As can be seen from Figs. 40(b-e), the extension of measurable electric fields around atomic column position increases with decreasing acceleration voltage. This is especially visible at the oxygen atomic columns and in good agreement to DPC image simulations by Edström et al. [152] which are based on the CoM signal and consider a 2.7 nm thick FePt structure and a convergence semi-angle of 25 mrad. Here, the colour wheels of Ti-O and Sr columns also increase in extension and reach the oxygen

sites already at an acceleration voltage of 80 kV. This increase in extension can be assigned to the stronger interaction of the electron beam with the specimen leading to increased deflection angles at low acceleration voltages. In addition, the electric field structure around the Ti-O and Sr columns loses its round shape presumably due to additional dynamical diffraction effects resulting in complex intensity redistribution in the beam. Furthermore, it should be emphasised that apparently only electric fields (colour wheels) in the vicinity of the O atom columns can be observed. This unexpected phenomenon will be further investigated in the next chapter and in Chapter A.2.4 in the Appendix. The insets in Figs. 40(b-e) display the diffraction pattern on the detector for the different acceleration voltages. At a convergence semi-angle of 25 mrad, the diffraction discs are not separated, leading to strong intensity modulations on the detector. This is in good agreement to the Bragg diffraction angles calculated in Fig. 40(a) and highlights the fact that the DPC signal might be more strongly influenced at lower acceleration voltages.

5.4. Real space probe intensity and the refocusing effect

In the previous chapter it was noticed that DPC images show very different DPC signal distributions depending on the acceleration voltage. In particular, the image at 30 kV in Fig. 40(e) unexpectedly showed no colour wheels around the Sr or Ti-O columns. Only the oxygen columns exhibit colour wheel-like signal distributions. Moreover, the extension of the electric field distribution of oxygen atomic columns at 30 kV is significantly greater than at 200 kV. To investigate the origin of these unexpected DPC signal distributions, the real space probe intensity inside the crystal is investigated for different specimen thicknesses in Fig. 41. This is achieved by using multislice simulations (Chapter 2.3) for three different positions of the beam impinging on a $SrTiO_3$ crystal assuming an acceleration voltage of 200 kV, a convergence semi-angle of 25 mrad and a defocus of 0 nm (entrance slice). Similar calculations have been utilised to study the influence of the defocus [43]. Further real space probe intensity distributions of this simulation series are depicted in Fig. 93 and Fig. 94 in the Appendix.

The beam positions which are considered for this investigation are sketched in Fig. 41(a) by the dark yellow (Sr atomic column), pink (O atomic column) and blue crosses (Ti-O atomic column) and are displaced by 0.05 nm in x-direction from the respective atomic. It is to note that only the beam position close to a Sr atomic column (yellow cross) is used for the real space probe intensities in Figs. 41(b-d).

Fig. 41(b) depicts the real space probe intensity of the incident electron beam which in the absence of lens aberrations exhibits a rotational symmetric Airy disc intensity distribution. Fig. 41(c) shows the intensity distribution of the beam after it has penetrated through a 7.6 nm thick slice of the crystal. It is observed that the maximum of beam intensity distribution is shifted in negative x-direction by approximately 0.12 nm from the initial beam position (white dot in Figs. 41(b-d)). This shift of intensity would lead to a measurable intensity redistribution in the detection plane and thus to a

measurable transferred momentum. A large fraction of the beam intensity, however, stays close to the initial beam position. In addition, an almost circular intensity distribution with rather large extension is observed (white dashed circle). This circular background is due to the convergence angle and broadening of the electron beam within the specimen. Additionally, several characteristic structures can be seen outside the dashed white circle. Those features are always composed of a local maximum in intensity and a tail-like extension. The tail-like extension is facing away from the initial beam position and the local maximum can be found close to it.

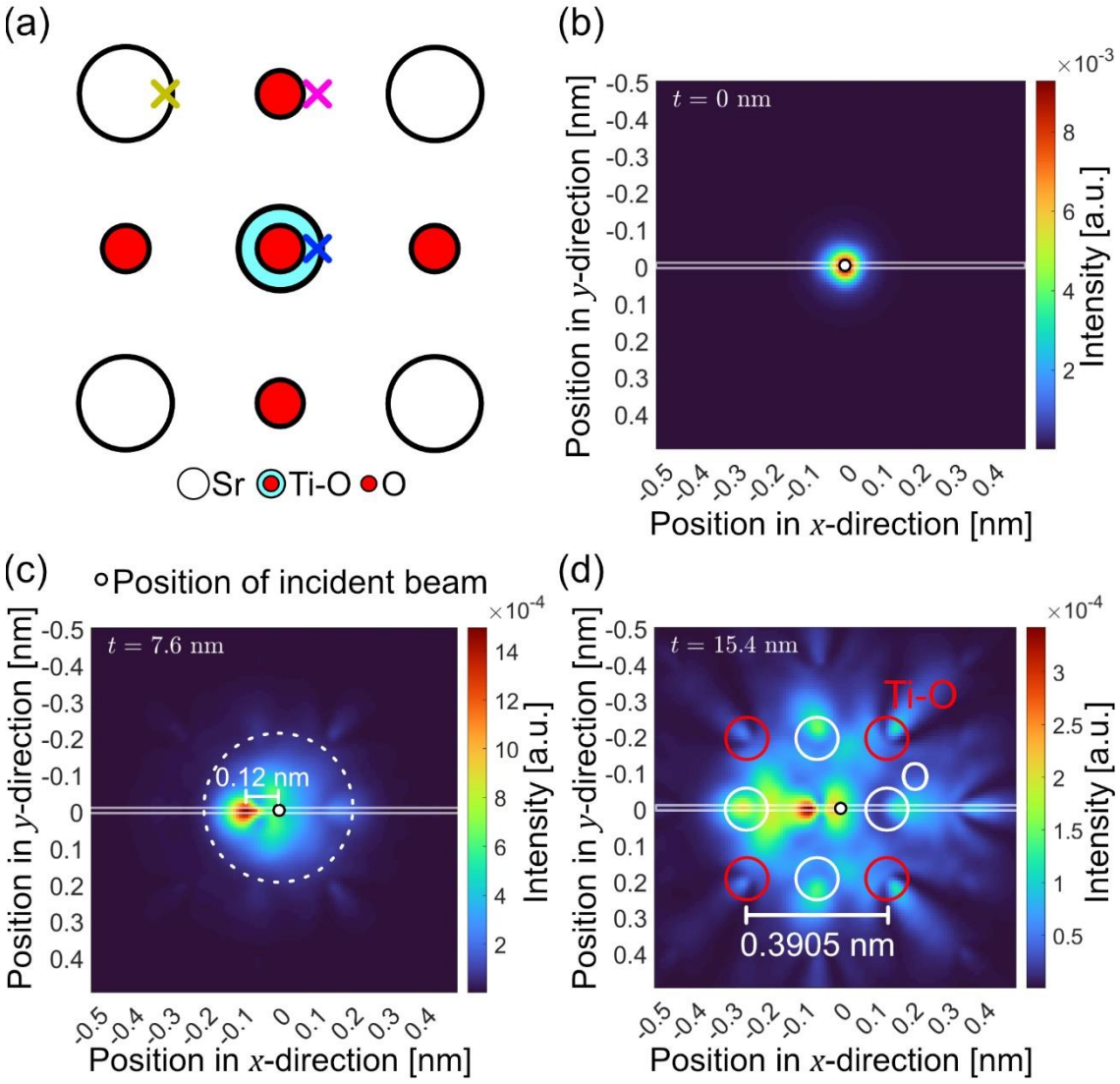

Figure 41: (a) Sketch of the $SrTiO_3$ crystal structure, including coloured crosses that mark the beam positions considered in this figure (yellow cross) as well as in Fig. 42 and Fig. 43. (b) Simulated real space probe intensity incident on a $SrTiO_3$ specimen at an acceleration voltage of 200 kV using a convergence semi-angle of 25 mrad. (c) Simulated real space probe intensity for the beam position marked by a yellow cross after the electron beam has interacted with a 7.6 nm and (d) a 15.4 nm thick crystal. The intensity is given as a fraction of complete beam intensity. The white parallel lines in (b-d) demarcate the area of the intensity distribution used for the acquisition of thickness dependent real space probe intensity profiles in x-direction (Fig. 42 and Fig. 43). For further explanations on the annotations in (c-d), the reader is referred to the main body of the text. Simulation parameters are given in Table 22 in the Appendix.

For a specimen thickness of 15.4 nm (Fig. 41(d)), these structures with tail-like extension become more pronounced. Here, the local maxima of features with tail-like extension form a pattern that matches the symmetry and atomic positions of the $SrTiO_3$ crystal structure. For highlighting this good matching, Fig. 41(d) contains white and red circles which are centred on the Ti-O and pure O atomic columns. Such patterns in the real space probe intensity have been observed in the literature and can be ascribed to a channeling of electrons along the atomic columns [153–155].
Summarising the results of Fig. 41(d), a major part of the intensity is deflected in the direction of the Sr column. It is still noteworthy that the overall maximum is still observed left to the initial beam position although a large part of the intensity is also found at the positions close to other atomic columns.

To further investigate this redistribution within the complete specimen, thickness dependent plots calculated from line profiles of the real space probe intensity for different initial beam positions are shown in Fig. 42 and Fig. 43. These thickness dependent plots are obtained for specimen thicknesses of up to 25 nm, for acceleration voltages of 200 kV and 30 kV, respectively, as well as for the three beam positions marked in Fig. 41(a). The thickness dependent plots are acquired from the area marked by two parallel white lines (for the x-direction in Figs. 41(b-d)).
Plots for an acceleration voltage of 200 kV are shown in Fig. 42. These approve that the redistribution of intensity is a dynamic process. This can be seen by the decrease of intensity directly below the initial beam position which is followed by an accumulation of intensity around several atomic columns with increasing specimen thickness. The latter is evident from the intensity in the vicinity of atomic columns especially at a specimen thickness of about 15 nm. Still, for all considered beam positions, a major part of the beam intensity is redistributed towards the nearest atomic column close by. Additionally, all three plots exhibit a cone-shaped background intensity, which can be seen by the triangular broadening of intensity within the specimen arising from the convergence semi-angle of 25 mrad.
For the beam position close to the Sr atomic column (Fig. 42(a)), it is observed that within the first 5 nm below the entrance plane, a large fraction of the beam intensity is found on the left side of the Sr atomic column. With increasing specimen thickness, the intensity on the left side of the Sr atomic column decreases as the beam broadens due its divergence. At larger specimen thicknesses a fraction of the real space probe intensity is again redistributed back to the right side of the Sr atomic column. This is particularly evident from the increased intensity on the right side of the Sr atomic column for a specimen thickness of 11 nm (upper white arrow). With further increase in thickness, the intensity oscillates along the Sr atomic column (both white arrows). This effect is also referred to as channeling effect and has been investigated for Z-contrast imaging [155–157]. In Fig. 42(b), the channeling effect is particularly pronounced along Ti-O atomic columns due to the smaller distance of Ti and O atoms in a Ti-O atomic columns than of the Sr atoms in a Sr atomic column. When the beam is placed next to

a pure O atomic column (pink cross in Fig. 41(a)), again a redistribution of intensity towards the next oxygen atomic column is observed in particular beyond a specimen thickness of 5 nm (Fig. 42(c)). However, the oscillation behaviour around this atomic column is not observed here which is assumed to be due to the weaker atomic potentials of the O atomic columns. The weaker potential landscape is also a possible explanation for the decreased amount of intensity redistributed towards the nearest O atomic column when comparing it to the intensity redistributed to a Sr or Ti-O atomic column for beam positions close to the Sr and Ti-O atomic columns.

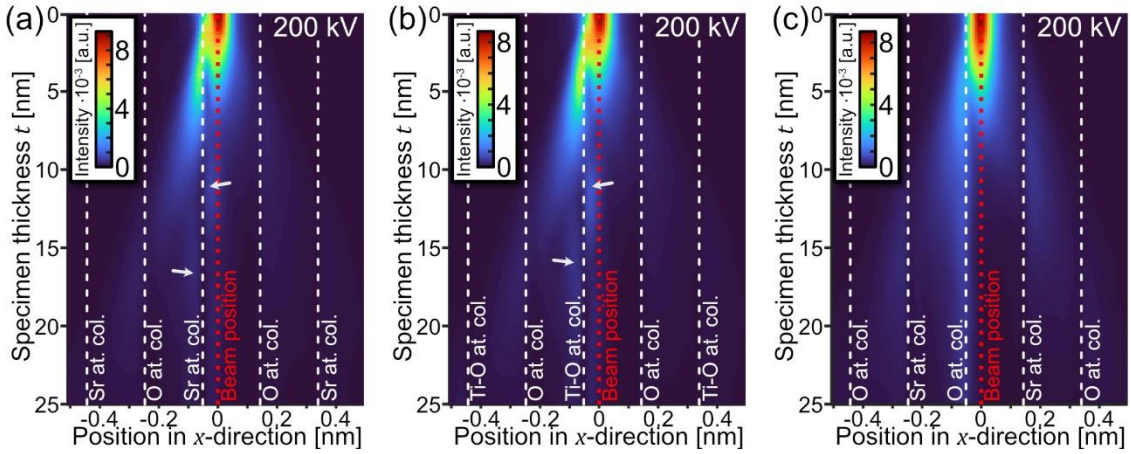

Figure 42: Real space probe intensity as a function of specimen thickness at an acceleration voltage of 200 kV if the beam is placed 0.05 nm next (right side) to a (a) Sr, (b) Ti-O and (c) O atomic column. Intensity profiles are obtained from the area marked by two parallel lines in Figs. 41(b-d). Atomic column positions are indicated by dashed lines. The reader is referred to the main body of the text for further explanations on the annotations. Simulation parameters are given in Table 22 in the Appendix.

Fig. 43 shows how the real space probe intensity behaves as a function of specimen thickness for the same beam positions and specimen structure but for an accelerating voltage of 30 kV. Here, already beyond a specimen thickness of less than a few nanometres, most of the beam intensity has left its original position (marked by the red dashed lines) and is deflected. This contrasts with the intensity distributions in Fig. 42 for an acceleration voltage of 200 kV. Additionally, the broadening of beam due to its divergence cannot be easily observed at this energy, presumably because of the stronger interaction of the incident electron beam with the specimen potentials.

Fig. 43(a) depicts the real space probe intensity if the beam is positioned close to an Sr atomic column. For such a beam position, a strong intensity redistribution towards the Sr atomic column is observed within the first few nanometres of the specimen. This can be seen by the global maximum of real space probe intensity, which is close to the nearest Sr atomic column. Despite the divergence of the electron beam, the intensity is focused into this global maximum through a dynamic coherent scattering process at the atomic potential.

It is expected that the intensity of the global maximum is further redistributed in negative x-direction and even beyond the Sr atomic column, as it is mostly found on the right sight of the Sr atomic column. Beyond a specimen thickness of 5 nm, however, most of the intensity is found on the right side of the initial beam position and

a channeling of intensity around the Sr atomic columns is not observed. A possible explanation is that the intensity of the global maximum is strongly deflected beyond the limits of the line profiles in negative x-direction due to the strong interaction with the Sr atomic potentials at this acceleration voltage.

The part of the intensity which propagates in positive x-direction due to the convergent shape of the electron beam, is split into one part, which is allocated on the O atomic column, and another part that is back deflected to the Sr atomic column. The latter is marked by a white curved line in Fig. 43(a).

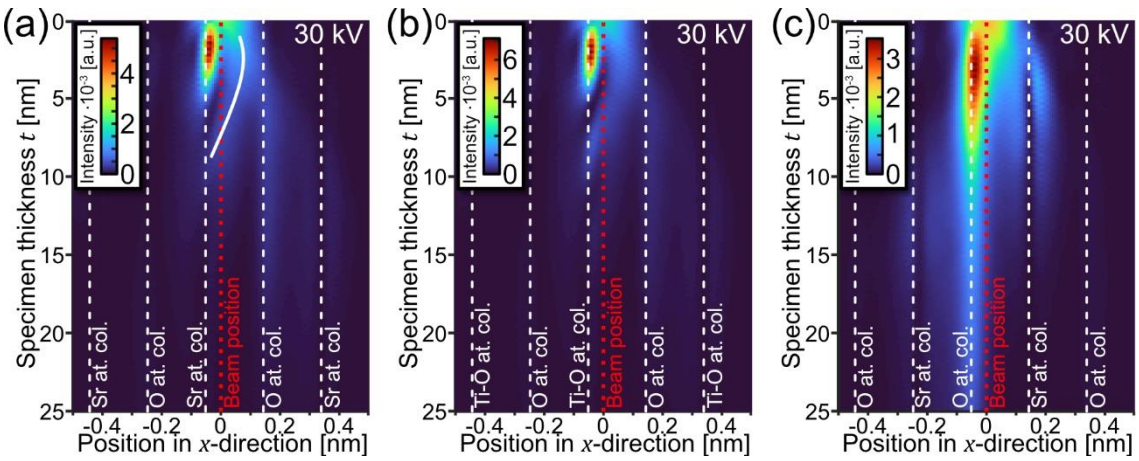

Figure 43: Contour plot of the line profiles in x-direction of the real space probe intensity for an acceleration voltage of 30 kV at three different beam positions (marked by coloured crosses in Fig. 41) at a distance of 0.05 nm in x-direction to the (a) Sr, (b) Ti-O and (c) O atomic columns. Simulation parameters are given in Table 23 in the Appendix.

Fig. 43(b) reveals that the real space probe intensity propagates in a similar manner when the beam is positioned close to a Ti-O or a Sr atomic column. This is due to similarity in projected atomic number ($Z_{\mathrm{Sr}} = 38$, $Z_{\mathrm{Ti-O}} = 30$). Similar to the real space probe intensity in Fig. 43(a), most of the intensity is found next to the Ti-O atomic column for a specimen thickness of approximately 2.5 nm.

When the beam is placed close to the pure O atomic columns, the resulting real space probe intensity as a function of specimen thickness behaves as in Fig. 43(c). After a thickness of approximately 1 nm a major part of the intensity can be found close to the pure O atomic column. With increasing thickness, a large proportion of the beam intensity aligns with the O atomic column position. In contrast to Fig. 42(c), no spatial oscillation of the real space probe intensity is observed for the considered acceleration voltage of 30 kV and specimen thicknesses. As a large proportion of the beam intensity is redistributed in direction of the O atomic column this would lead to a measurable redistribution of intensity in direction of the atomic column and a transferred momentum in the same direction.

The plots of real space probe intensity for the beam positions close to a pure O atomic column exhibit strong difference to the one depicted in Fig. 43(c) for a beam positions next to a Sr (Fig. 43(a)) or a Ti-O (Fig. 43(b)). These findings contrast with the findings for an acceleration voltage of 200 kV depicted in Fig. 42, which showed an almost

similar behaviour for all beam positions. The difference of the real space probe intensities for 200 kV and 30 kV are a possible explanation why colour wheels around the Sr and Ti-O atomic column positions are not observed at an acceleration voltage of 30 kV and a specimen thickness of 6.25 nm (Fig. 40(e)). Due to the atomic species-specific atomic potential and the resulting different redistribution of the beam intensity at different beam positions, the DPC image can exhibit drastically different features depending on the acceleration voltage.
Summarising the finding of Fig. 42 and Fig. 43, the beam intensity strongly varies with specimen thickness. More importantly, the beam intensity, which is propagated to a subsequent atom after it has interacted with a previous atom is strongly influenced by the potential of the previous atom and the intensity distribution incident on the previous atom.

To further understand the effect of the redistribution of real space probe intensity by previous atoms, which is then projected onto the next atom, the following investigations analyse the influence of the acceleration voltage, atomic species, and distance of two atoms on the DPC image. Fig. 44(a) schematically depicts two cases in a particle-based description and illustrates the trajectories of a single electron depending on the distance of two atoms.
In case (1), the electron moves in z-direction and first interacts with the atomic potential of the first atom. The electron is then projected with a certain deflection angle towards the second atom (deflected in negative x-direction). It moves no longer parallel to the z-direction. Therefore, it is incident with a certain angle to the z-direction and with a different impact parameter after traveling the distance $d_{\mathrm{atom},1}$.
In case (2), where the distance $d_{\mathrm{atom},2}$ between the two atoms is different and the electron impinges on the upper atom at the same impact parameter, the impact parameter of the electron and the second atom differs resulting in different final deflection angles.
A STEM electron beam consists of many electrons with different directions and impact parameters due to its convergent shape. For DPC signals and the complete description of the electron beam specimen interaction, all electrons must be considered. This is readily achieved by using the wave optical picture. The collective change in impact parameter of all beam electrons can be seen by the redistribution of real space probe intensity through a dynamic coherent scattering process in the wave optical picture. One example for the result of this dynamic coherent scattering process was already visible in Fig. 43(a) by the global maximum of intensity after the incident electron beam has already interacted with about 2.5 nm of the crystal. It is readily conceivable that the redistribution of intensity and the emergence of the global intensity maximum have an influence on the DPC signal. The influence of such a dynamic coherent scattering process on the DPC signal is in the following referred to as a refocusing effect. It is to note that term “refocusing effect” is introduced as an abbreviated description of the influence of intensity redistribution of beam intensity through a dynamic coherent

scattering process within the first few atomic slices on the DPC intensity. It also incorporates initial stages of a channeling phenomenon happening in the first few slices.

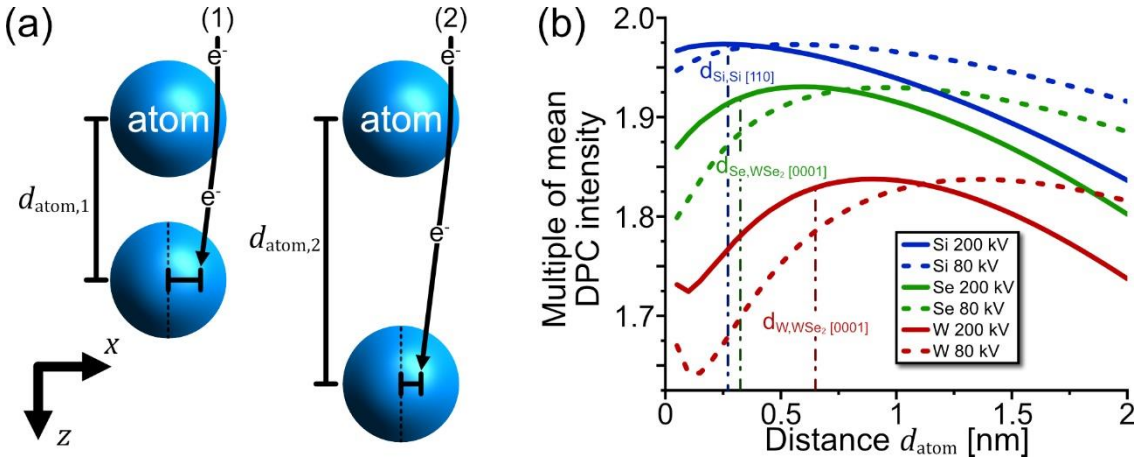

Figure 44: (a) sketch of the trajectories of a single electron incident in z-direction of an atomic column consisting of two atoms with different atomic distances (1) $d_{\mathrm{atom},1}$ and (2) $d_{\mathrm{atom},2}$ in z-direction. (b) Relative mean DPC signal magnitude as a function of the atomic distance in z-direction obtained from multislice image simulations with specimen structures consisting of only two atoms for the acceleration voltages of 80 kV and 200 kV. The mean DPC signal magnitude is related to the mean signal magnitude obtained from simulations of a single atom. A list of simulation parameters is compiled in Table 24 in the Appendix.

It is necessary to understand how and to what extend the refocussing effect influences the obtainable DPC image for different atomic distances and at different acceleration voltages. This is investigated in the following by calculating the mean DPC intensity of multislice DPC image simulations considering specimen structures consisting of two atoms displaced by distance d_{atom} in z-direction (similar to the sketch in Fig. 44(a)).
For this, Si ($Z = 14$), Se ($Z = 34$) and W ($Z = 74$), varying atomic distances in a range of 0.1 nm to 2 nm in steps of 0.05 nm and acceleration voltages of 200 kV and 80 kV are used. For the simulations, a structure size of 2.5 nm by 2.5 nm is assumed, subdivided into two slices. Each of the slices contains a single atom which is centred in the slice. In this hypothetical arrangement of two atoms, diffraction effects can be neglected. Moreover, the atomic positions are fixed (no frozen lattice approximations), as the goal of the simulations is to understand how the DPC signal is influenced by the arrangement of atoms in z-direction.
Fig. 44(b) shows the position averaged DPC image intensity of two atoms as a function of their distance d_{atom} in units of the mean intensity of a corresponding single atom. The mean DPC image intensity should be proportional to the number of atoms in projection and thus should lead to a factor of two when analysing two atoms. This is, however, not observed in Fig. 44(b), since none of the considered atomic species reaches a factor of two. All curves show a strong dependence on the atomic distance and an almost similar behaviour for the atomic species considered. With increasing distance, the mean DPC signal magnitude increases until it reaches a maximum. It is obvious from Fig. 44(b) that for all atomic species and acceleration voltages considered almost the same maximum heights are obtained. The distance at which the

maximum is found depends on the atomic species as well as the acceleration voltage. As a rule of thumb, two atoms of higher Z lead to the maximum mean DPC image intensity at larger distances. The atomic distance at which this maximum is observed also increases with decreasing the acceleration voltage indicating that the effect is more effective at smaller energies where the interaction between the electron and the first atom is stronger. Since the atomic distances are predetermined by the bonding length, Fig. 44(b) indicates that it might be useful to adjust the acceleration voltage to allow for measuring the highest possible mean DPC signal magnitude.

A possible explanation for the formation of this maximum could be that the refocusing effect leads to an increase in measurable DPC image intensity. With increasing atomic distance, the beam broadens at the second atom due its divergence. A broad beam would then "see" a strongly inhomogeneous potential landscape which subsequently results in a decrease in measurable DPC image intensity.

In case of two silicon atoms, a maximum of 1.974 times the mean DPC signal of a single atom is reached if the atoms are displaced by 0.3 nm in z-direction if an acceleration of 200 kV is used. At an acceleration voltage of 80 kV, a maximum of 1.973 is found for a displacement of 0.6 nm. When analysing silicon in [110] zone-axis orientation, the distance of atoms of an atomic column in beam direction amounts to 0.271 nm. Thus, analysing silicon in [110] zone-axis at an acceleration voltage of 200 kV gives an almost maximum obtainable DPC signal. When analysing two Se atoms, the maximum amounts to 1.931 at an acceleration voltage of 200 kV and 1.930 at an acceleration voltage of 80 kV, respectively. Two W atoms lead to a maximum of 1.836 at 200 kV and 1.837 at 80 kV. When analysing a monolayer of WSe_2 in [0001] zone axis orientation which consists of two Se atoms displaced in [0001] direction and a W atom (Fig. 65), the refocusing effect will have an influence on the measurable electric fields. Since the Se atoms in a monolayer are displaced by 0.324 nm, a maximum mean DPC signal of approximately 1.89 of the mean DPC signal of a single atom is measurable. This would decrease the electric fields measurable only on the Se atomic columns (consisting of two Se atoms) relative to a single Se atom, while the measurable DPC image intensity of the single W atom obviously corresponds well to the DPC image intensity of a single W atom. When analysing bilayers of WSe_2 (0001) in AA stacking (Fig. 65), the W atoms are displaced by 0.65 nm and 1.79 of the mean DPC signal of a single W atom is measurable. The Se atomic columns in a bilayer of WSe_2 consist of 4 atoms.

Summarising the results of Fig. 44, for quantitative DPC imaging, the refocusing effect needs to be considered to interpret atomic electric fields which scale non-linearly with the number of atoms and their distance in beam direction. The refocusing effect is expected to be enhanced with increasing number of atoms if the beam extension due to the convergent beam shape is not too broad within the crystal.

5.5. Lens aberrations

The true electrostatic field distribution around atoms in a crystal lattice may be difficult to determine because the incoming electron beam's wave front is altered by lens aberrations. Therefore, the intensity distribution in the detection plane and, thus, the difference signals do not necessarily represent the true electric field distribution. The measured electric field distribution might be drastically influenced by the aberration phase plate and its symmetry, superimposed on the true electrostatic field distribution. It is therefore a prerequisite to understand the influence of lens aberrations on measurable electric field distributions.

While defocus C_1 is a rotational symmetric lens aberration, two-fold astigmatism A_1 and third-order coma B_2 exhibit a certain symmetry corresponding to their aberration phase plate. Both A_1 and B_2 are correctable during STEM operation. All mentioned lens aberrations are typically only stable over a limited period of time. Therefore, they must be corrected and optimised frequently during operation. As the microscope operator manually corrects these lens aberrations, the remaining lens aberrations are unavoidable and might introduce artefacts to the DPC images. Therefore, the influence of lens aberrations on the DPC signal is investigated in the following.

Fig. 45(a) shows atomically resolved DPC and HAADF image simulations of $SrTiO_3$ for different combinations of two-fold Astigmatism A_1 (top to bottom) and third-order coma B_2 (left to right). The lens aberration coefficients resemble typical values present during STEM analysis. Both lens aberrations are here assumed to act in x-direction. The specimen thickness amounts to 3.51 nm and a defocus of -2 nm is used for the simulations. The atomic column positions in Fig. 45(a) are derived from the HAADF Z-contrast image and the positions of the Sr atomic columns are marked by white-contoured blue dots across the DPC image tableau.

The aberration free DPC and the corresponding HAADF images are depicted in the upper left corners of the DPC and HAADF image tableaus in Fig. 45(a). In the DPC image the colour wheels are visible in the aberration free image with a perfect rotational symmetry of deflections around individual atomic column positions. This simulation is in good agreement to the measurement of Shibata et al. [24]. The corresponding HAADF Z-contrast image only barely exhibits intensities at pure O atomic column positions. In the aberration free DPC image, O atomic columns can clearly be resolved.

The scattergram (Fig. 45(b)) of a DPC image which is free of any lens aberrations (except a defocus of -2 nm) shows a symmetric intensity distribution of the frequency of deflections. Here, the three major features inside the scattergram arise which have been investigated by scattergram filtering (Chapter 4.2): a square-like central feature with minor side lobes due to diffraction contrast at interatomic pixels, a disc up to deflections of approximately one third of the maximum deflection magnitude due to the atomic potentials of pure O columns and pixels with strong deflections outside the disc,

arising from the interaction at the Sr and Ti-O atomic columns with their higher Coulomb potential.

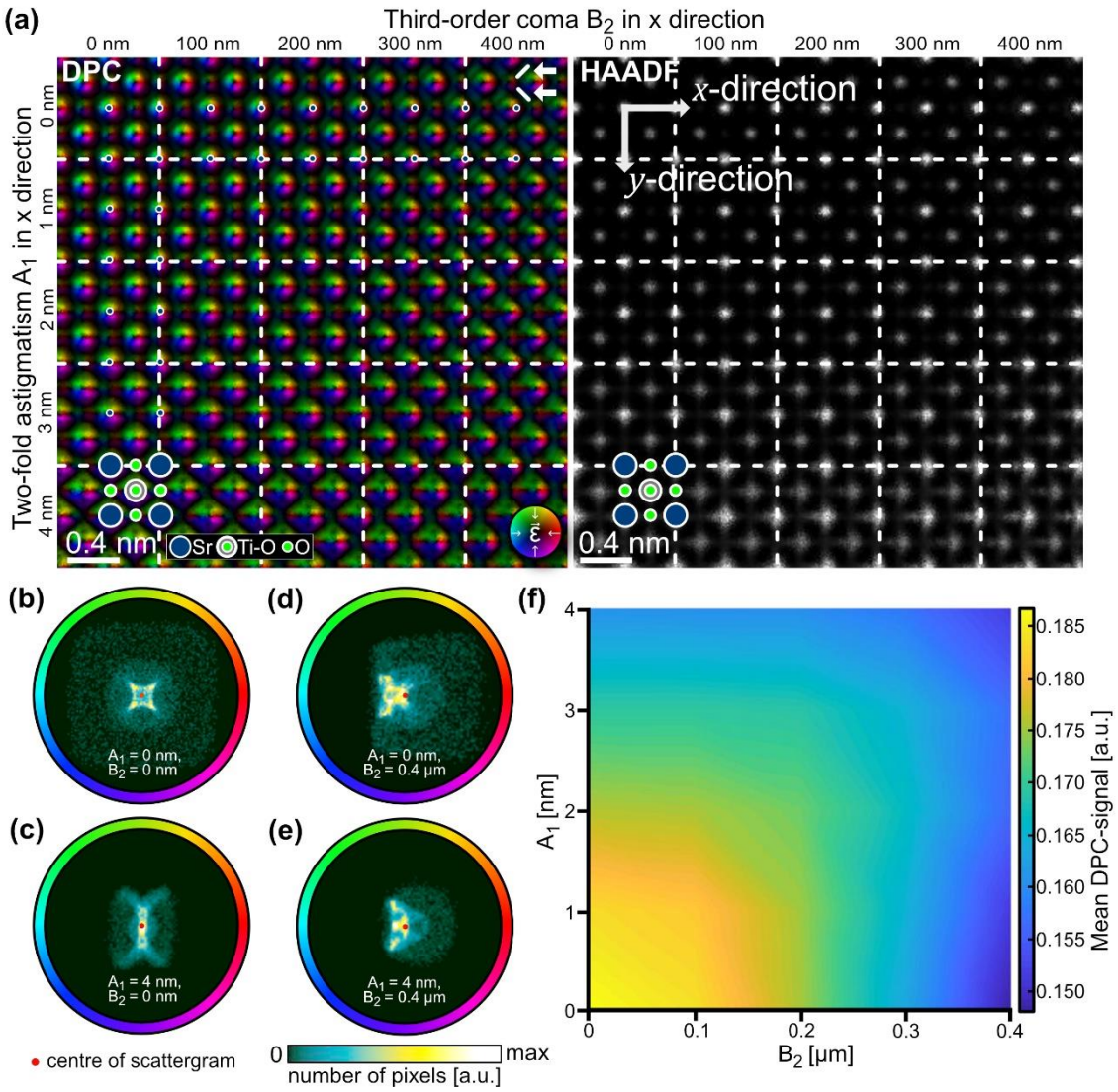

Figure 45: (a) Influence of two-fold astimgmatism A_1 and third-order coma B_2 on DPC and HAADF image simulations of $SrTiO_3$ in [001] zone-axis orientation. The images are simulated using a specimen thickness of 3.51 nm as well as a defocus of -2 nm and without other lens aberrations except of two-fold astigmatism and third-order coma. Sr atomic column positions are obtained form the HAADF image and marked by white-contoured blue dots. All images in (a) are normalised to their maximum DPC signal to visualise the changes resulting from the presence two-fold astigmatism and third-order coma. (b-e) Scattergrams of the considered extremal combinations of two-fold astigmatism and third-order coma. (f) mean DPC signal magnitude as a function of two-fold astigmatism A_1 and third-order coma B_2 within the range considered in (a). Limits of the scattergram are kept constant. This figure is taken from reference [91] and adapted. A list of simulation parameters are given in Table 25 in the Appendix.

With increasing two-fold astigmatism A_1, the colour wheels in the DPC image (Fig. 45(a)) get elongated. This elongation occurs mainly in the working direction of the two-fold astigmatism A_1, which ultimately results in an overlap of the colour wheels of the Sr and Ti-O atomic columns with those from O sites. The corresponding HAADF image reveals a square-like broadening of contrasts from Sr and Ti-O atomic columns. This square-like broadening is presumably a result of the used defocus due to the elliptical shape of the incident electron beam far off the focal plane. The influence of

the two-fold astigmatism on the DPC signal is also visible in the corresponding scattergrams in Fig. 45(c). Here, a characteristic change of the deflection distribution is observable as an elongated shape with inner features around the centre of the scattergram. This compression of deflection distribution, which dominantly acts in one direction and leads to an elongated feature with a long side perpendicular x-direction, can be ascribed to the two-fold astigmatism also working in x-direction. The inner features of the scattergram intensity distribution arise due the interaction of an electron beam having a symmetric intensity distribution and extension with the (symmetric) potential landscape inside the $SrTiO_3$ specimen.

In addition to two-fold astigmatism, third-order coma is a lens aberration that must be carefully corrected manually during operation. Unlike astigmatism, however, coma does not lead to an elongation of the features in the DPC images, but to a shift in the centres of the colour wheels and an anisotropic smearing as can be seen in Fig. 45(a). This shift is especially visible from the atomic column positions, marked by white-contoured blue dots. The shift of colour wheel centres is due to the asymmetric lens aberration phase plate, leading to directional phase gradients across the incident electron beam. In addition, the one-sided smearing is seen by halo-like features (exemplarily marked by white lines and arrows) that occur at positions of line-like features caused by diffraction effects and beam extension within the specimen. These halo-like features are therefore presumably due to the amplification of one of the line-like artefacts. The corresponding HAADF images in Fig. 45(a) also show changes in the presence of coma. However, although the behaviour is identical, changes are less obvious, especially in the case of coma. Coma is also observable as a characteristic change of features in the scattergram Fig. 45(d) and observed as a sidewise compressed deflection distribution. In addition, a high number of pixels from the halo-like features can be observed as very pronounced scattergram structures on the left side of the scattergram centre (Fig. 45(d)). Moreover, coma leads to an overall reduced deflection magnitude, as can be seen from the extension of the scattergram intensity distribution (Figs. 45(d, e)).

The combined influence of both lens aberrations on the features of the DPC image can be described as a superposition of the influence of individual lens aberrations (Fig. 45(a)). The corresponding scattergram in Fig. 45(e) furthermore confirms this assumption by the superposition of characteristic deformations of the deflection distribution in presence of both lens aberrations. Although a drastic change of the features in the DPC image is evident when both lens aberrations are present, the influence on the HAADF image might not yet be visible. This is due to the fact that the resolution of modern C_s-corrected microscopes is still lower than in the simulations considered here. Therefore, the influence of coma and astigmatism may not be visible during HAADF imaging. However, they can have a significant impact on the measurable features and magnitude of the electric field. Therefore, it is particularly important for DPC imaging to minimise them.

In the following the impact of two-fold astigmatism and third-order coma on the DPC signal magnitude is investigated. Fig. 45(f) depicts the mean DPC signal magnitude in dependency of the lens aberrations. Increasing two-fold astigmatism, third-order coma or a combination of both leads to a reduction in measurable mean DPC signal magnitude. For coma with an aberration coefficient below 100 nm and astigmatism below 1 nm, the influence on the obtainable mean DPC signal is negligible. As the third-order coma is a lens aberration of higher geometrical order than two-fold astigmatism, higher lens aberration coefficients are needed to have a strong impact on the phase aberration function. Moreover, combinations of certain lens aberrations can lead to reduced losses in mean DPC signals than each of the lens aberrations alone. This is particularly visible for a coma B_2 of 300 nm without and with a two-fold astigmatism A_1 of 3 nm.

In order to investigate the influence of astigmatism on the DPC signal in experiments, measurements of Si in [110] zone-axis orientation are analysed by utilizing the scattergram below. The Si TEM specimen is prepared by FIB lamella preparation and has an average specimen thickness of $t = (35 \pm 2)$ nm in the analysed area. Fig. 46 depicts measured DPC images (Figs. 46(a-d)), HAADF (Figs. 46(e-h)) images and corresponding scattergrams (Figs. 46(i-l)) with intentionally added two-fold astigmatism. On the one hand, this should prove that the simulations also reflect the behaviour of DPC measurements and, on the other hand, make it possible to estimate the influence of two-fold astigmatism as a correctable lens aberration in experiments.
Prior to image acquisition, the electron optical components of the column were aligned, and the microscope's C_s-corrector was tuned. After the specimen was tilted to [110] zone-axis orientation and the conventional alignment (defocus, two-fold astigmatism and third-order coma using the Ronchigram), last image optimisations were made using the DPC signal ultimately correcting two-fold astigmatism and defocus. These optimisations were conducted until the maximum possible mean DPC signal was reached.
The left column of Fig. 46 displays the DPC and HAADF image at optimum conditions. The DPC image in Fig. 46(a) clearly reveals the colour wheel distribution around dumbbells with overlapping potentials and dominant purple and green pixels. Moreover, the expected contrast of the silicon dumbbells is observed in the corresponding HAADF image in Fig. 46(e). Atomic column positions are exemplarily marked by bright blue dots. The scattergram in Fig. 46(i) shows an asymmetric deflection distribution with an off-centre maximum and very much blurred inner features. The formation of the off-centre maximum is due to a specimen tilt and residual lens aberrations (discussed below). The influence of specimen tilt is separately investigated in Chapter 5.6. A scattergram of a DPC image obtained from a perfectly oriented Si specimen is also shown in Chapter 5.6. Moreover, the blurring of features in the scattergram arises from noise during the detection process. The influence of noise is investigated in more detail in Chapter 5.7.

Two-fold astigmatism A_1 was intentionally added in equidistant steps as condenser lens astigmatism using the condenser lens (CL) stigmator (coarse steps of the CL stigmator on the JEM-ARM200F microscope) (Figs. 46(b-d)). It acts in the direction indicated by the double-sided arrow in Fig. 46(h). With increasing A_1 the shape of features in the DPC image gets elongated as one can see from Fig. 46(a) to Fig. 46(d). This elongation occurs in the direction of the astigmatism which is in perfect agreement with the findings on the influence of astigmatism derived from Fig. 45. It leads to a compression of corresponding scattergrams in working direction of A_1.

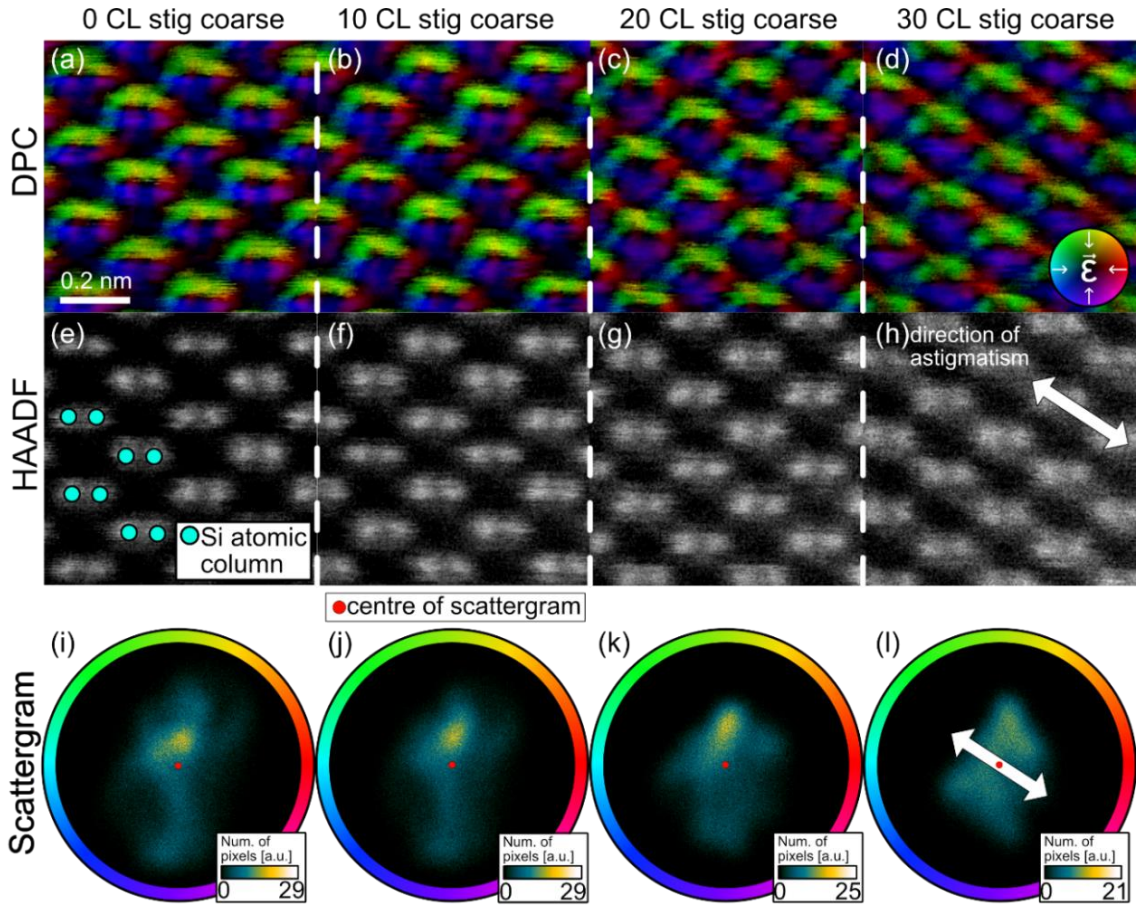

Figure 46: (a-d) Experimental DPC and (e-h) simultaneously acquired HAADF images with (i-l) corresponding scattergrams of Si[110] with varying two-fold astigmatism. The two-fold astigmatism is increased from left to right in steps of ten condenser lens stigmator coarse knob clicks on the ARM200F microscope. The double-sided arrows in (h) and (l) depict the working direction of astigmatism. All scattergrams show the same range of deflection distribution. Further experimental details are listed in Table 43 in the Appendix.

In addition to the change in the shape of the features, a reduction in the measurable field magnitude is also noticeable in the scattergrams in Fig. 46, which was also evident in Fig. 45 for $SrTiO_3$. At high A_1, the dumbbells exhibit visibly distorted, line-like features. These line-like features extend in a similar direction as the elongation of colour wheels. Such drastic distortions in the HAADF image could be corrected by the operator. Even though no drastic changes are observable in the HAADF image at small amounts of A_1 (e.g. ten CL stigmator coarse, shown in Fig. 46(f)), the DPC image (Fig. 46(b)) and the corresponding scattergram (Fig. 46(j)) show a reduced maximum

measurable DPC signal magnitude and also changes in the scattergrams inner structure. This again shows that the microscope must be aligned as perfectly as possible to guarantee the most accurate measurement of the electric field distribution present.

While two-fold astigmatism and third-order coma are correctable during operation using image features or the Ronchigram, higher order lens aberrations are typically not correctable during specimen analysis. On the one hand, this is due to the complexity of how lens aberrations of a higher geometric order influence the image. On the other hand, magnetic multipoles are necessary to counteract on the symmetrical phase plate of these lens aberrations which are typically not installed on non-corrected instruments. With the development of C_s-correctors consisting of two magnetic multipoles and several transfer lenses, it is possible to correct lens aberrations typically up to the fifth geometrical order depending on the number of poles. Hexapole correctors reduce the spherical aberration by adding six-fold astigmatism A_5 [5–7]. Since the influence of spherical aberration cannot be entirely eliminated despite modern correction of lens aberrations, it is important to understand how and to what extend the spherical aberration C_3 influences the obtainable DPC image. The influence of spherical aberration C_3 on atomically resolved DPC images with corresponding scattergrams of $SrTiO_3$ in [001] zone-axis orientation is investigated in Fig. 47. Fig. 47 additionally considers the influence of three-fold astigmatism A_2.
Fig. 47(a) displays simulated DPC images of $SrTiO_3$ achieved with different spherical aberration C_3 (left to right) and three-fold astigmatism A_2 (top to bottom) coefficients for a 3.51 nm thick specimen and the focus set to -2 nm below the entrance plane. With increasing spherical aberration C_3, stripe-like features are formed in the DPC images in Fig. 47(a). Since the spherical aberration C_3 is also a rotationally symmetric aberration like the defocus, an increase in spherical aberration leads to the formation of these stripe-like features in the DPC images. These stripe-like features again emerge parallel to low-index lattice planes, e.g. parallel to {010} and {100} lattice planes for a C_3 value of 10 µm. Further increasing of the spherical aberration results in inverted deflection distribution around the atomic column positions, e.g. at a spherical aberration of 20 µm. The inversion of deflection distribution corresponds to a rotation of all deflections by 180°. The influence of spherical aberration on DPC images is much larger than on corresponding HAADF images, as the comparison in Fig. 47(a) shows. This is evident from the fact that the colour wheels in DPC images are completely distorted, and stripe-like features arise, while the atomic columns in HAADF images just appear blurred. Despite this blurring, atomic columns and the Z-contrast can still be recognised. The scattergrams for the case with and without aberration Figs. 47(b, c) exhibit strong differences. Like defocus, spherical aberration drastically reduces the maximum measurable deflection, as can be seen from the extension of scattergram intensity distribution. This is particularly evident in the scattergram in Fig. 47(c) for a

spherical aberration of 20 µm, in which the largest portion of the measurable deflections is found near the scattergram centre.

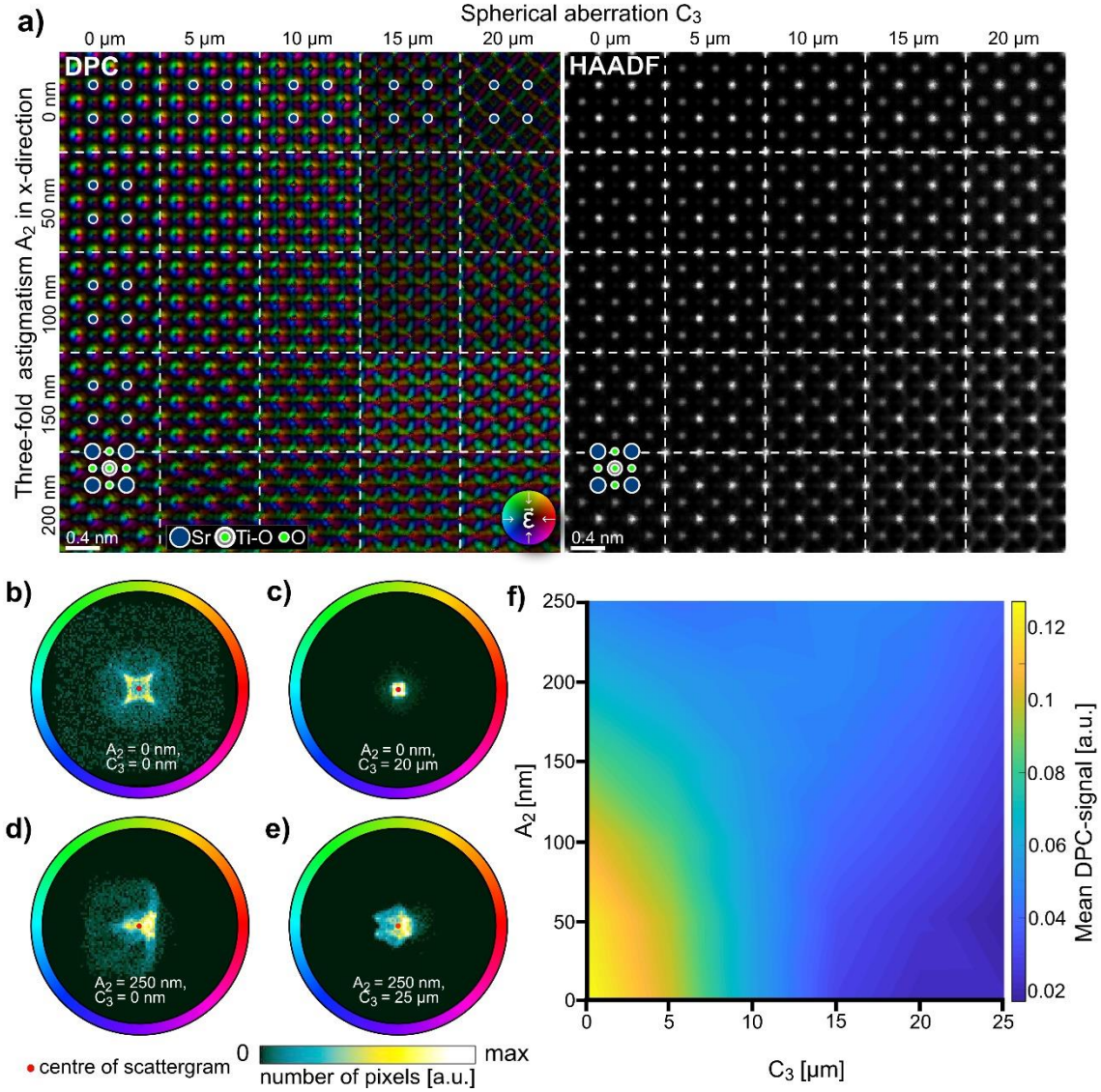

Figure 47: DPC images of a 3.51 nm thick $SrTiO_3$ crystal in [001] zone-axis orientation with a defocus of -2 nm beneath the specimen entrance plane with different additional three-fold astigmatisms A_2 and spherical aberrations C_3. All other lens aberrations are assumed to be zero in these simulations. (b-e) Corresponding scattergrams exhibiting a three-fold shape of the deflection distribution in case of three-fold astigmatism and an allocation of pixels close to the scattergram centre in the presence of spherical aberration. (f) Mean DPC signal magnitude as function of spherical aberration and three-fold astigmatism. Simulation parameters are listed in Table 26 in the Appendix.

Within the range of considered three-fold astigmatism A_2 in Fig. 47(a), the influence of just A_2 is small. This is evident from the colour wheels which can still be observed for $A_2 = 200$ nm. However, these colour wheels are slightly distorted, exhibiting a three-fold symmetry with increasing three-fold astigmatism. For better visibility, a zoomed in DPC image for a three-fold astigmatism coefficient of $A_2 = 200$ nm is displayed in Fig. 97 in the Appendix. Comparing the DPC images with pure three-fold astigmatism $A_2 = 200$ nm and pure two-fold astigmatism $A_1 = 4$ nm (Fig. 45(a)) a strong difference between the considered images can be observed. While rotational symmetric deflection distributions around individual columns cannot be observed in the DPC

image with $A_1 = 4\,\text{nm}$, these features are observable for $A_2 = 200\,\text{nm}$. A possible explanation for the difference is the order of the lens aberration since it determines the impact of the aberration coefficient on the aberration phase plate.

The intensity distribution of individual atomic columns in the HAADF images in Fig. 47(a) exhibits a three-fold symmetry with increasing three-fold astigmatism. A zoomed in version of the HAADF image assuming a three-fold astigmatism of $A_2 =$ 200 nm and without other lens aberrations is displayed in Fig. 98 in the Appendix. The scattergram of a DPC image of pure $A_2 = 250\,\text{nm}$ in Fig. 47(d) shows significant alterations compared to the aberration free scattergram in Fig. 47(b) although the impact of the considered A_2 on the DPC image seems small. The scattergram intensity distribution is a result of both. three-fold astigmatism introducing a certain three-fold symmetry and the $SrTiO_3$ specimen introducing the symmetry of the potential.

When both spherical aberration and three-fold astigmatism are present (Fig. 47(a)), the DPC image is significantly distorted. Features in the DPC image even arise which do not correspond to the typical or the inverted azimuthal ordering of deflections. The HAADF image, however, still does not exhibit such drastic changes, as atomic columns are clearly identifiable. Fig. 47(e) displays the scattergram of the DPC image simulated for a spherical aberration of C_3=25 µm and a three-fold astigmatism of A_2=250 nm. Since the extension of the scattergram distribution is much larger than in the case of only spherical aberration (Fig. 47(c); C_3=20 µm, A_2=0 µm), it also becomes apparent that certain combinations of lens aberrations can increase the measurable DPC signal magnitude.

Fig. 47(f) reveals the influence of spherical aberration and three-fold astigmatism on the mean DPC signal magnitude as a function of both lens aberrations. With increasing spherical aberration and three-fold astigmatism, the mean DPC signal magnitude is strongly reduced. The reduction of DPC signal amounts up to 80% in the considered range of three-fold astigmatism and spherical aberration. In case of spherical aberration this reduction can be attributed to the fact that the electrons experience a spatially inhomogeneous potential due to the increasing extension of the probe. In case of three-fold astigmatism, an overall reduction of the measurable mean DPC signal magnitude is also observable. This reduction depends on the initial beam position and the direction of electric fields present at that beam position as the extension of the incident electron probe's intensity distribution is not rotationally symmetric. Like in the case of two-fold astigmatism A_1 and defocus C_1 (Fig. 45(f)), certain combinations of three-fold astigmatism A_2 and spherical aberration C_3 can result in greater mean DPC signal magnitudes than in the presence of only A_2 or C_3. For example, this can be seen by the lower mean DPC signal magnitude for C_3=20 µm, A_2=0 µm than for C_3=20 µm, A_2=200 µm.

With state-of-the-art aberration correction, it is possible to keep the spherical aberration below 1 µm. As can be seen from Fig. 47(a), such spherical aberration values allow for DPC images exhibiting colour wheels around atomic column positions even if additional three-fold astigmatism is present. Nevertheless, any residual spherical

aberration might reduce the observable DPC signal magnitude, e.g. by 21.3 % for a spherical aberration of 5 µm. For quantitative DPC images and further calculations such as charge densities, it is, thus, particularly necessary to minimise spherical aberration as much as possible.

In summary, lens aberrations introduce characteristic features in the DPC image and change the intensity distribution of corresponding scattergrams depending on the symmetry of aberration phase plate and its aberration coefficients. For all considered lens aberrations, a reduction in obtainable mean DPC signal magnitude is observed, meaning that measured atomic electric fields are always lower than the true electric field if residual lens aberrations are present. This is also observable by the extension of scattergram features. The scattergram is, hence, a useful tool for an “in-line” detection, analysis, and correction of residual lens aberrations during high-resolution DPC-STEM investigations. A reliable recipe for optimising the DPC image quality is to isotropically increase the extension of scattergram features by manually tuning components of the microscopy, (simultaneously) compare the measured scattergram to a simulated scattergram without lens aberrations, and finally achieve a good agreement between both the measured and the simulated scattergram. Applying this recipe will maximise the obtainable deflection magnitude in all directions and thus decrease the influence of lens aberrations.

5.6. Specimen tilt

Like bright-field imaging in STEM, DPC primarily uses the direct beam of the intensity distribution in the detection plane. For bright-field images it is known that those are much more sensitive to the specimen tilt than HAADF images [116]. Since DPC also relies on the use of the direct beam, it is important to understand how the DPC signal is affected by the tilt of the specimen.

In the following, the influence of specimen tilt on the DPC signal is studied using simulations for $SrTiO_3$ in [001] zone-axis orientation. Fig. 48(a) investigates how specimen tilts ranging from 0 mrad to 25 mrad affect the measurable DPC image and the simultaneously acquirable HAADF image in $SrTiO_3$ near [001] zone-axis orientation. This is shown by multislice simulations for specimen thicknesses of 3.51 nm and 11.32 nm. The focus was always placed in the centre of the specimen and no other lens aberrations were used in the simulations. The tilt axis is denoted by a red line in the DPC image simulation of a specimen with a thickness of 3.51 nm that is not subjected to specimen tilt. For both thicknesses the features in the HAADF image and the DPC image are stretched in one direction with increasing specimen tilt. This behaviour is evident from elongated colour wheels in the DPC image. In the HAADF images, the atomic columns show an elliptical contour. The difference between the two thicknesses is also evident. Due to the larger number of scattering centres seen by the beam, the changes are stronger for larger specimen thickness. This can already be deduced from the DPC signal at a tilt of 10 mrad.

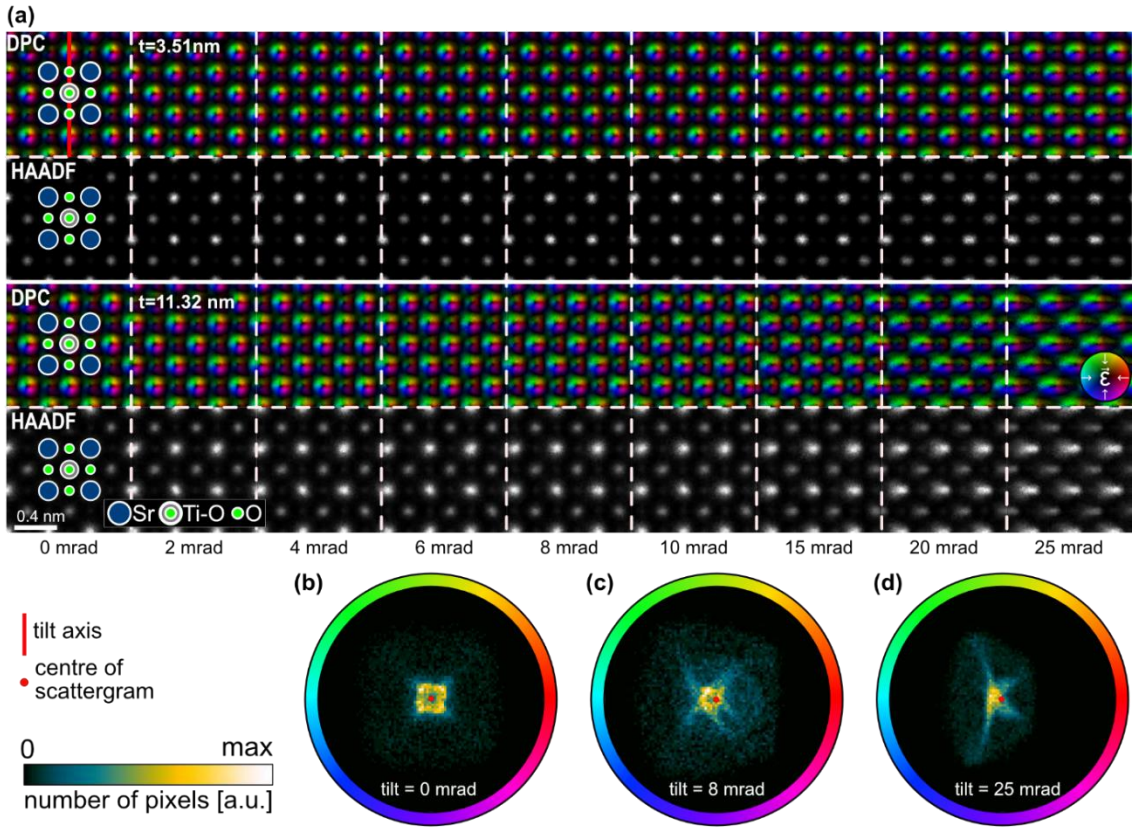

Figure 48: (a) Simulated DPC and HAADF images of $SrTiO_3$ near [001] zone-axis orientation as function of the specimen tilt. For the upper two rows of images a specimen thickness of 3.51 nm and for the lower two rows a specimen thickness of 11.32 nm is assumed. The defocus is for both rows set to half the specimen thickness. Other lens aberrations are assumed to be zero. (b-d) Scattergrams of the DPC images acquired with different specimen tilts for the specimen thickness of 11.32 nm. The tilt axis as well as a projection of the specimen structure are exemplarily marked in the first column of (a). Simulation parameters are given in Table 27 in the Appendix.

When analysing a specimen with a thickness of 3.51 nm (Fig. 48(a)), the DPC signal remains almost unchanged, while the DPC images of a specimen with a thickness of 11.32 nm already shows deviations from the perfectly round colour wheels above a tilt of 10 mrad. In the latter case, this is evident from the increasing number of green and blue pixels. The influence of specimen tilt is also observable in the scattergrams, which are exemplarily displayed for specimen tilts of 0 mrad, 8 mrad and 25 mrad in Figs. 48(b-d) for a specimen thickness of 11.32 nm. The specimen tilt leads to a redistribution of pixels in the scattergram and a change in the symmetry of the scattergram from initially four-fold to two-fold as can be derived from the one-side-compressed scattergram distribution shown in Fig. 48(d). A maximum in the scattergram distribution is found off-centre perpendicularly to the tilt axis at large tilt angles, e.g. in horizontal direction in Fig. 48(d) which is perpendicular to the tilt axis in Fig. 48(a). The redistribution of scattergram intensity due to tilt can be explained by the fact that the electrons of the beam propagate differently inside the specimen, because the atoms and their potentials above and below the focal plane are displaced perpendicular to the optical axis due to the tilt.

Similar to tilting the specimen, coma B_2 also leads to an off-centre maximum in the scattergram (Fig. 45(c)). Fortunately, the influence of specimen tilt differs from B_2 in a

way that it results in a dominant elongation of all features in the DPC image in one direction and does not involve changes in the phase front of the beam in the perpendicular direction leading to changed deflections in this direction. Specimen tilt can be also distinguished from two-fold astigmatism: Two-fold astigmatism results in more rectangular scattergram distributions with two lines of symmetry (one on the horizontal and one on the vertical axis in Fig. 45(d)), while the scattergram in case of tilt has only one horizontal symmetry line, as can be seen from a trapezoid-like contour with rounded sides of the scattergram intensity distribution (Fig. 48(d)).
The HAADF images (Fig. 48(a)) show only minor changes, e.g. for a specimen tilt of 10 mrad at a specimen thickness of 11.32 nm. Therefore, it is a good practice to check the orientation of the specimen directly in the DPC image or, even better, using the scattergram.

An off-centre maximum was also observed in the scattergram of the measured DPC image of Si[110] in Fig. 46(i). The formation of this off-centre maximum is not expected, for the symmetric projected electric field distribution of perfectly oriented silicon dumbbells in [110] zone-axis orientation. Therefore, the origin of this off-centre maximum is investigated in Fig. 49 using multislice image simulations of Si[110] with different specimen tilts ranging from 0 mrad to 5 mrad in steps of 1 mrad. The specimen thickness amounts to 30.72 nm, which is close to the measured thickness of $t = (35 \pm 2)$ nm. Besides a defocus of -6 nm (Chapter A.2.3) no other lens aberration was used in the simulation. The tilt axis is depicted as a red line in Fig. 49. It runs parallel to the projected connecting axis of atoms within a dumbbell, i.e. the [001] direction.

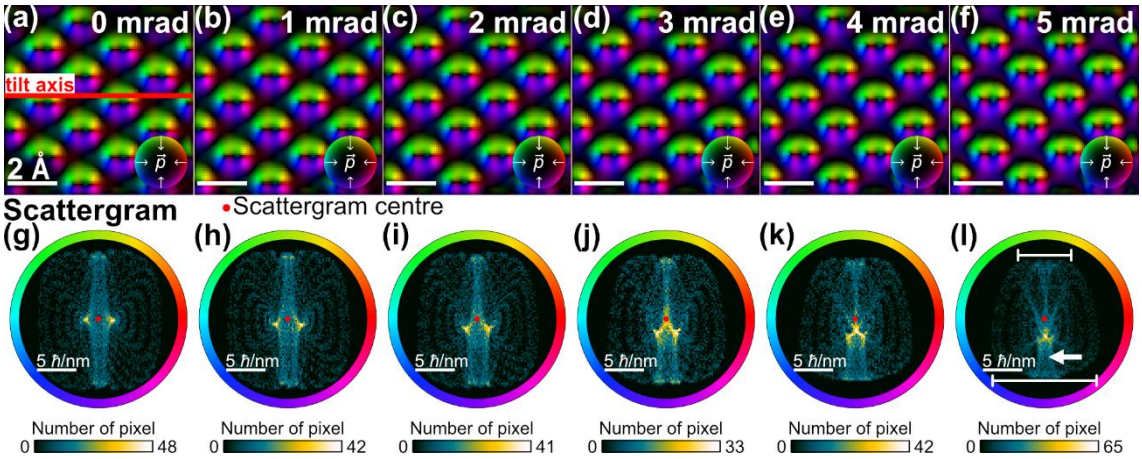

Figure 49: (a-f) DPC image simulations of Si[110] as a function of specimen tilt. The tilting axis is depicted by the red line in (a). Tilts in the range from 0 mrad to 5 mrad are considered. (g-l) Corresponding scattergrams revealing changes in the deflection distribution introduced by tilting the specimen. A list of simulation parameters is given in Table 28

With increasing specimen tilt, the DPC images in Figs. 49(a-f) show only slight differences. This is due to the fact that only tilt magnitudes up to 5 mrad are considered. The most dominantly observable change in the DPC images is an increase

of purple colour at interatomic regions far away from the dumbbells. Furthermore, the deflection distribution and thus the blue and purple colours around the atomic columns become more pronounced in the lower half of each dumbbell. The deflection distribution at the upper half of each dumbbell is slightly distorted (Fig. 49(f)) in comparison to the perfectly oriented crystal (Fig. 49(a)) and exhibits a more elliptical shape.

Although the DCP images show only minor differences in the considered tilt range, the scattergrams in Figs. 49(g-l) show clear differences even for these small tilt angles. The differences include a shift of the two local maxima towards the lower half of the scattergram (compare Fig. 49(g) and Fig. 49(h)) with increasing specimen tilt up to a tilt of 2 mrad. This is in good agreement to the findings for $SrTiO_3$ (Figs. 48(b-d)) where the dominant features were shifted perpendicularly to the tilt axis (please note that the tilt axes in Fig. 48 and Fig. 49 are perpendicular to each other). With further tilting, not only a shift of the two local maxima but the emergence of another maximum directly below the scattergram centre is observed in Figs. 49(j-l). This maximum initially is connected to the two local maxima (Fig. 49(j)) via line-like features. Increasing the tilt angle, this maximum becomes the dominant feature in the scattergram and further shifts towards the lower half of the scattergram. This means that with increasing specimen tilt the dominant feature in the scattergram, which in perfect orientation compromises two peaks adjacent to the scattergram centre, becomes a maximum below the scattergram centre. The off-centre maximum which is observed in the scattergram in Fig. 46(i) can therefore be ascribed to a specimen tilt with a tilt angle the range of a few mrad.

The features in the upper half of the scattergrams in Figs. 49(h-l) exhibit a decreased width while the features in the lower half exhibit an increased width with increasing tilt. The widths are exemplarily marked by white lines in the scattergram in Fig. 49(l). The increase in width of the scattergram distribution in the lower half of the scattergram with increasing tilt (Figs. 49(h-l)) can additionally be deduced from the bar-like structure extending from top to bottom of the scattergram. The lower half of the bar-like structure is marked by a white arrow in Fig. 49(l). This bar-like feature corresponds to those pixels of the DPC image where potentials of the individual atomic columns of a dumbbell overlap. It is interesting to note that the extension of this bar-like feature is larger in the lower half than in the upper half. This is in good agreement to the more pronounced purple and blue colours around the atomic columns because an increased scattergram feature width can only result from an increased difference of azimuthal directions of measured transferred momenta. Altogether, the extension of scattergrams decreases with increasing specimen tilt (Figs. 49(h-l)), indicating that the maximum measurable DPC magnitude decreases with increasing tilt.

As a redistribution of the scattergram distribution along with specimen tilt is observed, it might be possible to decouple the influence of specimen tilt from long range electric fields, which are, for example, piezo- and ferroelectric fields. To determine long range fields at atomic resolution, typically an unit cell averaging is conducted [30, 42]. To

measure long range electric fields with the help of the scattergram, one could define a small region of interest of the DPC image for scattergram calculation, which does not necessarily have to be a single unit cell, and calculate the position of the CoM as well as the position of the maximum of the scattergram. The position of the CoM of the scattergram distribution corresponds to the mean transferred momentum and the mean electric field. The position of the maximum of the scattergram distribution dominantly arises from interatomic pixels. The difference in position of the CoM of the scattergram distribution and the position of the maximum of the scattergram distribution therefore should indicate the presence of long-range electric fields. Further investigations are necessary to prove the applicability of this approach.

5.7. Image noise

Besides the good agreement of the scattergrams calculated from the DPC image simulation of Si[110] in Fig. 49(l) and the DPC measurement in Fig. 46(i) which is evident from the off-centre maximum, one particular difference is clearly visible: the features of measured scattergrams are less pronounced than the ones of simulated scattergrams as they appear strongly blurred. This is a result of image noise, which is not considered in the simulation.

Due to the finite dose conditions and the detection process of electrons, image noise cannot be prevented in scanning transmission electron microscopy [114, 115]. The detection process of electrons results in a Poisson distribution which approaches a Gaussian normal distribution for increasing number of electrons. Since the difference signals in DPC are based on a comparison of intensities of opposing detector segments, noises influence the derived electric field distributions. Müller-Caspary et al. [27] and Pöllath et al. [87] investigate the limitations of noise on the accuracy of electric field measurements utilising simulations for pixelated and non-pixelated detectors. They observed that modern instruments due to their high-brightness cold field-emission electron guns do not limit the attainable precision of the transferred momentum measurement [27]. Owing to the current state-of-the-art microsecond-fast segmented detectors, short dwell times can be achieved, e.g. to reduce drift at subatomic resolution [158]. Using short dwell times is also beneficial for beam sensitive materials [159]. However, noise levels might influence the accuracy of electric field quantifications as the number of detected electrons is low at short dwell times. To describe the impact of image noise on the DPC image, Seki et al. developed a noise model for DPC imaging with segmented detectors [114]. This noise model states that the standard deviation of the expectation value of the transferred momentum depends on the beam extension on the detector as well as the inverse square root $1/\sqrt{N_e}$ of the number of detectable electrons N_e [114]. While the number of electrons is proportional to the dwell time and the beam current, the extension of the beam on the detector is decisively determined by the convergence angle as well as the camera length. Pöllath et al. find the same dependency for pixelated and non-pixelated detectors [87]. In addition, they formulate an uncertainty relation which is based on the total number of

electrons allowing to determine the precision of the measurement of the transferred momentum and field quantities by using Heisenberg's uncertainty principle. The quantification of the number of detected electrons is a complex task and requires a Faraday cup as well as precise calibration [117, 160].

In the following, the influence of image noise on measured DPC images and corresponding scattergrams which are a representation of the momentum space is investigated. Since it is difficult to estimate the number of electrons incident on the detector during a measurement, a method is derived that allows to ensure the necessary precision without knowing the exact number of detected electrons.

For this, a noise model that describes the standard deviation of the DPC signal is developed. The derivation of the noise model is based on the formulations by Pöllath et al. [87] which start with an expression for the expectation value $\langle \vec{k}_\perp \rangle = 1/N_e \cdot \sum_j^{N_e} \vec{k}_{\perp,j}$ of the wavenumber $\vec{k}_\perp$ perpendicular to the optical axis. In this formulation $\vec{k}_{\perp,j}$ denotes the wavenumber of electron j. Analogously, this equation can be reformulated using the transferred momentum $\langle \vec{p}_\perp \rangle = 1/N_e \cdot \sum_j^{N_e} \vec{p}_{\perp,j}$.

The variance of the expectation value of transferred momentum is additive due to uncorrelated electron detection events during measurement [110] and can be reformulated using the Bienaymé [161] formula leading to an $1/N_e$ dependency [87]:

$$\mathrm{Var}(\langle \vec{p}_\perp \rangle) = \frac{1}{N_e^2} \sum_{j=1}^{N_e} \mathrm{Var}(\vec{p}_{\perp,\mathrm{j}}) = \frac{1}{N_e} \mathrm{Var}(\vec{p}_\perp). \tag{50}$$

It is to note that the standard deviation of the expectation value $\sigma(\langle \vec{p}_\perp \rangle) = \sqrt{\mathrm{Var}(\langle \vec{p}_\perp \rangle)}$ is the square root of the variance. Pöllath et al. [87] assume a homogeneously illuminated area with radius p_R in reciprocal space, finding that the standard deviation of the transferred momentum on a pixelated detector amounts to $\sigma_{\mathrm{Pixelated}}(\langle \vec{p}_\perp \rangle) = \left((p_R)/(2\sqrt{N_e}), (p_R)/(2\sqrt{N_e})\right)$ [87]. Please note that the standard deviation is given with components for p_x- and the p_y-direction.

Instead of measuring the exact number of incident electrons N_e, the segments of a segmented detector generate a signal from the detected electrons which can be described by the following equation (adapted from reference [37]):

$$S_i = A_i \cdot j_i \cdot \eta_i \cdot \tau, \tag{51}$$

where A_i[m^2] denotes the illuminated detector area, j_i[C/(s · m^2)] the current density of the electron beam on detector segment i, η_i[counts/C] the quantum efficiency converting incoming electrons into a signal, which also incorporates the gain of the photomultipliers and the analog-to-digital conversion, and τ[s] the dwell time. The index of A_i, j_i and η_i is used for assignment to detector segment i. The signal is given in counts signal units [counts]. It is to note that the dwell time is independent of the detector segment. It can be assumed that A_i is constant if the camera length is not changed and the beam is not too strongly deflected on the detector. The beam current incident on the specimen can be considered constant during the acquisition of a DPC

image because the current emitted by cold-field emission guns decreases on a much longer time scale.

The number of electrons incident on a detector segment does not only depend on the beam extension on the detector, the emission current of the gun, and the dwell time, but it is also influenced by incoherent scattering far off the detector segments by the specimen. The number of electrons incident on the detector thus changes if a specimen is present in the beam path. However, this effect is neglected in the following. By exchanging the number of detected electrons by a measured signal of the detector segments, the variance of the DPC signal is given by:

$$\mathrm{Var}(S) = \frac{1}{S^2}\sum_{j=5}^{8}\mathrm{Var}(S_i)\ . \tag{52}$$

Here, S_i is the signal generated by the ith detector segment and S is the overall intensity on all used detector segments, e.g. $S = S_5 + S_6 + S_7 + S_8$ if only Layer2 is used for the signal generation. Eq. 52 can be simplified using $\mathrm{Var}(S_i) = S_i$ due to Poisson distribution to

$$\mathrm{Var}(S) = a_\mathrm{m}/\tau, \tag{53}$$

in which a_m can be understood as a weighted mean of the variance of transferred momentum on all detector segments with

$$a_\mathrm{m} = \frac{\sum_{i=5}^{8} A_i \cdot j_i \cdot \eta_i}{\left(\sum_{i=5}^{8} A_i \cdot j_i \cdot \eta_i\right)^2}. \tag{54}$$

The standard deviation of the $\sigma_M(S) = \sqrt{\mathrm{Var}(S)}$ is given by

$$\sigma_M(S) = \sqrt{\frac{a_\mathrm{m}}{\tau}}. \tag{55}$$

Eq. 55 is a good estimation of the standard deviation and is in good agreement to the noise models described by Pöllath et al. [87] and Seki et al. [114] due to its $1/\sqrt{\tau}$ dependency. However, a few effects are not taken into account. These effects include read-out noise, dark currents arising from the analog-to-digital converters, and the impact of noise on the auto-gain calibration. A detailed description of a noise model which includes all these effects is prepared for publication. The essential steps are described in the following.

Noise arising from analog-to-digital conversion is often referred to as read-out noise. The corresponding process of converting an analogue signal to digital counts can be described by a Gaussian distribution [162] with a standard deviation of σ_RG which is independent of the dwell time.

Due to their typically low impact on the overall noise statistics, dark currents of the detector can be included in the read-out noise although they are typically poorly described by a Gaussian normal distribution [163].

Prior to DPC investigation, a gain calibration, which levels the amplification of individual photomultipliers, must be conducted. This is experimentally achieved by using the auto-gain calibration which is included in the software provided by the manufacturer. The impact of the gain calibration introduced by the auto-gain calibration is typically very small for good gain calibrations. Hence, noise arising from the gain calibration is for simplicity neglected in the following.
To account for these effects, the standard deviation of the signal can be approximated by

$$\sigma_M(S) \approx \sqrt{\frac{a_1}{\tau} + \frac{a_2}{\tau^2}} \tag{56}$$

with the parameters

$$a_1 = \frac{\sum_{i=1}^{d} A_i \cdot j_i \cdot \eta_i}{\left(\sum_{i=1}^{d} A_i \cdot j_i \cdot \eta_i\right)^2} \text{ and } a_2 = \frac{\sigma_{\mathrm{RG}}^2}{\left(\sum_{i=1}^{d} A_i \cdot j_i \cdot \eta_i\right)^2}. \tag{57}$$

The latter includes the standard deviation σ_{RG} for the read-out noise. Note that d denotes the number of detector segments. The standard deviation of read-out noise σ_{RG} can be assumed to be constant for a series of measurements if the gain of individual detector segments and the beam parameters are not changed.

Since the scattergram is a representation of the entire DPC measurement, e.g. in momentum space, its distribution is affected by noise. If the specimen contains a homogeneous electric field, one expects that the measured scattergram shows a noise-broadened distribution with a standard deviation according to Eq. 56. Furthermore, a scattergram of a DPC image acquired with a stationary beam (ideally in vacuum) is expected to show a transferred momentum distribution purely representing the probability distribution, i.e. the Poisson or Gaussian normal distribution or a mixture of both. The scattergram is therefore in the following used to investigate the probability distribution of transferred momenta.
Fig. 50(a) depicts scattergrams calculated from DPC images acquired with a stationary beam in vacuum and for dwell times ranging from 100 µs to 400 µs per pixel. All DPC images are captured without scanning the beam, i.e. the transferred momentum of a centred beam is measured for 512x512 times resulting in a DPC image with a size of 512x512 pixels. In this way, the measured transferred momenta are only influenced by image noise.
The beam was carefully centred on the SAAF detector prior to image acquisition. However, as this is done manually, the initial centring is corrected by subtracting a deflection corresponding to the centre of mass of the scattergram in a post processing step as explained in Chapter A.1.2 in the Appendix. Since this step subtracts a constant deflection, it can be assumed that this correction has no influence on the noise statistics. Furthermore, the rotation of deflection by the Lorentz force in the magnetic field of the lens system below the specimen was corrected. This correction

also has no influence on the overall signal distribution as it only changes the directionalities. All scattergrams are calibrated to depict the same range of transferred momentum. This allows for a direct comparison of transferred momentum distributions. It is evident from the scattergrams in Fig. 50(a) that the extension of the scattergram distribution decreases and the number of pixels within the same deflection magnitude and direction interval increases with increasing dwell time. This is in good agreement with the $1/\sqrt{\tau}$ dependence of the standard deviation resulting from the noise model.

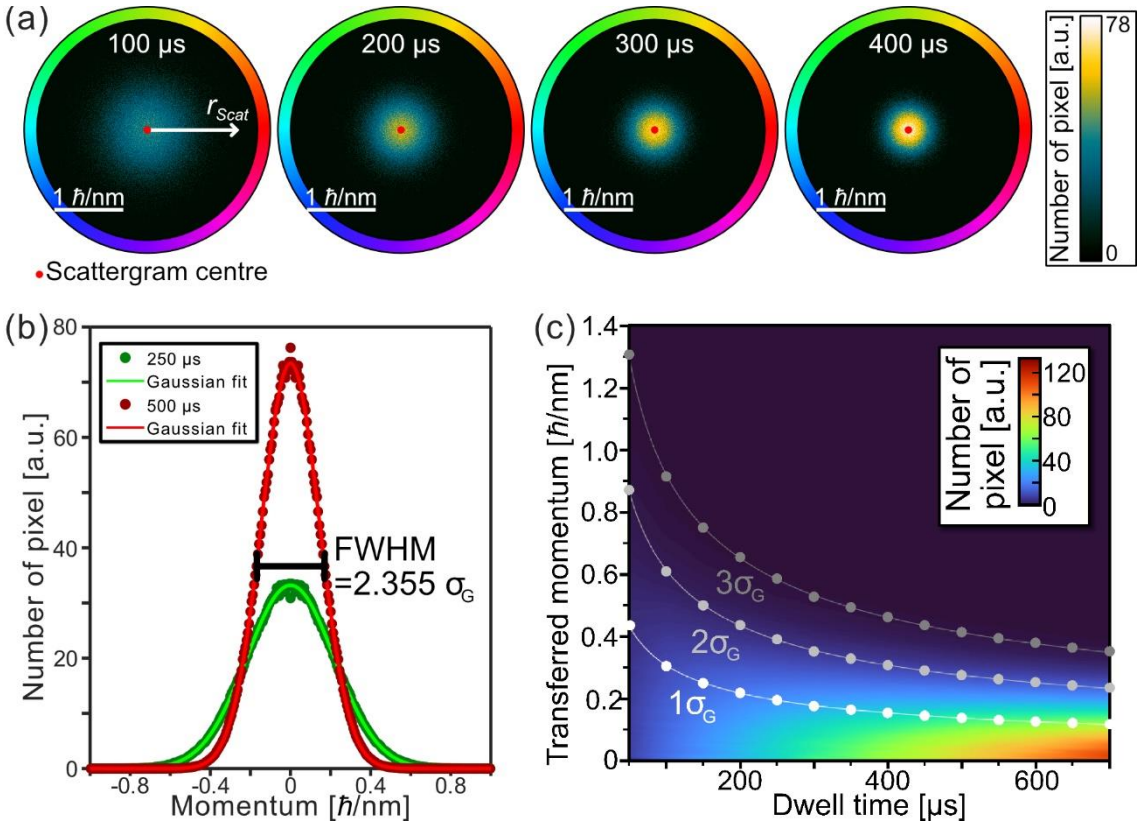

Figure 50: (a) Scattergrams of DPC images captured with a resolution of 512x512 pixel and, more importantly, with a stationary beam in vacuum for dwell times of 100 µs, 200 µs, 300 µs and 400 µs. (b) Radial intensity profiles of the scattergrams of dwell times of 250 µs and 500 µs obtained as described in Chapter 4.2. Profiles are acquired by calculating the mean value of scattergram intensity along a complete circumference at radius r_{Scat}. Furthermore, the right side of the plot is mirrored to the left side of the plot to allow for fitting a Gaussian function. (c) Contour plot of radial intensity profiles for dwell times ranging from 50 µs to 700 µs in steps of 50 µs. Standard deviations and their multiples, which are obtained by fitting Gaussian functions to each individual radial intensity profile, are marked by white (σ_G), grey ($2\sigma_G$) and dark grey ($3\sigma_{\mathrm{G}}$) dots. Fits of the dwell time dependent standard deviation are correspondingly marked. Further experimental details are given in Table 44 in the Appendix.

To quantify the standard deviation, Fig. 50(b) analyses the scattergram intensity for dwell times of 250 µs and 500 µs by acquiring radial intensity profiles. The radial intensity profiles are calculated as the mean value of scattergram intensity on a circle with radius r_{Scat} and are mirrored in Fig. 50(b). All mirrored radial profiles resemble a Gaussian function. Hence, a Gaussian function $G(r_{\mathrm{Scat}})$ is fitted to all mirrored radial intensity profiles. The Gaussian function is given by:

$$G(r_{\mathrm{Scat}}) = A_{\mathrm{Scat}} \cdot \exp\left(-\frac{r_{\mathrm{Scat}}^2}{2\sigma_{\mathrm{G}}^2}\right), \tag{58}$$

in which A_{Scat} denotes the amplitude and σ_G^2 the standard deviation. The fits confirm that the radial intensity profiles acquired for dwell times of 250 µs and 500 µs follow a Gaussian distribution and the same is observed for all dwell times up to 700 µs. Hence, it can be said that the noise is well approximated by a Gaussian distribution.

Fig. 50(c) displays a contour plot of radial intensity profiles for dwell times τ ranging from 50 µs to 700 µs. These radial intensity profiles are obtained in a similar way as those depicted in Fig. 50(b) for dwell times of 250 µs and 500 µs. However, the profiles are not mirrored. The white (σ_{G}), grey ($2\sigma_{\mathrm{G}}$), and dark grey ($3\sigma_{\mathrm{G}}$) dots demark multiples of the standard deviation, which are again obtained by fitting Gaussian functions to each mirrored line profile.

In Fig. 50(c), a decrease of σ_{G} with increasing dwell time τ is observable. The decrease in standard deviation in dependency of the dwell time τ is further investigated by fitting Eq. 56 to the determined standard deviations (σ_{G}). The constants determined with the help of the fit are $a_1' = (9.44 \pm 0.05)\cdot 10^{-6}$ s$(\hbar/\mathrm{nm})^2$ and $a_2' = (8 \pm 3)\cdot 10^{-14}$ $(\hbar\mathrm{s}/\mathrm{nm})^2$. It is to note that $a_1' = c_{\mathrm{cal,p}}^2 \cdot a_1$ and $a_2' = c_{\mathrm{cal,p}}^2 \cdot a_2$ are calibrated constants, where the constant $c_{\mathrm{cal,p}} = 7\cdot 10^{-9}\ \hbar/\mathrm{nm}$ is obtained from the calibration process described in Chapter 3.1.1. In the considered range of dwell times, a strong dependence on $1/\sqrt{\tau}$ is observed and thus the term with a_1' is dominating. This allows to conclude that the influence of the read-out noise is negligible for the considered dwell times. Read-out noise and dark currents would only significantly influence the standard deviation below a dwell time of $\tau' = a_2'/a_1' \approx 9\cdot 10^{-9}$ s, which is three orders of magnitude smaller than the dwell time possible with state-of-the-art segmented detectors.

A DPC measurement of a specimen exhibiting two dominant transferred momenta, which have an almost similar magnitude and direction, would in absence of noise lead to two peaks within the scattergram. Similar to the way noise blurs the scattergram for a stationary beam in vacuum, the peaks would be blurred by a Gaussian function. If the two peaks are only separated slightly in momentum space and extensively blurred by two Gaussian functions, they might not be resolvable within the scattergram, unless sufficiently long dwell times are used to render noise induced blur negligible. As the standard deviation is measurable with the scattergram from a stationary beam, one can derive a criterion for the minimum dwell time needed to resolve small features in the momentum space that only exhibit slight differences.

In the following this criterion for momentum space resolution is derived from the parameter a_1' since the contributions of read-out noise, dark currents and gain calibration are negligible. It follows the Sparrow resolution limit, which states that two features (Airy discs within the resolution limit by Sparrow [164] and here Gaussian functions) are resolvable if they exhibit a minimum midway between them [164, 165].

For two distinct transferred momenta $\vec{p}_{\perp,1}$ and $\vec{p}_{\perp,2}$, which lead to an almost equal intensity in the scattergram and are blurred by a Gaussian function with the same standard deviation σ_G, a local minimum arises if following condition is fulfilled [166]:

$$\left|\Delta\vec{p}_{\perp}^{\,2}\right| = \left|\vec{p}_{\perp,2} - \vec{p}_{\perp,1}\right| \geq 2\sigma_G. \tag{59}$$

By inserting Eq. 56, dropping the a_2' term and using the fit result of a_1', the minimum dwell time τ_{SP} necessary to resolve two distinct features is given by

$$\tau_{\mathrm{SP}} \geq \frac{4 \cdot a_1'}{|\Delta\vec{p}_{\perp}|^2}. \tag{60}$$

For example, to resolve two distinct scattergram features which exhibit a difference of 0.5 $\hbar$/nm a dwell time of 151 µs is necessary with the same microscope settings as used for the acquisition of scattergrams in Fig. 50. In contrast, a dwell time of 3.8 ms is necessary if transferred momenta which are different by 0.1 $\hbar$/nm should be resolvable. This criterion therefore allows to assess the necessary dwell time required to resolve features in momentum space without applying further noise reduction techniques. The result is only valid for a specific combination of convergence semi-angle, detector amplification and beam current.

A dwell time of 3.8 ms is typically not realistic for measurements at atomic resolution since it is limited by the specimen drift, specimen deterioration at high electron doses and the number of scan pixel. In addition, contamination build-up might also play a role. When analysing specimen at atomic resolution, low dwell times in the µs range are typically used. However, this would prevent measuring the transferred momentum with a resolution of 0.1 $\hbar$/nm.

The limitations arising from the lower dwell times can be overcome by applying rigid or non-rigid image registration techniques (Chapter 4.4.2). These techniques are based on superimposing registered images of an image series or image segments of an image with highly periodic features, e.g. an image of an atomically resolved crystalline material.

In the following image segments of sub-atomically resolved DPC and HAADF images are used. The registration is achieved using the HAADF image due to its Z-contrast and the comparably low influence of defocus. Fig. 51 shows DPC (Figs. 51(a-e)) and HAADF images (Figs. 51(f-j)) of Si in [110] zone-axis orientation calculated from a different number N of non-rigidly registered image segments. For the images shown, large-area DPC and HAADF images were simultaneously acquired at an image resolution of 512x512 pixels with a dwell time of 50 µs. The Si TEM specimen is prepared by FIB lamella preparation and has an average specimen thickness of $\bar{t} = (30 \pm 2)$ nm in the analysed area. The non-rigid registration is conducted using a 100x100 pixels image segment depicted in Fig. 51(a). This image also acts as a reference image for all other registered images. Before the image segments are non-rigidly registered, a rigid registration step selects image segments of the 512x512

pixels image surpassing a cross-correlation coefficient threshold of 0.75 with the reference image. All these image segments, which surpass the cross-correlation threshold, are subsequently registered in an order of decreasing cross-correlation coefficient and superimposed. Superimposing a number N of non-rigidly registered image segments is similar to increasing the dwell time $\tau = 50$ µs by a factor of N, i.e. $\tau^* = 50 \cdot N$.

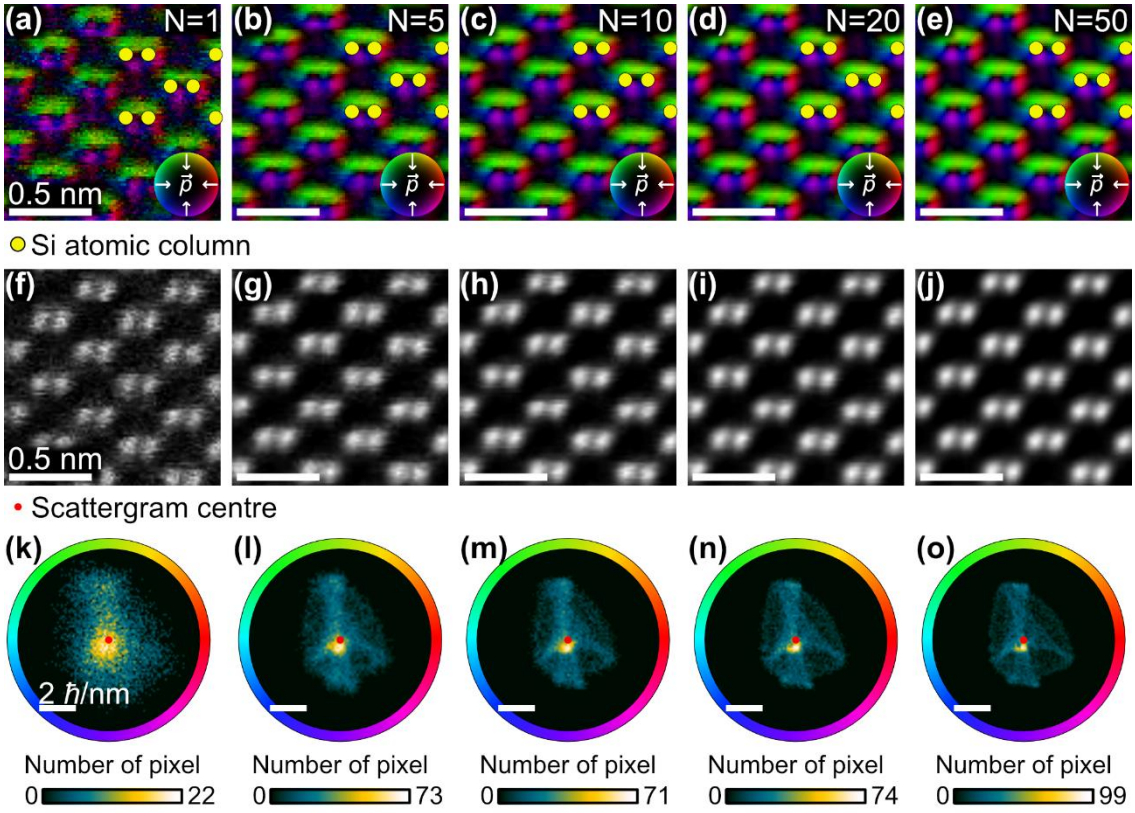

Figure 51: (a-e) DPC images of Si[110] with $N = 1$, $N = 5$, $N = 10$, $N = 20$, $N = 50$ images segments which are registered and superimposed during non-rigid registration. The average thickness of the FIB-prepared Si[110] specimen amounts to $\bar{t} = (30 \pm 2)$ nm in the analysed area. The dwell time during the measurement was set to 50 µs. (f-j) Corresponding HAADF image, which are simulateneously acquired and similarly registered. (k-o) scattergrams of the DPC images shown in (a-e). Each column consisting of a DPC image, HAADF image and scattergram refer to one specific number of registered images. The scalebar is the same for all HAADF and DPC images. Experimental parameters are listed in Table 45.

Fig. 51(a) and Fig. 51(f) display the as-measured DPC image and corresponding HAADF image with $N = 1$. The typical contrasts of the Si dumbbells can already be observed in the DPC and the HAADF images. This is evident from the colour wheels around individual atomic columns in the DPC image depicting the transferred momentum distribution and the Z-dependent intensity distribution of the atomic columns in the HAADF image. Despite revealing the expected contrasts, the DPC image as well as the HAADF image (Fig. 51(a) and Fig. 51(f), respectively) exhibit image distortions. These image distortions are due to noise and presumably due to the native SiO_x layer at the top and bottom of the TEM specimen. The latter broadens the beam due to scattering and leads to randomly distributed transferred momenta arising from its amorphous structure. It can be assumed that these randomly distributed

transferred momenta are suppressed by registering a high number of image segments. In addition, scan distortions including flags and skips due to mismatched scan line positions [135] are visible.

The corresponding scattergram in Fig. 51(k) shows a very blurred intensity distribution with almost no inner feature. Similar to the measured scattergrams in Fig. 32 and Fig. 46 as well as in the simulated tilt series in Fig. 49, which all considered Si near [110] zone-axis orientation as a specimen, an off-centre maximum in the scattergram is observed. This off-centre maximum is also observable in the scattergram in Fig. 51(k). The visibility of the off-centre maximum at such short dwell times underlines the potential of the scattergram. However, the scattergram barely shows the expected distribution of scattergram features, which are visible in the simulations in Fig. 49.

By superimposing five non-rigidly registered images to this reference image, the dwell time can artificially be increased to 250 µs. The resulting DPC image is shown in Fig. 51(b). Both the DPC image and the corresponding HAADF image (Fig. 51(g)) are less noisy than the ones for $N = 1$. This is also evident from the corresponding scattergram in Fig. 51(l) revealing that characteristic features within the scattergram are observable by only superimposing five images ($N = 5$). The observed features in the scattergram in Fig. 51(l) are in good agreement to the ones of the simulated, noise-free scattergram in Fig. 49(l). Similar as in the simulation in Fig. 49(l), one observes a vertical extension of the silhouette of the scattergram intensity and similar inner features. The DPC images in Figs. 51(c-e) correspond to dwell times τ^* of 500 µs ($N = 10$), 1 ms ($N = 20$) and 2.5 ms ($N = 50$). The corresponding HAADF images and scattergrams are displayed in Figs. 51(h-j) and Figs. 51(m-o), respectively. With increasing number of registered image segments and thus a simultaneous increase in dwell time, the DPC image as well as the corresponding HAADF image exhibit a reduced influence of noise and scan distortions. This is evident from the transferred momenta around dumbbells. Moreover, the intensity distribution of dumbbells in the HAADF image become more uniform. The corresponding scattergrams depicted in Figs. 51(k-o) reveal finer details with increasing number of registered image segments. This can be seen from the scattergram for a dwell time of 50 µs (Fig. 51(k)) exhibiting a very broad intensity distribution with barely any internal feature. The scattergram of DPC image comprising 50 non-rigidly registered images (Fig. 51(o)) exhibits fine details, as internal features, e.g. a bowtie-like feature, are clearly visible. These internal features are also in good agreement with the simulated scattergram in Fig. 49(l). The bowtie-like feature is marked by a white arrow in the simulated scattergram in Fig. 49(l). Summarising the findings of Fig. 51, image noise blurs all details in the scattergram of DPC image. To resolve small difference in electric field distributions, long dwell times or the registration of many image segments are necessary.

Chapter summary

DPC is a technique to measure electric fields in solid materials. Simultaneously it is sensitive to many other influences investigated in this chapter:

- Chapter 5.1: The interactions of an extended convergent electron beam and a specimen which include diffraction and other coherent scattering phenomena result in a symmetric CBED pattern which is incident on the detector. The symmetry is especially visible in the direct beam. Since DPC imaging mainly exploits the direct beam, the use of a symmetric segmented detector has a significant impact on the measurable DPC signal due to the way the individual segments intersect the symmetric CBED pattern. It was shown by measurements and simulations as well as detailed scattergram analyses that the directionality and position of features influenced by the detector are particularly dependent on the polar collection angles and detector rotation. The spatial distribution of pixels, which change with the rotation of the detector, are revealed by applying so-called scattergram filtering and with the help of a simulation series for different detector rotations. It is observed that mostly interatomic pixels are impacted by the detector rotation.
- Chapter 5.1: The camera length influences the extension of measured electric field distributions (not the actual electric field distribution!) around individual atomic columns.

- Chapter 5.2: Diffraction contrasts increase with increasing specimen thickness reducing the measurable DPC signal.
- Chapter 5.2: The optimum defocus in $SrTiO_3$ is below half the specimen thickness for highest mean DPC signal magnitude and close to the exit surface for highest cross-correlation to the DPC image of one unit cell.
- Chapter 5.2: A recipe to experimentally find the optimum defocus at which the DPC image is close to the one of a unit cell is presented. In the experiments, the optimum defocus is achieved by finding the maximum DPC signal and slightly moving the focus to an underfocus condition corresponding to the optimum defocus of a simulated tableau.

- Chapter 5.3: Features in the DPC image are impacted by the acceleration voltage, as the acceleration voltage influences the distance between diffraction discs in the detection plane and the interaction of the electron beam with the specimen.

- Chapter 5.4: The real space probe intensity distribution within the specimen is influenced by the acceleration voltage and by the specimen thickness. The potentials of previous layers of the specimen influence the interaction of the beam in subsequent layers. A channeling of probe intensity along atomic columns in real space and a redistribution of intensity to neighbouring atomic columns is observed.
- Chapter 5.4: The obtainable DPC signal is not only a function of the atomic potentials but also influenced by the spacings of atoms along the z-direction. The

former depends on the atomic number. This is investigated by DPC image simulations of two atoms displaced in z-direction. The overall maximum mean DPC signal magnitude is always lower than twice the mean DPC magnitude of a single atom. With increasing atomic number, the observable DPC signal magnitude decreases, however, it always exhibits a maximum depending on the atomic distance as well as the acceleration voltage. The atomic distance at which this maximum occurs is observed to increase with increasing atomic number and acceleration voltage.

- Chapter 5.5: Lens aberrations reduce the measurable DPC signal and introduce features in DPC images and corresponding scattergrams which exhibit symmetries corresponding to the symmetry of the aberration phase function.

- Chapter 5.6: In the considered range of specimen tilt (up to several mrad), specimen tilt leads to elongation of features in the DPC image and the formation of an off-centre maximum in the scattergram.

- Chapter 5.7: Image noise reduces the precision in momentum space. All features within the scattergram are blurred by the signal distribution function, which depends on the inverse square root of the dwell time and is Gaussian-like for all dwell times considered in this thesis.
- Chapter 5.7: A method for assessing the minimum dwell time required to resolve features in momentum space is given. This method is based on a noise model including read-out noise.
- Chapter 5.7: The influence of image noise can be suppressed by applying rigid and non-rigid image registration techniques.

6. DPC measurements at atomic resolution

In this chapter, different material systems are analysed using DPC. In addition to gaining new insights into the corresponding material systems, the focus is also on the investigation of the DPC technique and its limitations. In Chapter 6.1, a silicon TEM lamella is investigated and the atomic electric fields as well as charge densities are determined. Furthermore, images taken with segmented and pixelated DPC detectors are analysed and compared with each other. The atomic electric fields and charge densities in an InAs nanoisland are analysed in Chapter 6.2. Finally, DPC analyses are performed on two- and three-layer flakes of two-dimensional WSe_2 in Chapter 6.3. This analysis additionally comprises investigations on the impact of vacancy-type defects on the electric field distribution in WSe_2 bilayers.

6.1. Silicon

Silicon is not only the second most abundant element of the Earth's crust [167, 168] but also the key material in today's semiconductor industry with a market share of more than 90 % [169]. It is the basis of a variety of functional circuitry components, such as complementary-metal-oxide-semiconductor transistors. According to Moore's law, the number of transistors on a chip doubles every two years. This can only be achieved by making circuitry components smaller and smaller. In 2021, IBM announced the achievement of a prototype chip with 2 nm technology [170]. Although the smallest component is actually not 2 nm in size, it shows that the feature size of circuitry components is decreasing. Many components within such circuits rely on build-in electric fields and therefore, with ever decreasing feature sizes, the importance of electric fields of individual atoms is increasing. For this reason, the investigation of electric fields in silicon and also functional components on silicon is a key factor to design tomorrow's circuitry components. Hence, the atomic electric fields in silicon are investigated in the following.

6.1.1. TEM lamella preparation of Si[110]

Fig. 52(a) shows a TEM bright-field image of the Si specimen considered for DPC imaging. This specimen was obtained by focused ion beam (FIB) lamella preparation on a *Thermo Fisher Scientific* Helios G4 UX at *Thermo Fisher Scientific* in Eindhoven and was lifted out of a Si substrate ensuring that the [110] zone-axis orientation is almost perpendicular to the lamella surface. The aim of using FIB preparation here was to obtain a specimen of almost constant thickness. It is to note that the substrate was structured by nanosphere lithography for other research projects. Remains of polystyrene spheres, which sit on the substrate surface (indicated by a bright blue box in Fig. 52(a)), do not interfere with the following analysis as FIB backside milling [171] was used to prevent the curtaining effect [172] which would typically result in thickness modulations of the lamella. Backside milling is achieved by attaching the specimen

structure in an upside-down configuration to the TEM grid after lift-out. To obtain a lamella, which is ultimately thin and has only a minimal ion-irradiation-induced amorphous layer, the thinning of the lamella is conducted with different acceleration voltages of the ion beam. First, the complete lamella is milled at 30 kV in two milling directions. The two milling directions are indicated by the sketch shown in Fig. 52(b). This results in a wedge-shaped structure of the lamella. Second, a small section of the lamella (the bar of the H-like configuration visible in Fig. 52(a)) is thinned further at the same acceleration voltage. The third and final polishing step with an ion beam energy of 500 V ensures that only a minimum amorphous layer is present on top and bottom of the TEM lamella [173, 174].

In the TEM, the lamella is tilted to zone-axis orientation by using the bend contours (visible in the TEM bright-field image of the final lamella in Fig. 52(a)), the diffraction pattern and Kikuchi lines. It is also evident from the bend contours in Fig. 52(a) that the lamella is bent in the region of interest, which is marked by a red box. The specimen tilt is additionally checked and carefully adjusted before the DPC analysis using the symmetry of the CBED pattern (not shown here).

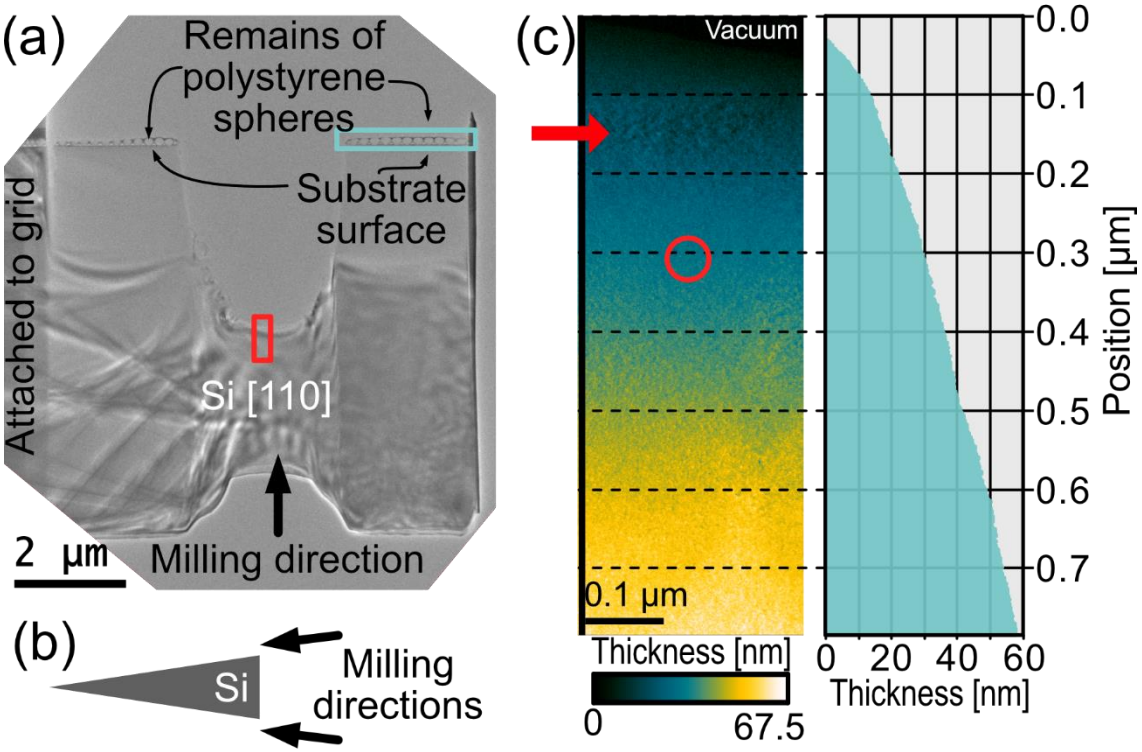

Figure 52: (a) TEM bright-field image of the TEM lamella of Si[110]. This lamella was obtained through FIB milling of a silicon substrate structured with PS nanospheres. Further details on the preparation process can be found in the main body of the text. (b) Milling directions for the preparation of a Si lamella for high-resolution imaging. (c) EFTEM thickness mapping and line profile of the specimen thickness of the red marked area in (a). The line profile was obtained by taking the average thickness of each pixel row in the EFTEM image. The red circle indicates the area of DPC measurement. Experimental details can be found in Table 46 in the Appendix.

Fig. 52(c) shows the specimen thickness profile obtained by the EFTEM t/λ-method [73]. The area of the thickness map is depicted by the red box in Fig. 52(a). Using the

model of Iakoubovskii [85], the measured relative thickness in units of mean free path is converted into the absolute thickness with an electron mean free path of 149.6 nm at an acceleration voltage of 200 kV. Fig. 52(c) additionally shows an integrated line profile of the average thickness along the thickness map. The EFTEM image as well as the corresponding line profile indicate a wedge-like shape of the lamella. Further EDS investigations in the area marked by a red circle in Fig. 52(c) (not shown here) reveal only a negligible amount of FIB implanted Ga.

The red circle in Fig. 52(c) also depicts the area of the DPC analysis. This area has a thickness of (30 ± 2) nm. Analysing such a thick specimen makes dynamic diffraction effects likely [91], as the thickness is a significant fraction of the extinction length ξ_g for electrons moving along the [110] direction in a Si crystal: ξ_{220}(Si, 200 kV) = 112 nm. Additionally, a thickness gradient of approximately (6.41 ± 0.03)% is observed. This value is obtained by fitting a linear profile to the region investigated by DPC and more accurately from 250 nm to 400 nm of the line profile in Fig. 52(c). For an analysed image area with a width of 2 nm, the maximum thickness difference amounts to 1.2 Å. Its influence on the DPC signal is neglected in the following, as the thickness gradient and its impact on the gradient of mean inner potential is rather moderate.

6.1.2. Atomic electric fields and charge densities

In this chapter, a DPC measurement and a DPC simulation, both for Si in [110] zone-axis and acquired with a segmented detector, are compared by analysing the maps of electric field and charge density distributions (Fig. 53). The DPC image was acquired at an acceleration voltage of 200 kV using a defocus guaranteeing the maximum possible DPC signal (Chapter 5.2). The camera length amounts to 12 cm leading to polar collection angles of β_{inner}=18 mrad and β_{outer}=35.4 mrad. The convergence semi-angle is 25 mrad. The detector was oriented such that the x-direction of the detector, in which the difference signal S_x is determined, is aligned with the dumbbell axis. This corresponds to a detector rotation of 0° in the detector rotation series shown in Fig. 31. In this chapter, all images are calibrated using the signal-based calibration method described in Chapter 3.1.1. All images shown in Fig. 53 are denoised using the non-rigid registration method (Chapter 4.4.2) for 300 image segments with a two-level scheme (coarse to fine registration) using 500 iterations at the coarse and 300 iterations at last level and a field smoothing with standard deviation of 1.5 pixels. Further details on the imaging and post-processing parameter can be found in Table 47 in the Appendix.

The dark-field image in Fig. 53(a), which is simultaneously acquired with the DPC image, clearly reveals the dumbbell structure of Si in [110] zone-axis orientation. Individual atoms of the dumbbells look deformed although a rotational symmetric intensity distribution is expected around the atomic column positions. This can be ascribed to a specimen tilt. The atomic column positions are determined from this dark-field image and are indicated by yellow discs. They are obtained using the procedure described in Chapter 4.5 and are projected onto all images in Fig. 53.

The colour-coded DPC image in Fig. 53(b) exhibits rotational electric fields around each atomic column position. This is visualised by the white arrows in the upper right corner of the image and evident from the colour wheels around the atomic columns. However, the colour wheels within the dumbbells are distorted due to the small distance between neighbouring atomic columns of 136 pm (projected in [110] orientation) resulting in an overlap of projected potentials. This overlap of potentials leads to a superposition of electric field vectors which can be seen by dominant green- and purple-coloured deflections at the top and the bottom of a dumbbell as well as a reduction in field magnitude between the two atomic columns.

The reduction in electric field magnitude in the middle of the connecting axis between the two atomic columns of a dumbbell is even better visible in the electric field magnitude map depicted in Fig. 53(c) and indicated by the central arrow of the three black arrows. The outer two minima which are additionally marked arise due to the nuclei at atomic column positions. At these pixels and more precisely on the atomic column no electric field perpendicular to the optical axis is expected. Furthermore, electric field magnitude maxima can be observed on the diagonal axis connecting two dumbbells. These local maxima are exemplarily highlighted by white circles with numbers (the numbers are used at the end of this section) in Fig. 53(c). Here again, to illustrate the direction of electric field vectors, an arrow plot with white arrows is partially overlayed.

Fig. 53(d) depicts the corresponding charge density map. The charge density is displayed in a colour code, in which blue coloured pixels denote negative charge densities and red coloured pixels positive charge densities. White pixels represent neutral regions. As can be seen in Fig. 53(d), a strongly localised positive charge density is evident at atomic column positions. Besides exhibiting the maximum absolute magnitudes of charge density, the charge density at atomic column positions also shows a certain rectangularity. This is indicated by the dashed green rectangle in Fig. 53(d). Moreover, regular changes in the charge density distribution at interatomic pixels can be observed. For example, line-like features which extend parallel to low order lattice planes can be observed. These line-like features are indicated by two black lines, which are connected by two dashed lines, and dominantly extend parallel to [001] and $[\bar{1}10]$. At positions, where these line-like features cross, even slightly positive charge densities can be observed, although no atomic column is present. A positive charge density is not expected for image regions, where no nucleus is present. As indicated in Chapter 5.1.2, this is due to the detector and its rotation. The influence of the detector on the DPC images can be also seen in the simulation series shown in Chapter A.2.1 in the Appendix.

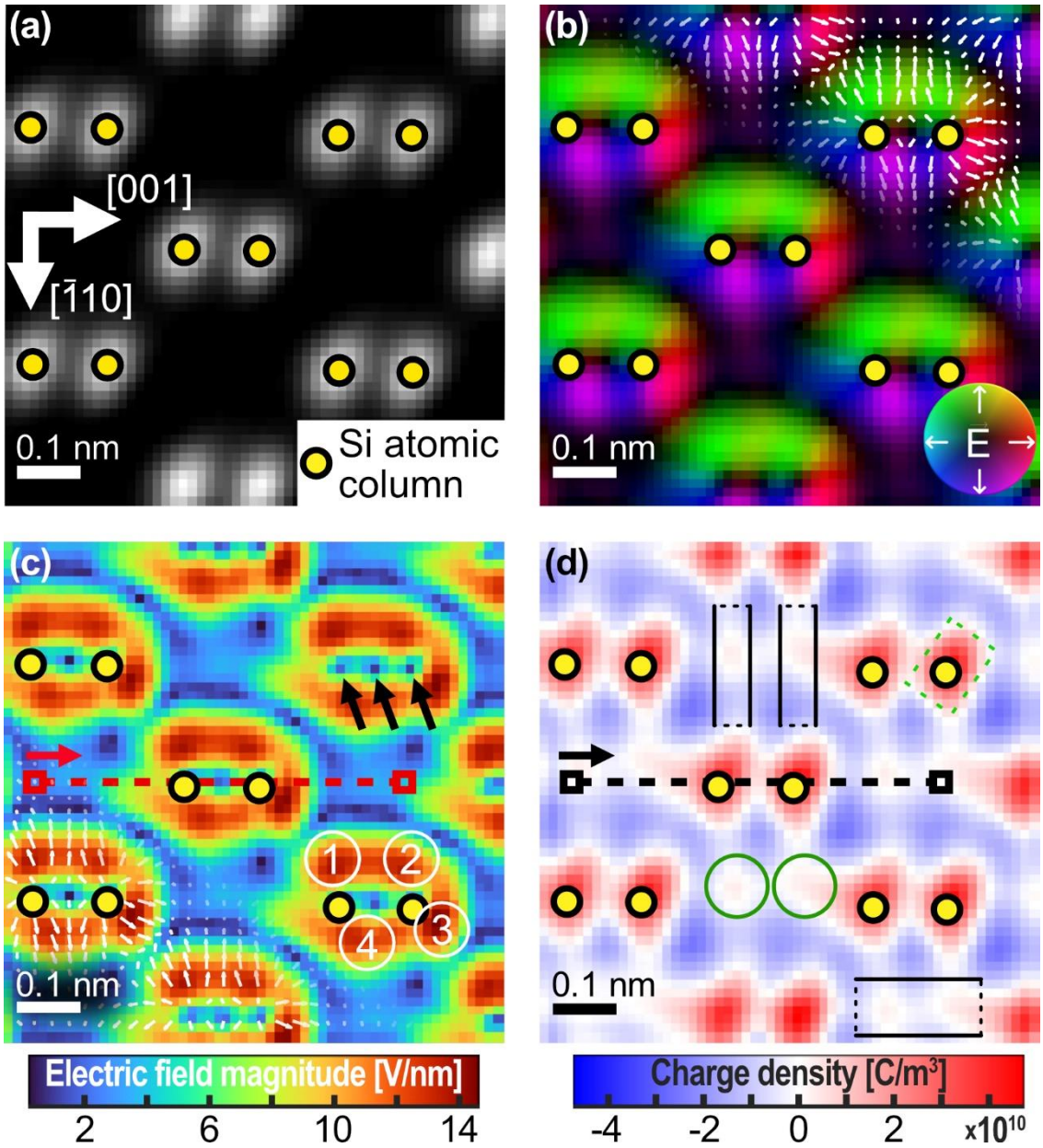

Figure 53: (a) Measured dark-field image of Si in [110] zone-axis orientation. (b) Colour-coded DPC image acquired with the segmented all-field detector. (c) Electric field magnitude obtained using the signal-based calibration process. (d) Charge density derived from (c). For the images shown in (a-d) a non-rigid registration for image noise minimisation was applied. Further details on the imaging parameters can either be found in the main body of the text or Table 47 in the Appendix.

For comparison to Fig. 53, Fig. 54 shows simulated images of Si[110] obtained by multislice image simulation using Dr. Probe [44]. This includes the dark-field (Fig. 54(a)) and colour-coded DPC (Fig. 54(b)) images as well as the electric field magnitude (Fig. 54(c)) and the derived charge density (Fig. 54(d)). The multislice simulation is performed with parameters similar to the ones used in the experiment. These particularly include a detector rotation of 0°, an acceleration voltage of 200 kV and no lens aberrations except of an underfocus of C_1 = -4 nm. The latter guarantees the maximum obtainable DPC signal for a 30.72 nm thick Si specimen. A simulative analysis of the defocus dependent DPC signal is shown in Chapter A.2.3. Further details on the simulation parameters can also be found in the Appendix in Table 29.

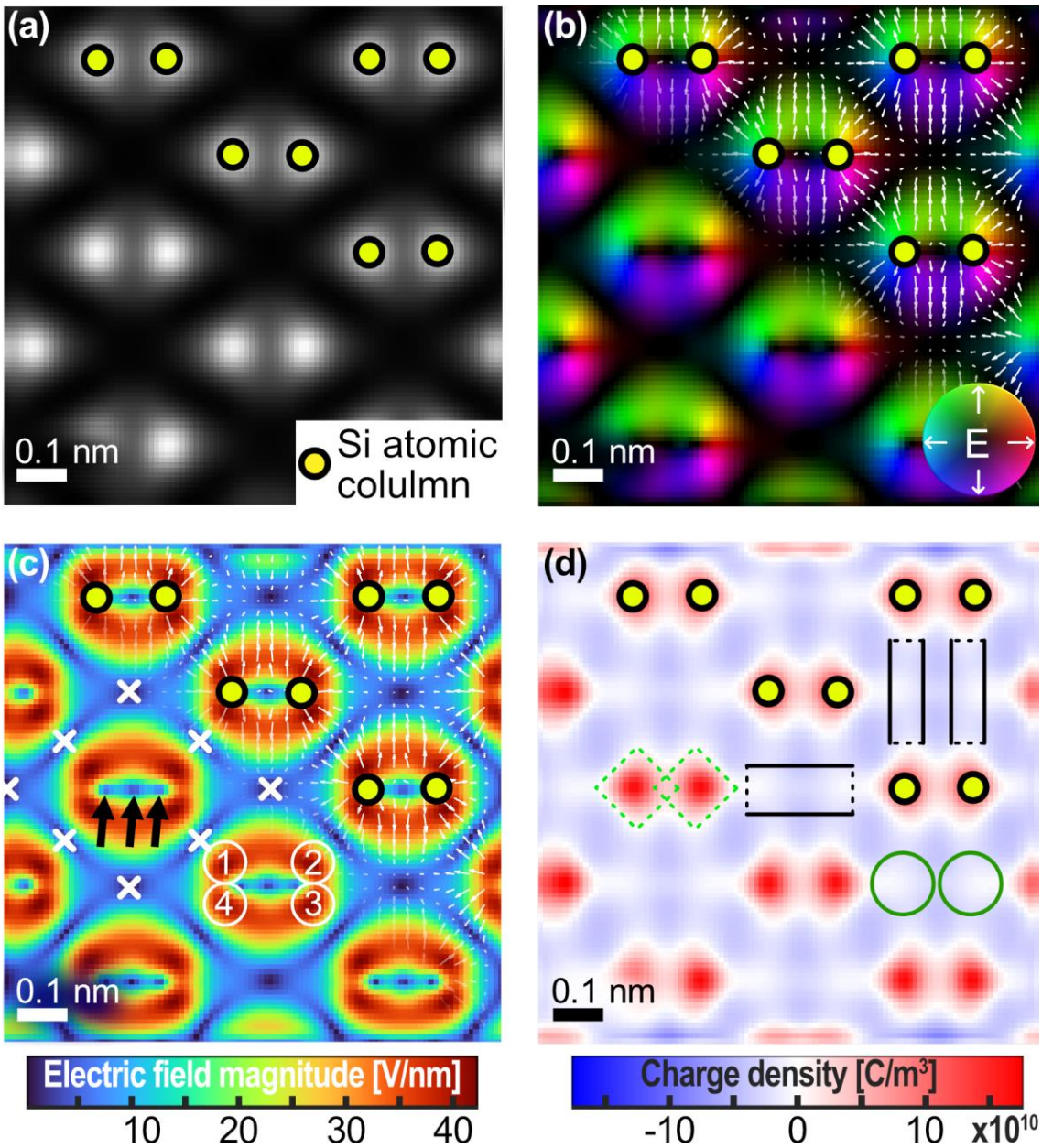

Figure 54: (a) Dark-field and (b) colour-coded DPC image as well as (c) electric field magnitude and (d) charge density of Si[110] obtained by multislice image simulations using Dr. Probe. The simulation parameters resemble the illumination and specimen parameters in the experiment. Here, the specimen thickness amounts to 30.72 nm and all simulations are conducted with a underfocus of C_1 = -4 nm. Further details can be found in Table 29 in the Appendix.

The dark-field image depicted in Fig. 54(a) clearly exhibits contrast at the Si dumbbells arising from scattering at atomic columns. However, the dumbbells do not show the expected perfectly rotational symmetric intensity distribution of individual atomic columns but a distorted and more triangular shape. This distortion arises from the defocus and is only visible due to the higher spatial resolution of the simulation than the measured image. A decrease in spatial resolution would correspond to a blurring of features. Blurring of the dark-field image would make the intensity distribution around atomic columns more rotational symmetric. An analysis of the influence of defocus on HAADF images is given in Fig. 99 in the Appendix. The atomic column positions are again determined by fitting two-dimensional Gaussian functions to the intensity

distribution of the dark-field image. Resulting atomic column positions are indicated by yellow discs in all images in Fig. 54.

Fig. 54(b) shows the colour-coded DPC image in which colour wheels around individual atomic columns can be observed. To illustrate the directions of electric field vectors, a vector plot is overlayed on the colour-coded DPC image, indicating the direction and magnitude of electric field vectors. The present electric field distribution is very similar to the measured DPC image displayed in Fig. 53(b). This is not only evident from the presence of colour wheels but can be particularly deduced from the areas of the image where the potentials of the individual atomic columns overlap. Like the measured DPC image, these areas also indicate a superposition of electric field direction and magnitude, leading to dominant purple and green areas above and below the dumbbell. Furthermore, a decrease in DPC signal on the connecting axis of the atomic columns of a dumbbell can be observed.

The decrease is also visible in the electric field magnitude shown in Fig. 54(c) and exemplarily indicated by the middle black arrow. The two outer arrows again point at the local minima of electric field magnitude arising from the scattering centres at atomic column position. These two local minima match the indicated atomic column positions which are marked by yellow discs. The simulated electric field magnitude distribution again shows local maxima of electric field close to the atomic columns, which sit on the connecting axis of two dumbbells. These local maxima are exemplarily marked by white circles with numbers (the numbers are used at the end of this section). Furthermore, local minima in the electric field magnitude are observed at interatomic pixels and more precisely at high symmetry points of the lattice. Several of these are exemplarily marked by white crosses.

The corresponding charge density map is shown in Fig. 54(d). The charge density exhibits local maxima at atomic column positions. These local maxima correspond to a positive charge density and arise from the potential of the nuclei. The charge density around each atomic column has a square-like shape. This is indicated by the dashed green squares. Furthermore, regular features at interatomic pixels are observable, which extend parallel to low order lattice planes, e.g. in [001] and [$\bar{1}$10] direction. These are exemplarily indicated by a set of two lines which are each connected by two dashed lines. At the crossings of the lines, local maxima in charge density are observable, which are marked by green circles.

Comparing the measured (Fig. 53) and simulated (Fig. 54) DPC images reveals a good qualitative match. In both cases rotational symmetric electric fields are evident around atomic column positions. However, the extension of the colour wheels is larger in case of the measured electric field distribution. This is presumably due to the different defocus used in the experiment, as discussed in Chapter 5.2 (see e.g. Fig. 36). The different defocus used in the experiment also possibly enhances the formation of line-like features, which arise due to the way the detector intersects the highly inhomogeneous CBED intensity distribution (Chapter 5.1). These line-like features are also referred to as an artefact resulting from dynamical diffraction effects and the beam

extension within the specimen. It is precisely these line-like features in the DPC measurement which lead to positive charge densities at interatomic pixels in the derived charge density map shown in Fig. 53(d). Due to the enhanced diffraction contrasts, the local charge density maxima at interatomic pixels (marked by a green circle in both the measured and simulated maps) exhibit higher positive values in the measured charge density than in the simulated one.

The magnitudes of the measured and simulated electric field distributions have very similar features. These include the local minima on the connecting axis of the atomic columns in a dumbbell and the local maxima on the connecting axis between neighbouring dumbbells. While the former is easy to recognise by the three arrows marked in both the simulation and experiment, the latter (indicated by white circles) reveals differences between simulation and experiment. These differences are particularly evident from the position of the local maxima. One possible explanation for these differences is a tilt of the specimen. The influence of the tilt is discussed in detail in Chapter 5.6 and is therefore only briefly addressed here by comparing the scattergrams of the measurement and the simulation in Fig. 55(a) and Fig. 55(b), respectively.

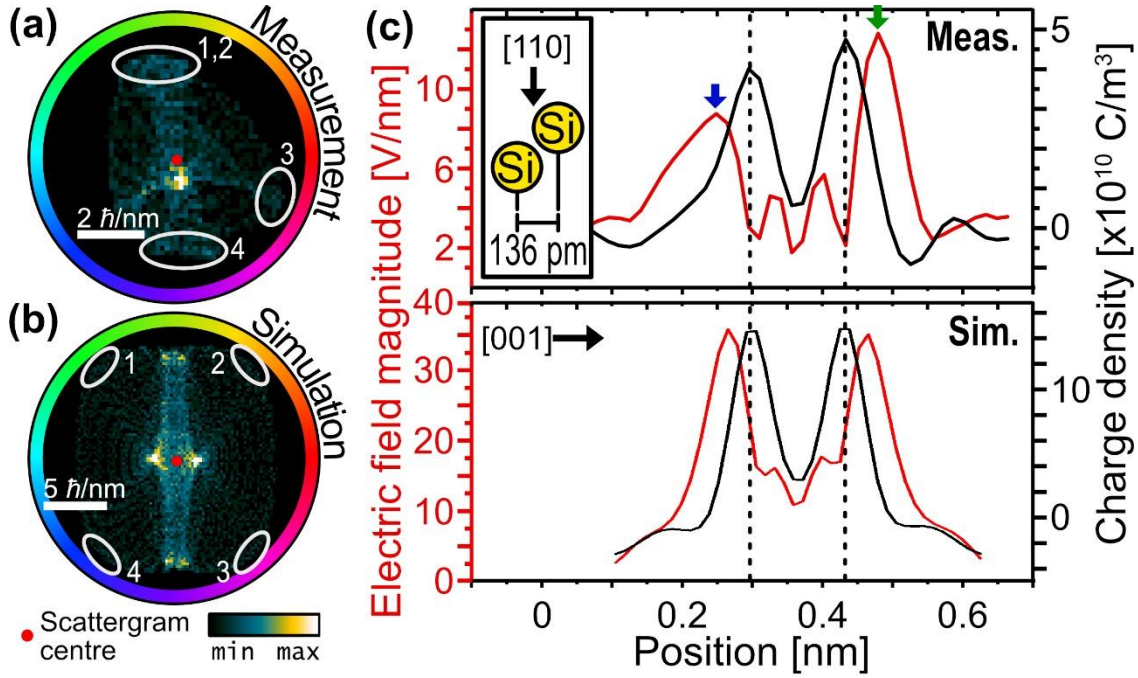

Figure 55: Scattergrams of (a) the simulated DPC image shown in Fig. 54 and (b) the measured DPC image shown in Fig. 53. Details on the annotations can be found in the main body of the text. It is to note that the numbers shown in the scattergrams do not point at similar features evident in the measurement and the simulation. (c) Line profiles of the measured electric field magnitude and charge density including an illustration of the ordering of Si atoms in a dumbbell with projected distance of 136 pm. The position of line profiles is indicated by the red and grey lines in Fig. 53. Further details on the imaging parameter can either be found in the description of Fig. 53 or Table 47 in the Appendix.

DPC imaging of a Si specimen, which is perfectly oriented in [110] zone-axis and has a thickness of about 30.7 nm, results in a scattergram with two off-centre maxima. As described in Chapter 5.6, one of the main results of the tilt of a Si specimen away from

[110] zone-axis orientation on the scattergram distribution is the formation of a single off-centre maximum (Fig. 49(l)). Such an off-centre maximum is evident in the scattergram in Fig. 55(a) which was calculated from the measured DPC image. The simulated DPC image of Si in [110] zone axis orientation is shown in Fig. 55(b). This scattergram obviously exhibits two off-centre maxima (close to the scattergram centre). The scattergrams also reveal that a different number of features with maximum electric field magnitude (marked by white circles in Fig. 53(c) and Fig. 54(c)) and different dominant electric field directions of the respective maximum are obtained by specimen tilt. The features of the scattergram correlated to the local maxima in the electric field distribution are marked by white circles in Figs. 55(a, b). For better classification, they are numbered in the measured and simulated electric field magnitudes (Fig. 53(c) and Fig. 54(c)) as well as in the corresponding scattergrams (Figs. 55(a, b)). It is to note that due to the high similarity in electric field direction of the local maxima of the measured electric field magnitude which are indicated by “1” and “2” in Fig. 53(c), scattergram maxima are merged in a single ellipse denoted by “1,2” in Fig. 55(a). Further explanations on features in the scattergrams of Si[110] are given in Chapter 5.1.2.

A quantitative discrepancy between simulated and measured electric field magnitudes terms can be observed (Fig. 53(c) and Fig. 54(c)). While the experimental mean value (averaging the whole map) amounts to 6.9 V/nm with a standard deviation of 3.7 V/nm, it amounts to 19.9 V/nm with a standard deviation of 11.6 V/nm in the simulation. A possible explanation is the difference in defocus, which influences the measurable electric field magnitude (Chapter 5.2, Fig. 38, or Chapter A.2.3, Fig. 92). Furthermore, an amorphous layer must be considered in case of the measurement. This amorphous layer is the native oxide layer, which Si forms on the top and bottom surface of the TEM lamella when stored at ambient conditions. Moreover, using a low keV ion beam for the final polishing step of the lamella, a small layer at the surface is amorphized [173, 174]. The influence of amorphous layers on obtainable DPC signals is beyond the scope of this thesis and has so far been mainly investigated for ADF STEM images [175].

Fig. 55(c) depicts line profiles of the experimental field magnitude and charge density along the dashed lines (dumbbell axis) in Figs. 53(c, d) including analogously obtained profiles for a simulation and atomic column positions (marked by black dashed lines in Fig. 55(c)). As can be seen, the overall minimum of electric field magnitude is observed in the middle of the two atomic columns. Additional local minima can be found exactly at the atomic column positions. It is to note that a non-zero electric field magnitude is measurable at all minima. This can be ascribed to the limited spatial resolution, which leads to a smearing of values, and the sampling, i.e. the scan positions do not coincide with the exact atomic column positions. Local maxima of the electric field magnitude are observed on both sides of each atomic column. However, the local maxima of electric field magnitude in between the atomic columns of a dumbbell show a reduced magnitude due to the overlap of potentials. The maximum of electric field magnitude

marked by a green arrow exhibits a larger magnitude than the one marked by a blue arrow. This is not observed in the corresponding simulation, which shows symmetric line profiles of electric field magnitude. A possible explanation for the difference in magnitude is the refocussing effect in combination with the specimen tilt. The atoms of the two atomic columns of a dumbbell sit at different z-positions along the [110] beam direction. This is illustrated in the inset in Fig. 55(c). The first atom thus redistributes the incident beam's intensity before the electron wave interacts with the potential of the second atom. This effect has also been observed in simulations with perfect specimen orientation and a defocus at the entrance plane (see Fig. 100 in the Appendix) and can be influenced by the defocus as well as the specimen tilt.

The charge density line profiles reveal localised positive charge density maxima at atomic column positions. At interatomic pixels, negative values of charge density can be observed. The influence of the refocussing effect and specimen tilt can also be possibly seen between the different positive charge density maxima of the atomic columns in the experiment. In the simulations, both atomic columns show similar positive charge densities.

Even though the absolute values of electric field magnitude and charge density obtained experimentally here are certainly affected by the large specimen thickness and all other errors discussed above, it should be finally mentioned that their maximum values (12.7 V/nm, $4.7 \cdot 10^{10}$ C/m^3) are of the same order of magnitude as corresponding values obtained in other quantitative DPC investigations (e.g. $SrTiO_3$ [9] and GaN [23]).

6.1.3. Comparison of segmented and pixelated DPC images

Although a quantitative analysis of the atomic electric field distribution of a (30 ± 2) nm thick Si specimen is not accurate due to the high specimen thickness and the fact that this thickness accounts for a substantial part of the extinction length, a quantitative comparison of the DPC images acquired with a segmented and a pixelated detector is still interesting. DPC imaging was therefore performed on the ARM200F at the university of Paderborn and on the NeoARM at the university of Augsburg, the first equipped with a segmented detector (*JEOL* SAAF detector) and the second with a pixelated detector (*GATAN* OneView camera).

The comparison is made based on the colour-coded electric field distributions as well as calibrated electric field magnitude and charge density maps. It includes two different ways of calculation and calibration for each detector type (Chapter 3.1 and Chapter 3.2). For the segmented detector, both DPC image acquisitions paired with the signal-based calibration (Chapter 3.1.1) and with the geometrical centre of mass (CoM) of the detector segments in momentum space (Chapter 3.1.2) are used. For the pixelated detector also two techniques are used to calculate the DPC signal: The calculation of the CoM of CBED intensity distribution and the difference signals from virtual segments on the detector (both Chapter 3.2). The latter calculates the DPC signal in a similar way as the segmented detector, using the geometrical CoM of the detector segments

in momentum space. All segmentation based DPC image acquisitions use Layer2 in a bisected way as well as an inner collection angle of $\beta_{\mathrm{inner}} = 18$ mrad and an outer angle of $\beta_{\mathrm{inner}} = 35.4$ mrad. The x-axis of the physical and virtual segmented detector is aligned with the connecting axis of atomic columns in a dumbbell ([001] direction). All images are smoothened by Gaussian denoising (Chapter 4.4.1) with a standard deviation of 0.02 nm corresponding to 1 pixel for the images acquired with segmented and pixelated detector. Rigid and non-rigid registration methods (Chapter 4.4.2) were not feasible, as the number of pixels of the DPC image captured with a pixelated detectors are limited by the storable amount of data.

The results of this comparison are only indicative and can only give a rule of thumb, as the DPC signal is influenced by many parameters. These parameters are given in the following and are based on the fact that two different microscopes are used. These influences include the defocus, which is manually adjusted and therefore inherently different. As described in Chapter 5.2, the defocus has a strong influence on the features and the signal magnitudes in a DPC image. Although both microscopes have similar spatial resolution capabilities, the spatial resolution might influence the obtainable DPC signal due to the different point spread functions and residual lens aberrations (Chapter 5.5). Since the spatial size of a pixel influences the derived charge density magnitudes (it's a density!), both image calibrations were carefully checked. These amount to 0.019 nm (ARM200F) and 0.018 nm (NeoARM). In order to prevent build-up of contamination during the image acquisition with the pixelated detector, the specimen was cleaned in an air plasma. Such a plasma leads to an oxidation of the Si and thus increases the thickness of amorphous layers on top and bottom of the Si lamella [176]. As a result, the amorphous layers might possess different thicknesses in the DPC images captured with the segmented and the pixelated detector, although the same Si TEM lamella is used.

To increase comparability, the defocus was carefully adjusted to obtain the maximum achievable DPC signal magnitude. In case of the 4D-STEM image, this was not achieved with the DPC image due to an acquisition time of approximately 1.5 minutes. It was achieved by optimising the measurable CBED pattern for a stationary beam (acquisition time corresponds to dwell time) and specifically by adjusting the focus until the CBED intensity is comparable to a simulated CBED pattern which was obtained with simulation parameters guaranteeing maximum DPC signal. All DPC images are acquired with carefully adjusted specimen tilt and at same area of the specimen described in Chapter 6.1.1. However, the images are not obtained from the same atomic columns.

Fig. 56 compares DPC analyses acquired with the segmented (SAAF detector) and pixelated detector (OneView camera) for the different image calculations and calibrations. This includes the colour-coded representation of electric field distribution in Figs. 56(a-d), the electric field magnitude in Figs. 56(e-h) and the derived charge density in Figs. 56(i-l). All images are normalised to their maximum and respective minimum magnitude. The DPC image and related quantities obtained with the

segmented detector are contained in Figs. 56(a, b, e, f, I, j). Analogously, Figs. 56(c, d, g, h, k, l) show the results of the pixelated detector.

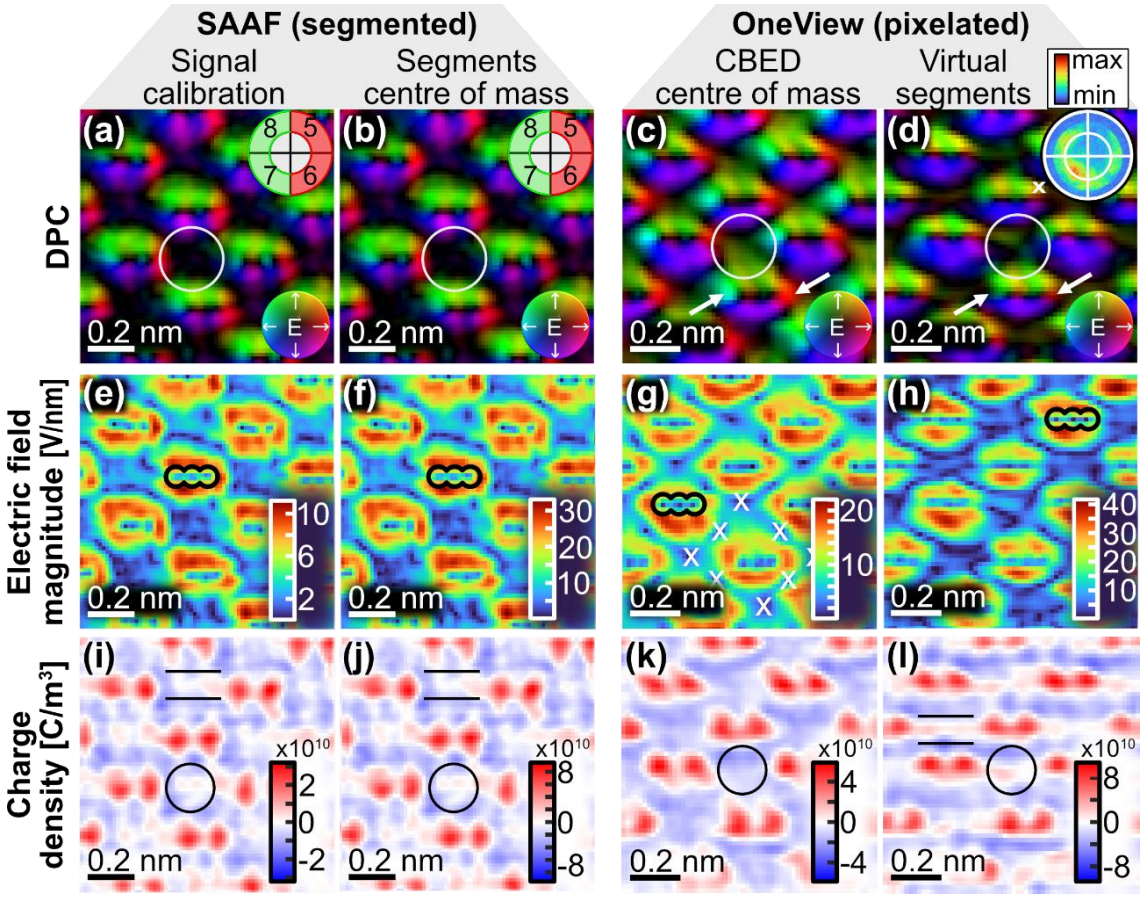

Figure 56: (a-d) Colour-coded DPC image of the electric field distribution obtained by using a segmented detector (SAAF) with (a) signal-based calibration and (b) with a calibration based on the detector segment's geometrical centre of mass as well as by using a pixelated detector (OneView) with (c) the centre of mass of the intensity distribution and (d) projected virtual detector segments on the pixelated detector. For (a,b,d) the detector is oriented in such a way that the x-direction of the detector is aligned with the direction of the connecting axis of the Si atomic columns in a dumbbell. The detector rotation is indicated by the insets in the respective subfigures (a,b,d) depicting the detector shape. Besides the inset detector shape and orientation, the inset in (d) furthermore includes a convergent-beam electron diffraction pattern (CBED). This CBED pattern was obtained from the pixel marked by a white cross in (d). (e-h) Corresponding electric field magnitudes and (i-l) charge densities. These are calculated from the DPC image in the top row of the respective column of the image tableau. The reader is referred to the main body of this thesis for explanations on the annotations. Experimental parameters can be found in Table 48 in the Appendix.

The colour-coded electric field distributions in Figs. 56(a-d) feature rotational symmetric fields around the atomic column positions. This can be deduced from the colour wheel-like colour-coded electric field distribution around the atomic columns. Nonetheless, the colour-coded electric field distributions exhibit several differences between the DPC images acquired with the two detector types. The electric field distributions of the dumbbells measured with the segmented detector and the virtual segments on the pixelated detector (Figs. 56(a, b, d)) have a smaller extension than the respective field measured by the centre of mass of intensity on the pixelated detector Fig. 56(c). This is evident from the difference in signal at interatomic pixels, which are exemplarily

marked by white circles. A possible explanation for the difference in extension of the electric field distribution of a dumbbell lies in the detector response function of the segmented detector and in particular the orientation of the detector to the symmetric CBED pattern. The influence of the response function of a segmented detector has been investigated in Chapter 5.1. One of the observations in Chapter 5.1 is a strong spatial compression of electric fields for a detector rotation of 0°. At this rotation the x-axis of the detector is aligned with the dumbbell's connecting axis, as it is the case in the DPC images in Figs. 56(a, b, d) and indicated by the detectors in the inset. The inset in Fig. 56(d) exemplarily shows a recorded convergent-beam electron diffraction (CBED) pattern for the electron beam positioned at the white cross in Fig. 56(d) to illustrate the extension of the direct electron beam on the detector and the intensity of diffracted beams. The influence of the use of a segmented detector is also directly observable, when comparing the DPC images in Figs. 56(c, d). Both result from the same 4D-STEM data and show the same area. Besides the smaller extension of electric fields also the electric fields with a direction resulting in red and bright blue pixels (indicated by white arrows) are suppressed in case of using virtual segments. The DPC images acquired with the segmented detector shown in Figs. 56(a, b) exhibit the same colour-coded electric field distribution for both calibrations and image calculation methods. This is because both calibrations use the same signal for image calculation and the colour-coded images are normalised to their maximum and minimum intensities.

Figs. 56(e-h) display the electric field distribution which are calculated from the differently determined DPC images. Obviously, the measured electric field magnitude at interatomic pixels is larger when the CoM of intensity on the pixelated detector (Fig. 56(g)) is used than if a detector with physical (Figs. 56(e, f)) or virtual detector segments (Fig. 56(h)) is used. Electric field magnitude maps which are based on the CoM of the intensity on the pixelated detector show eight local minima around each dumbbell (marked by white crosses in Fig. 56(g)). Such regular minima at interatomic regions are not observable in case of the other acquisition techniques (Figs. 56(e, f, h)). However, in all images, the three local electric field magnitude minima at and in between the atomic column positions are visible. These are exemplarily marked by black keyhole-shaped lines in Figs. 56(e-h). These three local minima have already been observed in Fig. 53 (marked by three arrows) and arise from the potential of the atomic nuclei and their overlap.

Despite the manifold of influences on the DPC signal, a good agreement regarding the maximum values of the electric field magnitude is observed between the measurements with a segmented and a pixelated detector. This is evident from the fact that all electric field maps exhibit electric field magnitudes within the same order of magnitude (10^{10} V/m) and is especially visible in case of maps acquired with the centre of mass of the detector segments in momentum space (Figs. 56(f, h)). This is expected, since both DPC images are calculated in a similar way. The difference in electric field magnitude possibly arises due to slightly different defoci, different convergence semi-

angles and different point-spread functions of the incident electron beam. The latter leads to a smearing of features and reduced measurable field magnitudes.

There is a difference by a factor of three in maximum electric field magnitudes obtained with the segmented detector and the two different calibrations (Figs. 56(e, f)). It can be explained by the fact that the signal-based calibration (Chapter 3.1.1) takes into account the illuminated area while the signal calculation, which is based on the segments centre of mass (Chapter 3.1.2), always uses the geometrical CoMs of the detector segment in momentum space even if the direct beam only barely extends into the Layer2. This could give rise to a systematic overestimation of electric field magnitudes when the CoMs of the segments are used. There is also a difference by a factor of two between the electric field magnitudes obtained with the pixelated detector, either calculated directly by the CoM or using virtual segments (Figs. 56(g, h)). They arise from the fact that the image based on the CoM of the intensity distribution is obtained with a much higher momentum space resolution than the image acquired with the help of virtual segments. The former determines the DPC signal by assigning each pixel of the camera a momentum space vector (Chapter 3.2). The latter can only account for intensity variation of the beam between the different areas covered by the limited number of (virtual) segments but cannot account for intensity variations within these segments. Here, DPC signal is calculated with the help of only four virtual segments and their respective geometrical centre of masses in momentum space (Chapter 3.1.2). Due to the fact that the local maximum of intensity is found close to the inner collection angle of the virtual segments (inset in Fig. 56(d)), the signal calculation with the virtual segments overestimates the DPC signal. This explains the increased measurable electric field magnitudes of the DPC signal acquired with the virtual segments on the detector.

Figs. 56(i-l) show the charge density maps obtained from the different detectors and the different calculation procedures. Local positive charge maxima are observed at atomic column positions. This is expected, since the DPC signal is dominated by the potential of the nuclei within atomic columns. The charge densities in Figs. 56(i-l) are in good agreement in terms of magnitude. Especially the charge densities derived with the help of the detector segments geometrical CoM in momentum space shown in Fig. 56(j) and Fig. 56(l) show a good agreement.

Certainly, the differences of the electric field maps are transferred to the derived charge density maps. These include positively charged pixels between the Si dumbbells as well as horizontal line-like features which are observed in all maps obtained from a (virtual) segmented detector (Figs. 56(i, j, l)). The interatomic pixels with a dominating positive charge density are indicated by the black circles, parallel black lines exemplarily highlight horizontal line-like features. As such features at interatomic pixel cannot be found in the CoM-based DPC image in Fig. 56(k), they arise from the detector response function intersecting the symmetric CBED pattern.

One insight obtained from the investigations shown in Fig. 56 is the strong influence of the detector and calibration technique on the DPC signal. Although a good agreement

in terms of electric field magnitude and charge density is obtained for both segmented and pixelated detectors, the electric field distribution exhibits significantly different electric field structures. It is to note again that these findings strongly depend on the specimen thickness which is responsible for the emergence of dynamical diffraction effects. It can be assumed that the influence of the detector type on the obtainable DPC signal decreases with decreasing specimen thickness.

To allow a more accurate quantification of electric field magnitude and direction as well as the corresponding charge density when using segmented detectors, the detector response function of segmented detectors must either be eliminated, reduced to a minimum or at least carefully considered in the interpretation. The following chapter therefore investigates the detector response function for which DPC signals very similar to the CoM signal can be measured. The subsequent chapter shows a method to reduce the influence of the detector response function by using an DPC image series of different detector rotations.

6.1.4. Segmented detector response function for CoM-similar signal

A segmented detector only uses a few segments for the acquisition of DPC images. In contrast, a pixelated detector has up to several hundred thousand pixels. It is therefore obvious that the pixelated detector offers a much higher momentum resolution. It can be assumed that the pixelated detector measures the true CoM of the intensity distribution, whereas the segmented detector only approximates the CoM. Hence, pixelated detectors measure the transferred momentum more reliably. As already shown in the previous chapter and discussed in Chapter 5.1, the low number of segments of a segmented detector has a non-negligible influence on the achievable DPC images and measurable electric field distributions. It is interesting to investigate the detector response function of a segmented detector and especially how it can be optimised to obtain a DPC image that is similar to one achieved with the CoM signal of pixelated detectors. In the following, this is accomplished for an eight-fold segmented detector and in particular by using virtual segments on the pixelated detector and a cross-correlation-based comparison with the CoM signal. The complete analysis is obtained from the 4D-STEM measurement that was already used in Fig. 56 and was acquired with the NeoARM at the university of Augsburg. Using a single 4D-STEM image provides the mandatory equality of the measurable potentials.

The detector response function is mainly governed by the inner β_{inner} and outer β_{outer} polar collection angles as well as the detector rotation φ. For a virtual segmented detector, it can be varied and is adjusted in post-processing of a 4D-STEM measurement by changing the rotation and extension of the virtual segments. For this purpose, a detector extension parameter d is introduced by which the detector's polar collection angles are determined. These are given by $\beta_{\mathrm{inner}} = 0.5 \cdot d \cdot \alpha$ and $\beta'_{\mathrm{outer}} = d \cdot \alpha$ in which α denotes the convergence semi-angle. The detector is completely illuminated at $d = 1$ while at $d = 2$ only Layer1 is illuminated by the direct

beam. However, at $d = 2$ also scattered and diffracted electrons are expected on Layer2. Experimentally, a decrease of d corresponds to an increase in camera length.
Imaging was conducted at the same area of the Si lamella as in Fig. 56 and at an acceleration voltage of 200 kV. The DPC images are determined from the intensity of the virtual segments of Layer2 by the geometrical centre of mass of detector segments (Chapter 3.2). The image is corrected by only correcting the basic rotation angle (rotation of beam in magnetic field of the projection lenses) and the detector rotation (Chapter A.1.1). No further post-processing such as denoising is applied.
Fig. 57(a) shows the colour-coded DPC image derived via the CoM evaluation. Since no denoising is applied, the influence of the image noise is much more visible than in Fig. 56. Fig. 57(b) shows the corresponding transferred momentum magnitude which exhibits the same structure as the electric field magnitude, as they are both multiplicatively coupled with each other. For a description of features see Chapter 6.1.3. Figs. 57(c-h) display the colour-coded DPC image and the transferred momentum magnitude maps for three different detector response functions. Figs. 57(c, d) are obtained with a detector response function of $d = 1$ and $\varphi = 0°$, Figs. 57(e, f) with $d = 1.3$ and $\varphi = 45°$ as well as Figs. 57(g, h) with $d = 1.6$ and $\varphi = 80°$, respectively. These are only examples. Investigations based on a systematic variation of d and φ and a quantitative comparison of CoM and segmented images will be presented in Fig. 58 below. To illustrate the detector response function, Fig. 57(i) depicts position averaged convergent-beam electron diffraction (PACBED) patterns overlayed with the detector silhouette. The red-, green- and violet-coloured dots in the upper left corner link the measured DPC images in Figs. 57(c-h) to the PACBED patterns.
It is evident from Figs. 57(c-h) that the detector response function drastically influences the obtained DPC images. Fig. 57(c) exhibits a rather small extension of intense colours around individual dumbbells and only negligible signal at interatomic pixels. This is particularly well visible from the separated features around individual dumbbells in the map of transferred momentum magnitude shown in Fig. 57(d). In Fig. 57(e), the colour wheel distributions around individual dumbbells exhibit a much larger extension due to the different detector response function. In addition, also intensities at interatomic pixels show a much higher intensity as it is also observable in the map of transferred momentum in Fig. 57(f). The position of features at interatomic pixels is indicated by a white circle in Figs. 57(e, f).
When the direct beam only extends barely into Layer2 (subfigures with green dots in Fig. 57), the measurable intensity within the virtual segments is small. Thus, the signal-to-noise-ratio is decreased, which ultimately prevents the detection of the typical rotational symmetric electric fields around individual atomic columns. This is particularly the case in Fig. 57(g) in which the colour wheels around atomic columns are only barely visible. This is similar in the transferred momentum magnitude map in Fig. 57(h), which shows almost no regular features.

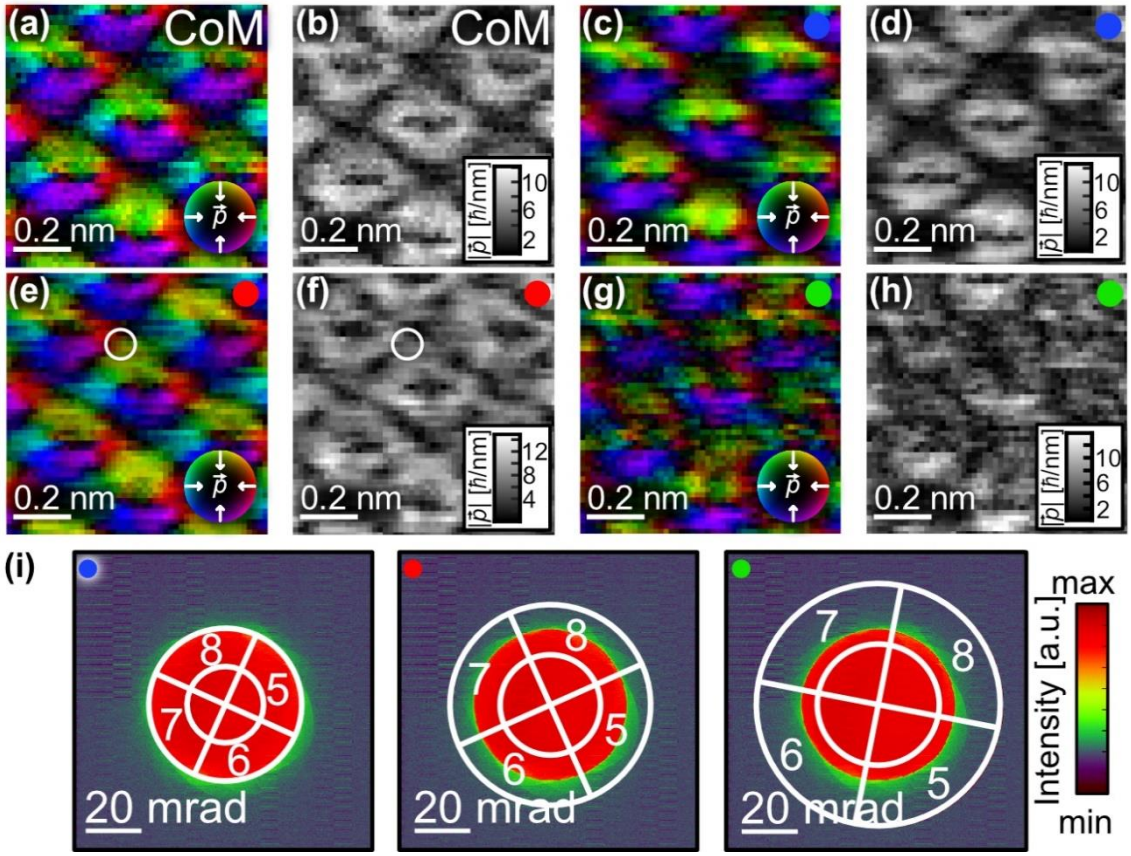

Figure 57: (a) Colour-coded DPC image obtained by the CoM signal of a pixelated detector with (b) corresponding transferred momentum magnitude map. (c, e, g) DPC images and (d, f, h) corresponding transferred momentum magnitude for a detector extension of $d = 1$ and detector rotation of $\varphi = 0°$ ((c, d) violet dot), $d = 1.3$ and $\varphi = 45°$ ((e, f) red dot) as well as $d = 1.6$ and $\varphi = 80°$ ((g, h) green dot), respectively. All DPC images (a, c, e, g) are obtained from the same 4D-STEM measurement which is conducted on (30 ± 2) nm thick Si[110] specimen. (i) Position averaged convergent-beam electron diffraction pattern with overlayed detector silhouette. The numbers in the detector segments indicate the segments used for the calculation of DPC signal in image (c, e, g). The coloured dots indicate the corresponding DPC image and transferred momentum magnitude. The coloured dots can also be found at the corresponding detector rotation and extension in Fig. 58. Experimental details are listed in Table 49 and Table 50 in the Appendix.

Fig. 58 shows the cross-correlation coefficient of the transferred momentum magnitude distribution $|\vec{p}|$ of the CoM image and the DPC image deduced via virtual segments in dependency of the detector response function, i.e. for detector rotations φ from 0° to 90° and detector extensions d from 0.5 to 2. Here, φ=0 corresponds to the alignment of the detector x-axis parallel to the dumbbell axis. A cross-correlation coefficient close to 1 resembles a case in which the transferred momentum magnitude derived from the virtual segments is similar to the one derived from the CoM signal. A cross-correlation coefficient of 1 therefore corresponds to an optimal situation. It is to note that this calculation does not include the direction of transferred momentum, since only the magnitude is considered in the calculation of this cross-correlation coefficient. For Fig. 58, again all images are obtained by using only Layer2 and projecting virtual segments on the pixelated detector (Chapter 3.2). The orientation of the detector is also deducible from the PACBED patterns in Fig. 57(i) as coloured dots for the three exemplary chosen detector response functions are also given in Fig. 58.

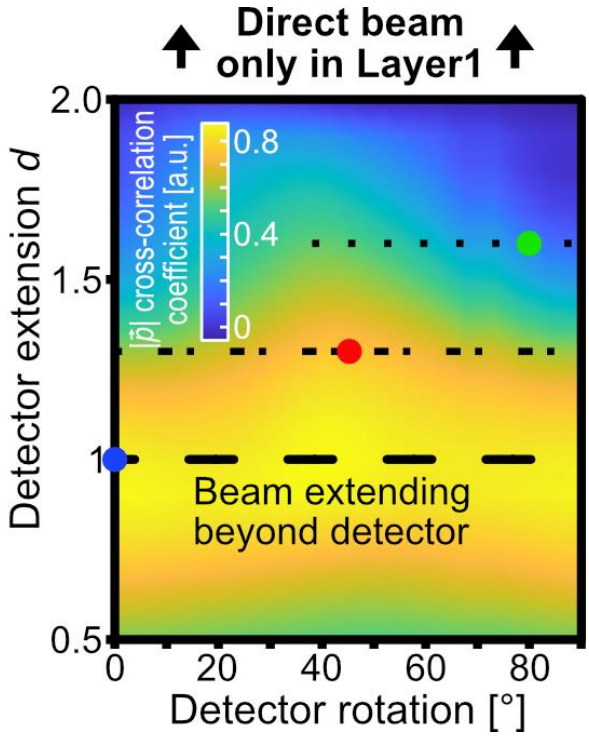

Figure 58: Cross-correlation coefficient of the transferred momentum magnitude of the DPC images determined via the CoM and the virtual segments on the pixelated detector as a function of the detector rotation and extension. The coloured dots mark the conditions for which DPC images were displayed in Fig. 57. All DPC images used for this surface plot are obtained from a single 4D-STEM image and measured on a (30 ± 2) nm thick Si[110] specimen at an acceleration voltage of 200 kV. The experimental details are the same as for the images in Figs. 57(a-h).

In Fig. 58, it can be seen that with increasing detector extension d the cross-correlation coefficient reaches its global maximum of 0.85 at a detector extension of d =0.95. This corresponds to a situation in which the direct beam has a larger extension than Layer2. This is rather unexpected, since an annular part close to the direct beam edge is not incident on the detector and hence not contributing to the signal. A possible explanation for the CoM-similar DPC image is based on the intensity distribution within the direct beam and in particular the dependence of the intensity on the polar angle. It can be seen in the inset in Fig. 56(d) that the intensity distribution within the direct beam can be very inhomogeneous. At such large specimen thicknesses of (30 ± 2) nm the global maximum of the intensity distribution can be found within and not necessarily at the edge of the direct beam. However, thinner specimens which fulfil the weak phase approximation but still possess inhomogeneous potentials would only result in an intensity gradient across the direct beam and a maximum of the intensity distribution at the edge of the direct beam. Thus, the intensity at polar angles close to the direct beam edge might play a decreased role for the quantification of transferred momenta at such large specimen thicknesses. It should be noted that this assumption cannot be generalised because the intensity distribution in the direct beam also depends, among others, on the defocus, convergence semi-angle and acceleration voltage. At d =1, a maximum cross-correlation coefficient of 0.842 is achieved for a detector rotation of 0°. With further increasing the detector extension, the cross-correlation coefficient decreases, and the detector rotation plays an important role. The latter can be seen

from the increased differences of cross-correlation coefficients for detector rotations of 0° and 45°. At detector extension at which the direct beam only partly illuminates Layer2, the best cross-correlation coefficient is obtained when the detector is rotated by 45° to the dumbbell axis. For example, assuming a detector extension of d =1.5 and a detector rotation of 45°, the segmented DPC image has a maximum cross-correlation coefficient of 0.668 with the CoM DPC image. As 0.668 does not render a high similarity, this investigation demonstrates that with such a detector response function, the DPC image is not similar to the CoM-derived DPC image. It is worthy to note that the optimum detector response function will also depend on the symmetry of the specimen potential as well as the specimen thickness and defocus. A comprehensive study of the specimen thickness dependent influence of the detector response function is required in the future.

This study shows that it is possible to increase the similarity of pixelated and segmented DPC images by optimising the detector response function. If a pixelated detector is not available, such investigations can be carried out with the help of a simulated 4D-STEM image.

6.1.5. Increasing azimuthal momentum space resolution

In this chapter, the increasing azimuthal momentum space resolution (IAMSR) method (Chapter 4.3) is applied. It is investigated how strongly the influence of the detector response function on DPC images can be reduced by applying the IAMSR method. This is achieved by applying the IAMSR method to a DPC image series obtained from a single 4D-STEM image, i.e. by calculating DPC images using virtual detector segments at different detector rotations (Chapter 3.2). Using a single 4D-STEM image instead of a series of separate genuine segmented DPC images is advantageous to investigate the improvement by the IAMSR method, because the potential landscape is the same for all images acquired with different detector rotations. The improvement is finally investigated by a comparison of the DPC image after application of the IAMSR method with the CoM DPC image of the same 4D-STEM image.

In the following, the IAMSR method is applied using 18 individual DPC images, i.e. the virtual detector segments were rotated in steps of 5°. Additionally, the influence of the polar collection angles of the detector segments were investigated by changing the beam extension parameter d (same definition as in Chapter 6.1.4). Moreover, the DPC images are calculated using segments of Layer1, Layer2 as well as a combination of Layer1 and Layer2. All images are denoised before applying the IAMSR method using a Gaussian denoising technique with a standard deviation of 19 pm (the size of one pixel). The comparison of the CoM and IAMSR images is based on determining their similarity via the cross-correlation coefficient of transferred momentum magnitude maps (without direction; Fig. 59(a)), colour-coded DPC images (including the direction; Fig. 59(b)) as well as charge density distributions (Fig. 59(c)). At this point it is to note that the DPC cross-correlation coefficient (Fig. 59(b)) is calculated by multiplying two cross-correlation coefficients: one cross-correlation coefficient calculated for images

only containing the individually normalised hue channel (direction) and another for the individually normalised value channel (magnitude) of DPC images in HSV colour space. All three quantities are plotted as a function of the beam extension d for the different detector segment layers.

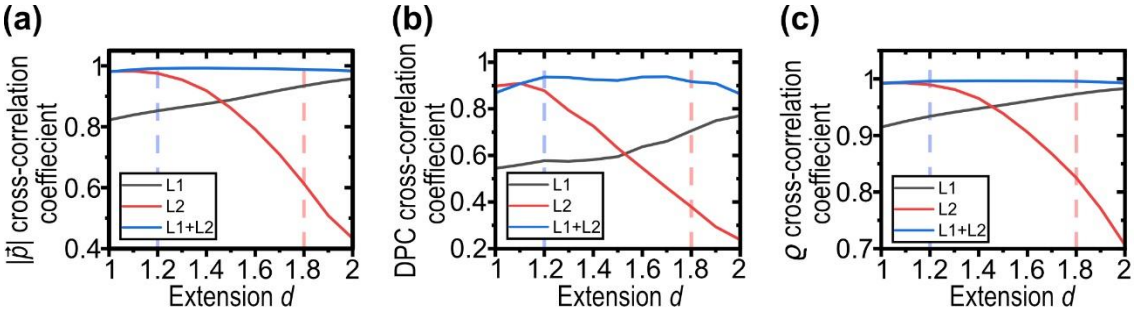

Figure 59: Cross-correlation coefficients of the (a) transferred momentum magnitude, (b) colour-coded DPC image and (c) charge density of the CoM derived signal and the signal obtained by applying the method to increase the azimuthal momentum space resolution. The dashed blue- and red-coloured vertical lines indicated the beam extension d of the IAMSR DPC images exemplarily shown in Fig. 60 and Fig. 61. Experimental details are listed in Table 51 in the Appendix.

For all three quantities, an almost similar trend for the layers is observable. Thus, the discussion in the following is ordered by the Layers considered for the IAMSR method.
When only Layer2 is used, the similarity of each of the considered three quantities with the CoM results is largest for d=1 and decreases with increasing the beam extension parameter d, corresponding to an increase in polar collection angles of the detector. This means that the highest cross-correlation coefficient of each quantity considering only Layer2 is measurable when the direct beam completely illuminates the detector. Hence, microscopist with a ring-shaped segmented detector can achieve good similarity between IAMSR and CoM results if a suitable beam extension on the detector is chosen. A decrease of cross-correlation coefficient with increasing d can be expected, since the proportion of the beam detected by Layer2 decreases with increasing the polar extension of Layer2. Although inhomogeneous fields are expected to result in an intensity gradient across the direct beam with highest intensity differences on opposing sites of the direct beam edge, at high specimen thicknesses the highest intensity differences might also be observable at smaller polar collection angles than the direct beam edge. If those intensity differences are not measurable due to the inner polar collection angle of ring-shaped Layer2, the detected transferred momenta strongly differ from those determined with the CoM signal reducing the similarity of both.
When using only Layer1 for the determination of the DPC signal, an increase in similarity can be observed with increasing polar collection angles. This is due to the fact that Layer1 only extends to half the direct beam at d=1 and, thus, a large fraction of the beam intensity is ignored in the evaluation and only the inner part of the beam is exploited. With increasing the extension parameter d and thus the polar detector angles, the proportion of the direct beam on Layer1 and therefore the similarities of the IAMSR and CoM images increase.

Using the complete detector, i.e. a combination of Layer1 and Layer2, the overall similarity with the results of a pixelated detector is highest. This is presumably due to the increased polar momentum space resolution and the fact that the entire direct beam is evaluated. At detector extensions close to d =1, IAMSR images obtained with a combination of Layer1 and Layer2 are very similar to the ones obtained from only Layer2. In contrast to the beam extension dependency of Layer2 the similarity of the IAMSR images from Layer1 and Layer2 and the CoM remains almost constant with increasing d. More precisely, even local maxima can be observed. It can be assumed that the position of these maxima depends on the inhomogeneity of the beam intensity in the detection plane and will therefore be a function of the specimen thickness.

Table 4 depicts the detector extensions d and cross-correlation coefficient at which the maximum cross-correlation coefficient $c_{\mathrm{Cross,Max}}$ of the three different signals are observed. The overall maximum cross-correlation coefficients are always observed when Layer1 and Layer2 are used for evaluation and amount to 0.993 for the transferred momentum magnitude, 0.938 for the colour-coded DPC signal and 0.997 for the charge density. Thus, it is beneficial to always use Layer1 and Layer2, i.e. all detector segments, for the IAMSR method. In Chapter 6.1.4 it was shown that the maximum achievable cross-correlation of a DPC image without the IAMSR method with a CoM detected $|\vec{p}|$ map was only about 0.85 (using Layer2). With IAMSR method, the cross-correlation coefficients of the transferred momentum magnitude are much higher. For example, using Layer2 with a detector extension of d =1.1 would give a cross-correlation coefficient for transferred momentum magnitude of 0.983. Consequently, the obtained DPC images and related quantities are much more similar to the images obtained by the CoM of pixelated detector by applying the IAMSR method.

Table 4: Overall maximum cross-correlation coefficients $c_{\mathrm{Cross,Max}}$ of the transferred momentum magnitude, colour-coded DPC and charge density IAMSR maps calculated from a 4D-STEM image with the maps derived from the CoM of the same 4D-STEM image. For this, an IAMSR enhanced virtual detectors with Layer1, Layer2 and Layer1+Layer2 geometry are assumed.

$(c_{\mathrm{Cross,Max}}, d)$	Layer1	Layer2	Layer1+Layer2
Transferred momentum magnitude	(0.958, 2)	(0.983, 1.1)	(0.993, 1.4)
DPC signal	(0.771, 2)	(0.909, 1.1)	(0.938, 1.7)
Charge density	(0.983, 2)	(0.993, 1.1)	(0.997, 1.4)

Several of the DPC images extracted from the 4D-STEM data set of Si[110] assuming the IAMSR method are exemplarily given in Fig. 60 and Fig. 61. For comparison Figs. 60(a-c) also include the CoM derived DPC images of the same area. These images comprise the colour-coded DPC image, the transferred momentum magnitude, and the derived charge density map. All images have been calculated assuming a detector extension of d=1.2 and exploiting either Layer1, Layer2, or a combination of

Layer1 and Layer2. All images in Figs. 60(d, g, i) show similar colour wheel distributions and more importantly a high similarity to the CoM derived colour-coded DPC image. However, the colour-coded DPC image in Fig. 60(d) where only Layer1 is used shows a much higher overall colour saturation. This is in particular observable from the central Si dumbbell, which is marked in all images by a white circle. Regarding the DPC signal magnitude, this means that the DPC signal of individual dumbbells is more similar on Layer1 than on Layer2 or a combination of Layer1 and Layer2. This is presumably due to a higher similarity of the inner part of direct beam around all dumbbells. When Layer2 or a combination of Layer1 and Layer2 is used, the magnitude of the DPC image is different from dumbbell to dumbbell. However, the IAMSR images are more similar to the CoM signal. This cannot only be deduced from cross-correlation coefficients as a function of the detector extension in Fig. 59(b) but is correspondingly visible in Figs. 60(a, g, j). In all three images, the white encircled dumbbell shows a dimmer contrast than the dumbbell below (marked by a white dashed square). These contrast characteristics of the dumbbells are also apparent in the map of transferred momentum in Figs. 60(b, e, h, k) and particularly evident from the white encircled dumbbells.

It can be shown that the dumbbell extension is larger when Layer1 (Fig. 60(e)) instead of Layer2 (Fig. 60(h)) is used. Both, Layer1 and Layer2 in combination (Fig. 60(k)) give an intermediate dumbbell extension. The transferred momentum magnitude closely matches the one determined by the CoM signal (Fig. 60(b)) when a combination of Layer1 and Layer2 is used (Fig. 60(k)). If only Layer1 or Layer2 is utilised within the IAMSR method, the measured transferred momentum is lower (Fig. 60(e)) or higher (Fig. 60(h)) than the one determined by the CoM signal. This is due to the fact that the intensity differences on the Layer1 are possibly smaller than those on Layer2 since intensity differences are expected at the edges of the direct beam. DPC signals on Layer1 are typically smaller than on Layer2 even if Layer1 would measure an increased intensity difference because the geometrical centre of masses of Layer1 are closer to the optical axis than the ones of Layer2.

Figs. 60(c, f, i, l) show the calculated charge densities, derived from the transferred momentum magnitudes assuming a specimen thickness of (30±2) nm. No line-like features at interatomic pixels are observable in any of the charge density maps after applying the IAMSR method. This is highlighted by the black circles and is in contrast to the DPC images acquired with the segmented detector at one fixed detector rotation, e.g. shown in Fig. 53(d) and Figs. 56(i, j, l). No positive charge densities are observed at these regions, as it was the case if the DPC images were captured without the IAMSR method. The emergence of positive charge density at interatomic pixels was explained by the influence of the detector response function and especially the momentum space resolution of the detector (Chapter 5.1). This would possibly mean that the influence of the detector response function and the low momentum space resolution of segmented detectors can be drastically optimised by acquiring an image

series with different rotations of a segmented detector and by applying the IAMSR method. This is in good agreement to the findings of Li et al. [112].

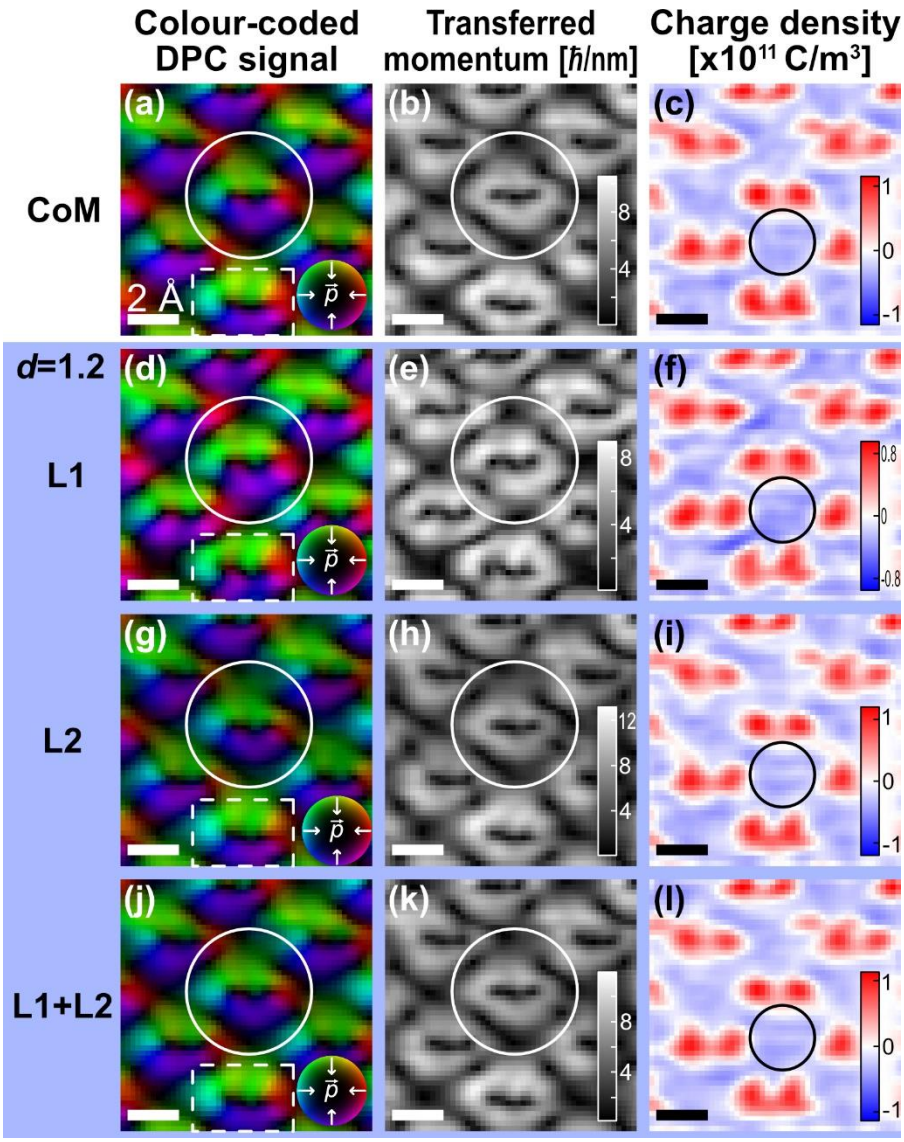

Figure 60: (a) Colour-coded DPC image, (b) transferred momentum magnitude and (c) charge density obtained from the CoM signal of a 4D-STEM image of Si[110]. The same quantities for a detector extension d = 1.2 and after applying the IAMSR method using (d-f) Layer1, (g-i) Layer2 and (j-l) a sum of Layer1 and Layer2. The images (j, k, l) have the highest similarity to the CoM signal as can be deduced from plots of cross-correlation coefficient as a function of the detector extension d (Fig. 59). All images are normalised to their respective maximum and minimum. Experimental details are listed in Table 51 in the Appendix.

For comparison with the results for d=1.2, Fig. 61 depicts colour-coded DPC images, the transferred momentum magnitude maps and the charge density distributions calculated with the IAMSR method for Layer1 (Figs. 61(a-c)), Layer2 (Figs. 61(d-f)) as well as the sum of Layer1 and Layer2 (Figs. 61(g-i)) for a detector extension $d = 1.8$. For this configuration, the direct beam of the CBED pattern barely hits Layer2 of the detector and mainly illuminates the inner Layer1. Comparing the images acquired only with Layer1 for the different detector extensions of d=1.2 in Fig. 60 and d=1.8 in Fig. 61, almost no qualitative changes are visible. However, when only using Layer2 for

the image calculation, the larger detector extension strongly alters the colour distribution around the dumbbells (highlighted by white circles in Fig. 61). Then, the colour-coded DPC map solely shows a strong green and blue colour. These colours can either be explained by a small specimen tilt, leading to increased intensities of diffraction discs on one side of the CBED pattern or by a slightly misaligned virtual detector. The colour-coded DPC images obtained using Layer1 (Fig. 61(a)) or Layer1+Layer2 (Fig. 61(g)) are in good agreement to the ones obtained from a detector extension of d=1.2 (Figs. 60(d, g, j)) as well as the CoM DPC image Fig. 60(a). This is due to the fact that in these cases the largest part of the CBED discs is exploited. Similar to the colour-coded DPC signal, the transferred momentum (Figs. 61(b, e, h)) is also affected by the detector extension leading to a strong change in measurable magnitude especially on Layer2 (Fig. 61(e)). Layer1 (Fig. 61(b)) and the sum of Layer1 and Layer2 (Fig. 61(h)) again are in a good qualitative agreement to their respective counterparts shown in Figs. 60(e, k).

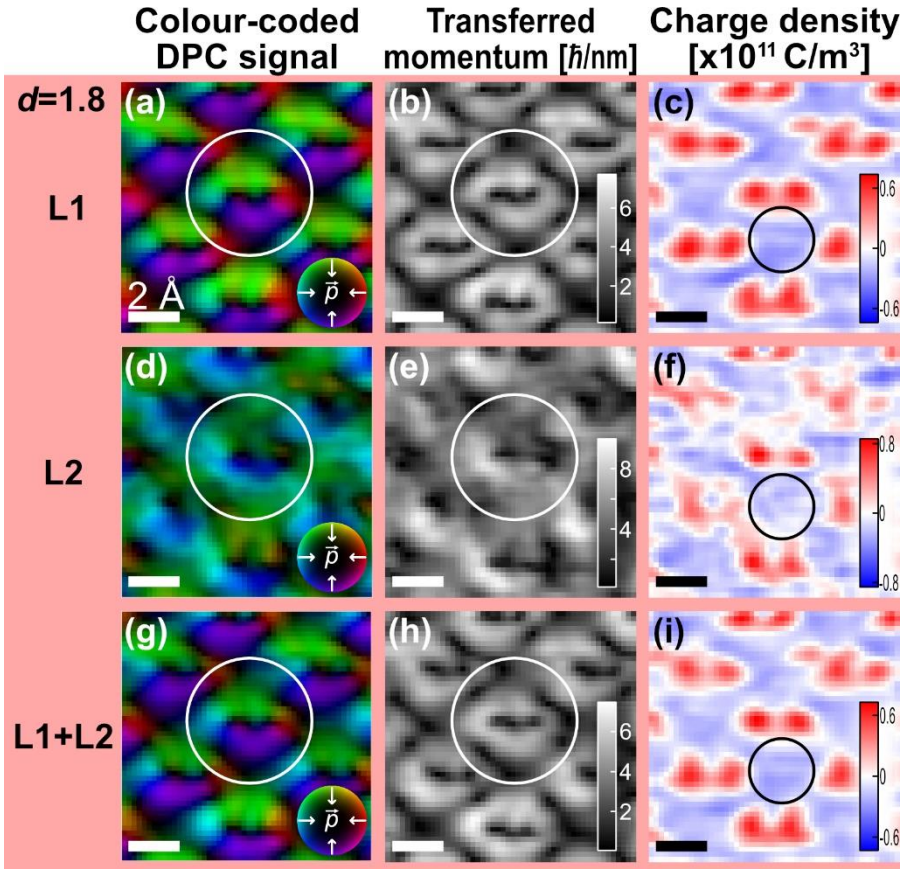

Figure 61: Colour-coded DPC image, transferred momentum magnitude and charge density after applying the IAMSR method on a 4D-STEM image using Layer1 (a-c), Layer2 (d-f) and a sum of Layer1 and Layer2 (g-i) with a detector extension d= 1.8. The images acquired with the sum of Layer1 and Layer2 (g, h, i) have the highest similarity with the CoM images (Fig. 60(a-c)). All images are normalised to their respective maximum and minimum. Experimental details are listed in Table 51 in the Appendix.

It is interesting that although almost no colour wheels and rotational electric fields around the atomic columns are visible if only Layer2 is used, the combination of Layer1 and Layer2 still features the expected electric field distribution and charge density. This supports the conclusion that it is beneficial to use a combination of Layer1 and Layer2

for the IAMSR method. This conclusion, however, requires further investigations, as only one 4D-STEM image of Si[110] and a fixed specimen thickness is considered.
It is important that both detector extensions (Fig. 60 and Fig. 61) do not result in positive charge densities at interatomic pixels. The IAMSR method is therefore a possible candidate to reduce artefacts in DPC images acquired with segmented detectors. It is interesting to further investigate the IAMSR method and more importantly to apply this method on a series of DPC images captured with a segmented detector considering different detector rotations. It needs to be emphasised that the IAMSR technique was only applied here for virtually projected detector segments on the CBED patterns of a 4D-STEM image. A crucial point for applying the IAMSR method on an image series captured with a segmented detector will be the alignment of images, which can certainly be achieved by the non-rigid registration and the alignment of the detector rotational axis with the centre of the CBED pattern. However, optimisation and quantitative characterisation of the alignment are tasks of future research.

6.2. Indium arsenide

Although most electronic devices are based on silicon, photon generation and detection in optoelectronic devices are mainly achieved with direct band gap materials [177] such as III-V semiconductors. Indium arsenide quantum dots (QDs) are one of the most promising nanostructures for future optoelectronic applications. Applications of InAs QDs include high-performance lasers and photodetectors [177] for infrared light as well as single photon emitters [178]. These applications are particularly made possible by indium arsenide's narrow and direct band gap of 0.36 – 0.40 eV [179, 180], high electron mobility and good alloying capability with other III-V semiconductors such as GaAs.
For advanced optoelectronic applications, the quality and uniformity of the QDs are crucial. Measures for the quality of QDs are the shape and the crystalline structure perfection. The latter includes the strain as well as the type and number of defects [181] present in an InAs QD. It is advantageous for QD-based devices that both strain and defects are avoided, reduced to a minimum or at least included in a controlled manner [180, 181] as they change the band structure and thus the optical properties. Defects also lead to new band gap states due to present dangling bonds [180]. Different crystal structure types (e.g. zinc blende and wurtzite) can lead to a band alignment at grain boundaries [182, 183]. To reduce the strain as well as the number of defects, InAs is often grown on lattice-matched substrates such as InP or GaSb [180]. However, the growth on lattice mismatched substrates such as Si or GaAs is of high interest and could lead to low-cost devices [177, 180]. Growth of InAs on lattice mismatched substrates typically introduces misfit defects at the InAs/substrate interface which alter the optoelectronic properties.
In this context, Riedl et al. investigate if the formation of misfit dislocations in InAs QDs can be avoided by using nanopatterned substrates allowing for strain partitioning [181].

The prepatterned substrates consist of GaAs pillars with a diameter of 25 nm and a height of approximately 70 nm. Pre-patterning was achieved by a combination of nanosphere lithography and reactive ion etching. InAs islands are subsequently grown on top of the GaAs pillars in [111] direction by molecular beam epitaxy [181, 184–186]. It is observed [181] that no misfit dislocation at the InAs/GaAs interface is observed for InAs QDs with a diameter below 7 nm.

One of the heteroepitaxial InAs nanoislands is displayed in $[110]$ zone-axis orientation in the HAADF images in Fig. 62(a) and Fig. 62(b). The specimen is prepared using a FIB and is covered with a protective carbon layer to reduce damage during the FIB milling process. In addition, the protective carbon layer also reduces the formation of native surface oxide layers. Nevertheless, a thin oxide layer is evident from a dim contrast and EDS line profiles (not shown here) around InAs island as well as the GaAs pillar in Fig. 62(a). The final thickness of the FIB lamella was measured with the EFTEM t/λ-method and amounts to t =(75.6 ± 11.6) nm. According to the STEM HAADF image in Fig. 62(a), the InAs island sits approximately in the middle of the GaAs pillar. However, the position in the projection is displaced from the centre of the pillar. This is evident from different defoci which are necessary to obtain atomic resolution in GaAs and InAs and particularly visible in Fig. 62(b), which shows an image of the InAs nanoisland at increased magnification. Such off-centre positions are energetically favourable for InAs QDs on GaAs(111)A nanopillars, as molecular static simulations have shown [186].

The InAs nanoisland has a lateral diameter of approximately 6.3 nm and it can be assumed that the extension of the nanoisland in direction of the optical axis is similar. Even though the QD is embedded in a thick amorphous carbon film, due to the small crystalline volume it can be expected that the QD shows little dynamic diffraction effects, making it well suited for a DPC analysis of atomic level electric fields.

Close to the GaAs pillar interface, InAs on the zinc-blende GaAs(111)A substrate has a zinc-blende structure (Fig. 62(c)), as it is obvious from the Z-contrast (Chapter 2.1.5) of arsenic (Z=33) and indium (Z=49) atoms. With increasing distance to the GaAs pillar interface, several twin boundaries occur, some of which are marked by dashed lines. At the top of the island, InAs is finally present in wurtzite (WZ) phase (Fig. 62(d)).

Due to different band structures of WZ and ZB InAs, a type II band alignment is expected for bulk material [182, 183] as well as nanowires [182, 187, 188]. Theoretical values for the band offset in bulk material range from 86 meV to 104 meV for the conduction band and 45 meV to 46 meV for the valence band [188, 189] (a sketch of the band diagram at a ZB-WZ InAs interface is depicted in Fig. 101 in the Appendix). The type II band alignment leads to a selective confinement of holes in the WZ region and electrons in the ZB region different. Thus, electric fields with field vectors from the WZ to the ZB region are expected. However, as nanoislands or QDs are small in three dimensions, a change in electronic band structure has to be expected due to confinement effects, ultimately influencing the band alignment and resulting charge separation.

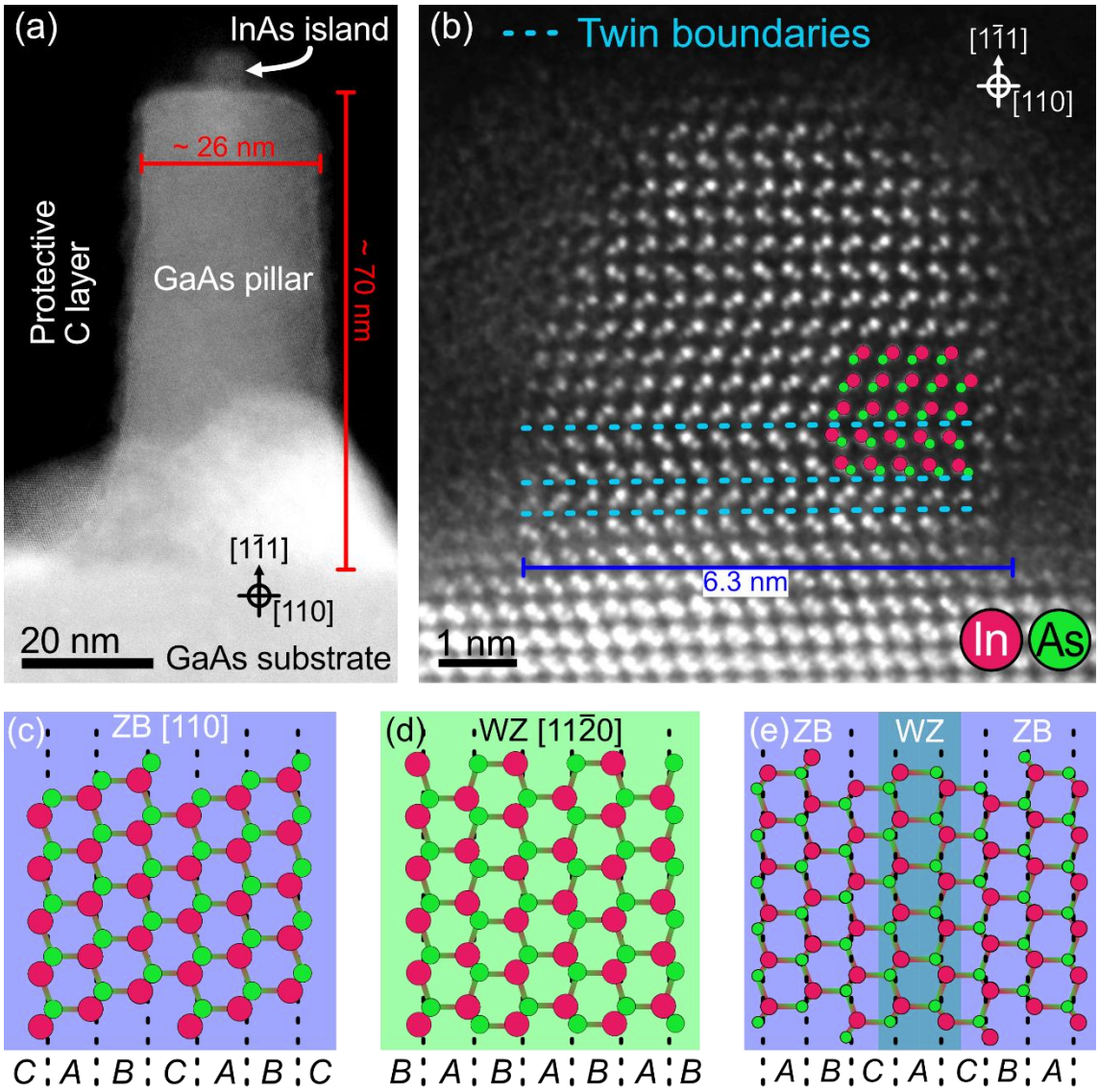

Figure 62: (a) STEM HAADF image of an InAs nanoisland on top of a GaAs pillar both in [110] zone-axis orientation. The specimen structure is protected by a carbon layer, which was deposited prior to FIB lamella preparation. (b) STEM HAADF image of the InAs nanoisland. Atomic species of atomic columns are indicated by red and green dots. The dots shown were determined using the atomic column fitting method described in Chapter 4.5. Sketches of the (c) zinc blende (ZB) and (d) wurtzite (WZ) InAs crystal structures. (e) Sketch of the ZB atomic lattice containing a rotational Σ3(111) twin boundary. All sketches in (c-e) are shown in [110] zone-axis orientation. Imaging conditions are listed in Table 52 in the Appendix.

Furthermore, due to the lower symmetry of the InAs WZ phase and the resulting separation of positive and negative charge centres in strained WZ InAs, also polarization fields are expected at the WZ-ZB interface. This straining arises from the slightly different lattice constants of WZ and ZB and is expected to be present in <111> direction. It introduces a separation of charges with a polarization charge density in the range of (10^{-3}-10^{-2}) C/m^2 [187, 190], which was measured by electron holography in reference [189]. This would lead to a measurable charge density in the range of (10^{6}-10^{7}) C/m^3. In the following, the same InAs island, which as used in [181], is analysed in [110] zone axis orientation with the help of DPC. This allows to investigate the atomic electric fields in ZB InAs as well as electric fields due to band alignment and polarization effects at ZB/WZ interfaces.

6.2.1. Atomic electric fields in zinc blende InAs

Fig. 63(a) shows a DPC image of the electric field distribution of InAs island on top of a GaAs pillar from Fig. 62(b). The investigation was done at an acceleration voltage of 200 kV, a convergence semi-angle of 25 mrad using a 40 µm aperture and using only the outer layer for image acquisition. At a camera length of 12 cm, the detector segments of Layer2 intersect the electron beam intensity distribution at polar angles from 18 mrad to 35.6 mrad. The calibration process for these illumination and detection settings is described in 3.1. It is to note that the DPC image in Fig. 63(a) was acquired with a different defocus than the image in Fig. 62(b), as the optimum defocus for HAADF and DPC images are different [91, 148]. For the DPC image shown in Fig. 63(a) a defocus guaranteeing the maximum possible DPC signal is chosen.

As the InAs island is encapsulated in an amorphous protective carbon film, the superposition of an electric field background can be expected. Although the influence of amorphous material in under- and overfocus conditions is not investigated sufficiently, in the following it is assumed for simplicity that the influence of the amorphous layer is like noise on the DPC image but with a broader spatial frequency than typical image noise. Similar to the reduction of image noise, it is possible to reduce the influence of amorphous layer by using a Gaussian denoising technique as described in Chapter 4.4.1. However, as the spatial frequency of features in the DPC image arising from the atomic electric fields is in the same range as the fluctuation induced by the amorphous layer, reducing the influence of the amorphous layer is only possible to a certain extent by Gaussian denoising. This is due to the fact that the Gaussian functions necessary for a strong reduction extend over the typical distance of atoms in InAs leading to a smearing of features as well as an averaging of DPC signal. Here, the image noise as well as the randomly distributed transferred momenta due to amorphous layers are only slightly removed using a Gaussian function with a standard deviation of 3 pixels (equal to 0.48 pm). Other techniques such as a Fourier filtering or rigid and non-rigid registration are not practicable. Fourier filtering would drastically alter the features of the InAs electric field distribution, as the features of the InAs island and amorphous layer are in the same range of spatial frequency. Taking an image series plus aligning the images by rigid or non-rigid image registration techniques cannot remove the influence of the amorphous layer because the amorphous layer is static without the build-up of further contamination and constant for subsequent scans.

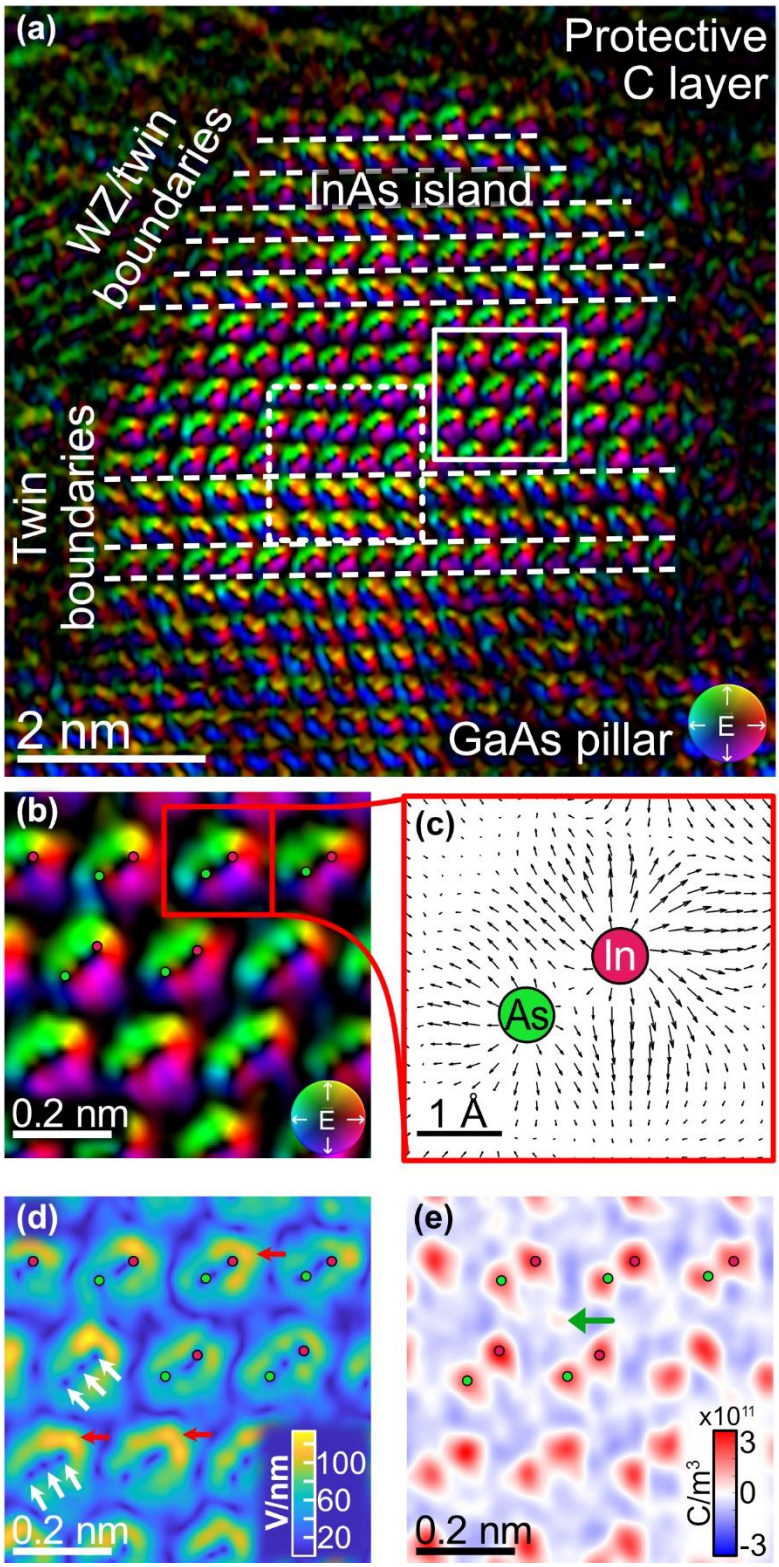

Figure 63: (a) DPC image of a twin boundary-containing 6.3 nm wide InAs island on top of a GaAs pillar which is encapsulated in a 70 nm thick protective carbon layer for FIB lamella preparation. The colour distribution depicts the measured electric field distribution as indicated by the colour wheel in the lower right corner of the image. The white box indicates the area used for the images in (b, d, e). Additionally, a white dashed box in (a) indicates the area of the DPC image used for the investigations shown in Fig. 64. White dashed lines reveal the position of rotational twin boundaries. (b) DPC image of the electric field distribution in the ZB phase of the InAs island (white box). (c) Vector plot of the electric field distribution around an exemplary pair of In and As atomic columns. (d) Measured electric field magnitude and (e) respective charge density. The atomic column positions in (b-e) are calculated using the HAADF intensity-based fitting algorithm described in Chapter 4.5 and marked in all images by red and green dots. A list of imaging parameters is compiled in Table 53 in the Appendix.

In Fig. 63(a) the rotational electric fields around each atomic column in the InAs island are visible. They are particularly obvious in the magnified view of a ZB area in Fig. 63(b) and the electric field vector map of a InAs dumbbell in Fig. 63(c). The atomic column positions of In and As atomic columns in Fig. 63(b) are determined with the HAADF intensity-based fitting algorithm described in Chapter 4.5 and represented by red and green dots. In Fig. 63(b) the DPC signals around the atomic columns are not uniform for all dumbbells. This is, besides the changes in local thickness arising from the dot-like shape of the InAs island, particularly due to the amorphous layer above and below the nanoisland. The influence of the amorphous layer is visible at interatomic pixels and can be detected by the different extensions of the green areas. The influence of the amorphous layer can also be seen in the electric field vector map in Fig. 63(c), which is dominated by the diverging fields around the In and As atomic columns. There, at interatomic pixels, small fluctuations of the measured electric field direction are evident. In addition, these fluctuations might also arise due to noise and applied Gaussian denoising method. Nonetheless, as the DPC signal in Fig. 63(b) and Fig. 63(c) is dominated by the atomic electric fields, they are investigated in the following in more detail.

The measurable electric field in Fig. 63(c) shows an increased magnitude around the In atoms, a reduced strength (Fig. 63(d)) on the connecting axis between In and As atomic columns, and no electric field at the positions of the atomic columns as it was the case for silicon (Chapter 6.1). The change in electric field magnitude of In and As can be ascribed to the difference in atomic number. The In atomic column comprising the atoms with the larger atomic number generates increased measurable field magnitudes. The difference in atomic number is also responsible for the dominance of In in the region of overlapping potentials, which is visible by the fact that the field vectors which are close to the As atomic column away still point away from the In atomic column. In addition, along the connection axis between two atomic columns or at highly symmetric points of the crystal lattice no electric field is measurable, since opposing electric fields cancel each other out. Both the reduced electric field at atomic column positions and at the high symmetry points, which can be found at the connecting axis of In and As atoms, are exemplarily marked by white arrows in Fig. 63(d).

Moreover, the measured electric field distribution shows a crescent-like feature with increased magnitude around the In atomic column. This is evident in Fig. 63(d) and is exemplarily pointed at by the red arrows. A possible explanation for the crescent-like features is bonding. However, this needs further investigations such as DFT simulations. Another possible explanation is some tilt of the specimen, which leads to an increased overlap of potentials in the In-As region, while the In-vacuum region is less affected by overlapping potentials.

The corresponding charge density depicted in Fig. 63(e) shows positively charged areas at atomic column positions. The average charge density of the local maxima at In atomic columns amounts to $(2.8 \pm 0.3) \cdot 10^{11}$ C/m^3. In case of As atomic columns

$(2.2 \pm 0.3) \cdot 10^{11}$ C/m^3 is measured. The values are averaged over all atomic columns shown in Fig. 63(e). The precision is given by the standard deviation. The In atomic columns exhibit a (1.3 ± 0.2) times higher positive charge density than the As atoms, which is qualitatively expected, since In has a higher atomic number than As, however, one might expect a ratio of 49/33=1.48. Possible explanations for the difference between measured and expected charge density ratios include the screening of atomic potentials, residual lens aberrations, image noise, and the redistribution of intensity along the atomic columns due to a coherent scattering effect, which is different for the In and As atomic columns. Note that all above-mentioned effects only influence the measured values. Another approach to calculate the charge density ratios of In and As atomic columns which is based on the position of local minima is investigated in Chapter A.2.9.

The HAADF intensities (not shown here) of the atomic columns of the same area as in Fig. 63(e) amount to $I_{\mathrm{HAADF,In}} = (2.03 \pm 0.05)$ for In and $I_{\mathrm{HAADF,As}} = (1.81 \pm 0.03)$ for As columns in arbitrary units. It is interesting that the relative accuracy of the HAADF intensities (~2 %) is much better than the one for the charge densities (~10 - 14 %). A possible explanation is the influence of the amorphous layer, which might be stronger on the DPC signal than on the HAADF signal. The impact of the amorphous layer on ADF image intensities has been investigated in detail [175, 191] finding that the magnitude of the influence of the amorphous layer for ADF imaging depends on several parameters: 1) The atomic species of the atomic column which is surrounded by the amorphous layers, 2) the defocus, 3) the thickness, and 4) more importantly if it sits in front of or behind the structure of interest. An amorphous layer in front of the crystalline material in beam direction significantly reduces the measurable contrast and resolution in ADF-STEM imaging. An amorphous layer additionally adds a base-signal to the overall HAADF signal with a small spatial modulation due to the irregularly ordered scattering centres within the amorphous film [175]. As DPC mainly exploits the direct beam, its signal strongly depends on coherent scattering. Coherent scattering might be more strongly affected by the irregular ordering of scattering centres than the incoherent scattering in ADF imaging. The effect of amorphous layers on DPC imaging is therefore an interesting subject for future research. In addition, its influence on the HAADF and DPC images of the InAs island can only be qualitatively assessed, as the position of the InAs island in the protective carbon layer was not investigated: The amorphous carbon film introduces a broadening of the electron beam and an intensity redistribution and acts differently on DPC signal and HAADF intensity.

To estimate the contrast of the In and As atomic columns, the contrasts of individual atomic columns are compared. Since brightness and contrast are freely adjustable during HAADF imaging and the measurement of the exact number of scattered electrons is a tedious process requiring a Faraday cup [160], these values can only be regarded as an approximation for the contrast. In the following, the contrast of an atomic column is calculated by determining the intensity at the atomic column positions and subtracting the minimum value of the HAADF image I_{min} to account for the manual

brightness setting. The contrast of two atomic columns is then given by $(I_{In} - I_{min})/(I_{\mathrm{As}} - I_{\mathrm{min}})$ which amounts to 1.66 for the In and As atomic columns in Figs. 63(b, d, e). Neglecting the influence of the amorphous layer as well as the contrast and brightness settings of the microscope, this would lead to a $Z^{(x\approx 1.28)}$ contrast dependency with $x\approx$1.28 estimated by $(49/33)^x$ = 1.66.

Calculating the Z dependency of the charge density image in an analogous way results in an exponent x of about 0.6. This is lower than the theoretical linear Z dependency of DPC images. The lower exponent is assumed to be due to the amorphous layer at the top and bottom of the film, as well as the defocus, which leads to varying electric fields around atomic columns of heavier and lighter atomic species (Chapter 5.2).

In Fig. 63(e), negatively charged areas around the atomic columns are evident. However, as the amorphous layer at the top and bottom of the InAs nanoisland influences the signal at interatomic pixels and modulates the DPC signal solely arising from the interaction of the electron beam with the InAs island, local changes in the negative part of the charge density are not expected to only arise from atomic bonding effects. In addition, the amorphous layer at the top and bottom of the nanoisland is a possible explanation for positively charged regions at interatomic pixels, which are marked by a green arrow in Fig. 63(e). Therefore, it is necessary to investigate the influence of the amorphous layer on the DPC signal, also considering different atomic species, defoci and thicknesses of amorphous layers as it has been done for ADF-STEM in [175].

In addition to the atomic electric fields in InAs, periodic electric fields are also observable in the GaAs pillar in Fig. 63(a). These electric field distributions do not exhibit rotational symmetric field vectors around each individual atomic column position. This is due to the fact that the extension of the GaAs pillar in beam direction is much larger than the extension of the InAs island and that the InAs island has an off-centre position. At such thicknesses the measurable electric field distribution is expected to be strongly affected by influences such as specimen tilt and dynamic diffraction. Both in combination may be a possible explanation for the dominant blue, yellow and red colours in the electric field map of the GaAs substrate.

6.2.2. Electric field distribution at an InAs twin boundary

The InAs nanoisland contains several rotational twin boundaries which are visible in Fig. 63(a) (marked with white dashed lines). As the crystal structure in the vicinity of the twin boundaries is similar to a WZ InAs lattice and the InAs island otherwise has a ZB InAs lattice, a type II band alignment can be expected. A type II band alignment has been experimentally observed in WZ-ZB InAs nanowires with a diameter of several tens of nanometres [192]. However, with decreasing diameter there is a critical diameter of nanowires, as the band gap changes due to quantum confinement effects. According to tight binding simulations by Akiyama et al., the valence band maximum offset at ZB/WZ interfaces in nanowires approaches the offset of the bulk material if the

diameter of the nanowire is above approximately 6.5 nm [183]. Thus, also a critical diameter for nanoislands can be expected.

To investigate the electronic structure of small WZ phase inclusions in ZB InAs, the electric field and charge density across a twin boundary (indicated by the white dashed line) are shown in Fig. 64. The analysed area is depicted in Fig. 63(a) by the dashed white box.

Fig. 64(a) displays the electric field magnitude in the defect region. It is interesting to note that the InAs dumbbells show completely different electric field distributions. While the electric field distributions of individual dumbbells above the twin boundary (in $[1\bar{1}1]$ direction) exhibit a crescent like structure around the In atom, the dumbbells below show a one-sided increased electric field magnitude, which spans from In to As atomic columns.

As the type II band alignment should lead to a separation of charges perpendicular to the twin boundary, the electric field magnitude in y-direction is shown in Fig. 64(b), which comes close to the electric field distribution in $[\bar{1}1\bar{1}]$ direction. Here also a difference between the electric field of the dumbbells above and below is evident from the difference in electric field in y-direction. This difference is particularly visible in the negative part of the electric field in y-direction and exemplarily marked by two white boxes. A possible explanation is the presence of specimen tilt, which introduces a certain directionality to the features.

Fig. 64(c) shows the experimentally derived charge density. Here the In atoms, which always are the first in $[\bar{1}1\bar{1}]$ direction, possess the higher positive charge density. However, at the twin boundary, this is no longer true, as some of the upper atoms show a decreased positive charge density. One could expect that the decreased positive charge density is due to a lower number of atoms in the atomic columns. However, this is not the case, as can be seen from the HAADF image in Fig. 64(d). Examples for this behaviour are highlighted by the black (Fig. 64(c)) and white arrows (Fig. 64(d)). While the atomic columns marked by the left arrows exhibits a lower positive charge density than the right one, it simultaneously generates more HAADF intensity. It is possible that the separated charges lead to a screening of the atomic columns and thus to a different ratio of the positive charge densities of In and As atomic columns. However, this needs further investigations and in particular a removal of the influence of the amorphous layer on top and below the InAs nanoisland.

To investigate the changes arising from the twin boundary further, Fig. 64(d) depicts integrated line profiles in $[\bar{1}1\bar{1}]$ direction of the overall electric field magnitude, the electric field magnitude in y-direction and the charge density. The line profile direction as well as the region, from which the line profiles are obtained, are depicted in the respective images in Figs. 64(a-c). It can be seen here that there is no clear change in the electric field distribution across the twin boundary. This is evident from the line profile of the overall electric field magnitude as well as the electric field magnitude in y-direction of the image. Both electric field components do not show any strong influence of the twin boundary. An electric field vector map of a small area at the twin boundary

showing no characteristic field is additionally displayed in Fig. 103(b) in the Appendix. Thus, changes in the electric field distribution due to charge separation by a band alignment are not detected in case of this nanometre sized island.

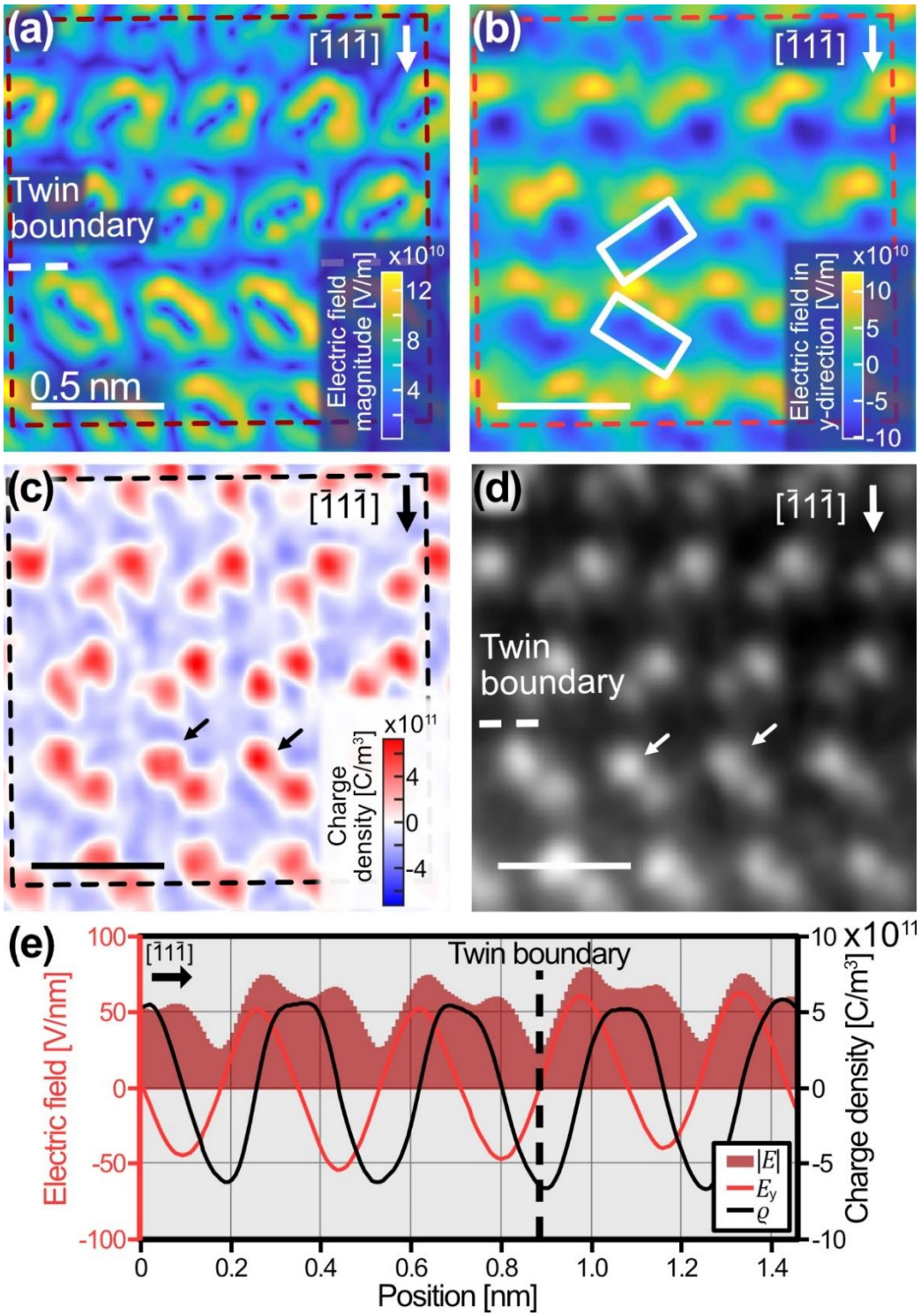

Figure 64: (a) Measured overall electric field magnitude of the twin boundary containing area indicated by the white dashed rectangle in Fig. 63. The twin boundary is indicated by a white dashed line. (b) Electric field magnitude in y-direction (vertical image direction). (c) Respective charge density. (d) Line profiles of the overall electric field magnitude and electric field magnitude in y-direction as well as the charge density. The line profile are obtained from the dashed boxes marked in (a-c) and are calculated by an integration of pixels perpendicular to the [$\bar{1}1\bar{1}$] direction. The direction of line profiles is indicated by the arrows. In (d) the position of the twin boundary is depicted by a dashed line. A list of imaging parameters is compiled in Table 53 in the Appendix.

The absence of electric fields could be advantageous for certain optical applications, as the recombination of charge carriers is not influenced by electric fields. In addition, it is in good agreement to the findings by Akiyama [183], who state that the charge separation due to band alignment might vanish for very small nanometre sized twin boundaries. However, the changes in electric field distribution due to the separation of charges induced by the band alignment or polarisation charge might be too low to be measured by DPC in high-resolution mode of a STEM [37]. This is due to the fact that typically very small camera lengths are used resulting in limited sensitivities of DPC imaging. A possible route to increase the field sensitivity is the use of the low magnification (LowMag) mode which uses very small convergence angles and large camera lengths. However, as the resolution of the LowMag mode is typically in the single digit nanometre regime, investigations of twin boundaries in nanoislands which consist of several twin boundaries would not be possible with sufficient spatial resolution. And again, the influence of the amorphous layer at the top and bottom of the InAs nanoisland needs to be removed or reduced to a minimum, to see differences in field distribution due to charge redistribution effects.

6.3. Two-dimensional tungsten diselenide

One of the most promising material systems for atomically thin and also flexible optics and electronics at present are mono-, bi- and multilayers of transition metal dichalcogenides (TMDs) [193–195]. The material class of TMDs includes MoS_2, $MoSe_2$, WS_2 and WSe_2, whose monolayers each consist of a layer of hexagonally arranged metal atoms sandwiched between two layers of hexagonally arranged chalcogen atoms typically in a trigonal prismatic coordination [194–196]. The layers in TMD bulk materials and multilayers of TMDs are bonded via van-der-Waals interaction [197, 198]. TMDs offer exciting optoelectronic properties [199–202]. For example, TMDs are semiconductors with a direct or indirect bandgap depending on the number of layers. Monolayers of WSe_2 have a direct bandgap of 1.6 – 1.66 eV [194, 203]. With further increasing the number of layers, the band gap energy is narrowed and approaches that of bulk WSe_2 with an indirect band gap of 1.35 eV [204]. In addition, strong many-body Coulomb interactions are found in WSe_2 [200], e.g. leading to stable excitons [199, 205, 206].

Moreover, lateral WSe_2 homojunctions of flakes with different number of layers are of interest, as a type I band alignment is expected due to the different band structures of WSe_2 with different number of layers [207]. The largest difference in band structure is observed for a WSe_2 homointerface between a monolayer and a bilayer, and transfer of electrons and holes into the bilayer is expected due to the type I band alignment. As the band offset of conduction band minimum is larger than the one for the valence band, it is more efficient to transfer electrons from monolayer to bilayer than holes [207]. Thus, an electric field at the homointerface is expected.

TMDs' exciting electrical properties make them an ideal material to used them in novel transistor approaches. For example, Zhang et al. fabricated a back-gate field effect

transistors consisting of nanosheets of WSe_2 and Platinum electrodes on a Si/SiO_2 substrate with high on/off current ratios as well as high charge mobilities [193]. Due to the broken centrosymmetry their crystalline structure, TMDs are piezoelectric materials when they are present in two or more layers [193]. Tensile stress in the material therefore might introduce macroscopic electric fields due to the piezoelectric displacement of the positive and negative charge distribution centres of mass. Tensile stress also changes the optoelectronic properties. This can e.g. change the indirect bandgap of TMD multilayers to a direct bandgap [208]. Thus, strain patterning of 2D TMDs has drawn a lot of interests recently.

Apart from the promising optoelectronic properties, 2D TMDs are also of interest for DPC measurements due to the atomically thin specimen thickness. Monolayers and multilayers of TMDs can be produced in a comparatively simple and reliable way, even without an amorphous surface layer since no ion beam treatment is required in specimen preparation. Therefore, monolayers of TMDs are an ideal material system for performing DPC measurements without the dynamic diffraction effects described in Chapter 5. Measurements of electrostatic properties have already been conducted by DPC or other phase related techniques for 2D materials such as graphene [209], hexagonal boron nitride (h-BN) [32], MoS_2 [31, 33–35, 210] and WS_2 [210, 211].

The crystal structure and possible stacking of multilayers are illustrated in Fig. 65. Fig. 65(a) shows a top view of a monolayer of WSe_2 with lattice constant a=3.28 Å. The straight black lines mark the boundaries of unit cells. In each layer the tungsten atoms are present in a trigonal prismatic coordination [194, 196] and bond to six surrounding selenium atoms in an ionic-covalent character [198, 212]. Since the layers are bonded to other layers only via van der Waals forces, sliding of adjacent layers is possible. Different stacking configurations or polytypes have been proposed in literature, five of which have high symmetry stacking orders. They are depicted in Fig. 65(b) using side and top view models of the crystal structure. Here, the nomenclature of He et al. [213] is adopted. The AA' (polytype: 2H; space group $P6_3/mmc$) stacking in which the two layers are stacked with W sitting over Se and Se over W is the energetically most favourable. The other stackings are denoted as follows: AA with W over W and Se over Se, A'B displaced and rotated (rotation about c-axis) with Se over Se, AB' displaced and rotated with W over W and AB (polytype: 3R; space group R3*m*) displaced and rotated with W over W. The latter is almost degenerate in energy with the AA' stacking [213]. The lattice parameter c amounts to $c = 12.96$ Å [214] for the dominant AA' stacking and deviates in range of 0.5 Å depending on the stacking [213]. The minimum interlayer distance between the selenium atoms in the direction perpendicular to the basal plane also varies depending on the stacking. For example, Se atoms have a distance of 3.152 Å in AA' and a distance of 3.165 Å in AB [215]. For different stackings, differences of the band structure [213] along with difference in the optical properties [215, 216] are observed.

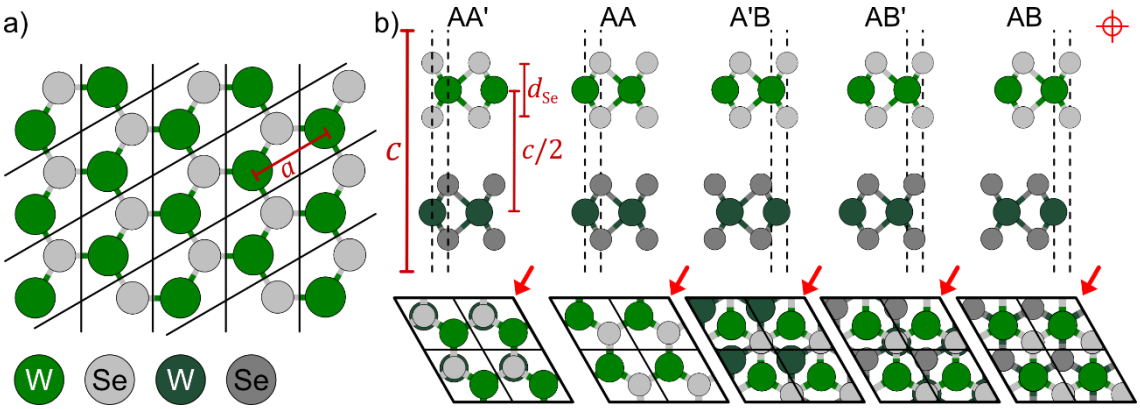

Figure 65: (a) Top-view of a monolayer of WSe_2. It is to note that for each Se position marked in this model, two Se atoms are present in projection. Black lines demark the boundaries of unit cells. (b) Side-views of the five high-symmetry stackings AA', AA, A'B, AB' and AB (upper row) and basal plane projections (lower row) of WSe_2 bilayers. For explanations on the stackings and on the parameters a, c and d_{Se} the reader is referred to the main body of the text (adapted from ref. [213]). The red arrows in the lower row of atomic structure models indicate the viewing direction (indicated by a crosshair in the upper right corner) of the upper row of structure models.

In the following, DPC analyses are carried out on bi- and trilayers of 2D-WSe_2. The focus of this study is on measuring the electric field and charge density distribution for different numbers of molecular layers. In addition, the electric field in the vicinity of defects is investigated. This chapter is structured as follows. Chapter 6.3.1 describes the preparation of the WSe_2 specimen. Chapter 6.3.2 shows DPC measurements of WSe_2 bi- and trilayers. This is followed by a determination of the stacking sequence of the WSe_2 multilayers in Chapter 6.3.3. The determination of stacking sequence is achieved by comparing the measurements to analogous simulations of AA, AA', AAA, and AA'A stacked WSe_2 multilayers. Finally, the changes of electric field which are introduced by vacancy-type defects in a WSe_2 bilayer are revealed in Chapter 6.3.4 by subtracting the electric field distribution of a pristine lattice.

6.3.1. Preparation of WSe_2 for (S)TEM investigation

For the preparation of TMD monolayers or multilayers, exfoliation techniques from bulk material [195] such as the scotch tape method to peel off a monolayer [193, 217] or mechanical cleavage similar to graphene [218, 219] are used. However, due to the limited controllability of size and number of layers when using exfoliation techniques, large-area TMD materials are challenging to produce [193]. Other preparation methods include atomic layer deposition [220] and molecular beam epitaxy (MBE) [221]. Another method to produce TMD monolayers is a chemical vapor deposition (CVD) [194, 203, 222, 223] using solid precursors [193, 202] and thermally robust substrates such as SiO_2 [222] and Al_2O_3 [202, 223]. This gives TMD layers with a controllable number of layers as well as a larger area and better crystal quality [193] than using a preparation based on the exfoliation of a few layers from bulk TMD materials [193]. Furthermore, CVD processes allow to create lateral homojunctions, i.e. the transition from a monolayer to a bi- or multilayer [207], and heterostructures of WSe_2 and another TMD such as $MoSe_2$ [222].

Two approaches for the transfer of TMD flakes are described in literature, namely a wet chemical transfer using poly(methyl methacrylate) (PMMA) [201] and a dry transfer with polydimethylsiloxane (PDMS) [202, 207]. In the following, only the dry transfer is considered since it allows for a reduced contamination build-up during STEM analysis as it does not include the dissolution of any component during the preparation. However, in comparison to the PMMA-based transfers, WSe_2 flakes prepared by a PDMS transfer might be subjected to increased mechanical strain as the elastomer is typically pressed onto the substrate.

Fig. 66 shows the used specimen preparation route based on the dry transfer of WSe_2 flakes onto *Pelco*® silicon nitride support grids (TED PELLA Inc., CA, USA). Monocrystals of WSe_2 are purchased from *2Dsemiconductors* (2Dsemiconductors Inc., AZ, USA). Monolayers are obtained using mechanical exfoliation by the scotch tape technique. For the mechanical exfoliation, a single crystal of WSe_2 (thick flake with a lateral diameter in range of 0.3 cm to 0.5 cm) is placed onto a scotch tape. The latter is fixed onto a flat surface. Using a *Nitto SPV-224 PR-MJ* tape, several WSe_2 flakes are exfoliated, as illustrated in Fig. 66(a). Especially the fixation of the scotch tape to a flat surface and a careful prevention of air bubbles between the *Nitto* and the scotch tape promotes a successful exfoliation of WSe_2 flakes. By releasing the *Nitto* tape in a small angle γ, the probability to obtain a high yield of WSe_2 monolayers is increased [224]. The WSe_2 flakes on the *Nitto* tape can then be analysed directly with the aid of a light microscope due to the transparency of the *Nitto* tape in the optical range of the spectrum. The colour of the WSe_2 flakes (not shown here) can be used as a rough indication of the layer thickness. Too thick flakes can be thinned out with a further peeling process using a *Nitto* tape.

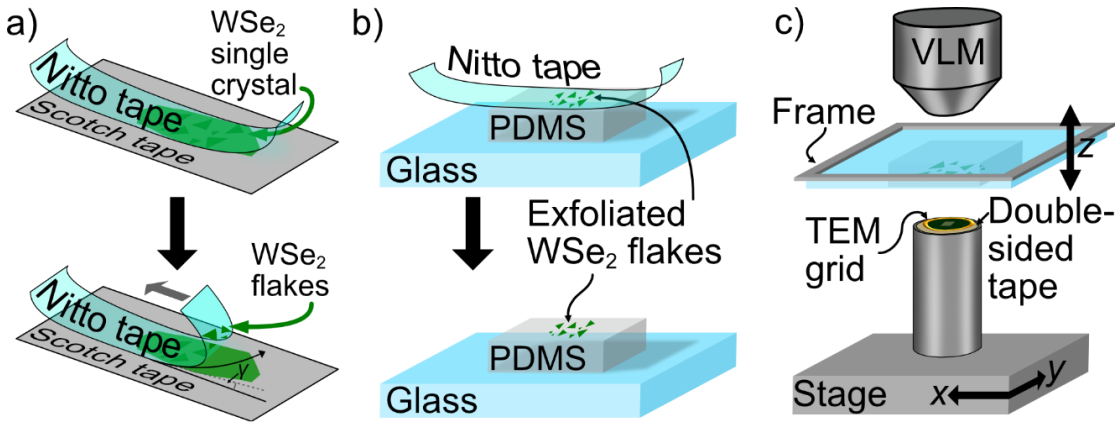

Figure 66: General procedure for the preparation of WSe_2 TEM specimen. (a) Exfoliation of WSe_2 flakes using a WSe_2 bulk crystal attached to a scotch tape and a *Nitto* tape for peel-off. Here, γ denotes the peel-off angle. (b) Transfer of WSe_2 flakes, which are attached to the *Nitto* tape, onto a PDMS stamp. (c) Preparation of TEM specimen by pressing the PDMS stamp supported by a glass slide mounted to a frame onto a SiN_x TEM window grid using a self-made drivable stage and a visual light microscope (VLM) for precise control of movement. The TEM grids are attached to the stage using a double-sided tape.

During the next step depicted in Fig. 66(b), the WSe_2 flakes attached to the *Nitto* tape are transferred onto a PDMS stamp (*Sylgard 184* is used as a PDMS) on top of a cleaned glass slide. The PDMS stamp is obtained by curing PDMS at 130 °C on top of

a GaAs wafer which serves to provide a smooth surface. After curing, a stamp with a size of 1 cm by 1 cm is cut out and gently released from the GaAs using tweezers. The PDMS stamp is placed on a glass slide with the surface that was previously in contact with GaAs now facing upwards. This surface exhibits a lower roughness than the surface, which was previously in contact to air, and, thus, promotes a reduced deformation and crack formation during the transfer process. The *Nitto* tape containing the WSe_2 flakes is pressed by hand on the PDMS stamp and a heat treatment at 60 °C in air is performed to promote adhesion between PDMS and WSe_2. Again, it is necessary to prevent air pockets between the *Nitto* tape and the PDMS. Afterwards, the *Nitto* tape is released at a small angle leaving several WSe_2 flakes on top of the PDMS stamp.

The general procedure and setup for transferring the WSe_2 flakes from the PDMS to the TEM grid is depicted in Fig. 66(c). The set up includes a visual light microscope (VLM) from *Keyence Deutschland GmbH*, a frame which is used to fix the glass slide and is movable in z-direction, as well as a stage to which a TEM grid is attached to. The latter is movable in x- and y-direction. Before attaching the silicon nitride TEM grid to the stage, the TEM grid is cleaned using a sequence of wet chemical cleaning in acetone, isopropyl alcohol, and deionized water each for 5 min. After an additional cleaning in an oxygen-based plasma for 5 min at a flow rate of 10 sccm using a Tergeo EM plasma cleaner (*PIE Scientific LLC*), the silicon nitride grid is attached to the stage via a double-sided tape as can be seen in Fig. 66(c). This prevents a gliding of the TEM grids and a sticking to the PDMS during the transfer. The glass slide with the PDMS stamp is mounted to the frame. By moving the PDMS stamp in contact to the TEM grid and releasing it with a slow speed of approximately 0.5 µm/s, WSe_2 flakes are transferred to the TEM grid due to the viscoelastic properties of the PDMS. The VLM is used to select and transfer a specific flake with a promising thickness, as both the PDMS and the glass slide are transparent, and the stage and frame allow for precise lateral positioning. In addition, the VLM can be used to directly check the success of the transfer before inserting the TEM grid into the TEM. However, the characterisation of transferred flakes by means of VLM does not allow for an accurate quantification of the number of TMD layers.

There are several methods which allow the determination of specimen thickness in the TEM and are already applied on 2D materials [225]. One of these methods is the EELS and EFTEM log-ratio method [73, 226]. Other methods exploit intensity variations in selected area electron diffraction (SAED) pattern upon specimen tilting, the CBED zero-disc fringes, the EDS signal, nano beam electron diffraction [227] or relative STEM-ADF intensities of chalcogen and metal atomic columns arising due to the Z-contrast, supplemented by corresponding image simulations. However, the suitability of these techniques is still under debate [225]. Most TEM studies of TMD materials are therefore typically accompanied by other measurement techniques such as AFM, photoluminescence (PL) and Raman measurements of the same flake [225]. However, the precise thickness measurement, e.g. by AFM imposes several challenges, since

the flakes need to be transferred to a planar substrate for thickness characterisation and subsequently to a TEM grid without any damages and further thinning.
In this thesis, the number of layers is determined using PL and the local specimen thickness measured using EFTEM and EELS utilizing the log-ratio method despite the possible inaccuracy. An electron mean free path of 33.4 nm was calculated using the model of Malis et al. [84] for an electron energy of 80 kV and a take-off angle of 157 mrad given by the entrance aperture of the GIF. Two WSe_2 flakes are investigated in the following, one of which consists of two layers and the other of three layers. The thicknesses amount to t=(1.31 ± 0.07) nm for the bilayer and t=(2.39 ± 0.01) nm for the trilayer, respectively. They differ from the theoretical thicknesses of 1.3 nm and 2.6 nm, respectively. This is due to the fact that both values are average thicknesses across the analysed area of the EFTEM and STEM-EELS maps, which might be subject to specimen contamination and thickness modulations due to point defects (as seen later).

6.3.2. Electric fields in pristine bi- and trilayer

Fig. 67 shows the comparative HAADF and DPC investigations of a bi- and a trilayer of WSe_2. In all images in Fig. 67, image noise is reduced by applying the non-rigid registration described in Chapter 4.4.2. For this purpose, 300 image segments were aligned, superimposed, and the average intensity of individual pixels in all aligned images calculated. Further experimental parameters are compiled in Table 54 in the Appendix.
Investigations of the bilayer are displayed in Figs. 67(a-d). The HAADF image in Fig. 67(a) clearly shows the hexagonal lattice of WSe_2 in [0001] zone-axis orientation. From the HAADF image two distinct atomic column types are evident exhibiting two different intensities. As will be shown in Chapter 6.3.3, the bilayer is probably present in an AA stacking. Hence, the brighter atomic columns are assigned to W, the darker to Se. Atomic column positions are determined using the fitting of 2D Gaussian functions as described in Chapter 4.5 resulting in a list of positions for W (green) and Se (grey) atomic columns. For better visibility some of these positions marked in Fig. 67(a).

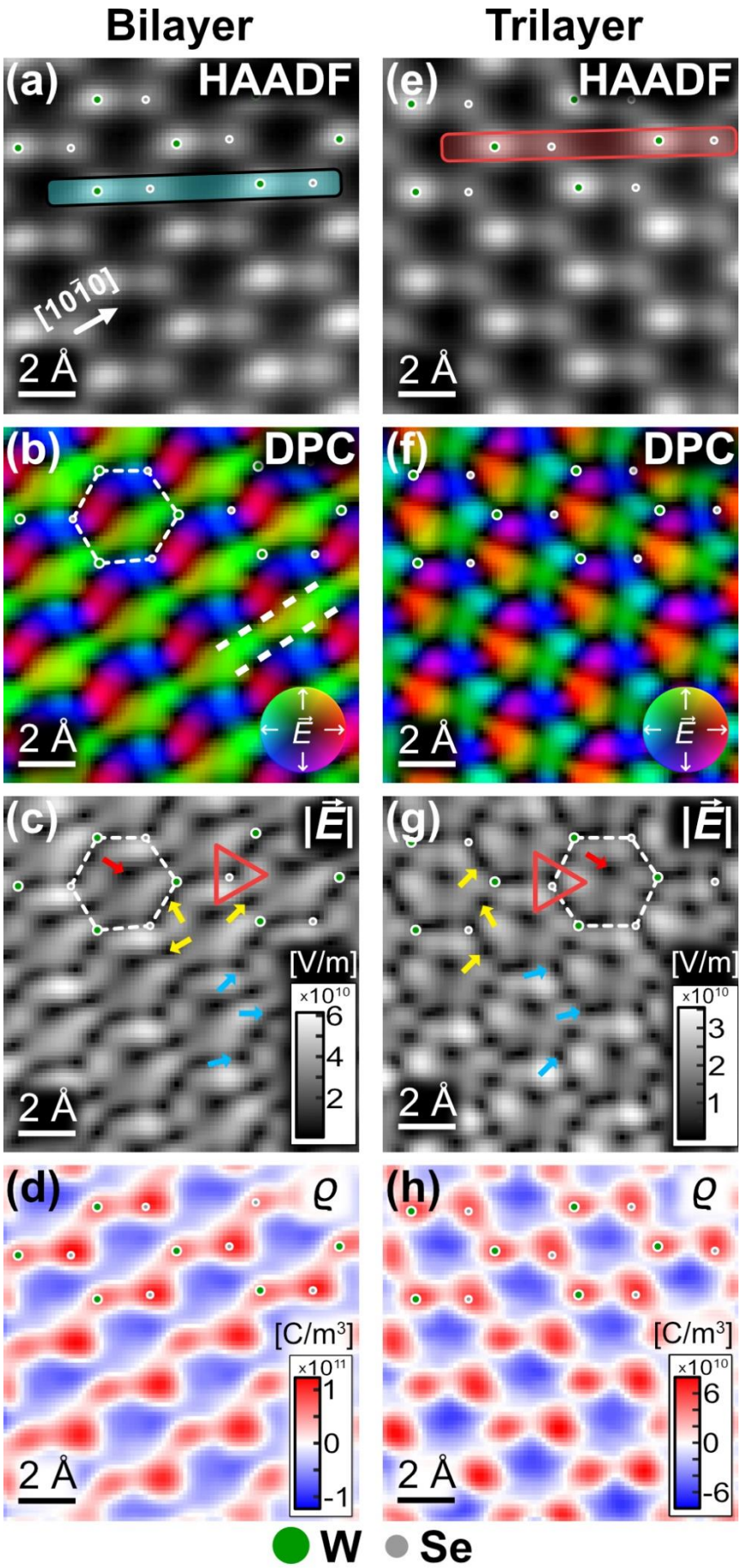

Figure 67: DPC-STEM investigations of a bi- (a-d) and a trilayer (e-h) of WSe_2. (a,e) HAADF images, (b,f) colour-coded electric field distributions, (c,g) electric field magnitude maps, and (d,h) charge density distributions.

The colour-coded electric field distribution shown in Fig. 67(b) exhibits colour wheels around each atomic column position. Some directions are less pronounced since the potentials of atomic nuclei overlap. This is particularly the case at positions close to the middle of two atomic columns and perpendicular to their connecting axis. In a hexagonal arrangement of three W and three Se_2 atomic columns (exemplarily marked by a dashed hexagon in Fig. 67(b)), an inverted colour wheel is observed. This inverted colour wheel arises due to the potentials of the six atomic columns. Furthermore, a dominant green line-like feature in $[10\bar{1}0]$ direction can be observed, which is exemplarily marked by two parallel dashed white lines. This green feature can presumably be explained by a slight tilt or bending of the WSe_2 film. Bending of 2D films across holes of a holey silicon nitride film has also been observed in the literature for MoS_2 [228]. There, bending arises due to the fact that the holey silicon nitride film with hole diameters of 200 nm is not perfectly flat but exhibits gradients towards the hole edges. MoS_2 follows its surface leading to valleys in the 2D material with peak to valley heights of up to 29 nm and a strain of 2% (determined by TEM diffraction techniques) [228].

Fig. 67(c) shows the corresponding electric field magnitude map determined from the colour-coded electric field distribution displayed in Fig. 67(b). The electric field magnitude map exhibits minima at high symmetry points of the WSe_2 lattice, sitting at the atomic column positions (blue arrows), halfway between the atomic column positions (yellow arrows) and at the centre of a hexagonal WSe_2 ring (red arrow). This is in good agreement to other DPC investigations of TMDs [31, 33, 34, 210, 211], graphene [209], and h-BN [32], and arises from the overlapping potentials of hexagonally arranged nuclei. The minimum at the centre of such a hexagon shows a tail-like extension. The positions of minima arising at atomic column positions are slightly shifted compared to the positions determined from the HAADF image. Both the shift of positions and the tail-like extension of the minima might be due to a specimen tilt as described in Chapter 5.6. It can also be explained by the presence of residual three-fold astigmatism as further simulative investigations of the influence of three-fold astigmatism on the achievable DPC images of a WSe_2 monolayer in Chapter A.2.11 in the Appendix show. One should probably emphasise that the HAADF and DPC images are acquired in the same scan, such that any erroneous image shift between HAADF and DPC images is excluded. The maximum electric field magnitude of up to $|\vec{E}_{\max}| \approx 6 \cdot 10^{10}$ V/m is observed close to the atomic column positions, which is in the same order of magnitude as reported for MoS_2 [33, 34, 210]. However, it is to note that the obtained magnitudes strongly depend on the defocus (Chapter 5.2).

Due to the proportionality of the DPC signal to the projected atomic number of $Z_{\mathrm{p;W,BL}} = 148$ and $Z_{\mathrm{p;Se,BL}} = 136$, W columns of a bilayer are expected to have an approximately 8.8% higher DPC signal and thus an increased charge density if only the atomic numbers are considered. However, the calculated charge density (Fig. 67(d)) shows a higher value for Se than for W atomic columns. In addition, the positive charge density around Se atomic columns has a larger extension. A similar behaviour is

observable in references [31, 35] where the electric field distributions and charge densities in bilayer MoS_2 are investigated using 4D-STEM. In those publications it is evident but not discussed in detail that S columns have a higher measured charge density than Mo columns, while the projected atomic number of $Z_{p;Mo,BL}$=84 of Mo columns is larger than the one of S columns $Z_{p;S,BL}$=64. A possible explanation for this unintuitive charge density ratio is the refocusing effect (Chapter 5.4): the signal of a certain number of Se atoms is generally closer to the corresponding multiple of the signal of one atom than in the case of W. Fig. 67(d) also reveals a deviation between the atomic column position determined with the HAADF signal and the position of the maximum positive charge density of individual atomic columns. As the charge density distribution is derived from the DPC signal, the deviation can be possibly attributed to specimen tilt and three-fold astigmatism.

An analogous investigation of a WSe_2 trilayer near [0001] zone-axis orientation is depicted in Figs. 67(e-h). The HAADF image shown in Fig. 67(e) exhibits similar contrasts as the one of the bilayer in Fig. 67(a). Again, the hexagonal lattice consists of two types of atomic columns with different brightnesses. The brighter columns presumably consist of pure W and the less bright columns of pure Se. This is deduced from the investigations in Chapter 6.3.3. Atomic column positions are again determined using the algorithm described in Chapter 4.5.
The colour-coded electric field map and the corresponding electric field magnitude are displayed in Fig. 67(f) and Fig. 67(g), respectively. Especially the electric field magnitude shows a high similarity to the one of a bilayer. This is evident from the fact that minima at high symmetry points of the crystal lattice are visible again. However, the overall electric field magnitude with its maximum measuring $\left|\vec{E}_{\max}\right| \approx 4{\cdot}10^{10}$ V/m is lower in case of a trilayer. The reduction in electric field magnitude is possibly due to the normalisation by higher specimen thickness and the fact that for thick specimen always a decreased DPC signal is measurable due to dynamical effects (Chapter 5.2). Although dynamical effects are typically neglected at a specimen thickness of about 2.4 nm, the measured electric field magnitudes indicate that a dynamical treatment is necessary for quantitative DPC at such small specimen thicknesses. Among the differences of the measured electric field magnitude between a bi- and a trilayer, there is also an increased and more pronounced electric field magnitude around the Se atoms in case of a trilayer. This electric field around the Se atomic column is exemplarily marked by a triangle. The electric field distribution at interatomic pixels (in hexagons of W and Se atomic columns; exemplarily highlighted by a white dashed hexagon Fig. 67(g)) again shows an inverted colour wheel which is less distorted than for the WSe_2 bilayer. The minimum local electric field magnitude minimum (exemplarily marked by a red arrow) is located closer to the geometrical centre of the hexagon than for the bilayer. In addition, no tail-like extension for this minimum is observable and the colour-coded DPC image exhibits no dominant electric field direction and thus no

dominant colour. This can be assigned to a good alignment and the absence of bending in the specimen.
Fig. 67(h) displays the charge density map calculated from the electric field distribution. Similar to the charge density of a bilayer, the positive charge around the Se atomic columns has a broader extension than the one of W atomic columns. The maximum positive charge at the Se and the W atomic columns does not exhibit obvious differences. This is in contrast to the charge density of a bilayer. The good alignment also seems to influence the detectable atomic columns positions, as a good agreement of positions determined from the HAADF signal and the positions of positive charge maxima is observed, which is much better than for the bilayer measurement. This highlights once more the importance of specimen tilt and the three-fold astigmatism for DPC measurements.

For a quantitative comparison, line profiles of the HAADF intensity, the electric field magnitude $|\vec{E}|$ and the charge density ρ of the bi- (dark grey profiles) and trilayer (red profiles) are shown in Figs. 68(a-c). The line profiles are acquired in $[11\bar{2}0]$ direction, cross two pairs of W and Se atomic columns, and are laterally aligned.
Fig. 68(a) depicts the line profiles of the HAADF intensity. Since brightness and contrast can be adjusted manually on the microscope during the analysis, the absolute numbers are meaningless. The line profiles were therefore normalised to allow for a comparison of relative peak heights. It should be emphasised that the contrast and brightness settings can even change the ratio of absolute peak heights between Se and W atomic columns. After normalisation, however, this has little effect on the relative peak heights $I_{\mathrm{W;BL}}$, $I_{\mathrm{Se;BL}}$, $I_{\mathrm{W;TL}}$ and $I_{\mathrm{Se;TL}}$ which are indicated in Fig. 68(a). From Fig. 68(i) it is evident that the Se atomic columns exhibit less intensity than the W atomic columns for both the bi- and the trilayer. The relative peak height of the W and Se atomic columns in the HAADF image of a bilayer are calculated using $H_{\mathrm{BL}} = (I_{\mathrm{Se;BL}} - I_{\mathrm{min;BL}})/(I_{\mathrm{W;BL}} - I_{\mathrm{min;BL}})$ including the minimum intensity $I_{\mathrm{min;BL}}$of the HAADF image. The relative peak height for the bilayer amounts to H_{BL}=(0.67 ± 0.01). For a trilayer, the relative peak height is decreased and measures H_{TL}=(0.547 ± 0.001). These are mean values of relative peak heights for 50 different pairs of W and Se atomic columns. The accuracies are the standard deviations. The smaller accuracy of the bilayer values although being noise reduced using the non-rigid registration can be explained by the crystallinity of WSe_2 bilayer structures, which show an increased probability of defect formation. Present defects change the obtainable standard deviation after noise reduction, as they are contained in individual images which are aligned during the non-rigid registration.
Line profiles of the electric field magnitude (Fig. 68(b)) exhibit strong difference between the bi- and trilayer. The measured electric field magnitude of a bilayer has higher maxima of the electric field magnitude than the trilayer. This again might arise from the thickness normalisation necessary for the calculation of electric field magnitudes. While the maximum electric field magnitude in the trilayer can be found

always on the right side of the Se atomic columns in line profile direction, the maximum electric field magnitude of the bilayer can be observed on the left side of the W atomic columns. This might arise from the specimen tilt and three-fold astigmatism, since the dominant green line-like feature visible in Fig. 67(c) which also leads to an increased electric field magnitude extends to the left and upper side of the W atomic columns.

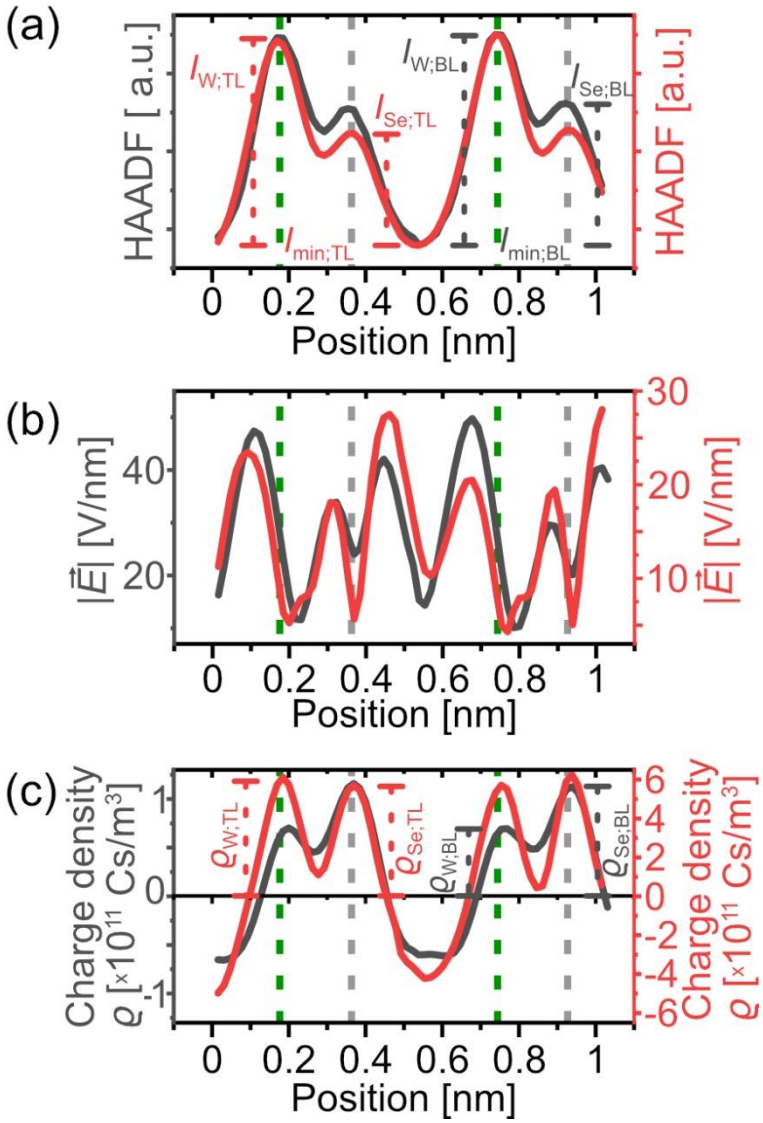

Figure 68: (a-c) Line profiles of (a) the HAADF intensity, (b) electric field magnitude and (c) charge density. The line profiles are obtained from the regions depicted in Figs. 67(a, e) with a line profile width of one pixel. The HAADF intensities are normalised to allow for a comparison between intensities at W and Se atomic columns. Atomic column positions are marked by green (W) and grey (Se) dashed lines. A list of measurement parameters is compiled in Table 54.

Although the line profiles of HAADF intensity reveal that the Se atomic columns have a lower intensity, this is not the case for the charge density depicted in Fig. 68(c). As visible in the corresponding charge density map in Fig. 67(d), the Se atomic columns have a $C_{BL} = \rho_{\mathrm{Se;BL}}/\rho_{\mathrm{W;BL}} = (1.64 \pm 0.01)$ times higher charge density than the W columns in case of the bilayer. This is not evident in the WSe_2 trilayer. In WSe_2 trilayers, the Se and W atomic columns have almost identical positive charge density maxima which differ only by a factor of $C_{TL} = (1.01 \pm 0.05)$. As discussed below, the

relative HAADF peak intensity and charge density ratios allow to determine the stacking of WSe_2 multilayers.

6.3.3. Stacking of bi- and trilayers

Since all quantities depend on the stacking of WSe_2 layers, it is important to know the stacking to allow comparability between the investigations of WSe_2 with a different number of layers and with the literature. Since electron micrographs only represent a projection of the lattice potential, the determination of the stacking sequence is not straight forward. This becomes more difficult as the number of layers increases, as there are multiple possible stacking sequences. As can be seen below, however, it is possible to determine the stacking taking into account the HAADF images and the charge density distributions, since both are based on different signals and show different dependencies on machine-dependent parameters such as the defocus [91]. In the following, identification of stacking sequence is achieved by using Dr. Probe [44] for multislice HAADF and DPC image simulations.

Fig. 69 shows investigations of different stacking sequences of a WSe_2 bilayers and displays the simulated HAADF images, the colour-coded electric field maps, the electric field magnitude maps, and charge density distributions for structures with AA and AA' stackings. Among all possible stacking sequences (displayed in Fig. 65), these two have been chosen because they do not involve layer shifts (like for AB-type stacking) and projected atom positions form a hexagonal lattice, as it is experimentally observed. Simulation parameters match the microscope parameters used in the measurements discussed above and comprise an acceleration voltage of 80 kV, a convergence semi-angle of 30 mrad and a Gaussian-like effective source profile with a full width at half maximum of 70 pm. No frozen-lattice configurations are applied since noise levels are not included in the discussion and thermal lattice vibrations are assumed to have a negligible influence on the relative electric field magnitudes and HAADF intensities of W and Se atomic columns. For the detection, the outer collection angles of the detector are 18 mrad for Layer1 and 36 mrad for Layer2. A list of further simulation parameters is given in Table 30 in the Appendix. Atomic column positions are determined from the HAADF intensities in the same way as in the experiment and are again indicated by green (pure and mixed W) and grey (pure and mixed Se) dots. In case of AA' stacking no pure W and Se atomic columns are present. The marked dots, therefore, depict the atomic species in the upper layer (first three slices of considered layer stack).

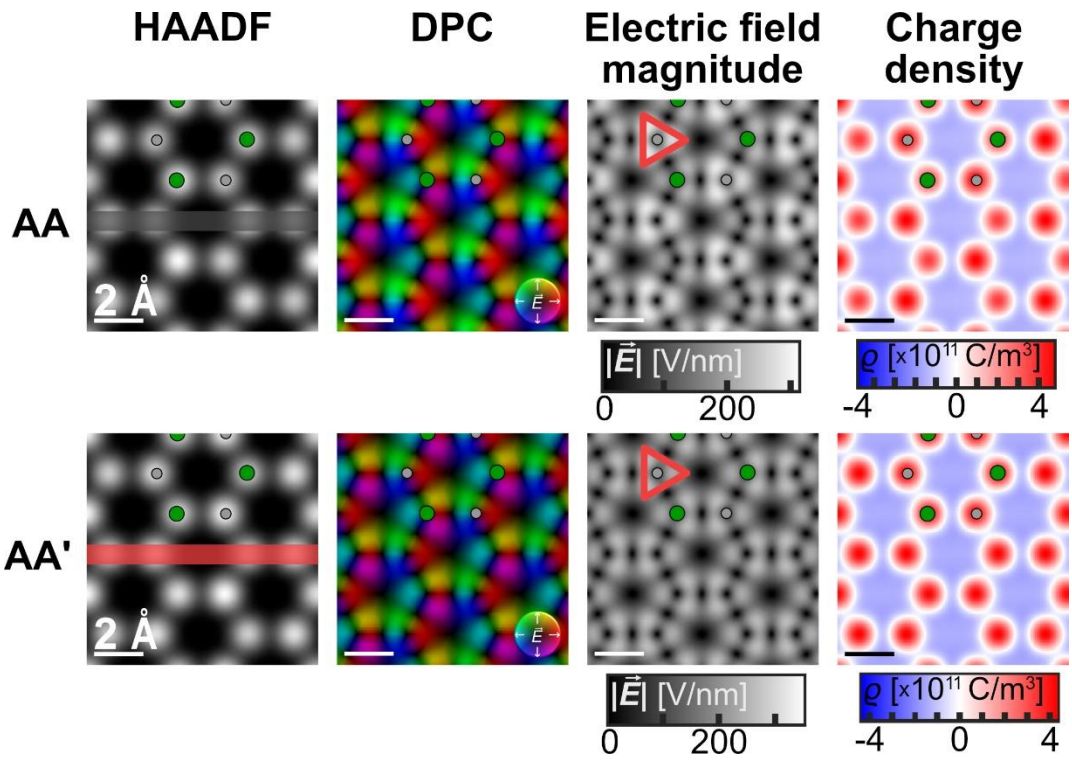

Figure 69: Multislice image simulations of HAADF intensity, charge density and electric field distribution as well as colour-coded electric field distribution for different stackings for a bilayer of WSe_2. All image simulations are acquired exactly in [0001] zone-axis orientation. A list of simulation parameters is given in Table 30 in the Appendix.

The simulated HAADF images of a bilayer with an AA and AA' stacking (see Fig. 65(b)) are shown in the left column of Fig. 69. W atomic columns exhibit a higher intensity than Se atomic columns for the AA stacked WSe_2. Such relative intensities of Se and W atomic columns cannot be observed in the case of the AA' stacking. There, the atomic columns in which two Se atoms are followed by one W atom in beam direction exhibit a higher intensity than the atomic column consisting of a W atom followed by two Se atoms. Such contrast ratios have also been experimentally observed by Wan et al. for WSe_2 [229] and by Xia et al. for MoS_2 [230]. Thus, in stacked 2D materials, the HAADF intensity is not solely determined by the projected atomic potentials, but also by the ordering of atoms along the beam axis. A possible explanation is different channeling of the electron (probably its initial stage) initiated by the first atom in beam direction [157].

At a glance, the colour-coded electric field distribution and corresponding map of the electric field magnitude of both, the AA as well as the AA' stacking (Fig. 69), are seemingly in good agreement to the experimental images (Figs. 67(b, c)), as far as minima at high symmetry points are observable. In addition, a colour wheels exist around each atomic column and inverted colour wheels in each hexagon (exemplarily indicated by the six dots). Due to overlapping potentials of the atoms and a finite effective source profile leading to a smeared simulated electric field magnitude, triangularly shaped electric field structures of particularly high magnitude and a non-evenly distributed colour brightness in the colour wheels are observable. This intensity modulation is evident but less obvious in the measurement and marked by red

triangles in Fig. 67(c) and Fig. 69. Such triangular features are also visible for A'A stackings, but the intensity is not modulated (difference of fields around W and Se atomic columns as described below). Similar to the measurement, the simulated electric field magnitude of the AA stacked WSe_2 structure exhibits increased intensities close to the Se atomic columns. This is not observed in the DPC image simulations of an AA' stacked structure. However, due to strain and slight tilt of the specimen in the measured electric field magnitude map Fig. 67(c), the electric field magnitude distribution in the triangles of the simulated image is more uniform.
Due to the difference in electric field distribution, the calculated charge density distribution of an AA stacked WSe_2 structure differs from the AA' structure. While in the AA stacked structure the Se atomic columns have a higher positive charge density, almost identical positive charge densities are observed for both the W and Se atomic columns in case of the AA' stacked WSe_2. Furthermore, a broader extension of positive charge densities around the Se atomic columns than around W atomic columns is only observed in the case of AA stacked structure. This is a strong indication that the measured bilayer specimen is AA stacked WSe_2.

For a stronger proof, quantifications of relative HAADF intensities and charge densities of different atomic columns are necessary. Therefore, Fig. 70 shows line profiles of the HAADF intensity and charge density. The line profiles extend across two pairs of W and Se atomic columns as can be seen by the transparent dark grey and red lines in the HAADF and charge density images in Fig. 69. Atomic column positions of pure W and Se (AA stacking) or mixed W/Se_2 and Se_2/W (AA' stacking with the first always denoting the atomic species of the first layer in propagation direction of the electron beam) columns are indicated by the green and grey dashed lines in Fig. 70.
The pure Se and pure W atomic columns of the AA stacked structure have a HAADF intensity ratio of $H_{AA} = (I_{\mathrm{Se;AA}} - I_{\mathrm{min}})/(I_{\mathrm{W;AA}} - I_{\mathrm{min}})$ =0.805 . The intensities $I_{\mathrm{Se;AA}}$, $I_{\mathrm{W;AA}}$, and I_{min} are determined in the same way as the intensities $I_{\mathrm{Se;BL}}$, $I_{\mathrm{W;BL}}$ and $I_{\mathrm{min;BL}}$ in Fig. 68(a). Although the projected atomic number in AA' stacked WSe_2 is the same for both mixed atomic column types, the atomic column in which two Se atoms interact first with the electron beam exhibits a $H_{AA'}$= 1.131 of the HAADF intensity of an atomic column in which a W atom is followed by two Se atoms in beam direction. These contrast ratios were also observed by Wan et al. for WSe_2 [229] and by Xia et al. for MoS_2 [230].

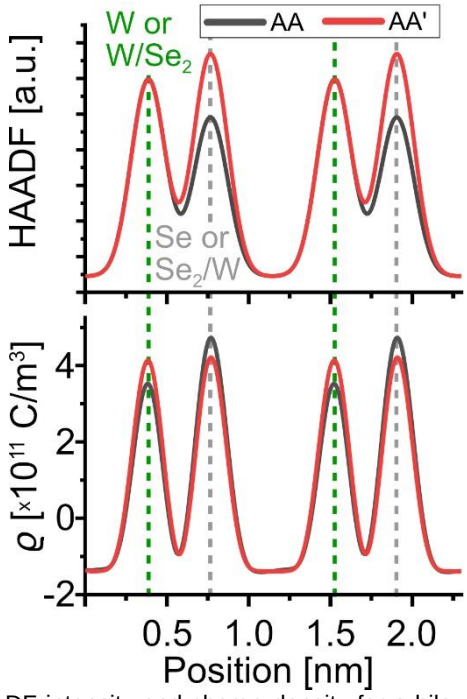

Figure 70: Line profiles of HAADF intensity and charge density for a bilayer of WSe_2[0001]. Areas of line profiles are indicated by red and grey boxes in Fig. 69. A list of simulation parameters is given in Table 30 in the Appendix.

Line profiles of the corresponding charge density reveal that in the simulations the pure Se atomic column has a 1.34 times higher maximum positive charge density than the pure W atomic column in case of AA stacking, i.e. $C_{AA} = \rho_{\mathrm{Se;AA}}/\rho_{\mathrm{W;AA}} = 1.34$. The ratio of maximum charge density for mixed Se_2/W and W/Se_2 atomic columns in an AA' stacked WSe_2 structure amounts to $C_{AA'} = \rho_{\mathrm{Se;AA'}}/\rho_{\mathrm{W;AA'}} = 1.02$. The simulated and experimental HAADF intensity and charge density ratios are given in Table 5.

Table 5: HAADF intensity ratios and charge density ratios deduced from simulated and experimental HAADF and DPC images of WSe_2 bilayers. Two different stackings, namely AA and AA', are considered for the simulated values.

	Simulated AA	**Simulated AA'**	**Experimental**
HAADF intensity ratio H	0.805	1.131	(0.67 ± 0.01)
Charge density ratio C	1.34	1.02	(1.64 ± 0.01)

The experimentally observed relative HAADF intensity and charge density peak height ratios of $H_{\mathrm{BL}} = (0.67 \pm 0.01)$ and $C_{\mathrm{BL}} = (1.64 \pm 0.01)$ and the corresponding values in Table 5 lead to the conclusion that the measured WSe_2 bilayer is an AA-stacked layer stack. This is especially obvious from the different charge densities of W and Se atomic columns. The difference of the measured and simulated HAADF intensity ratio can be explained by an increased background signal in the measurement due to contamination and a broadened effective source profile.

Analogous investigations for the trilayer are given in the following. Fig. 71 displays the simulated HAADF images, the colour-coded electric field maps, the maps of the electric field magnitude and the charge density distributions of AAA and AA'A stacked WSe_2 trilayers. Again, these two have been chosen based on the experimentally observed hexagonal lattice contrast and do not involve lateral layer translations (like for AB-type stacking). Besides the different specimen structure due to the additional layer, the simulations are achieved with the same simulation parameters as the simulations for the bilayer. A complete list of simulation parameters can be found in Table 30 in the Appendix.

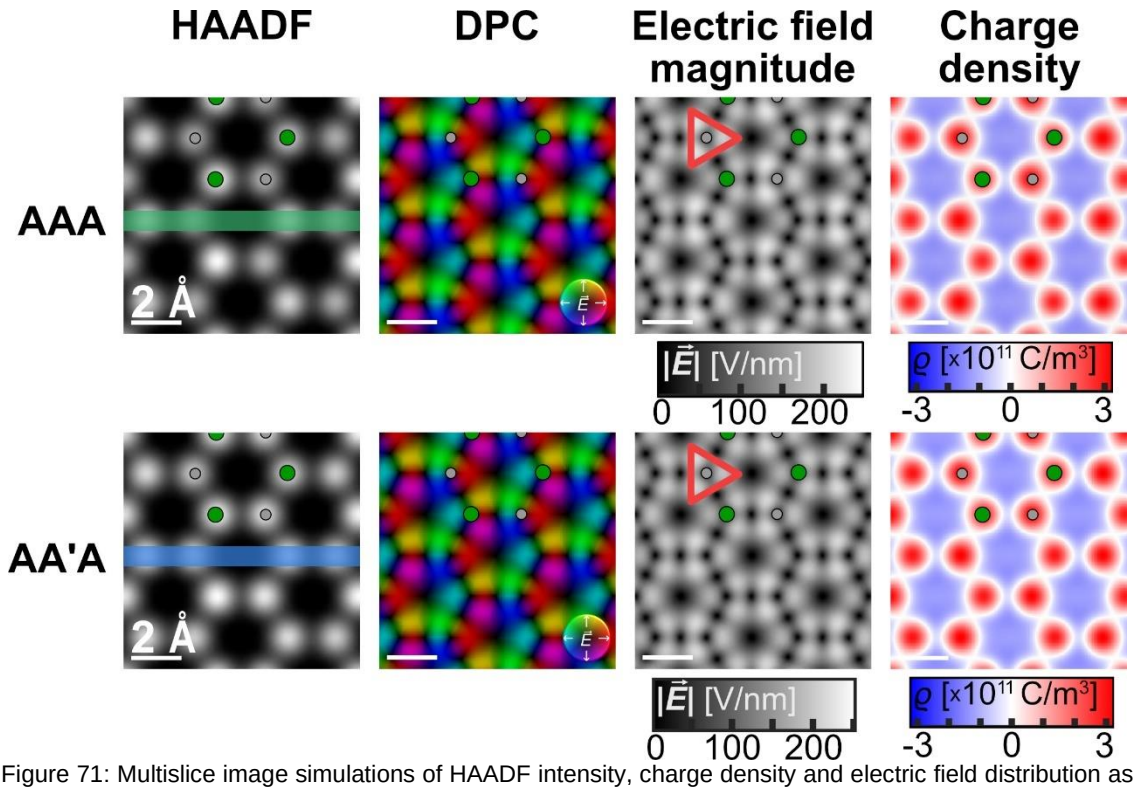

Figure 71: Multislice image simulations of HAADF intensity, charge density and electric field distribution as well as colour-coded electric field distribution for different stackings for a trilayer of WSe_2 in [0001] zones axis orientation. A list of simulation parameters is given in Table 30 in the Appendix.

In case of the image simulations for WSe_2 trilayers, both the AAA and AA'A stacked structures do not exhibit obvious differences in the HAADF images, the colour-coded electric field maps, the maps of the electric field magnitude as well as the charge density distributions as can be seen in Fig. 71. In the HAADF image of the AAA image, the pure or mixed W atomic columns always have a lower intensity than the pure or mixed Se atomic columns. This contrasts with the findings for the AA and AA' stacked bilayers, for which a contrast inversion was observed between pure and mixed atomic columns. Still, a small difference between HAADF images of the AAA and AA'A stacked WSe2 trilayers can be seen by the increased contrast of 2Se+W+2Se atomic column (AA'A stacking, marked by green dot) compared to the pure Se atomic column (AAA stacking, marked by green dot). In the electric field magnitude maps and the charge density distribution, a small difference around pure and mixed W and Se atomic columns is obvious. This can be particularly seen from the triangular features in the

electric field magnitude maps around pure and mixed Se atomic columns (indicated by red triangles) and from the extension of positive charge density around the pure and mixed W atomic columns. Again, differences are smaller and less obvious than for the different stackings of a WSe_2 bilayer.

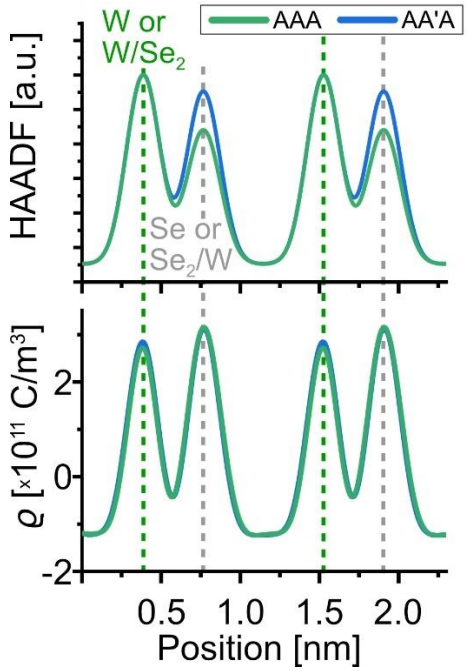

Figure 72: Line profiles of HAADF intensity and charge density for a trilayer of WSe_2[0001]. Areas of line profiles are indicated by green and blue boxes in Fig. 71. A list of simulation parameters is given in Table 30 in the Appendix.

The small but existing differences between both stackings are further investigated by line profiles in Fig. 72. Here, the HAADF intensity ratios amount to H_{AAA}=0.71 and $H_{AA'A}$=0.91. The charge density ratios exhibit smaller differences, which are C_{AAA}=1.16 and $C_{AA'A}$= 1.09. These values make it more likely that the investigated trilayer has an AAA stacking, as the comparison of simulated and measured ratios in Table 6 show.

Table 6: HAADF intensity ratios and charge density ratios deduced from simulated and experimental HAADF and DPC images of WSe_2 bilayers. Two different stackings, namely AA and AA', are considered for the simulated values.

	Simulated AAA	**Simulated AA'A**	**Experimental**
HAADF intensity ratio H	0.71	0.91	(0.547 ± 0.001)
Charge density ratio C	1.16	1.09	(1.01 ± 0.05)

6.3.4. Electric fields of Se vacancies

The mechanical, electrical, and optical properties are not only determined by the properties of a material present in a perfect (infinitely expanded) crystal, but defects in the crystal structure have a dominant influence on the properties of a material and its possible applications. This obviously also applies to 2D films of transition metal dichalcogenides, where the defects largely affect the opto-electronic, morphological and magnetic properties [231–233]. Like in 3D materials, one should expect that single and multiple vacancies may occur at different charge states, resulting in different opto-electronic properties.

Possible defects in 2D-WSe_2 include vacancies of metal (Mo, W) or chalcogen (S, Se) atoms [234, 235], antisite defects [235, 236] where the metal atom takes the position of a chalcogen atom (or vice versa), adatoms [231] on interstitial lattice positions, ternary doping atoms [234] as well as grain boundaries [237], large-scale holes [237] and rotational defect clusters resembling the shape of a trifoliate leaf induced by a rotation of metal-chalcogen bond [233]. Vacancies might result in an intrinsically n- or p-doped material even without the incorporation of a third atomic species in the lattice [238]. Regarding the optical properties, point defects such as Se vacancies introduce new states in the bandgap [238, 239] and change the photoluminescence quantum yield since they act as charge-traps and nonradiative recombination centres [231, 235, 236]. Furthermore, Se vacancies facilitate the adsorption of adatoms [232, 240] and especially can lead to a dissociation of O_2 into two separated oxygen atoms. One oxygen atom is bound at the initial Se vacancy site, passivating the otherwise existing defect gap states, and the other one at an interstitial lattice point [240]. Especially the latter renders 2D-WSe_2 into a promising material for the creation of single photon emitting devices [241] since the interstitial oxygen together with strain gradients give localised excitons, necessary for single photon emission [240].

In WSe_2 monolayers, Se mono- (one missing Se atom) and bivacancies (a completely missing Se atomic column) are the dominant defect types regardless of the 2D material preparation technique. This is due to their lower formation energy compared to other defects such as antisite defects and W vacancies [238–240, 242]. Densities of such point defects in WSe_2 are in the range of 10^{10} cm^{-2} to 10^{13} cm^{-2} [241]. However, it has been observed that the type and density of defects largely depend on the fabrication method: 2D-WSe_2 grown by chemical vapor deposition has typically a higher point defect density than 2D-WSe_2 which has been mechanically exfoliated from bulk WSe_2 [236, 243]. In addition, the ratio of W and Se vacancies is influenced by the preparation technique [236, 239].

While a large number of defects can already occur at room temperature in the as-produced WSe_2 layer, they can also be created by various processes, such as chemical [231], plasma [231], ozone [231], alpha particle [232] as well as laser [231], ion [244] or electron beam treatment [233, 237]. Due to the good controllability of the

electron beam, the latter in particular makes top-down fabrication of tailored defect structures possible.

The formation of defects by electron beam irradiation can be classified by different formation mechanisms including knock-on collisions (displacement of an atom), radiolysis, charging and heating [245]. In addition, contamination on 2D TMDs might locally mediate the defect formation under an electron beam and thus acts as catalyst [231]. In particular, the displacement driven by the knock-on collisions is one of the most dominant damage mechanisms, which gives rise to point defects like e.g. Frenkel defects [245]. For defects to occur due to knock-on damage, the energy of the electron beam [246] and the electron dose on the specimen [247] must exceed threshold values. Komsa et al. [246] calculated this energy for various 2D TMDs under the assumption that the knock-on energy must exceed a threshold value at which the atom leaves its bound position in the crystal lattice and does not return. The threshold displacement energy is thus characteristic for the atomic species present in the material and is also dependent on the binding energy and the crystal structure. The threshold displacement energy for a single Se atom amounts to 2.2 eV – 2.8 eV to form a Se monovacancy [240]. This is much smaller than the threshold displacement energy of a single W atom for the formation of a W monovacancy which is above 3.6 eV [240, 246]. To calculate the energy which is transferred to the atom by the incident electron beam, it is appropriate to assume elastic scattering [248]. The transferred energy then depends on the atomic mass of the atom, the scattering angle and the incident electron beam [248]. The incident electron energy to create a Se vacancy in WSe_2 is roughly 200 keV [246]. However, also irradiation damage in WS_2 is observed even at 30 kV acceleration voltage [211, 239] which can be ascribed to radiolysis. The impact of radiolysis increases at lower acceleration voltages [245] and as a result, defect formation is observed at acceleration voltages lower than 200 kV in case of WSe_2 [233]. The irradiation of a monolayer of WSe_2 with electrons primarily generates mono-vacancies of Se (V_{Se}), i.e. one missing Se atom in a Se atomic column, and selenium divacancies (V_{Se2}), i.e. a completely missing Se atomic column. Both are the most stable defects in WSe_2 and have the lowest formation enthalpy [239, 242]. In WSe_2 bilayers in an AA stacking, it is also possible that three (V_{Se3}) and four Se atoms (V_{Se4}) are missing in a pure column of Se atomic sites. Also, the evolution of defects and formation of vacancy clusters (vacancies at neighbouring sites) is observed under electron beam irradiation [233]. Since vacancies are readily created, they are likely to diffuse through the material by a rearrangement of Se atoms [211, 233]. A single point defect can also alter the lattice in the vicinity around the defect [233], e.g. leading to a relaxation of neighbouring W atoms in direction of V_{Se} and V_{Se2} vacancies [242]. In addition, phase transitions are possible, e.g. the transformation from the 2H to the metallic 1T polymorph of MoS_2 via lattice plane gliding has been described [249], which can be provoked by an illumination with the electron beam.

To create future devices which rely on the functionalities of defects in WSe_2, precise control is necessary, thus electron microscopy is inevitable, as it offers sub-atomic

resolution with a manyfold of analytical techniques [237]. In addition, as the electric properties and thus the electric field at defects play a key role in the device's property and performance, investigations of the electric field distribution at defects are necessary.

In the following, a line-like defect cluster in a bilayer of WSe_2 comprising several Se vacancy-type defects of different numbers of missing Se atoms is investigated. The HAADF image as well as the DPC image are depicted in Fig. 73. Images are acquired with the same microscope settings as described in Chapter 6.3.2 and more importantly at very low dwell times, since it is observed that as soon as one or more defects have occurred many further defects arise or accumulate within a short time, ultimately leading to the formation of holes with a diameter of several nanometres in the WSe_2 layer. This is in good agreement to the findings in reference [211].
In contrast to the post-processing applied on the images in the previous chapter, the presence of defects does not allow to use the non-rigid image registration, as the registration would overlay images of pristine lattice with the ones containing defects. Therefore, image noise is reduced only using the Gaussian noise reduction algorithm described in Chapter 4.4.1. For this, a Gaussian function with a full width at half maximum of 120 pm was used which also reduces the spatial resolution. Atomic column positions are again assigned using the algorithm described in Chapter 4.5. The atomic columns with the brighter contrast are assigned to the W atomic column, the darker ones to the Se atomic column, respectively. However, due to the reduced resolution arising from the noise reduction, the accuracy of atomic column positions might be reduced. Thus, marked atomic column positions serve only as a guide to the eye. A large-area HAADF image of the defect region is depicted in Fig. 109 in the Appendix. From this figure, it can be deduced that the increased intensities at the upper left and lower right image corner in Fig. 73(a) are presumably arising from contamination.
The HAADF image depicted in Fig. 73(a) shows several vacancy-type defects (marked by white dashed circles which are additionally annotated with numbers) arranged in a line. As can be seen from the different intensities which are observable at the exact positions of the defect sites, different types of Se vacancies are present. The defects numbered with 1, 3 and 4 show remaining intensities at the defect sites. It can thus be assumed that one or more Se atoms are remaining in the atomic column of this bilayer. Almost no contrast is observable at the defect site marked with 2. Furthermore, all W atomic columns exhibit an almost identical intensity. This is in good agreement to the fact that the Se atoms are prone to form defects due to their lower threshold displacement energy [246].

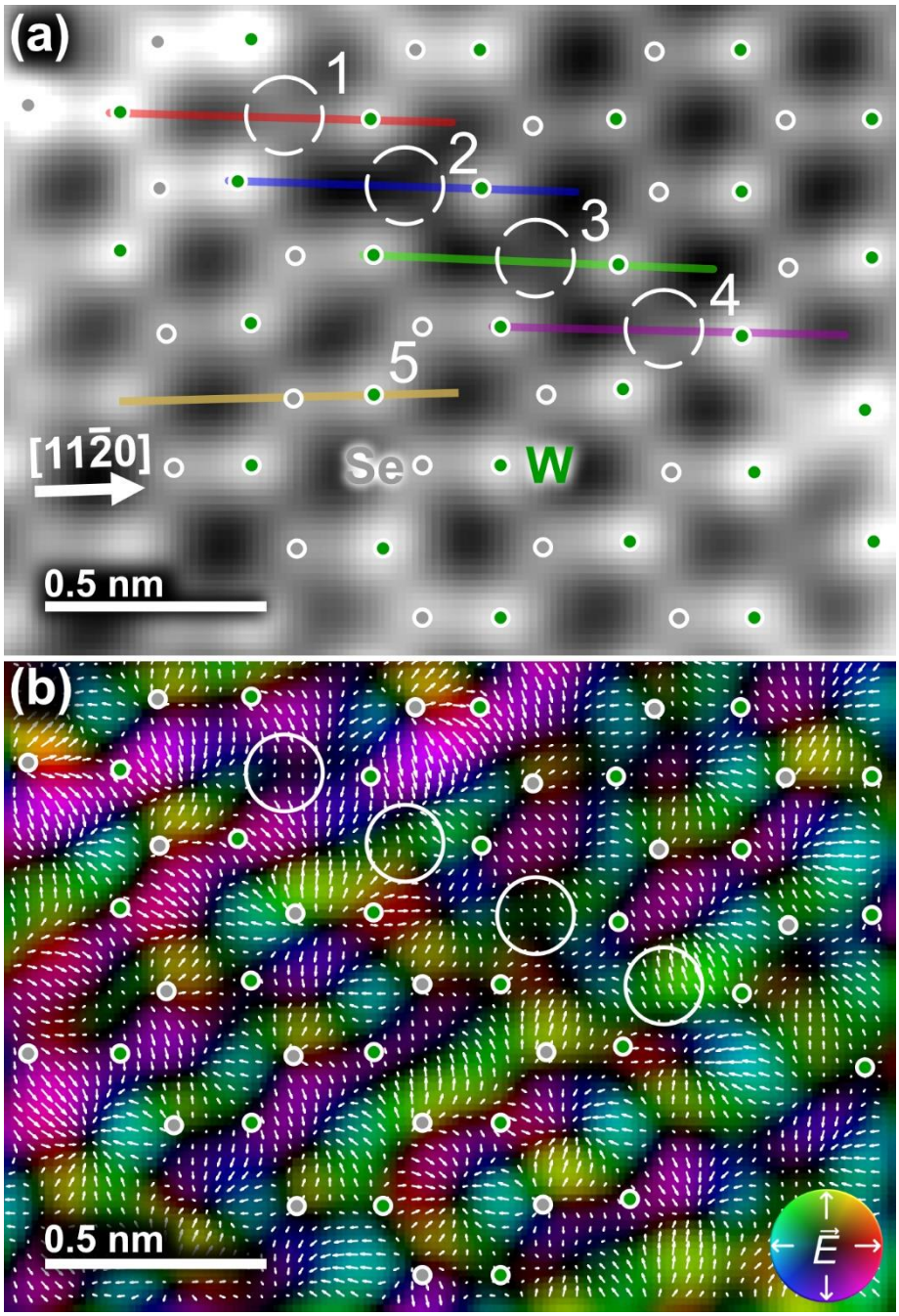

Figure 73: (a) HAADF image of WSe_2 close to [0001] zone-axis orientation. The WSe_2 structure contains several point defects, some of them are indicated by white circled. (b) Simultaneously acquired DPC image of the same area. The same defects are encircled. Experimental details are listed in Table 55 in the Appendix.

These conclusions are supported by line profiles of the HAADF intensity (Fig. 74) for the four defects highlighted in Fig. 73. They are obtained from the region marked by red, blue, green, and purple lines in Fig. 73(a) and span across the defect sites in $[11\bar{2}0]$ direction. The yellow line profile corresponds to a perfect Se site. The dashed black line reveals the line profiles of HAADF intensity of a pristine lattice which is analogously obtained from a rigidly registered defect free image. All line profiles are laterally aligned via the W atomic columns. The line profiles in Fig. 74 show an almost identical HAADF intensity W atomic columns, while the observed intensities at the

perfect Se columns and defect sites show strong variations. This is attributed to a different number of remaining Se atoms.

For quantification, the intensity ratios of intensities at Se (I_{Se}) and at W atomic columns (I_{W}) are given in Table 7 for the five line profiles. The intensity ratios are calculated as $H = (I_{\mathrm{Se}} - I_{\mathrm{min}})/(I_{\mathrm{W}} - I_{\mathrm{min}})$. Here, I_{min} is the overall minimum of the HAADF image. Table 7 additionally contains the ratio of simulated HAADF intensity at W and Se atomic columns. The simulated value assumes an AA stacked WSe_2. The intensity ratios obtained from the perfect Se Site and the pristine lattice nicely match the simulated. The small difference of the simulated and measured intensity ratio is presumably due to different reasons: 1) the fact that the intensity is derived without averaging of image segments, 2) surface contamination, and 3) the image noise. Because of the small difference to the predicted intensity ratio, it is assumed that four Se atoms are present at the Se atomic column of the HAADF intensity line profile labelled with 5.

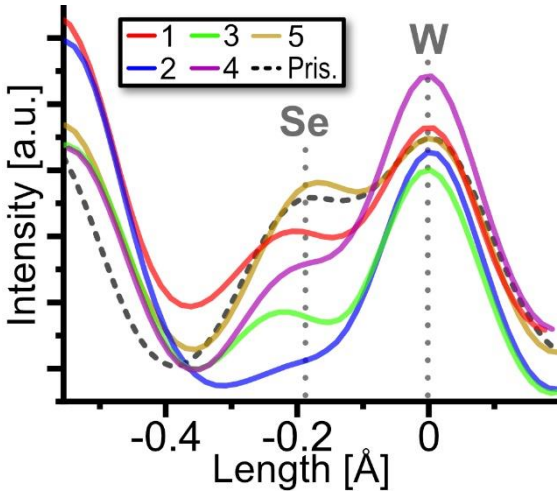

Figure 74: Line profiles of HAADF intensity. Line profile areas are indicated in Fig. 73(a) by the colour. The line profile indicated as “Pristine” is obtained from rigidly registered HAADF image. Experimental details are listed in Table 55 in the Appendix.

Table 7: HAADF intensity ratio $H = (I_{\mathrm{Se}} - I_{\mathrm{min}})/(I_{\mathrm{W}} - I_{\mathrm{min}})$ of intensities at the Se and W atomic columns sites for the line profiles shown in Fig. 74. Additionally, the ratio of simulated HAADF intensity at W and Se atomic column sites is shown. The right column shows the ratios $S = (I_{\mathrm{Se},i} - I_{\mathrm{min}})/(I_{\mathrm{Se},5} - I_{\mathrm{min}})$ of the HAADF intensities at the different Se vacancies ($I_{\mathrm{Se},i}$) and the Se atomic column containing four Se atoms ($I_{\mathrm{Se},5}$) with I_{min} the minimum intensity of the HAADF image.

Line profile	HAADF intensity ratio H	Se site intensity ratio S
1	0.62	77.5%
2	0.15	16.6%
3	0.38	40.2%
4	0.42	62.9%
5	0.83	-
Pristine	0.82	-
Simulation	0.805	-

By comparing the intensities at the Se vacancies ($I_{\mathrm{Se},i}$ of profile i) with the intensity of a perfect Se atomic column containing four Se atoms ($I_{\mathrm{Se},5}$; yellow line profile), the type of defect should be detectable as the HAADF contrast scales with the projected atomic number. Basically, for Se vacancy-type defects in an AA stacked WSe_2 bilayer, where

instead of four Se atoms in a column there are only one, two or three Se atoms left, one would expect 25%, 50% or 75% of the HAADF intensity of a four atom column, since the atomic column consists of atoms of the same atomic number [45, 47]. The ratios of intensities at the Se vacancy sites ($I_{\mathrm{Se},i}$) and the intensity at the Se atomic column ($I_{\mathrm{Se},5}$) comprising four atoms are calculated by $S = (I_{\mathrm{Se},i} - I_{\mathrm{min}})/(I_{\mathrm{Se},5} - I_{\mathrm{min}})$ with the minimum intensity I_{min} of the HAADF image. Results are given in Table 7.
Several reasons might lead to the deviation from the expected ratios: First, the position of the Se atomic column is slightly shifted as compared to the Se in a pristine lattice. This might be due to the fact that the lattice in the vicinity of defects can be distorted [233, 242] or that just a particular moment of the dynamic process of defect evolution is captured [233]. The latter would lead to a smaller intensity measured at the defect site. Second, as the incorporation of oxygen atoms at such vacancy defects is likely [240], an oxygen atom might increase the obtainable contrast at the point defect site. A single O atom would just generate 8.5% of the intensity of a Se atom following a $Z^{1.7}$ contrast. Third, surface contamination, which is typically composed of hydrogen, carbon, and oxygen, only consists of weakly scattering atoms. A random distribution of such elements cannot be easily identified but might change the local contrasts. Fourth, due to the applied Gaussian denoising, all features are blurred. The intensity of W atomic columns might thus extend into the area of the line profile.
In the following, it is assumed that the defect labelled with 1 is a V_{Se} monovacancy as an intensity of 75% of the intensity of a perfect Se atomic column corresponds well to the expected intensity of a three Se atom atomic column. The defect labelled with 2 is a completely missing Se atomic column (V_{Se4}), showing residual HAADF contrast either due to two oxygen adatoms or a moving Se atom. The defect labelled with 3 is assumed to be a V_{Se2} or a V_{Se3} defect in an AA bilayer, i.e. two or three Se atoms are missing in the atomic column. In case of a V_{Se2} defect, a moving Se atom is snapshot at a certain stage of the dynamical process. In case of a V_{Se3} defect, the residual atomic column consists of one Se atom plus two substitutional oxygen atoms. If one imagines that one Se atom and two oxygen atoms are present at the defect site, one obtains in total about 42 % of the intensity of a Se atomic column consisting of four atoms. However, this needs further investigations and chemical mappings of the atomic species to prove that oxygen atoms are present at the defect site. The defect labelled with 4 is assumed to be a V_{Se2} defect which probably contains additional substitutional atoms or shows an increased intensity due to contamination. The presence of contamination can be inferred from the increased intensity at the lower right corner of the HAADF image in Fig. 73(a).

The DPC image in Fig. 73(b) shows that pronounced colour wheels similar to those of the pristine WSe_2 bilayer exist in defect free areas and particularly at W atomic columns. However, differences between the measured electric field distribution and the expected electric field distribution in a pristine lattice are observable in the vicinity of defects. In order to reveal those differences, Fig. 75(a) shows the difference of

measured electric field magnitudes $\Delta\left|\vec{E}\right| = |E_{\mathrm{defect}}| - \left|E_{\mathrm{pristine}}\right|$ between the defect containing area and a pristine area of the WSe_2 specimen. In addition, Fig. 75(b) shows the colour-coded difference map of electric field vectors $\Delta\vec{E} = \vec{E}_{\mathrm{defect}} - \vec{E}_{\mathrm{pristine}}$. The images of defective and the pristine regions are obtained from a single large-area DPC image which is shown in Figs. 109(a, b). This ensures that the defective and the pristine images are obtained with the same acquisition parameter. The post processing steps are the same as for the images in Fig. 73. The DPC and HAADF image containing the defects is obtained by cropping (Figs. 109(c, d)). The pristine region is obtained by using the rigid registration technique with a pristine image region for the rigid registration reference image (Figs. 109(e, f)). By selecting a pristine region far off the defect containing area, but still using the same image, the calculated difference maps $\left|\Delta\vec{E}\right|$ and $\Delta\vec{E}$ are less influenced by imaging conditions and are assumed to be most sensitive to the effects of a crystal defect. Before the images are subtracted, the DPC and HAADF images were aligned using the non-rigid image registration to account for lattice distortions. The HAADF images are used for the non-rigid registration with the defect containing area as the reference image. By choosing the defect containing image as the non-rigid registration reference image, the registered image of a pristine lattice can act as background which is subtracted from the defect containing image to reveal the difference induced by the defects. The non-rigid registration is applied with a high field smoothing of four pixels to prevent atoms which should be aligned with the defect to be falsely aligned with the nearest neighbour.

Fig. 75(a) shows that the electric field magnitude difference is mostly small, except for areas next to the defect and contaminated areas (upper left and lower right corner; also see increased HAADF intensities in Fig. 73(a)). The difference arising from contamination is not investigated in the following.

As can be seen from Fig. 75(a), a reduction in electric field magnitude is observed at defects 1, 2 and 3 (black circles). This is reasonable, as atomic nuclei are missing, which otherwise would lead to strong electric field magnitudes. Directly at the defect position, almost no difference in electric field distribution is observable. This can be explained by the fact that the projected electric field of an atom is also zero at the geometrical centre of the atomic potential. Removing or adding an atom with any atomic number would thus not change the measurable electric field at this position. This is particularly evident at the defect marked with a 3. The other defects might show a non-negligible difference of electric field magnitude due to slightly shifted atoms and a distortion of the electric field due to the presence of lattice distortions or different orientations of the WSe_2 areas due to bending. Moreover, the difference of electric field magnitude reveals an increased electric field magnitude close to the three W atoms surrounding the Se vacancy. These positions at which an increased electric field magnitude is observable are exemplarily marked by dashed circles. This increase in electric field magnitude occurs geometrically at the connection lines between W atoms and nearest Se vacancies and thus might be misinterpreted as dangling bonds arising due to missing Se atoms. Instead, as the Se atoms are missing at the defect sites, no

overlap of electric field is possible leading to an increasing the electric field magnitude close to the W atomic columns. Such an effect was also observed around a B vacancy cluster in hexagonal boron nitride [32]. In addition, also a decreased electric field magnitude resembling a trident star is observed in Fig. 75(a) (exemplarily indicated by dashed triangles). This is particularly the case for the defect labelled as 2 (V_{Se4} vacancy) and for the defect labelled as 3 (possibly a V_{Se3} vacancy with additional O atoms). Such a feature was also observed in electric field difference map for vacancies in h-BN [32].

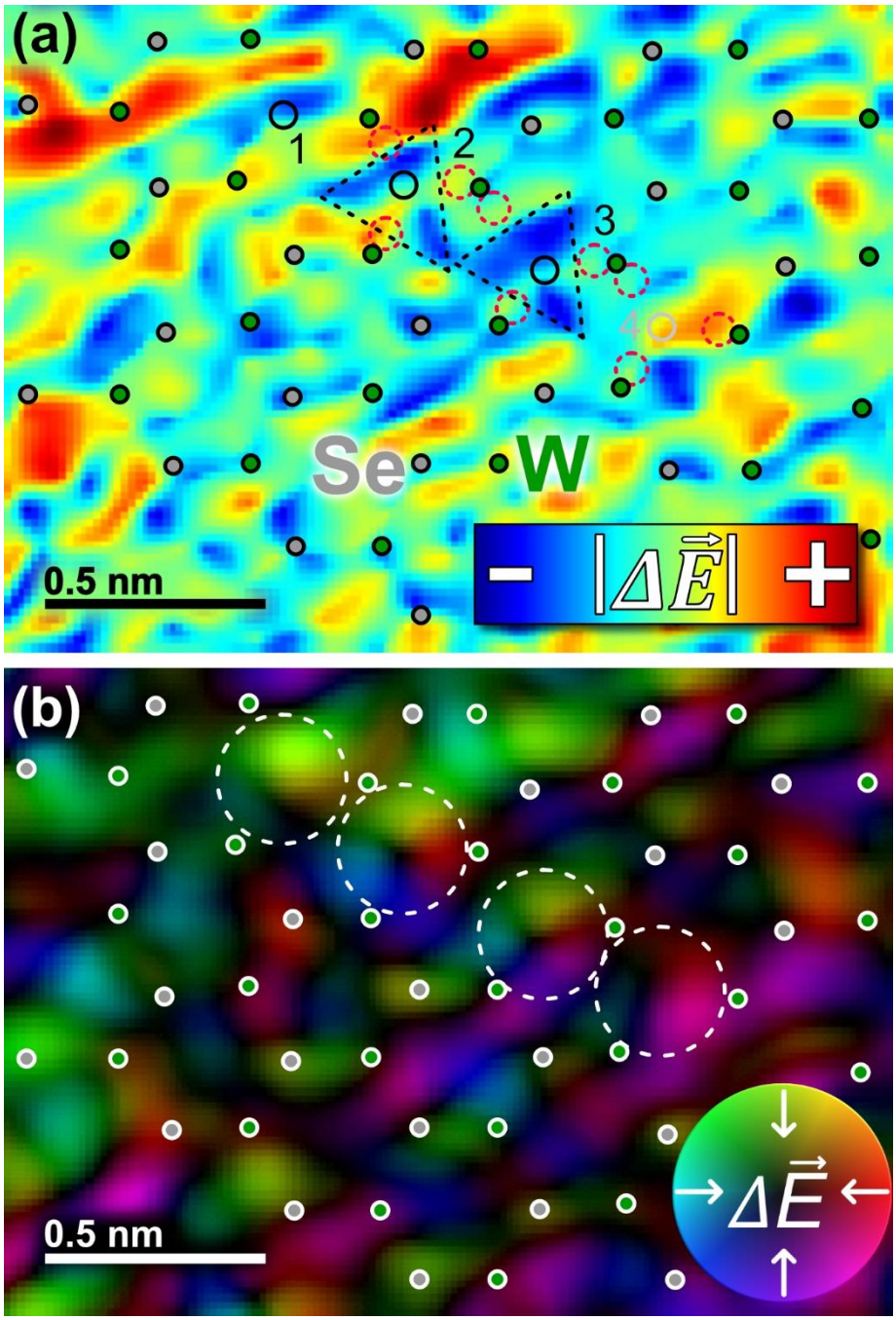

Figure 75: (a) Difference map $\Delta|\vec{E}| = |E_{\mathrm{defect}}| - |E_{\mathrm{pristine}}|$ of the electric field magnitude. (b) Colour-coded difference $\Delta\vec{E} = \vec{E}_{\mathrm{defect}} - \vec{E}_{\mathrm{pristine}}$ of the electric field vectors.

In the colour-coded difference map of electric field vectors in Fig. 75(b), colour wheels arise at the defect positions, resembling the electric field of atoms. Apart from the distinct colour wheels at defect positions, almost no other regular or periodic difference electric field distribution is observable. However, the difference in electric field distribution above the defect complex exhibits a dominant green colour, which might be due to bending of the lattice because of the line-like defect cluster or contamination.

Chapter summary

- This chapter shows application examples of differential phase contrast imaging. In each material system, rotationally symmetrical fields around atomic columns and consequently positive charge densities at the atomic column positions are measurable due to the dominant potential of nuclei. This confirms the applicability of DPC imaging for the characterisation of the electronic structure of various material systems. However, further methods and investigations are necessary to remove the strong influence of the atomic nuclei. In general, a good agreement between measurements and multislice image simulations for segmented detectors is observed.

- Chapter 6.1: The comparison of measurements with a segmented detector and a pixelated detector reveals that measurable electric field magnitudes and charge densities match in the order of magnitude but have significantly different features of measured electric field distribution due to different detector response functions.
- Chapter 6.1: It is demonstrated by using a 4D-STEM image of silicon in [110] zone-axis orientation with a sample thickness of (30 ± 2) nm that the signal most identical to the CoM signal is obtained with a segmented detector at 45° rotation to the dumbbell axis. Furthermore, it is advantageous if the direct beam completely illuminates the outer Layer2 as long as only Layer2 is used for the measurement of the DPC signal.
- Chapter 6.1: Using the increased azimuthal momentum space resolution (IAMSR) method, very good correlations can be obtained between the CoM signal and the signal from a multisegmented detector (up to a cross-correlation coefficients of 0.997 for derived charge densities). Interatomic pixels of IAMSR optimized DPC images do not show unexpected features, such as positive charge densities at positions where no atomic column is present. The IAMSR method is therefore promising to reduce diffraction artefacts even at such high specimen thicknesses.

- Chapter 6.2: For the first time, an InAs nanoisland with a width of 6.3 nm is analysed by STEM-DPC. The measurable electric field distribution in zinc blende InAs projected along the [110] zone-axis exhibits rotational electric fields around In and As atomic columns. The In atomic columns possess higher electric field magnitudes than the As atomic columns. In addition, a crescent-like feature around the In atomic column on the side opposite to the As atomic column is observed.

One possible cause for this crescent-like feature could be atomic bonds.

- Chapter 6.2: No characteristic change in the electric field distribution is measured across a twin boundary.

- Chapter 6.3: Two-dimensional WSe_2 is analysed by STEM-DPC. It is demonstrated that the DPC signal in combination with the HAADF intensity is promising to determine the stacking order of two-dimensional transition metal dichalcogenides. Simulations give evidence that in 2D materials the contrast of atomic columns is not solely determined by the projected depth integral of atomic numbers in atomic columns, but that the contrast is also influenced by the vertical order of atomic species in a column. This is due to a redistribution of electron probe intensity by the uppermost atomic layer, noticeable in extremely thin specimen.
- Chapter 6.3: In bi- and trilayers of WSe_2, a discrepancy between the expected and measured magnitudes of electric field and positive charge density between W and Se atomic column is observed, which can possibly be explained by a refocussing effect.
- Chapter 6.3: For the first time, vacancy-type defects in 2D-WSe_2 and their impact on the electric field distribution are investigated. By subtracting the field of an undisturbed lattice, a trident-star-shaped decrease of the electric field magnitude precisely around the defect site and an increase towards the adjacent W atomic columns for a completely missing Se atomic column are revealed.

7. Conclusions

In this work, contributions to the advancement of differential phase contrast (DPC) imaging in the STEM are made to investigate the electric field and charge density distributions of solids at sub-atomic resolution. While the DPC signal is sensitive to electric fields, it is concurrently sensitive to many influences, which make the correct image interpretation difficult, especially when using a segmented detector. For quantitative DPC imaging with segmented detectors it is crucial to know all influences, to understand how and to what extent they affect the DPC images, and to ideally be able to minimise their impact.

Therefore, key influences on DPC images acquired with a segmented detector are investigated in this work. The investigated influences include properties of the incident electron beam, dynamical diffraction effects, specimen tilt, detector type, shape, and orientation, as well as image noise. This is accomplished with multislice simulations of Si[110] and $SrTiO_3$[001] as well as comparative measurements of Si[110] and by using a disc-shaped segmented detector consisting of eight segments. Even though most influences are investigated for DPC images acquired with a segmented detector, many of the results also apply to other detector types.

The investigations utilise the scattergram which is a two-dimensional histogram of the quantity (e.g. electric field or beam deflection) displayed in the entire DPC image. Throughout this work, the scattergram has proven to be an excellent tool to investigate and detect the influences on DPC images, as they alter the scattergram characteristically. This allows to minimise the impact of the influences by using dedicated software for the scattergram calculation “in-line” with the DPC measurement. Furthermore, a novel method, the so-called scattergram filtering, is presented which enables to reveal the spatial distribution of DPC image features leading to characteristic scattergram features. Since the impact of many influences on the DPC signal are described and methods to minimise specific influences are presented, the results presented here may be of great interest to others and help to improve the accuracy of future DPC measurements.

It is shown that the use of a segmented detector has a significant impact on the features in the DPC image. This is caused by the fact that the DPC signal is deduced from an inhomogeneous and complex convergent beam electron diffraction (CBED) intensity distribution and the way the individual segments intersect the CBED pattern. The polar collection angles of the detector, which are experimentally adjustable by the camera length, influence the extension of measured electric field around individual atomic columns. The azimuthal collection angles can be adjusted by the detector rotation. The detector rotation significantly influences the directionality and magnitude of DPC image features, e.g. leading to unexpected positive charge densities at interatomic pixels. By applying the scattergram filtering technique, it was revealed that the detector rotation mostly impacts the DPC image features at interatomic pixels.

Changes of directionality and magnitude arising from the detector rotation make up a significant part of the measurable DPC signal at interatomic pixels.

To investigate the influence of the detector type, DPC images of Si[110] acquired with a segmented detector and a pixelated detector are compared. The comparison reveals that measurable electric field magnitudes and charge densities match in order of magnitude but have significantly different features. It is demonstrated for a (30 ± 2) nm thick Si specimen in [110] zone-axis orientation that the highest similarity of DPC images acquired with a segmented detector and a pixelated detector is obtained if the segmented detector is rotated by 45° to the Si dumbbell axis.

A promising method to increase the azimuthal momentum space resolution of segmented detectors is presented and experimentally validated. This method is introduced as the IAMSR (increasing azimuthal momentum space resolution) method and uses a series of DPC images at different detector rotations. By applying the IAMSR method, very high similarities up to cross-correlation coefficients of 0.997 can be obtained between DPC images acquired with segmented and pixelated detectors. After application of the IAMSR method, interatomic pixels do not show unexpected features, such as positive charge densities at positions where no atomic column is present.

Simulative investigations of the influence of the specimen thickness reveal that the measurable DPC signal is reduced with increasing specimen thickness. This is due to the increasing beam extension in the specimen, the extended beam experiencing increasingly inhomogeneous specimen potentials, and dynamic diffraction effects. These effects additionally result in line-like features in the DPC image arising from the symmetry of the CBED patterns and the detector.

The combined influence of defocus and specimen thickness is investigated by multislice image simulations of $SrTiO_3$[001]. It is observed that the optimum defocus to obtain the highest mean DPC signal magnitude in $SrTiO_3$ is below half the specimen thickness. In contrast, the optimum defocus to obtain a DPC image exhibiting the highest similarity to the DPC image of one unit cell is close to the specimen exit surface. It is worth to note that the optimum defocus values are different for other materials. In this work, a recipe is presented, which allows to experimentally find the defocus at which the highest similarity to the DPC image of one unit cell is achieved. For this, the defocus is first set to obtain the maximum DPC signal in the experiment. Afterwards, the defocus is adjusted according to the simulated difference between the defocus guaranteeing the maximum DPC signal and the defocus for the highest similarity to the image of a unit cell.

It is shown by using image simulations for $SrTiO_3$[001] that the acceleration voltage significantly influences the features in a DPC image, as it impacts the interaction of the electron beam with the specimen potentials and the distance of diffraction discs in the detection plane. The acceleration voltage influences the measured extension of electric fields around individual atomic columns. Notably, its impact depends on the atomic species in the atomic column. For an acceleration voltage of 30 kV and a 6.25 nm thick

$SrTiO_3$ specimen, rotational symmetric electric fields are only observed around O atomic columns. This can be explained by the propagation of the electron beam intensity which depends on the acceleration voltage. This dependency is investigated by simulations of the real space probe intensity distribution as a function of the $SrTiO_3$ specimen thickness for acceleration voltages of 30 kV and 200 kV.

The impact of the propagation of the electron wave within a specimen on the obtainable DPC image is further investigated by considering multislice image simulations of two atoms which are displaced in incident beam propagation direction. By varying the spacing of the atoms and acceleration voltage, it is found for the considered atomic species (Si, Se, and W) that the mean DPC signal magnitude obtainable for two atoms is always lower than two times the mean DPC signal magnitude of a single atom. This reduction in mean DPC signal can be ascribed to a redistribution of intensity by a coherent scattering of the electron wave at the first atom. This emphasises the fact that dynamic effects must be considered in the interpretation of the interaction of an electron beam and the specimen for accurate quantitative DPC imaging even in the case of ultimately thin specimens.

Besides the defocus, also the impact of higher order lens aberrations on the DPC signal is investigated by using multislice image simulations of $SrTiO_3$[001]. The higher order lens aberrations include two-fold astigmatism, coma, third-order spherical aberration and six-fold astigmatism. All lens aberrations reduce the measurable DPC signal and introduce features according to the symmetry of their respective aberration phase plate. The influences of the lens aberrations are also detectable in the corresponding scattergrams which characteristically deviate from a scattergram of an aberration free image. The deviations particularly depend on the symmetry of the aberration phase plate.

Moreover, the influence of specimen tilt is investigated by simulations of $SrTiO_3$[001] as well as a comparison of simulated and measured DPC images of Si[110]. With increasing tilt, an elongation of features in the DPC image and the formation of an off-centre maximum in the scattergram distribution is evident. Even for tilts below 5 mrad, the scattergram distribution exhibits significant differences to the one obtained with a perfectly oriented specimen although almost no differences of the DPC images are visible to the naked eye.

Image noise which is present due to the finite dose conditions reduces the precision of the transferred momentum measurement and results in a blurring of features of the scattergram distribution. It is shown in this work that the magnitude of blurring depends on the inverse square root of the dwell time. To guarantee the necessary precision in momentum space, a method to assess the minimum dwell time is described.

The present thesis also includes application examples of differential phase contrast imaging of monocrystalline Si, an InAs nanoisland containing several rotational twin boundaries, and pristine as well as defective multilayers of 2D-WSe_2. These are accomplished by using state-of-the-art C_s-corrected scanning transmission electron

microscopes (STEM) which are equipped with a segmented or a pixelated detector. Independent of the material system, rotationally symmetric fields around atomic columns, electric field minima at high symmetry points of the crystal lattice, and positive charge densities exactly at the atomic column position are observed. Additionally, good agreements between the measurements and multislice image simulations are evident. All the measurements and in particular the measurement of a 30 nm thick Si specimen in [110] zone axis orientation showed the expected strong influence of the atomic nuclei on the DPC measurement. The DPC measurements on the 30 nm thick Si specimen also confirmed the sensitivity of DPC imaging to the previously investigated influences.

Investigations of the 6.3 nm thick InAs nanoisland revealed that the In atomic columns exhibit higher electric field magnitudes and higher positive charge density values than the As atomic columns in zinc blende InAs[110]. This is in good agreement to the expectations, as In atoms have a higher atomic number. In addition, crescent-shaped features of increased electric field magnitude are observed around the In atomic columns, which can presumably be explained by the presence of atomic bonds. DPC measurements of an InAs rotational twin boundary revealed no characteristic change in the electric field distribution due to the presence of the defect.

Investigations of the electric field and charge density distributions in bi- and trilayers of 2D-WSe_2 are presented. Due to its very small thickness, 2D-WSe_2 is an excellent material to explore the capabilities of DPC. It is shown that the DPC signal in combination with the HAADF intensity is promising to determine the stacking order of WSe_2 layers, as both the DPC and the HAADF are characteristically influenced by the vertical order of atomic species in a column. Moreover, it is observed that higher electric field magnitudes and positive charge densities are observed around pure Se atomic columns in WSe_2 bi- and trilayers, although higher values expected for pure W atomic columns due to their higher projected depth integral of atomic number. This discrepancy can possibly be explained by the redistribution of electron probe intensity by the uppermost atomic layer. The impact of vacancy-type defects in 2D-WSe_2 on the electric field distribution is revealed by subtracting the field of an undisturbed lattice. A trident-star-shaped decrease of the electric field magnitude precisely at the defect sites and increased magnitudes at adjacent W atomic columns are observed for a completely missing Se atomic column and there are indications that this is a common feature of vacancy-type defects in hexagonally ordered 2D materials.

All in all, these results render DPC imaging a very promising technique to accurately quantify electric field distributions and charge densities in solid materials at atomic resolution if residual influence of the experimental technique itself are minimised or at least included in the interpretation. Besides the electric field and charge distributions, DPC imaging can provide additional information, such as the stacking of WSe_2 layers. Since such additional information is not accessible with conventional STEM techniques, DPC is one of the most interesting methods in the research field of electron microscopy.

Appendix

The Appendix includes the description of the correction of image artefact, further supporting information, such as additional DPC image simulations, as well as the parameter for the acquisition of DPC images and multislice image simulations.

A.1. Correction of image artefacts

This chapter describes the corrections of machine-induced artefacts which are typically present in DPC images. Although several routines for the optimisation and analysis of DPC images already exist [250, 251], a customised, self-written *MATLAB* application (*DPCToolbox*) was developed for DPC imaging using an eight-fold segmented SAAF detector. The corrections, which are possible with the *DPCToolbox* and applied to most of the experimental data of this thesis, are explained in the following. These include the correction of the rotation of the deflection direction in the DPC images (Chapter A.1.1), the correction of imperfect beam centring during the measurement (Chapter A.1.2), the correction of the background due to missing or imperfectly tuned descanning coils (Chapter A.1.3) and the correction of anisotropy of detector sensitivity in Chapter A.1.4. All these corrections are carried out in post-processing and can be applied in an arbitrary order.

Most of the corrections exploit a characteristic signal, the so-called background which arises due to missing descanning coils. The beam is not redirected back to the optical axis at every scan position resulting in an analogous scanning of the beam on the detector. Hence, a transferred momentum distribution is measurable due to the displacement of the beam on the detector. The magnitude of displacement depends on the extension of the scanning area (determined by magnification), as well as the camera length.

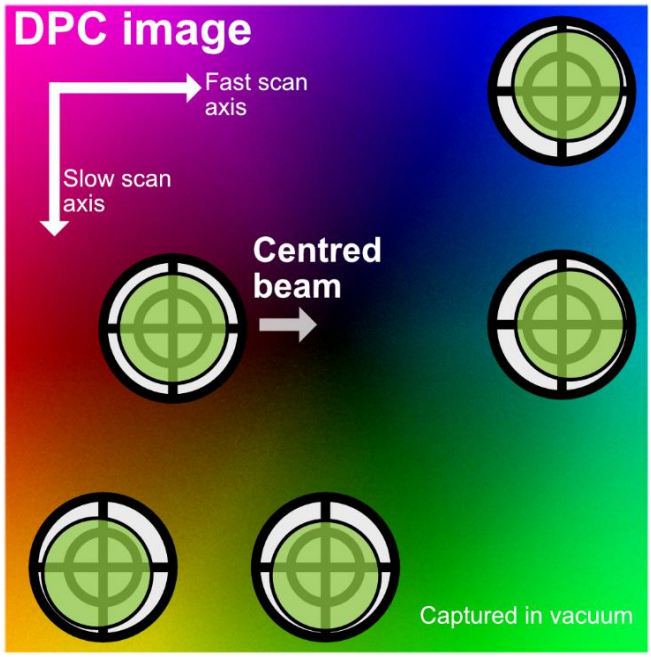

Figure 76: DPC image recorded from an area only containing vacuum. Such a DPC image is used for the explanation of the origin and characterization of a so-called background in DPC images at intermediate magnification. The background arises due to large-area scanning of the beam without descanning coils. The scanning of the beam on the specimen is projected on the detector.

A typical background is exemplarily shown in Fig. 76. This background is visible as an inverted colour wheel distribution which is centred in the DPC image. It is to note that for the DPC image shown in Fig. 76, a pure vacuum area without any specimen material was chosen, as the presence of material might otherwise interfere with the characterisation of the background. Fig. 76 additionally

contains schematics of the scan-position-dependent displacement of the beam on the detector and highlights the fast and slow scan axes. For example, if the beam is scanned from the centre to the right (in direction of the fast scan axis), a displacement of the beam on the detector to the right is visible resulting in a light blue colour in the DPC image. It can also be seen in Fig. 76 that transferred momenta with small magnitudes (centre of the inverted colour wheel) are measurable in the centre of the DPC image. The position of the inverted colour wheel centre is influenced by the initial beam centring. If the beam centring is properly conducted the beam is also centred on the detector in the middle of the image.

Although the background itself is considered an artefact, it facilitates the corrections of some of the other artefacts. In the following, the rotation, centring and background corrections are exemplarily shown using a DPC measurement of SiO_2 spheres with a mean diameter of about 130 nm, which were deposited on a lacey carbon grid by casting and drying of a suspension droplet. Fig. 77 shows the HAADF and DPC images as well as images of the difference signals S_x and S_y of the SiO_2 spheres without any processing. The HAADF image in Fig. 77(a) shows several spheres on the lacey. A material accumulation on the connecting axes between the spheres can be observed (marked by a red circle in Fig. 77(a)) that can be attributed mainly to residuals in the liquid phase of the suspension and material diffusion to minimise surface energies [252].
The difference signals, S_x and S_y, in Fig. 77(b) and Fig. 77(c) exhibit increased signal difference at the edges of the spheres. Here, the background is visible as a long-range gradient in the images. As the spheres consist of amorphous material, the DPC signal is expected to only arise from gradients of projected mean inner potential and thus from local changes of the specimen thickness. As the thickness increases towards the geometrical centre of each individual sphere, a colour wheel is expected for each sphere in the DPC image in Fig. 77(d). However, the spheres show a dominant blue to purple colour, and an increased intensity at the edges of the spheres.
The corresponding scattergram (for more information on the scattergram see Chapter 4.2) is depicted in Fig. 77(e). It exhibits several dominant features, e.g. a square-like feature, which can be assigned to the background. This square-like feature is rotated clockwise by an angle of about 40°. Furthermore, two dominant triangular features (corresponding to deflections represented by purple and green colours) and a tail-like extension of the scattergram which protrudes towards the left (bright blue) can be observed. It can clearly be seen that the scattergram distribution is not centred on the scattergram. The deviations can be attributed to an imperfect beam centring on the detector which was conducted prior to taking the image.

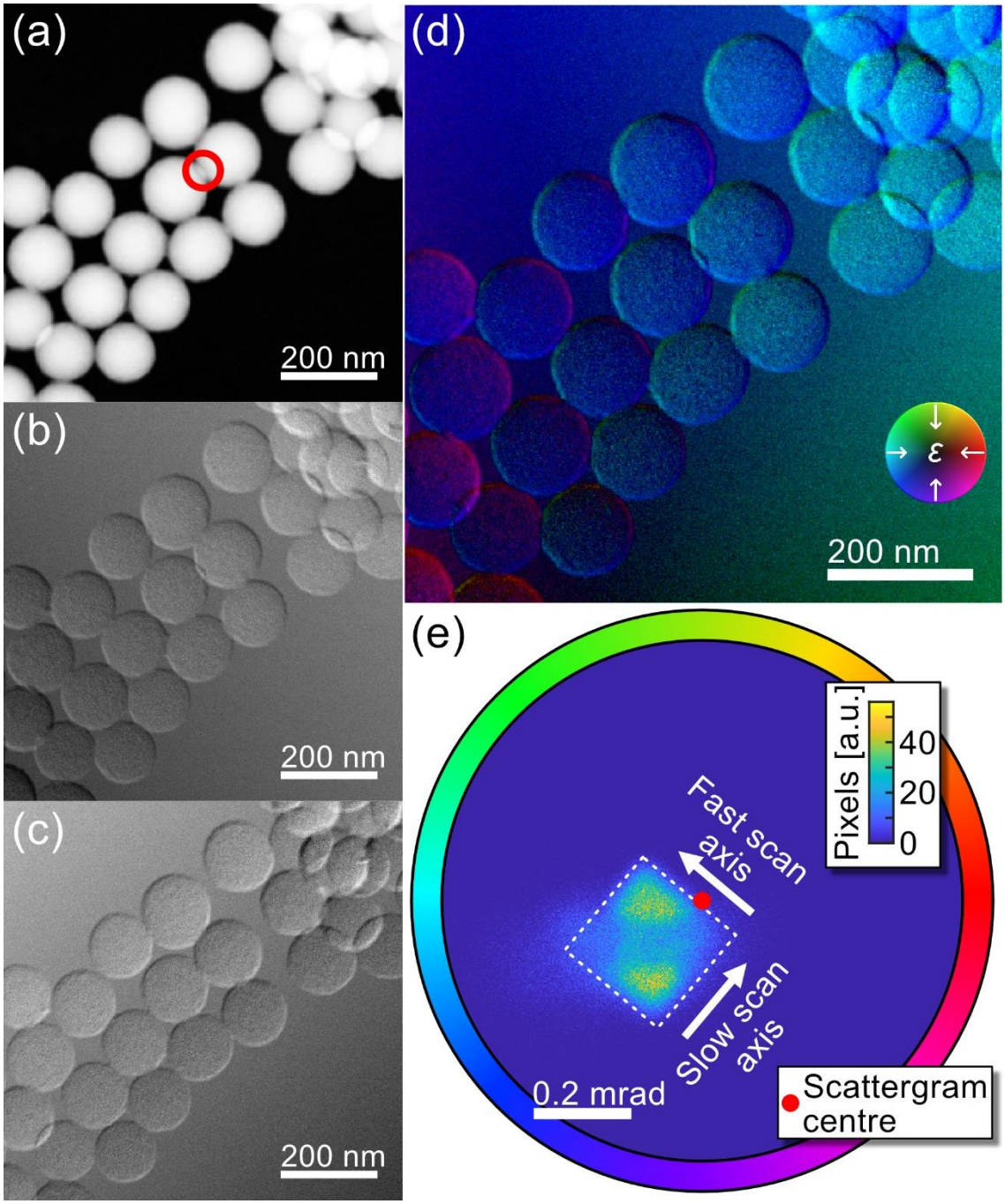

Figure 77: (a) HAADF image of SiO_2 spheres on a lacey grid. The carbon film of the lacey grid completely covers the image areas. The images based on the difference signals in (b) x- and (c) y-direction show an intensity gradient in the background. (d) Colour-coded DPC image of the measured deflection angle which was calculated from the difference signals S_x and S_y. (e) Scattergram of the DPC image.

A.1.1. Basic rotation angle

One of the necessary corrections is the rotation correction. This correction aligns the detector directions (S_x and S_y or k_x and k_y) with the image directions (x and y). Only a proper rotation correction allows to obtain reliable quantitative information including accurate charge densities. The charge density particularly depends on accurate directions as it is calculated from the two-dimensional divergence of the electric field vectors.

The difference of detector directions and image directions results from three different factors: (1) the Lorentz force in the magnetic field of the projection lenses rotating the CBED pattern by a basic rotation angle φ_{Basic}, (2) the detector rotation $\varphi_{\mathrm{Detector}}$ and (3) the scan rotation φ_{Scan}.
Several things are to note for the individual contributions. The basic rotation angle is determined by the imaging mode (low magnification or high-resolution mode), the camera length and the acceleration voltage, as it depends on the impact of the Lorentz force on accelerated electrons in the magnetic field of the projection lenses. Furthermore, it is not absolutely necessary to know whether the beam is rotated in a range of 0° to 360° or plus multiples of 360°.
Rotating the detector also azimuthally rotates the x- and y-directions of the detector around the optical axis resulting in a different orientation between the x- and y-directions of the DPC image and the k_x- and k_y-directions of the detector. It is to note that the detector is typically not installed in a way that its k_x- and k_y-directions are aligned with the image directions. This results in an angle which is included in the basic rotation angle φ_{Basic} and not in the detector rotation angle $\varphi_{\mathrm{Detector}}$ as it is constant.
The scan rotation changes the x- and y-directions of the image leading to a different orientation between x- and y-directions of image and detector. The scan rotation does not rotate the CBED pattern on the detector.

All three above-mentioned contributions can be included in a single correction rotation angle $\varphi_{\mathrm{Correction}}$ given by:

$$\varphi_{\mathrm{Correction}} = \varphi_{\mathrm{Scan}} + \varphi_{\mathrm{Basic}} + \varphi_{\mathrm{Detector}}. \tag{61}$$

The rotation correction is based on the recalculation of the S_x and S_y signals using $\sin$ and $\cos$ functions. For the corrected difference signal $S_{x,\mathrm{Rotation}}(\vec{R})$ in x-direction follows

$$S_{x,\mathrm{Rotation}}(\vec{R}) = -\sqrt{\left(\mathrm{S}_x^2(\vec{R}) + \mathrm{S}_y^2(\vec{R})\right)} \cdot \sin\left(\varphi_{\mathrm{DPC}}(\vec{R}) + \varphi_{\mathrm{Correction}}\right), \tag{62}$$

and for the $S_{y,\mathrm{Rotation}}$ signal

$$S_{y,\mathrm{Rotation}}(\vec{R}) = -\sqrt{\left(\mathrm{S}_x^2(\vec{R}) + \mathrm{S}_y^2(\vec{R})\right)} \cdot \cos\left(\varphi_{\mathrm{DPC}}(\vec{R}) + \varphi_{\mathrm{Correction}}\right), \tag{63}$$

in which S_x and S_y depict the original difference signals in x- and y-direction and φ_{DPC} the azimuthal deflection direction at probe position $(\vec{R})$. The colour-coded DPC image is afterwards recalculated based on the $S_{x,\mathrm{Rotation}}(\vec{R})$ and $S_{y,\mathrm{Rotation}}(\vec{R})$ images. It is to note that the minus signs are included in the correction to account for the definition of directionalities and the colour-code.

As the scan rotation and the detector rotation can be precisely adjusted, the only unknown rotation angle is the basic rotation angle φ_{Basic}. One possible method to determine φ_{Basic} is explained in the following. This method is based on two-steps and exploits a background which is experimentally acquired with both φ_{Scan} and $\varphi_{\mathrm{Detector}}$ set to 0°, i.e. the difference of image and detector directions results only from φ_{Basic}.
First, two-dimensional polynomial functions are fitted to the S_x and S_y images. The polynomial functions are based on the following models:

$$S_{x/y,\mathrm{fit}}\left(\vec{R}=(x,y)\right)=\mathrm{p}_{x/y,00}+\mathrm{p}_{x/y,10}\cdot\mathrm{x}+\mathrm{p}_{x/y,01}\cdot\mathrm{y}. \tag{64}$$

Here, $S_{x/y,\mathrm{fit}}\left(\vec{R}\right)$ denotes the resulting fit for the individual difference signal of S_x and S_y, $\mathrm{p}_{x/y,00}$, $\mathrm{p}_{x/y,10}$, $\mathrm{p}_{x/y,01}$ the fitting coefficients and $\vec{R}=(x,y)$ the beam position. Using such a first order polynomial function for the background is reasonable, as the displacement of the beam on the detector is relatively small when an intermediate magnification is used and the difference signals S_x and S_y are expected to be linear in dependence of the beam position.
Second, the basic rotation angle is calculated from the angular difference of the directions of the intensity gradients of the fitted $S_{x/y,\mathrm{fit}}$ images and an ideal S_x and S_y images with perfect rotation alignment. In a DPC image with perfect rotation alignment, the intensity gradient in the $S_{x,\mathrm{fit}}\left(\vec{R}\right)$ only has directional components in the x-direction of the image, while the intensity gradient in the $S_{y,\mathrm{fit}}\left(\vec{R}\right)$ only exhibits components in the y-direction of the image. In presence of a basic rotation, the individual intensity gradients of the $S_{x/y,\mathrm{fit}}$ images exhibit components in both the x- and y-direction. The corresponding angles can be derived from $\mathrm{p}_{x/y,10}$ and $\mathrm{p}_{x/y,01}$ by using a tangent relation. The overall basic rotation angle is then determined from the mean angular difference of the $S_{x/y,\mathrm{fit}}$ intensity gradients to the ideal intensity gradients.

The determination of φ_{Basic} and the subsequent correction is shown in the following. Fig. 78(a) depicts a DPC image which is captured with φ_{Scan} and $\varphi_{\mathrm{Detector}}$ set to 0°, a camera length of 12 cm and at an acceleration voltage of 200 kV. The corresponding difference signals, which are individually normalised, are displayed in Fig. 78(b) and Fig. 78(c). The resulting fitted signals $S_{x/y,\mathrm{fit}}\left(\vec{R}\right)$ as well as the calculated directions of the gradients are depicted in Fig. 78(d) for the S_x signal and in Fig. 78(e) for the S_y signal, respectively. The individual directions of the gradients of the individual fits are depicted by blue arrows. In addition, the directions of the gradients for a background without the presence of basic rotation are given by the orange arrow. For φ_{Basic}, the mean angular difference between the orange and the blue direction are calculated. Here, φ_{Basic} amounts to $(40.8\pm0.07)°$.

To investigate the magnification range for which this approach to measure the basic rotation angle is reasonable, Fig. 78(f) displays the calculated basic rotation angles (without scan and detector rotation) for magnifications ranging from 20k to 5M. All

determined basic rotation angles are found close to 41°. For magnifications below 200k, an increased basic rotation angle is observed. This increase in basic rotation angle with decreasing magnification originates from the fact that the scanning of the direct beam on the detector is influenced by the initial beam position (beam centring) as well as the anisotropy of the detector sensitivity (Chapter A.1.4). These influences lead to nonlinear S_x and S_y signals, different directions of the gradients of the S_x and S_y images and thus to a background deviating from a perfect background. For magnifications above 1M, strongly fluctuating basic rotation angles are observed which arise due to the presence of image noise and decreasing background signal.

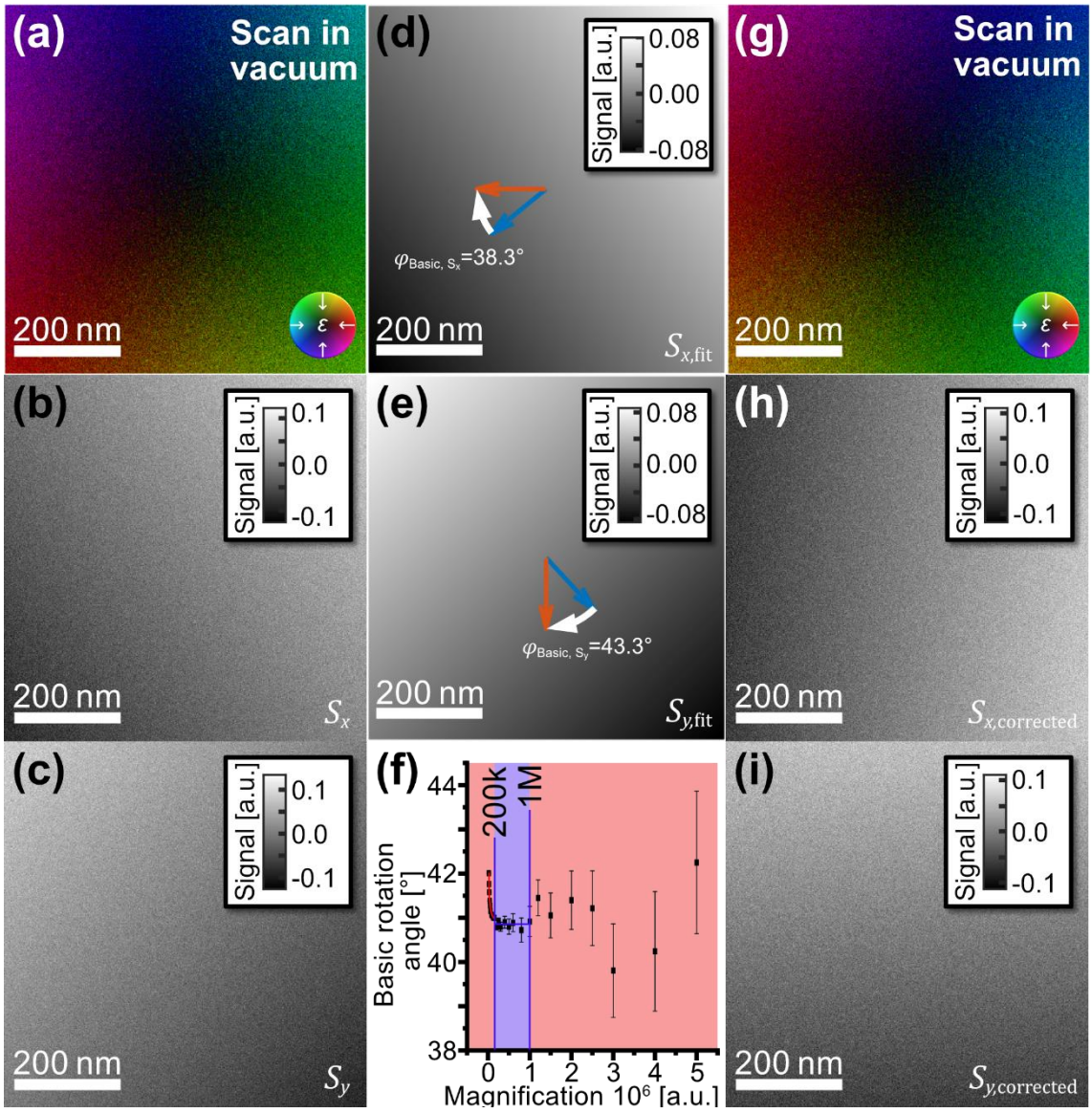

Figure 78: (a) DPC image of a large scan in vacuum, with corresponding (b) S_x and (c) S_y images. (d) Resulting fit for the S_x image and (e) for the S_y image, respectively. The blue arrows depict the direction of negative gradient of the surface fits in (d) and (e). For rotation corrected image, the ideal directions of negative gradient in S_x and S_y image are depicted by the orange arrows. (f) Rotation angles determined via the fit function in dependence of the magnification.

To calculate the basic rotation angle for the considered microscope settings (high-resolution mode, acceleration voltage of 200 kV and camera length of 12 cm), a fit of

form $y = a_{\mathrm{rotation}}$ is considered in the magnification range from 200k to 1M. Here, $a_{\mathrm{rotation}} = \varphi_{\mathrm{Basic}}$ is the fit parameter which corresponds to the basic rotation angle. The resulting rotation angle amounts to $\varphi_{\mathrm{Basic,200\,kV}} = (40.8 \pm 0.06)°$. This basic rotation angle is considered in all experiment DPC images shown in this thesis which are obtained at an acceleration voltage of 200 kV using a camera length of 12 cm. For an acceleration voltage of 80 kV, the basic rotation angle is analogously determined and amounts to $\varphi_{\mathrm{Basic,80\,kV}} = (180 \pm 1)°$ for the same camera length.

The rotation corrected DPC, $S_{x,\mathrm{Rotation}}$ and $S_{y,\mathrm{Rotation}}$ images are displayed in Figs. 78(g-i). An inverted colour wheel is observed in the DPC image in Fig. 78(g). In addition, the gradient inside the $S_{x,\mathrm{Rotation}}$ and $S_{y,\mathrm{Rotation}}$ point towards their respective x- or y-directions.

In the following, the rotation correction is applied to the DPC image of the spheres on Lacey film, which was already shown in Fig. 77. As a camera length of 12 cm and an acceleration voltage of 200 kV were used during acquisition and the scan and detector rotation amounts to 0°, a rotation correction with $\varphi_{\mathrm{Basic}} = 40.8°$ is applied.

Fig. 79(a) shows the DPC image after rotation correction. While the uncorrected DPC image in Fig. 77(d) is dominated by purple and green colours, the rotation corrected DPC image exhibits dominant purple and blue colours. This is evident in the scattergram in Fig. 79(b), which shows a strong accumulation of pixels in the interval of deflection distribution which corresponds to a purple colour in the DPC image. Compared to the uncorrected scattergram in Fig. 77(e), the entire scattergram is rotated around the scattergram centre by an angle of 40.8°.

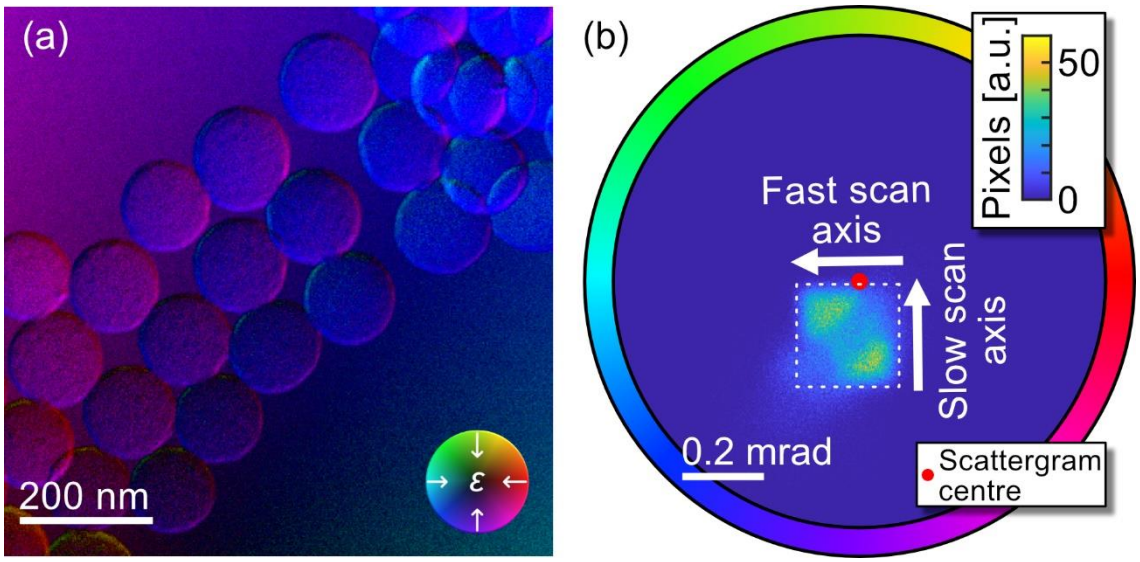

Figure 79: (a) DPC image of the SiO_2 spheres on lacey grid shown in Fig. 77 after rotation correction. (b) corresponding scattergram.

A.1.2. Initial beam centring

The beam is centred on the detector using a manual centring routine before each measurement, which is guided via a crosshair function implemented in the *SAAF Center* (software delivered by the manufacturer for the acquisition of DPC images with the segmented annular all-field detector). The crosshair function displays an uncalibrated centre of mass (CoM) of the intensity on all detector segments. By aligning the CoM with crosshair, centring is achieved.

This routine is ideally performed in vacuum, without specimen structure and with a stationary beam (or at the maximum magnification). Since this procedure is conducted manually, it is prone to errors. As subsequent traveling to the desired specimen area is required, any instability in the projection lens system or the presence of stray fields can introduce additional displacements of the beam on the detector prior to the acquisition of the DPC image. It is therefore likely that the DPC measurements show a strong dominant deflection due to the displacement of the CBED pattern before DPC image acquisition.

In the following a post-processing correction of the initial beam centring is described, which utilises the scattergram distribution. The correction is explained with the help of a DPC image recorded in vacuum. Fig. 80(a) shows a DPC image which is dominated by a deflection direction due to the imperfect centring of the beam prior to image acquisition. Here, the imperfect centring of the beam results from an intentional deflection using the projector lens alignment (see also Chapter 3.1). More precisely, the beam was deflected by ten coarse steps of the projector lens deflectors resulting in a dominance of green colour in the DPC image. The initial beam position and its deflection angle ε are schematically indicated in the inset in Fig. 80(a). It can be assumed that the projector lens alignment is stable during a measurement and the deflection due to the initial centring is significantly less than the maximum measurable deflection before the detector exhibits non-linear dependencies of the signal on the deflection angle [38]. The measured offset due to the initial beam centring is therefore constant and can be subtracted from each pixel.

Fig. 80(b) shows the corresponding scattergram which exhibits a square-like distribution of deflections which is found off-centre. The off-centre position of the scattergram feature arises precisely because of the initial centring. The square shape of the distribution results from the background signal.

The correction of the initial beam centring is typically achieved by subtracting average signals $S_{x,\mathrm{Offset}}$ and $S_{y,\mathrm{Offset}}$ from each pixel of the $S_x(\vec{R})$ and $S_y(\vec{R})$ images [251]. This results in the beam position corrected image $S_{x,\mathrm{Centred}}(\vec{R})$ for the x-direction

$$S_{x,\mathrm{Centred}}(\vec{R}) = S_x(\vec{R}) - S_{x,\mathrm{Offset}}, \tag{65}$$

and for the $S_{y,\mathrm{Centred}}(\vec{R})$ signal in y-direction

$$S_{y,\mathrm{Centred}}(\vec{R}) = S_y(\vec{R}) - S_{y,\mathrm{Offset}}. \tag{66}$$

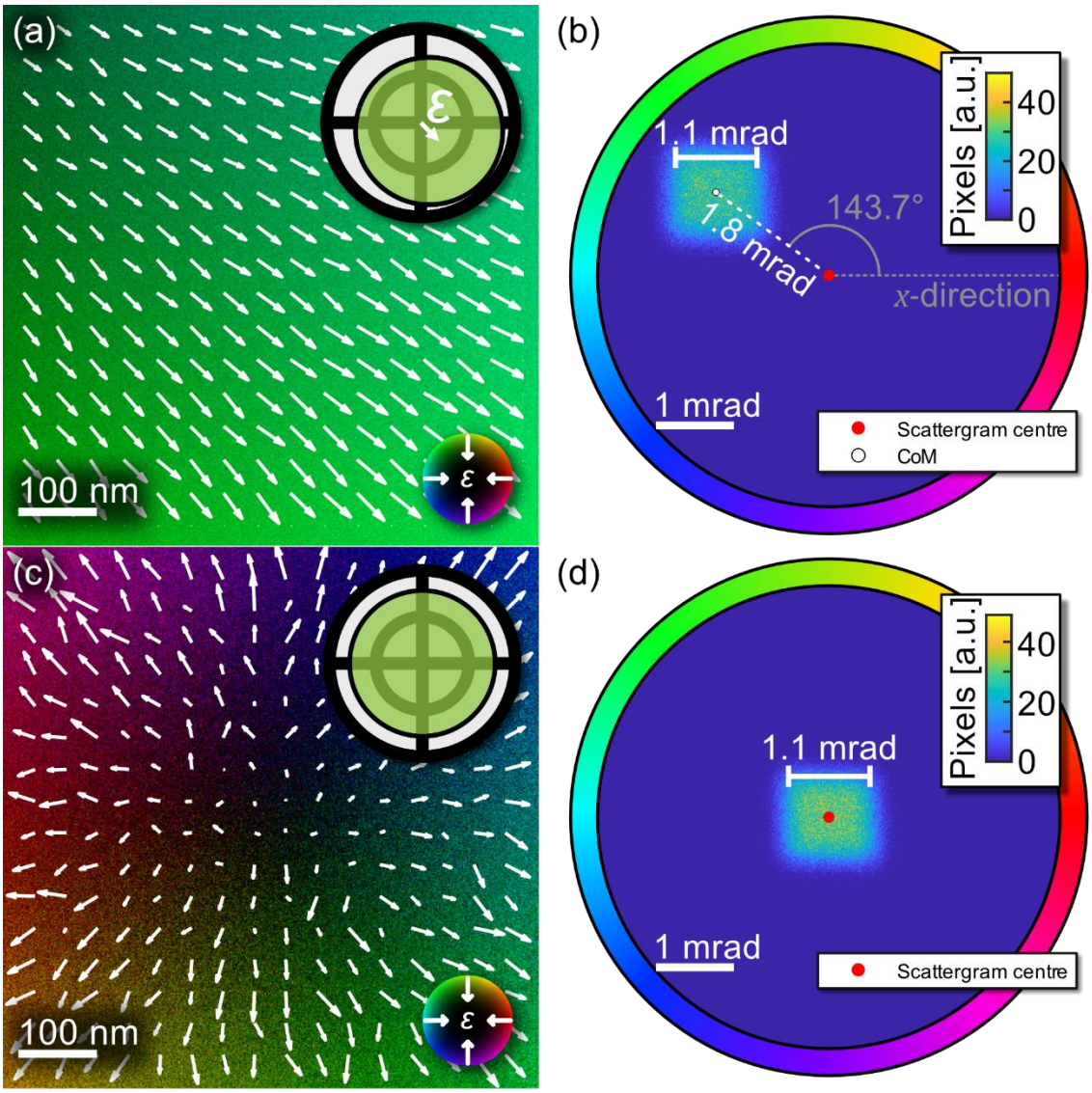

Figure 80: (a) DPC image of a scan in vacuum, with an initial imperfect centring of the beam and the corresponding scattergram in (b). The quiver plot on top of the DPC image in (a) depicts the deflection directions. For information on the annotations inside the scattergram in (b) the reader is referred to the main body of the text. (c) DPC image with quiver plot after beam centring correction of the DPC image shown in (a). For the centring the CoM method (described below) is used. The sketches in (a) and (b) display the beam position before DPC image acquisition and the corresponding beam position after centring. (d) Scattergram after centring correction.

There are several methods to determine $S_{x,\mathrm{Offset}}$ and $S_{y,\mathrm{Offset}}$. For example, the average difference signals S_x and S_y of areas or the entire DPC image are used in the literature [251]. Since stray fields or other artefacts such as specimen tilt have an influence on the mean signal, the correction is prone to errors. In the following, the correction of initial beam centring is conducted with the help of the scattergram, which offers several approaches to correct for the initial beam centring. Here two approaches are explained, which are based on the centre of mass (CoM) and the overall maximum

of the scattergram intensity distribution. It is to note that the scattergram also allows for centring using any arbitrary feature of the scattergram distribution. Technically, this can also be achieved by clicking with the mouse on a certain coordinate inside the scattergram which is displayed in the *DPCtoolbox*.

For both approaches the coordinates of the CoM or the overall maximum $\vec{P}_{\mathrm{Max}}$=$(P_{x,\mathrm{Max}}, P_{y,\mathrm{Max}})$ must be determined. With $\vec{P} = (P_x, P_y)$ being the pixel coordinates of the scattergram pixels, the beam centring corrected difference signals $S_{x,\mathrm{Centred}}$ and $S_{y,\mathrm{Centred}}$ are given by

$$S_{x,\mathrm{Offset}} = c_{\mathrm{Scattergram}} \cdot (P_{x,\mathrm{CoM/Max}} - b/2) \tag{67}$$

and

$$S_{y,\mathrm{Offset}} = c_{\mathrm{Scattergram}} \cdot (P_{y,\mathrm{CoM/Max}} - h/2). \tag{68}$$

Here, $c_{\mathrm{Scattergram}}$ denotes the calibration factor of the scattergram, which defines the difference signal per scattergram pixel. The parameters b and h represent the pixel width and pixel height of the scattergram. After correction, the colour-coded DPC image calculated from $S_{x,\mathrm{Offset}}$ and $S_{y,\mathrm{Offset}}$.
While the determination of the pixel coordinates of the global scattergram maximum $\vec{P}_{\mathrm{Max}}$ is straightforward, the calculation of the CoM requires an additional step. The calculation of the coordinates of the CoM is achieved using

$$\vec{P}_{\mathrm{CoM}} = \left(\left(\left(\sum_{j=1}^{N} I_{j,\mathrm{Scat.}} \cdot P_{x,j} \right) \Big/ N \right), \left(\left(\sum_{j=1}^{N} I_{j,\mathrm{Scat.}} \cdot P_{y,j} \right) \Big/ N \right) \right), \tag{69}$$

in which $I_{j,\mathrm{Scat.}}$ denotes the intensity and $P_{x,j}$ as well as $P_{y,j}$ represent the coordinates of the jth scattergram pixel, $N_{\mathrm{px}} = \mathrm{b} \cdot \mathrm{h}$ is the total number of scattergram pixels.

There are different cases in which one of the above-mentioned methods is more suitable for correction. If the measured deflection distribution features a strong image noise, for example, the CoM method is usually more suitable. In Chapter 5.5, in which the influence of specimen tilt on the DPC signal and the corresponding scattergram was studied, an off-centre maximum was observed. This off-centre maximum does not necessarily coincide with the coordinates of the scattergram's CoM. It might therefore be beneficial to use the overall scattergram maximum for correction.

In the scattergram in Fig. 80(b), a square-like feature can be observed. The CoM of the scattergram intensity is indicated by a white dot, which is found at a deflection angle of 1.8 mrad from to the scattergram centre and at an azimuthal angle of 143.7° to the x-axis in the scattergram. Fig. 80(c) displays the centring corrected DPC image. Instead of a dominant deflection which was evident from the green colour in the colour-coded

DPC image in Fig. 80(a), Fig. 80(c) shows typically colour distribution of the background due to the missing descanning coils (Chapter A.1). The corresponding scattergram in Fig. 80(d) also exhibits a square-like feature, which is allocated around the scattergram centre after centring correction. Lines, indicating a deflection interval of 1.1 mrad are given as reference to illustrate that the correction just shifts the scattergram feature to the scattergram centre.

The correction of initial beam centring on the example of the SiO_2 spheres on the lacey grid is shown in Fig. 81. In this case, the correction is based on the CoM of the scattergram distribution. The DPC image prior to correction is depicted in Fig. 79(a). A deflection offset of 0.14 mrad in the azimuthal direction of 256.4° to the x-axis was subtracted. As can be seen from Fig. 81(a), the inverted colour wheel due to the missing descanning coils is visible and contrasts at the sphere edges are more pronounced.

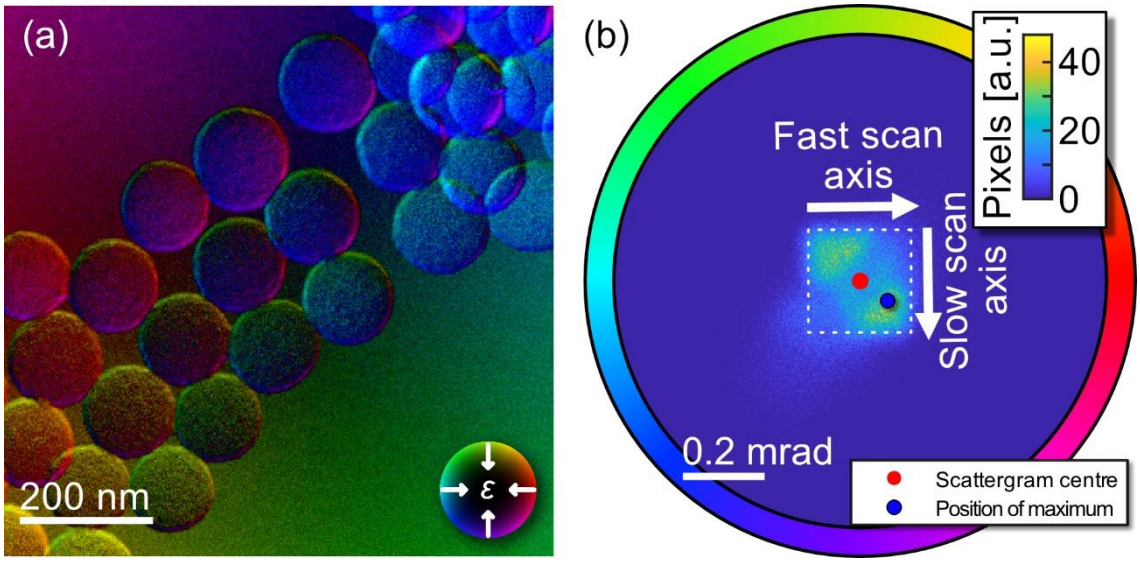

Figure 81: (a) DPC image of SiO_2 spheres on a lacey grid after centring and rotation correction. The uncorrected image can be found in Fig. 79(a). (b) Corresponding scattergram.

The corresponding scattergram in Fig. 81(b) shows that the square-like feature, which is resulting from the background and marked by a white dashed square, is aligned with the centre of the scattergram. Furthermore, the position of the intensity maximum of the scattergram is marked by a blue dot. In this case, a correction based on the global maximum of the intensity distribution of the scattergram would not have been appropriate.

A.1.3. Descanning background

The background which was introduced in Chapter A.1 can have a strong influence on the measurable DPC signal. This is particularly true for DPC image acquired with low magnifications or in other words for large-area scans. For the interpretation of the electric field, it is necessary to correct the background. Present backgrounds might result in a reduction or even cancellation of measurable transferred momenta in areas where the specimen-induced transferred momenta are in opposite direction to the transferred momenta of the background. It is also possible that the background enhances the measurable transferred momenta. It is therefore particularly important to correct the background before calculating the charge density (dDPC) or the specimen potential (iDPC).

In the following, a method to correct the background is presented which is based on a subtraction of pure background signals $S_{x,\mathrm{Back}}(\vec{R})$ or $S_{y,\mathrm{Back}}(\vec{R})$. This results in the background corrected signal $S_{x,\mathrm{Back.-Corrected}}$ in x-direction

$$S_{x,\mathrm{Back.-Corrected}}(\vec{R}) = S_x(\vec{R}) - S_{x,\mathrm{Back}}(\vec{R}) \tag{70}$$

and the signal $S_{y,\mathrm{Back.-Corrected}}$ in y-direction

$$S_{y,\mathrm{Back.-Corrected}}(\vec{R}) = S_y(\vec{R}) - S_{y,\mathrm{Back}}(\vec{R}). \tag{71}$$

The pure background signals $S_{x/y,\mathrm{Back}}$ are obtained from fitting a background model to the difference signals S_x and S_y of the original data or of a separate DPC image acquired in vacuum. In this thesis, several models based on polynomial functions are considered, which are given by

$$S_{x/y,\mathrm{Back}} = \sum_{i=0}^{l}\sum_{j=0}^{m} p_{i,j} x^i y^j . \tag{72}$$

Here, l and m represent the order of polynomial function. It is to note that only functions with the same order in x-and y-direction are used ($l = m$). In addition, polynomial functions up to the third order are considered. Consequently, the models denoted as Poly11, Poly22 and Poly33 are used for the calculation of the background. The numbers in the nomenclature of the models determine the parameters l and m.

Generally, the pure background signals can be determined from the DPC image, which is to be corrected, or from a DPC image without a specimen. The former approach is reasonable for DPC images with almost isotropically distributed transferred momenta, such as DPC images at atomic resolution. The latter must be captured with the same microscope settings.

In the following, all models are examined to test the magnifications for which they result in a reasonable approximation of the pure background. Fig. 82(a) shows the DPC images acquired in vacuum with magnifications of 25k, 50k, 100k and 200k (split into rows). These DPC images are captured with a camera length of 12 cm and a convergence semi-angle of 25 mrad. Fig. 82(a) additionally depicts the deflection magnitude. The deflection magnitude in case of the 25k DPC image amounts up to approximately 6 mrad, which is much larger than typical deflections resulting from the interaction of the electron beam with the electric fields inside the specimen.

To investigate this further, Fig. 82(b) displays profiles of the deflection magnitude as a function of the distance to the centre of the DPC image. These profiles are obtained by calculating the mean deflection magnitude on the complete circumference of a circle with radius r_{Back} (red arrow in Fig. 82(a)). An almost linear increase of measurable deflection magnitude with increasing distance to the image centre is observed. This is in good agreement to the findings of Zweck et al. [38] on the detector linearity. Assuming linear detector response and a linear background is therefore reasonable for all considered magnifications. Still, a knee is observed in the radial profile for a magnification of 25k. This knee can be assigned to a too strong displacement of the beam on the detector due to the background. The knee is observed at a distance of approximately 150 pixels to the centre of the image (25k). Using the image calibration, the knee is therefore strongly apparent in DPC images which extend over a scanning area of 5.8 µm.

Fig. 82(a) additionally shows the resulting images of deflection magnitude after applying the background corrections using the Poly11, Poly22 and Poly33 methods. After correction, the deflection magnitude images reveal a significant reduction of measurable deflection magnitude. While for a magnification of 25k features with a residual deflection magnitude are evident even after correction with the Poly11, Poly22 and Poly33 method, for higher magnifications only fluctuations in the measurable deflection magnitude due to image noise are present. The emergence of areas of increased deflection can be attributed to the deviation of the actual background from the background models.

Fig. 82(c) shows the mean deflection magnitude of the DPC measurement, before and after correction with the three different background models and considers magnifications ranging from 20k to 5M. It is found that the corrections significantly reduce the mean measurable deflection magnitude. With increasing order of polynomial function considered for the background correction, the influence of the background is decreased. Thus, corrections based on the Poly33 background model always show a lower residual mean deflection than the corrections based on the Poly11 and Poly22 method. At high magnifications, the average deflection magnitude in the background corrected signals converge until the level of the image noise is reached.

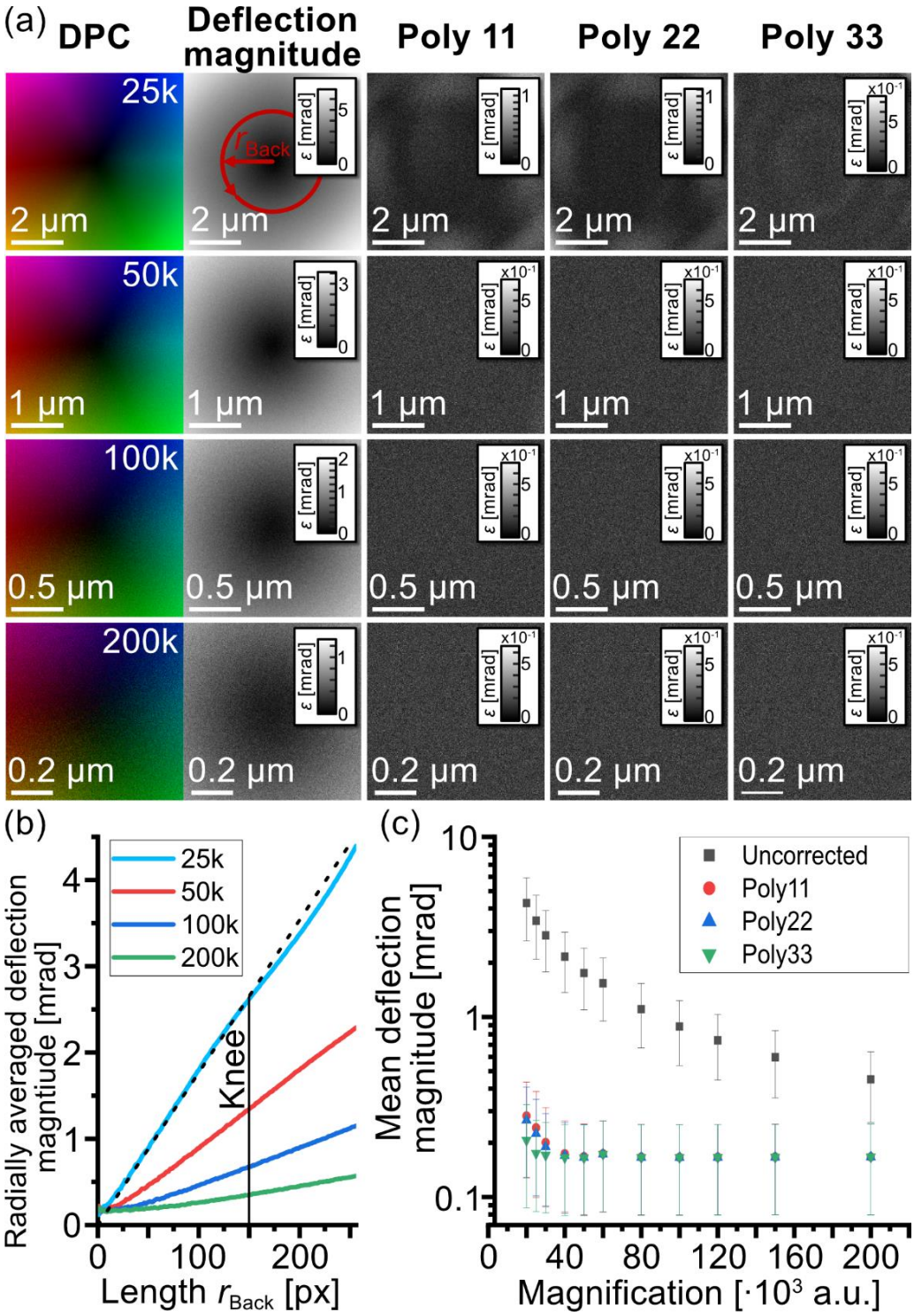

Figure 82: (a) DPC images with corresponding deflection magnitude and the residual deflection magnitude after background correction using the Poly11, Poly22 and Poly33 models. The measurement consider magnifications of 25k, 50k, 100k and 200k. In addition, all images are acquired in vacuum without the presence of any specimen structure. (b) Radial profiles of the deflection of the deflection magnitude displayed in (a). The length r_{Back} denotes the distance to the centre of the deflection map as indicated by the red arrow in (a). Deflections for each distance are obtained by measuring the mean value on the complete circumference of a circle with radius r_{Back}. (c) Mean deflection magnitude of the uncorrected and corrected deflection magnitude images. Here the mean deflection magnitude is depicted for magnifications ranging from 20k to 5M.

Fig. 83 shows the DPC image and corresponding scattergram of the SiO_2 spheres on a lacey grid after application of the rotation, the centring, and the background correction. Here, the Poly11 background model is used, and the background is derived from the same DPC image. The inverted colour wheel which is typical for the background is no longer visible in the corrected DPC image in Fig. 83(a). Each individual sphere exhibits a radially symmetric deflection distribution, as can be seen from the deflections in direction of the sphere centres. This is in good agreement to the expected deflection distribution arising from local gradients of the projected mean inner potential. In addition, reduced deflection magnitudes are measurable at the connecting axes of the spheres (exemplarily marked by white circles in Fig. 83(a)). It is possible to identify stacked spheres (white arrow).

The background-corrected scattergram in Fig. 83(b) does no longer exhibit a square-like feature which is observable in the uncorrected scattergram in Fig. 81(b). Instead, the corrected scattergram exhibits a round feature with global maximum and a tail-like extension. The global maximum (marked by a white arrow in Fig. 83(b)) arises from many pixels with weak deflections. These weak deflections are a result of the interaction with the lacey and the central areas of the SiO_2 spheres. The tail-like extension corresponds to strong deflections at peripheral areas of the spheres.

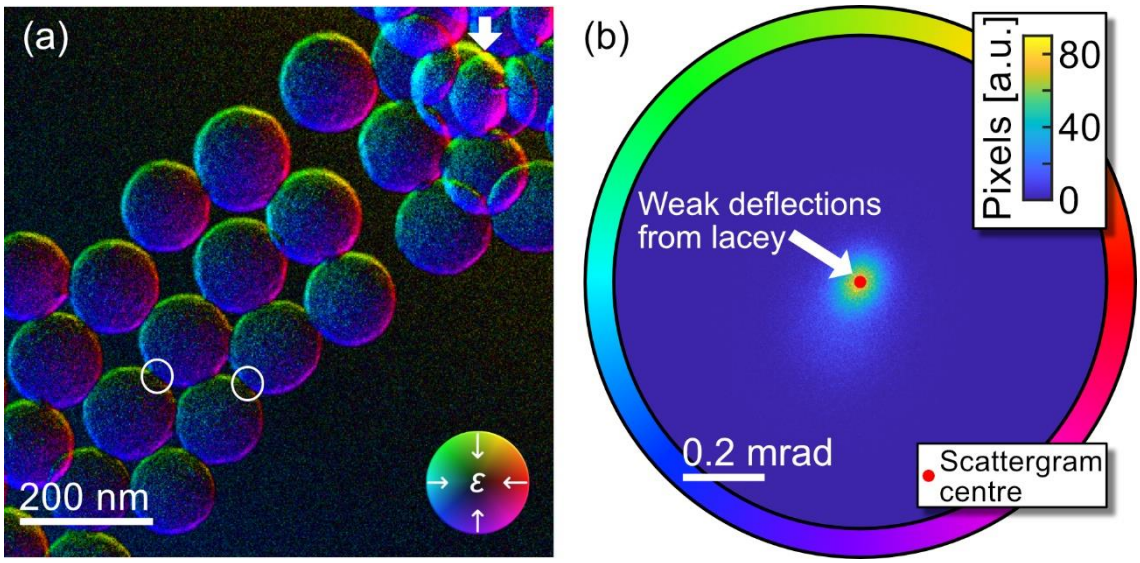

Figure 83: (a) DPC image and (b) corresponding scattergram of SiO_2 spheres on Lacey grid after rotation, centring and background correction. The corresponding uncorrected DPC image is depcited in Fig. 77(d).

A.1.4. Anisotropy of detector sensitivity

In Chapter 3.1.2 it was observed that the detector exhibits an elliptical silhouette, which possibly arises due to a tilted installation. It is expected that the detector will measure a greater difference signal in the direction of the detector's short semi-axis than in direction of the longer semi-axis. Additionally, it can be expected that this anisotropy of detector sensitivity is observable with the scattergram. In the following, a scattergram-based method to evaluate and correct the anisotropy of detector sensitivity is given.

To measure the anisotropy of detector sensitivity, deflections, which are uniformly distributed in all directions, are required. For this purpose, the background arising from missing descanning coils can be exploited. It is assumed that the scattergram intensity of the measured deflections for a scan in vacuum exhibit a square-like distribution as long as the scan area corresponds to an undistorted square and the magnification lies within the linear response range of the detector. Fig. 84(a) shows a DPC image acquired at a magnification of 200k guaranteeing a linear detector response function. The image was rotation and beam centring corrected. The corresponding scattergram in Fig. 84(b) shows a rectangle-like feature.

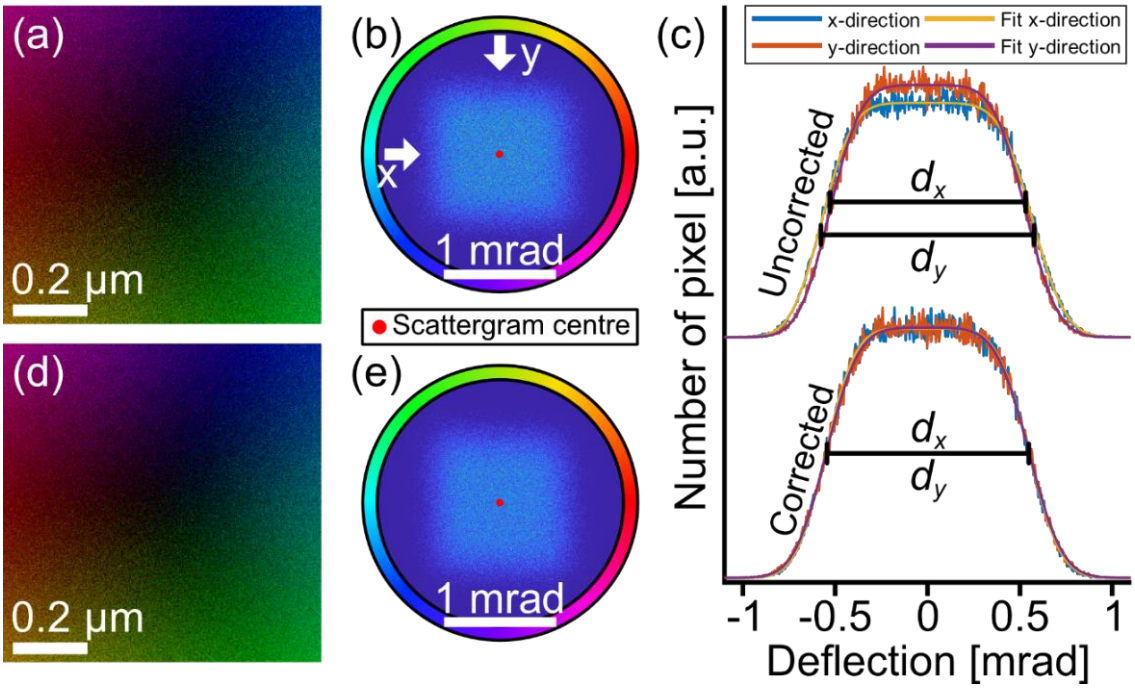

Figure 84: (a) DPC image and (b) corresponding scattergram before correction of momentum space anisotropy. (c) Intensity profiles with corresponding two-sided error function fits of the scattergram distribution in x- and y-direction (marked by white arrows in (b)) before and after correction of momentum space anisotropy. For these profiles, the intensity is integrated along the complete height or width for the x- and y-direction, respectively. (d) DPC image and (e) corresponding scattergram after correction of momentum space anisotropy.

Line profiles of the scattergram intensity in x- and y-direction which are integrated across the full height and full width, respectively, are depicted in Fig. 84(c). These line profiles reveal a difference in detector sensitivity that is particularly visible in the

extension and height of the line profiles. In y-direction, the profile is wider compared to the x-direction, which means that the detector has an increased sensitivity in this direction. The increased sensitivity results from a decreased extension of the detector in the same direction. The fluctuations in the two intensity profiles in the x- and y-directions as well as the edge steepness result from present image noise (further details in Chapter 5.7).

By comparing the widths of both line profiles, the difference in sensitivity in x- and in y-direction can be calculated and afterwards corrected by applying a factor to the difference signals. To obtain this factor, the widths of the line profiles are determined by fitting two-sided error functions $l_{\mathrm{Fit}}(r_{x/y})$ with the form of

$$l_{\mathrm{Fit}}(r_{x/y}) = a_{1,x/y} \cdot \left(\mathrm{erf}\left(\frac{r_{x/y}}{a_{2,x/y}} - a_{3,x/y} \right) - \mathrm{erf}\left(\frac{r_{x/y}}{a_{4,x/y}} - a_{5,x/y} \right) \right) + a_{6,x/y}. \tag{73}$$

to each individual line profile. These two-sided error functions include the parameters $a_{i,x/y}$ which account for the height, the width, the steepness and base level of the two-sided error function. The parameter $r_{x/y}$ represents the position of the line profile.
The width of the two sided error function is the given by the fitting parameters. As $\mathrm{erf}(0) = 0$, the width $d_{x/y}$ in x- and y-direction at half maximum is given by

$$d_{x/y} = a_{3,x/y} \cdot a_{2,x/y} - a_{5,x/y} \cdot a_{4,x/y}. \tag{74}$$

And thus the ratio $r_{\mathrm{Anisotropy}}$ of width in y- and x-direction is given by

$$r_{\mathrm{Anisotropy}} = \frac{d_y}{d_x}. \tag{75}$$

This ratio allows to find a correction factor $c_{\mathrm{Anisotropy}}$ that can be applied to adjust the difference signals in x- and y-direction due to difference in sensitivity. This correction factor is given by

$$c_{\mathrm{Anisotropy}} = \frac{\sqrt{d_x^2 + \left(r_{\mathrm{Anisotropy}} \cdot d_y^2 \right)}}{\sqrt{d_x^2 + d_y^2}}. \tag{76}$$

The correction factor is applied on the S_x signal using

$$S_{x,\mathrm{Anisotropy\ corrected}} = S_x \cdot c_{\mathrm{Anisotropy}} \tag{77}$$

and on the S_y signal using the following equation:

$$S_{y,\mathrm{Anisotropy\ corrected}} = \frac{S_y}{c_{\mathrm{Anisotropy}}}. \tag{78}$$

The ratio of widths of the scattergram profiles in x- and y-direction in Fig. 84(c) amounts to $r_{\mathrm{Anisotropy}}$ =1.077. Thus, the detector exhibits a difference in sensitivity of 7.7 % in x- and y-directions. The DPC image and corresponding scattergram after correction are depicted in Figs. 84(d, e). This clearly shows that the detection anisotropy needs to be carefully checked for quantitative DPC imaging.

Although the difference between colour-coded DPC images shown in Fig. 84(a) and Fig. 84(d) seems negligible, a difference between the uncorrected and corrected scattergram distributions is observable as the scattergram in Fig. 84(e) exhibits a square-like instead of a rectangle-like distribution. The resulting line profiles in x- and y-direction (Fig. 84(c)) are in good agreement.

The anisotropy of the detector sensitivity needs careful investigation because it might have a significant impact on, e.g. calculated charge densities. Such investigations might also be beneficial for other detector types. For the atomically resolved images in this thesis, the correction factor $r_{\mathrm{Anisotropy,total}}$ amounts to 1.07 ±0.01 which is obtained from an image series of magnifications ranging from 50k to 500k. Note that this correction factor is not transferable to other machines.

A.2. Supporting information

This chapter covers further DPC measurements and image simulations.

A.2.1. Influence of detector rotation

The influence of detector rotation on DPC measurements and image simulations of Si[110] is shown in Fig. 85 and Fig. 86. For different detector rotations between 0° and 80°, the HAADF and DPC images are shown, and the corresponding scattergrams are depicted for the measurements on the left and for the corresponding simulations on the right. Experimental details can be found in Table 42. A list of simulation parameters is given in Table 17.

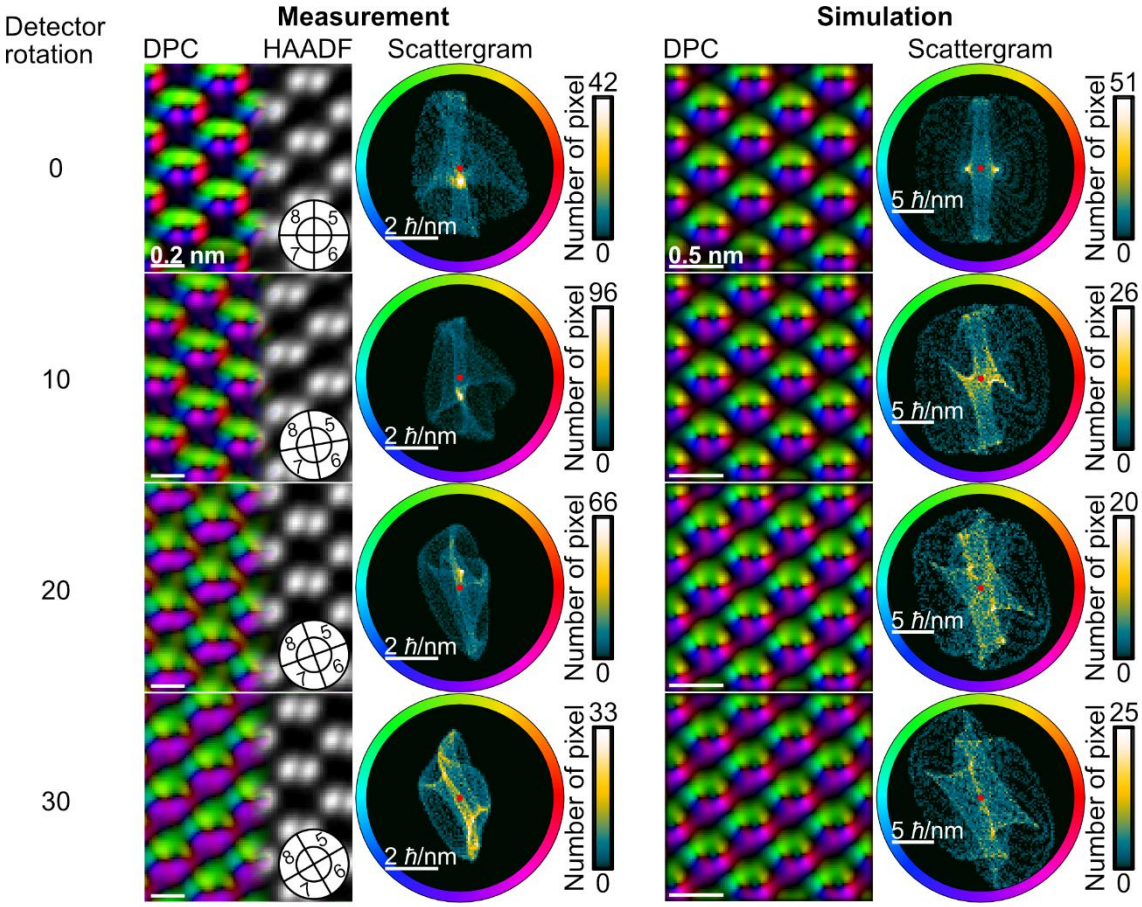

Figure 85: DPC measurement and image simulations as well as corresponding scattergrams of Si[110] for detector rotations of 0°, 10°, 20° and 30°. The specimen thickness amounts to (30 ± 2) nm in the measurements and 30.72 nm in the simulations. Sketches in the lower right corner of the measurements illustrate the detector orientation to the crystal structure. Simulations are obtained using -6 nm of underfocus. Further experimental parameters can be found in Table 42. Simulation parameters of the multislice image simulations are listed in Table 17.

A good agreement of all measurements and simulations and more importantly for all detector rotations is evident from the scattergram intensity distributions. The defocus for the measured DPC images was set prior to each measurement to obtain the maximum DPC signal. Slight differences can be expected, due to specimen drift as well as manual error, slightly influencing the obtainable DPC image. The wave-like

features in the scattergrams of simulated DPC images results from a combination of sampling (grid of pixels) of the scan as well as the neglect of frozen lattice configurations.

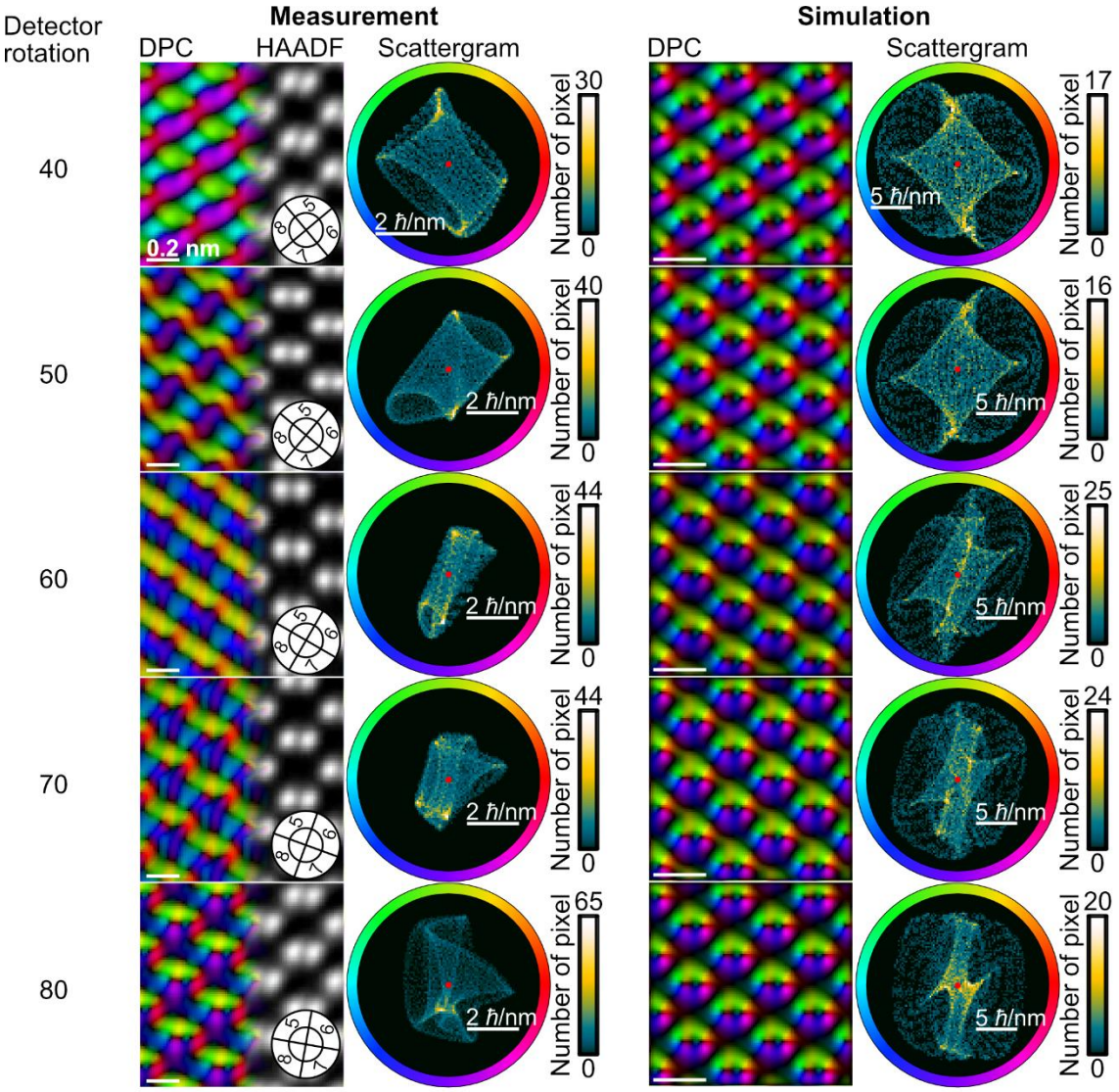

Figure 86: DPC measurement and image simulations as well as corresponding scattergrams of Si[110] for detector rotations of 40°, 50°, 60°, 70° and 80°. Experimental parameters are given in Table 42. Simulation parameters of the multislice image simulations are compiled in Table 17.

As shown above, the detector rotation has a drastic influence on the intensity distribution within the scattergram. As the scattergram is a representation of transferred momentum distribution, changes within the electric field distribution are expected. Therefore, the influence of detector rotation on the electric field is investigated in the following.

Fig. 87 and Fig. 88 show the simulated HAADF and DPC images, maps of the electric field magnitude and the charge density for detector rotations from 0° to 80° in steps of 10°. These image simulations are considered for the investigation of the changes in magnitude and azimuthal direction of the DPC signal along the detector rotation

(Fig. 34). A strong influence of the detector rotation on the DPC image is visible. This is particularly visible in the electric field magnitude maps as well as the charge density maps showing strongly varying features in the vicinity of atomic columns.

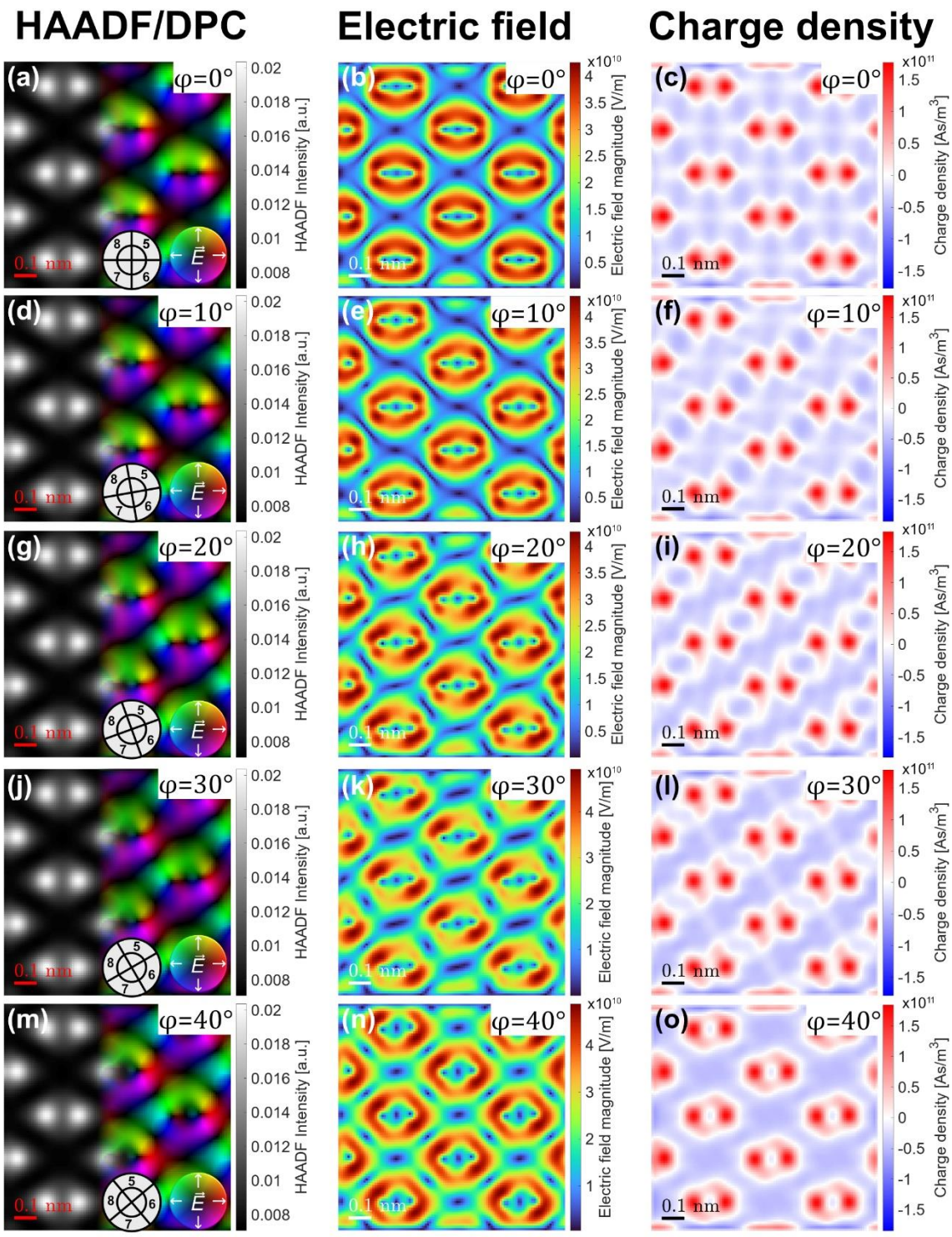

Figure 87: (a, d, g, j, m) HAADF and DPC images, (b, e, h, k, n) electric field magnitude and (c, f, i, l, o) charge density for Si[110] at detector rotations of (a, b, c) 0°, (d, e, f) 10°, (g, h, i) 20°, (j, k, l) 30°, and (m, n, o) 40°.

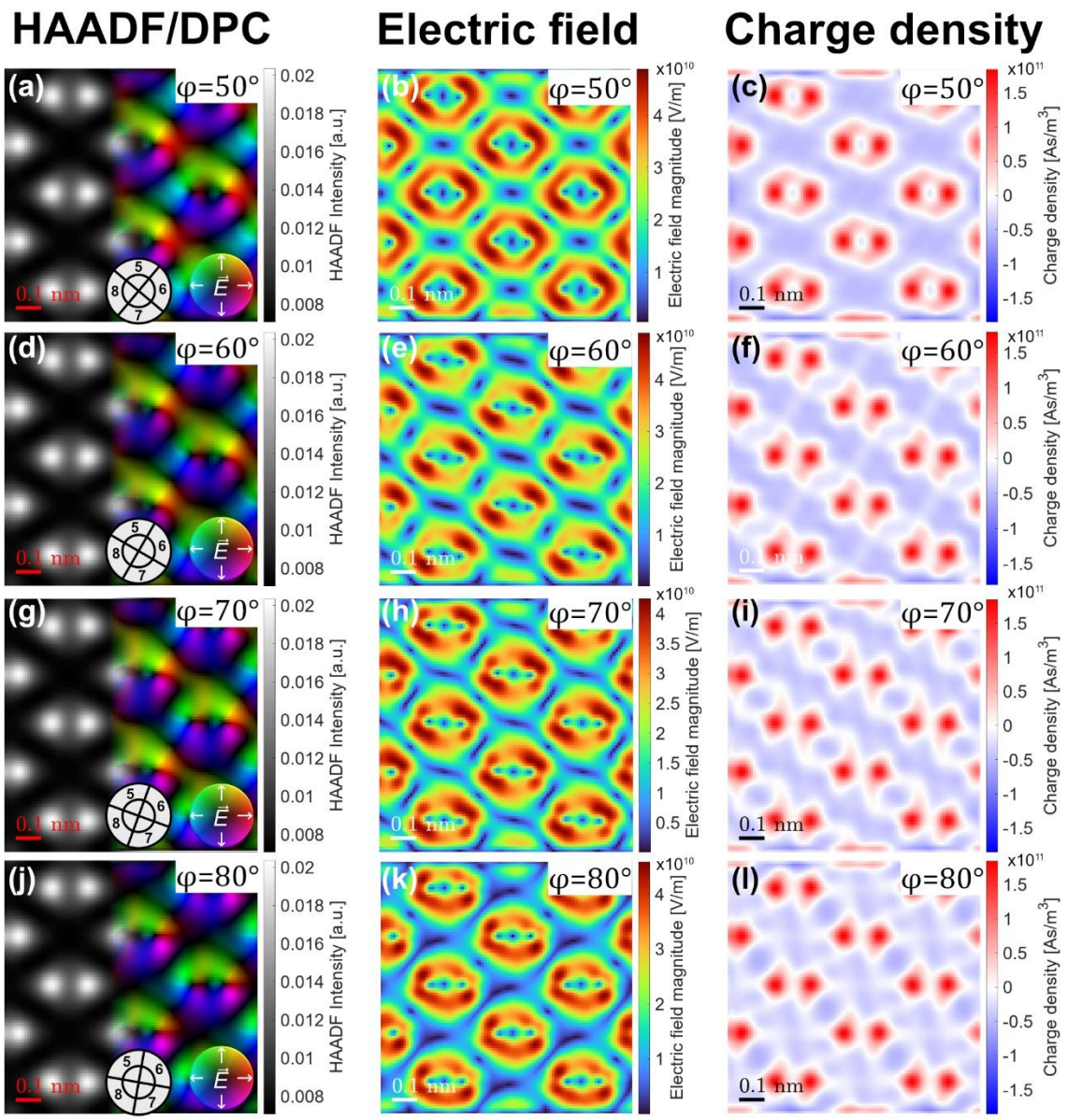

Figure 88: (a, d, g, j) HAADF and DPC images, (b, e, h, k) electric field magnitude and (c, f, i, l) charge density for Si[110] for detector rotations of (a, b, c) 50°, (d, e, f) 60°, (g, h, i) 70°, and (j, k, l) 80°.

A.2.2. Influence of defocus and specimen thickness

In this chapter, the influence of defocus and specimen thickness on the DPC image intensity is investigated using multislice image simulations of $SrTiO_3$ in [001] zone-axis orientation for defoci ranging from 5 nm (overfocus) to -10 nm (underfocus) and specimen thicknesses ranging from 0.39 nm (one unit- cell of $SrTiO_3$). All individual DPC images are normalised to their individual maximum to reveal the changes introduced by altering the defocus. The tableau which is normalised to the overall maximum is displayed in Fig. 37. Simulation parameters are listed in Table 20.

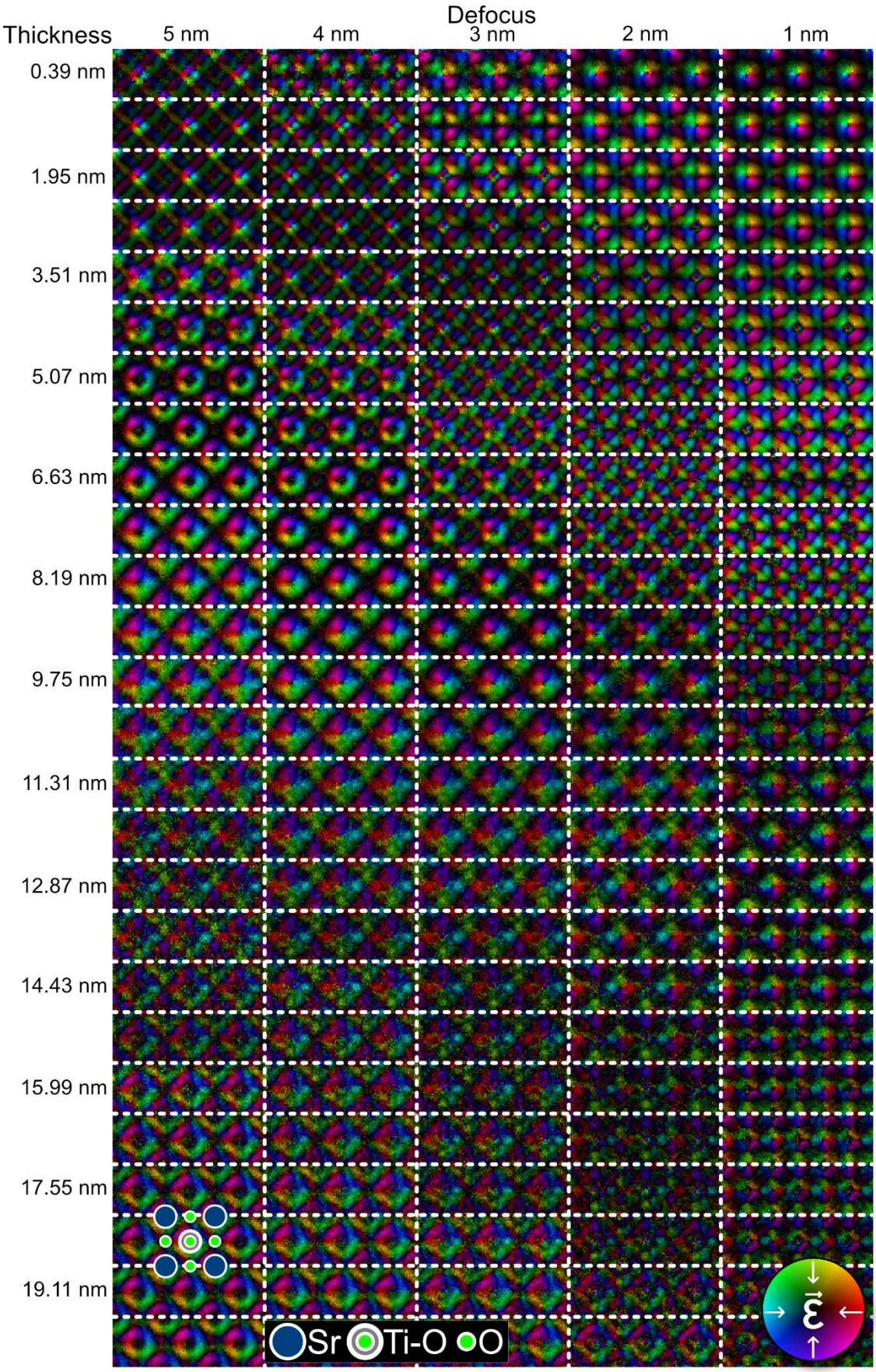

Figure 89: DPC image simulations with defocus values ranging from 5 nm to 1 nm (overfocus) for specimen thicknesses between 0.39 and 19.92 nm. All individual DPC image simulations are normalised to their maximum intensity [91]. Simulation parameters are compiled in Table 20.

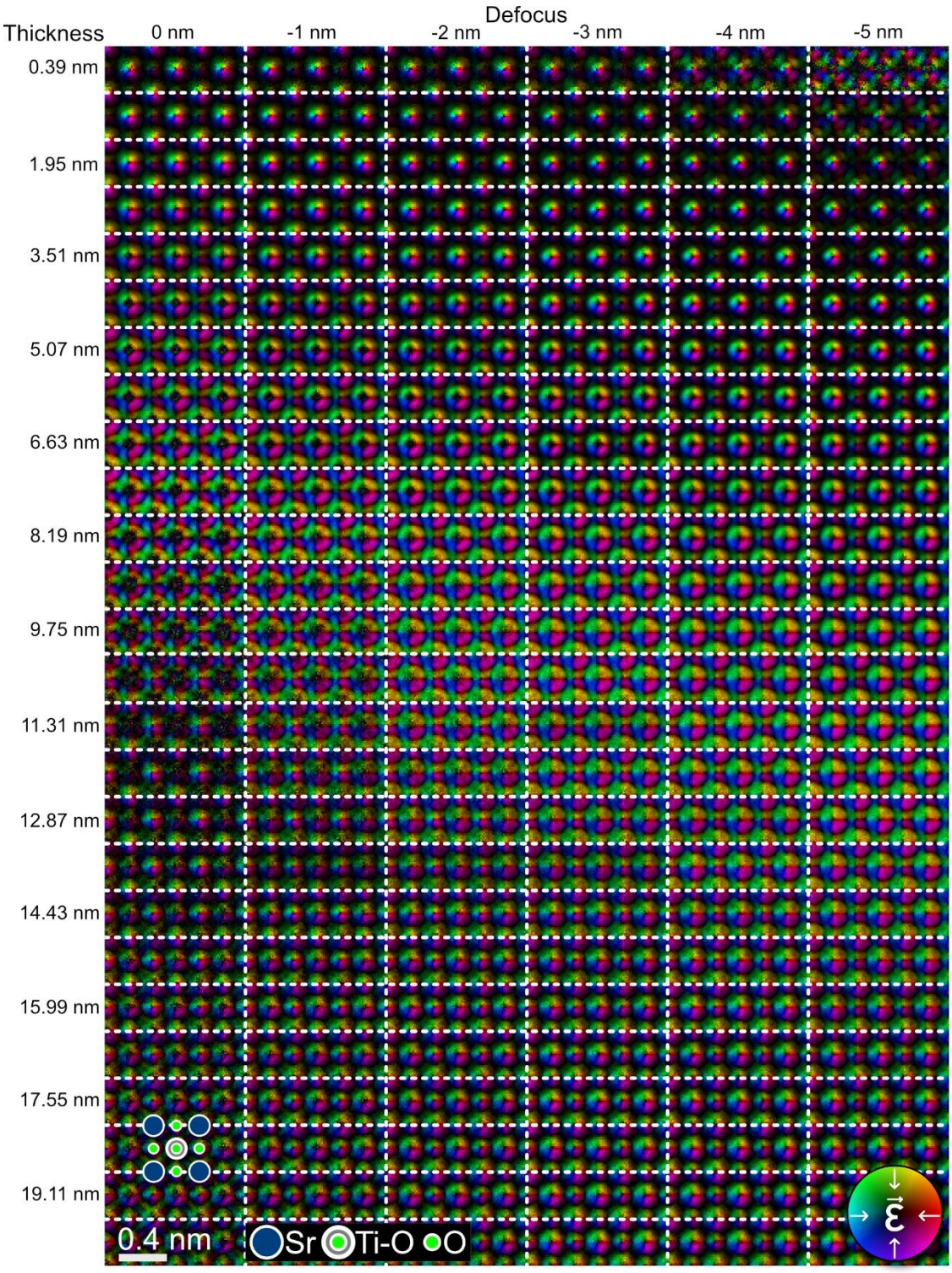

Figure 90: DPC image simulations with defocus values ranging from 0 nm to -5 nm (underfocus) for specimen thicknesses between 0.39 and 19.92 nm. All individual DPC image simulations are normalised to their maximum intensity [91]. Simulation parameters are compiled in Table 20.

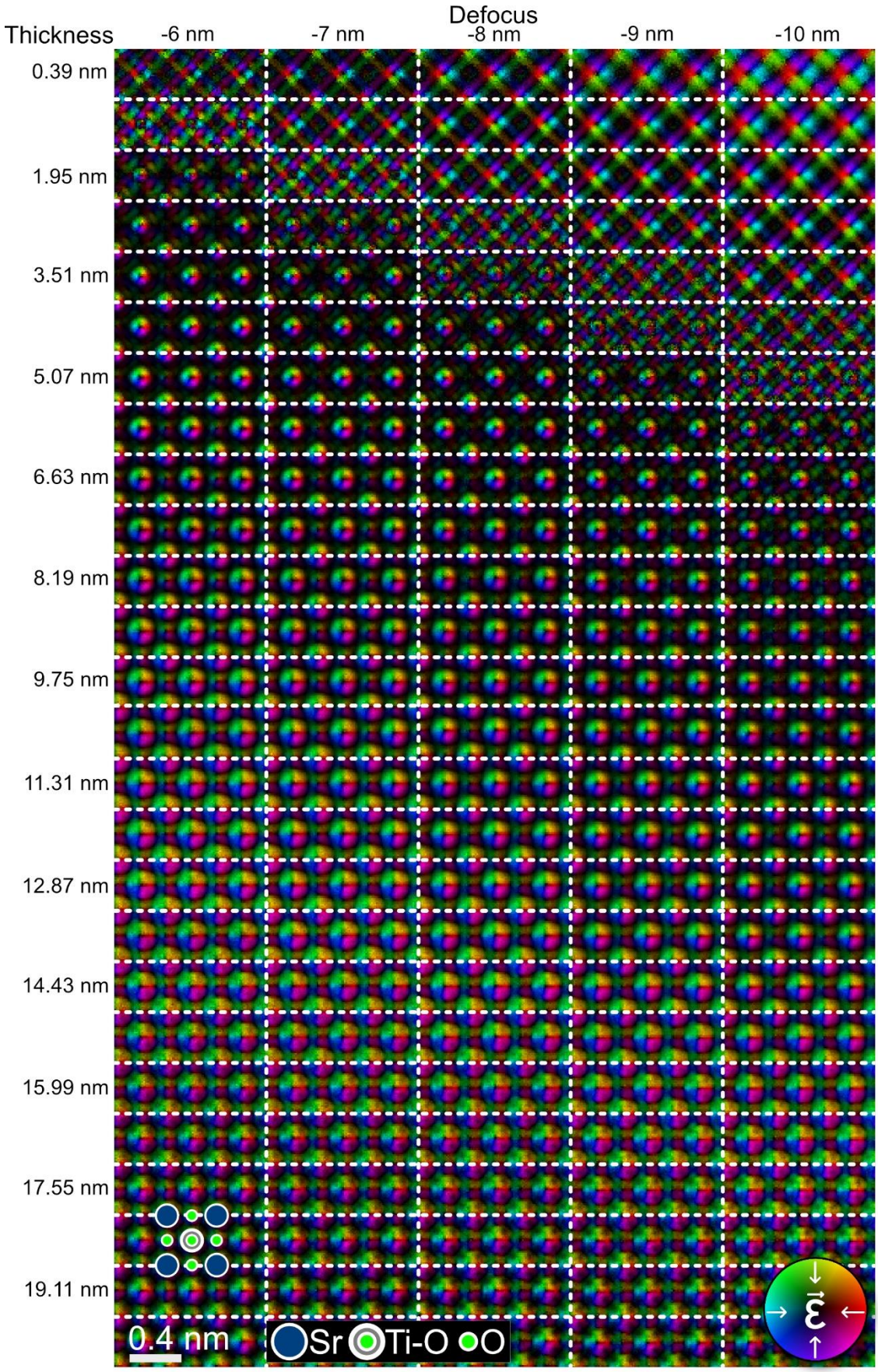

Figure 91: DPC image simulations with defocus values ranging from -6 nm to -10 nm (underfocus) for specimen thicknesses between 0.39 and 19.92 nm. All individual DPC image simulations are normalised to their maximum intensity [91]. Simulation parameters are compiled in Table 20.

A.2.3. Defocus dependent DPC signal of 30.72 nm thick Si[110]

In this chapter, the optimum defocus for Si[110] with a thickness of 30.72 nm is investigated by using multislice image simulations to calculate the mean DPC signal magnitude as well as the cross-correlation coefficient with the DPC image of one unit cell of Si[110] (Fig. 92). Simulation parameters are compiled in Table 31.

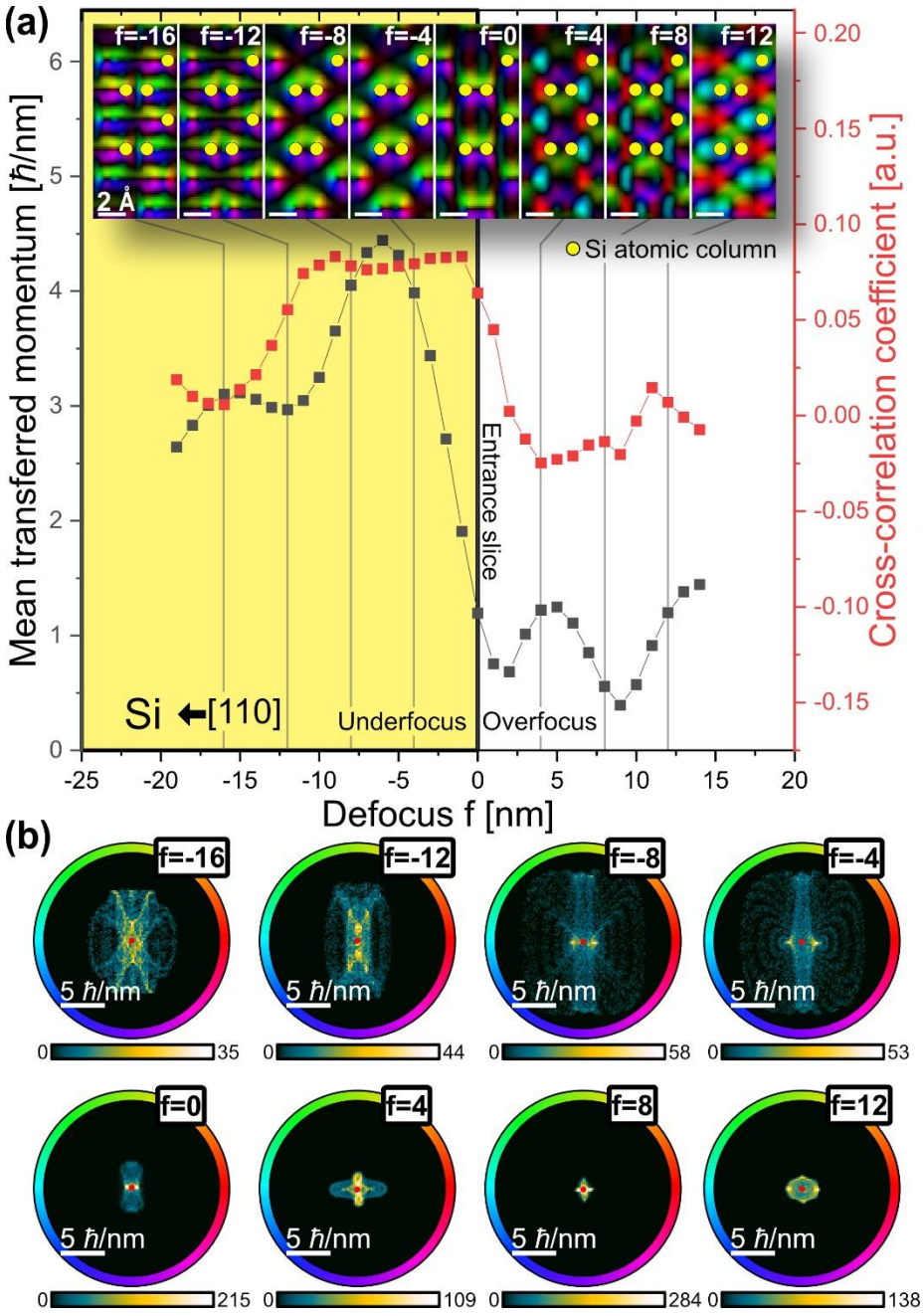

Figure 92: Investigation of defocus-dependent mean DPC signal magnitude and cross-correlation coefficient to the image of one unit cell for 30.72 nm thick Si[110]. (a) Plots of mean DPC signal magnitude and cross-correlation coefficient with inset showing exemplary DPC image for different defoci. (b) Corresponding scattergrams of the exemplary DPC images. A list of simulation parameters is given in Table 31.

As can be seen from Fig. 92(a), the highest mean DPC signal magnitude is achieved for a defocus of -6 nm. The highest cross-correlation coefficient is evident for a defocus of -9 nm. It is to note that the cross-correlation coefficient is almost constant for defoci

of -13 nm to -1 nm (underfocus; in the specimen). The maximum of mean DPC signal magnitude and cross-correlation coefficient are observed for defoci slightly below the entrance plane and definitely above half the specimen thickness. These results contrast with the findings for $SrTiO_3$ in Fig. 38, where the optimum defocus for both the maximum mean DPC signal magnitude and the maximum cross-correlation is below half the specimen thickness – at least for the considered of specimen thicknesses. A possible explanation for the diffent optimum defocus is the difference of atomic potentials. The inset in Fig. 92(a) shows exemplary DPC images and Fig. 92(b) the corresponding scattergrams. The DPC images and scattergrams highlight the strong influence of defocus on obtainable DPC image features.

A.2.4. Real space probe intensity

This chapter covers supplementary real space probe intensities and analyses of the thickness dependent area-averaged real space probe intensity as well as thickness dependent line profiles in y-direction.

Fig. 93 shows the real space probe intensity distributions in $SrTiO_3$[001] for different thicknesses and beam positions. These real space probe intensity distributions are obtained from multislice simulations using an acceleration voltage of 200 kV. The beam positions were assumed to be 0.05 nm to the right of a Sr, a Ti-O or a pure O column and the defocus according to the entrance slice is chosen. The thicknesses are exemplarily selected and range from 0 nm (focal plane and entrance slice) to 15.4 nm. Simulation parameters are listed in Table 22. Fig. 94 displays the simulated real space probe intensity distributions for the same specimen structure, thicknesses, beam positions and defocus, but for an acceleration voltage of 30 kV. Simulation parameters for the multislice simulations at 30 kV are given in Table 23. Both figures are split into three columns for the three different beam positions. Each column depicts the real space probe intensity for five different specimen thicknesses in increasing order. Both figures additionally contain sketches of the $SrTiO_3$ crystal structure and squares for further investigations in Fig. 95.

Comparing the real space probe intensities in Fig. 93 and Fig. 94, several statements can be made:

First, the redistribution of intensities is quite similar for the beam positions close to the Sr and Ti-O atomic columns for one acceleration voltage. This statement individually holds for both acceleration voltages. However, intensity redistributions at 200 kV and 30kV for the Sr and Ti-O atomic columns are not similar.

Second, the real space probe intensities for beam positions close to the pure O atomic columns advance differently to the beam positions in the vicinity of Sr and Ti-O atomic columns. This holds for both acceleration voltages and is particularly evident from the position of local maxima and minima of the real space probe intensity (compare Figs. 93(m, n) to Fig. 93(o) as well as Figs. 94(m, n) to Fig. 94(o)). The difference in redistribution of real space probe intensity can be explained by the difference in projected atomic potential (Sr column: $Z = 38$; Ti-O column: $Z = 30$; O column: $Z = 8$).

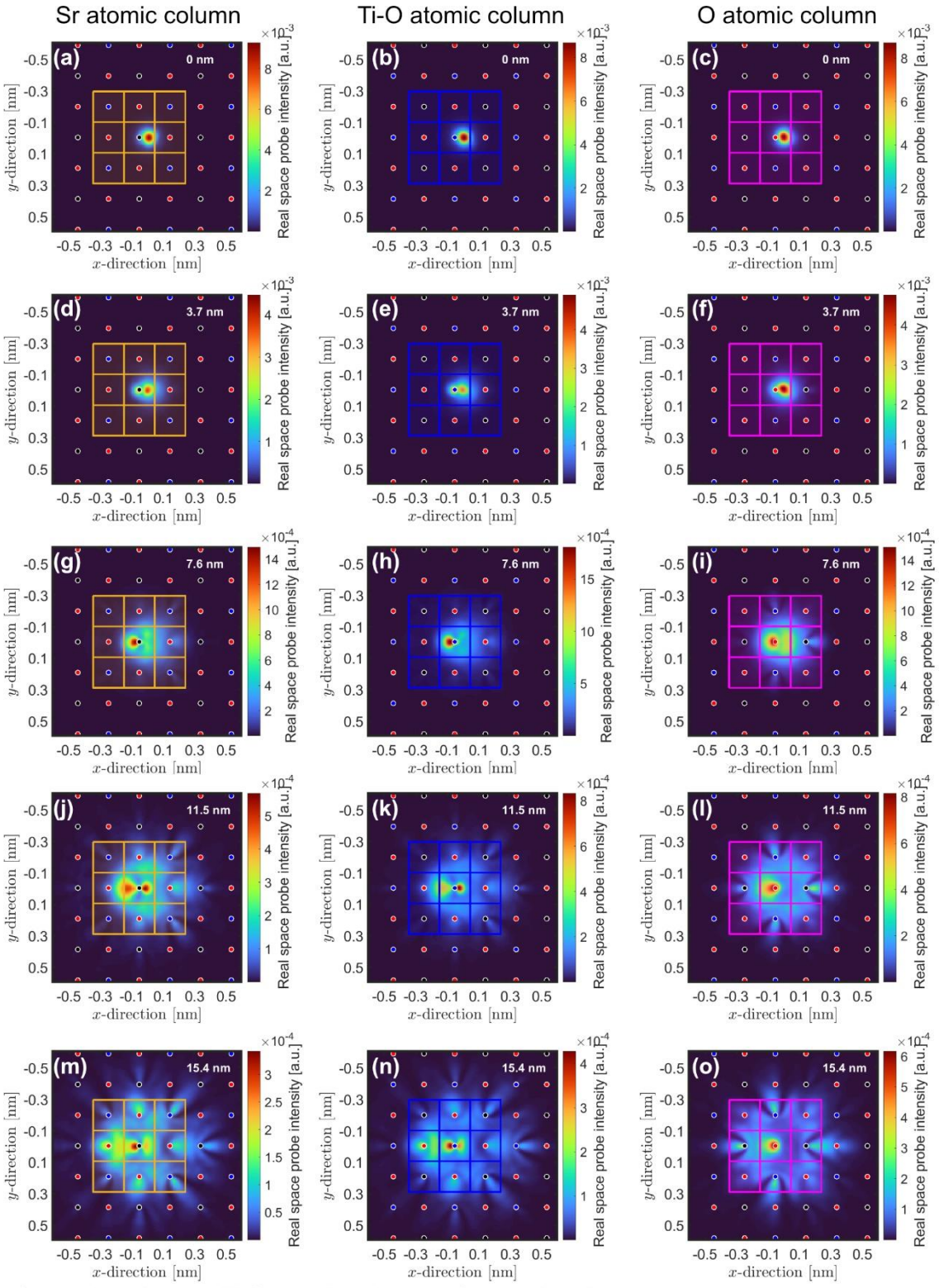

Figure 93: Real space probe intensities in $SrTiO_3$[001] at different specimen thickness of (a-c) 0 nm (entrance slice), (d-f) 3.7 nm, (g-i) 7.6 nm, (j-l) 11.5 nm, (m-o) 15.4 nm and for different beam positions, which are 0.05 nm right of (a, d, g, j, m) a Sr, (b, e, h, k, n) a Ti-O and (c, f, I, l, o) a pure O atomic column. The simulations are obtained using the multislice algorithm of Dr. Probe and assuming an acceleration voltage of 200 kV, a defocus of 0 nm and no other lens aberrations. The position of Sr, Ti-O and pure O atomic columns are marked by black, blue, and red dots. The yellow, blue, and magenta squares which individually cover the area of one quarter of a projected unit cell are used for the analysis presented in Fig. 95. Further explanations on the squares are therefore given in the section describing Fig. 95. A list of simulation parameters is given in Table 22.

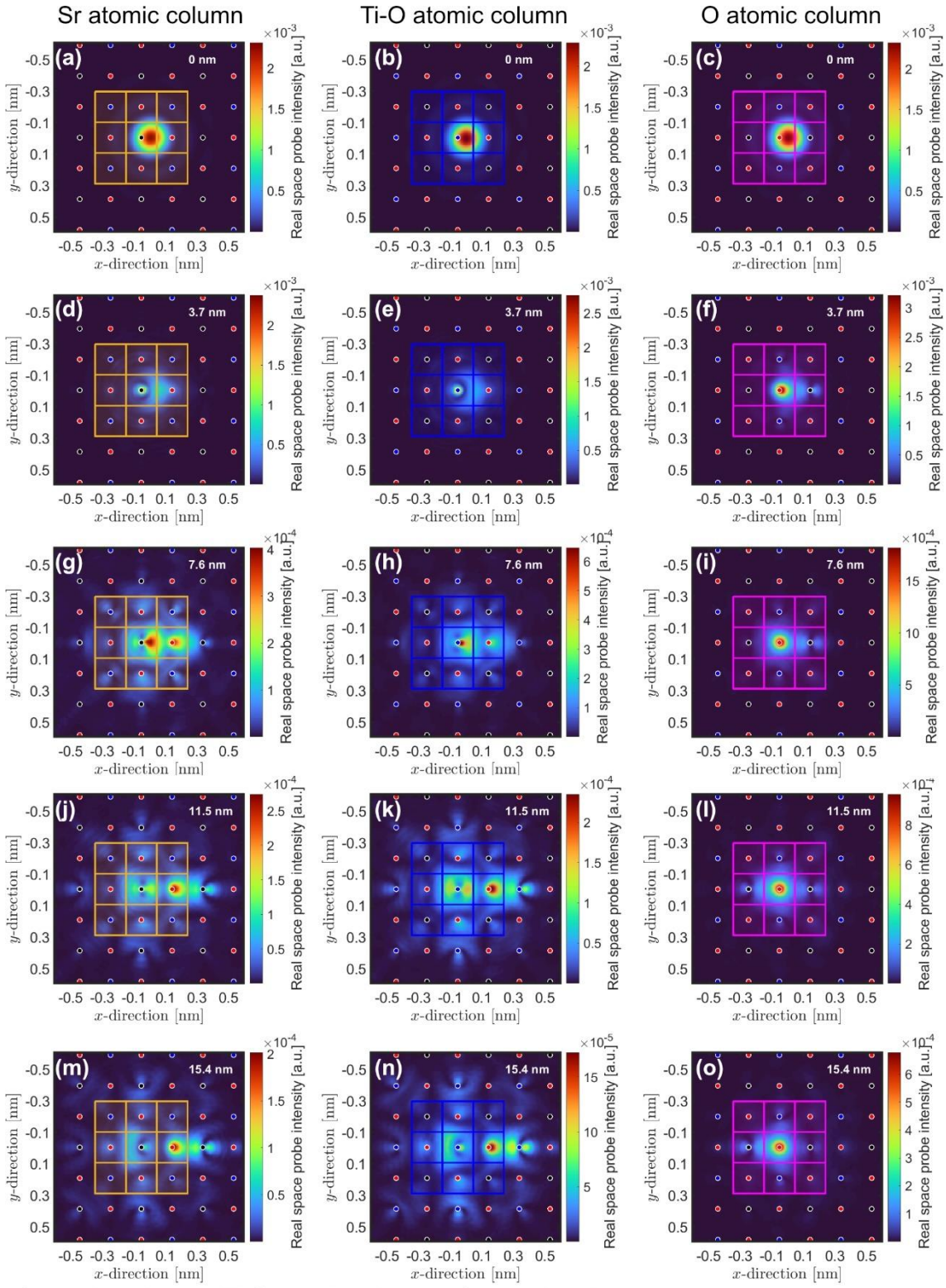

Figure 94: Real space probe intensities in $SrTiO_3$[001] at different specimen thickness of (a-c) 0 nm (entrance slice), (d-f) 3.7 nm, (g-i) 7.6 nm, (j-l) 11.5 nm, (m-o) 15.4 nm and for different beam positions, which are 0.05 nm right of (a, d, g, j, m) a Sr, (b, e, h, k, n) a Ti-O and (c, f, I, l, o) a pure O atomic column. The simulations are obtained using the multislice algorithm of Dr. Probe and assuming an acceleration voltage of 30 kV, a defocus of 0 nm and no other lens aberrations. The position of Sr, Ti-O and pure O atomic columns are marked by black, blue, and red dots. The yellow, blue, and magenta squares which individually cover the area of one quarter of a projected unit cell are used for the analysis presented in Fig. 95. Further explanations on the squares are therefore given in the section describing Fig. 95. Simulation parameters are listed in Table 23.

Third, the redistribution of intensity differs significantly between the real space probe intensities for acceleration voltages of 200 kV and of 30 kV. This is particularly visible for beam positions close to the Sr and Ti-O atomic columns (Fig. 93 and Fig. 94) and can be explained by the difference in interaction with the specimen potentials due to the difference in electron energy (the interaction constant changes!). While most of the intensity is redistributed in direction of the nearest atomic column (and even beyond that!) in case of 200 kV, most of the intensity is found in opposite direction at 30 kV. This behaviour is particularly visible at a specimen thickness of 15.4 nm for an acceleration voltage of 30 kV (Figs. 94(m, n)), where the overall intensity maximum is found around the next pure O atomic column. However, this difference is not observable for initial beam positions close to the pure O columns (Fig. 94(o)). When the beam is positioned close to a pure O column, its intensity is redistributed in direction of the next pure O atomic column.
Fourth, the full width at half maximum of the incident probe is influenced by the acceleration voltage (compare Figs. 93(a-c) and Figs. 94(a-c)). The considered source profile and aperture diameter (25 mrad) are the same for all real space probe intensities.
Fifth, a significant broadening of the real space probe intensity is observable for both acceleration voltages. Most of the real space probe intensity covers a larger area than that of a single unit cell (2x2 of the marked yellow, blue and magenta squares in both figures). Even though the electron beam interacts with all atoms inside a specimen, the contribution to the electrostatic potential is negligible for atoms, which are at a far distance to the electron beam. As can be seen from Fig. 93 and Fig. 94, due to the broadening of intensity, the electron beam is strongly influenced not only by the potential of one atom, but by that of several atoms. This is further investigated in Fig. 95.

Fig. 95 shows profiles of the area-integrated real space probe intensity in $SrTiO_3$[001] for areas around individual atomic columns for acceleration voltages of 200 kV and 30 kV as well as three different beam positions as a function of the specimen thickness (same data as in Fig. 93 and Fig. 94). The nine individual areas used for the calculation of the nine profiles are marked by the yellow, blue and magenta squares in the real space probe intensity profiles (Fig. 93 and Fig. 94). These areas are centred on individual atomic columns and cover an area equal to one quarter of the projected area of a single $SrTiO_3$ unit cell. The insets in Fig. 95 depict a sketch of the same areas including the atomic columns and the yellow-, blue- and magenta-framed squares. Additionally, the individual areas are labelled by “Sr#”, “Ti-O#” and “O#” in which “#” represents a number. The same labels are also used for the area-integrated real space probe intensity profiles.

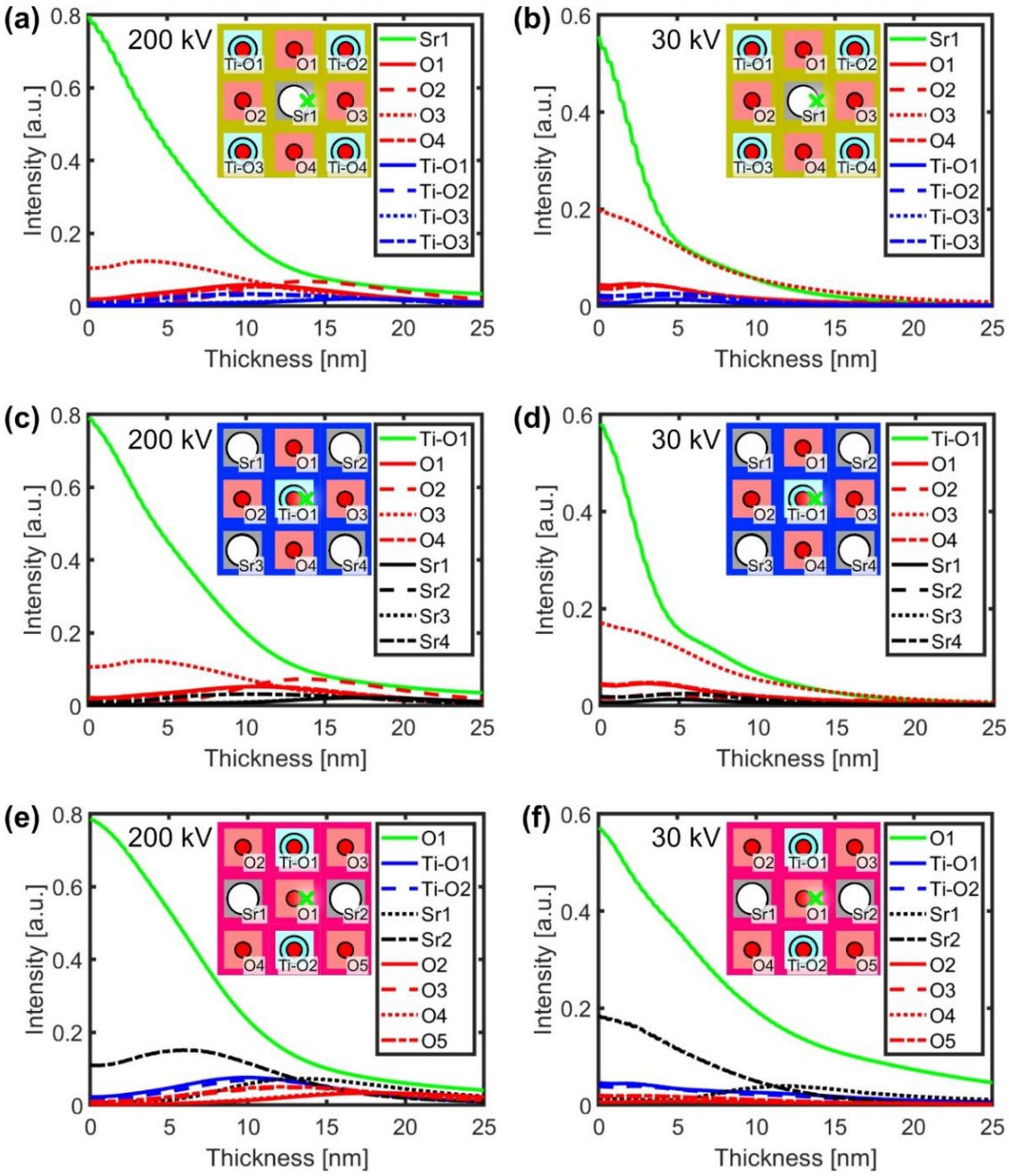

Figure 95: Area-integrated real space probe intensity as a function of the $SrTiO_3$ specimen thickness for beam positions, which are 0.05 nm right of (a, b) a Sr, (c, d) a Ti-O and (e, f) a pure O atomic, and for acceleration voltages of (a, c, e) 200 kV and (b, d, f) 30 kV. For the intensity profiles areas around individual atomic columns are considered.

Several findings can be made from the area-integrated real space probe intensity profiles shown in Fig. 95. The findings are in good agreement to the statements derived from Fig. 93 and Fig. 94 and are given below:

First, all area-integrated intensities decrease with increasing specimen thickness due to beam broadening within the specimen.

Second, most of the intensity is found around the central atomic column (the one close to the beam position, i.e. Sr1, Ti-O1, O1) if the specimen is thin. At increased thicknesses, the potentials of other atomic columns contribute significantly to the interaction of specimen and electron beam.

Third, the thickness dependent behaviour of the area-integrated real space probe intensity profiles is influenced by the full width at half maximum of the incident electron beam as well as the acceleration voltage.
Fourth, the area-integrated real space probe intensities of the beam positions close to the Sr and Ti-O atomic columns behave similarly for a specific acceleration voltage. This can be deduced from the ratio of area-integrated intensities and particularly seen from the area-integrated intensity of Sr1 and O3 or Ti-O1 and O3 atomic columns (Figs. 95(a-d)). This is also expected as the projected atomic numbers and, hence, the potentials are comparable. Additionally, the area-integrated real space probe intensities for a beam position close to a pure O atomic column are quite similar to those of beam positions close to Ti-O and Sr atomic columns at an acceleration voltage of 200 kV (Fig. 95(e)). At 30 kV, the thickness dependent area-integrated real space probe intensity behaves differently if the incident beam's position is close to an O atomic column (Fig. 95(f)). This can be derived from the observation that most of the intensity can be found in the projected area around the O1 atomic column. In contrary to this, much of the intensity is also found in the area of the atomic column on the right sight of the central atom if the beam is positioned close to a Sr and Ti-O atomic column ((Figs. 95(b, d)). Assuming a beam close to a Sr atomic column and an acceleration voltage of 30 kV, most of the intensity is found around the pure O atomic column, O3, if the specimen thickness is larger than 9.8 nm. As the O3 is on the right of the Sr1 atomic column, this is rather unintuitive as a deflection and thus an analogous redistribution of intensity to the left is expected for such a beam position.
All these findings could lead to a possible explanation why the DPC image for an acceleration voltage of 30 kV only shows dominant deflections (colour wheels) around the pure O atomic columns (Fig. 40(e)): While the intensity is distributed mostly across two atomic columns if the beam is placed close to a Sr or a Ti-O atomic column, most of the beam intensity interacts with the potential of the O1 atomic column for a beam position close to the O atomic column.

The line profiles of the real space probe intensity in x-direction as a function of the specimen thickness were shown in the main body of this thesis. In the following, the real space probe intensity profiles in y-direction is shown. These line profiles are obtained in a similar way and more importantly from the same data as the profiles in x-direction shown in Fig. 42 (200 kV) and Fig. 43 (30 kV). The positions of the incident electron beam are depicted in Figs. 96(a-c). All profiles (Figs. 96(d-i)) are mirror symmetrical around the position of the incident electron beam. The dominant direction of intensity redistribution (Fig. 42 and Fig. 43) is in x-direction. Thus, a spiral trajectory of the electron intensity is not evident from the real space probe intensities for the considered beam position.

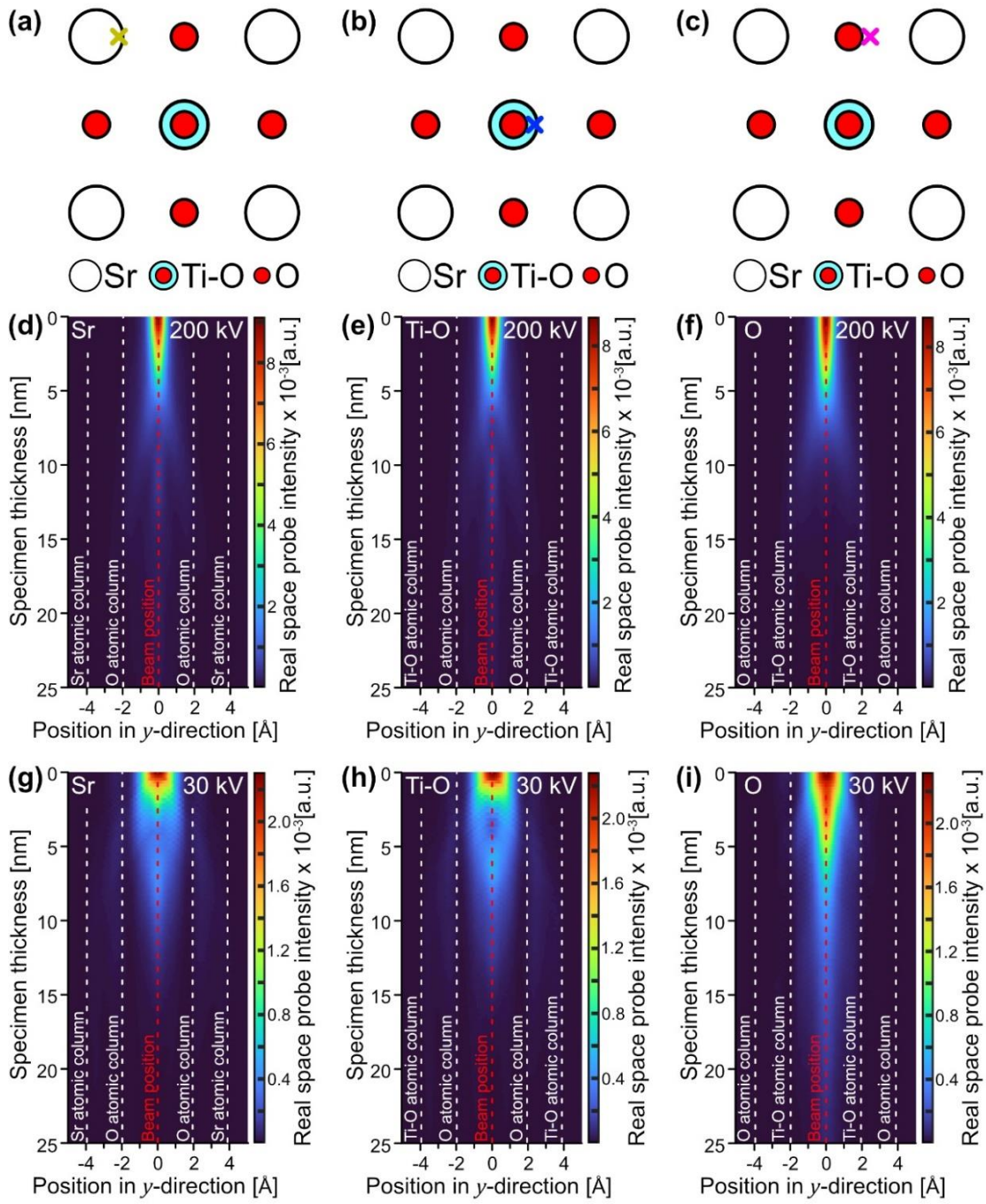

Figure 96: (a-c) Beam positions used for the simulations of real space probe intensities in dependency of the specimen thickness in $SrTiO_3$[001]. Beam positions are 0.05 nm on the right side of (a) a Sr, (b) Ti-O and (c) a pure O atomic column. Real space probe intensity profiles in y-direction for an acceleration voltage of (d-f) 200 kV and (g-i) 30 kV. Simulation parameters for the 30 kV profiles are given in Table 22 and the ones for the 200 kV in Table 23.

A.2.5. Three-fold astigmatism A_2 in images of $SrTiO_3$[001]

A zoomed in version of the DPC image of a 3.51 nm thick $SrTiO_3$[001] is shown in Fig. 97. This image is part of the investigations on the influence of three-fold astigmatism A_2 and spherical aberration C_3 on the DPC images displayed in Fig. 47. Simulation parameters are listed in Table 26 in the Appendix.

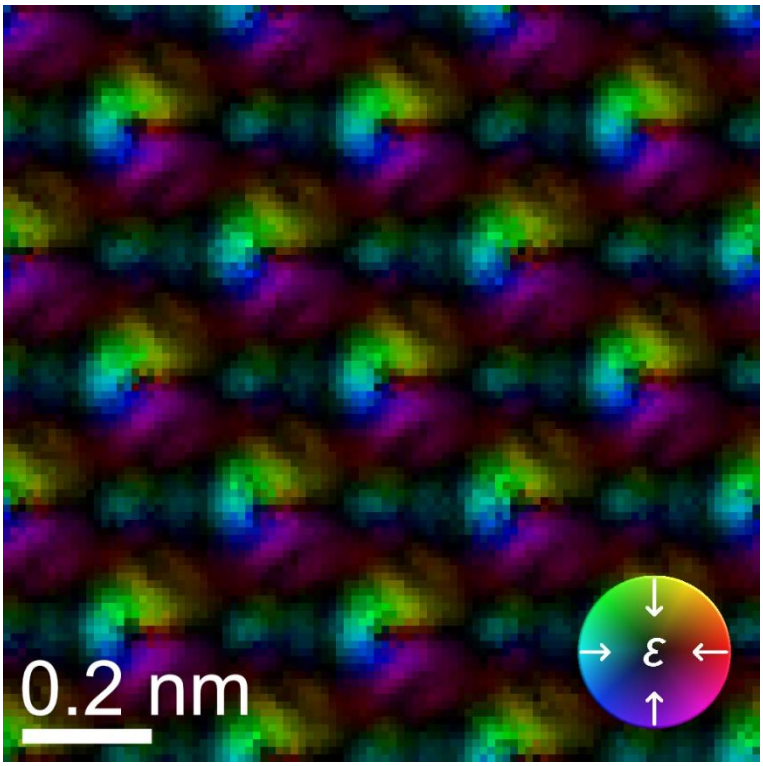

Figure 97: Simulated DPC image of a $SrTiO_3$[001] crystal with a thickness of 3.51 nm. Simulation parameters are found in Table 26.

Fig. 98 displays the HAADF image corresponding to the DPC image shown in Fig. 97. The red triangle highlights the three-fold symmetry of intensity around one exemplarily chosen atomic column.

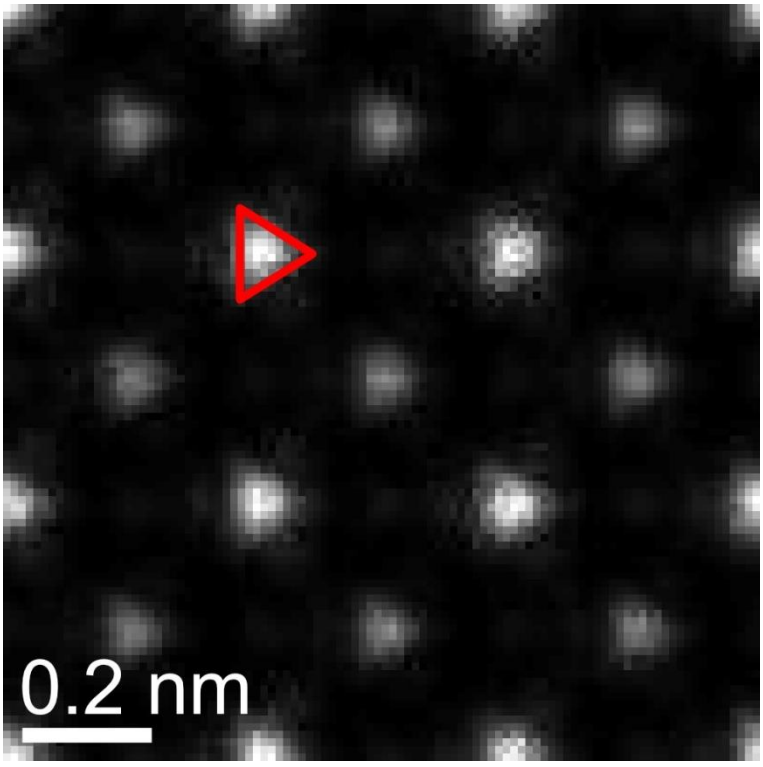

Figure 98: Simulated HAADF image of a $SrTiO_3$[001] crystal with a thickness of 3.51 nm corresponding to the DPC image simulation in Fig. 97. The Simulation parameters are found in Table 26.

A.2.6. Defocus dependent HAADF images of Si[110]

This chapter reveals the influence of defocus on obtainable HAADF images for a 30.7 nm thick Si[110] specimen using multislice image simulations. The HAADF images are displayed in Fig. 99, the simulation parameters are given in Table 31. A strong dependency on the defocus is observable in Fig. 99 because the intensity distribution of individual atomic columns exhibits rectangular shapes for under- and overfocus conditions.

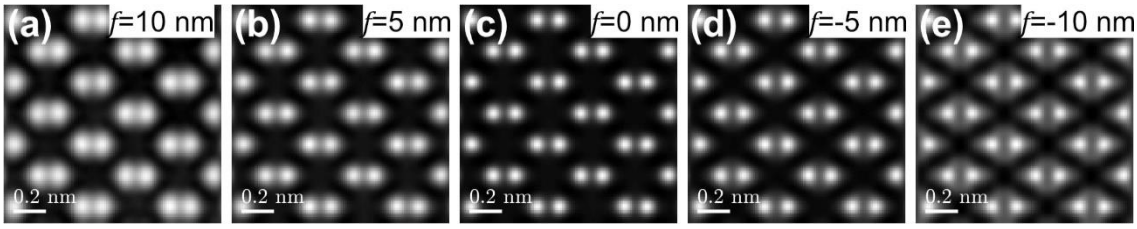

Figure 99: Simulated HAADF images of a 30.7 nm thick Si[110] specimen assuming a defocus of (a) f=10 nm, (b) f=5 nm, (c) f=0 nm, (d) f=-5 nm, and (e) f=-10 nm. Positive defoci correspond to overfocus conditions, negative defoci to underfocus conditions. A defocus of 0 nm corresponds to a focus at the entrance slice of the specimen. Simulation parameters are compiled in Table 31.

A.2.7. Charge density and electric field magnitude maps of Si[110]

In the following, the influence of defocus on electric field magnitude maps and charge density distribution for a 30.72 nm thick Si[110] specimen is investigated using multislice image simulations. The maps and additionally line profiles are displayed in Fig. 100. The defocus value is depicted in the upper left corner of the electric field magnitude map. A defocus of 0 nm corresponds to the case where the beam is focused to the entrance slice. Positive values correspond to overfocus conditions, and negative values to underfocus conditions (focal plane in the specimen). A list of simulation parameters is compiled in Table 31.

The defocus has a strong influence on electric field magnitude maps and obviously also on calculated charge density maps, as the latter is derived from the former. Rotational symmetric field around dumbbells are only detectable in case of underfocus conditions. This can be recognised by the specific shape of the dumbbells: three local minima, which are surrounded by an elliptical feature of high electric field magnitude (further explanation given in Chapter 6.1.2). For underfocus conditions, separated positive charge densities in the vicinity of the atomic nucleus can be observed. For f=0 nm, the electric field magnitude map exhibits bar-like features of high magnitude around atomic column. The observable charge density in the vicinity of the atomic column positions for f=0 nm is still positive. A reduced distance of positive maxima and the decreased ratio of minimum (midway between the atomic columns) and maximum charge density is observable compared to underfocus conditions. It is interesting to note that a difference of peak charge densities $\Delta\rho$ of left and right atomic columns of a dumbbell is observable only for f=0 nm. For overfocus conditions (f>0 nm), three

minima but no elliptical feature of high magnitude are observable for the electric field magnitude map and atomic columns show negative charge densities.

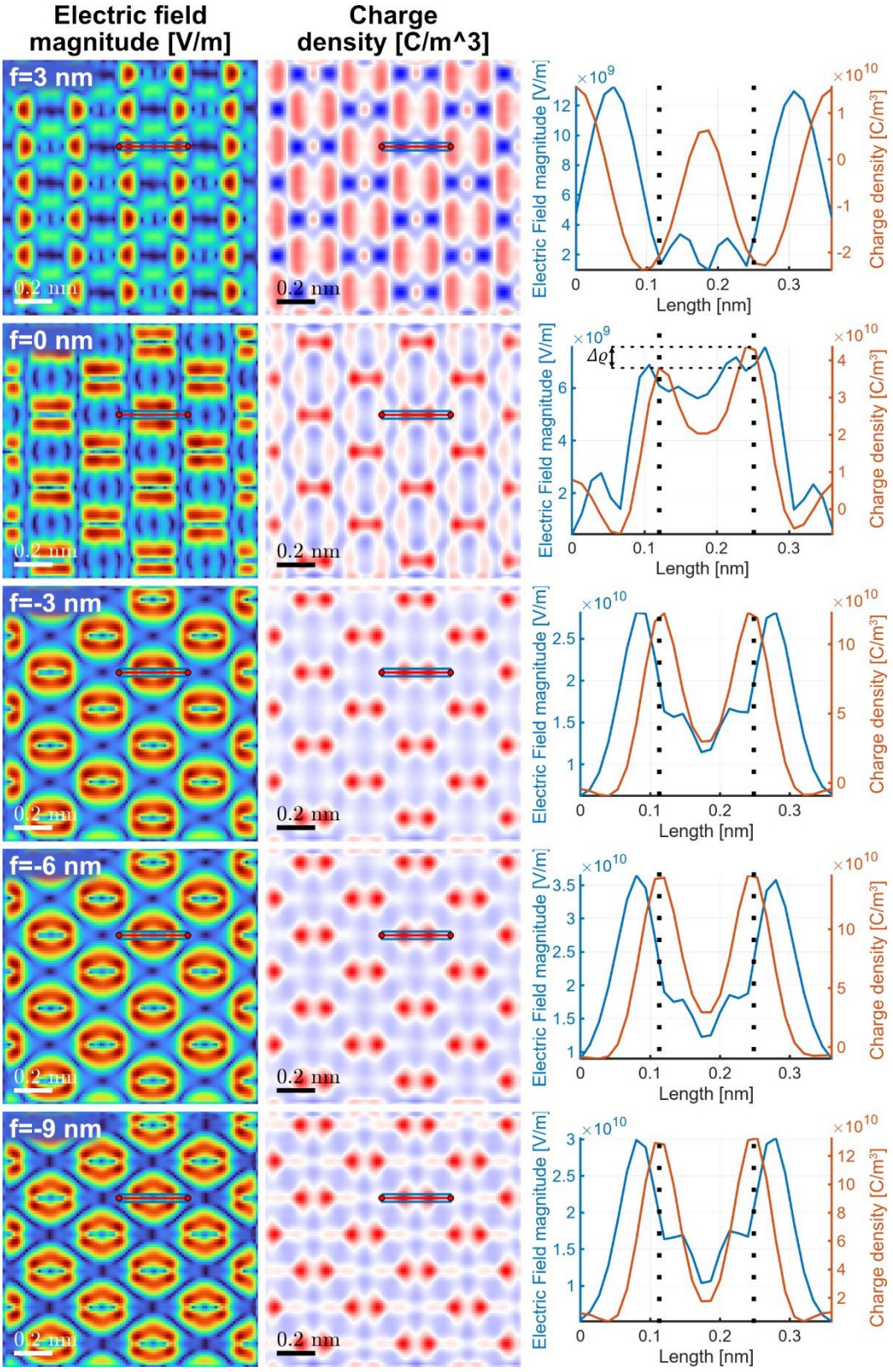

Figure 100: Simulated maps of the electric field magnitude and charge density of a 30.7 nm thick Si[110] specimen in dependency of the defocus. Line profiles which are calculated from the marked areas (red line surrounded by blue box) are additionally included. Simulation parameters can be found in Table 31.

A.2.8. Schematic band diagram of InAs at ZB-WZ heterointerface

Fig. 101 shows a schematic band of the band structure at a zinc blende-wurtzite (ZB-WZ) interface in InAs [188]. Values are derived from DFT calculations of electronic band diagrams at the Γ-point of the Brillouin zone.

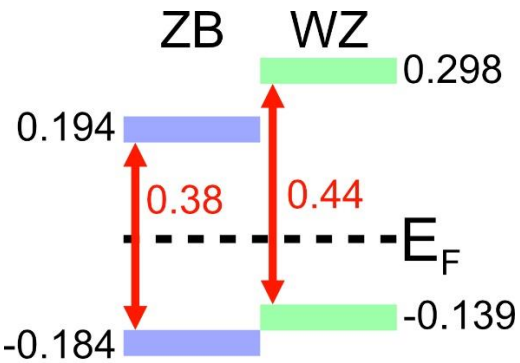

Figure 101: Schematic of the band alignment near the fundamental bandgap E_0 at the Γ-point of the Brillouin zone of InAs at a ZB-WZ heterointerface. Red values indicate the bandgaps of wurtzite and zinc blende InAs. Energy values are given in units of eV. E_F=0 eV denotes the Fermi energy. This figure is adapted from [188].

A.2.9. Distance of electric field minima in InAs

Field minima are visible in the measured electric field magnitude map at regions in which the field vectors resulting from overlapping potentials cancel each other out. In an ideal DPC image, the local field minima are evident exactly at atomic column positions and on the connecting axes between neighbouring atomic columns if the measured electric field distribution is only influenced by the atomic potentials, i.e. dynamical effects and the influence of lens aberrations and specimen tilt can be neglected. As the relative position of the field minimum on the connecting axis is influenced by the contributing charges, this ultimately allows to calculate the effective charge density ratio of two atomic columns by using the distance of the atomic columns and the minimum midway between them as detailed below.

The inset in Fig. 102(a) illustrates two point charges ($q_1 \neq q_2$) with respective distances r_2 and r_1 to the point where the opposing electric field vectors cancel each other out on the q_1-q_2-connecting axis. From a superposition of the electric fields $\vec{E}_i$ of individual point charges, it follows that

$$\left|\vec{E}_1\right| = \left|\vec{E}_2\right| \Rightarrow \frac{1}{4\pi\varepsilon_0}\frac{q_1}{r_1^2} = \frac{1}{4\pi\varepsilon_0}\frac{q_2}{r_2^2} \Rightarrow \frac{r_2^2}{r_1^2} = \frac{q_2}{q_1}. \tag{79}$$

Here, ε_0 is the vacuum permittivity. By assuming that each atomic column acts like a point charge and by measuring the distances r_2 and r_1 in the experimental electric field magnitude map, the effective ratio of charge densities of the two atomic columns of a dumbbell can be calculated.

This is exemplarily shown for InAs[110] (Fig. 102(a)) with line profiles of the HAADF intensity and charge density, which span across one dumbbell as it is indicated in the HAADF image in Fig. 102(b). In the following, point charge q_1 corresponds to the In

atomic column and q_2 to the As atomic column. By assuming that the atomic columns positions are exactly on the position of the two outer local minima of the electric field magnitude profile, the measured distances to the central field minimum amount to r_1=0.084 nm and r_2=0.075 nm resulting in a q_2/q_1 ratio of 1.23.

Averaging the q_2/q_1 ratio of 25 dumbbells results in 1.79±1.21 (precision given by standard deviation). This differs from the expected q_2/q_1 ratio of 1.48 for InAs (In: Z=49; As: Z=33). Possible explanations for the difference include the screening of atomic potentials in the measurement, residual lens aberrations, image noise, and the redistribution of intensity along the atomic columns due to a coherent scattering effect, which is different for the In and As atomic columns. The amorphous layer at the top and bottom of the InAs island as well as different numbers of atoms in the atomic columns of the considered 25 dumbbells (manually selected!) influence the standard deviation. As the experimentally deduced q_2/q_1 ratio is close to the expected q_2/q_1 ratio (despite the image quality), the approach presented above is promising for future research.

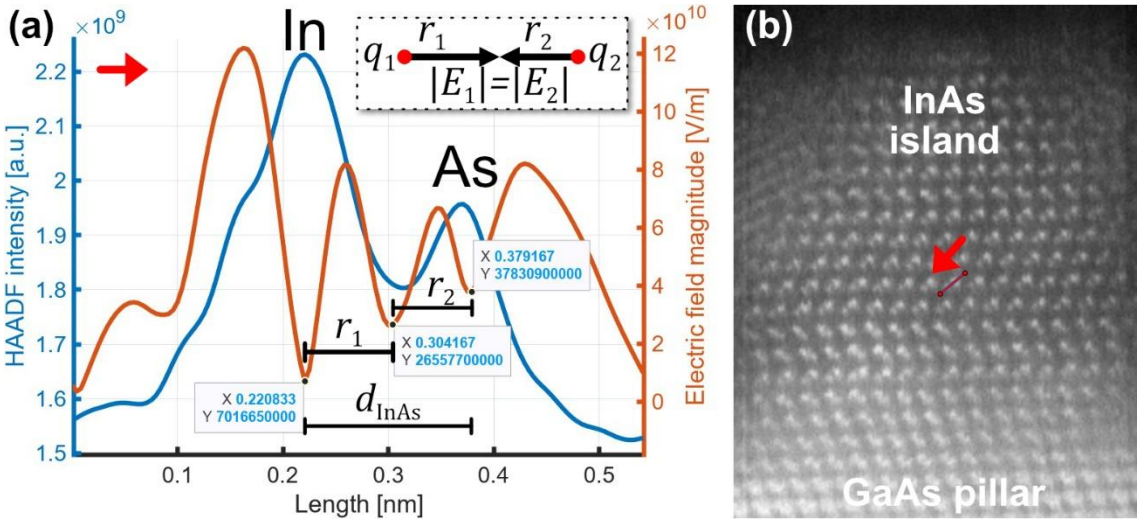

Figure 102: (a) Line profiles of HAADF intensity and charge density measured over a InAs dumbbell as indicated in the HAADF image of (b). The inset and the annotations in (a) indicate the parameters used for the calculation of effective charge density ratio. The X values in the annotations denote the position of the line profile and the Y values the electric field distribution at point X. A list of imaging parameters is compiled in Table 53 in the Appendix.

A.2.10. HAADF and electric field vectors at InAs twin

In Chapter 6.2.2, the electric field distribution at a twin boundary in InAs is investigated. Fig. 103(a) displays an HAADF image of an area close to the defect. The electric field vectors are depicted in Fig. 103(b). The atomic column positions are marked by green and red dots. These positions are deduced from the position of HAADF peak intensity of individual atomic columns. Here, no characteristic field at the twin boundary can be seen.

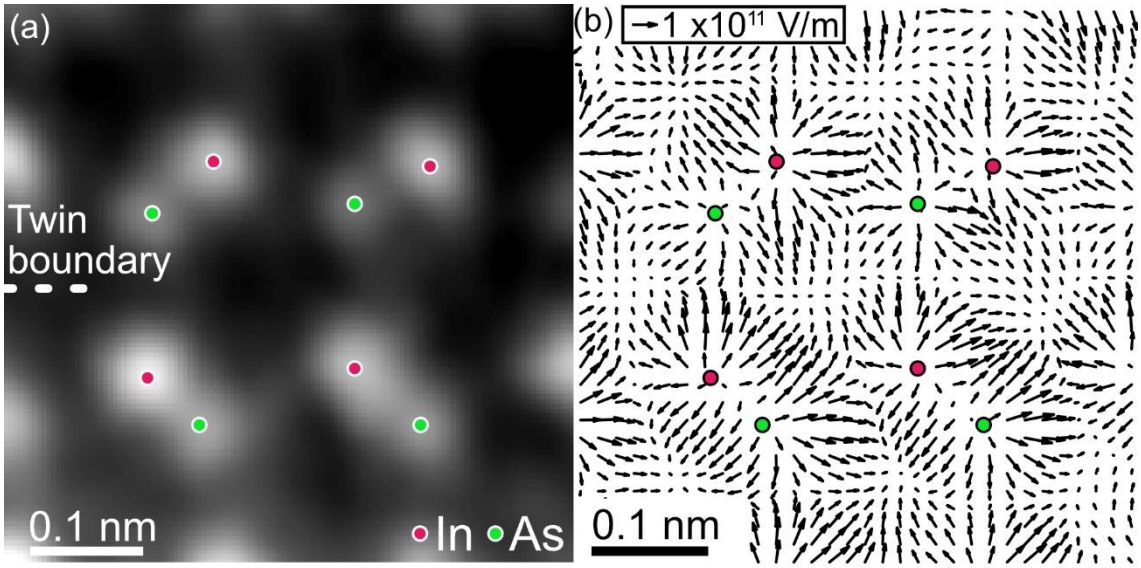

Figure 103: (a) HAADF image and (b) electric field vector map calculated from DPC image. A list of imaging parameters is compiled in Table 53 in the Appendix.

A.2.11. WSe_2: Influence of three-fold astigmatism and specimen tilt

In this chapter, the combined influence of three-fold astigmatism A_2 and specimen tilt on HAADF and DPC images as well as electric field maps and charge density distributions for a WSe_2[0001] monolayer are studied. Three-fold astigmatism ranges from 500 nm to -500 nm in steps of 100 nm. Specimen tilt is assumed to act in x-direction of the image and specimen tilt from -20 mrad to 25 mrad in steps of 5 mrad are assumed. The tilting axis as well as the specimen structure are indicated in Fig. 104. A list of simulation parameters is compiled in Table 32.

Fig. 104 shows the resulting HAADF images in which several trends can be observed. With increasing A_2, the intensity around individual atomic columns exhibits a triangular shape. The typical Z-contrast from the WSe_2 crystal can be recognised for A_2 magnitudes lower than 200 nm. At absolute values of A_2 of above 200 nm HAADF intensity at interatomic pixels is visible as a result of the probe extension. In the considered range of specimen tilt no significant change is visible. This is also possibly due to the fact that the specimen structure is only a monolayer, i.e. W atomic columns only consist of a single W atom.

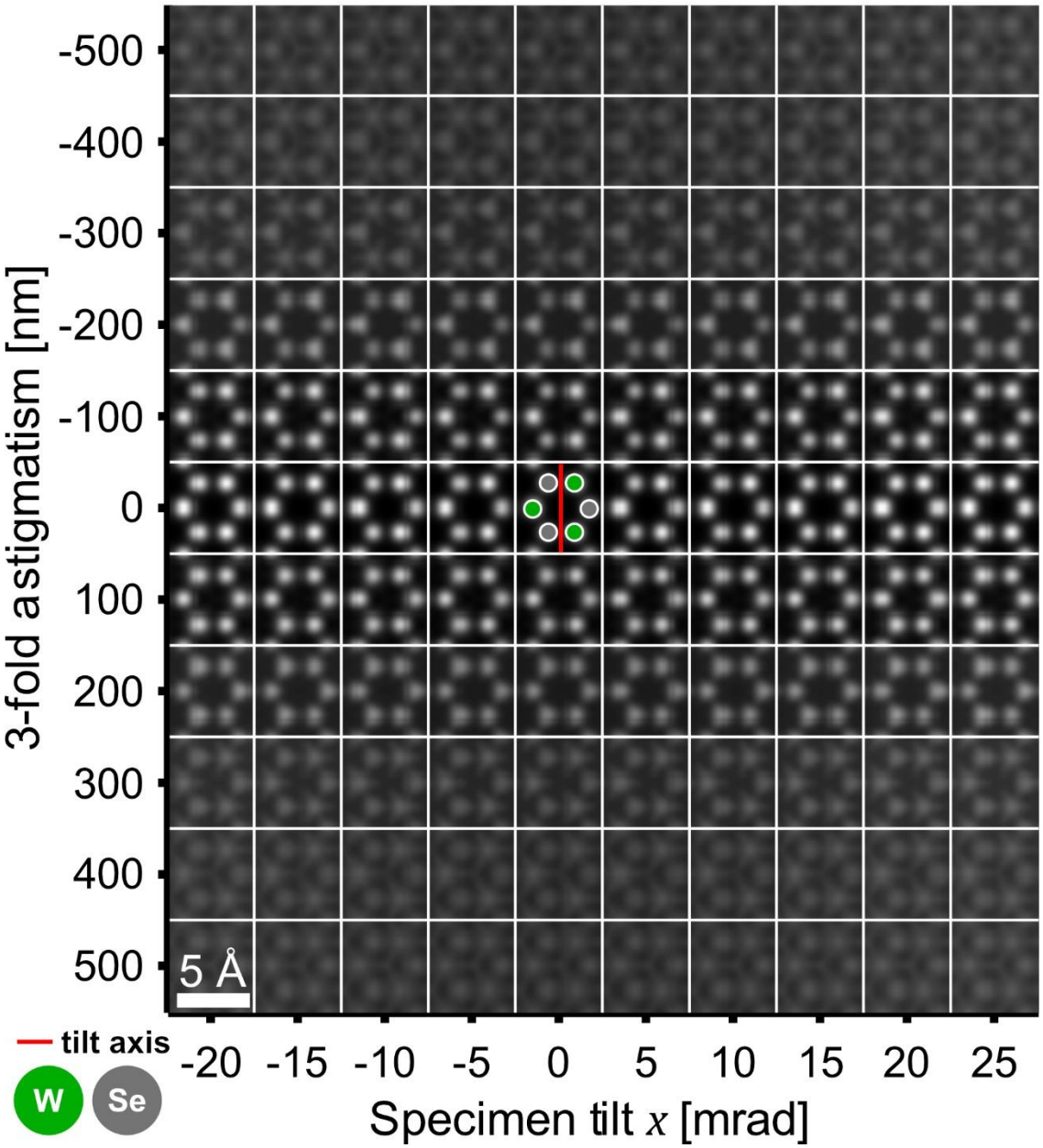

Figure 104: HAADF images of WSe_2[0001] in dependency of three-fold astigmatism and specimen tilt in x-direction. Simulation parameters are listed in Table 32.

Fig. 105 depicts the corresponding DPC images. The DPC images are individually normalised to optimise the visibility of features in the DPC images. With increasing A_2 a distortion of colour wheels at individual atomic columns is observed. While colour wheels are recognisable for A_2 magnitudes below 300 nm, above absolute A_2 values of 300 nm a dominance of red and bright blue colours is obvious. In addition, inverted colour wheels at interatomic pixels (a description of this feature is given in Chapter 6.3.2) are distorted in presence of A_2 and a shift of the central minimum in the inverted colour wheel with respect to the atomic column positions is visible. This shift is exemplarily indicated by three white arrows. In the considered range of specimen tilt, no change of the DPC signal is obvious. This can be explained by the fact that the atomic columns only contain a single W atom or just two Se atoms.

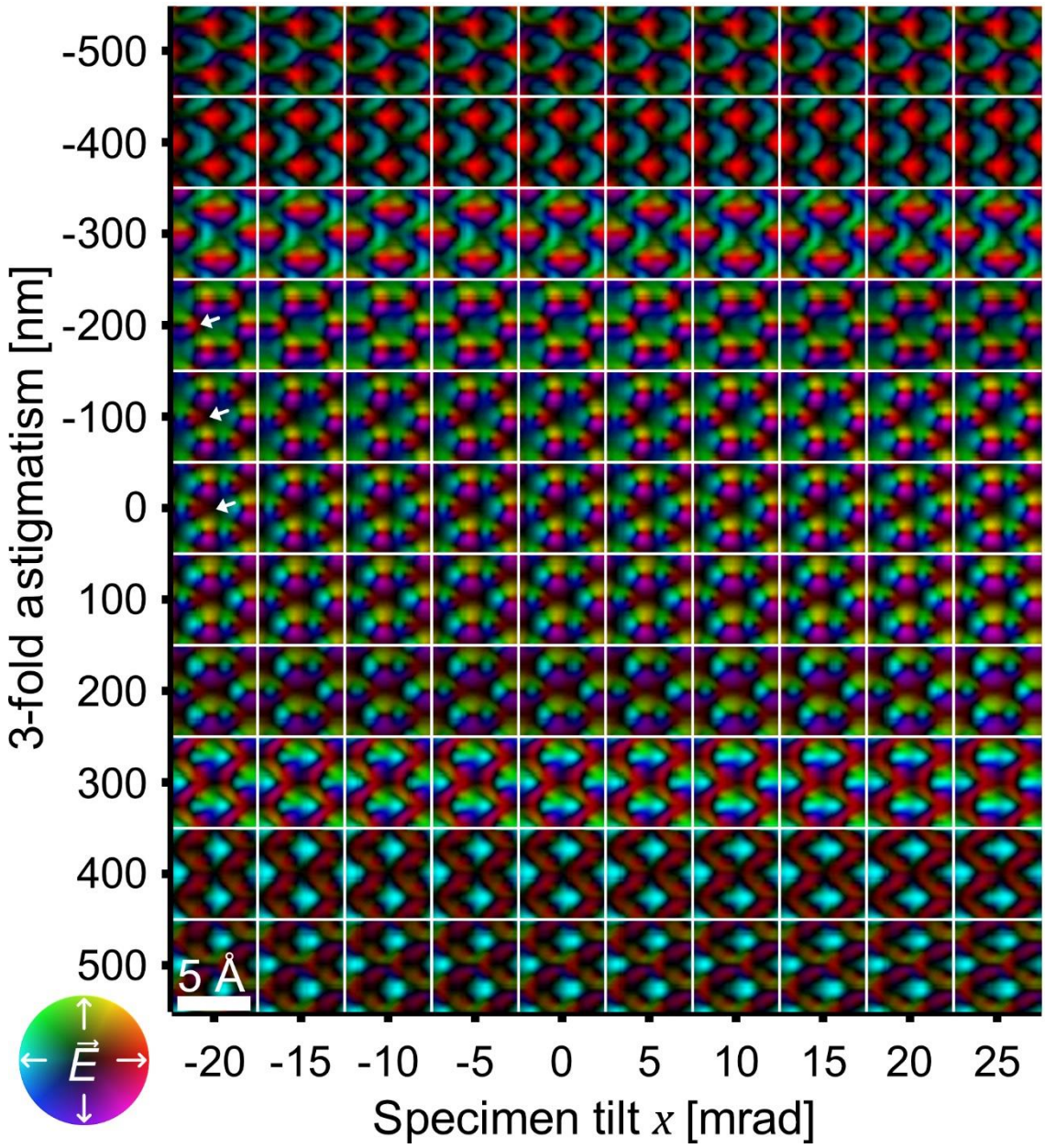

Figure 105: Individually normalised DPC images of WSe_2[0001] in dependency of three-fold astigmatism and specimen tilt in x-direction. Simulation parameters are listed in Table 32.

Fig. 106 displays all DPC images normalised to the overall maximum DPC signal of the complete image series. It can be seen that any presence of A_2 reduces the overall DPC signal magnitude as the intensity vanishes with increasing A_2. This is in good agreement with the findings on the influence of lens aberrations (Chapter 5.5). In the considered range of specimen tilt no significant change of DPC image is obvious.

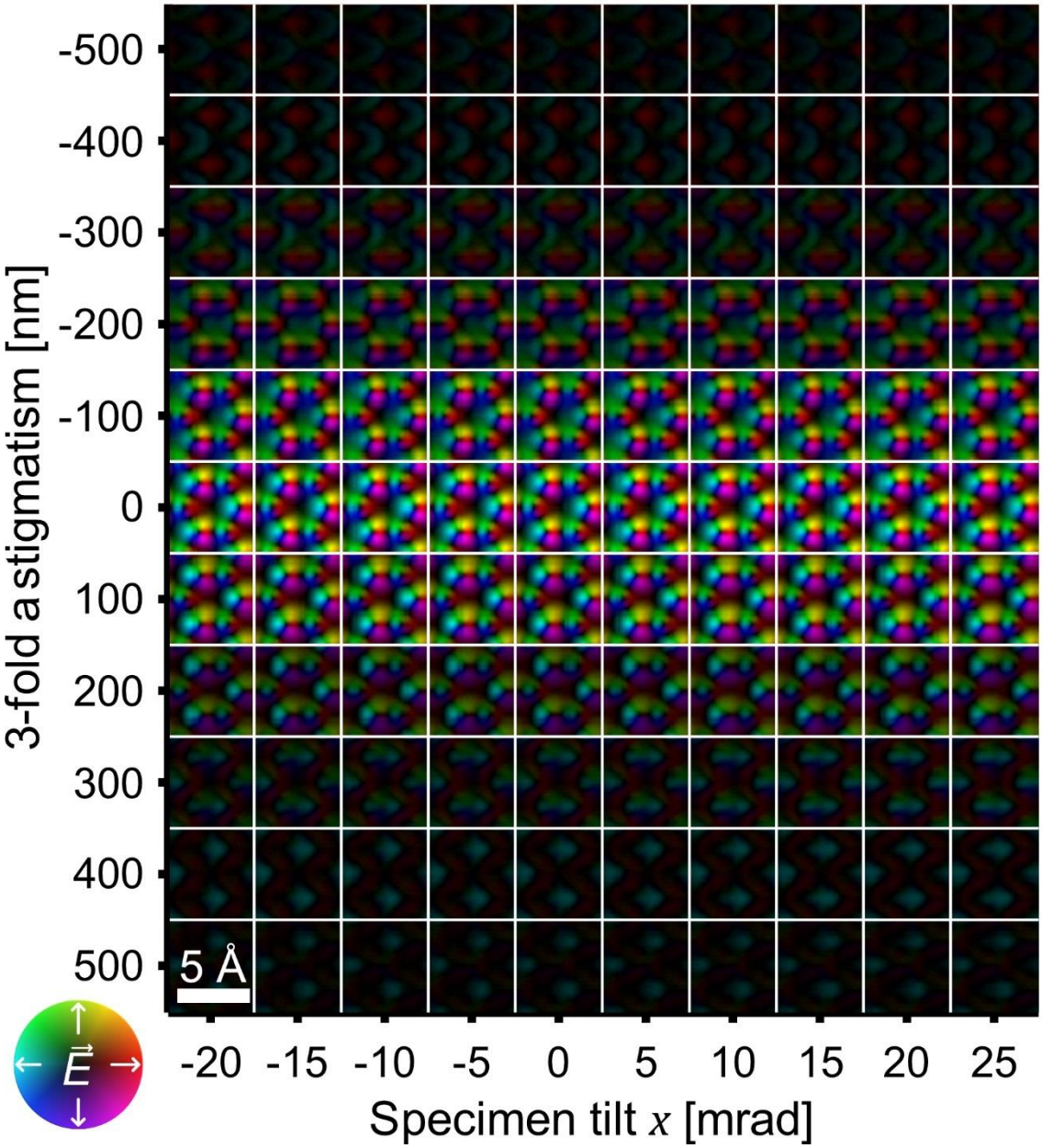

Figure 106: DPC images of WSe_2[0001] in dependency of three-fold astigmatism and specimen tilt in x-direction. All images are normalised to the overall maximum DPC signal magnitude and a list of simulation parameters is given in Table 32.

Fig. 107 displays maps of the electric field magnitude which is derived from the DPC images in Fig. 106. As the electric field magnitude is directly derived from the DPC image, it is likewise influenced by the present three-fold astigmatism A_2 and specimen tilt.

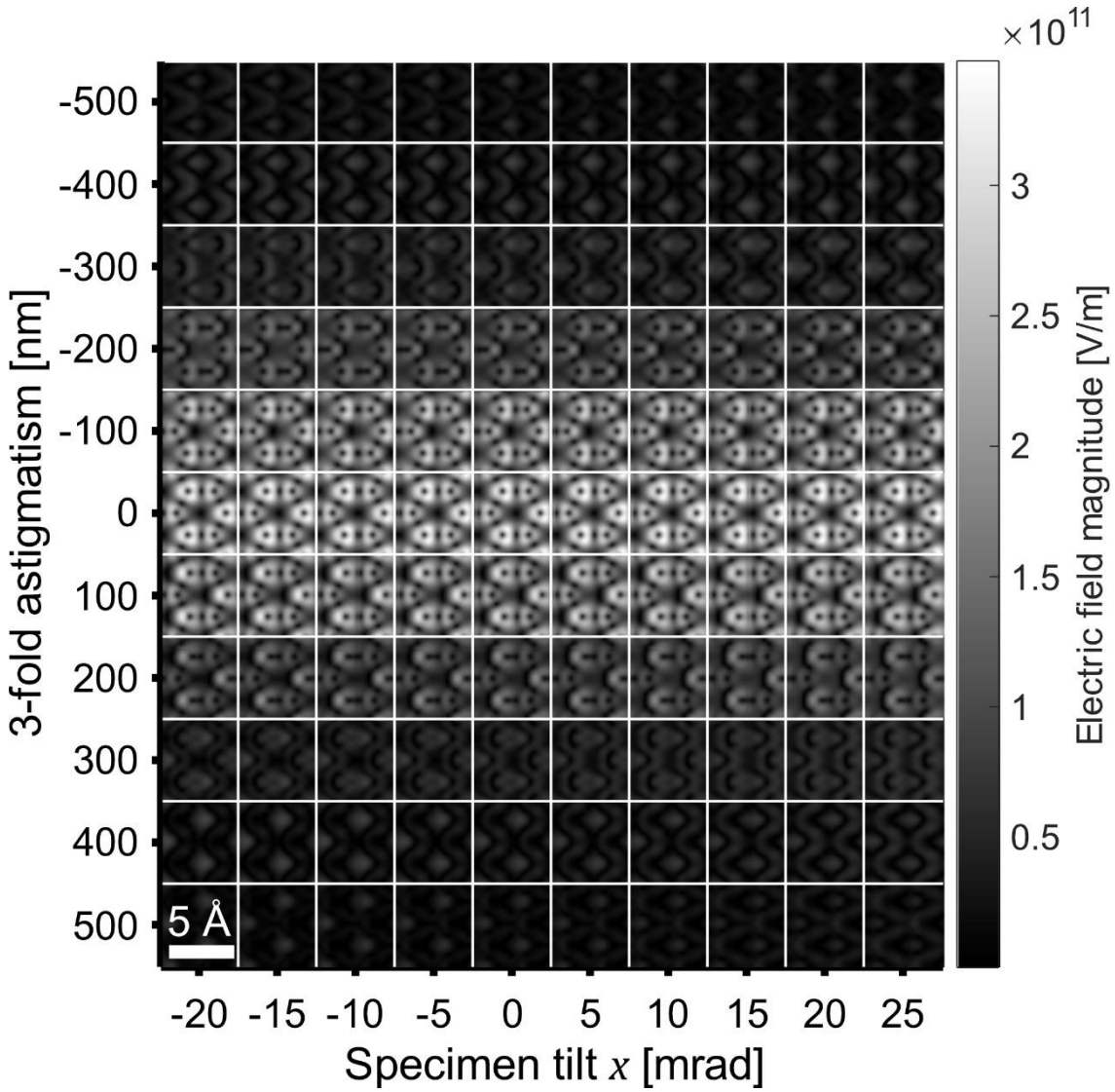

Figure 107: Maps of the electric field magnitude of WSe_2[0001] in dependency of three-fold astigmatism and specimen tilt in x-direction. These maps are obtained from the DPC images in Fig. 106. A list of simulation parameters is compiled in Table 32.

Fig. 108 displays the charge density distributions which are derived from the electric field maps. Again, a strong influence of three-fold astigmatism for the considered range of lens aberration coefficients is obvious. While positive charge densities at atomic column positions can be recognised for absolute values of A_2 below 300 nm, individual atomic columns can no longer be detected after further increasing A_2. In addition, positive charge densities at individual atomic columns are already distorted below absolute A_2 values below 300 nm. This can be seen from the positive charge density at the W atomic column exhibiting a triangular shape for negative values of A_2 (indicated for A_2=-200 nm by a black triangle) and at the Se atomic column for positive values of A_2 (indicated for A_2=200 nm by a green triangle). No significant impact of specimen tilt on the charge density is observed for the considered range of specimen tilt.

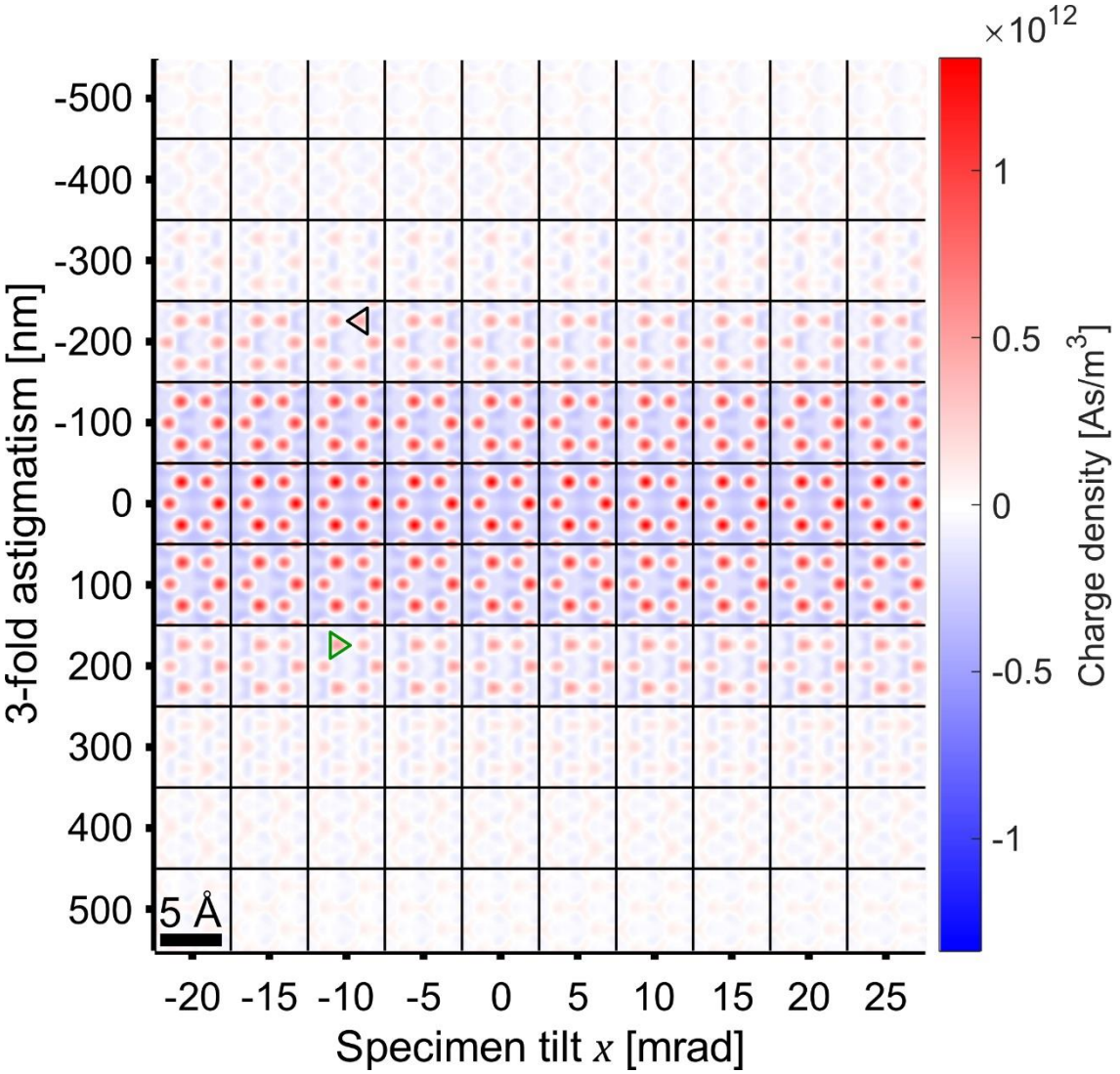

Figure 108: Charge density distributions of WSe_2[0001] in dependency of three-fold astigmatism and specimen tilt in x-direction. These maps are obtained from the DPC images in Fig. 107. Simulation parameters are compiled in Table 32.

A.2.12. Investigation of Se vacancies

Images supporting the investigation on the impact of vacancy-type defects on the electric field distributions in a WSe_2 bilayer (Chapter 6.3.4) are displayed in Fig. 109. Information on the imaging conditions and post-processing parameters are given in Table 55.

Fig. 109(a) shows the large-area HAADF image containing several defects. The corresponding DPC image is depicted in Fig. 109(b). One defective area is exemplarily marked by a red box and magnified in Figs. 109(c, d, g). It is exactly this area which is used in Chapter 6.3.4. Besides vacancy-type defects, also other defects including substitutional and interstitial atoms are visible. While the presence of the former can explain bright intensities at atomic column positions (exemplarily marked by white arrows), the latter is seen by strong intensities in between the atomic columns (blue arrow). Contamination, which is sitting at the top and the bottom of the bilayer lead to island like modulations of HAADF intensity (low spatial frequency). The area which is highlighted by a green box in Fig. 109(a) is used for the calculation of the electric field

of a pristine lattice which is considered for the calculation of electric field difference due to the presence of defects. The final image of electric field of a pristine lattice is obtained by using the green marked area as the reference image in a rigid registration (Chapter 4.4.2). The registration is based on the HAADF image assuming a threshold cross-correlation coefficient of 0.73. Such a threshold coefficient guarantees that only almost defect free areas are superimposed. This reduces the impact of defects on the electric field distribution and thus the resulting images can be assumed to be defect free. In total, 300 images are superimposed by this technique. The resulting HAADF image and DPC image are displayed in Figs. 109(e, f). Here, very regular HAADF intensities and electric field distributions are visible.

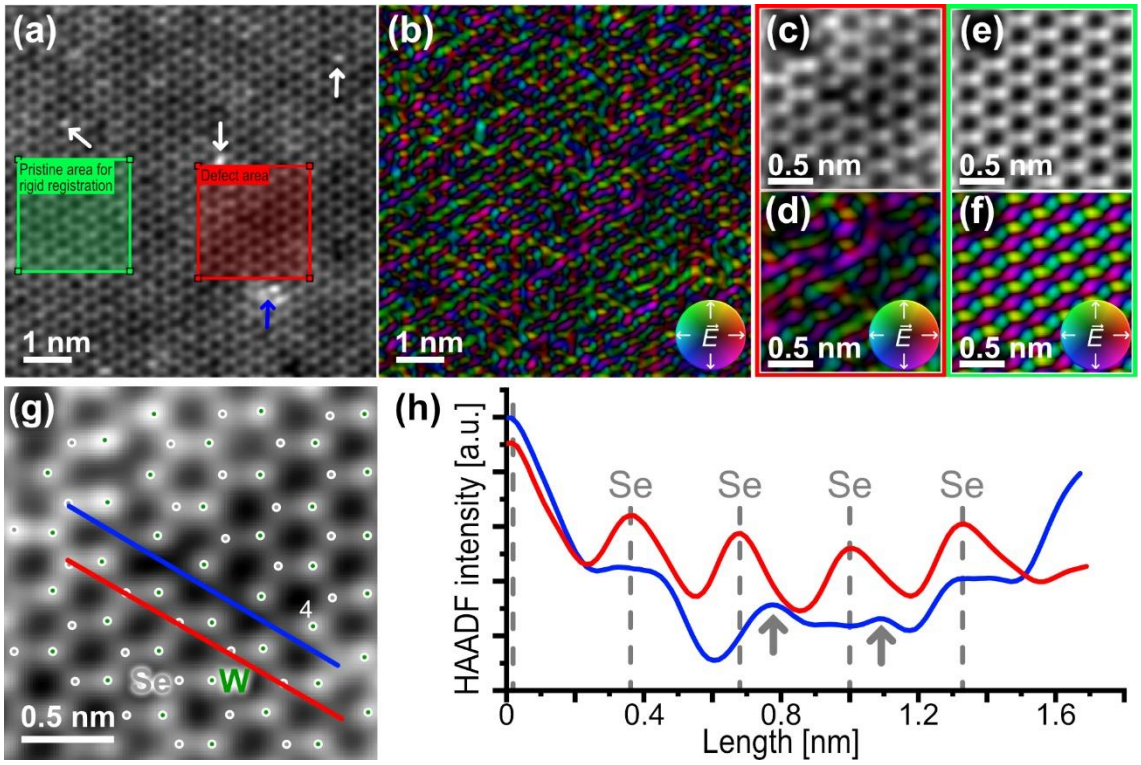

Figure 109: (a) Large-area HAADF image of a bilayer of WSe_2 near [0001] zone axis orientation. (b) Corresponding DPC image. The DPC image and HAADF image of the area used for the investigation of the impact of defects are displayed in (c) and (d), respectively. (e) HAADF image and (f) DPC image after rigid registration using the green marked area in (a). (g) Magnified view of the defective area additionally indicating the position of HAADF intensity line profiles displayed in (h).

Line-profiles of HAADF intensity in $[01\bar{1}0]$ direction which are indicated by blue and red lines in Fig. 109(g) are depicted in Fig. 109(h). By comparing the line profile intensity of a pristine lattice (red curve) with the one across the line-like defect cluster, it is obvious that the line-like defect cluster comprises different types of Se vacancies, i.e. different number of missing Se atoms in an atomic column.

A.3. Simulation parameters

This chapter lists the parameters for the multislice simulations.

Table 8: Parameters for the CBED multislice simulations displayed in Fig. 8(d) and Figs. 9(d-f).

Figures	Fig. 8(d), Figs. 9
Type of simulation	CBED pattern simulation
Material system and zone-axis orientation	$SrTiO_3$[001]
Unit cell size (x-, y-, z-direction)	0.3905 nm x 0.3905 nm x 0.3905 nm
Unit cell repetitions for supercell (x-, y-, z-direction)	15, 15, 1
Unit cell slice along z-direction	2
Slice structure	0: 225 Sr, 225 O 1: 225 Ti, 450 O
Frozen lattice configurations	100
Supercell discretisation	864 x 864
Mean square displacements [nm^2]	Sr: 0.0066 Ti: 0.0051 O: 0.0108
Fixed absorption parameter	0.1
Repetitions per scan position	100
Defocus [nm]	0 (entrance slice)
Other lens aberrations	All zero
Acceleration voltage [kV]	200 kV
Effective source profile	Gaussian (HWHM = 0.04 nm)
Aperture radius [mrad]	25
Aperture centre [mrad]	X=0, Y=0
Structure thickness [nm]	2.73
Specimen tilt [°]	0

Table 9: Simulation parameter of the DPC and HAADF multislice simulations of Fig. 10.

Figure	Fig. 10	
Type of simulation	Image simulation	
Material system and zone-axis orientation	$SrTiO_3$[001]	
Unit cell size (x-, y-, z-direction)	0.3905 nm x 0.3905 nm x 0.3905 nm	
Unit cell repetitions for supercell (x-, y-, z-direction)	10, 10, 1	
Unit cell slice along z-direction	2	
Slice structure	0: 100 Sr, 100 O 1: 100 Ti, 200 O	
Frozen lattice configurations	50	
Supercell discretisation	1000 x 1000	
Mean square displacements [nm^2]	Sr: 0.0066 Ti: 0.0051 O: 0.0108	
Fixed absorption parameter	0.1	
Repetitions per scan position	1	
Defocus [nm]	-5.5 (underfocus)	
Other lens aberrations	All zero	
Acceleration voltage [kV]	200 kV	
Effective source profile	Gaussian (HWHM = 0.04 nm)	
Aperture radius [mrad]	25	
Aperture centre [mrad]	X=0, Y=0	
SAAF detector collection angles [mrad]	β_{inner}=18.0	β_{outer}=35.8
Detector rotation [°]	φ=0	
HAADF detector collection angles	$\beta_{\mathrm{inner,HAADF}}$=51.0	$\beta_{\mathrm{outer,HAADF}}$=180
Structure thickness [nm]	11.32	
Specimen tilt [°]	0	
Detector configuration	Layer2, bisected (Chapter 3.1)	

Table 10: Simulation parameter of the multislice DPC and HAADF simulations of Fig. 17 and Fig. 18.

Figures	Fig. 17, Fig. 18	
Type of simulation	Image simulation	
Material system and zone-axis orientation	$SrTiO_3$[001]	
Unit cell size (x-, y-, z-direction)	0.3905 nm x 0.3905 nm x 0.3905 nm	
Unit cell repetitions for supercell (x-, y-, z-direction)	10, 10, 1	
Unit cell slice along z-direction	2	
Slice structure	0: 100 Sr, 100 O 1: 100 Ti, 200 O	
Frozen lattice configurations	50	
Supercell discretisation	1000 x 1000	
Mean square displacements [nm^2]	Sr: 0.0066 Ti: 0.0051 O: 0.0108	
Fixed absorption parameter	0.1	
Repetitions per scan position	1	
Defocus [nm]	-2 (underfocus)	
Other lens aberrations	All zero	
Acceleration voltage [kV]	200 kV	
Effective source profile	Gaussian (HWHM = 0.04 nm)	
Aperture radius [mrad]	25	
Aperture centre [mrad]	X=0, Y=0	
SAAF detector collection angles [mrad]	β_{inner}=18.0	β_{outer}=35.8
Detector rotation [°]	φ=0	
HAADF detector collection angles	$\beta_{\mathrm{inner,HAADF}}$=51.0	$\beta_{\mathrm{outer,HAADF}}$=180
Structure thickness [nm]	3.51	
Specimen tilt [°]	0	
Detector configuration	Layer2, bisected (Chapter 3.1)	

Table 11: Parameters for multislice image simulation shown in Fig. 19(b) and Fig. 20(b).

Figures	Fig. 19(b) and Fig. 20(b)
Type of simulation	CBED simulation
Material system and zone-axis orientation	Si[110]
Unit cell size (x-, y-, z-direction)	0.768 nm x 0.5431 nm x 0.768 nm
Unit cell repetitions for supercell (x-, y-, z-direction)	10, 10, 1
Unit cell slice along z-direction	4
Slice structure	0: 400 Si 1: 400 Si 2: 400 Si 3: 400 Si
Frozen lattice configurations	50
Supercell discretisation	500 x 500
Mean square displacements [nm^2]	Si: 0.0070
Fixed absorption parameter	0.1
Repetitions per scan position	100
Defocus [nm]	-6 (underfocus)
Other lens aberrations	All zero
Acceleration voltage [kV]	200 kV
Effective source profile	Gaussian (HWHM = 0.04 nm)
Aperture radius [mrad]	25
Aperture centre [mrad]	X=0, Y=0
Structure thickness [nm]	30.72 (40 unit cells)
Specimen tilt [°]	0

Table 12: Parameters for multislice image simulation shown in Figs. 19(c, d, f) and Figs. 20(a, c).

Figures	Fig. 19(c, d, f) and Fig. 20(a, c)	
Type of simulation	Image simulation series of DPC images at different detector rotations for calculation of intensity on detector segments and increase azimuthal momentum space resolution method	
Material system and zone-axis orientation	Si[110]	
Unit cell size (x-, y-, z-direction)	0.768 nm x 0.5431 nm x 0.768 nm	
Unit cell repetitions for supercell (x-, y-, z-direction)	10, 10, 1	
Unit cell slice along z-direction	4	
Slice structure	0: 400 Si 1: 400 Si 2: 400 Si 3: 400 Si	
Frozen lattice configurations	50	
Supercell discretisation	1000 x 1000	
Mean square displacements [nm^2]	Si: 0.0070	
Fixed absorption parameter	0.1	
Repetitions per scan position	1	
Defocus [nm]	-6 (underfocus)	
Other lens aberrations	All zero	
Acceleration voltage [kV]	200 kV	
Effective source profile	Gaussian (HWHM = 0.04 nm)	
Aperture radius [mrad]	25	
Aperture centre [mrad]	X=0, Y=0	
SAAF detector collection angles [mrad]	β_{inner}=18.0	β_{outer}=35.8
Detector rotation [°]	Varying as described in main body of the text	
HAADF detector collection angles	$\beta_{\mathrm{inner,HAADF}}$=51.0	$\beta_{\mathrm{outer,HAADF}}$=180
Structure thickness [nm]	30.72 (40 unit cells)	
Specimen tilt [°]	0	
Detector configuration	Layer2, bisected (Chapter 3.1)	

Table 13: Parameters for the CBED multislice simulations displayed in Fig. 26.

Figure	Fig. 26
Type of simulation	CBED pattern simulation
Material system and zone-axis orientation	$SrTiO_3$[001]
Unit cell size (x-, y-, z-direction)	0.3905 nm x 0.3905 nm x 0.3905 nm
Unit cell repetitions for supercell (x-, y-, z-direction)	10, 10, 1
Unit cell slice along z-direction	2
Slice structure	0: 100 Sr, 100 O 1: 100 Ti, 200 O
Frozen lattice configurations	50
Supercell discretisation	1000 x 1000
Mean square displacements [nm^2]	Sr: 0.0066 Ti: 0.0051 O: 0.0108
Fixed absorption parameter	0.1
Repetitions per scan position	100
Defocus [nm]	0 (entrance slice)
Other lens aberrations	All zero
Acceleration voltage [kV]	200 kV
Effective source profile	Gaussian (HWHM = 0.04 nm)
Aperture radius [mrad]	25
Aperture centre [mrad]	X=0, Y=0
Structure thickness [nm]	1.95, 3.51, 5.47, 8.97 (denoted in figure)
Specimen tilt [°]	0

Table 14: Parameters considered for the multislice image simulation used in Fig. 27(b).

Figure	Fig. 27(b)
Type of simulation	Image simulation
Material system and zone-axis orientation	$SrTiO_3$[001]
Unit cell size (x-, y-, z-direction)	0.3905 nm x 0.3905 nm x 0.3905 nm
Unit cell repetitions for supercell (x-, y-, z-direction)	10, 10, 1
Unit cell slice along z-direction	2
Slice structure	0: 100 Sr, 100 O 1: 100 Ti, 200 O
Frozen lattice configurations	Not considered
Supercell discretisation	576 x 576
Fixed absorption parameter	0.1
Repetitions per scan position	1
Defocus [nm]	-3 (underfocus)
Other lens aberrations	All zero
Acceleration voltage [kV]	200 kV
Effective source profile	Gaussian (HWHM = 0.04 nm)
Aperture radius [mrad]	25
Aperture centre [mrad]	X=0, Y=0
SAAF detector collection angles [mrad]	β_{inner} and β_{outer} are function of parameter d
Detector rotation [°]	φ=0
Structure thickness [nm]	6.25
Specimen tilt [°]	0
Detector configuration	Layer2, bisected (Chapter 3.1)

Table 15: Parameters considered for the multislice image simulation used in Fig. 28.

Figure	Fig. 28
Type of simulation	Image simulation
Material system and zone-axis orientation	$SrTiO_3$[001]
Unit cell size (x-, y-, z-direction)	0.3905 nm x 0.3905 nm x 0.3905 nm
Unit cell repetitions for supercell (x-, y-, z-direction)	10, 10, 1
Unit cell slice along z-direction	2
Slice structure	0: 100 Sr, 100 O 1: 100 Ti, 200 O
Frozen lattice configurations	Not considered
Supercell discretisation	576 x 576
Fixed absorption parameter	0.1
Repetitions per scan position	1
Defocus [nm]	-3 (underfocus)
Other lens aberrations	All zero
Acceleration voltage [kV]	200 kV
Effective source profile	Gaussian (HWHM = 0.04 nm)
Aperture radius [mrad]	25
Aperture centre [mrad]	X=0, Y=0
SAAF detector collection angles [mrad]	β_{inner} and β_{outer} are function of parameter d
Detector rotation [°]	φ=0
Structure thickness [nm]	6.25
Specimen tilt [°]	0
Detector configuration	Layer1+Layer2, bisected (Chapter 3.1)

Table 16: Simulation parameters for multislice image simulation depicted in Fig. 30.

Figure	Fig. 30	
Type of simulation	Image simulation	
Material system and zone-axis orientation	Si[110]	
Unit cell size (x-, y-, z-direction)	0.768 nm x 0.5431 nm x 0.768 nm	
Unit cell repetitions for supercell (x-, y-, z-direction)	10, 10, 1	
Unit cell slice along z-direction	4	
Slice structure	0: 400 Si 1: 400 Si 2: 400 Si 3: 400 Si	
Frozen lattice configurations	Not considered	
Supercell discretisation	500 x 500	
Fixed absorption parameter	0.1	
Repetitions per scan position	1	
Defocus [nm]	-2 (underfocus)	
Other lens aberrations	All zero	
Acceleration voltage [kV]	200 kV	
Effective source profile	Gaussian (HWHM = 0.04 nm)	
Aperture radius [mrad]	25	
Aperture centre [mrad]	X=0, Y=0	
SAAF detector collection angles [mrad]	β_{inner}=18.0	β_{outer}=35.8
Detector rotation [°]	Varying, as described in Fig. 30	
HAADF detector collection angles	$\beta_{\text{inner,HAADF}}$=51.0	$\beta_{\text{outer,HAADF}}$=180
Structure thickness [nm]	24.58	
Specimen tilt [°]	0	
Detector configuration	Layer2, bisected (Chapter 3.1)	

Table 17: Parameters for multislice image simulation in Figs. 31(b, d, f), Fig. 32(c, g, k, o, s), Fig. 33(c, g, k, o, s), Fig. 85, Fig. 86, Fig. 87 and Fig. 88.

Figures	Fig. 31(b, d, f), Fig. 32(c, g, k, o, s), Fig. 33(c, g, k, o, s), Fig. 85, Fig. 86, Fig. 87 and Fig. 88	
Type of simulation	Image simulation	
Material system and zone-axis orientation	Si[110]	
Unit cell size (x-, y-, z-direction)	0.768 nm x 0.5431 nm x 0.768 nm	
Unit cell repetitions for supercell (x-, y-, z-direction)	10, 10, 1	
Unit cell slice along z-direction	4	
Slice structure	0: 400 Si 1: 400 Si 2: 400 Si 3: 400 Si	
Frozen lattice configurations	Not considered	
Supercell discretisation	1000 x 1000	
Fixed absorption parameter	0.1	
Repetitions per scan position	1	
Defocus [nm]	-6 (underfocus)	
Other lens aberrations	All zero	
Acceleration voltage [kV]	200 kV	
Effective source profile	Gaussian (HWHM = 0.04 nm)	
Aperture radius [mrad]	25	
Aperture centre [mrad]	X=0, Y=0	
SAAF detector collection angles [mrad]	β_{inner}=18.0	β_{outer}=35.8
Detector rotation [°]	Varying, as denoted in the figures and the main body of the text.	
HAADF detector collection angles	$\beta_{\text{inner,HAADF}}$=51.0	$\beta_{\text{outer,HAADF}}$=180
Structure thickness [nm]	30.72	
Specimen tilt [°]	0	
Detector configuration	Layer2, bisected (Chapter 3.1)	
Post-processing	Optional scattergram filtering as described in the figure caption	

Table 18: Multislice image simulation parameters for the DPC images shown in Fig. 34.

Figure	Fig. 34	
Type of simulation	Image simulation	
Material system and zone-axis orientation	Si[110]	
Unit cell size (x-, y-, z-direction)	0.768 nm x 0.5431 nm x 0.768 nm	
Unit cell repetitions for supercell (x-, y-, z-direction)	10, 10, 1	
Unit cell slice along z-direction	4	
Slice structure	0: 400 Si 1: 400 Si 2: 400 Si 3: 400 Si	
Frozen lattice configurations	Not considered	
Supercell discretisation	1000 x 1000	
Fixed absorption parameter	0.1	
Repetitions per scan position	1	
Defocus [nm]	-6 (underfocus)	
Other lens aberrations	All zero	
Acceleration voltage [kV]	200	
Effective source profile	Gaussian (HWHM = 0.04 nm)	
Aperture radius [mrad]	25	
Aperture centre [mrad]	X=0, Y=0	
SAAF detector collection angles [mrad]	β_{inner}=18.0	β_{outer}=35.8
Detector rotation [°]	Varying, as denoted in the main body of the text.	
HAADF detector collection angles	$\beta_{\text{inner,HAADF}}$=51.0	$\beta_{\text{outer,HAADF}}$=180
Structure thickness [nm]	30.72	
Specimen tilt [°]	0	
Detector configuration	Layer2, bisected way (Chapter 3.1)	

Table 19: Simulation parameters of the multislice DPC and HAADF simulations of Fig. 36.

Figure	Fig. 36	
Type of simulation	Image simulation	
Material system and zone-axis orientation	$SrTiO_3$[001]	
Unit cell size (x-, y-, z-direction)	0.3905 nm x 0.3905 nm x 0.3905 nm	
Unit cell repetitions for supercell (x-, y-, z-direction)	10, 10, 1	
Unit cell slice along z-direction	2	
Slice structure	0: 100 Sr, 100 O 1: 100 Ti, 200 O	
Frozen lattice configurations	50	
Supercell discretisation	1000 x 1000	
Mean square displacements [nm^2]	Sr: 0.0066 Ti: 0.0051 O: 0.0108	
Fixed absorption parameter	0.1	
Repetitions per scan position	1	
Defocus [nm]	0 (entrance slice)	
Other lens aberrations	All zero	
Acceleration voltage [kV]	200	
Effective source profile	Gaussian (HWHM = 0.04 nm)	
Aperture radius [mrad]	25	
Aperture centre [mrad]	X=0, Y=0	
SAAF detector collection angles [mrad]	β_{inner}=18.0	β_{outer}=35.8
Detector rotation [°]	φ=0	
HAADF detector collection angles	$\beta_{\text{inner,HAADF}}$=51.0	$\beta_{\text{outer,HAADF}}$=180
Structure thickness [nm]	Varying, as described in the figure	
Specimen tilt [°]	0	
Detector configuration	Layer2, bisected (Chapter 3.1)	

Table 20: List of parameters for multislice DPC image simulations and corresponding calculations depicted in Fig. 37, Fig. 38, Fig. 89, Fig. 90 and Fig. 91.

Figures	Fig. 37, Fig. 38, Fig. 89, Fig. 90 and Fig. 91	
Type of simulation	Image simulation	
Material system and zone-axis orientation	$SrTiO_3$[001]	
Unit cell size (x-, y-, z-direction)	0.3905 nm x 0.3905 nm x 0.3905 nm	
Unit cell repetitions for supercell (x-, y-, z-direction)	10, 10, 1	
Unit cell slice along z-direction	2	
Slice structure	0: 100 Sr, 100 O 1: 100 Ti, 200 O	
Frozen lattice configurations	50	
Supercell discretisation	1000 x 1000	
Mean square displacements [nm^2]	Sr: 0.0066 Ti: 0.0051 O: 0.0108	
Fixed absorption parameter	0.1	
Repetitions per scan position	1	
Defocus [nm]	Varying from 5 (overfocus) to -10 (underfocus)	
Other lens aberrations	All zero	
Acceleration voltage [kV]	200	
Effective source profile	Gaussian (HWHM = 0.04 nm)	
Aperture radius [mrad]	25	
Aperture centre [mrad]	X=0, Y=0	
SAAF detector collection angles [mrad]	β_{inner}=18.0	β_{outer}=35.8
Detector rotation [°]	φ=0	
Structure thickness [nm]	Varying, as denoted in the figure	
Specimen tilt [°]	0	
Detector configuration	Layer2, bisected (Chapter 3.1)	

Table 21: Parameters of multislice image simulations in Figs. 40(b-e).

Figures	Figs. 40(b-e)	
Type of simulation	Image simulation	
Material system and zone-axis orientation	$SrTiO_3$[001]	
Unit cell size (x-, y-, z-direction)	0.3905 nm x 0.3905 nm x 0.3905 nm	
Unit cell repetitions for supercell (x-, y-, z-direction)	10, 10, 1	
Unit cell slice along z-direction	2	
Slice structure	0: 100 Sr, 100 O 1: 100 Ti, 200 O	
Frozen lattice configurations	Not considered	
Supercell discretisation	576 x 576	
Mean square displacements [nm^2]	Sr: 0.0066 Ti: 0.0051 O: 0.0108	
Fixed absorption parameter	0.1	
Repetitions per scan position	1	
Defocus [nm]	-3 (underfocus)	
Other lens aberrations	All zero	
Acceleration voltage [kV]	(b) 200, (c) 80, (d) 60, (e) 30	
Effective source profile	Gaussian (HWHM = 0.04 nm)	
Aperture radius [mrad]	25	
Aperture centre [mrad]	X=0, Y=0	
SAAF detector collection angles [mrad]	β_{inner}=18.0	β_{outer}=35.8
Detector rotation [°]	φ=0	
Structure thickness [nm]	6.25	
Specimen tilt [°]	0	
Detector configuration	Layer2, bisected (Chapter 3.1)	

Table 22: Parameters of real space probe intensity simulations in Figs. 41(b, c, d), Fig. 42 and Fig. 93.

Figures	Fig. 41(b, c, d), Fig. 42, Fig. 93
Type of simulation	Real space probe intensity simulation
Material system and zone-axis orientation	$SrTiO_3$[001]
Unit cell size (x-, y-, z-direction)	0.3905 nm x 0.3905 nm x 0.3905 nm
Unit cell repetitions for supercell (x-, y-, z-direction)	15, 15, 1
Unit cell slice along z-direction	2
Slice structure	0: 225 Sr, 225 O 1: 225 Ti, 450 O
Frozen lattice configurations	Not considered
Supercell discretisation	864 x 864
Mean square displacements [nm^2]	Sr: 0.0066 Ti: 0.0051 O: 0.0108
Fixed absorption parameter	0.1
Repetitions per scan position	1
Defocus [nm]	0 (entrance slice)
Other lens aberrations	All zero
Acceleration voltage [kV]	200
Effective source profile	Gaussian (HWHM = 0.04 nm)
Aperture centre [mrad]	X=0, Y=0
Structure thickness [nm]	Varying as denoted in the figures.
Specimen tilt [°]	0

Table 23: Parameters of real space probe intensity simulations shown in Fig. 43 and Fig. 94.

Figure	Fig. 43, Fig. 94
Type of simulation	Real space probe intensity simulation
Material system and zone-axis orientation	$SrTiO_3$[001]
Unit cell size (x-, y-, z-direction)	0.3905 nm x 0.3905 nm x 0.3905 nm
Unit cell repetitions for supercell (x-, y-, z-direction)	15, 15, 1
Unit cell slice along z-direction	2
Slice structure	0: 225 Sr, 225 O 1: 225 Ti, 450 O
Frozen lattice configurations	Not considered
Supercell discretisation	864 x 864
Mean square displacements [nm^2]	Sr: 0.0066 Ti: 0.0051 O: 0.0108
Fixed absorption parameter	0.1
Repetitions per scan position	1
Defocus [nm]	0 (entrance slice)
Other lens aberrations	All zero
Acceleration voltage [kV]	30
Effective source profile	Gaussian (HWHM = 0.04 nm)
Aperture centre [mrad]	X=0, Y=0
Structure thickness [nm]	Varying as described in the figures.
Specimen tilt [°]	0

Table 24: Parameters of multislice image simulations in Fig. 44(b).

Figure	Fig. 44(b)		
Type of simulation	Image simulation (image size of 1 nm by 1 nm)		
Atomic species	Si	Se	W
Unit cell size (x-, y-, z-direction)	2.5 nm x 2.5 nm x d_{atom} (d_{atom} varying)		
Unit cell repetitions for supercell (x-, y-, z-direction)	5, 5, 1		
Unit cell slice along z-direction	2		
Slice structure	0: 5 Si 1: 5 Si	0: 5 Se 1: 5 Se	0: 5 W 1: 5 W
Frozen lattice configurations	Not considered		
Supercell discretisation	1000 x 1000		
Fixed absorption parameter	0.1		
Repetitions per scan position	1		
Defocus [nm]	0 nm (entrance slice)		
Other lens aberrations	All zero		
Acceleration voltage [kV]	200, 80		
Effective source profile	Gaussian (HWHM = 0.04 nm)		
Aperture radius [mrad]	25		
Aperture centre [mrad]	X=0, Y=0		
SAAF detector collection angles [mrad]	β_{inner}=18.0	β_{outer}=35.8	
Detector rotation [°]	φ=0		
Structure thickness [nm]	Varying as a function of d_{atom}		
Specimen tilt [°]	0		
Detector configuration	Layer2, bisected (Chapter 3.1)		

Table 25: List of parameters multislice parameters for DPC simulations considered for Fig. 45.

Figure	Fig. 45	
Type of simulation	Image simulation	
Material system and zone-axis orientation	$SrTiO_3$[001]	
Unit cell size (x-, y-, z-direction)	0.3905 nm x 0.3905 nm x 0.3905 nm	
Unit cell repetitions for supercell (x-, y-, z-direction)	10, 10, 1	
Unit cell slice along z-direction	2	
Slice structure	0: 100 Sr, 100 O 1: 100 Ti, 200 O	
Frozen lattice configurations	50	
Supercell discretisation	1000 x 1000	
Mean square displacements [nm^2]	Sr: 0.0066 Ti: 0.0051 O: 0.0108	
Fixed absorption parameter	0.1	
Repetitions per scan position	1	
Defocus [nm]	-2 (underfocus)	
Other lens aberrations	A_1 from 0 nm to 4 nm in steps of 1 nm B_2 from 0 nm to 400 nm in steps of 100 nm	
Acceleration voltage [kV]	200	
Effective source profile	Gaussian (HWHM = 0.04 nm)	
Aperture radius [mrad]	25	
Aperture centre [mrad]	X=0, Y=0	
SAAF detector collection angles [mrad]	β_{inner}=18.0	β_{outer}=35.8
Detector rotation [°]	φ=0	
HAADF detector collection angles	$\beta_{\mathrm{inner,HAADF}}$=51.0	$\beta_{\mathrm{outer,HAADF}}$=180
Structure thickness [nm]	3.51	
Specimen tilt [°]	0	
Detector configuration	Layer2, bisected (Chapter 3.1)	

Table 26: List of parameters multislice for DPC image simulations shown in Fig. 47, Fig. 97 and Fig. 98.

Figure	Fig. 47, Fig. 97, Fig. 98	
Type of simulation	Image simulation	
Material system and zone-axis orientation	$SrTiO_3$[001]	
Unit cell size (x-, y-, z-direction)	0.3905 nm x 0.3905 nm x 0.3905 nm	
Unit cell repetitions for supercell (x-, y-, z-direction)	10, 10, 1	
Unit cell slice along z-direction	2	
Slice structure	0: 100 Sr, 100 O 1: 100 Ti, 200 O	
Frozen lattice configurations	50	
Supercell discretisation	1000 x 1000	
Mean square displacements [nm^2]	Sr: 0.0066 Ti: 0.0051 O: 0.0108	
Fixed absorption parameter	0.1	
Repetitions per scan position	1	
Defocus [nm]	-2 (underfocus)	
Other lens aberrations	A_2 from 0 nm to 200 nm in steps of 50 nm C_3 from 0 µm to 20 µm in steps of 5 µm	
Acceleration voltage [kV]	200	
Effective source profile	Gaussian (HWHM = 0.04 nm)	
Aperture radius [mrad]	25	
Aperture centre [mrad]	X=0, Y=0	
SAAF detector collection angles [mrad]	β_{inner}=18.0	β_{outer}=35.8
Detector rotation [°]	φ=0	
HAADF detector collection angles	$\beta_{\text{inner,HAADF}}$=51.0	$\beta_{\text{outer,HAADF}}$=180
Structure thickness [nm]	3.51	
Specimen tilt [°]	0	
Detector configuration	Layer2, bisected (Chapter 3.1)	

Table 27: Multislice simulation parameter of DPC simulations in Fig. 48.

Figure	Fig. 48	
Type of simulation	Image simulation	
Material system and zone-axis orientation	$SrTiO_3$[001]	
Unit cell size (x-, y-, z-direction)	0.3905 nm x 0.3905 nm x 0.3905 nm	
Unit cell repetitions for supercell (x-, y-, z-direction)	10, 10, 1	
Unit cell slice along z-direction	2	
Slice structure	0: 100 Sr, 100 O 1: 100 Ti, 200 O	
Frozen lattice configurations	50	
Supercell discretisation	1000 x 1000	
Mean square displacements [nm^2]	Sr: 0.0066 Ti: 0.0051 O: 0.0108	
Fixed absorption parameter	0.1	
Repetitions per scan position	1	
Defocus [nm]	-2 (3.51 nm), -5.5 (11.32 nm)	
Other lens aberrations	All zero	
Acceleration voltage [kV]	200	
Effective source profile	Gaussian (HWHM = 0.04 nm)	
Aperture radius [mrad]	25	
Aperture centre [mrad]	X=0, Y=0	
SAAF detector collection angles [mrad]	β_{inner}=18.0	β_{outer}=35.8
Detector rotation [°]	φ=0	
HAADF detector collection angles	$\beta_{\text{inner,HAADF}}$=51.0	$\beta_{\text{outer,HAADF}}$=180
Structure thickness [nm]	3.51, 11.32	
Specimen tilt	Varying from 0 to 25 mrad	
Detector configuration	Layer2, bisected (Chapter 3.1)	

Table 28: Parameters for multislice image simulation in Fig. 49.

Figure	Fig. 49	
Type of simulation	Image simulation	
Material system and zone-axis orientation	Si[110]	
Unit cell size (x-, y-, z-direction)	0.768 nm x 0.5431 nm x 0.768 nm	
Unit cell repetitions for supercell (x-, y-, z-direction)	10, 10, 1	
Unit cell slice along z-direction	4	
Slice structure	0: 400 Si 1: 400 Si 2: 400 Si 3: 400 Si	
Frozen lattice configurations	Not considered	
Supercell discretisation	1000 x 1000	
Fixed absorption parameter	0.1	
Repetitions per scan position	1	
Defocus [nm]	-6 (underfocus)	
Other lens aberrations	All zero	
Acceleration voltage [kV]	200 kV	
Effective source profile	Gaussian (HWHM = 0.04 nm)	
Aperture radius [mrad]	25	
Aperture centre [mrad]	X=0, Y=0	
SAAF detector collection angles [mrad]	β_{inner}=18.0	β_{outer}=35.8
Detector rotation [°]	Varying, as denoted in the figures and the main body of the text.	
HAADF detector collection angles	$\beta_{\text{inner,HAADF}}$=51.0	$\beta_{\text{outer,HAADF}}$=180
Structure thickness [nm]	30.72	
Specimen tilt	Varying from 0 mrad to 5 mrad	
Detector configuration	Layer2, bisected (Chapter 3.1)	

Table 29: Parameters for multislice image simulation in Fig. 54.

Figure	Fig. 54	
Type of simulation	Image simulation	
Material system and zone-axis orientation	Si[110]	
Unit cell size (x-, y-, z-direction)	0.768 nm x 0.5431 nm x 0.768 nm	
Unit cell repetitions for supercell (x-, y-, z-direction)	10, 10, 1	
Unit cell slice along z-direction	4	
Slice structure	0: 400 Si 1: 400 Si 2: 400 Si 3: 400 Si	
Frozen lattice configurations	Not considered	
Supercell discretisation	1000 x 1000	
Fixed absorption parameter	0.1	
Repetitions per scan position	1	
Defocus [nm]	-4 (underfocus)	
Other lens aberrations	All zero	
Acceleration voltage [kV]	200 kV	
Effective source profile	Gaussian (HWHM = 0.04 nm)	
Aperture radius [mrad]	25	
Aperture centre [mrad]	X=0, Y=0	
SAAF detector collection angles [mrad]	β_{inner}=18.0	β_{outer}=35.8
Detector rotation [°]	0	
HAADF detector collection angles	$\beta_{\text{inner,HAADF}}$=51.0	$\beta_{\text{outer,HAADF}}$=180
Structure thickness [nm]	30.72	
Specimen tilt [mrad]	0	
Calibration	Signal-based	
Detector configuration	Layer2, bisected (Chapter 3.1)	

Table 30: Parameters of the multislice DPC and HAADF image simulation for WSe_2 shown in Fig. 69 and Fig. 70, Fig. 71 and Fig. 72.

Figures	Fig. 69, Fig. 70, Fig. 71, Fig. 72			
Type of simulation	Image simulation			
Material system and zone-axis orientation	WSe_2[0001]			
Unit cell of structure size (x-, y-, z-direction)	5.69 Å, 3.29 Å, 12.97 Å			
Unit cell repetitions for supercell (x-, y-, z-direction)	10, 10, 1			
Unit cell slices along z-direction	6			
Stacking	AA	AA'	AAA	AA'A
Slice structure Slices 0-2 and 3-5 have different projected positions of Se and W atoms.	0: 200 Se 1: 200 W 2: 200 Se 0: 200 Se 1: 200 W 2: 200 Se	0: 200 Se 1: 200 W 2: 200 Se 3: 200 Se 4: 200 W 5: 200 Se	0: 200 Se 1: 200 W 2: 200 Se 0: 200 Se 1: 200 W 2: 200 Se 0: 200 Se 1: 200 W 2: 200 Se	0: 200 Se 1: 200 W 2: 200 Se 3: 200 Se 4: 200 W 5: 200 Se 0: 200 Se 1: 200 W 2: 200 Se
Frozen lattice configurations	Not considered			
Supercell discretisation	1000 x 1000			
Fixed absorption parameter	0.1			
Repetitions per scan position	1			
Defocus [nm]	0 (underfocus)			
Other lens aberrations	All zero			
Acceleration voltage [kV]	200 kV			
Effective source profile	Gaussian (FWHM = 0.07 nm)			
Aperture radius [mrad]	30			
Aperture centre [mrad]	X=0, Y=0			
SAAF detector collection angles [mrad]	β_{inner}=18.0		β_{outer}=36.0	
Detector rotation [°]	Varying, as denoted in the figures and the main body of the text.			
HAADF detector collection angles	$\beta_{\mathrm{inner,HAADF}}$=51.0		$\beta_{\mathrm{outer,HAADF}}$=180	
Structure thickness [nm]	1.29	1.29	1.94	1.94
Specimen tilt [mrad]	0			
Detector configuration	Layer2, bisected (Chapter 3.1)			

Table 31: Parameters for multislice image simulation shown in Fig. 92, Fig. 99 and Fig. 100.

Figures	Fig. 92, Fig. 99, Fig. 100	
Type of simulation	Image simulation	
Material system and zone-axis orientation	Si[110]	
Unit cell size (x-, y-, z-direction)	0.768 nm x 0.5431 nm x 0.768 nm	
Unit cell repetitions for supercell (x-, y-, z-direction)	10, 10, 1	
Unit cell slice along z-direction	4	
Slice structure	0: 400 Si 1: 400 Si 2: 400 Si 3: 400 Si	
Frozen lattice configurations	50	
Supercell discretisation	500 x 500	
Mean square displacements [nm^2]	Si: 0.0070	
Fixed absorption parameter	0.1	
Repetitions per scan position	100	
Defocus [nm]	Varying from -19 nm to + 14 nm (underfocus)	
Other lens aberrations	All zero	
Acceleration voltage [kV]	200 kV	
Effective source profile	Gaussian (HWHM = 0.04 nm)	
Aperture radius [mrad]	25	
Aperture centre [mrad]	X=0, Y=0	
SAAF detector collection angles [mrad]	β_{inner}=18.0	β_{outer}=36.0
Detector rotation [°]	0	
Structure thickness [nm]	30.72	
Specimen tilt [mrad]	0	
Calibration	Signal-based	
Detector configuration	Layer2, bisected (Chapter 3.1)	

Table 32: Parameters for multislice image simulation shown in Fig. 104, Fig. 105, Fig. 106, Fig. 107 and Fig. 108.

Figures	Fig. 104, Fig. 105, Fig. 106, Fig. 107 and Fig. 108	
Type of simulation	Image simulations	
Material system and zone-axis orientation	WSe_2[0001]	
Unit cell size (x-, y-, z-direction)	5.69 Å, 3.29 Å, 6.5 Å	
Unit cell repetitions for supercell (x-, y-, z-direction)	10, 10, 1	
Unit cell slice along z-direction	3	
Slice structure	0: 200 Se 1: 200 W 2: 200 Se	
Frozen lattice configurations	Not considered	
Supercell discretisation	480 x 480	
Fixed absorption parameter	0.1	
Repetitions per scan position	1	
Defocus [nm]	0 nm	
Three-fold astigmatism A_2 [nm]	From -500 to +500 in steps of 100	
Other lens aberrations	All zero	
Acceleration voltage [kV]	80 kV	
Effective source profile	Gaussian (HWHM = 0.05 nm)	
Aperture radius [mrad]	30	
Aperture centre [mrad]	X=0, Y=0	
SAAF detector collection angles [mrad]	β_{inner}=18.0	β_{outer}=36.0
Detector rotation [°]	0	
Specimen tilt [mrad]	From -20 to +25 in steps of 5	
Calibration	Signal-based	
Detector configuration	Layer2, bisected (Chapter 3.1)	

A.4. Imaging parameters

The parameters for the experimental DPC images are given below.

Table 33: Experimental details for Fig. 5.

Figure	Fig. 5	
Material system and zone-axis orientation	Si[110]	
Preparation method	FIB	
Image type	HAADF	
Microscope and detectors	*JEOL* JEM-ARM200F, *JEOL* HAADF deetector	
Acceleration voltage [kV]	200	
Convergence semi angle [mrad]	25	
HAADF detector collection angles [mrad]	53	180
Camera length [cm]	12	
Dwell time [µs]	50	
Denoising	Non-rigid registration of 300 images; Iteration on levels (coarse to fine registration): [500,300]; Field smoothing: 1.5 px	
Specimen thickness [nm]	(30 ± 2)	

Table 34: Experimental details for Fig. 13(c).

Figure	Fig. 13 (c)
Material system and zone-axis orientation	Si[110]
Preparation method	FIB
Image type	CBED
Microscope and detectors	*JEOL* JEM-ARM200F, *GATAN* OneView
Acceleration voltage [kV]	200
Condenser lens aperture size [µm]	150
Camera length [cm]	20
Integration time [s]	1
Specimen thickness [nm]	> 50

Table 35: Experimental details for Fig. 13(g-i).

Figure	Fig. 13(g-i)
Material system and zone-axis orientation	No specimen (vacuum area of specimen)
Image type	DPC
Microscope and detectors	*JEOL* JEM-ARM200F, *JEOL* SAAF detector
Acceleration voltage [kV]	200
Condenser lens aperture size [µm]	40
Convergence semi angle [mrad]	25
Inner polar angle [mrad]	18
Outer polar angle [mrad]	35.4
Camera length [cm]	20
Dwell time [µs]	100
Projector lens alignment	Varying
Detector configuration	Layer2, bisected (Chapter 3.1)

Table 36: Experimental details for Fig. 14(b).

Figure	Fig. 14(b)
Image type	Image of Detector (Imaging system in alignment mode with excitation of lenses similar to TEM mode)
Microscope and detectors	*JEOL* JEM-ARM200F, *JEOL* SAAF detector
Acceleration voltage [kV]	200
Corresponding camera length [cm]	12
Dwell time [µs]	100
Calibration	From CBED pattern and scanning of beam on OneView Camera

Table 37: Experimental details for Fig. 15.

Figure	Fig. 15
Material system and zone-axis orientation	Si[110]
Image type	CBED (with stationary beam)
Microscope and detectors	*JEOL* JEM-ARM200F NeoARM, *GATAN* OneView
Acceleration voltage [kV]	200
Condenser lens aperture size [µm]	40
Convergence semi angle [mrad]	27.3
Camera length [cm]	40
Dwell time [ms]	3.3
Specimen thickness [nm]	(23.0 ± 0.7)

Table 38 Experimental details for Fig. 16.

Figure	Fig. 16
Image type	Image of Detector (Imaging system in alignment mode with excitation of lenses similar to TEM mode)
Microscope and detectors	*JEOL* JEM-ARM200F, *JEOL* HAADF detector
Acceleration voltage [kV]	200
Corresponding camera length [cm]	12
Dwell time [µs]	100
Calibration	From CBED pattern and scanning of beam on OneView Camera

Table 39: Experimental details for Figs. 22(a-c).

Figures	Figs. 22(a-c)	
Material system and zone-axis orientation	Si[110]	
Preparation method	FIB	
Image type	HAADF	
Microscope and detectors	*JEOL* JEM-ARM200F, *JEOL* HAADF detector	
Acceleration voltage [kV]	200	
HAADF detector collection angles [mrad]	53	180
Camera length [cm]	12	
Dwell time [µs]	50	
Denoising	(a) Rigid registration of 200 images, (b) None (c) None	
Image type for non-rigid registration	(a) Reference (b) Moving image (c) Result after warping	
Non-rigid registration settings	Iterations on levels (coarse to fine registration): [300,300], Field smoothing: 2 px	
Specimen thickness [nm]	(30 ± 2)	

Table 40: Experimental details for DPC and HAADF images shown in Fig. 23.

Figure	Fig. 23	
Material system and zone-axis orientation	Si[110]	
Preparation method	FIB	
Image type	HAADF, S_x, S_y, DPC	
Microscope and detectors	*JEOL* JEM-ARM200F, *JEOL* HAADF detector, *JEOL* SAAF detector	
Acceleration voltage [kV]	200	
Convergence semi-angle [mrad]	25	
SAAF detector collection angles (Layer2)	18	35.4
HAADF detector collection angles [mrad]	53	180
Camera length [cm]	12	
Dwell time [µs]	50	
Corrections (Chapter A.1)	Rotation, centring, background, momentum space anisotropy	
Denoising	(a) Rigid registration of 200 images, (d) None (e) None (f) Rigid registration (200 images) (g) Non-rigid registration (200 images)	
Non-rigid registration settings	Iterations on levels (coarse to fine registration): [300,300], Field smoothing: 1.5 px	
Specimen thickness [nm]	(30 ± 2)	
Detector configuration (DPC)	Layer2, bisected (Chapter 3.1)	

Table 41: Experimental details for Fig. 24.

Figure	Fig. 24	
Material system and zone-axis orientation	Trilayer WSe_2[0001]	
Preparation method	Mechanical exfoliation as described in Chapter 6.3.1	
Image type	HAADF	
Microscope and detectors	*JEOL* JEM-ARM200F, *JEOL* HAADF detector	
Acceleration voltage [kV]	80	
Convergence semi-angle [mrad]	30	
HAADF detector collection angles [mrad]	54.2	191
Camera length [cm]	12	
Corrections (Chapter A.1)	Rotation, centring, background	
Denoising	(a) Non-rigid registration of 300 images, (b) Image of (a) with additional Gaussian blurring with $\sigma = 2.5$ pixels (c) Same as (a) (e) Same as (a) since area of (c) (g) Same as (a)	
Non-rigid registration settings	Iterations on levels (coarse to fine registration): [100,50,25], Field smoothing: 2.5 px	
Specimen thickness estimated via EFTEM [nm]	(2.39 ± 0.01)	

Table 42: Experimental details for Fig. 31(a, c, e), Fig. 32(a, e, i, m, q), Fig. 33(a, e, i, m, q), Fig. 85 and Fig. 86.

Figures	Fig. 31(a, c, e), Fig. 32(a, e, l, m, q), Fig. 33(a, e, i, m, q), Fig. 85, Fig. 86	
Material system and zone-axis orientation	Si[110]	
Preparation method	FIB	
Specimen thickness [nm]	(30 ± 2)	
Image type	HAADF, DPC	
Microscope and detectors	*JEOL* JEM-ARM200F, *JEOL* HAADF detector, *JEOL* SAAF detector	
Acceleration voltage [kV]	200	
Convergence semi-angle [mrad]	25	
HAADF detector collection angles [mrad]	53	180
SAAF detector collection angles (Layer2)	18	35.4
Detector rotation φ [°]	Fig. 31 (a) 0 (c) 30 (e) 40 Fig. 32 (a) 0 (e) 0 (i) 0 (m) 0 (q) 0 Fig. 33 (a) 30 (e) 30 (i) 40 (m) 40 (q) 40 Fig. 85 • As denoted in the figure Fig. 86 • As denoted in the figure	
Camera length [cm]	12	
Dwell time [µs]	50	
Detector configuration (DPC)	Layer2, bisected (Chapter 3.1)	
Corrections (Chapter A.1) before denoising	Rotation, centring, background, momentum space anisotropy.	
Denoising and other post-processing steps	Fig. 31 (a) Non-rigid registration of 300 images (c) Non-rigid registration of 300 images (e) Non-rigid registration of 300 images Fig. 32 (a) Same as Fig. 31(a) (e) Same as Fig. 31(a), scattergram filtering (i) Same as Fig. 31(a), scattergram filtering (m) Same as Fig. 31(a), scattergram filtering (q) Same as Fig. 31(a), scattergram filtering Fig. 33 (a) Same as Fig. 31(c) (e) Same as Fig. 31(e), scattergram filtering (i) Same as Fig. 31(e) (m) Same as Fig. 31(e), scattergram filtering (q) Same as Fig. 31(e), scattergram filtering Fig. 85 • Non-rigid registration of 300 images for all DPC and HAADF images Fig. 86 • Non-rigid registration of 300 images for all DPC and HAADF images	
Non-rigid registration settings	Iterations on levels (coarse to fine registration): [500,300], Field smoothing: 1.5 px	

Table 43: Experimental details for Fig. 46.

Figure	Fig. 46	
Material system and zone-axis orientation	Si[110]	
Preparation method	FIB	
Specimen thickness [nm]	(35 ± 2)	
Image type	HAADF, DPC	
Microscope and detectors	*JEOL* JEM-ARM200F, *JEOL* HAADF detector, *JEOL* SAAF detector	
Acceleration voltage [kV]	200	
Convergence semi-angle [mrad]	25	
HAADF detector collection angles [mrad]	53	180
SAAF detector collection angles (Layer2)	18	35.4
Detector rotation φ [°]	0	
Camera length [cm]	12	
Dwell time [µs]	80	
Condenser stigmator	Varied using the Condenser lens stigmator in steps of 10 coarse knob clicks	
Detector configuration (DPC)	Layer2, bisected (Chapter 3.1)	
Corrections (Chapter A.1) before denoising	Rotation, centring, background	
Denoising	None	

Table 44: Experimental details for Fig. 50.

Figure	Fig. 50	
Material system and zone-axis orientation	No specimen (vacuum area of specimen)	
Image type	DPC	
Microscope and detectors	*JEOL* JEM-ARM200F, *JEOL* SAAF detector	
Acceleration voltage [kV]	200	
Convergence semi-angle [mrad]	25	
SAAF detector collection angles (Layer2)	18	35.4
Detector rotation φ [°]	0	
Camera length [cm]	12	
Dwell time [µs]	Varied from 50 to 700	
Corrections (Chapter A.1)	Rotation, centring.	
Detector configuration (DPC)	Layer2, bisected (Chapter 3.1)	

Table 45: Experimental details for DPC and HAADF images shown in Fig. 51.

Figure	Fig. 51	
Material system and zone-axis orientation	Si[110]	
Preparation method	FIB	
Image type	HAADF, DPC	
Microscope and detectors	*JEOL* JEM-ARM200F, *JEOL* HAADF detector, *JEOL* SAAF detector	
Acceleration voltage [kV]	200	
Convergence semi-angle [mrad]	25	
SAAF detector collection angles (Layer2)	18	35.4
HAADF detector collection angles [mrad]	53	180
Camera length [cm]	12	
Dwell time [µs]	50	
Corrections (Chapter A.1) before denoising	Rotation, centring, background, momentum space anisotropy	
Denoising	(a, f, k) None (b, g, l) 5 non-rigidly aligned images (c, h, m) 10 non-rigidly aligned images (d, i, n) 20 non-rigidly aligned images (e, j, o) 50 non-rigidly aligned images	
Non-rigid registration settings	Iterations on levels (coarse to fine registration): [300,300], Field smoothing: 1.5 px	
Specimen thickness [nm]	(30 ± 2)	
Detector configuration (DPC)	Layer2, bisected (Chapter 3.1)	

Table 46: Experimental details TEM bright-field image and EFTEM thickness mapping shown in Fig. 52.

Figure	Fig. 52
Material system and zone-axis orientation	Si[110]
Preparation method	FIB
Image type	TEM BF, EFTEM t/λ
Microscope and detectors	*JEOL* JEM-ARM200F, (a) *GATAN* OneView, (c) *GATAN* GIF Quantum ER with GIF CCD
Acceleration voltage [kV]	200
Aperture(s)	150 µm (condenser lens) (a) No objective lens aperture for contrast enhancement (c) Filter entrance aperture (Imaging)
Integration time [s]	(a) 0.0798 (c) 0.3082 for the elastic and unfiltered images
Mean free path of electrons [nm]	149.6
Filter energy width [eV]	10 (centred on 0 eV)
Filter energy position [eV]	0

Table 47: Imaging parameters for Fig. 53 and Figs. 55(a, c).

Figures	Fig. 53, Fig. 55	
Material system	Si[110]	
Preparation method	FIB	
Microscope and detectors	*JEOL* JEM-ARM200F, *JEOL* HAADF detector, *JEOL* SAAF detector	
Acceleration voltage [kV]	200	
Convergence semi-angle [mrad]	25	
SAAF detector collection angles (Layer2)	18	35.4
HAADF detector collection angles [mrad]	53	180
Detector rotation [°]	0° to dumbbell axis	
Camera length [cm]	12 cm	
Dwell time [µs]	80	
Corrections (Chapter A.1) before denoising	Rotation, centring, background, momentum space anisotropy	
Denoising	Non-rigid registration of 300 images; Iterations on levels (coarse to fine registration): [500,300]; Field smoothing: 1.5 px	
Calibration	Signal-based	
Specimen thickness [nm]	(30 ± 2)	

Table 48: Imaging parameters for Fig. 56.

Figure	Fig. 56
Material system	Si[110]
Preparation method	FIB
Microscope and detectors	(a, b, e, f, i, j) *JEOL* JEM-ARM200F, *JEOL* SAAF detector (c, d, g, h, k, l) *JEOL* JEM-ARM200F NeoARM, *GATAN* OneView
Acceleration voltage [kV]	200
Convergence semi-angle [mrad]	(a, b, e, f, i, j) 25 (c, d, g, h, k, l) 27.4
SAAF and virtual detector collection angles (Layer2)	18 | 35.4
SAAF and virtual detector rotation [°]	0° to dumbbell axis
Camera length [cm]	(a, b, e, f, i, j) 12 (c, d, g, h, k, l) 20
Signal generation (DPC)	(a, b, d, e, f, h, i, j, l) Layer2, bisected (Chapter 3.1) (c, g, k) Centre of Mass of CBED intensity
Dwell time [µs]	(a, b, e, f, i, j) 80 (c, d, g, h, k, l) 3300
Corrections (Chapter A.1) before denoising	(all) Rotation, (all) centring, (all) background, (a, b, e, f, i, j) momentum space anisotropy
Denoising	(all) Gaussian denoising with $\sigma = 1$ px
Calibration	(a, e, i) Signal-based (b, f, j) CoM of Segments (c, g, k) Com (d, h, l) Virtual segments CoM
Specimen thickness [nm]	(30 ± 2)

Table 49: Imaging parameters for Figs. 57(a-h).

Figures	Fig. 57(a-h)
Material system	Si[110]
Preparation method	FIB
Imaging type	DPC
Microscope and detectors	*JEOL* JEM-ARM200F NeoARM, *GATAN* OneView
Acceleration voltage [kV]	200
Convergence semi-angle [mrad]	27.4
Virtual detector collection angles (Layer2)	Varying inner layer | Varying outer layer
Virtual detector rotation [°]	Varying
Camera length [cm]	20
Virtual detector configurations (DPC)	Layer2, bisected (Chapter 3.1)
Dwell time [µs]	3300
Corrections	Rotation, Centring
Denoising	No denoising
Calibration	(a, b) Com (c-h) Virtual segments CoM
Specimen thickness [nm]	(30 ± 2)

Table 50: Imaging parameters for Fig. 57(i).

Figure	Fig. 57(i)
Material system	Si[110]
Preparation method	FIB
Imaging type	PACBED obtained from a full 4D-STEM image (150x150 pixels)
Microscope and detectors	*JEOL* JEM-ARM200F NeoARM, *GATAN* OneView
Acceleration voltage [kV]	200
Convergence semi-angle [mrad]	27.4
Camera length [cm]	20
Dwell time [s]	74.25
Specimen thickness [nm]	(30 ± 2)

Table 51: Imaging parameters for Fig. 59, Fig. 60 and Fig. 61.

Figures	Fig. 59, Fig. 60, Fig. 61	
Material system	Si[110]	
Preparation method	FIB	
Imaging type	DPC	
Microscope and detectors	*JEOL* JEM-ARM200F NeoARM, *GATAN* OneView	
Acceleration voltage [kV]	200	
Convergence semi-angle [mrad]	27.4	
Virtual detector collection angles (Layer2)	Varying inner layer	Varying outer layer
Virtual detector rotation [°]	Varying	
Camera length [cm]	12	
Corrections	Rotation, Centring	
SAAF and virtual detector configurations (DPC)	L1=Layer1, bisected (Chapter 3.1) L2=Layer2, bisected (Chapter 3.1) L1+L2=Layer1+Layer2, bisected (Chapter 3.1) Except for Fig. 60(a, b, c), all by using the increased azimuthal momentum space resolution method	
Dwell time [µs]	3300	
Denoising	Gaussian denoising with σ =1 px = 0.01889 nm	
Calibration	All virtual segments in combination with increased azimuthal momentum space resolution method except Fig. 60(a-c)	
Specimen thickness [nm]	(30 ± 2)	

Table 52: Imaging parameters for the HAADF images in Figs. 62(a, b).

Figures	Figs. 62(a, b)	
Material system	InAs[110]	
Preparation method	FIB	
Imaging type	HAADF	
Microscope and detectors	*JEOL* JEM-ARM200F, *JEOL* HAADF detector	
Acceleration voltage [kV]	200	
Convergence semi-angle [mrad]	27.4	
HAADF detector collection angles [mrad]	53	180
Camera length [cm]	12	
Dwell time [µs]	80	
Denoising	None	
Specimen thickness [nm]	(75.6 ± 11.6) (Measured at carbon layer)	

Table 53: Imaging parameters for the HAADF and DPC images in Fig. 63, Fig. 64, Fig. 102 and Fig. 103.

Figures	Fig. 63, Fig. 64, Fig. 102, Fig. 103	
Material system	InAs[110]	
Preparation method	FIB	
Imaging type	DPC	
Microscope and detectors	*JEOL* JEM-ARM200F, *JEOL* HAADF detector, *JEOL* SAAF detector	
Acceleration voltage [kV]	200	
Convergence semi-angle [mrad]	27.4	
SAAF detector collection angles (Layer2)	18	35.4
HAADF detector collection angles [mrad]	53	180
Camera length [cm]	12	
Calibration	Signal-based	
Dwell time [µs]	80	
Corrections before denoising	Rotation, centring, background, momentum space anisotropy	
Denoising	Gaussian denoising with standard deviation of 3 px = 0.48 pm	
Specimen thickness [nm]	(75.6 ± 11.6) (Measured at carbon layer)	

Table 54: Imaging parameters for the HAADF images in Fig. 67 and Fig. 68.

Figures	Fig. 67, Fig. 68	
Material system	(a-d) Bi- and (e-h) trilayer WSe_2[0001]	
Preparation method	Mechanically exfoliated and transferred using PDMS as described in Chapter 6.3.1	
Imaging type	HAADF, DPC	
Microscope and detectors	*JEOL* JEM-ARM200F, *JEOL* HAADF detector, *JEOL* SAAF detector	
Acceleration voltage [kV]	80	
Convergence semi-angle [mrad]	30	
SAAF detector collection angles (Layer2)	18.2	36.1
HAADF detector collection angles [mrad]	54.2	191
Camera length [cm]	12	
Calibration	Signal-based	
Dwell time [µs]	70	
Corrections before denoising	Rotation, centring, background	
Denoising	Non-rigid registration of 300 images; Iterations on levels (coarse to fine registration): [500,300]; Field smoothing: 1.5 px	
Specimen thickness [nm]	(a-d) (1.31 ± 0.07) (e-h) (2.39 ± 0.01)	

Table 55: Imaging parameters for the HAADF images in Fig. 73, Fig. 74, Fig. 75 and Fig. 109.

Figures	Fig. 73, Fig. 74, Fig. 75, Fig. 109	
Material system	Bilayer WSe_2[0001]	
Preparation method	Mechanically exfoliated and transferred using PDMS as described in Chapter 6.3.1	
Imaging type	HAADF, DPC	
Microscope and detectors	*JEOL* JEM-ARM200F, *JEOL* HAADF detector, *JEOL* SAAF detector	
Acceleration voltage [kV]	80	
Convergence semi-angle [mrad]	30	
SAAF detector collection angles (Layer2)	18.2	36.1
HAADF detector collection angles [mrad]	54.2	191
Camera length [cm]	12	
Calibration	Signal-based	
Dwell time [µs]	70	
Corrections before denoising	Rotation, centring, background	
Denoising	Gaussian denoising with a Full width half maximum of 120 pm	
Calculation of difference map	Alignment of pristine lattice (moving image) on defective lattice (reference image).	
Specimen thickness [nm]	(1.31 ± 0.07)	

References

[1] J. Zweck, *J. Phys.: Condens. Matter* **28**, 403001 (2016).

[2] H. Rose, *Optik* **39**, 416 (1974).

[3] H. Rose, *Ultramicroscopy* **2**, 251 (1976).

[4] N.H. Dekkers, H. de Lang, *Optik* **41**, 452 (1974).

[5] M. Haider, S. Uhlemann, J. Zach, *Ultramicroscopy* **81**, 163 (2000).

[6] H. Müller, S. Uhlemann, P. Hartel, M. Haider, *Microsc. Microanal.* **12**, 442 (2006).

[7] P. Hartel, V. Gerheim, M. Linck, H. Müller, S. Uhlemann, Z. Zach, M. Haider, *Ultramicroscopy* **206**, 112821 (2019).

[8] N. Shibata, S.D. Findlay, Y. Kohno, H. Sawada, Y. Kondo, Y. Ikuhara, *Nat. Phys.* **8**, 611 (2012).

[9] K. Müller, F.F. Krause, A. Béché, M. Schowalter, V. Galioit, S. Löffler, J. Verbeeck, J. Zweck, P. Schattschneider, A. Rosenauer, *Nat. Commun.* **5**, 5653 (2014).

[10] M. Krajnak, D. McGrouther, D. Maneuski, V.O.‘ Shea, S. McVitie, *Ultramicroscopy* **165**, 42 (2016).

[11] J.N. Chapman, P.E. Batson, E.M. Waddell, R.P. Ferrier, *Ultramicroscopy* **3**, 203 (1978).

[12] T. Matsumoto, Y.-G. So, Y. Kohno, H. Sawada, Y. Ikuhara, N. Shibata, *Sci. Adv.* **2**, e1501280 (2016).

[13] S. McVitie, J.N. Chapman, *Microsc Microanal* **3**, 146 (1997).

[14] M. Lohr, R. Schregle, M. Jetter, C. Wächter, T. Wunderer, F. Scholz, J. Zweck, *Ultramicroscopy* **117**, 7 (2012).

[15] W. Gao, C. Addiego, H. Wang, X. Yan, Y. Hou, D. Ji, C. Heikes, Y. Zhang, L. Li, H. Huyan, T. Blum, T. Aoki, Y. Nie, D.G. Schlom, R. Wu, X. Pan, *Nature* **575**, 480 (2019).

[16] C. Mahr, T. Grieb, F.F. Krause, M. Schowalter, A. Rosenauer, *Ultramicroscopy* **236**, 113503 (2022).

[17] N. Shibata, S.D. Findlay, H. Sasaki, T. Matsumoto, H. Sawada, Y. Kohno, S. Otomo, R. Minato, Y. Ikuhara, *Sci. Rep.* **5**, 10040 (2015).

[18] H.G. Brown, N. Shibata, H. Sasaki, T.C. Petersen, D.M. Paganin, M.J. Morgan, S.D. Findlay, *Ultramicroscopy* **182**, 169 (2017).

[19] L. Clark, H.G. Brown, D.M. Paganin, M.J. Morgan, T. Matsumoto, N. Shibata, T.C. Petersen, S.D. Findlay, *Phys. Rev. A* **97,** 043843 (2018).

[20] B.C. da Silva, Z.S. Momtaz, L. Bruas, J.-L. Rouviére, H. Okuno, D. Cooper, M.I. den-Hertog, *Appl. Phys. Lett.* **121**, 123503 (2022).

[21] A. Beyer, M.S. Munde, S. Firoozabadi, D. Heimes, T. Grieb, A. Rosenauer, K. Müller-Caspary, K. Volz, *Nano Lett.* **21**, 2018 (2021).

[22] M. Wu, A. Tafel, P. Hommelhoff, E. Spiecker, *Appl. Phys. Lett.* **114**, 13101 (2019).

[23] G. Sánchez-Santolino, N.R. Lugg, T. Seki, R. Ishikawa, S.D. Findlay, Y. Kohno, Y. Kanitani, S. Tanaka, S. Tomiya, Y. Ikuhara, N. Shibata, *ACS Nano* **12**, 8875 (2018).

[24] N. Shibata, T. Seki, G. Sánchez-Santolino, S.D. Findlay, Y. Kohno, T. Matsumoto, R. Ishikawa, Y. Ikuhara, *Nat. Commun.* **8**, 15631 (2017).

[25] K. Müller-Caspary, T. Grieb, J. Müßener, N. Gauquelin, P. Hille, J. Schörmann, J. Verbeeck, S. van Aert, M. Eickhoff, A. Rosenauer, *Phys. Rev. Lett.* **122**, 106102 (2019).

[26] L. Wang, R. Xie, B. Chen, X. Yu, J. Ma, C. Li, Z. Hu, X. Sun, C. Xu, S. Dong, T.-S. Chan, J. Luo, G. Cui, L. Chen, *Nat. Commun.* **11**, 5889 (2020).

[27] K. Müller-Caspary, F.F. Krause, T. Grieb, S. Löffler, M. Schowalter, A. Béché, V. Galioit, D. Marquardt, J. Zweck, P. Schattschneider, J. Verbeeck, A. Rosenauer, *Ultramicroscopy* **178**, 62 (2017).

[28] M.J. Zachman, Z. Yang, Y. Du, M. Chi, *ACS Nano* **16**, 1358 (2022).

[29] T. Grieb, F.F. Krause, K. Müller-Caspary, R. Ritz, M. Simson, J. Schörmann, C. Mahr, J. Müßener, M. Schowalter, H. Soltau, M. Eickhoff, A. Rosenauer, *Ultramicroscopy* **228**, 113321 (2021).

[30] A. Strauch, B. März, T. Denneulin, M. Cattaneo, A. Rosenauer, K. Müller-Caspary, Microsc. *Microanal*. **29**, 499 (2023).

[31] K. Müller-Caspary, M. Duchamp, M. Rösner, V. Migunov, F. Winkler, H. Yang, M. Huth, R. Ritz, M. Simson, S. Ihle, H. Soltau, T. Wehling, R.E. Dunin-Borkowski, S. van Aert, A. Rosenauer, *Phys. Rev. B* **98** (2018).

[32] O. Cretu, A. Ishizuka, K. Yanagisawa, K. Ishizuka, K. Kimoto, *ACS Nano* **15**, 5316 (2021).

[33] S. Calderon V, R.V. Ferreira, D. Taneja, R.T. Jayanth, L. Zhou, R.M. Ribeiro, D. Akinwande, P.J. Ferreira, *Nano Lett.* **21**, 10157 (2021).

[34] Y. Wen, S. Fang, M. Coupin, Y. Lu, C. Ophus, E. Kaxiras, J.H. Warner, *ACS Nano* **16**, 6657 (2022).

[35] J. Martis, S. Susarla, A. Rayabharam, C. Su, T. Paule, P. Pelz, C. Huff, X. Xu, H.-K. Li, M. Jaikissoon, V. Chen, E. Pop, K. Saraswat, A. Zettl, N.R. Aluru, R. Ramesh, P. Ercius, A. Majumdar, *Nat. Commun.* **14**, 4363 (2023).

[36] R. Close, Z. Chen, N. Shibata, S.D. Findlay, *Ultramicroscopy* **159**, 124 (2015).

[37] F. Schwarzhuber, P. Melzl, J. Zweck, *Ultramicroscopy* **177**, 97 (2017).

[38] J. Zweck, F. Schwarzhuber, J. Wild, V. Galioit, *Ultramicroscopy* **168**, 53 (2016).

[39] N. Shibata, Y. Kohno, S.D. Findlay, H. Sawada, Y. Kondo, Y. Ikuhara, *J. Electron Microsc.* **59**, 473 (2010).

[40] T.J. Pennycook, A.R. Lupini, H. Yang, M.F. Murfitt, L. Jones, P.D. Nellist, *Ultramicroscopy* **151**, 160 (2015).

[41] T. Seki, G. Sánchez-Santolino, R. Ishikawa, S.D. Findlay, Y. Ikuhara, N. Shibata, *Ultramicroscopy* **182**, 258 (2017).

[42] K. Müller-Caspary, F.F. Krause, F. Winkler, A. Béché, J. Verbeeck, S. van Aert, A. Rosenauer, *Ultramicroscopy* **203**, 95 (2019).

[43] C. Addiego, W. Gao, X. Pan, *Ultramicroscopy* **208**, 112850 (2020).

[44] J. Barthel, *Ultramicroscopy* **193**, 1 (2018).

[45] S.J. Pennycook, P.D. Nellist, *Scanning transmission electron microscopy: Imaging and analysis*, New York: Springer (2011).

[46] J. Liu, *Microsc. Microanal.* **27**, 943 (2021).

[47] N. Tanaka, *Scanning Transmission Electron Microscopy of Nanomaterials: Basics of Imaging and Analysis*, Singapore: World Scientific Publishing Company (2014).

[48] D.A. Muller, *Nat. Mat.* **8**, 263 (2009).

[49] K. Müller, A. Rosenauer, M. Schowalter, J. Zweck, R. Fritz, K. Volz, Microsc. *Microanal* . **18**, 995 (2012).

[50] D.B. Williams, C.B. Carter, *Transmission Electron Microscopy: A Textbook for Materials Science*, Boston: Springer (1996).

[51] L. Reimer, *Transmission Electron Microscopy: Physics of Image Formation and Microanalysis*, Berlin, Heidelberg: Springer (2013).

[52] S.J. Pennycook, P.D. Nellist, *Scanning Transmission Electron Microscopy: Imaging and Analysis*, New York: Springer (2011).

[53] R. Erni, M.D. Rossell, C. Kisielowski, U. Dahmen, *Phys. Rev. Lett.* **102**, 96101 (2009).

[54] S. Morishita, R. Ishikawa, Y. Kohno, H. Sawada, N. Shibata, Y. Ikuhara, *Microsc.* **67**, 46 (2018).

[55] R. Ishikawa, S. Morishita, T. Tanigaki, N. Shibata, Y. Ikuhara, *Microsc.* **72***,* 78 *(2023)*.

[56] M.T. Otten, *J. Electron Microsc. Tech.* **17**, 221 (1991).

[57] H. Sawada, T. Sannomiya, F. Hosokawa, T. Nakamichi, T. Kaneyama, T. Tomita, Y. Kondo, T. Tanaka, Y. Oshima, Y. Tanishiro, K. Takayanagi, *Ultramicroscopy* **108**, 1467 (2008).

[58] J.M. Cowley, *Ultramicroscopy* **2**, 3 (1976).

[59] J.M. Cowley, *J. Electron Microsc. Tech.* **3**, 25 (1986).

[60] J.M. Cowley, *Ultramicroscopy* **4**, 435 (1979).

[61] O. Scherzer, *J. Appl. Phys.* **20**, 20 (1949).

[62] B.D. Forbes, A.J. D'Alfonso, S.D. Findlay, D. van Dyck, J.M. LeBeau, S. Stemmer, L.J. Allen, *Ultramicroscopy* **111**, 1670 (2011).

[63] J. Murray Gibson, *Ultramicroscopy* **56**, 26 (1994).

[64] M. Vulović, L.M. Voortman, L.J. van Vliet, B. Rieger, *Ultramicroscopy* **136**, 61 (2014).

[65] P. Hartel, H. Rose, C. Dinges, *Ultramicroscopy* **63**, 93 (1996).

[66] S.J. Pennycook, *Annu. Rev. Mater. Sci.* **22**, 171 (1992).

[67] M.M.J. Treacy, *Microsc. Microanal.* **17**, 847 (2011).

[68] S.J. Pennycook, D.E. Jesson, *Ultramicroscopy* **37**, 14 (1991).

[69] S. Yamashita, J. Kikkawa, K. Yanagisawa, T. Nagai, K. Ishizuka, K. Kimoto, *Sci. Rep.* **8**, 12325 (2018).

[70] A. de Backer, G.T. Martinez, A. Rosenauer, S. van Aert, *Ultramicroscopy* **134**, 23 (2013).

[71] S. van Aert, A. de Backer, G.T. Martinez, B. Goris, S. Bals, G. van Tendeloo, A. Rosenauer, *Phys. Rev. B* **87,** 064107 (2013).

[72] A. de Wael, A. de Backer, I. Lobato, S. van Aert, *Ultramicroscopy* **230**, 113391 (2021).

[73] R.F. Egerton, *Electron Energy-Loss Spectroscopy in the Electron Microscope*, New York: Springer (2011).

[74] M. Watanabe, E. Okunishi, T. Aoki, *Microsc. Microanal.* **16**, 66 (2010).

[75] J. Nelayah, M. Kociak, O. Stéphan, García de Abajo, F. Javier, M. Tencé, L. Henrard, D. Taverna, I. Pastoriza-Santos, L.M. Liz-Marzán, C. Colliex, *Nat. Phys.* **3**, 348 (2007).

[76] J. Nelayah, L. Gu, W. Sigle, C.T. Koch, I. Pastoriza-Santos, L.M. Liz-Marzán, P. A. van Aken, *Opt. Lett.* **34**, 1003 (2009).

[77] O. Nicoletti, F. de La Peña, R.K. Leary, D.J. Holland, C. Ducati, P.A. Midgley, *Nature* **502**, 80 (2013).

[78] J. Bürger, V.S. Kunnathully, D. Kool, J.K.N. Lindner, K. Brassat, *Nanomaterials* **10**, 141 (2020).

[79] K. Varlot, J.M. Martin, C. Quet, *J. Microsc.* **191**, 187 (1998).

[80] K. Varlot, J.M. Martin, C. Quet, *Micron* **32**, 371 (2001).

[81] J.J. Ritsko, L.J. Brillson, R.W. Bigelow, T.J. Fabish, *J. Chem. Phys.* **69**, 3931 (1978).

[82] J.T. Titantah, D. Lamoen, *Carbon* **43**, 1311 (2005).

[83] B. Rafferty, L.M. Brown, *Phys. Rev. B* **58**, 10326 (1998).

[84] T. Malis, S.C. Cheng, R.F. Egerton, *J. Electron Microsc. Tech.* **8**, 193 (1988).

[85] K. Iakoubovskii, K. Mitsuishi, Y. Nakayama, K. Furuya, *Microsc. Res. and Tech.* **71**, 626 (2008).

[86] W. Wang, J. Cui, Z. Sun, L. Xie, X. Mu, L. Huang, J. He, *Adv. Mater.* **33**, 2106359 (2021).

[87] S. Pöllath, F. Schwarzhuber, J. Zweck, *Ultramicroscopy* **228**, 113342 (2021).

[88] B. Bauer, J. Hubmann, M. Lohr, E. Reiger, D. Bougeard, J. Zweck, *Appl. Phys. Lett.* **104**, 211902 (2014).

[89] I. Lazić, E.G.T. Bosch, S. Lazar, *Ultramicroscopy* **160**, 265 (2016).

[90] A. Lubk, J. Zweck, *Phys. Rev. A* **91,** 023805 (2015).

[91] J. Bürger, T. Riedl, J.K.N. Lindner, *Ultramicroscopy* **219**, 113118 (2020).

[92] J.N. Chapman, I.R. McFadyen, S. McVitie, *IEEE Trans. Magn.* **26**, 1506 (1990).

[93] M. Nord, R.W.H. Webster, K.A. Paton, S. McVitie, D. McGrouther, I. MacLaren, G.W. Paterson, *Microsc. Microanal.* **26**, 653 (2020).

[94] F. Schwarzhuber, P. Melzl, S. Pöllath, J. Zweck, *Ultramicroscopy* **192**, 21 (2018).

[95] C. Ophus, *Microsc. Microanal.* **25**, 563 (2019).

[96] I. MacLaren, L. Wang, D. McGrouther, A.J. Craven, S. McVitie, R. Schierholz, A. Kovács, J. Barthel, R.E. Dunin-Borkowski, *Ultramicroscopy* **154**, 57 (2015).

[97] M.W. Tate, P. Purohit, D. Chamberlain, K.X. Nguyen, R. Hovden, C.S. Chang, P. Deb, E. Turgut, J.T. Heron, D.G. Schlom, D.C. Ralph, G.D. Fuchs, K.S. Shanks, H.T. Philipp, D.A. Muller, S.M. Gruner, Microsc. *Microanal.* **22**, 237 (2016).

[98] T. Mawson, D.J. Taplin, H.G. Brown, L. Clark, R. Ishikawa, T. Seki, Y. Ikuhara, N. Shibata, D.M. Paganin, M.J. Morgan, M. Weyland, T.C. Petersen, S.D. Findlay, *Ultramicroscopy* **233**, 113457 (2022).

[99] M. Krajnak, J. Etheridge, *Proc. Natl. Acad. Sci. U.S.A.* **117**, 27805 (2020).

[100] T. Seki, Y. Ikuhara, N. Shibata, *Microsc.* **70**, 148 (2021).

[101] H. Wang, L. Liu, J. Wang, C. Li, J. Hou, K. Zheng, *Molecules* **27**, 3829 (2022).

[102] L. Liu, N. Wang, C. Zhu, X. Liu, Y. Zhu, P. Guo, L. Alfilfil, X. Dong, D. Zhang, Y. Han, *Angew. Chem. Int. Ed.* **59**, 819 (2020).

[103] L. Wang, M. Ma, H. Wang, H. Xiong, X. Chen, F. Wei, B. Shen, *ACS Nano* (2023).

[104] X. Li, J. Wang, X. Liu, L. Liu, D. Cha, X. Zheng, A.A. Yousef, K. Song, Y. Zhu, D. Zhang, Y. Han, *J. Am. Chem. Soc.* **141**, 12021 (2019).

[105] X. Zhang, H. Zhao, J. Zhu, *Mater. Today Phys.* **23**, 100629 (2022).

[106] W. Lin, Y. Li, S. de Graaf, G. Wang, J. Lin, H. Zhang, S. Zhao, D. Chen, S. Liu, J. Fan, B.J. Kooi, Y. Lu, T. Yang, C.-H. Yang, C.T. Liu, J.-j. Kai, *Nat. Commun.* **13**, 5990 (2022).

[107] A. Weickenmeier, H. Kohl, *Acta Crystallogr. A* **47**, 590 (1991).

[108] R.F. Loane, P. Xu, J. Silcox, *Acta Crystallogr. A* **47**, 267 (1991).

[109] D. Zhou, K. Müller-Caspary, W. Sigle, F.F. Krause, A. Rosenauer, P.A. van Aken, *Ultramicroscopy* **160**, 110 (2016).

[110] R.R. Meyer, A. Kirkland, *Ultramicroscopy* **75**, 23 (1998).

[111] S.D. Findlay, J.M. LeBeau, *Ultramicroscopy* **124**, 52 (2013).

[112] Z. Li, J. Biskupek, U. Kaiser, H. Rose, *Microsc. Microanal.* **28**, 611 (2022).

[113] A.B. Yankovich, B. Berkels, W. Dahmen, P. Binev, S.I. Sanchez, S.A. Bradley, A. Li, I. Szlufarska, P.M. Voyles, *Nat. Commun.* **5**, 4155 (2014).

[114] T. Seki, Y. Ikuhara, N. Shibata, *Ultramicroscopy* **193**, 118 (2018).

[115] G. Y. Fan, M. H. Ellisman, *J. Microsc.* **200**, 1 (2000).

[116] P. Gao, A. Kumamoto, R. Ishikawa, N. Lugg, N. Shibata, Y. Ikuhara, *Ultramicroscopy* **184**, 177 (2018).

[117] R. Ishikawa, A.R. Lupini, S.D. Findlay, S.J. Pennycook, *Micros. Microanal.* **20**, 99 (2014).

[118] C. Ravi, D. James, V. Sarma, B. Datta Sahoo, A. Inamdar, in *2017 IEEE International Symposium on Circuits and Systems (ISCAS)* 2017, p. 1.

[119] R.H. Walden, *IEEE J. Select. Areas Commun.* **17**, 539 (1999).

[120] J.R. Prescott, *Nucl. Instrum. Methods* **39**, 173 (1966).

[121] J.A. Baicker, *IRE Trans. Nucl. Sci.* **7**, 74 (1960).

[122] H. Ikoma, M. Broxton, T. Kudo, G. Wetzstein, *Sci. Rep.* **8**, 11489 (2018).

[123] D. Bernecker, *Image Processing*, in: *Medical Imaging System,* Eds. A. Maier, S. Steidl, V. Christlein, J. Hornegger, Cham: Springer (2018).

[124] B. Berkels, R. Sharpley, P. Binev, A. Yankovich, F. Shi, P. Voyles, W. Dahmen, *Microsc. Microanal.* **18**, 300 (2012).

[125] B. Berkels, P. Binev, D.A. Blom, W. Dahmen, R.C. Sharpley, T. Vogt, *Ultramicroscopy* **138**, 46 (2014).

[126] L. Shapiro and G.H. Stockman, *Computer vision*. Prentice-Hall (2001).

[127] Ling Shao, Ruomei Yan, Xuelong Li, Yan Liu, *IEEE Trans. Cybern.* **44**, 1001 (2014).

[128] R.F. Egerton, P. Li, M. Malac, *Micron* **35**, 399 (2004).

[129] J. Modersitzki, *Numerical methods for image registration*. New York: Oxford University Press (2003).

[130] L. Jones, H. Yang, T.J. Pennycook, M.S.J. Marshall, S. van Aert, N.D. Browning, M.R. Castell, P.D. Nellist, *Adv. Struct. Chem. Imag.* **1**, 1 (2015).

[131] J.M. Fitzpatrick, D.L.G. Hill, C.R. Maurer, *Image registration*, in: *Handbook of Medical Imaging, Volume 2. Medical Image Processing and Analysis*, Eds. M. Sonka, J.M. Fitzpatrick, Bellingham: SPIE (2000).

[132] J.-P. Thirion, *Med. Image Anal.* **2**, 243 (1998).

[133] A.B. Yankovich, C. Zhang, A. Oh, T.J.A. Slater, F. Azough, R. Freer, S.J. Haigh, R. Willett, P.M. Voyles, *Nanotechnology* **27**, 364001 (2016).

[134] C.A. Glasbey, K.V. Mardia, *J. Appl.Stat.* **25**, 155 (1998).

[135] N. Braidy, Y. Le Bouar, S. Lazar, C. Ricolleau, *Ultramicroscopy* **118**, 67 (2012).

[136] R. Mishra, R. Ishikawa, A.R. Lupini, S.J. Pennycook, *MRS Bull.* **42**, 644 (2017).

[137] S. van Aert, J. Verbeeck, R. Erni, S. Bals, M. Luysberg, D. van Dyck, G. van Tendeloo, *Ultramicroscopy* **109**, 1236 (2009).

[138] W. Wang, W. Cai, *RSC Adv.* **11**, 11057 (2021).

[139] Y. Wang, U. Salzberger, W. Sigle, Y. Eren Suyolcu, P.A. van Aken, *Ultramicroscopy* **168**, 46 (2016).

[140] M. Nord, P.E. Vullum, I. MacLaren, T. Tybell, R. Holmestad, *Adv. Struct. Chem. Imag.* **3**, 1 (2017).

[141] A. de Backer, G.T. Martinez, K.E. MacArthur, L. Jones, A. Béché, P.D. Nellist, S. van Aert, *Ultramicroscopy* **151**, 56 (2015).

[142] M. Alania, T. Altantzis, A. de Backer, I. Lobato, S. Bals, S. van Aert, *Ultramicroscopy* **177**, 36 (2017).

[143] T. Nilsson Pingel, M. Jørgensen, A.B. Yankovich, H. Grönbeck, E. Olsson, *Nat. Commun.* **9**, 1 (2018).

[144] H. E, K.E. MacArthur, T.J. Pennycook, E. Okunishi, A.J. D'Alfonso, N.R. Lugg, L.J. Allen, P.D. Nellist, *Ultramicroscopy* **133**, 109 (2013).

[145] I.F. Sbalzarini, P. Koumoutsakos, *J. Struct. Biol.* **151**, 182 (2005).

[146] S. Schulze, M. Gruschwitz, H. Schletter, I. Alexandrou, M. Hietschold, C. Tegenkamp, *Imaging* (2020).

[147] S.D. Findlay, N. Shibata, Y. Ikuhara, R. Huang, E. Okunishi, H. Sawada, Y. Kohno, Y. Kondo, *Micros. Today* **25**, 36 (2017).

[148] H.L. Robert, I. Lobato, F.J. Lyu, Q. Chen, S. van Aert, D. van Dyck, K. Müller-Caspary, *Ultramicroscopy* **233**, 113425 (2022).

[149] N. Tanaka, J.J. Hu, N. Baba, *Ultramicroscopy* **78**, 103 (1999).

[150] H.H. Rose, *Philos. Trans. Royal Soc. A* **367**, 3809 (2009).

[151] S. Korneychuk, B. Partoens, G. Guzzinati, R. Ramaneti, J. Derluyn, K. Haenen, J. Verbeeck, *Ultramicroscopy* **189**, 76 (2018).

[152] A. Edström, A. Lubk, J. Rusz, *Phys. Rev. B* **99**, 174428 (2019).

[153] N.R. Lugg, G. Kothleitner, N. Shibata, Y. Ikuhara, *Ultramicroscopy* **151**, 150 (2015).

[154] C. Ophus, *Adv Struct Chem Imag* **3**, 1 (2017).

[155] R.J. Wu, A. Mittal, M.L. Odlyzko, K.A. Mkhoyan, *Microanal* **23**, 794 (2017).

[156] P.M. Voyles, D.A. Muller, E.J. Kirkland, *Microsc. Microanal.* **10**, 291 (2004).

[157] M. Haruta, H. Kurata, H. Komatsu, Y. Shimakawa, S. Isoda, *Ultramicroscopy* **109**, 361 (2009).

[158] D. Jannis, C. Hofer, C. Gao, X. Xie, A. Béché, T.J. Pennycook, J. Verbeeck, *Ultramicroscopy* **233**, 113423 (2021).

[159] Q. Chen, C. Dwyer, G. Sheng, C. Zhu, X. Li, C. Zheng, Y. Zhu, *Adv. Mater.* **32**, 1907619 (2020).

[160] F.F. Krause, M. Schowalter, O. Oppermann, D. Marquardt, K. Müller-Caspary, R. Ritz, M. Simson, H. Ryll, M. Huth, H. Soltau, A. Rosenauer, *Ultramicroscopy* **223**, 113221 (2021).

[161] A. Klenke, *Wahrscheinlichkeitstheorie*, Berlin, Heidelberg: Springer (2020).

[162] S.M. Ross, *Introduction to probability models*, London: Academic Press (2019).

[163] R.L. Baer*, A model for dark current characterization and simulation,* in: *Sensors, Cameras, and Systems for Scientific/Industrial Applications VII*, Ed. M.M. Blouke, SPIE (2006).

[164] C.M. Sparrow, *Astrophys. J.* **44**, 76 (1916).

[165] D. van Dyck, S. van Aert, A.J. den Dekker, A. van den Bos, *Ultramicroscopy* **98**, 27 (2003).

[166] R. Shinnar, G.H. Weiss, *Sep. Sci.* Tech. **11**, 377 (1976).

[167] F.W. Clarke, H.S. Washington, *The Composition of the Earth's Crust*, Washington: Government Printing Office (1924).

[168] A.A. Yaroshevsky, *Geochem. Int.* **44**, 48 (2006).

[169] K. Pandey, A. Sharma, A.K. Singh, *Silicon*, 1 (2022).

[170] P. Ball, *Nat. Mater.* **21**, 132 (2022).

[171] S.M. Schwarz, B.W. Kempshall, L.A. Giannuzzi, M.R. McCartney, *Microsc. Microanal.* **9**, 116 (2003).

[172] E. Montoya, S. Bals, M.D. Rossell, D. Schryvers, G. van Tendeloo, *Microsc. Res. Tech.* **70**, 1060 (2007).

[173] L.A. Giannuzzi, R. Geurts, J. Ringnalda, *Microsc. Microanal.* **11**, 828 (2005).

[174] Z. Zhang, W. Wang, Z. Dong, X. Yang, F. Liang, X. Chen, C. Wang, C. Luo, J. Zhang, X. Wu, L. Sun, J. Chu, *Adv. Electron Mater.* **8**, 2101401 (2022).

[175] K.A. Mkhoyan, S.E. Maccagnano-Zacher, E.J. Kirkland, J. Silcox, *Ultramicroscopy* **108**, 791 (2008).

[176] S Taylor, J F Zhang, W Eccleston, *Semicond. Sci. Technol.* **8**, 1426 (1993).

[177] B. Tossoun, G. Kurczveil, C. Zhang, A. Descos, Z. Huang, A. Beling, J.C. Campbell, D. Liang, R.G. Beausoleil, *Optica* **6**, 1277 (2019).

[178] M.V. Rakhlin, K.G. Belyaev, G.V. Klimko, I.S. Mukhin, D.A. Kirilenko, T.V. Shubina, S.V. Ivanov, A.A. Toropov, *Sci. Rep.* **8**, 5299 (2018).

[179] S. Adachi, *J. Appl. Phys.* **61**, 4869 (1987).

[180] A. Murat, M. Matsubara, B.-M. Nguyen, E. Bellotti, *Phys. Rev. Mater.* **2**, 123604 (2018).

[181] T. Riedl, V.S. Kunnathully, A. Trapp, T. Langer, D. Reuter, J.K.N. Lindner, *Adv. Mater. Interfaces.* **9**, 2102159 (2022).

[182] M. Hjort, S. Lehmann, J. Knutsson, A.A. Zakharov, Y.A. Du, S. Sakong, R. Timm, G. Nylund, E. Lundgren, P. Kratzer, K.A. Dick, A. Mikkelsen, *ACS Nano* **8**, 12346 (2014).

[183] T. Akiyama, T. Yamashita, K. Nakamura, T. Ito, *Nano Lett.* **10**, 4614 (2010).

[184] T. Riedl, J.K.N. Lindner, *Phys. Status Solidi A* **211**, 2871 (2014).

[185] V.S. Kunnathully, T. Riedl, A. Trapp, T. Langer, D. Reuter, J.K.N. Lindner, *J. Cryst. Growth* **537**, 125597 (2020).

[186] T. Riedl, V.S. Kunnathully, A. Trapp, T. Langer, D. Reuter, J.K.N. Lindner, *Phys. Rev. Mater.* **4**, 14602 (2020).

[187] I.-J. Chen, S. Lehmann, M. Nilsson, P. Kivisaari, H. Linke, K.A. Dick, C. Thelander, *Nano Lett.* **17**, 902 (2017).

[188] J.K. Panda, A. Chakraborty, D. Ercolani, M. Gemmi, L. Sorba, A. Roy, *Nanotechnology* **27**, 415201 (2016).

[189] L. Li, Z. Gan, M.R. McCartney, H. Liang, H. Yu, W.-J. Yin, Y. Yan, Y. Gao, J. Wang, D.J. Smith, *Adv. Mater.* **26**, 1052 (2014).

[190] S.A. Dayeh, D. Susac, K.L. Kavanagh, E.T. Yu, D. Wang, *Adv. Funct. Mater.* **19**, 2102 (2009).

[191] T. Yamazaki, K. Watanabe, N. Nakanishi, I. Hashimoto, *Ultramicroscopy* **99**, 125 (2004).

[192] M. Möller, de Lima Jr, M. M., A. Cantarero, T. Chiaramonte, M.A. Cotta, F. Iikawa, *Nanotechnology* **23**, 375704 (2012).

[193] Z. Zhang, Y. Liu, C. Dai, X. Yang, P. Chen, H. Ma, B. Zhao, R. Wu, Z. Huang, Di Wang, M. Liu, Y. Huangfu, S. Xin, J. Luo, Y. Wang, J. Li, B. Li, X. Duan, *Chem. Mater.* **33**, 1307 (2021).

[194] Y. Ma, B. Liu, A. Zhang, L. Chen, M. Fathi, C. Shen, A.N. Abbas, M. Ge, M. Mecklenburg, C. Zhou, *ACS Nano* **9**, 7383 (2015).

[195] M. Xu, T. Liang, M. Shi, H. Chen, *Chem. Rev.* **113**, 3766 (2013).

[196] Y. You, X.-X. Zhang, T.C. Berkelbach, M.S. Hybertsen, D.R. Reichman, T.F. Heinz, *Nat. Phys.* **11**, 477 (2015).

[197] H. Sahin, S. Tongay, S. Horzum, W. Fan, J. Zhou, J. Li, J. Wu, F. M. Peeters, *Phys. Rev. B* **87**, 165409 (2013).

[198] A. Klein, S. Tiefenbacher, V. Eyert, C. Pettenkofer, W. Jaegermann, *Phys. Rev. B* **64**, 205416 (2001).

[199] T. Yan, X. Qiao, X. Liu, P. Tan, X. Zhang, *Appl. Phys. Lett.* **105**, 101901 (2014).

[200] W. Lan, J. Wang, M. Xin, Y. Huang, C. Gu, B. Liu, *Appl. Phys. Lett.* **117**, 83107 (2020).

[201] Z. Chu, A. Han, C. Lei, S. Lopatin, P. Li, D. Wannlund, Di Wu, K. Herrera, X. Zhang, A.H. MacDonald, X. Li, L.-J. Li, K. Lai, *Nano Lett.* **18**, 7200 (2018).

[202] K.M. McCreary, A.T. Hanbicki, S. Singh, R.K. Kawakami, G.G. Jernigan, M. Ishigami, A. Ng, T.H. Brintlinger, R.M. Stroud, B.T. Jonker, *Sci. Rep.* **6**, 35154 (2016).

[203] J. Gusakova, X. Wang, L.L. Shiau, A. Krivosheeva, V. Shaposhnikov, V. Borisenko, V. Gusakov, B.K. Tay, *Phys. Status Solidi (A)* **214**, 1700218 (2017).

[204] C.-x. Yang, X. Zhao, S.-y. Wei, *Solid State Commun.* **245**, 70 (2016).

[205] P. Tonndorf, R. Schmidt, P. Böttger, X. Zhang, J. Börner, A. Liebig, M. Albrecht, C. Kloc, O. Gordan, D.R.T. Zahn, S. Michaelis de Vasconcellos, R. Bratschitsch, *Opt. Express* **21**, 4908 (2013).

[206] P. Rivera, J.R. Schaibley, A.M. Jones, J.S. Ross, S. Wu, G. Aivazian, P. Klement, K. Seyler, G. Clark, N.J. Ghimire, J. Yan, D.G. Mandrus, W. Yao, X. Xu, *Nat. Commun.* **6**, 6242 (2015).

[207] Z. Jia, J. Shi, Q. Shang, W. Du, X. Shan, B. Ge, J. Li, X. Sui, Y. Zhong, Q. Wang, L. Bao, Q. Zhang, X. Liu, *ACS Appl. Mater. Inter.* **11**, 20566 (2019).

[208] S.B. Desai, G. Seol, J.S. Kang, H. Fang, C. Battaglia, R. Kapadia, J.W. Ager, J. Guo, A. Javey, *Nano Lett.* **14**, 4592 (2014).

[209] R. Ishikawa, S.D. Findlay, T. Seki, G. Sánchez-Santolino, Y. Kohno, Y. Ikuhara, N. Shibata, *Nat. Commun.* **9**, 3878 (2018).

[210] S. Fang, Y. Wen, C.S. Allen, C. Ophus, G.G.D. Han, A.I. Kirkland, E. Kaxiras, J.H. Warner, *Nat. Commun.* **10**, 1127 (2019).

[211] S. de Graaf, M. Ahmadi, I. Lazić, E.G.T. Bosch, B.J. Kooi, *Nanoscale* **13**, 20683 (2021).

[212] K.F. Mak, C. Lee, J. Hone, J. Shan, T.F. Heinz, *Phys. Rev. Lett.* **105**, 136805 (2010).

[213] J. He, K. Hummer, C. Franchini, *Phys. Rev. B* **89**, 075409 (2014).

[214] W.J. Schutte, J.L. de Boer, F. Jellinek, *J. Solid State Chem.* **70**, 207 (1987).

[215] K.M. McCreary, M. Phillips, H.-J. Chuang, D. Wickramaratne, M. Rosenberger, C.S. Hellberg, B.T. Jonker, *Nanoscale* **14**, 147 (2022).

[216] A.A. Puretzky, L. Liang, X. Li, K. Xiao, K. Wang, M. Mahjouri-Samani, L. Basile, J.C. Idrobo, B.G. Sumpter, V. Meunier, D.B. Geohegan, *ACS Nano* **9**, 6333 (2015).

[217] H. Li, J. Wu, Z. Yin, H. Zhang, *Acc. Chem. Res.* **47**, 1067 (2014).

[218] A.K. Geim, K.S. Novoselov, *Nat. Mater.* **6**, 183 (2007).

[219] K.S. Novoselov, D. Jiang, F. Schedin, T.J. Booth, V.V. Khotkevich, S.V. Morozov, A.K. Geim, *Proc. Natl. Acad. Sci.* **102**, 10451 (2005).

[220] R. Browning, N. Kuperman, R. Solanki, V. Kanzyuba, S. Rouvimov, *Semicond. Sci. Technol.* **31**, 095002 (2016).

[221] M. Nakano, Y. Wang, Y. Kashiwabara, H. Matsuoka, Y. Iwasa, *Nano Lett.* **17**, 5595 (2017).

[222] Y. Gong, S. Lei, G. Ye, B. Li, Y. He, K. Keyshar, X. Zhang, Q. Wang, J. Lou, Z. Liu, R. Vajtai, W. Zhou, P.M. Ajayan, *Nano Lett.* **15**, 6135 (2015).

[223] A. Han, A. Aljarb, S. Liu, P. Li, C. Ma, F. Xue, S. Lopatin, C.-W. Yang, J.-K. Huang, Y. Wan, X. Zhang, Q. Xiong, K.-W. Huang, V. Tung, T.D. Anthopoulos, L.-J. Li, *Nanoscale Horiz.* **4**, 1434 (2019).

[224] E. Gao, S.-Z. Lin, Z. Qin, M.J. Buehler, X.-Q. Feng, Z. Xu, *J. Mech. Phys. Solids* **115**, 248 (2018).

[225] R.J. Wu, M.L. Odlyzko, K.A. Mkhoyan, *Ultramicroscopy* **147**, 8 (2014).

[226] R. Saha, H.L. Meyerheim, B. Göbel, B.K. Hazra, H. Deniz, K. Mohseni, V. Antonov, A. Ernst, D. Knyazev, A. Bedoya-Pinto, I. Mertig, S.S.P. Parkin, *Nat. Commun.* **13**, 3965 (2022).

[227] J. Sickel, M. Asbach, C. Gammer, R. Bratschitsch, H. Kohl, *Microsc. Microanal.* ***28***, 701 (2022).

[228] Y. Zhang, M.-K. Choi, G. Haugstad, E.B. Tadmor, D.J. Flannigan, *ACS Nano* **15**, 20253 (2021).

[229] Y. Wan, J.-K. Huang, C.-P. Chuu, W.-T. Hsu, C.-J. Lee, A. Aljarb, C.-W. Huang, M.-H. Chiu, H.-L. Tang, C. Lin, X. Zhang, C.-M. Wei, S. Li, W.-H. Chang, L.-J. Li, V. Tung, *ACS Mater. Lett.* **3**, 442 (2021).

[230] M. Xia, B. Li, K. Yin, G. Capellini, G. Niu, Y. Gong, W. Zhou, P.M. Ajayan, Y.-H. Xie, *ACS Nano* **9**, 12246 (2015).

[231] J. Jiang, T. Xu, J. Lu, L. Sun, Z. Ni, *Res.* **2019**, 4641739 (2019).

[232] S. Tongay, J. Suh, C. Ataca, W. Fan, A. Luce, J.S. Kang, J. Liu, C. Ko, R. Raghunathanan, J. Zhou, F. Ogletree, J. Li, J.C. Grossman, J. Wu, *Sci. Rep.* **3**, 2657 (2013).

[233] Y.-C. Lin, T. Björkman, H.-P. Komsa, P.-Y. Teng, C.-H. Yeh, F.-S. Huang, K.-H. Lin, J. Jadczak, Y.-S. Huang, P.-W. Chiu, A.V. Krasheninnikov, K. Suenaga, *Nat. Commun.* **6**, 6736 (2015).

[234] A.A. Tedstone, D.J. Lewis, P. O'Brien, *Chem. Mater.* **28**, 1965 (2016).

[235] L. Li, E.A. Carter, *J. Am. Chem. Soc.* **141**, 10451 (2019).

[236] D. Edelberg, D. Rhodes, A. Kerelsky, B. Kim, J. Wang, A. Zangiabadi, C. Kim, A. Abhinandan, J. Ardelean, M. Scully, D. Scullion, L. Embon, I. Zhang, R. Zu, E.J.G. Santos, L. Balicas, C. Marianetti, K. Barmak, X.-Y. Zhu, J. Hone, A.N. Pasupathy, *arXiv preprint arXiv:1805.00127* (2018).

[237] R.G. Mendes, J. Pang, A. Bachmatiuk, H.Q. Ta, L. Zhao, T. Gemming, L. Fu, Z. Liu, M.H. Rümmeli, *ACS Nano* **13**, 978 (2019).

[238] S. Zhang, C.-G. Wang, M.-Y. Li, Di Huang, L.-J. Li, W. Ji, S. Wu, *Phys. Rev. Lett.* **119**, 046101 (2017).

[239] G. Moody, K. Tran, X. Lu, T. Autry, J.M. Fraser, R.P. Mirin, L. Yang, X. Li, K.L. Silverman, *Phys. Rev. Lett.* **121**, 57403 (2018).

[240] Y.J. Zheng, Y. Chen, Y.L. Huang, P.K. Gogoi, M.-Y. Li, L.-J. Li, P.E. Trevisanutto, Q. Wang, S.J. Pennycook, A.T.S. Wee, S.Y. Quek, *ACS Nano* **13**, 6050 (2019).

[241] L. Linhart, M. Paur, V. Smejkal, J. Burgdörfer, T. Mueller, F. Libisch, *Phys. Rev. Lett.* **123**, 146401 (2019).

[242] S. Haldar, H. Vovusha, M.K. Yadav, O. Eriksson, B. Sanyal, *Phys. Rev. B* **92**, 235408 (2015).

[243] S. Ding, F. Lin, C. Jin, *Nanotechnology* **32**, 255701 (2021).

[244] T. Shi, R.C. Walker, I. Jovanovic, J.A. Robinson, *Sci. Rep.* **7**, 4151 (2017).

[245] Q. Chen, C. Dwyer, G. Sheng, C. Zhu, X. Li, C. Zheng, Y. Zhu, *Adv. Mater.* **32**, e1907619 (2020).

[246] H.-P. Komsa, J. Kotakoski, S. Kurasch, O. Lehtinen, U. Kaiser, A.V. Krasheninnikov, *Phys. Rev. Lett.* **109**, 035503 (2012).

[247] S. de Graaf, B.J. Kooi, *2D Mater.* **9**, 015009 (2021).

[248] R.F. Egerton, P. Li, M. Malac, *Micron* **35**, 399 (2004).

[249] Y.-C. Lin, D.O. Dumcenco, Y.-S. Huang, K. Suenaga, *Nat. Nanotechnol.* **9**, 391 (2014).

[250] B.H. Savitzky, S.E. Zeltmann, L.A. Hughes, H.G. Brown, S. Zhao, P.M. Pelz, T.C. Pekin, E.S. Barnard, J. Donohue, L.R. DaCosta, E. Kennedy, Y. Xie, M.T. Janish, M.M. Schneider, P. Herring, C. Gopal, A. Anapolsky, R. Dhall, K.C. Bustillo, P. Ercius, M.C. Scott, J. Ciston, A.M. Minor, C. Ophus, *Microsc. Microanal.* **27**, 712 (2021).

[251] A. Ishizuka, K. Ishizuka, *JEOL NEWS* **55** (2020).

[252] T. Riedl, J.K.N. Lindner, Microsc. *Microanal.* **28**, 185 (2022).

List of publications

Peer-reviewed articles

- *Two-dimensional switchable blue phase gratings manufactured by nanosphere lithography,*
  M. Wahle, K. Brassat, J. Ebel, J. Bürger, J. K. N. Lindner, H.-S. Kitzerow, *Optics Express 25*(19), 22608 (2017).

- *Hierarchical nanopores formed by block copolymer lithography on the surfaces of different materials pre-patterned by nanosphere lithography,*
  K. Brassat, D. Kool, J. Bürger, J. K. N. Lindner, *Nanoscale 10*(21), 10005 (2018).

- *On the adsorption of DNA origami nanostructures in nanohole arrays,*
  K. Brassat, S. Ramakrishnan, J. Bürger, M. Hanke, M. Doostdar, J. K. N. Lindner, A. Keller, *Langmuir 34*(49), 14757 (2018).

- *Spray coating of poly (acrylic acid)/ZnO tetrapod adhesion promoting nanocomposite films for polymer laminates,*
  D. Meinderink, K. J. Nolkemper, J. Bürger, A. G. Orive, J. K. N. Lindner, G. Grundmeier, *Surface and Coatings Technology 375*, 112 (2019).

- *Nano-architectural complexity of zinc oxide nanowall hollow microspheres and their structural properties,*
  K. Engelkemeier, J. K. N. Lindner, J. Bürger, K. Vaupel, M. Hartmann, M. Tiemann, K.-P. Hoyer, M. Schaper, *Nanotechnology 31*(9), 095701 (2019).

- *Characterisation of the PS-PMMA interfaces in microphase separated block copolymer thin films by analytical (S)TEM,*
  J. Bürger, V. S. Kunnathully, D. Kool, J. K. N. Lindner, K. Brassat, *Nanomaterials 10*(1), 141 (2020).

- *Influence of lens aberrations, specimen thickness and tilt on differential phase contrast STEM images,*
  J. Bürger, T. Riedl, J. K. N. Lindner, *Ultramicroscopy 219*, 113118 (2020).

- *In situ backside Raman spectroscopy of zinc oxide nanorods in an atmospheric-pressure dielectric barrier discharge plasma,*
  S. Knust, L. Ruhm, A. Kuhlmann, D. Meinderink, J. Bürger, J. K. N. Lindner, G. Grundmeier, *Journal of Raman Spectroscopy 52*(7), 1237 (2021).

- *Quality or Quantity? How Structural Parameters Affect Catalytic Activity of Iron Oxides for CO Oxidation,*
  S. Schlicher, N. Prinz, J. Bürger, A. Omlor, C. Singer, M. Zobel, R. Schoch, J. K. N. Lindner, V. Schünemann, S. Kureti, M. Bauer, *Catalysts 12*(6), 675 (2022).

- *High-Resolution Study of Changes in Morphology and Chemistry of Cylindrical PS-b-PMMA Block Copolymer Nanomasks during Mask Development,*
  J. Bürger, H. Venugopal, D. Kool, T. de los Arcos, A. G. Orive, G. Grundmeier, K. Brassat, J. K. N. Lindner, *Advanced Materials Interfaces 9*(26), 2200962 (2022).

- *Die steel design for additive manufacturing. Part 1: Analysis & CALPHAD design,*
  F. Hengsbach, J. Bürger, A. Andreiev, K. Biggs, J. Fischer-Bühner, J. K. N. Lindner, K.-P. Hoyer, G. Olson, M. Schaper, *submitted to Acta Materialia* (2023). Preprint available via https://papers.ssrn.com/sol3/papers.cfm?abstract_id=4340381.

- *Die steel design for additive manufacturing. Part 2: Experimental validation,*
  F. Hengsbach, J. Bürger, A. Andreiev, K. Biggs, J. Fischer-Bühner, J. K. N. Lindner, K.-P. Hoyer, G. Olson, M. Schaper, *submitted to Acta Materialia* (2023). Preprint available via https://papers.ssrn.com/sol3/papers.cfm?abstract_id=4340382.

- *Investigation of the electric field and charge density distribution of pristine and defective 2D WSe2 by Differential Phase Contrast Imaging,*
  M. Groll, J. Bürger, I. Caltzidis, K. D. Jöns, J. K. N. Lindner, (2023) *submitted to SMALL*. Preprint available via https://arxiv.org/abs/2304.01068.

- *The impact of noise on differential phase contrast STEM images,*
  J. Bürger, C. Zietlow, J. K. N. Lindner, (2023) (to be submitted).

Conference paper

- *Selective area growth of cubic Gallium Nitride in nanoscopic Silicon Dioxide masks,*
  F. Meier, M. Littmann, J. Bürger, T. Riedl, D. Kool, J. K. N. Lindner, D. Reuter, D. J. As, *physica status solidi(b)* (2022).

Contributions to books

- *Climate Protection, Resource Efficiency, and Sustainable Engineering,*
  Ilona Horwath and Swetlana Schweizer (eds.), transcript Verlag, ISBN: 978-3-8376-6377-8

Conference contributions (presenting author is marked in bold font)

- *Site-selective protein immobilization on regular antidot patterns fabricated by nanosphere lithography,*
  Brassat K., Rüdiger A., Bürger J., Bremser W., Strube O., Lindner J.K.N.,
  E-MRS Fall Meeting 2016, 19–22 September 2016, Warsaw, Poland.

- *Electrode patterning by nanosphere lithography for switchable 2D blue phase gratings,*
  Wahle M., Brassat K., Ebel J., Bürger J., Lindner J.K.N., Kitzerow H.-S.,
  2nd Joint Conference of the German & British Liquid Crystal Societies, 3–5 April 2017, Würzburg, Germany.

- *Large area nanopatterns in elastomers by nanosphere mask replication,*
  Bürger J., Brassat K., Meyers T., Hilleringmann U., Lindner J.K.N.,
  Frühjahrstagung der Deutschen Physikalischen Gesellschaft, 4–9 March 2018, Berlin, Germany.

- *Nanostructure Research using Transmission Electron Microscopy at the new OWL Analytic Centre,*
  Riedl T., Bürger J., Kunnathully V., Wiegand M.C., Duschik K., Ramermann D., Ennen I., Hertle Y., Schaper M., Hellweg T., Hütten A., Lindner J.K.N.,
  8th NRW Nanoconference, 21–22 November 2018, Dortmund, Germany.

- *Pattern transfer of self-assembled block copolymer nanopores into silicon and silicon dioxide by reactive ion etching,*
  Stratmann A., Kool D., Bürger J., Brassat K., Lindner J.K.N.,
  Frühjahrstagung der Deutschen Physikalischen Gesellschaft, 31 March – 05 April 2019, Regensburg, Germany.

- *Atomic Resolution Differential Phase Contrast STEM investigations of electric fields in ZnO nanostructures,*
  Bürger J., Weiß J., Meinderink D., Engelkemeier K., Grundmeier G., Schaper M., Lindner J.K.N.,
  Frühjahrstagung der Deutschen Physikalischen Gesellschaft, 31 March – 05 April 2019, Regensburg, Germany.

- *Influences of lens aberration and specimen tilt on atomic resolution differential phase contrast STEM images,*
  Bürger J., Lindner J.K.N.,
  EMRS Spring Meeting 2019, 27–31 May 2019, Nice, France.

- *Differential phase contrast imaging with an 8-fold segmented detector in the STEM: Recent Applications and Limits,*
  Bürger J., **Lindne**r **J.K.N.,**
  Max-Planck Workshop on “Current Topics in Transmission Electron Microscopy: Magnetic and optical properties of functional materials“ at Ringberg Castle, 3–5 July 2019, Lake Tegernsee, Germany.

- *Characterization of Laser Beam Modified Carbon Fibres,*
  Engelkemeier K., Duschik K., Bürger J., Hoyer K.-P., Buitkamp N., Bremser W., Schaper M., **Lindner J.K.N.**,
  Microscopy Conference 2019, 01–05 September 2019, Berlin, Germany.

- *Atomic resolution differential phase contrast imaging of defect structures in heteroepitaxial GaAs grown on Si3N4 nanohole-masked Si(001),*
  Bürger J., Riedl T., Langer T., Trapp A., Reuter D., Lindner J.K.N.,
  Microscopy Conference 2019, 01–05 September 2019, Berlin, Germany.

- *Influence of lens aberrations, specimen tilt and thickness on differential phase contrast images of crystalline specimens,*
  Bürger J., Riedl T., Lindner J.K.N.,
  Microscopy Conference 2019, 01–05 September 2019, Berlin, Germany.

- *GaAs heteroepitaxy on Si_3N_4 nanohole-masked Si(001) patterned by nanosphere lithography,*
  Riedl T., Langer T., Trapp A., Bürger J., Reuter D., Lindner J.K.N.,
  Euromat 2019 Conference, 1–5 September 2019, Stockholm, Sweden.

- *DPC-STEM observation of magnetic domains in Fe-Si alloy manufactured by laser beam melting,*
  Pramanik S., Tasche L., Bürger J., Lindner J.K.N., Hoyer K.-P., Schaper M.,
  Materials Science and Engineering Congress 2020, 22–25 September 2020, Darmstadt, Germany (virtual).

- *Analytical (S)TEM of the morphology and interfaces of microphase domains in PS-b-PMMA block copolymers*
  Bürger J., Brassat K., Lindner J.K.N.
  Symposium M on ALTECH 2021 - Analytical techniques for precise characterization of nano materials, European Materials Research Society Spring Meeting 2021, 31 May – 4 June 2021, Strasbourg, France (virtual).

- *XPS Study of the selective removal of PMMA from microphase separated PS-b-PMMA thin films,*
  Venugopal H., de los Arcos T., Gonzalez Orive A., Grundmeier G., Bürger J., Kool D., Brassat K., Lindner J.K.N.,
  13th international conference on Physics of Advanced Materials (ICPAM-13), 24–30 September 2021, Sant Felio de Guixols, Spain.

- *Analytical high-resolution STEM investigations of interfacial widths and line-edge roughnesses in microphase separated cylindrical block copolaymer thin films,*
  Bürger J., Venugopal H., Kool D., de los Arcos T., Gonzalez Orive A., Grundmeier G., Brassat K., Lindner J.K.N.,
  13th international conference on Physics of Advanced Materials (ICPAM-13), 24–30 September 2021, Sant Felio de Guixols, Spain **(Best Poster Award)**.

- *Investigation of interfacial widths and line-edge roughnesses in microphase separated cylindrical block copolymer films,*
  Bürger J., Venugopal H., Kool D., de los Arcos T., Gonzalez Orive A., Grundmeier G., Brassat K., Lindner J.K.N.,
  EMRS Spring Meeting 2022, 30 May – 03 June 2022 (virtual) **(Best Poster Award)**.

- *Scattergram analysis and filtering of differential phase contrast STEM images,*
  Bürger J., Groll M., Riedl T., Lindner J.K.N.,
  Frühjahrstagung der Deutschen Physikalischen Gesellschaft, 4–9 September 2022, Regensburg, Germany.

- *Characterization of 2D WSe_2 via sub-atomic resolution STEM Differential Phase Contrast imaging,*
  Groll M., Bürger J., Lindner J.K.N.,
  Frühjahrstagung der Deutschen Physikalischen Gesellschaft, 4–9 September 2022, Regensburg, Germany.

- *Atomic electric fields in InAs measured by scanning transmission electron microscopy,*
  Bürger J., Kunnathully V.S., Riedl T., Lindner J.K.N.,
  14th international conference on Physics of Advanced Materials (ICPAM-14), 8–15 September 2022, Dubrovnik, Croatia.

- *Investigation of atomic electric fields in 2D WSe_2 by STEM differential phase contrast,*
  Groll M., Bürger J., Lindner J.K.N.,
  14th international conference on Physics of Advanced Materials (ICPAM-14), 8–15 September 2022, Dubrovnik, Croatia.

- *Influences of DPC images captured with segmented detectors,*
  Bürger J., Groll M., Riedl T., Lindner J.K.N.,
  DGE Arbeitskreistreffen Differentieller Phasenkontrast, 25 September – 27 September 2022, Munich, Germany.

- *Characterization of 2D WSe_2 by STEM differential phase contrast,*
  Groll M., Bürger J., Lindner J.K.N.,
  DGE Arbeitskreistreffen Differentieller Phasenkontrast, 25–27 September 2022, Munich, Germany.

- *Ultra-High-Resolution Characterization of Cylindrical mask Openings Created by Microphase Separation in PS-b-PMMA,*
  Bürger J., Venugopal H., Kool D., de los Arcos T., Gonzalez Orive A., Grundmeier G., Brassat K., **Lindner J.K.N.**,
  The 6th DSA Symposium at KAIST, 19–21 October 2022, Daejeon, Korea.

- *Revealing interfacial widths and line-edge roughnesses in cylinder-forming block copolymers using low keV analytical transmission electron microscopy,*
  Bürger J., Venugopal H., Kool D., de los Arcos T., Gonzalez Orive A., Grundmeier G., Brassat K., Lindner J.K.N.,
  Microscopy Conference 2023, 26 February – 02 March 2023, Darmstadt, Germany.

- *DPC-Toolbox, a software for post-processing and analysis of differential phase contrast STEM images,*
  Bürger J., Groll M., Lindner J.K.N.,
  Microscopy Conference 2023, 26 February – 02 March 2023, Darmstadt, Germany.

- *Characterization of two-dimensional WSe_2 using differential phase contrast STEM,*
  Groll M., Bürger J., Lindner J.K.N.,
  Microscopy Conference 2023, 26 February – 02 March 2023, Darmstadt, Germany.

- *Increasing azimuthal momentum space resolution of segmented detectors for differential phase contrast STEM imaging,*
  Bürger J., Groll, M., Ulrich, A., Albrecht, M., Lindner, J.K.N., International Microscopy Congress 20 (IMC20), 10–15 September 2023, Busan, South Korea.

- *Electric field and charge density distributions of 2D mono- and multilayers of WSe_2 by high-resolution STEM DPC,*
  Groll M., Bürger J., Caltzidis, I., Jöns, K.D., Lindner J.K.N., International Microscopy Congress 20 (IMC20), 10–15 September 2023, Busan, South Korea.

- *Differential Phase Contrast STEM Investigation of Interatomic Electric Fields in Pristine and Defective 2D-WSe_2 Multi- and Monolayers,*
  Groll M., Bürger J., Caltzidis, I., Jöns, K.D., **Lindner J.K.N.**, The 15th International Conference on Physics of Advanced Materials (ICPAM-15), 19–26 November 2023, Sharm El Sheikh, Egypt.

Acknowledgements

I would like to thank all those who have contributed to this thesis in terms of scientific as well as mental support. A few exceptionally kind people deserve a special mention and thanks in this context:

- I would like to thank **Prof. Dr. Jörg K. N. Lindner**, *Nanopatterning – Nanoanalysis – Photonic Materials* (NNP), Dept. of Physics at Paderborn University for his unwavering scientific and personal support, teaching me all kinds of TEM as well as STEM techniques possible with the ARM200F, giving me a lot of freedom in my scientific decision making, and the many opportunities he has given me to participate in conferences, workshops as well as exciting, interdisciplinary research projects.

- **Prof. Dr. Knut Müller-Caspary** from Ludwig-Maximilians-Universität in Munich, for agreeing and finding the time to assess this thesis.

- **Prof. Dr. Donat J. As** *Optoelectronic semiconductors – Group III-nitrides,* Dept. of Physics at Paderborn University, for spontaneously agreeing to evaluate this thesis.

- **Dr. Katharina Brassat**, NNP, who was my supervisor during my bachelor's and master's theses and gave me a great start to the doctoral phase with her excellent supervision and discussions. I would also like to take this opportunity to thank her for the many successful collaborations in the research field of block copolymer lithography.

- **Dr. Thomas Riedl**, NNP, for the many precise discussions and fruitful collaborations on the GaAs and InAs material system.

- Most important, I would like to thank my student helpers, **Jan Shames**, NNP, for the work on the rigid and non-rigid registration algorithms, and **Maja Groll**, NNP, for the work on WSe_2 multilayers. Without their help and the extraordinarily good cooperations and accompanying scientific discussions, this work would not have been possible to this extent. I would also like to thank Maja Groll for the countless hours of proofreading.

- The research team of **Prof. Dr. Manfred Albrecht**, University of Augsburg, for the opportunity to use the JEOL JEM-ARM200F NeoARM. In particular, I would like to thank **Dr. Aladin Ulrich** for the good supervision at the TEM in Augsburg and the very good discussions about (S)TEM techniques and alignment tricks.

- The research team of **Prof. Dr. Klaus Jöns**, *Hybrid Quantum Photonic Devices*, Dept. of Physics at Paderborn University, for the cooperation in the area of WSe_2. Special thanks go to **Ioannis Caltzidis**, who was significantly involved in the preparation of WSe_2 specimens.

- **Prof. Dr. Dirk Reuter**, *Optoelectronic materials and devices*, Dept. of Physics at Paderborn University, and his research team for the MBE growth of the InAs nanoislands on the prepatterned GaAs substrates.

- The whole NNP research team and especially **Daniel Kool** and **Christian Zietlow** for the nice and sometimes even motivating atmosphere in the office. In addition, I would like to thank Christian Zietlow for the joint work on the influence of noise on DPC images and the development of the noise model for DPC imaging.

- **Prof. Dr. Josef Zweck,** University of Regensburg, and his research team for the introduction to the scattergram at the DGE Workshop on DPC imaging as well as **Dr. Juri Barthel,** ER-C Jülich**,** for the consistently helpful support for the use of Dr. Probe.

- In addition, I would like to thank *Zeiss* (Oberkochen, Germany) for the FIB lamella preparation of the InAs nanoisland on GaAs substrate and *Thermo Fisher Scientific* (Eindhoven, Netherlands) for the preparation of the Si[110] TEM lamella.

At this point, I would also like to take the opportunity to thank all my colleagues with whom I worked on (interdisciplinary) research projects that lead to many successful publications. Thank you for always expanding my horizon of knowledge:

- All those involved in the FK-LEM (Fortschrittskolleg "*Leicht-Effizient-Mobil*" at Paderborn University), which was a transdisciplinary research team consisting of 13 doctoral students from the fields of mechanical engineering, chemistry, physics, and social sciences. **Prof. Dr. Ilona Horwarth** and **Dr. Swetlana Schweizer** are particularly deserving of mention here, for the multitude of discussions that went far beyond the horizon of a physicist. Since my position as a doctoral student was financed for a large part by the FK-LEM, I would like to acknowledge the state government of North Rhine-Westphalia for the funding.

- The research team of **Prof. Dr. Mirko Schaper**, *Lehrstuhl für Werkstoffkunde* (LWK), Dept. of Mechanical Engineering at Paderborn University, and in particular **Florian Hengsbach** for the research on the novel die steel and being a good colleague, **Dr. Sudipta Pramanik** for the many many many discussions on TEM techniques and DPC investigations of magnetic material as well as **Kristina Duschik** for the discussions about (conventional) TEM techniques, for

being a good office neighbour and for providing **h**ighly **a**nnealed **a**nd **d**elicious **f**ood (HAADF = delicious cookies) on my birthday. I would also like to thank **Katja Engelkemeier** for the opportunity to test the DPC technique on ZnO hollow-body spheres.

- The research team of **Prof. Dr. Guido Grundmeier**, *Technical and macromolecular Chemistry* (TMC), Dept. of Chemistry at Paderborn University, for the collaboration on many block copolymer related projects. I would also like to thank **Dr. Dennis Meinderink** for the work on the ZnO tripods.

- The research team of **Prof. Dr. Donat J. As**, *Optoelectronic semiconductors – Group III-nitrides,* Dept. of Physics at Paderborn University*,* and specifically **Dr. Falco Meier** for the collaboration on the selective area growth of cubic GaN on prepatterned substrates.

- The research team of **Prof. Dr. Matthias Bauer**, *Inorganic Chemistry*, Dept. of Chemistry at Paderborn University, and in particular **Dr. Steffen Schlicher** for the collaborations on the iron oxide catalysts.

In addition, I would like to take this opportunity to thank all my fellow students, many of whom I can proudly count among my friends, for the super exciting and fun time during my studies. These include **Maximilian Protte**, **Christian Kießler**, **Julian Brockmeier** and **Daniel Kool**.

Besides the scientific part, I would also like to thank some people who kept the “life” in my work-life balance alive. These include my current flatmate and best friend **Martin Sramko** as well as **Lennart Vater**, and **Dennis Kolesnikow**. Thank you for the many trips and adventures! Moreover, I would like to thank **Sara Kiel** for sharing a horse with me.

Last but not least, I would like to thank my sister **Johanna Bürger** for proofreading this thesis and my family for all the support, especially in stressful times.

Declaration of plagiarism

I hereby certify that I, Julius Bürger, have independently written this thesis that I have used no sources other than those indicated or cited, and that I have explicitly indicated all material that has been quoted, either literally or by content, from the sources used. This dissertation was neither submitted nor made public for a degree at this or any other institute or university.

Paderborn, 22. Dezember 2023